Cranfield University

School of Mechanical Engineering
Department of turbomachinery and engineering mechanics

PhD Thesis

Academic year 1998/99

Peter A Lyes

Low Speed Axial Compressor Design and Evaluation; High Speed Representation and Endwall Flow Control Studies.

Supervisors:-

Prof R Elder (Chairman)

Dr P Ivey (Academic)

Dr R B Ginder (Industrial)

28th January 1999

Abstract

This Thesis reports the design, build and test of two sets of blading for the Cranfield University low speed research compressor. The first of these was a datum low speed design based on the fourth stage of the DERA high speed research compressor C147. The emphasis of this datum design was on the high-to-low speed transformation process and the evaluation of such a process through comparing detailed flow measurements from both compressors.

Area traverse measurements in both the stationary and rotating frame of reference were taken at Cranfield along with overall performance, blade surface static pressure and flow visualisation measurements. These compare favourably with traverse and performance measurements taken on C147 before commencement of the PhD work. They show that despite the compromises made during the transformation process, due to both geometric and aerodynamic considerations, both the primary and secondary flow features can be successfully reproduced in the low speed environment.

The aim of the second design was to improve on the performance of the datum blading through the use of advanced '3D' design concepts such as lean and sweep. The blading used nominally the same blade sections as the datum, and parametric studies were conducted into various lean/sweep configurations to try to optimise the blade performance. The final blade geometry also incorporated leading edge recambering towards the fixed endwalls of both the rotor and stator. The '3D' blading demonstrated a 1.5% increase in efficiency (over the datum blading) at design flow rising to around 3% at near stall along with an improvement in stall margin and pressure rise characteristic.

The design work was completed using the TRANSCode flow solver for both the blade-to-blade solutions (used in the S1-S2 datum design calculation) and the fully 3D solutions (for the advanced design and post datum design appraisal). The 3D solutions gave a reasonable representation of the mid-span and main 3D flow features but failed to model the corner and tip clearance flow accurately. An interesting feature of the low speed flowfield was the circumferential variation in total pressure observed at exit from all rotors for both designs. This was not present at high speed and represents one of the main differences between the high and low speed flow. Unsteady modelling of mid-height sections from the first stage indicate that part of this variation is due to the potential interaction of the rotor with the downstream stator while the remainder is due to the wake structure from the upstream stator convecting through the rotor passage. Finally, the implications for a high speed design based on the success of the 3D low speed design are considered.

PREFACE

The work reported in this thesis was carried out between January 1995 and January 1999, while the author was registered as an industry based research student with the School of Mechanical Engineering, Cranfield University, and a full time employee of the Defence Evaluation and Research Agency at Pyestock. Except where specifically stated to the contrary, the contents of the Thesis is the work of the author alone and has not been submitted for any other academic or professional award. This Thesis is submitted on the conditions contained in the Regulations document. The work included in this study was completed as part of the PhD study and has not been carried out previously or subsequently.

P A Lyes

28th January 1999

Acknowledgements

The work reported in this thesis was carried out between January 1995 and January 1999 while the author was registered as an industry based research student with the School of Mechanical Engineering, Cranfield University, and a full time employee of the Defence Evaluation and Research Agency at Pyestock. The work was funded by the UK Ministry of Defence under the Applied Research Programme package 7b and by the Department of Trade and Industry CARAD programme.

During the course of this work I have become indebted to many people who deserve mention in these acknowledgements. Professor Robin Elder (panel chairman), Dr Paul Ivey and Dr Bob Ginder have acted as supervisors to the work providing encouragement and guidance throughout. I would specially like to thank Dr Paul Ivey for his diplomacy and patience during difficult times as project manager of the Cranfield measurement programme. I am also indebted to Dr Bob Ginder for his guidance, insight and diligent attention to detail.

Special thanks are made to Bernard Charnley, Brian Stapleton and Pat Sweeney. It is due to their hard work and commitment to the low speed facility that the measurements made for this project were among the most successful and comprehensive ever taken.

I would also like to draw attention to my colleagues at Pyestock for their help during this period. Thanks are due to Dr Mike Cherrett for initiating the PhD programme of work and to Judith Parker for project managing the core compressor programme during the majority of the project. I would like to thank Dr Brian Angel and Dr Bob Jackson for their help and guidance with the un-NEWT modelling and to Mike Spruce for the C147 TRANSCode modelling. I would like to thank Phil Moss for project managing the last stages of the project and to Dan Cooper for providing project support. I would also like to thank Pete Lord for drawing the blades and producing their manufacturing data files. I would especially like to thank Bob Ginder for taking the time to read the draft of the Thesis and in providing detailed and valuable comments.

Finally, I would like to thank my wife Lek, for her support and patience during the work.

Nomenclature

C147	5-stage core compressor
DERA1	Datum low speed compressor design
DERA2	Advanced '3D' low speed compressor design
LSRC	Low speed research compressor
M	Mach number
P	Pressure
PS	Pressure surface
SS	Suction surface
U	Mid height blade speed
V	Velocity
V_a	Axial velocity
V_p	Pressure surface velocity
V_s	Suction surface velocity
ΔH	Enthalpy rise across rotor
α_2	Stator exit flow angle
β_2	Rotor relative exit flow angle

SUBSCRIPTS

ave	Mass average quantity
bar	Bulk mass weighted average
t	Stagnation quantity
te	Trailing edge quantity
wall	Casing wall quantity
0	Stator exit quantity
∞	Free stream value

LIST OF CONTENTS

		Page
ABSTRACT		i
PREFACE		ii
ACKNOWLEDGEMENTS		iii
NOMENCLATURE		iv
LIST OF CONTENTS		v
CHAPTER 1:	**INTRODUCTION**	**1**
	1.1 GENERAL BACKGROUND	1
	1.2 SCOPE OF THE WORK	1
	1.3 AIMS AND OBJECTIVES OF THE WORK	2
	1.4 THESIS STRUCTURE	2
CHAPTER 2:	**COST BENEFIT ANALYSIS**	**4**
	2.1 THE EVOLUTION AND ROLE OF THE DEFENCE EVALUATION AND RESEARCH AGENCY	4
	2.1.1 INTRODUCTION	4
	2.1.2 ORIGINS OF THE DERA	4
	2.1.3 THE ROLE OF DERA	5
	2.1.4 THE DERA ORGANISATION	5
	2.1.5 AIR SYSTEMS SECTOR	7
	2.1.6 PROPULSION DEPARTMENT	7
	2.2 BENEFITS OF THE PROJECT TO THE CUSTOMER	8
	2.2.1 INTRODUCTION	8
	2.2.2 THE AIM OF THE LOW SPEED CORE COMPRESSOR RESEARCH PROJECT	8
	2.2.3 TECHNOLOGY CONSIDERATIONS	9
	2.2.4 MILITARY APPLICATIONS	11
	2.2.5 BENEFITS OF IMPROVED COMPRESSOR TECHNOLOGY	13
	2.3 MANAGING THE PROJECT	17
	2.3.1 INTRODUCTION	17
	2.3.2 PROJECT SCOPE, PLANNING AND SCHEDULING	17
	2.3.3 PROJECT PROBLEMS ENCOUNTERED	18
	2.4 JUSTIFICATION FOR THE PROJECT	19
	2.4.1 COST OF PROJECT	19
	2.4.2 BENEFIT ANALYSIS OF THE PROJECT	20
CHAPTER 3:	**REVIEW OF PREVIOUS WORK**	**22**
	3.1 INTRODUCTION	22
	3.2 ENDWALL FLOW PHENOMENA	23
	3.2.1 TIP CLEARANCE FLOWS	23
	3.2.2 SECONDARY FLOWS	25
	3.2.3 INLET SKEW	25
	3.3 LOW SPEED BLADING	25
	3.3.1 THE HIGH-TO-LOW SPEED TRANSFORMATION	26
	3.4 3D DESIGN FOR ENDWALL REGIONS	28
	3.4.1 INTRODUCTION	28
	3.4.2 ENDBENDS	28

Page

3.4.3 BLADE SECTION MODIFICATION AND ENDWALL CONTOURING 29
3.4.4 LEAN AND SWEEP 29
3.5 CRANFIELD LOW SPEED COMPRESSOR 31
3.6 C147 COMPRESSOR 31
3.7 CONCLUSIONS 32

CHAPTER 4: DATUM DESIGN 33
4.1 INTRODUCTION 33
4.2 LOW SPEED RIG FACILITY 33
4.3 LOW SPEED CODE DEVELOPMENT 34
4.3.1 THE INCOMPRESSIBLE MODEL 35
4.3.2 CHANGES TO TRANSCODE 36
4.3.3 CODE VERIFICATION AND VALIDATION 36
4.3.4 V2-CASCADE 36
4.3.5 NEB1D 38
4.4 AERODYNAMIC LOW SPEED MODELLING 39
4.5 BLADE DESIGN 40
4.5.1 HIGH SPEED STAGE 40
4.5.2 DESIGN METHODOLOGY 41
4.5.3 THROUGHFLOW CALCULATION 42
4.5.4 BLADE-TO-BLADE CALCULATION 43
4.6 BLADE PROFILE GENERATOR 44
4.7 FINAL DESIGN 45
4.7.1 ROTOR AND STATOR 45
4.7.2 INLET GUIDE VANE 46
4.7.3 OUTLET GUIDE VANE 47
4.8 DISCUSSION 48
4.9 CONCLUSIONS 48

CHAPTER 5: LOW SPEED COMPRESSOR AND INSTRUMENTATION 50
5.1 INTRODUCTION 50
5.2 LOW SPEED COMPRESSOR PROCUREMENT 50
5.2.1 RIG ARRANGEMENT AND PROCUREMENT 50
5.2.2 BLADING PROCUREMENT 51
5.3 INSTRUMENTATION DESCRIPTION 53
5.3.1 OVERALL PERFORMANCE 53
5.3.2 BLADE SURFACE STATIC PRESSURE MEASUREMENTS 54
5.3.3 STATIONARY FRAME AREA TRAVERSING 55
5.3.4 2D AND 3D TRAVERSE PROBES 55
5.3.5 ROTATING FRAME TRAVERSING 57
5.3.6 FLOW VISUALISATION 58
5.4 CONCLUSIONS 58

CHAPTER 6: DATUM DESIGN AERODYNAMIC MEASUREMENTS 60
6.1 INTRODUCTION 60
6.2 OVERALL PERFORMANCE 60
6.3 BLADE SURFACE STATIC SCANS 61
6.4 STATIONARY FRAME AREA TRAVERSING 62
6.5 ROTATING FRAME AREA TRAVERSING 65
6.6 FLOW VISUALISATION 66
6.7 THROUGHFLOW ANALYSIS 68
6.8 CONCLUSIONS 70

		Page
CHAPTER 7:	**DATUM DESIGN APPRAISAL**	**72**
	7.1 INTRODUCTION	72
	7.2 HIGH-TO-LOW-SPEED READ-ACROSS	72
	7.2.1 OVERALL PERFORMANCE	73
	7.2.2 RADIAL PROFILES	75
	7.2.3 STATOR EXIT FLOW FIELD	75
	7.2.4 ROTOR EXIT	76
	7.2.5 FLOW VISUALISATION	77
	7.3 COMPARISONS WITH TRANSCODE PREDICTIONS	78
	7.3.1 RADIAL PROFILES	78
	7.3.2 STATOR EXIT FLOW FIELD	79
	7.3.3 ROTOR EXIT FLOW FIELD	80
	7.3.4 BLADE SURFACE PRESSURE DISTRIBUTIONS	80
	7.4 FULL INLET FLOW FIELD MODELLING	81
	7.5 UN-NEWT MODELLING OF DATUM STAGE	83
	7.6 CONCLUSIONS	85
CHAPTER 8:	**3D BLADE DESIGN**	**88**
	8.1 INTRODUCTION	88
	8.2 3D BLADE DEFINITION	88
	8.3 COMPUTATIONAL APPROACH	89
	8.4 3D DESIGN APPROACH	90
	8.4.1 INITIAL STUDIES	90
	8.4.2 PHYSICAL EFFECTS OF 3D MODIFICATIONS	91
	8.4.3 COMBINED LEAN/SWEEP APPROACH	93
	8.4.4 EFFECTS OF LEADING EDGE RECAMBERING	94
	8.4.5 EFFECTS OF PROFILE MODIFICATION	94
	8.4.6 EFFECTS OF SECTION RE-STAGGER	95
	8.5 FINAL DESIGN	95
	8.6 MULTISTAGE CONSIDERATIONS	98
	8.7 CONCLUSIONS	98
CHAPTER 9:	**3D DESIGN AERODYNAMIC MEASUREMENTS**	**100**
	9.1 INTRODUCTION	100
	9.2 OVERALL PERFORMANCE	100
	9.3 BLADE SURFACE STATIC SCANS	101
	9.4 STATIONARY FRAME AREA TRAVERSING	102
	9.4.1 2D COBRA PROBE MEASUREMENTS	102
	9.4.2 3D COBRA PROBE MEASUREMENTS	104
	9.5 ROTATING FRAME AREA TRAVERSING	105
	9.6 FLOW VISUALISATION	107
	9.7 THROUGHFLOW ANALYSIS	108
	9.8 CONCLUSIONS	109
CHAPTER 10	**3D DESIGN APPRAISAL**	**111**
	10.1 INTRODUCTION	111
	10.2 PERFORMANCE IMPROVEMENT	111
	10.2.1 OVERALL PERFORMANCE	111
	10.2.2 RADIAL PROFILES	112
	10.2.3 STATOR EXIT FLOW FIELD	113
	10.2.4 ROTOR EXIT FLOW FIELD	115
	10.2.5 BLADE SURFACE PRESSURE DIFFERENCES	115

Page

10.2.6 FLOW VISUALISATION 116
10.3 UN-NEWT MODELLING 117
10.4 HIGH SPEED 3D DESIGN 119
10.5 CONCLUSIONS 121

CHAPTER 11 CONCLUSIONS 123
11.1 DATUM DESIGN WORK 123
11.2 INSTRUMENTATION AND RIG CHANGES 124
11.3 DATUM PERFORMANCE 124
11.4 CFD COMPARISONS 125
11.5 DERA2 DESIGN WORK 126
11.6 DERA2 PERFORMANCE 127
11.7 RECOMMENDATIONS FOR FUTURE CFD AND DESIGN WORK 128
11.8 RECOMMENDATIONS FOR FUTURE TESTING 129

APPENDIX A CYCLE EFFICIENCY CALCULATION **130**

APPENDIX B PROPULSIVE EFFICIENCY CALCULATION **132**

APPENDIX C CALCULATION OF SPECIFIC THRUST **134**

APPENDIX D PROBE CALIBRATION COEFFICIENTS **135**

APPENDIX E HIGH SPEED LEAN ANGLE CALCULATION **136**

REFERENCES 137

TABLES 145

FIGURES 155

Chapter 1 - Introduction

1.1 General background

Recent research into core compressors has focused to a large extent on understanding the loss mechanisms present in the blade endwall regions where annulus wall and tip leakage flows interact with blade boundary layer and mainstream flows. These interactions result in complex flow phenomena which can have a major influence on compressor efficiency and stall margin. There is also considerable related interest in exploiting '3D' blading design approaches, such as incorporating lean, sweep and endbends to achieve improvements in efficiency and/or stable operating range. Such performance improvements are in great demand in the highly competitive aeroengine market. For example, improvements in compressor efficiency enable fuel consumption and operating costs to be reduced and aircraft range to be increased. This is important for both military and civil applications. Peak cycle temperature can also be reduced, giving more thrust growth potential, together with longer turbine life and therefore reduced cost of ownership and maintenance requirements. Higher levels of blade loading are also sought so that stage numbers can be reduced along with a reduction in the number of parts, weight and cost.

Understanding 3D aerodynamics and developing new design concepts through high-speed testing can be very costly, and this has lead to increased use of low speed research compressors. These aim to reproduce the flow physics found in high-speed core compressors at a comparatively low set-up and running cost.

1.2 Scope of the work

The aim of the work in this Thesis is to investigate the application of 3D blading design approaches to highly loaded compressors. However, before embarking on a programme of work on the Cranfield low speed compressor it was felt that a careful comparison between the aerodynamics of closely related high and low speed blading of relevant duty was needed. The first part of the Thesis therefore involves the design and test of low speed conventional blading whose design was based on an embedded stage from a previous highly loaded high speed research compressor. Detailed traverse measurements were taken at rotor and stator exit along with overall performance measurements and compared with measurements from the high speed research compressor. These have been used to evaluate the high to low speed transformation process and the low speed blading. This design was then used as a datum on which an improved 3D design was based. The second design incorporated a combination of lean, sweep and leading edge recambering. The 3D blading was also manufactured and tested and the results used to evaluate the 3D design approach. The opportunity was also taken

to use the test data to evaluate flowfield predictions carried out using the DERA TRANSCode 3D viscous flow solver (Calvert et al, 1997).

1.3 Aims and objectives of the work

The main aims of the work reported in this Thesis are threefold:

AIM 1: To evaluate the high to low speed transformation process through comparing detailed flow measurements taken in both the high and low speed environments. Emphasis is placed on how well secondary flow features are modelled in addition to the primary and overall performance comparison.

The datum low speed blading was designed to represent as closely as possible the high speed blading of the target stage. Along with the overall performance parameters, the blade sections were carefully designed to replicate the same non-dimensional velocity distributions as the high speed blading over both the suction and pressure surfaces.

AIM 2 To develop a 3D design approach and use it to design and evaluate an advanced set of blading based on the datum design. This design is appraised through comparing detailed flowfield measurements with those from the datum build.

These flow measurements include; stationary frame measurements at most axial locations using pneumatic steady state 3-hole cobra probes, rotating frame traverses around rotor 3 (the study stage) using similar probes, performance mapping, flow visualisation and blade surface static pressure measurements.

AIM 3 To use the detailed flowfield measurements to evaluate the DERA 3D viscous flow solver TRANSCode.

The option of running TRANSCode at low speed was added to the code's capability, this was undertaken by the author before design work at low speed could commence. Since the TRANSCode was instrumental in both low speed designs its use as a design tool is also evaluated.

1.4 Thesis structure

The work reported in this Thesis has been carried while the author has been registered for a Total Technology PhD. To fulfill the requirements of this type of PhD a cost benefit analysis, focusing on the benefits of this research to the military customer, has been included. This is presented in chapter 2.

Chapter 3 describes the work carried out on low speed compressors and endwall flows by other workers while chapter 4 describes the datum design work and the low speed modifications made to TRANSCode. Chapter 5 describes the Cranfield low speed

research compressor and instrumentation while chapter 6 describes the measurements made on the datum design. These measurements are appraised in more detail in chapter 7 where they are also compared with CFD results.

The 3D design is described in chapter 8 and the traverse measurements are reported in chapter 9. Chapter 10 draws on measurements from both builds to appraise the 3D blading design while chapter 11 draws conclusions from the work and recommendations for further work.

Chapter 2 Cost benefit analysis

2.1 The evolution and role of the Defence Evaluation and Research Agency (DERA)

2.1.1 Introduction

The Defence Evaluation and Research Agency (DERA) was launched in April 1995 and is the largest single research organisation of its kind in Western Europe bringing together in one agency the core of the Ministry of Defence's non-nuclear scientific and technical assets. DERA offers a range of services from operational studies and analysis, basic and applied research to consultancy advice on the procurement process, and test and evaluation of specific equipment.

90% of DERA's billion pound turnover comes from the UK Ministry of Defence who rely on the Agency's scientific and technical know-how and facilities to assist in the definition of future defence needs and the procurement of costly and complex equipment for the Armed Forces. The breadth of research carried out by the divisions of DERA is such that many of their discoveries and technology are used in the civil sector with rewarding commercial consequences for DERA and benefit to industry.

2.1.2 The origins of DERA

The Defence Evaluation and Research Agency was launched on 1st April 1995, born out of the success of the Defence Research Agency (DRA) which was launched as a trading fund on 1st April 1993. The DRA was formed in 1991 from the rationalisation of the MOD's four main non-nuclear research establishments:-

Royal Aircraft Establishment	(RAE)
Royal Signals and Radar Establishment	(RSRE)
Admiralty Research Establishment	(ARE)
Royal Armaments Research and Development Establishment	(RARDE)

The rationalisation reduced overhead costs by over £100M while maintaining the same level of scientific output relevant to the military needs. DERA has gone one step further and grouped together a wider range of scientific and technical services than were previously covered by the DRA. DERA was formed by the merger of the DRA with the following establishments:-

Chemical and Biological Defence Establishment
Defence Operational Analysis Centre
Directorate General of Test and Evaluation
Operational Analysis Units in MOD and in Commands
Defence Research Information Centre

The organisational structure of DERA has evolved since its inception and the organisations from which it was composed no longer exist independently. DERA has a corporate turnover of just over £1 billion and has over 11000 staff.

2.1.3 The role of DERA

At its most fundamental level, DERA exists to serve the needs of the Ministry of Defence by providing scientific and technical advice that ensures that the nation has the military capability necessary for the successful implementation of the Government's defence and security policies. This is achieved by DERA scientists and engineers working closely with the military staff at every stage of planning. DERA are involved from early conceptual work, as the military decide what capabilities they need, to the procurement, test and evaluation of equipment.

In order to be able to give this advice, DERA carries out programmes of research aimed at pushing back the frontiers of technical knowledge. DERA needs to be able to tell the military what the technical options are going to be in the next century rather than next year so that the military equipment is always at the leading edge and not obsolete technology.

DERA's role does not stop at giving advice to the MOD. It must also ensure that the producers of military equipment maintain their technological lead so that they are ready when the military specify new equipment with a range of futuristic capabilities. That is why DERA works closely with industry, sometimes as formal sub contractor to major defence manufacturers, sometimes funding EM research to build capability in industry on MOD's behalf.

Much of the technology needed to provide the military with a war winning edge is also of significant value in civil applications, in other words the technology often has dual use potential. Consequently DERA is also supported by DTI and has a commitment that its technology is exploited in ways that also bring maximum benefit to the nation at large.

The DERA mission statement reads:

> *To harness science and technology to UK defence needs*
>
> Corporate Plan 1998.

2.1.4 The DERA organisation

DERA originated as a managing organisation bringing overall management cohesion to its business sectors. The separate divisions that composed the DERA are now known simply as DERA and their individual titles have disappeared. The fact that the organisation is a trading fund means that all its income has to be earned from

customers, even though 90% of these are in the MOD they still have to be persuaded that the DERA product is worth purchasing and offers value for money. It is this commercial environment that has driven the need for rationalisation leading to improved efficiency and customer service. By grouping together a larger range of scientific services the DERA hopes to ensure a quality and coherence of service to its customers.

DERA Consultancy services

The primary role of DERA is to provide impartial expert advice to the Government and Armed forces staff to ensure that the MOD can be an expert customer during equipment procurement programmes which may cost several millions or billions of pounds over several years. Operational and technical insight are essential if one is to get value for money from today's increasingly sophisticated defence market. DERA consultancy and technical expertise is relevant to customers, before, during and after key procurement decisions.

DERA conduct suitability studies for off-the-shelf purchases or development projects and provide expert support to write requirements and technical specifications. They also carry out evaluations of contractor proposals using technical assessment, simulation and modelling. DERA can provide technical consultancy during negotiations with contractors and assess contractor performance during technical projects. The DERA consultancy support role spans the entire life of defence projects from the long term policy setting stage through to the operational in service stage.

DERA and Industry

The second main role of DERA is to ensure that UK industry benefits from the results of DERA research and development programmes so that defence contractors are able to improve their equipment design and integration. Also, by applying the basic understanding of the technical challenges involved the risk of proposed defence solutions are reduced. DERA's framework document states a specific obligation for the Agency to manage its affairs to the best advantage of wealth creation in the UK

Wealth creation is a key element for both the MOD and DERA. Techniques to monitor the transfer of technology into UK or UK-based civil and defence industries, include Technology Transfer. In addition, dual-use technology centres (DUTCs) are being used to transfer the research undertaken and the expertise gained from MOD's research for civil exploitation

DERA's position of impartiality allows staff to work with both the procurement agents and industry and thereby support both the MOD's needs and those of the industry contractors at the same time. A proposal has recently been published in a

Government Green Paper to set up a Defence Diversification Agency (DDA) aimed at commercially exploiting the military technology developed within DERA. The agency would be part of DERA and would seek to exploit civil markets through improving access to DERA knowledge and laboratories, and by creating industry partnership opportunities for programmes of co-development. The DDA would also provide knowledge to civil companies to enable them to discover the potential for their products in UK defence programmes. The diversification initiative would therefore be a two-way process maximising commercial spin-offs from the defence sector and civil spin-ins into the defence sector.

2.1.5 Air Systems Sector

Air Systems sector is the DERA business sector concerned with research relating to both military and civil aircraft. Research activities include; systems performance assessment, avionics, control systems, air traffic management, aerodynamics, airworthiness and CFD code development. The Air Systems Sector's mission statement reads:

To provide the best possible support to MOD in Air Environment systems engineering, integration and the harnessing of technology to enhance military air capabilities, and to our partners in Government and Industry alike.

Air Systems Sector Business Plan 1998

2.1.6 Propulsion Department

The Propulsion Department of the Air Systems Sector specialises in the field of gas turbine technology and its customer base can be divided into four basic types: UK Ministry of Defence, other UK government departments, commercial customers and the European Union through collaborative programmes.

Most of the work of the department is by direct contract from MOD. This is in the form of scientific research and technical advice. The MOD also contracts to a wide range of other departments in the DERA and often these other DERA groups task the department on behalf of the MOD. In addition to the MOD, other UK government departments have an interest in gas turbine technology and associated environmental issues; notably the Department of Trade and Industry (DTI). The propulsion department is involved in the DTI Civil Aircraft Research and Demonstration (CARAD) programme which aims to increase the competitiveness of the UK aero industry in world markets.

A large number of companies are engaged in propulsion technology from manufacturers to users. These companies often require assistance with the development of a product or confirmation of the performance of a product in a

working environment and use the department's expertise and resources in this role. The propulsion department is active in participating and co-ordinating research projects in collaboration with commercial and other research organisations. These projects are funded by the EU, member government departments and private industry.

The Propulsion Department's mission statement reads:

To provide well founded advice and technical assessments in propulsion and air vehicle performance to MOD, DTI and other government departments and to use our facilities and technical capabilities to work with and support the aerospace industry, providing this does not conflict with our primary role as independent advisor to government.

Propulsion Department Business Plan 1998

2.2 Benefits of the project to the customer

2.2.1 Introduction

The overall performance of an aeroengine is restricted by the limitations of its various components. These components impose aerodynamic, thermal and mechanical limits on the engine cycle. The upper limit on turbine entry temperature for example, is governed by the mechanical limitations of the downstream turbine stages and the quality of the aero-thermal design of the blade cooling systems. The application of the aircraft (military combat or civil transport) and the planned service life also have an influence on the choice of engine cycle parameters.

The success of the compressor design has an important influence on the overall engine performance. The process of defining the engine cycle involves a compromise between choosing efficiency targets, thrust/weight ratio, surge margin and various mechanical considerations such as stress and vibration limits which will limit the service life. The number of compressor stages used will depend on the stage loading achieved by the compressor, size and weight considerations and the permitted deficit in efficiency that decreasing the number of stages will produce.

In this section the design considerations of military combat aeroengines will be examined and how the benefits of improved compressor technology affect the overall engine performance. This is contrasted with civil applications although the emphasis will be on the military aeroengine and how this project will benefit the military customer.

2.2.2 The aim of the low speed core compressor research project

The overall aim of the core compressor research programme at DERA Pyestock is to improve the technology of core compressor design through an integrated

programme of design method development and experimental testing. Prior to this current programme of work, experimental testing has centred around the C147 high speed research compressor at Pyestock. Due to the high cost of refurbishing the C147 module and maintaining the compressor test facility at Pyestock, it was not possible to retain the capability hence DERA no longer has a high speed compressor test facility.

In order to fulfil its programme need for experimental testing the Turbomachinery Group of the Propulsion Department has started to use the Low Speed Research Compressor (LSRC) facility at Cranfield University. The current programme of work is the first time DERA has used the LSRC facility. The programme of work is in two phases, the first phase of the programme aims to determine the validity of low speed compressor testing relative to high speed compressor testing. This will be achieved through the careful high-to-low speed transformation of a stage from C147 into a low speed blading design that will be tested on the LSRC. The transformation process will be evaluated through comparing detailed flow measurements taken in both the high and low speed environments.

The second phase of the work involves the design and test of advanced low speed blading incorporating 3D design concepts. The aim of the design is to improve compressor efficiency by reducing the losses found towards the endwalls. Whilst this work concentrates on low speed work the programme is expected to feed into a future high speed core compressor research programme which will utilise the lessons learnt at low speed.

This project supports the intelligent customer role of DERA through improving the understanding of low speed compressor aerodynamics and of the new 3D design methodologies that are becoming popular among engine manufacturers. The extensive low speed test measurements will also help to support the department's ongoing programme of computational methods development. By combining DERA's core compressor research activities with Cranfield's low speed research compressor the aim is to provide both the military (MOD) and civil (DTI) customers with cost effective research that is at the leading edge of technology. DTI provides joint funding for this project as part of the CARAD programme which supports UK industry in maintaining a competitive position in the air transport market. The needs of these customers are not mutually exclusive and are met by the generic nature of the project.

2.2.3 Technology Considerations

The ultimate design requirement of any compressor is to achieve as high a pressure ratio as possible, in the least number of stages, at the highest possible efficiency with an acceptable surge margin. Unfortunately these four requirements conflict with each other and a compromise has to be found. It will be shown that this

compromise depends heavily on the application of the engine and the service requirements.

Figure 2.1 shows the trends in pressure ratio per stage for in-engine efficiencies at the engine aerodynamic design point. In general increasing the work done by each stage reduces the compressor's efficiency. The number of stages required will therefore depend on the target pressure ratio and efficiency. If efficiency is of main concern then the number of stages must be increased along with the overall length, weight and cost of the engine. If efficiency is less of a concern, the number of stages may be decreased and the loading increased to achieve an improvement in thrust/weight ratio and cost.

The surge margin is another important consideration and the margin needed will depend on the application of the engine. The engine must remain stable over a range of transient conditions and allowance must also be made for intake flow distortions due to cross-wind and severe manoeuvring, build tolerances and in service component deterioration.

Figure 2.2 shows a typical HP compressor performance map of pressure ratio varying with mass flow for various spool speeds. The surge line is the dashed line defining the left most edge of the map and it represents the limit of stability where the compressor can be operated stably. Reducing the mass flow beyond this line will result in the stall or surge of the compressor. The nature of the instability will depend on the spool speed and the presence of any inlet flow distortions.

At design speeds the pressure rise will typically increase up to the instability line and peak efficiency will often be close to the surge line. The need to maintain an adequate surge margin will therefore reduce the pressure ratio and efficiency available at the design spool speed. The shift to a realistic surge margin may cost 3% or more in compressor efficiency and a compressor designer must be aware of this in evaluating compressor technology achievements.

Another important factor that has to be taken into account when considering the design and performance of an aeroengine is the Reynolds number. Reynolds number has a serious effect on compressor efficiency. It operates in a complex way and is therefore difficult to model numerically. The effect of Reynolds number on compressor efficiency is therefore generally modelled empirically and a typical experimentally based relationship may be:-

$$(1 - \eta_{isen}) \propto Re^{-0.1} \qquad \text{(Philpot, 1992)}$$

From sea level to cruise at altitude Reynolds number can change by a factor of around 2.5 giving a compressor efficiency loss of around 1.5%. As well as affecting

efficiency this reduction causes the engine to rematch to a slightly higher compressor running line and this must be included in the surge margin assessment.

2.2.4 Military Applications

Future Military Requirements

This section outlines the main combat aircraft programmes which the UK will require early in the next century (Paramour, 1995). The Royal Navy's requirement is for a Sea Harrier Replacement to fulfil both ground attack and air defence roles. It will be required to operate from the current Invincible class ships and will therefore need short take-off and vertical landing (STOVL) capability. The Royal Navy foresee that future replacements of their ships would be with larger aircraft carriers for which STOVL gives several advantages over conventional take off and landing (CTOL) aircraft; a 20-40% better sortie rate, lower speed on departure and fewer weather constraints than would occur when operating from smaller carriers. At take-off the STOVL aircraft requires a high level of installed dry power, but less power in afterburner than a CTOL aircraft.

The Royal Navy want an aircraft with better missile capability that is able to carry its weapon back to the ship. Since only one fixed wing aircraft type will be carried it must have good multi-role capability. The aircraft must have moderate supersonic capability and there will be no need for supercruise (otherwise a large and uneconomical engine would be required).

The Royal Air Force requirement is for a replacement for the Harrier and Tornado in their offensive roles. The replacement concept is known as the Future Offensive Air System (FOAS) and this could take the form of a missile, UAV or a manned aircraft. If the FOAS is to be an aircraft the requirement will be for a long range ground attack aircraft since air superiority needs will be met by EF2000. The aircraft must be able to operate in all weathers, day and night, at low and medium level. The aircraft engines must provide the aircraft with a good range, a good payload with an appropriate compromise between performance, low observability and a reasonable self-defence capability. The RAF want a twin engined aircraft for FOAS and it must be able to return to base on one engine. The RAF's second requirement will be for upgrades of the EF2000 for some time in the first 20 years of the next century.

Technology Requirements

The main aspects of military aircraft performance on which the engine has most influence are thrust/weight ratio and fuel consumption. Thrust/weight ratio is arguably the most important factor in military engine design because of the benefits it provides

in both combat and take-off performance. The engine thrust/weight ratio contributes both directly because of the benefit of a lighter engine and therefore increased payload/range and indirectly because it allows a lighter and smaller airframe to fulfil the same mission. Thrust/weight ratio is particularly important for carrier operations where the takeoff runway is small and the range crucial.

Thrust/weight ratio can be increased through improved cycle and component efficiencies, and higher aerodynamic loadings leading to fewer turbomachinery stages. As mentioned earlier, these requirements are to some extent in conflict and the right compromise has to be found. Current thrust/weight levels are limited to a maximum of around 10:1 using conventional materials and aerodynamic design. Improvements on this can only be achieved through significant weight reduction by the use of advanced materials and advanced aerodynamic blading design.

In order to meet the range requirements for future military aircraft improvement to the engine's fuel consumption is important. This can be achieved by improving component and cycle efficiencies. Also the use of variable cycle engines could allow better fuel consumption at both low and medium level flight. This does however, add an extra level of complexity to the engine and may make the engine more costly, heavier and reduce reliability.

The other most important design considerations besides outright performance are the durability, reliability and maintainability of the military engine. The engine must have a good resistance to foreign object damage, sand erosion and battle damage. It must be capable of continuing to run after sustaining a moderate amount of damage such as small arms fire. For the RAF a reliable affordable engine is the predominant requirement. Although a high thrust/weight ratio is desirable, a robust engine with lower thrust/weight ratio would be preferable to a delicate unreliable one with a higher ratio. Maintainability can be improved by using simpler engine concepts with fewer turbomachinery stages and fewer parts. The need for longer engine lives, reduced need for part life overhaul and a reduction in the overall cost of ownership is of paramount importance.

Another feature which is increasingly becoming important is the requirement of stealth. The infra-red, radar, acoustic and visible signatures of the engine are important in maintaining the overall stealthiness of the aircraft. In addition the visible emissions such as smoke and nitrogen oxides also contribute to the visible signatures of the aircraft. The engine frontal area, intake, fan design and exhaust nozzle design will all affect the signatures of the engine while the performance of the combustor will have an impact on the emission signature.

Technology Trade-offs

So far we have considered the conflicting performance requirements and restrictive economic and operational requirements of the military engine. Trade-offs have to be made in seeking the optimum combination of requirements.

> *The UK Services are adamant that they must not all be made in favour of performance, and that reduced life-cycle costs must be an equally important objective.* (Paramour, 1995)

An important trade-off that has to be considered is engine life cycle cost vs thrust/weight ratio. Better turbine technology is required to improve both engine life and thrust/weight ratio but one of these will be at the expense of the other. In order to achieve very high thrust/weight ratios advanced materials are required. The most cost-effective compromise needs to be found which will take into account performance, engine production cost, and the cost and usage rate of spares.

Thrust/weight ratio vs specific fuel consumption is another important trade-off that has to be considered. In order to achieve high thrust/weight ratios turbomachinery with few highly loaded stages is desirable and this also benefits the life cycle cost and durability. However, high loading produces penalties in efficiency and also therefore fuel consumption. These trade-offs affect the engine sizing for the aircraft and a compromise between the conflicting requirements is determined by the proposed role and mission of the aircraft. Mission analysis is also necessary to determine other factors such as bypass ratio and stealth.

2.2.5 Benefits of improved Compressor Technology

Improvements in compressor design can be used in a variety of ways to improve either thrust/weight ratio, fuel consumption, surge margin or cost. The benefits do not have to be focused on just one aspect of engine performance but can be used in a balanced way to obtain a better all round engine. The balance of where the improvements will be used will depend on the trade-offs already mentioned which depend on the aircraft role and mission.

For simplicity each aspect of engine performance will be taken in turn and the impact of a 1% improvement in the compressor component efficiency on improving that characteristic of the engine will be assessed. These may be achieved through redesigning the whole compression system in order to fully realise the potential of the improved compressor blading ie. by reducing the number of stages.

Benefits to fuel consumption

A compressor efficiency improvement can be utilised in two ways to improve overall engine fuel consumption. The first is to keep the compressor pressure ratio constant and let the efficiency improvement be carried through to the overall cycle. The second method would be to exchange the efficiency improvement for increased pressure ratio and thereby improve the cycle thermal efficiency. In the second method we are effectively 'cashing in' the efficiency gain for pressure ratio with an exchange rate similar to that shown in Figure 2.1.

Figure 2.3 shows the ideal (no losses) Joule cycle for a simple gas turbine on a temperature-entropy diagram. Air enters the compressor at atmospheric conditions at state (A) and passes through the inlet ducting to state (1). The air is then isentropically compressed through the compressor to state (2). The work input during the compression phase is:-

$$W_C = C_p(T_2 - T_1)$$

The air then reaches the combuster and heat energy is added by the burning of fuel in the chamber to reach state (3). This takes place at approximately constant pressure and the heat addition is:-

$$Q = C_p(T_3 - T_2)$$

The amount of heat that can be added at this stage is limited by the maximum turbine entry temperature T_{max} . This temperature is limited by the turbine blade melting point, the level of thermal creep stress and the amount and effectiveness of cooling available to the blades. The cooling available will allow the blades to operate in a free stream gas at a temperature above the melting point of the blades. However, a safety margin will have to be imposed and the blade life will be greatly reduced if too high a temperature is chosen.

The air is expanded through the turbine from stage (3) to stage (4). This provides the turbine with just sufficient work to drive the compressor. The work output from the turbine is:-

$$W_T = C_P(T_4 - T_3)$$

From state (4) to (5) further expansion occurs through the propelling nozzle producing a net thrust. Further fuel can be burned in the nozzle to produce extra thrust in a process called afterburning. Afterburning is used in military engines when more thrust is temporarily needed for example, for carrier take-offs or to outrun an enemy. The use of the afterburners will be at the expense of efficiency since the fuel is burned at a lower pressure and therefore the thermal efficiency will be low.

The overall cycle efficiency (ignoring afterburning) is a function of pressure ratio and γ for ideal cycles. The calculation for ideal efficiency (ignoring change in γ) is shown in Appendix A and is:-

$$\eta = 1 - \left(\frac{1}{r}\right)^{\frac{\gamma-1}{\gamma}} \quad \text{where } r=P_{02}/P_{01}$$

The cycle efficiency is therefore dependent only on the pressure ratio if we assume no losses and we are not restricted by turbine entry temperature. If we now assume that the compressor does not compress isentropically but has an efficiency η_c (defined in Appendix A) and the other components are still ideal then :

$$\eta = 1 - \left(\frac{\left(\frac{1}{r}\right)^{\frac{\gamma-1}{\gamma}} - \left(\frac{1}{t}\right)}{1 - \left(\frac{r^{\frac{\gamma-1}{\gamma}} - 1}{\eta_c} + 1 \right) \cdot \left(\frac{1}{t}\right)} \right) \text{, where } t = \left(\frac{T_{03}}{T_{01}}\right)$$

This function is shown graphically in figure 2.4 as a series of curves for temperature ratios of 4.5 to 7.25. A typical military engine will have a pressure ratio of between 25:1 and 30:1 and a temperature ratio of around 7.25:1. The regions for typical military and civil applications are shown ringed on the diagram. The dashed lines are for η_c values of 85% and the solid for 86%. The case of an engine operating at a pressure ratio of 25:1, temperature ratio of 7.25:1 and compressor efficiency of 85% is marked on the plot. If the compressor efficiency is improved by 1% to 86% and the pressure ratio maintained then the cycle efficiency increases by 0.2% which will improve the specific fuel consumption (s.f.c.) by ~0.35 %.

Figure 2.5 shows how this improvement in cycle efficiency (due to a 1% increase in compressor efficiency) changes with pressure ratio and initial compressor efficiency at a temperature ratio of 7.25:1. As the initial compressor efficiency is improved, further 1% improvements create less of a cycle improvement. This implies that not only does the task of improving compressor efficiency become more difficult at higher efficiencies (since there is less loss generated in the bladerows and therefore less to 'clean up') but also the pay back from this effort becomes increasingly less. The improvement also becomes greater at larger pressure ratios.

Another way of using the improved compressor efficiency is to operate the compressor at a higher pressure ratio until the efficiency drops to its former level. The

efficiency vs stage pressure ratio relationship shown in figure 2.1 suggests that a 1% improvement in efficiency might pay for an 8% increase in pressure ratio. The efficiency improvement could therefore increase the pressure ratio from 25:1 to 27:1. This is shown on figure 2.4 as the point on the 85% line (dashed) at 27:1 pressure ratio. The improvement to cycle efficiency now becomes 0.8% which represents a 1.4% improvement in s.f.c.

As the starting point pressure ratio is increased the steepness of the lines decreases so that the improvement from an increase in pressure ratio will have less effect on the cycle efficiency. This is shown in figure 2.6 where the effect of an increase in pressure ratio to:-

$$r \rightarrow \left(r^{\frac{\gamma-1}{\gamma}} + \frac{\Delta T_{Pr=25}}{T_1} \right)^{\frac{\gamma}{\gamma-1}}, \text{ where } \Delta T_{Pr=25} = \left(27^{\frac{\gamma-1}{\gamma}} - 25^{\frac{\gamma-1}{\gamma}} \right) \cdot T_1$$

is shown for a range of initial pressure ratios. The pressure ratio has been increased in a way which assumes that the efficiency improvement produces a uniform increase in blade loading. The increase in the pressure ratio is a consequence of this increased loading. In reality at higher pressure ratios the improvement to pressure ratio will not simply factor up by say 8% per 1% improvement in efficiency but will be a function of the payoff function shown in figure 2.1.

For high pressure ratio compression systems such as civil airliner engines the choice of whether to increase the pressure ratio or component efficiency becomes less clear. A typical case for a civil engine is shown in figure 2.4 where a 1% improvement in compressor performance produces a similar improvement in cycle efficiency to that which an increase in pressure ratio would achieve.

Benefits to thrust/weight ratio

The level of specific thrust achieved by an engine will depend heavily on the temperature ratio and cycle pressure ratio employed. Military engines operate at higher temperature ratios and relatively lower pressure ratios than civil engines in order to obtain higher levels of specific thrust. This higher level of temperature ratio and lower pressure ratio is at the expense of propulsive efficiency as shown in figure 2.7 (and Appendix B). For a given turbine entry temperature, and therefore temperature ratio, the amount of energy that can be added to the flow by burning fuel will be limited by the combustor inlet temperature. The higher the pressure ratio, the higher will be the temperature at inlet to the combustor and therefore the lower the amount of fuel that can be burnt. The specific thrust will therefore be low for high pressure ratios. At low pressure ratios the lower cycle efficiency will reduce the amount of thrust achieved.

The specific thrust therefore increases to a maximum at a certain pressure ratio and falls off at higher pressure ratios.

Figure 2.8 shows the relationship between specific thrust and pressure ratio for four different temperature ratios. The calculation is shown in Appendix C and is for a simple turbojet cycle and assumes that the nozzle is choked. The figure shows results for a compressor isentropic efficiency of 85% and 86%, turbine and mechanical efficiency are assumed to be ideal. For the 25:1 pressure ratio used in the cycle efficiency study figure 2.8 shows that a 1% increase in compressor efficiency would yield a 0.4% increase in specific thrust. This compares to a 0.9% increase for the higher pressure ratio cycle of a civil aircraft.

Alternatively the increased compressor efficiency could be used to reduce turbine entry temperature (TET) and therefore increase turbine life at the same level of specific thrust. For the 25:1 pressure ratio case the temperature ratio could be dropped to 6.97:1 which corresponds to a temperature drop at turbine entry of 8.6K below a base TET of 2000K

2.3 Managing the project

2.3.1 Introduction

The experimental work presented in this thesis has been carried out on the Low Speed Research Compressor (LSRC) based at Cranfield University. The project is unusual for the Propulsion Department since a large amount of the work (the manufacturing and testing) has been subcontracted and the context of the research (low speed aerodynamics) is new to the department. This chapter outlines the management aspects of the project with particular emphasis on some of the problems encountered and how they were overcome.

2.3.2 Project scope, planning and scheduling

Initially the programme of work associated with the Cranfield measurements was linked as a sub item of a larger project covering all the core compressor research in the department. The project manager for the cores programme was responsible for placing the contract of work with Cranfield University while the item manager (the author) was responsible for planning and executing the programme of work. These roles changed slightly when the management for the cores programme was reorganised at DERA. This resulted in a change of emphasis for the item manager to concentrate more on the technical work and less on the contractual and management issues. The original arrangement produced a potential conflict of interest when

contractual problems of the project conflicted with the student-supervisor relationship of the PhD.

The project comprised two builds of the rig along with extensive periods of testing for each build. The first build involved the complete re-manufacture of many of the components that make up the rig since the hub-to-casing ratio was to be increased from 0.85 to 0.91. A stator indexing mechanism was also designed and manufactured along with a new inlet bell mouth and intake arrangement. Considerable delays were incurred when problems arose with the new rings. Many were out of tolerance and had to be sent back to the manufacturer for modification. The second build was simpler and only involved the manufacture and fitting of new blades.

The initial contract placed with Cranfield was not specific regarding the contents of the tests and this created problems later on. DERA's experience of making high speed measurements at Pyestock had led DERA staff to assume that an extensive set of measurements would be made, the detail of which would be decided nearer the time. Cranfield however, was used to making a more limited set of measurements for Rolls-Royce and therefore had different expectations of the set of tests.

2.3.3 Project problems encountered

The main overriding problem encountered by the project was the conflict with Rolls-Royce over the occupancy of the facility caused by a series of slippages. These slippages were due to a number of separate problems which included; leaking pneumatic pipes, Scanivalve homing problems, software problems and problems with the torquemeter signal. More serious problems such as a persistent drive motor failure caused more lengthy delays and lead to a shortening of the test programme for the datum build. The Rolls-Royce programme of LSRC work supported the development of advanced derivatives of the Trent core and was therefore on a tight timescale.

Since many of the problems that were encountered were common to both the DERA and RR builds it was often more important to resolve the problem rather than cut a set of measurements out to make way for the next build. During the first DERA build however, the delays due to manufacture and build had set the test schedule back to such an extent that serious problems were created for the RR schedule. After negotiations between DERA, Cranfield and RR it was decided that the DERA build would be split in two with the second phase of testing commencing after the RR test. This was only possible because enough data had been collected on the datum build to assist the design of the DERA 3D blading.

Splitting the datum build test schedule created further problems when the overall performance measurements failed to match those from the first phase. In

addition, measurements downstream of the inlet guide vane (IGV) showed a one degree difference in flow angle from the first set of measurements. Because the IGV blades had been removed to accommodate the RR build it was thought that they may have been reset differently. Further delays were introduced by the exhaustive instrumentation checking needed to resolve the performance discrepancy which was caused by a temperamental torquemeter signal. An important lesson learnt from the datum build was that splitting a test on the LSRC can extend the on-test time considerably due to the temperamental nature of the instrumentation and difficulty in rebuilding the module to the original specification. Splitting a test should therefore be avoided wherever possible.

The lack of detail in the original contract with Cranfield caused problems when time pressures started to build due to the delays in testing. Since the contents of the test programme were loosely defined DERA were under pressure to reduce the content of test programme. This situation was improved to some extent for the second DERA build by agreeing a specific test schedule with Cranfield prior to the tests.

2.4 Justification for the project

2.4.1 Cost of project

The cost of the total project breaks down as follows.

Cranfield costs:-

Manufacture of datum build	£200.00k
Manufacture of additional components	£38.30k
Testing of datum build - Phase 1	£35.00k
Testing of datum build - Phase 2	£22.62k
Manufacture of 3D build	£58.14k
Testing of 3D build	£49.86k
Final report	£16.44k
Total Cranfield costs	**£420.36k**

DERA costs:-

Manpower (per year)	£48.30k
Travel and subsistence (per year)	£ 2.00k
Workstation (per year)	£10.70k
Total yearly cost	**£61.00k**
Printing costs	£ 5.00k
Total DERA costs for 3 years	**£188.00k**
Overall Cost	**£608.36k**

2.4.2 Benefit analysis of the project

Section 2.2 outlined the potential benefits of the project to the military customer. in this section these benefits are compared with the overall project costs so that justification for the project can be assessed. The benefits were calculated for a military engine with a pressure ratio of 25:1 and a temperature ratio of 7.25:1. The compressor efficiency is 85% and the calculations assumed a 1% improvement of this to 86% with all other components modelled as ideal. The benefits may be summarised as follows:-

Using component improvement with same pressure ratio

Cycle efficiency	+0.2%
Specific fuel consumption	-0.35%

Using compressor improvement with higher pressure ratio

Cycle efficiency	+0.8%
Specific fuel consumption	-1.4%

Using compressor improvement to improve specific thrust for the same turbine inlet temperature (turbojet cycle)

Specific thrust	+0.4%

Using compressor improvement to reduce turbine entry temperature for the same specific thrust (turbojet cycle)

Temperature ratio	-8.6K (from 2000K)

The aim of the project is to improve understanding of compressor core aerodynamics so that component efficiency can be improved. Since this improvement in efficiency can be used in different ways it is difficult to quantify the payback of the project. For example, how can the ability to improve the manoeuvrability of a military aircraft be quantified in monetary terms?

Table 2.1 shows the breakdown of flying hours for the RAF Harrier and Tornado fleet for 1997 along with the total fuel consumed and fuel costs (Saunders,1998). The total fuel bill for these aircraft for 1997 amounts to £43.2M. If the component improvement is simply used to reduce the military's fuel bill with the engine cycle parameters kept the same then the project could expect to save the military £0.6M per year (assuming s.f.c. -1.4%). This yearly saving compares well with the total project costs of £0.6M.

However, it is likely that the military are more interested in seeking improvements in specific thrust and thereby improve the overall thrust/weight ratio of

their aircraft. Since fuel consumption is also important for range and endurance the cycle choice remains a careful balance between thrust capability and endurance. The compressor efficiency improvement will therefore feed into this optimisation process. The application of the military aeroengine has a bearing on this optimisation process; for example combat/attack aircraft have different priorities from aircraft with air patrol or intercept roles. Although the payoff is hard to quantify it is clear that improved compressor efficiency can improve; efficiency, range, payload, thrust, cost of maintenance and/or unit cost (through reduced bladerow count).

Chapter 3 Review of previous work

3.1 Introduction

The most important region for axial compressors from a performance point of view is the endwall region. These include corner flow and tip-clearance flows. In core compressors these regions provide the greatest source of loss and therefore also the greatest potential for improvement. They are, however, the most challenging and least well understood region of the compressor.

Modelling of these flows has usually been made practicable by employing a tidy division between the bulk 'inviscid' flow and the endwall viscous flow. Such a division is desirable due to the simplifications that can be made both computationally and phenomenologically. In an S1-S2 system, for example, the bulk flow is computed on smooth quasi-3D blade-to-blade surfaces using well validated codes and boundary layer models. The important endwall flow is usually dealt with by the throughflow calculation where correlations and blockage factors are used with the assumption of circumferential uniformity. Attempts have been made to account for the 3D endwall effects within the throughflow calculation by the use of conventional 2D boundary layer methods and 'corrections' for overtip vortices and endwall boundary layers. These methods lack the appropriate coupling and the necessary degrees of freedom found in real compressors where highly 3D flow effects such as tip vortices, boundary layer skew, and corner separations interact with one another and with the 'bulk' inviscid flow. Cumpsty (1989) gives a comprehensive description of the viscous flow found in compressors and their study by experimental and theoretical means.

Calculation methods based on the 3D Navier-Stokes equations are ideal for endwall flows where the overall features such as tip leakage vortices and regions of separation can be well predicted. However, they can be inaccurate in their prediction of loss and computer size and power currently restrict the size of practical calculations. While 3D Navier-Stokes solvers are useful for assessing isolated 3D flow phenomena the only conclusive way to assess a compressor design is by experimental measurement. In the past experimental testing had a greater focus on linear cascades to help improve the blade-to-blade flow. This has lead to the improvement and validation of boundary layer models and viscous-inviscid blade-to-blade codes. The subsequent gains in compressor performance arose from the use of controlled diffusion type blading.

As the compressor aerodynamics to be investigated becomes more challenging by the need to address problems such as boundary layer skew, blade-to-blade interaction, overtip flow and unsteadiness the more complex the tools must be to analyse these. From

the experimental point of view this implies that complete compressor modules must be tested and that cascade testing is no longer appropriate. The consequence of this is the increased cost of testing new blade types and configurations.

The following review outlines the study of endwall flows and how this work has precipitated research into the design of 3D blading. This is followed by an outline of how low speed testing has been used as a cost effective alternative to high speed testing in the study of endwall flows and the assessment of 3D blading variants.

3.2 Endwall Flow Phenomena

3.2.1 Tip Clearance Flows

The effect of tip clearance on compressor performance is not straightforward due to the overwhelming effect the tip flow has on the endwall flow development and on the blade-to-blade flow near the tip. In multistage core compressors the problem is compounded by the effect of the tip flow on subsequent blade rows especially since this flow is unsteady relative to the next blade row.

Experimental investigations of tip clearance have been carried out to study the effect of different clearances on overall performance. Wennerstrom (1984) tested a high speed single stage compressor at tip clearances of 0.42, 0.68 and 0.94 per cent of chord. This study showed the clearance of 0.68 per cent to be the most efficient and suggests that an optimum clearance exists below which losses start to increase. This theory is supported by investigations by Inoue et al (1986) into the effect of clearance between 0.43 and 4.3 per cent and found an optimum to exist at less than 1 per cent. Unfortunately the optimum clearance for rotors is generally smaller than that which can be tolerated for mechanical reasons.

The benefit of tip clearance is sometimes explained by considering the clearance flow as opposing the secondary flow which is usually moving toward the suction surface due to the pressure gradient set up by the bulk freestream flow. This flow into the suction surface endwall corner region tends to become involved in a three dimensional separated flow region caused by the high incidence from inlet skew. The introduction of tip clearance flow at small clearances can re-energise this stalled region and therefore reduce the losses. At greater clearances, however, the overtip flow dominates the flow field and greater losses are incurred.

Studies into tip clearance have also been carried out on low speed multi-stage compressors. Wisler (1984) reported that for a low speed four-stage compressor the effect of increasing rotor tip clearance by 1.44% height was to reduce the efficiency by 1.5 per cent, the flow range by 11 per cent and the peak pressure rise by 9.7 per cent.

Howard et al (1993) investigated the effect of rotor tip clearances at 1.2% and 3.0% of chord on both the rotor losses and the losses of the following stator. They found that the losses increased for both rotor and stator at increased rotor clearance and that the additional stator loss caused 30% of the drop in stage efficiency while the remaining 70% was attributed to loss increases in the rotor.

Lakshminarayana et al (1986) investigated the evolution of loss through a rotor passage for a low speed compressor at the peak efficiency condition. The loss core was found to start at the suction surface close to the endwall and move towards the pressure surface as the over tip vortex progressed towards the rear of the passage. Inoue et al (1986) measured the relative loss just downstream of a rotor trailing edge for five different levels of tip clearance from 0.43 to 4.3 per cent. For the smaller clearances the centre of the loss core moved only a small distance from the suction surface but as the clearance was increased the high loss region moved over toward the pressure surface.

The effect of tip clearance on blade pressure distribution and loss was investigated by Lakshminarayana and Horlock (1967). A linear cascade was used with the blades cut at mid height so that the two halves cantilevered in from the endwall. The clearance between the two halves could be adjusted and different inlet flow conditions were used. At a clearance of 1 per cent chord the pressure distributions were very similar to the 2D distributions with no gap. At larger gaps the effect on pressure distribution was quite marked with a large drop in the pressure at the rear of the suction surface. Due to this drop in pressure at the suction surface the total blade normal force was increased by the presence of the gap. This increase continued until the clearance became around 6 per cent of chord and then the normal blade force decreased.

By far the most important effect of the tip clearance flow is the effect it has on separated flow in the endwall suction surface region. MacDougall (1988) carried out oil flow visualisation studies on stator blades with and without clearance close to stall. The stator without clearance showed a very large corner stall region extending up most of the span while the stator with clearance (approx 1 per cent of chord) and operating at the same flow coefficient showed no corner separation. This behaviour was also predicted by MacDougall and Dawes (1987) using a Navier-Stokes solver on the same stator geometry with and without clearance. Storer and Cumpsty (1990) carried out experimental measurements in a linear cascade along with three-dimensional calculations to investigate the tip leakage flow. The numerical predictions of leakage flow rate agreed well with measurements and indicated that the mechanism of tip leakage is primarily inviscid.

3.2.2 Secondary Flows

The primary source of loss in turbomachines at design condition is in the endwall region. Howell (1945) estimated the contribution to loss by different loss sources as a function of flow function. This is shown in figure 3.1 where contributions from the annulus loss, secondary flow loss and profile loss are illustrated. The results show that the profile losses contribute most significantly at flow coefficients above the design intent while at design and toward surge the annulus and secondary losses dominate.

The secondary flow and annulus loss included in the above analysis includes all the losses other than profile loss and therefore includes tip clearance flow loss also. Other losses which are more usually referred to as secondary are those arising from the movement of the endwall boundary layer flow under the influence of the cross passage pressure gradient. This secondary flow arises because the boundary layer moves at a lower velocity than the mainstream flow. The mainstream flow turns through the passage and therefore a cross passage pressure gradient is set up. The lower velocity fluid in the boundary layer must follow a tighter radius of curvature since it experiences the large pressure gradient of the faster moving mainstream flow. This results in the endwall boundary layer overturning, sweeping up the suction surface and rolling into a vortex. Dong et al (1987) carried out a flow visualisation experiment on a non-rotating hub which illustrates this overturning effect.

3.2.3 Inlet skew

The endwall flow features discussed so far serve as an insight into the mechanisms present within blade rows for degrading the performance of the compressor. This picture is further compounded by the effect of inlet boundary layer skew. This arises primarily from the translation of the boundary layer from one frame of reference to another. A collateral boundary layer in one frame of reference will look highly skewed in the next with the flow direction approaching 90 degrees at the wall. In a multi-stage compressor the endwall boundary layers will be skewed on exit to each blade row due to the secondary and clearance flows within the passage. This implies that the boundary layer entering the next blade row will be highly skewed and complex leading to high incidences near the blade ends.

3.3 Low-speed blading

Low speed testing has been used for a number of years as a cost effective way of testing novel and often risky blade designs before committing such designs to real high speed compressors. The aim of any low speed research compressor is to reproduce the aerodynamic flow physics found in today's high speed core compressors at a

comparatively low set up and running cost. The larger scale and better instrumentation access of low speed compressors allow for improved spatial resolution from area traverse measurements compared to high speed compressors. However, the lower pressure and temperature levels provide a unique challenge at low speed; requiring a higher level of accuracy and relying on throughflow analysis to provide the individual stage work profiles. Another limitation of low speed testing is the restriction to emulating sub-sonic high speed blading, found in the rear stages of the HP compressor.

3.3.1 The high-to-low speed transformation

The principle of low speed modelling is to reproduce the non-dimensional aerodynamic quantities found in the high speed flow field. For turbomachinery flows this process involves the simulation of aerodynamically similar blades and aerodynamically similar boundary conditions. Keuthe and Chow (1976) and Liepmann and Roshko (1957) show that geometrically similar isolated bodies that move through a fluid with equal non-dimensional aerodynamic parameters (ie Reynolds number and Mach number) experience equal dimensionless forces. When the Mach number of the two bodies differ, the angle of attack, camber and thickness have to be modified to maintain aerodynamic similarity. This modification takes the form of a simple transformation when the bodies considered are isolated aerofoils.

The transformation comes from the combination of Gothert's rule with the incompressible similarity law of linearised perturbation theory (Shapiro, 1953) and states that the camber, thickness and angle of attack of the incompressible aerofoil be increased by the factor $(1-M_\infty^2)^{1/2}$. This is known as an affine transformation since it is equivalent to a uniform stretch of the aerofoil shape in the y-direction.

For turbomachinery flows this transformation is inadequate mainly because the theory is for isolated aerofoils and the v and u-velocities on the surface are considered perturbations on the larger mainstream U-velocity. Since the 'aerofoils' in turbomachinery are arranged in cascade and the level of turning and diffusion is high then neither of these assumptions hold. The turbomachinery case is further complicated by the unsteady interaction between the rotating and stationary blade rows and the 3D effects of blade aspect ratio, solidity, axial-gap/chord ratio, blade row number ratios, hub/tip ratio and tip clearance/chord ratios.

The incompressible similarity law does tell us to expect thicker and more cambered profiles and it has been used to generate profile shapes from a target high speed design as a starting point in the blade design iteration of low speed compressor blades (Robinson, 1991).

For true aerodynamic similarity the blades must have the same scaled surface roughness, Reynolds number and be tested in fluid of the same turbulence intensity. Schäffler (1979) investigated the effects of Reynolds Number and blade surface roughness on multistage axial flow compressors. The investigation included tests carried out on two 6-stage high pressure compressors. The first was from a flight engine that had experienced foreign object damage and as a result the rotor blade leading edges were reworked. The second compressor was the same design but used new production type blades. The results show that, while the damaged compressor was generally 0.5 per cent down on efficiency, degradation of the compressor performance became more significant as Reynolds numbers fell below ~2-3 x 10^5 and at 2.5 x 10^5 the degradation could produce an extra 1% fall in efficiency. This was attributed to laminar separation of the boundary layer at the lower Reynolds number. For the undamaged compressor the drop in efficiency due to laminar separation bubbles occurred at Reynolds numbers below 1 x 10^5 with the effect of surface roughness also playing an important part in the behaviour of the boundary layer.

Wisler (1984) presents a detailed description of the high-to-low speed modelling process used at the GE low speed rig. The process starts by establishing the high speed pitchline design quantities by averaging radial distributions of flow parameters such as; exit swirl angles, loss coefficients, flow coefficient and normalised rotor exit total pressure. Once this is established the low speed pitchline design is created starting with the low speed vector diagrams. This is achieved using the pitchline quantities from the high speed design and iterating the level of the rotor exit pressure until the target pressure rise coefficient is achieved. After the vector diagrams are set up the blade aerofoils are designed to achieve the same normalised suction surface velocity distribution as the high speed blades. The chord lengths and number of blades are based on the values of solidity and aspect ratio to be modelled.

Robinson (1991) presents the low speed design of blading based on stage 7 of the V2500 compressor. The hub/tip ratio of the study stage differed from the low speed compressor so blade numbers were altered to keep the desired solidity. A throughflow analysis was set up using radial profiles of loss coefficient from the V2500 stage 7 design values and the mass flow rate was set to achieve the target Va/U at stage 3. The rotor pressure ratio was adjusted to give the target $\Delta H/U^2$ at stage 3 and the blade profiles were tailored to give similar non-dimensional suction surface velocities as the high speed blades.

While the work of Wisler (1984) and Robinson (1991) outline the methods employed in designing their low speed model there appears to be no reporting of the measured low speed performance comparing the flowfield of the low speed study stage

with the high speed target stage. The low speed models are used as datums from which more adventurous 3D designs are based and referred back to so that performance improvement can be assessed. It is somewhat surprising that the level of high-low speed read across and the limitations of low speed compressor models have not been fully assessed. This would surely help in the interpretation of 3D low-speed designs and their applicability to a high speed environment.

3.4 3D Design for endwall regions

3.4.1 Introduction

The complex viscous endwall flow phenomena outlined in chapter 3.2 can seriously reduce the performance of multi-stage axial flow compressors. Recent research work has focused on alleviating these endwall losses through the use of '3D' blade design approaches. This design work has been facilitated by the development of fully 3D Navier-Stokes flow solvers and the increased computer speed and memory needed to make run times viable within a sensible design time frame. The use of computer simulation has allowed more adventurous exploration of different geometry configurations on a shorter timescale and at greatly reduced risk and cost. Such explorations would have been too risky with traditional empirically based design systems where the region of interest extends beyond the database of tested geometries and the build and test of iteratively improved designs can be very costly.

The 3D design approaches attempt to control the endwall flows by locally reducing the loading in these regions. Several methods have been used to achieve this with varying degrees of success, these include; end-bends, leading edge recambering, section modification, lean and sweep. End-bends are near endwall blade twists that off-load the endwalls by reducing the level of turning required while leading edge recambering reduces loading by aligning the leading edge with the skewed inlet boundary layer flow thereby decreasing the incidence at the endwall.

These methods by their nature are design for a certain flow angle and operating point in order for the benefits of the design to be fully realised. Recent interest has focused on the more generic methods of lean and sweep to control the endwall flows. These methods involve stacking the blade on a non-radial stacking axis either forwards/backwards (sweep) or perpendicular to the flow (lean).

3.4.2 Endbends

Endbends are used in many aircraft applications to improve compressor efficiency by reducing endwall losses. Endbends are camber or stagger angle changes that are made localised to blade ends and are often introduced as a perturbation to a conventionally

designed blade. They are usually designed to align the leading edges at the endwalls with the skewed inlet flow and the trailing edges with the overturning secondary flow at blade exit. Losses are decreased by the reduction in incidence and/or a change in flow turning of the endwall sections.

Wisler (1985) shows that a 10% reduction in stator endwall loss along with improved stall range is achievable due to the application of endbends. Robinson et al (1989) show that endbends can relieve the corner separation at the shrouded end of a stator.

3.4.3 Blade section modification and endwall contouring

Controlled Diffusion (CD) airfoils have been incorporated into conventional '2D' blade designs since the late seventies allowing increased pressure rise per stage and efficiency improvements of around 2% over standard airfoils. Behlke (1986) takes the controlled diffusion airfoil philosophy further by applying it to the full span including the viscous endwall regions in what the author calls 'second generation controlled diffusion airfoils'. The blade endwall sections were tailored to produce an optimum chordwise loading distribution. Behlke reports a 1.5 % increase in efficiency and 30 percent increase in surge-free operation relative to a standard 'first generation' CD airfoil blade. The resulting blade shape looks very similar to an endbend blade with distinctive leading and trailing edge re-cambers.

LeJambre et al (1995) describe a method to reduce corner separation in the hub region of a compressor rotor blade by contouring the hub endwall. The concept was initially employed in the design as a means of increasing the choke margin of the high Mach number rotors. The resulting shape of the hub flow path wall had the additional benefits of creating a radial force almost the same as an aerofoil bow. This force redistributes flow and reduces the tendency of the boundary layer to separate at the endwall corner between the aerofoil suction surface and endwall. In the case studied the contoured wall not only eliminated flow separation but enabled the blade to achieve higher levels of diffusion.

3.4.4 Lean and Sweep

Lean and/or sweep of the blade stacking axis has been successfully employed by many researchers to obtain further efficiency improvements of the order of 1 percent over conventionally stacked blading. Weingold et al (1995) report the design and test of a redesigned stator and explain the aerodynamic effect of using bowed blading through the use of a simplified lifting line model. Tweedt et al (1986) introduced leading edge forward sweep to a stator endwall with three stator hub configurations; a running

clearance, a stationary clearance and a shroud. They reported a 11.5% reduction in loss using sweep for the shrouded case. Leading edge sweep was reported to increase loss on the hub end of the stator when a running hub clearance was used.

Denton and Xu (1998) provide a detailed discussion of the effects of lean and sweep and the aerodynamic mechanisms that produce these effects. They also describe how these mechanisms can be exploited, using 3D CFD design tools, to improve turbomachinery design.

Emmerson and Buchanan (1996) investigated numerically the effects of lean and sweep on a stator cascade geometry using a 3D Navier-Stokes flow solver. A range of lean and sweep combinations were used along with different stacking axis shapes. The best geometry achieved a 9% reduction in pressure loss coefficient. A highly skewed inlet boundary layer case was also investigated to assess the benefits of lean and sweep on the performance of the stator downstream of a rotor bladerow. The datum case produced greater losses with the skewed inlet but much larger loss reductions (up to 40% on loss coefficient) were achieved using either lean or swept blades.

The implication is that the larger the endwall losses the more benefit lean or sweep will produce. However, Emmerson et al (1996) show that the nature of the endwall losses is also important when considering the benefits of lean and sweep. They investigated the effects of lean and sweep on a single stage transonic fan stator known to suffer from a significant hub corner stall. Sweep and lean were predicted to be much less effective in reducing the hub endwall corner stall than for the stator cascade case. This was attributed to a severe separation of the flow from the leading edge in the hub region which was not present in the cascade case at design inlet conditions. At higher incidences the benefit of lean/sweep diminished. Experimental studies at V.K.I. by Breugelmans (1987) show similar trends when lean was applied to a compressor cascade operating at a high flow incidence.

Shang et al (1993) show how the behaviour of endwall flows differs for straight and leaned blades through a series of flow visualisation and area traverse measurements made downstream of a compressor cascade. A straight blade, a straight lean (incorporating an acute and obtuse angle of the suction surface with the endwall) and curved lean (obtuse angle at both ends) blade were investigated. The ink trace flow visualisations show how blade lean delays the migration of endwall flow onto the suction surface for obtuse lean angles but is increased for acute angles. For the curved blade both endwalls were improved while the midspan loss increased. Zhongqi et al (1994) confirm this result which turns out to be a general observation for subsonic compressor bladerows.

The multistage implications of using bowed blades is an important design consideration since the potential improvements to the endwall flow of one bladerow could greatly change the flow onto the next bladerow and this interaction has to be modelled if bladerows are to be optimised. Rhie et al (1995) modelled the multistage performance of a multistage HP compressor incorporating both bowed and straight bladerows. Body forces and deterministic stresses were used to model the effects of up and downstream bladerows. The calculation showed good agreement with experimental data and predicted the mid span losses of the bowed blades to increase greatly at the near stall flow condition.

3.5 Cranfield low speed compressor

The low speed rig at Cranfield is a 120kW, 1200 rpm, four stage compressor with a parallel annulus and a casing diameter of 1.22m. Identical rotor and stator blading is used for each stage, with the third stage used as the study stage while the first and second stages set up the inlet conditions to it. The fourth stage provides an appropriate downstream pressure field for the study stage.

The low speed research facility was made in the early eighties and has been used almost exclusively by Rolls-Royce to test various conventional and endbend blade designs, Robinson, (1991) and Casey (1990) report on some of the blade types used. Initially these were based around two datum blade types, a free vortex double circular arc (DCA) design (based on the RB211) and a low reaction design (based on V2500). Various endbend philosophies have been tried on these datum builds including; inviscid endbends proposed by Freeman (1978) viscous endbends, controlled vortex and inverted velocity profile. More recent work has focused on a New End Bend design (Barton, 1992b) and BRITE/EURAM funded builds aimed at studying overtip flow and comparing shrouded and unshrouded stators (Swoboda et al, 1998). Current Rolls-Royce low speed tests involve 3D blades incorporating bowed stacking axes. The design of C147 type blading will be the first LSRC build to have military loading levels.

3.6 C147 Compressor

The compressor used as the high speed reference for this work was the third build of the DERA five stage research compressor designated C147. The first build had four stages and conventional blading, mainly with double circular arc (DCA) profiles. This build exceeded its design pressure ratio of 4.0 and achieved a peak polytropic efficiency at design speed of 89% (Calvert et al 1989). The second build incorporated a complete new set of blading with controlled diffusion (CD) profiles, a constant α_o (~12.5°) and an extra zero stage (Ginder 1991). This demonstrated a 1½ % efficiency improvement over

the first build. The third build used the same blade design as the second build but had increased blade numbers to improve the surge margin.

3.7 Conclusions

This literature survey has highlighted the current research trends within axial compressor community. There is particular emphasis on the continued investigation of 3D design concepts and the development and improvement of 3D Navier-Stokes flow solvers to meet these design objectives. There is also a need for a detailed investigation of low speed compressor testing to evaluate the relevance to the high speed environment. This Thesis hopes to meet this need through the design and test of a datum low speed blade set (based on an existing high speed stage) and an advanced low speed blade set, incorporating 3D design concepts.

Chapter 4 - Datum design

4.1 Introduction

The aim of a low speed research compressor is to reproduce the aerodynamic flow physics found in high speed core compressors at a comparatively low set up and running cost. The performance of an embedded stage is strongly influenced by those around it and therefore an essential ingredient of the modelling process is to simulate the likely stage entry and exit conditions. This is most readily achieved by using identical blading in each stage. In a four stage compressor the first two stages set up repeating flow conditions and endwall boundary layers so that the axial velocity profile is representative of an embedded stage. The third is the study stage and the fourth sets up the appropriate downstream pressure field. The larger scale of a low speed research compressor allows better instrumentation access and more detailed measurements to be made.

This chapter outlines the design of a set of low speed blades for the Cranfield Low Speed Research Compressor (LSRC) that aim to represent a high speed stage as closely as possible. The Pyestock research compressor C147 (Calvert et al 1989, Ginder 1991) was chosen as the high speed reference. This is a highly loaded compressor with controlled diffusion blading, cantilevered stators and detailed flow measurements around most blade rows. Previous low speed designs at Cranfield have generally been of lower loading and have not attempted to correspond directly to an existing high speed counterpart. The blading set will become the datum on which a further design and test will be based. This later design, incorporating '3D' design concepts, is reported in chapter 8. The datum design has been built and tested and these measurements are reported in chapter 6.

4.2 Low speed rig facility

The low speed rig at Cranfield is a 120kW, 1200 rpm, four stage compressor with a parallel annulus. Identical rotor and stator blading is used for each stage, with the third stage used as the study stage while the first and second stages set up the inlet conditions to it. The fourth stage provides an appropriate downstream pressure field for the study stage. While no inlet turbulence grids are employed on the rig, the unsteadiness generated by the first two stages should provide realistic levels of turbulence to the study stage. The casing diameter is 1.22m and for the current work the annulus height is 54.8mm and the hub/tip ratio 0.91. The large scale allows easy access between blade rows for traverse measurements and good spatial resolution at the end walls. A photo and the layout of the current build of the Cranfield rig are shown in figures 5.1 and 5.2 respectively.

Performance measurements are made by a torquemeter and eight total pressure rakes up and downstream of the module. The mass flow measurement is obtained by a calibrated bellmouth air intake and the mass flow is controlled by a conical throttle at the rear of the exhaust ducting. For a full description of the low speed compressor and the instrumentation employed in the test series see chapter 5.

The low speed research facility was made in the early eighties and has been used almost exclusively by Rolls-Royce to test various conventional and endbend blade designs, Robinson, (1991) and Casey (1990) report on some of the blade types used. Initially these were based around two datum blade types, a free vortex double circular arc (DCA) design (based on the RB211) and a low reaction design (based on V2500). Various endbend philosophies have been tried on these datum builds including; inviscid endbends proposed by Freeman (1978) viscous endbends, controlled vortex and inverted velocity profile. More recent work has focused on a New End Bend design (Barton, 1992b) and BRITE/EURAM funded builds aimed at studying overtip flow and comparing shrouded and unshrouded stators (Swoboda et al, 1998). Current Rolls-Royce low speed tests involve 3D blades incorporating bowed stacking axes. The design of C147 type blading will be the first LSRC build to have military loading levels.

For the DERA tests the Cranfield rig has been extensively re-worked to incorporate a higher hub line (to increase the hub/tip ratio from 0.85 to 0.91) and a new intake bullet and flare. A new inlet duct with two gauze planes has been manufactured to fit over the new intake bullet and this acts as a settling chamber for the incoming air. The duct extends beyond the front doors of the test facility so that air is drawn directly from the outside rather than the circulating air inside the cell. New rotor, stator and hub spacer rings have been procured along with a new stator-stator indexing mechanism that allows the movement of the second stator blade row relative to the others.

4.3 Low speed code development

The success of the datum and 3D blade designs for the LSRC at Cranfield is strongly dependent on how well the bladerow flow can be modelled at low Mach numbers. For the datum design, accurate blade-to-blade modelling of the near blade surface velocity distributions is necessary for the high-to-low speed transformation process. For a successful 3D design, good modelling of the 3D flowfield including the endwall and overtip flows is desirable so that the optimum blade shape can be found. This section describes the modifications that were made to the DERA TRANSCode flow solver to enable the code to achieve convergence at low speed. It was important to

the success of the project that a reliable low speed modelling capability be established at Pyestock and TRANSCode proved to be a good starting point for this work.

The blade-to-blade code used in the S1-S2 design of the high speed compressor C147 was the inviscid-viscous quasi-3D solver S1BYL2 (Calvert and Ginder, 1985). This code could not be used for the LSRC since it cannot converge at the low Mach numbers found in the Cranfield compressor. Also, the solution method was not well suited to the thick blunt leading edges of the low speed blades because S1BYL2 models a cusp at the leading and trailing edges.

The CFD options for the LSRC datum design work were either to use the Rolls-Royce code FINSUP, which is a quasi-3D solver, write a new incompressible code or modify an existing DERA code. The Propulsion Department at Pyestock has been developing a cell centred time marching Navier-Stokes flow solver, TRANSCode (Calvert 1995) for 3D and 2D (quasi-3D) flows derived from Professor Dawes' BTOB3D code (Dawes, 1986). The solver is more suited to high speed compressible flows and does not converge well for low speed flows. It was decided that modifying TRANSCode would be the simplest and most effective way of meeting the requirements for the low speed blading designs. TRANSCode has been developed and improved within the department for many years and has proved to be a reliable code for modelling high speed flows. It can be run as a blade-to-blade solver or fully 3D so that the same code can be used for both the datum and 3D LSRC designs.

4.3.1 The Incompressible Model

The convergence method implemented into the low speed version of DERA TRANSCode is based on the method of "Pseudo compressibility", originally proposed by Chorin (1967) and developed by Chang and Kwak (1984) and later employed by Walker (1987). The method relies on the unsteady flow information in the converging flowfield solution being transmitted via pressure waves rather than density waves. This is achieved by time-marching pressure instead of density. Consider a sound wave propagating through the medium with speed a and an associated pressure and density change of δP and $\delta\rho$ respectively. The sound speed can be shown to be:

$$a^2=(\delta P/\delta\rho)$$

This means that incompressible flows (where $\delta\rho=0$) have an infinite sound speed, and therefore zero Mach number. The pseudo compressibility method works by replacing $\delta\rho$ in the continuity equation with the term $\delta P/\beta^2$ so that:

$$\delta\rho/\delta t + \nabla\rho\underline{v} = 0$$

becomes:

$$(1/\beta^2)\delta P/\delta t + \nabla\rho\underline{v} = 0$$

where β is analogous to the sound speed. The other conservation equations remain unchanged. When the solution has reached convergence $\delta P = 0$ and $\nabla \rho \underline{v} = 0$. and therefore continuity is satisfied. The use of pseudo compressibility results in a system of hyperbolic-type equations of motion and the value of β is carefully selected (see Chang and Kwak, 1984) to ensure convergence stability.

4.3.2 Changes to TRANSCode

TRANSCode is a cell-centred, finite volume Navier-Stokes solver employing a 2 or 4 step Runge-Kutta scheme and multigrid algorithm. A low-speed version of this code has been developed which can be operated in both compressible and incompressible modes by use of a additional parameter (XLS) within the .CON control file.

The variable RO within the time-marching part of the code has been replaced by an additional variable TRO (or Time-marched RO). When XLS = 0, TRO becomes RO and the code operates in its original compressible mode. With XLS greater than 0, TRO becomes the time-marched pressure field and the code operates in the incompressible mode. In this mode β is a field variable based on the local velocity and is scaled by XLS. RO everywhere is updated at the end of each loop by an average value of density at the inlet plane. In this way the density field is not allowed to spatially vary and hence $\nabla \rho = 0$.

The changes to TRANSCode involved the addition of a few variables and the alteration of a number of subroutines to include the extra logic needed to handle both modes of operating. The momentum equation was unaffected as were the boundary layer and stress routines. The energy equation was no longer necessary.

4.3.3 Code verification and validation

In order to evaluate the effects of the modifications made to TRANSCode a number of test cases have been run using the modified code. Two cases are shown here; one a quasi-3D compressor cascade and the other a 3D stage. The validation of the code has two parts; the first is to verify that the low speed modifications have been correctly applied and produce similar results to the high speed option running at low Mach number. The second part is to validate how well the low speed predictions match test data so that its capability as a design tool can be assessed.

4.3.4 V2-Cascade

The V2 cascade (Fottner, 1990) is a high turning compressor cascade tested in the high speed wind tunnel of DFVLR Braunschweig. An evaluation of the standard TRANSCode for the V2 cascade, compared with both experimental and S1BYL2 predictions, has been reported by Stapleton (1997). In order to fully assess the

modifications to TRANSCode a code-code comparison was carried out. The modified and the original versions of TRANSCode were run on the V2 blade geometry in quasi-3D mode at five different Mach numbers ranging from 0.13 to 0.56. The quasi-3D mode uses a blade-to-blade 2D grid of one cell height and a stream tube thickness distribution is imposed by the cell height to obtain the correct axial velocity ratio. For the V2 cascade the test measurement of endwall boundary layer growth gave the distribution of stream tube thickness needed to model the mid-height section. Figure 4.1 shows the normalised near surface velocity distributions and convergence history for solutions at five inlet Mach numbers. Nominal Mach number increases up the page.

For the incompressible solutions the Mach number is zero so strictly it is the inlet velocity that increases up the page for these solutions (nominal Mach number is the Mach number a compressible flow would have if it was operating at the same inlet velocity). For comparison with the high speed solutions a nominal Mach number based on the inlet total and static pressure has been calculated and this represents the flow condition that the solution is trying to achieve. The first point to note is that convergence is obtained far earlier for the low speed code when the Mach number is reduced and the high speed code takes progressively longer. The two codes take equal convergence time for the 0.56 Mach number case. The unmodified high speed code failed to converge at all for 3-D test cases such as NEB1D at Mach numbers below ~0.3.

The non-dimensional velocity distributions plotted in the left hand column show the distributions for the low speed option are generally constant, although there are some minor changes near the leading edge, while the peak suction surface velocity increases at high Mach numbers for the high speed code. This is the effect of compressibility; from the peak suction surface velocity to the lower trailing edge velocity the density has increased so the velocity change across the same region has to increase (compared with the incompressible case) to maintain mass continuity.

The high speed code predicts large oscillations towards the leading edge at low Mach numbers which suggests that the code is struggling to cope with the incompressible flow around the blade in this region. This is the same region where some discrepancies in the incompressible solutions occur. The low speed velocity distributions agree with the high speed distributions fairly well at Mach numbers relevant to the LSRC. This is encouraging for the design of the datum LSRC blading since these sections are designed using TRANSCode to produce the same velocity distributions as the C147 blading.

Figure 4.2 shows the displacement thickness, momentum thickness and shape factor for the two solutions at 0.26 indicated Mach number. The displacement thicknesses agree well for both options on the suction surface and this is also the case for

the momentum thickness and shape factor. The pressure surface however is predicted to be thicker for both displacement and momentum thickness for the high speed solution. This could be due to the oscillations seen in the velocity distributions for the high speed solution at the leading edge of the pressure surface producing false entropy generation. These oscillations highlight a difficulty with predicting the flow in this region with the compressible option and the consequence is a thicker pressure surface boundary layer.

The results of this test confirm that the implementation of the low speed option into TRANSCode has been successful. The poor convergence of the unmodified code at low Mach numbers and its inability to produce good solutions in this flow regime confirm the necessity of the low speed modifications. For low speed flows the low speed option converges quickly and produces sensible results. At 0.3 Mach, the boundary between compressible and incompressible flow, the low speed option performs in a manner consistent with the high speed un-modified code.

4.3.5 NEB1D

NEB1D (Young, 1993) is a low speed compressor designed for the Cranfield LSRC by Rolls-Royce. It is a straight stacked design with cantilevered stators and a 0.85 hub/tip ratio based on the NEB1 3D design (Place 1995, Young 1993). Both the rotor and stator were modelled in isolation and figure 4.3 shows the grid used to model the NEB1D stator geometry. The clearance end of the blade is modelled by a pinched tip and the 41x135x41 grid is typical of the grids used to model the DERA low speed blades. Radial profiles from an experimental throughflow calculation at design flow were used for the inlet boundary conditions for both the rotor and stator predictions.

Figure 4.4 shows the circumferentially mass averaged radial profiles from the stator prediction and compares them to the experimental profiles. The predictions show fairly good agreement with the measurements over most of the span. The most difference occurs towards the hub where the centre of the whirl velocity deficit is predicted to occur around 5% height instead of 15%. The swirl angle profile shows TRANSCode overpredicting the stator deviation by around 1° at mid-height.

Figure 4.5 compares contours of total pressure downstream of the stator from the TRANSCode prediction with an experimental area traverse taken with a three hole cobra probe. The wake widths and wake deficit agree well with the measurement and the contour map shows the same overall contour levels and trends. Towards the hub however the measurements show a large region of low total pressure at the centre of the passage, probably associated with the clearance vortex. The prediction captures a similar feature in the same location but fails to predict the same shape and structure, the solution appears washed out and lacking in detail. This shortcoming of the TRANSCode solver was also apparent later on for the 3D predictions of the datum and 3D DERA low speed

blading. Different numbers of grid points in the clearance gap were tried along with various tip shapes to try to improve the predictions at the clearance end. Increasing the number of points in the gap had little effect while decreasing the clearance or squaring-off the tip had the effect of increasing the size of the total pressure loss core and moving it closer to the wake losses.

Figure 4.6 shows the NEB1D TRANSCode solution for the rotor and compares the exit radial profiles of relative swirl angle and total pressure with the experimental throughflow results. The swirl angle results show very good agreement with the test data, especially at mid-height where the differences are only around 0.25°. This small under-prediction of deviation compares to a 1° over-prediction for the stator and does not suggest that a systematic correction to deviation angles should have to be applied when using the code for design purposes[1].

The total pressure levels in the contour plot and radial profile at rotor exit show a similar trend in tip clearance flow prediction to that of the stator. The loss core associated with the clearance vortex is not well defined and is smeared across the passage, and the tip losses appear greater than in the experiment.

4.4 Aerodynamic low speed modelling

The principle of low speed modelling is to produce aerodynamically similar blades operating under equivalent boundary conditions to their high speed counterparts. Keuthe and Chow (1976) and Liepmann and Roshko (1957) show that 2-D geometrically similar isolated bodies that move through a fluid with equal non-dimensional aerodynamic parameters (*ie* Reynolds and Mach Number) experience equal dimensionless forces. When the Mach number of the two bodies differ, the angle of attack, camber and thickness have to be modified to maintain aerodynamic similarity. This modification takes the form of a simple transformation when the bodies considered are isolated airfoils. This transformation comes from the combination of Gothert's rule with the incompressible similarity law of linearised perturbation theory (Shapiro, 1953) and states simply that the camber, thickness and angle of attack of the incompressible airfoil be increased by the factor $(1-M^2_\infty)^{1/2}$ where M_∞ represents the freestream Mach number.

For turbomachinery flows this transformation is inadequate since the bodies are three dimensional, are in an annular cascade and experience both steady and unsteady

---

[1] It was therefore difficult to foresee (due to the differences between the rotor and stator deviations error) the over-prediction of stator deviation in the datum DERA design which lead to an increase in work over the target level (see chapter 7 for a discussion on the datum design overall performance). Although with hindsight the DERA1 rotor and stator predicted deviation errors were fairly consistent with the NEB1D stage.

blade row interaction effects. Many other parameters such as blade aspect ratio. solidity, axial-gap/chord ratio and blade row number ratios also have an influence. However, the rule tells us to expect thicker, more cambered profiles for the low Mach number blades and a different level of incidence. Ideally the blades would also have the same Reynolds number, scaled surface roughness and be tested in fluid of the same turbulence intensity. The boundary layer momentum integral equation shows that Mach number will have an effect on boundary layer development but this is expected to be small compared to the velocity and pressure gradients.

The present work is restricted, for simplicity and cost, to a parallel annulus (hence essentially constant axial velocity) and geometrically identical blade rows. This restriction introduces problems because for the high speed compressor Va/U reduces across the fourth stage. Exact equivalence between low and high speed cannot be maintained and some compromise must be accepted. In the present work, the low speed blading was designed for the same $\Delta H/U^2$ across the rotor and Va/U at inlet to the rotor. A consequence of this is that the de Haller numbers (blade exit-to-inlet velocity ratios) are not maintained[2]. However, the blade sections were designed to produce the same distribution of local to trailing-edge-velocity distribution so that blade local diffusion is maintained.

The Reynolds number based on rotor chord turned out at about 3×10^5 and is unavoidably lower than the high speed value of 1.1×10^6. This is due to the physical and mechanical constraints of the Cranfield rig. The situation could have been improved by increasing the chord of the blades but there were practical constraints on this, and it would have also been at the expense of maintaining blade aspect ratio and possibly axial-gap/chord ratio. Schäffler (1979) shows the degradation in axial compressor performance becomes more significant as Reynolds numbers fall below ~ $2\text{-}3 \times 10^5$ and at 3×10^5 the degradation could produce a 1% fall in efficiency. Thus the Reynolds number achieved, while not ideal, was considered acceptable.

4.5 Blade design

4.5.1 High speed stage

The compressor used as the high speed reference for this work was the third build of the DERA five stage research compressor C147. The first build had four stages and conventional blading, mainly with double circular arc (DCA) profiles. This build exceeded its design pressure ratio of 4.0 and achieved a peak polytropic efficiency at design speed of 89% (Calvert et al 1989). The second build incorporated

---

[2] However the higher than intended level of work achieved on test resulted in De Haller numbers close to high speed values

a complete new set of blading with controlled diffusion (CD) profiles, a constant α_o (~12.5°) and an extra zero stage (Ginder 1991). This demonstrated a 1½ % efficiency improvement over the first build. The third build used the same blade design as the second build but had increased blade numbers to improve the surge margin. All designs had cantilevered stators.

The choice of which high speed stage to model is restricted to some extent by fundamental limitations of the low speed modelling procedure. For example, if a blade is to be designed to produce a prescribed velocity distribution, it follows that the distribution must be both smooth and continuous. This rules out the modelling of stages where significant shock waves are present and therefore limits the study to the rear stages of a HP compressor.

The fourth stage of C147 Build 3 (operating at peak efficiency) was modelled in the low speed compressor, because this stage is embedded, subsonic, unlike the earlier stages, and has good test measurement coverage at entry and exit. These measurements include radial traverses (behind the rotors) and area traverses (behind the stators) using both steady state and high-frequency response pressure probes. The measurements were facilitated by having abnormally large axial gaps between the blade rows and this feature is maintained in the low speed design. Figure 4.7 shows the layout of the C147 compressor and the aerodynamic and geometric parameters for the fourth stage are listed in Table 4.1. Where two values of any parameter are given, these correspond to stage inlet and outlet.

4.5.2 Design methodology

The method adopted for the low-speed design follows the same principle as that used in the original high speed design, namely an axisymmetric quasi-3D S1-S2 approach which iterates between two basically 2D methods for the blade-to-blade and throughflow planes. Ideally the same design system would be used for both high and low speed compressors to ensure full consistency of approach. The original design used the DERA S1-S2 system (Calvert and Ginder, 1985) which incorporates the S1BYL2 inviscid-viscous time-marching solver for the blade-to-blade calculation and the SC90 (Dunham et al, 1990) streamline curvature code for the throughflow. As described in 4.3 an alternative blade-to-blade code was used, which was a version of the existing Navier-Stokes flow solver TRANSCode (Calvert et al, 1997) modified to run at low speed.

TRANSCode uses a Baldwin-Lomax turbulence model and can be run for quasi-3D or fully 3D geometries. It was run with a fully turbulent boundary layer as opposed to S1BYL2 which calculates boundary layer transition. For the design work, seven sections, each at constant radius, were chosen to define both the rotor and stator.

Quasi-3D calculations were carried out on grids of 41 pitchwise x 135 axial points and were typically run to 1200 time steps producing convergence of about three orders of magnitude on axial-momentum residuals. For the later fully 3D calculations used to analyse the design, the sheared H mesh employed in the code is extended around the clearance end of the blade using a simple pinched tip model which produces a highly skewed grid in the overtip region. The 3D calculations were carried out on grids of 41 x 135 x 41 and run for 2500 time steps giving similar convergence to the quasi-3D calculations.

SC92H (Dunham, 1994) was used for the design throughflow calculation since this has been validated against low speed data. This incorporates endwall effects and spanwise mixing modelling. The losses and blockage due to 3D overtip and endwall effects are calculated within the code, eliminating the need for the imposed endwall loss coefficients or blockage factors used in SC90.

The design method flowchart is illustrated in figure 4.8. An initial throughflow calculation was carried out on the LSRC annulus using blade positions scaled from the high speed stage and guessed profile losses. The radial profiles of work and stator exit flow angle were also input into the calculation. The calculation provides a radial distribution of flow angle and stream tube thickness at inlet and exit to each blade row. The seven blade-to-blade solutions for each blade-row are calculated using preliminary blade shapes and these are then modified to achieve the target normalised velocity distributions calculated for the high speed stage. The iteration is continued until the normalised velocity distributions are acceptable, the outlet flow angles agree with the throughflow results to within 0.1° and the profile losses are consistent.

Finally the sections are stacked radially on their centroids and the blade shape is checked for radial smoothness. This is most easily achieved by ensuring the blade section definition parameters vary smoothly. The sections defining the smoothed blade are re-run to check that the normalised velocity distributions and outlet flow angle are still acceptable.

4.5.3 Throughflow calculation

Figure 4.9 shows the results for the third stage from the throughflow calculation. The figure shows the C147 curves (SC90) and the results from the SC92H calculation. The SC90 results are derived from an S1-S2 calculation having small corrections to S1BYL2 deviations to align the overall pressure ratio with prediction (Ginder, 1991). The SC92H solution calculates the 3D endwall effects and adds these to the inviscid solution. The results have been used without these 3D effects to give an essentially 2D design comparable with the high-speed case. These 2D results are also shown on

figure 4.9 to facilitate comparison with the SC90 results. The mass flow for SC92H was adjusted until the rotor inlet Va/U distribution matched the high speed target.

The difference in rotor relative inlet angle between the high and low speed design is due to small discrepancies in α_0 arising from differences in annulus contraction and blockage growth from the preceding stator exit (where values of α_0 were set equal). Generally, the 2D radial variations of flow angle agree well with the high speed results, however, an angle offset is apparent for both blade rows. The rotor has about 3° more turning than the high speed case and the stator about 2° less. This difference is due to the varying Va/U across the high speed stage (due to compressibility, which is also offset to some extent by annulus contraction) and the small difference in α_0 at inlet. Va/U remains fairly constant for the low speed model due to the parallel annulus and negligible density change. A consideration of velocity triangles across a rotor with constant $\Delta H/U^2$ and different levels of Va/U show that different levels of turning are required. The consequence of this is that the rotor has to achieve more turning and the stator less for this particular case.

Fully 3D TRANSCode calculations were also carried out using the inlet conditions from the SC92H solution. The pitchwise averaged results from this calculation are also shown in figure 4.9 for both the rotor and stator exit flow angles. The results show encouraging agreement with SC92H.

4.5.4 Blade-to-blade calculation

A blade geometry generator (described in section 4.6 below) was set up to produce blade shapes with a bi-cubic spline pressure surface and a parabolic arc suction surface. This is the same family of curves as in the original high speed design and gave velocity distributions of a similar shape to the high speed target. Designing the blade sections to match the high speed non-dimensional velocity distributions was a lengthy and time consuming process. The main difficulty is in increasing the peak suction surface velocity sufficiently. This can be achieved by either increasing the amount of turning/camber, increasing incidence/stagger, increasing the thickness or decreasing the number of blades.

Since the inlet and outlet flow angles are effectively fixed by the throughflow calculation the blade designer has a restricted amount of freedom. Increasing camber produces more turning so more stagger is required to match the outlet flow angle. The resulting re-staggered section now operates at lower incidence and therefore lower peak velocity, producing the opposite result. The most useful parameter to change in setting up the design was the solidity. Although ideally this would have been kept at the high-speed value. Changes in solidity were also constrained because the blade

taper ratio was held constant. Typically, hub sections would have required a different change in solidity from the tip sections due to the different turning requirements. In the final design solidity had to be reduced to match the velocity distributions of the high speed stage. This is due, at least in part, to the higher value of de Haller number that resulted from the choice to fix $\Delta H/U^2$ at the high speed value.

After the blade sections were set up and the solidity was nearly finalised then fine tuning of the profiles was achieved by iterating through the cycle of "change-blade-shape, evaluate, re-stagger, re-evaluate". This process is speeded up by learning from a well-matched section and applying to an ill-matched section.

4.6 Blade profile generator

The blades used in the fourth stage of C147 build 3 were defined with a parabolic arc suction surface and a bi-cubic arc pressure surface. Parameters such as point of maximum thickness, wedge and camber angle were used to change the two surfaces and give the designer aerodynamic control over the section. The design parameters used in the fourth stage of C147 build 3 are listed in table 4.2. The advantage of defining a section in this manner is that a complete blade can be defined with only a handful of parameters and the sections are completely defined geometrically, ie interpolation is not required.

Initially the low speed blades were defined using the C147 definition but it quickly became apparent that the considerably thicker low speed sections caused problems for the bi-cubic surface generator for the pressure surface. This surface proved to be extremely sensitive to camber and wedge angle variations, small changes of these often resulted in a large 'bulge' appearing on the pressure surface. To circumvent this problem the pressure surface was set up first with a dummy suction surface using parameters to control the camber, thickness etc. of a dummy section, then the suction surface was replaced with a parabola controlled by another set of parameters. In this way the suction surface could be considerably thickened up independently of the pressure surface geometry.

During the design process extra terms were added to the blade definition program. The initial change was to increase the leading edge thickness to achieve the higher non-dimensional suction surface velocities of the high speed blades. This was done by linearly stretching the suction surface parabola outwards at the leading edge by adding an offset that ramped up toward the leading edge. When the leading edge became thicker the leading edge circle joining the suction and pressure surface became inadequate. Instead, an ellipse was fitted with a controllable aspect ratio and inclination. This gave more control of the leading edge loading and also resulted in a smoother change in curvature at the blend point with the upper and lower surfaces. An

extra term was added later to thicken the trailing edge radii when it became apparent that the sections designed were too thin for manufacturing reasons. The final blade profile generator is illustrated in figure 4.10. The dummy section used to define the pressure surface is shown on the left and the actual suction surface definition on the right.

4.7 Final design

4.7.1 Rotor and stator

The final rotor and stator normalised velocity distributions are shown by the chained lines in figure 4.11. The distributions have been plotted against normalised surface length from the stagnation point. They show good agreement with the C147 velocity distributions (solid lines) over most of the span and chord. Most discrepancy occurs at the leading edge. This is mainly because the thicker low speed blades experience a larger stagnation region at the leading edge and the incidence differs between the high and low speed. For the rotor, discrepancies also occur at the pressure surface trailing edge towards the hub. Here the high speed blades show more diffusion and very 'hooked' trailing edges would have been required in the low speed blades to achieve this.

The radial variation of parameters used to define the rotor and stator are shown in tables 4.3 and 4.4 respectively. The overall design parameters for the low speed design are shown in Table 4.1 along with the equivalent high speed values.

The radial variations of blade and flow inlet angles and blade incidence have been plotted in figure 4.12 for both the low speed and C147 stage. The low speed leading edge blade angle was calculated using the centre line of each section, defined by fitting circles within the section. There are some uncertainties in this calculation towards the thick leading edge and the absolute values calculated may not therefore be significant. Note that the flow angles used are from the '2D' throughflow result and the incidences are therefore '2D' distributions. The incidence varies from -10 to 9 degrees for the low speed rotor and -2 to 1.5 for the high speed rotor. Variations are rather smaller for the stator. The large incidence variation for the low speed cases is due mainly to the metal angle variation rather than the flow angle and is therefore subject to the uncertainties of the leading edge angle calculation.

Figure 4.12 also shows the loss buckets for the high and low speed sections at mid-height for both blade rows and also the hub case for the low speed rotor. These were generated using TRANSCode and S1BYL2 for the low and high speed sections respectively. Because of uncertainties in calculating off-design losses, these results are indicative only, but they do help in interpreting the large differences in incidence. For

the high speed rotor, the loss bucket is higher and narrower than its low speed counterpart due mainly to the effects of Mach number. However. the rotor is operating near the bottom of its loss bucket near zero incidence. In spite of their very different geometric incidences, both sections of the low speed rotor also operate close to minimum loss and hence their incidences appear sensibly chosen. The stator incidence and loss buckets show similar trends to the rotor except that the radial variation of incidence is much less. The narrower loss buckets for the high speed case indicate greater sensitivity to off design incidences than at low speed (whether due to spanwise variations or changes in operating point). This is an accepted limitation of low speed testing.

A boundary layer analysis has been carried out for the low speed blades. the results are shown in figure 4.13. These show similar growth rates for the displacement and momentum thicknesses resulting in the shape factors remaining fairly level along most of the chord length. This is in contrast to the rising shape factors of the high speed blades which arise from the more rapid growth in displacement thickness. However, the high speed results were obtained using S1BYL2 while the low speed results used TRANSCode. Comparison of the boundary layer parameters predicted for the V2 cascade using TRANSCode and S1BYL2, as shown by Stapleton (1997) also show this trend. They show S1BYL2 overpredicting the rise in form factor with TRANSCode predicting form factors very close to experimental values.

The final design is shown fully in figure 4.14 where the stage layout including tip clearances are also shown. Final axial gap/chord ratios vary slightly from the high speed design due to the change in stagger introduced during the detailed design phase and because the true scaled chord was fixed. This is only a minor change and the meridional view shown in the figure closely matches the high speed layout.

Figure 4.15 shows a photograph of the final design low speed rotor and stator along with the corresponding rotor and stator from the fourth stage of C147 build 3. The LSRC blades are cast from aluminium while the C147 blades are machined from titanium.

4.7.2 Inlet guide vane

The inlet guide vane (IGV) was designed to turn the incoming flow to the correct swirl angle for the first stage. The angle used was the design interstage swirl angle α_0. This was used to ensure that the first stage operated at similar inlet conditions to the other three stages and therefore helps the stages to repeat. The radial distribution of swirl was chosen to be constant (ignoring endwall effects) to simplify the design. The previous build of the LSRC used 96 blades for the IGV and so the new

IGV was designed to have this number of blades so that the same annulus outer ring could be used. This saved a significant amount of manufacturing cost and time.

The IGV design used the same blade profile generator as the rotors and stators and had a constant section up the span for simplicity (the target α_0 variation was only ~0.5° across the span). The loading and velocity levels were considerably lower than the rotor and stator due to the lower amount of turning (α_0 = 13.5°). A design point that had not been noticed until the general assembly drawing of the compressor annulus was produced was that the IGV blades were cantilevered over the junction between the stationary bullet and the rotating hub. Since the loading on the IGV's was low this was not considered to be a problem.

4.7.3 Outlet guide vane

Previous builds of the LSRC had used an outlet guide vane (OGV) to straighten the flow to axial before the flow enters the throttle. Since the downstream instrumentation, such as the exit total pressure rakes, are situated at stator 4 exit and the exit whirl angle is fairly low it was decided that OGV's were not necessary for this design. The downstream total pressure rakes were set at 13.5° to the axial so that true total pressure is measured. The existing OGV blade ring was used to save money and aluminium tape was used to cover over the existing blade mounting holes.

4.8 Discussion

The high-to-low speed transformation process is not straight forward and during the design process several key decisions have been made. Compromises have to be made due to both geometric and aerodynamic constraints. For example, the size and power of the rig restrict the Reynolds number that can be achieved. They also influence decisions over which high speed geometric factors are to be reproduced at low speed. For example, reproducing the high speed hub/tip ratio involved increasing the LSRC hub/tip ratio from 0.85 to 0.91. Although this is expensive due to the extra rings that have to be made it allows other geometric factors such as blade aspect ratio to be reproduced. Also, because of the smaller annulus area, the rig was able to run at 1100 rpm without power limitations. This enables the Reynolds Number to be maintained at as high a value as is practical.

The other main design choices were to try to match $\Delta H/U^2$ and Va/U at rotor inlet. A consequence of maintaining the same $\Delta H/U^2$ across the rotor is that the de Haller numbers (blade exit-to-inlet velocity ratios) are not maintained (see footnote 2). However, the blade sections were designed to produce the same distributions of trailing edge velocity so that blade local diffusion is maintained. The decision to match non-dimensional surface velocity distribution was based on previous work on

low speed compressor design and the hope that this approach would result in a boundary layer aerodynamically similar those at high speed. The boundary layer momentum integral equation shows that the effects of Mach number on boundary layer development is small compared to the effect of local velocity and pressure gradients. An alternative approach may be to model the boundary layer directly, in other words design a section keeping the boundary layer non-dimensionals constant. This would be extremely difficult to achieve since problems with transition position and the accuracy of boundary layer models could prove insurmountable and/or produce blade sections with bumps or inflections.

The design method adopted (S1-S2) has not been calibrated although the different elements used, ie SC92H and low speed TRANSCode, have been evaluated on other test cases. The method is similar to the high speed S1-S2 method but the S1 and S2 calculations have not been linked and are run separately after making the appropriate file edits. Full S1-S2 convergence (to the same level as the C147 S1-S2 calculation) is therefore never attained although exit flow angles agree to within 0.1^{o}. This is due partly to the fact that the S1 stream surfaces remain fixed at constant radii.

The normalised velocity distributions compare well with their high speed counterparts but the accuracy of these are subject to the correct flow angle being used in the calculation. In order to quantify the effect of flow angle on the velocity distributions a calculation has been carried out for the mid-height stator section operating at three inlet flow angles. Figure 4.16 shows the results of the study comparing velocity distributions at the datum, $+2^{o}$ and -2° inlet flow angles. They show a 4% variation in peak velocity for each 2° variation in flow angle. Only the first 30% of the blade chord appears affected by the change with the rest of the chord showing almost no difference in normalised velocity. The consequences of a flow angle error, although affecting the design, would not be too serious and the blades could be restaggered to compensate should this be necessary.

4.9 Conclusions

The TRANSCode flow solver has been modified to run at the low Mach numbers found in low speed research compressors by implementing the method of pseudo-compressibility. The modifications were implemented as an alternative running option so that either compressible or incompressible flows can be modelled with the same code.

The implementation of the new option was tested by comparing results with those obtained from the unmodified method applied to the V2 compressor cascade. These comparisons were completed at various Mach numbers and confirm the improved convergence of the low speed method over the original code. Validation work has also been completed on the NEB1D rotor and stator to assess the code's ability to model real

low speed flows by comparing the predictions with low speed test data. Generally the results appear encouraging with good modelling of the mid-height and fixed ends of the blades. Modelling of the clearance ends of both rotor and stator proved to be inadequate and the stator solution was unable to predict the shape and structure of the loss core associated with the clearance vortex.

The stator exit flow angle was over-predicted by about a degree at mid-height while the rotor relative exit swirl angle was under-predicted by about 0.25 degrees. These conflicting results together with the uncertainty associated with experimental test data meant that it was difficult to foresee the error in deviation predicted for the datum DERA design (discussed in chapter 7) which lead to an increased level of work over the design intent.

A low speed blade set has been designed for the Cranfield LSRC representing the fourth stage of C147 build 3. The design has focused closely on the high-to-low speed transformation process with a view to evaluating such a process through low speed testing. The approach used was a manual S1-S2 method which used the low-speed TRANSCode solver to calculate the blade-to-blade flow (S1) and SC92H to calculate the throughflow (S2). This method ensured consistency of approach with the high-speed stage design which used a coupled S1-S2 method employing S1BYL2 and SC90.

A blade geometry generator was coded to facilitate the design process. This used a number of parameters to control the suction surface, pressure surface, leading and trailing edges so that each section shape was easily controlled. The generator used a parabola for the suction surface and a bi-cubic spline for the pressure surface.

The blade sections were designed to match the high speed normalised surface velocity distributions. Good agreement has been achieved for both blade rows and their variation with incidence appears to be small.

The hub/tip ratio of the low speed research compressor at Cranfield has been designed for a 0.91 hub/tip ratio to match that of the high speed stage. The inlet guide vane (IGV) has been designed with 96 blades so that existing hardware can be re-used. Outlet guide vanes (OGV) will not be used since the exit flow angle is low and the OGV ring is downstream of any instrumentation.

The high-to-low speed transformation process has involved compromises due to both geometric and aerodynamic constraints. Geometric constraints include the size and power of the rig which restrict the Reynolds number. Aerodynamically the effects of Mach number on loss buckets and boundary layer limit the extent to which full high-low speed readacross can be achieved.

Chapter 5 - Low-speed compressor and instrumentation

5.1 Introduction

This chapter describes the low speed research compressor (LSRC) based at Cranfield University. The process and nature of the aerodynamic measurements used to assess and quantify both the datum and advanced 3D design performance are described and discussed. The rig was significantly modified for the DERA tests, the most significant change was the increase in hub/tip ratio from 0.85 to 0.91. This involved the procurement of new hub spacer rings along with new blade rings and a new inlet bullet arrangement. The opportunity was taken to improve the intake arrangement so that the intake air is drawn directly from outside the building and a settling chamber was incorporated to reduce inlet flow distortion.

The compressor instrumentation is described and discussed along with methods employed to try to improve measurement accuracy. In addition to the standard instrumentation used for testing, 3D probes were designed and manufactured at Cranfield University. These were successfully used for the first time during the DERA2 test programme. Flow visualisation studies using fluorescent dye were also successfully executed for both DERA1 and DERA2 stator blading.

Details of the experimental results obtained for the datum design along with results from a throughflow analysis using radial profiles from the stationary frame traverse data are presented in chapter 6. Results of the advanced 3D design are reported in chapter 9. Appraisal of the datum design and comparison of the datum test results with CFD and design intent are presented in chapter 7. The appraisal of the 3D design is presented in chapter 10.

5.2 Low speed compressor procurement

5.2.1 Rig arrangement and procurement

The Cranfield low speed research compressor was originally built with a 0.85 hub/tip ratio and extensive re-manufacturing of rings was necessary to bring the hub line up to the 0.91 hub/tip ratio needed for the DERA build. This introduced the need for a new inlet bullet and the opportunity was also taken to improve the intake arrangement which was known to suffer from inlet disturbances.

Figure 5.1 shows sections through the Cranfield rig for the 0.85 hub/tip ratio build and the 0.91 hub/tip ratio (DERA) build. Along with the rotor and stator blade rings which had to be specially made due to the increased blade number count (over previous builds) and raised hub line, new hub spacer rings also had to be made. All the rings have to be

made very accurately since any warping out of plane or ovality will make building the rig difficult and could introduce leakage paths and uneven blade clearance gaps. The casing spacer rings are all ganged together by two diametrically opposing cross bars and a stepper motor drives the rings around circumferentially so that any probes that are mounted in the casing are traversed in unison relative to the stators. Movement of the second stage stator relative to the others is also possible, this feature was designed into the rig during the DERA procurement phase but was not used during testing; tests were completed with stator 2 aligned with the other stators.

The rig also benefits from a rotating frame traverse mechanism which is built into the hub. This mechanism allows for rotor relative traversing upstream and downstream of the third rotor. While specifying the new hub/tip ratio and blade numbers was the responsibility of the author, the modified rig design and procurement was Cranfield's responsibility. The rig procurement process lasted for around five months and problems with warped rings caused delay to the programme when some rings had to be returned to the manufacturers for improvement.

Figure 5.2 shows the new inlet bullet and outer flare arrangement for the DERA build. The previous build had used a mirror image of the same profile for both the inner and outer flares and both were made from fibreglass. The new arrangement incorporated an inner bullet based on an earlier unused Cranfield design and a smaller scroll outer flare. Both components were made from perspex for improved rigidity and trueness of form. The new bullet extended further upstream than the previous intake and a new intake cover was necessary. The second photo in figure 5.2 shows this intake cover in position over the inlet bullet. The cover consists of two cylindrical sections that are rolled into position on castors and clamped to each other and to the back plate by G-clamps. The first section is simply a cylinder which covers the large inner bullet while the second section has gauze material at either end of it and acts as a settling chamber. The increased length of the whole assembly allows the intake plane of the second section to be just outside of the test room so that air is drawn directly from the outside. The new intake arrangement was found to be more aerodynamically stable than the previous arrangement and it was easier to set the compressor up on flow condition due to the reduction of outside flow disturbances.

5.2.2 Blading procurement

All the blading used in this project was made from cast aluminum by R D Castings Ltd. In the aerodynamic design each blade was defined at seven sections up the span. Further sections were interpolated and extrapolated into the endwalls producing 23 sections defined by x,y,z co-ordinates; these data were sent to the drawing office at Pyestock. The data were read into the PRO Engineer CAD package and 3D surface definitions were

generated. The end boss was then added to the blade along with details for cropping the blade to the correct height. There were some difficulties with the surface generation early on when repeat points were included in the definition at the leading and trailing edges. These repeats caused the surface spline to form a cusp. The problem disappeared when the repeat points were taken out of the data set.

Figure 5.3 shows the layout of a rotor blade including the endboss arrangement. 10:1 drawings were produced of the sections shown in the figure, these were printed out on acetate and five of them were used for the shadowgraph inspection. The drawing office calculated the angle-setting-jig contact points on the pressure surface and the angle that they make with the circumferential direction. The drawing office also produced the CAD data for the diecutters who then generated the cutter path data for the dies. The die was made from a blade die and a separate endboss die. The blade die was made in two sections; a suction surface half and a pressure surface half with a join at the leading and trailing edges. The join created flashing at the leading and trailing edges during the casting process that had to be removed by hand. This hand finishing process is carried out by rubbing used emery cloth over the leading and trailing edges. It was not performed adequately on the first batch of blades that were inspected (due to a fear of creating a flat at the leading edge) and they had to be sent back for further finishing. After casting, each blade is bolted to a jig at the correct setting angle and a cutter is passed over their ends in a radial arc to crop the blade to the correct height. For the stators an internal radius was machined at the clearance end.

A batch of five blades was cast for each blade type (not including the IGV) and thin slices were wire-eroded from them at different heights. These sections were then inspected on a shadowgraph and compared to 10:1 section drawings. The inspection was carried out at AQA premises in Shefford by R D Castings with DERA and Cranfield personnel present. The tolerance criteria used was the same as for the C147 build 3 blades; 0 to +0.08mm over both blade surfaces, reducing to 0 to +0.05 mm at the leading and trailing edges. Apart from a few points at some heights where the section became too thick at the trailing edge and too short at the leading edge the overall comparison was good for the datum DERA1 blades. For the DERA2 blades the quality was even better with most of the sections lying on the line of the 10:1 drawing over most of the chord. Spot checks were also made on complete blades to check for radial stacking accuracy.

The blades were mounted into the rings and set to the correct angle using specially made jigs. The blades are sealed to their fixed endwall using silicon sealant so that there are no gaps under the fixed ends of the blades. Also the end pennies are reasonably flush with the endwalls. After the DERA1 build a sample of blades from the IGV, rotor and stator were inspected for setting angle by an independent inspection team from DERA. The same

team inspected the DERA2 blades before the rings were built into the module and noticed a consistent setting angle discrepancy with the stators. It was found that the jig had been damaged and had opened up by about one degree. A new jig was manufactured and the blades were removed and re-positioned using the new jig.

5.3 Instrumentation description

5.3.1 Overall Performance

The overall performance of the rig is measured by eight total pressure rakes at inlet, four at outlet, a torquemeter, two NPL probes mounted in the calibrated bellmouth and an array of static pressure tappings in the same plane as the NPL probes. Sixteen new total pressure rakes were made for the DERA programme to accommodate the smaller passage height produced by the 0.91 hub/tip ratio. Figure 5.4 shows a photo of a rake; each contains twelve total pressure ports which are more closely spaced towards the endwalls. The rake design was based on previous Cranfield rakes and they were set axially at inlet and at 12° at exit (to approximate the stator exit swirl). The original aim was to have eight rakes at inlet and exit verniered relative to their closest stationary bladerow so that good coverage of the machine was achieved (previous builds used four rakes). The ring holding the rake instrumentation moves circumferentially with the traverse rings and it is known from previous tests that the relative position of the rakes can significantly affect the overall performance measured. This effect is discussed in more detail in chapter 6.

Although all the rakes were made and fitted, there were only enough spare Scanivalve channels to plumb up half the ports. In addition, owing to an oversight, the rakes were not verniered relative to their upstream stator passage. It was decided that only six of the ports on all eight rakes would be plumbed at inlet so that any circumferential inlet distortion would be averaged out and twelve of the ports on only four rakes at exit would be plumbed so that better coverage of the exit boundary layer be obtained.

The signal from the torquemeter is amplified and passed through slip rings and into the control room where it is sampled 50 times and an average obtained. This is carried out 48 times during an instrumentation scan at a given operating point and the final value is found from the average of these averages. Problems with the torquemeter signal occurred during the second half of the datum build tests and for all the 3D design (DERA2) tests when the signal behaved erratically and contained a significant level of noise. During the datum tests this noise was attributed to drive motor problems; the voltage supply to the motor was noisy and it was thought that this could cause the torque output to jump about. A low pass filter was used and this helped to improve the measured signal. A tare torque measurement was not obtained during testing due to time constraints. Instead a tare torque

was derived using a measurement from an earlier build with a 0.85 hub/tip ratio and using a correlation to correct for hub/tip ratio.

The mass flow measurement is made by finding the mid-height inlet dynamic head at a plane in the inlet duct and applying a discharge coefficient calculated from a detailed radial traverse at the measurement plane. The density is calculated from the atmospheric pressure and temperature measurements and the flow is assumed to be incompressible. The measurement of inlet dynamic head is made by measuring the pressure difference between the two NPL probes (which are plumbed together) and five evenly spaced inner wall statics and five outer wall statics (also all plumbed together). The advantage of this is that an average inlet dynamic head is measured. However, if one port is leaking this will change the overall reading in a manner that may be difficult to detect. The atmospheric temperature measurement is made using a thermopile of 6 thermocouples evenly spread over the inlet gauze and referenced to a junction in an ice bucket.

5.3.2 Blade surface static pressure measurements

Figure 5.5 shows two of the surface static instrumented datum blades with static pressure tappings at 50 % height on the suction and pressure surfaces respectively. Also shown is a pair of instrumented 3D (DERA2) blades mounted on a ring and positioned with their instrumentation facing each other, the position of the inlaid tubing of the nearest full blade is clearly visible although the ports on the pressure side of the opposite blade are more difficult to discern. Blades were instrumented at seven radial heights with 15 tappings on the suction surface and 8 or 3 on the pressure surface. Due to the limited number of Scanivalve channels available four of the heights on the pressure surface were instrumented with 3 tappings only and these were placed near the leading edge. These were used to get an indication of the operating incidence at these heights. The full blade instrumentation schedule is shown for the rotor in figure 5.6. The stators were instrumented in a similar manner at the same percentage heights and chord positions. The same instrumentation scheme was used for both the datum and 3D builds.

Blades were generally paired up so that a blade instrumented at say 50% height on the suction surface was positioned next to a blade instrumented at 50% height on the pressure surface so that the instrumentation faced each other and measured flow conditions of the same passage. The reference ports on the suction surface blade were used to reference both the suction surface and pressure surface data. The paired instrumented blades were spread over the circumference of the stator 3 and rotor 3 bladerows and the reference ports used to correct for any circumferential variation in pressure so that the results could be combined to produce pressure variations for a single blade. Details of the instrumented blading is documented in the instrumentation schedule. The rotor static

pressure measurements were made using a rotating Scanivalve mounted close to the centre line. The effect of rotation on the pressure measurements were corrected for using the rotational speed measurement and knowing the effective radius of the instrumentation.

5.3.3 Stationary frame area traversing

Stationary frame area traversing was undertaken on a grid of 21 radial by 60 circumferential points (covering 7.5° of the circumference or 2.79 stator passages). The radial height spacing was reduced close to the endwalls to improve resolution of the endwall flow but the circumferential grid spacing was kept constant for simplicity and because it would be difficult to determine where the wakes would be before testing. Two traverse sets were measured for each flow condition so that all nine axial locations could be recorded. The data acquisition software used at Cranfield (RICARDA) allows for up to six traverse probes to be recorded in any one sweep so the second set allowed the other three locations and repeats to be measured. The traverse rings in which the probes are mounted are all connected together and driven by a large stepper motor. Before a sweep each probe is set manually to the correct radial height and yaw angle (determined by the design calculation and repeated if measured probe incidence is outside ±5° tolerance) and the rings are driven to the start position. A sweep of sixty points takes about an hour including the probe setup times (this is approximately 1 minute per point due mainly to scanning time of all channels and settling time). This means that a full area traverse of 21 sweeps takes around twenty one hours (or more when breaks are taken into account) and one traverse set usually takes a few working days to complete.

In previous test series the probe angle was set for each sweep by holding a digital inclinometer against the probe holding cradle of the actuator mechanism. This proved to be inaccurate when the axis of the probe was significantly away from the horizontal. A series of measurements were made using a dividing head to mimic the probe inclination. After the inclinometer method was proved to be too unreliable, a mechanical protractor mechanism was devised for each of the probe cradles. The protractor comprised a large metal semi circular plate with one degree intervals etched on to it. The plate was bolted to the outer cradle and a large pointer was attached to the inner cradle that rotates with the probe. The pointer is zeroed before use by locking the cradle in the datum position using the locating pin between the inner and outer cradles. It is estimated that the mechanism should be capable of setting the probe angle consistently to an accuracy of better than ±0.1°.

5.3.4 2D and 3D traverse probes

The traverse probes used throughout the DERA work were all steady state pneumatic cobra probes. These were mainly 2D three hole probes, however two 3D probes were also designed and used for the DERA2 test measurements to complement the 2D probe

measurements. These are both shown in the photograph in figure 5.7. The 2D probes comprise three hypodermic tubes running through the stem of the probe and bent through 90° in a swan-necked shape so that the head of the probe lies within the envelope of the stem. The side ports are chamfered back at 45° to the plane of the central pitot port. The 3D probe uses basically the same design but has a fourth port directly above the pitot port and this is chamfered back at 45° in the vertical plane. The 3D probes were particularly difficult to make due to their small size and limited turning space available for the extra port. One major concern with the basic design was that the fourth port would be so close to the stem that the port reading may be influenced by stagnant fluid at the stem and make it less sensitive to pitch variations. The first 3D probes that were made at Cranfield suffered from a misalignment of the side ports, highlighting the technical difficulty of making the probes. A second attempt was made which were visibly much better and the tunnel calibrations confirmed that they behaved sensibly.

Figures 5.8 and 5.9 show the calibration maps for the 2D and 3D probes respectively, the coefficients are defined in Appendix D. Variations in total pressure coefficient, yaw coefficient and static pressure coefficient are shown for variations in yaw angle at zero pitch for the six 2D probes in figure 5.8. Figure 5.9 shows the same variations for the 3D probe C010 at 7 pitch angles along with the variation of pitch coefficient with pitch angle at the various calibrated yaw angles. Calibrations are carried out manually in a low speed wind tunnel using an inclined manometer to measure the port pressures. Each probe is positioned in its respective cradle and mounted in the tunnel. The probe is rotated until the side port readings agree, then the probe is locked into position for the calibration and throughout testing. Originally the 2D probe coefficients suffered from steps in level near the zero yaw position which were particularly noticeable in the total pressure coefficient curves. This was traced to a lack of resolution in the measurement of the raw pressure data. The inclined manometer was set to 45° and read to the nearest 1mm of water. This was improved by inclining the manometer to 60° and rounding the reading to the nearest 0.5mm. This is a difficult measurement because the pressure levels often fluctuate slightly and the calibrations were hard to repeat consistently.

For the 3D probes a special adapter was fitted to the wind tunnel to allow the probe to be pitched at -15°, -10°, -5°, 0°, +5°, +10° and +15° . The 3D calibration was applied to the raw measured data through a simple iterative program written by the author. The program takes advantage of the two-dimensional surface B-spline lookup routine BSINTERP which comes with the PV-Wave Advantage programming language. A two-dimensional tensor product B-spline is found for each coefficient at the start of the program and the lookup routine SPVALUE is used to apply the spline to find the value of the coefficient for a given pitch and yaw angle. Initial values for the yaw, pitch, total and static

pressure are found and then the yaw coefficient (Cyaw) is found from the measured data. The yaw angle that this Cyaw and pitch angle corresponds to is then found and then the pitch angle that this new yaw angle and Cyaw corresponds to is found. This inner loop is iterated until the yaw and pitch angles converge and then the corresponding total and static pressure coefficients are found. From these, new values of total and static pressure are calculated, Cyaw is updated and the whole process continues until certain convergence criteria are met.

5.3.5 Rotating frame traversing

The rotating frame traverse mechanism enables two probes to be traversed at rotor 3 inlet and exit over approximately 1.7 rotor pitches (~6°) using a grid of 21 radial by 49 pitchwise points. The mechanism has been designed so that when one probe retracts the other probe moves out to a higher radius. The probes are located 180° apart and each probe has a counter weight that moves in the opposite direction to maintain the balance of the drum. The traverse planes are in the same axial plane as the stationary traverses at stator 2 and rotor 3 exit. This means that stationary probes have to be fully retracted before starting a rotating traverse and also the traversing has to be completed separately for the two probes since the drive mechanism pulls one probe well into the hub when the other is out near the casing.

The pressures from the probes are measured by a rotating Scanivalve head and the signals are passed through a slipring located in the inlet bullet. The main problems encountered with the rotating traverse work arose from the sliprings and the lack of feedback in controlling the probe position. The sliprings would produce spurious signals after completing about three sweeps and this could usually be cured by stopping the rig and blowing out the rings with an air line. At some points during a sweep the probe did not move on to the next point when the signal to move was sent. This means that a repeat measurement is made at the same grid point and creates a kink in the traverse results since it is often unknown where the stop occurred. When this occurs in the radial movement an entire sweep can be unintentionally repeated at the same probe height. At the end of the traverse the sweeps are checked for quality and individual sweeps are repeated until a good data set is obtained.

The backlash present in the drive mechanism causes problems in setting the start position for a sweep since the amount of backlash changes from when the rig is stationary to when it is rotating at full speed. A stroboscope is therefore used to view the probe through the perspex rotor window and the probe is driven past and then back to a scribed line on the hub endwall. This process can also be hit and miss due to the viewing difficulties and can produce wiggles in the traverse data due to offsets in the start positions

of sweeps. The rotating probes are nulled in-situ before the rig is fully built up by using a DISA calibrating nozzle which is clamped into an axial position in front of each probe and blows air over the head of the probe. The probe is nulled by rotating the stem until the two side ports are equalised. This procedure is repeated when the rig is stripped down at the end of testing to check that the probe has not slipped.

The pressure measurements are corrected for centrifugal effects, as for the rotor surface static pressure measurements. The rotating frame traverse measurements could be speeded up significantly by having encoders on the traverse actuators. This would improve the positional accuracy of the traverse grid and reduce the need to repeat sweeps due to the probe being at the wrong position.

5.3.6 Flow visualisation

The flow visualisation is carried out on a removable cassette that holds a pair of stators located at stator 3. The experiment is carried out at the end of the test programme in case the oil based fluorescent dye blocks downstream instrumentation ports. A sample of fluorescent dye was obtained from John Bolger of Rolls Royce and was mixed with some Tellus oil until the correct consistency was achieved. Three colours were employed, red on the suction surface, green/yellow on the casing endwall and blue on the suction surface. Before the dye is painted on, the cassette is removed, cleaned, sprayed with primer and finally given a coat of black paint. It proved important to remove as much of the excess silicon used to seal under the fixed end of the blades as possible (although under platform sealing was not affected). The silicon surface repelled the oil from it and on the initial test oil migrated rapidly from the endwalls after only a few seconds of being painted on. The paint was used mainly to act as a base to support the oil but also produced a good neutral background for the photographs.

After the cassette was painted it was inserted into the rig and the rig run up to condition without delay. The rig was held on condition for around twenty minutes (about ten minutes was used during the datum measurements due to a motor problem) and then the rig was stopped, the cassette removed and photographed in a dark room. This process was repeated for each condition (high flow condition was not achieved for the datum build due to the drive motor failing).

5.4 Conclusions

The Cranfield University research compressor facility has been significantly modified for the DERA tests. The most significant change was the increase in hub/tip ratio from 0.85 to 0.91 and the alterations that had to be made to accommodate this. The procurement of new hub spacer rings along with new blade rings and a new inlet bullet

arrangement was necessary. The opportunity was taken to improve the intake arrangement so that the intake air is drawn directly from outside the building and a settling chamber was incorporated to reduce inlet flow distortion. This intake arrangement proved to be successful in producing a clean steady inlet flow, enabling the compressor to be readily setup on flow condition.

The compressor instrumentation and measurement methods have also been improved. These include improvements to the method of setting the probe angles, improving the resolution of the probe calibration data and improving the measurement of overall total pressure rise through increased rake coverage. The probe setting angle arrangement was improved by incorporating a large pointer and protractor at each probe cradle and the calibration data resolution was improved by inclining the manometer to 30°.

In addition to the standard instrumentation used for testing, 3D probes were designed and manufactured at Cranfield University. These were successfully used for the first time during the DERA2 test programme. Flow visualisation studies using fluorescent dye were also successfully executed for both DERA1 and DERA2 stator blading.

Chapter 6 - Datum design aerodynamic measurements

6.1 Introduction

This chapter describes the aerodynamic measurements made on the datum (DERA1) build of the Cranfield low speed research compressor. Experimental results from overall performance instrumentation, stationary frame area traverses, rotating frame area traverses, blade surface static pressure measurements at stage 3 and flow visualisation results are presented. In addition a throughflow analysis has been completed at each of the three test flow points using radial profiles derived from the stationary frame traverse data.

Appraisal of the datum design performance and comparison with the high speed stage and CFD results are presented in chapter 7. Results of the advanced 3D design are reported in chapter 9.

6.2 Overall performance

Testing of the datum build was interrupted in the middle of the test programme to accommodate the urgent test of a Rolls-Royce design. The datum build was therefore tested in two phases nominated part 1a and part 1b. Overall performance characteristics were measured before and after traversing during the 1a measurements and a total of five characteristics were taken with very good agreement between all of them. The first three (for clarity) of these are shown in figure 6.1 where Va/U (bulk mean Va and mid-height U) has been plotted against pressure rise, $\Delta H/U^2$ and efficiency. A probe sweep at mid-height to rotor 3 inlet was used to determine how the local Va/U at entry to the study stage differed from the bulk Va/U measured for characteristics, the design flow of 0.6 into the third stage corresponded to 0.588 at compressor inlet. The choice of the design point flow coefficient is discussed in more detail in chapter 7. The efficiency reaches a peak of around 88% at a flow coefficient slightly higher than design. This implies that the blades are operating at a slightly higher incidence than optimum. The left hand limit is determined by the onset of rotating stall which is clearly audible to the test operator.

The design point $\Delta H/U^2$ is also shown (by the square symbol in the figure) and this shows that the work is around 10% higher than intended. This higher than expected level of work in the low speed compressor is due to a number of reasons, these are; the choice of design flow point, inadequacies in the SC92H design calculation and some deviation error in the TRANSCode blade-to-blade design calculations. These are discussed in more detail in chapter 7.

During the part 1b phase of the datum build measurements the torquemeter reading suffered from noise and some inconsistent readings. The limited motor life restricted the

time available for investigation and a number of better performance measurements were obtained at the end of the test series at design flow with the instrumentation stepped across a stator pitch. These are also shown in the figure as the 'totem pole' at design flow. While the indicated performance at the instrumentation set point (the circumferential location where characteristic measurements are made) is higher than that indicated in the part 1a measurements the performance range is close to the earlier data. The figure demonstrates the range of performance that can be measured when the instrumentation is indexed circumferentially. An overall performance difference of nearly 2% was recorded from the worst case to best case. This is due to the limited number of rakes used and because they were not verniered relative to their closest stationary row so that a true representation of the inlet and exit flow field was not achieved.

Figure 6.2 shows the results of a study of this effect using data from an area traverse at stator 4 exit taken during the part 1b phase. The positions of the four downstream rakes relative to their respective upstream stator passage were calculated and total pressure data was interpolated from the stator 4 traverse at these relative positions onto the rake ports. The overall performance was then calculated based on this imaginary rake measurement and the rakes were stepped around to make another reading until a whole stator pitch was covered. The first figure shows the relative positions of the rakes showing that they are grouped fairly closely in pairs. This grouping produces the two distinct drops in pressure ratio and efficiency shown in the other two figures of 6.2. The performance variation predicted from this study is of the order of 1.5% which agrees fairly closely with measured characteristic performance.

The implication for any back-to-back comparison with another design is that any measured performance difference could be due in part to the repositioning of wakes relative to instrumentation. This could easily occur in bowed blades where midspan sections have moved circumferentially relative to the mounting boss when compared to straight datum blades. An instrumentation sweep was carried out for the 3D design performance measurements to add confidence to the indicated performance improvement shown by the standard performance measurements.

6.3 Blade surface static scans

The blade surface static pressure measurements are shown in figures 6.3 and 6.4 for the rotor and stator respectively. Seven heights up the span were instrumented and these are shown as a column of plots for each of the three flow conditions. The coefficient used is the difference in pressure from an average of the three reference ports normalised by the inlet dynamic head to the compressor.

The difference in pressure between the suction surface and pressure surface at the leading edge is a good indicator of the operating incidence of each section. From high flow to near stall the incidence increases, as would be expected. In addition, the incidence appears to be higher towards the hub of the rotor and towards the casing at the stator. Contour plots of the suction surface for each blade at each operating condition is shown in figure 6.5. The blade surface is represented as a normalised square extending from 0% to 100% chord and from 0% to 100% passage height. The extent of the instrumentation is indicated by the white space surrounding the colour filled contours. The contours for the stator indicate that both ends of the blade operate at a slightly higher load than the mid-span sections (as indicated by the increased peak in suction towards the leading edge). This is trend is seen in the data for all operating conditions. For the rotor data the high flow and design flow data show slightly more loading at the ends although it is less clear than the stator data.

6.4 Stationary frame area traversing

All the stationary frame area traversing for the datum design was completed using the 2D pneumatic probes described in chapter 5. Each traverse was made from a number of sweeps (nominally 21) made over a series of days. Initially the probe angles were set to a constant mid-height value across the span and these were later modified for repeat sweeps at the endwalls where the flow incidence onto the probe was higher than $\pm 5^{o}$. Further repeats were also made where the data was of poor quality. The traverse control files used in the final data sets are shown in table 6.1. Good quality data were not obtained for the near stall condition at 14.68% and 19.17% heights during the part 1a measurements and no high flow data was obtained during the part 1b measurements.

Table 6.2 shows the axial locations the traverse measurements were made for each data set. The data presented in the following figures use mainly results from the part 1a measurements with part 1b measurements used in the axial locations that were not covered. Where repeat measurements were made, for example at stator 3 exit, the agreement between the part 1a and part 1b measurements was good.

Figures 6.6 to 6.8 show area contour plots of total pressure coefficient (defined as {Pt-Pswall}/{Ptave-Pswall} where Pswall is wall static and Ptave is mass average of Pt) for the design, near stall and high flow conditions respectively. The rotor results are shown in the left hand column and the stators on the right; the stages run from first stage at the top to fourth stage at the bottom. The rotor rotates from left to right and the view is looking upstream so that flow to the right of the stator wakes is from the suction surface and flow to the left from the pressure surface. All the stators are axially in line as are all the stator exit

probes. Probes at rotor exit were positioned in line on the starboard side while the stator exit probes were positioned on the port side of the compressor.

The contours at rotor exit show that there is a strong circumferential non-uniformity in the flow field at exit from all the measured rotors. This could be due in part to the wake structure from the upstream stationary blade row persisting through the rotor row. However, a close look at the rotor 1 exit flow field reveals that the wavelength of the circumferential variation towards the hub is the same as those at rotor 2 and rotor 3 exit and corresponds to the stator pitch. The only stationary blade row upstream of rotor 1 is the IGV and this is significantly further upstream (approx 3 rotor chords) and has 96 blades whereas the stator rows have 134 blades. The circumferential variation towards the casing at rotor 1, however, looks more like the IGV exit wavelength. The circumferential variation in total pressure seen towards the hub at rotor 1 exit could therefore be the result of a potential interaction between rotor 1 and stator 1. The circulation around the rotor waxes and wanes as it passes the downstream stationary pressure field even though this is over half a chord downstream. This is probably amplified by a flow separation at the rotor hub which could be more sensitive to load variations than at the top half of the blade where predominantly IGV wavelengths are seen. For the subsequent rotor rows the circumferential variation due to the potential interaction is probably reinforced by the upstream stationary row wakes persisting through the rotor though it is difficult to speculate the relative influence of these two effects without using a fully unsteady 3D calculation. A mid-height unsteady calculation is described in chapter 7 and this estimates that approximately 65% of the circumferential variations downstream of an embedded rotor can be attributed to the upstream stator and 35% to the downstream stator.

The circumferential variation in total pressure at exit from the rotors enters the stators and convects through the mid-passage region becoming a strong feature of the stator exit flow field. The off-design measurements shown in figures 6.7 and 6.8 show how the circumferential position of this flow feature relative to the stators varies with operating point. At near stall the higher total pressure region moves towards the pressure surface side of the stator passage and at high flow it moves towards the suction side and is split by the next stator blade.

The relative position of a stator row clocked relative to a downstream stator row can have a measurable effect on performance. Barankiewicz and Hathaway, 1997 show that stator indexing can account for a 0.2% change in efficiency for a four stage low speed research compressor. The circumferential movement of the higher total pressure region with flow condition is therefore likely to have a similar effect and the off-design performance characteristic will therefore be a function of this in addition to the usual influence of incidence on losses.

At design flow the stationary frame traverses downstream of the stators reveal a region of higher wake loss from 65% passage height up towards the casing. This radial distribution of wake thickness is consistent through all four stages and from passage to passage (with the exception of the second wake shown at stator 1 exit which is considerably reduced compared to the other two wakes). At the hub the wake merges with a region of low total pressure that extends some way across the passage from the pressure side of the wake. This loss core is thought to be the clearance vortex from the previous blade that has moved across the passage and reached the wake by the time it has reached the measurement plane which is approximately 32% of the stator chord downstream. Measurements shown in chapter 9 for the 3D design using a four sensor probe support this conclusion. They show velocity vectors in the axial plane which reveal a vortex structure at the same position.

At near stall the stator wakes thicken considerably in the top 40% of the passage indicating that the loading has increased here more than at the lower half of the passage. The wakes at stator 2 exit have increased the most with stator 4 wakes showing considerably less increase. This result is highlighted in the throughflow analysis presented towards the end of this chapter which show the stator 4 losses considerably lower than the other stators and subsequently the fourth stage efficiency is the highest of all the stages at all flow conditions. Close inspection of the clearance vortex structure, discussed in the above paragraph, for the three operating points show that the low total pressure region associated with it moves progressively to the left (away from the pressure side of the passage) with increased flow coefficient. This is most readily viewed at stator 1 exit where the region of low total pressure moves from covering approximately 25% of the passage at near stall to 40% at high flow. The convection trajectory of the clearance vortex therefore moves from right to left across the passage (as viewed in the figures) with increased flow coefficient in a similar manner to the inlet total pressure distortion.

Figure 6.9 show radial profiles of total pressure ratio behind the rotors and stators at design flow, near stall and high flow respectively. The profiles were calculated from pitchwise mass averages of the stationary frame area traverse data. The radial profile at a total pressure ratio of around 1.0 is for the IGV and the following pairs of profiles are for the four stages from front to back. The Z shaped profiles correspond to rotor exit and the profiles immediately to the left of them correspond to their respective stator; the difference between them represents the pressure loss through the stator. Some axial stations were not measured during testing and therefore do not appear in this figure. The pressure drop across stator 2 appears to be larger than for stators 1 and 3 at design flow and near stall. This is reflected in the results of the throughflow analysis, shown later, where stator 2 has the highest pressure loss coefficient distribution. The figure also shows that the rotor hub

endwall boundary layer grows radially as the compressor approaches stall and that all the profiles generally maintain their same shape (ie there is no sudden performance change towards stall).

Absolute yaw angles at rotor and stator exit at near stall, design and high flow are shown in figure 6.10 for all the measured planes. The yaw angle distribution at IGV exit is more uniform (at around 12.5°) than those at stator exit which vary from 10° to over 15°. This will mean that the first rotor operates at a higher incidence than the remaining rotors from 60% towards the casing, and at a lower incidence over the lower half of the annulus. The results at rotor exit show that rotor 1 does less turning and therefore has a greater deviation over the outer half of the annulus than the remaining rotors. However the performance over the inner half of the annulus for rotor 1 is very similar to the other rotors. The rotor loading in this region is therefore generally less affected by decreases in incidence than by increases, this suggests they are operating at the lower right hand corner of their loss buckets. This is supported by the analysis of the loss buckets shown in chapter 4. After the first stage the stages repeat relatively well in terms of both total pressure and yaw angle distribution.

6.5 Rotating frame area traversing

Rotating frame traverses were completed at rotor 3 exit for design flow, near stall and high flow conditions. At rotor 3 inlet a mid height sweep was obtained at design flow after which traversing had to be abandoned due to a persistent drive motor problem. The results from the rotating frame traverse work are shown in figures 6.11 to 6.13 for near stall, design flow and high flow respectively. Contour plots of total pressure coefficient are presented, these have been calculated in a similar manner to the stationary frame results except that the mid-height static pressure (derived from the probe measurements) was used instead of P_{wall} because the effect of the radial pressure gradient changed the coefficients significantly from the stator results. Contour plots of relative flow angle are also shown along with radial profiles of total pressure ratio (ratioed to atmospheric pressure) and relative yaw angle. The view in the contour plots is looking upstream and the rotor rotates from left to right.

From the hub to 50% passage height the rotor wakes are considerably thicker than in the top half of the passage at all flow conditions. At design flow (figure 6.12) the hub endwall boundary layer extends to around 10% of passage height with more of the endwall boundary layer fluid accumulating towards the rotor suction surface. This is due to an overturning of the slower endwall flow moving under the influence of a strong cross-passage pressure gradient. This is highlighted by the relative yaw angle contours towards the hub which indicate that the flow is approaching the axial direction.

Since the traverse plane is approximately 30% chord downstream of the rotor trailing edge it is likely that the large wake loss region centred at around 20% height is the result of a 3D interaction of the suction surface boundary layer with the thick hub endwall flow (ie a corner separation) rather than the result of a 2D blade stall. By the time the flow reaches the traverse plane this 3D corner stall region appears to have moved radially outward from the hub with endwall boundary layer flow beginning to sweep under it. This view is also supported by the measurements obtained at the near stall operating condition.

At the high flow condition (figure 6.13) the blade loading (and therefore also the cross-passage pressure gradient) has reduced and the hub endwall boundary layer fluid is positioned more towards the middle of the blade passage. The angle contours at the endwall show less over-turning than at design flow and the hub endwall boundary layer appears to be thicker and more prominent indicating that less fluid has swept up the suction surface of the adjacent rotor. The high loss region of the rotor wake has reduced in size with less radial extent of the losses (when compared to design flow). At near stall (figure 6.11) the endwall flow shows the opposite of this trend with the hub endwall boundary layer reduced in thickness at the measuring plane and the rotor wake losses increased slightly over the design flow condition.

At the casing the pressure coefficient contours show a region of low total pressure close to the pressure side of the rotor wakes. This feature looks very similar to the clearance vortex measured behind the stators at the hub endwall. At near stall the centre of the low total pressure region is furthest from the nearest rotor wake and gets slightly closer as the flow coefficient is increased. This is in contrast to the stator vortex feature which moves closer to its adjacent wake at lower flows. This unexpected result is possibly explained by the cross-passage pressure gradient having a greater influence on the rotor clearance flow position than for the stator clearance flow. At a low flow coefficient when the blade is highly loaded and the cross-passage pressure gradient is strong the overtip vortex is influenced by an 'overturning' effect similar to endwall boundary layer flows (although it is not necessarily overturned relative to the main flow stream).

6.6 Flow visualisation

Flow visualisation studies were undertaken for the datum design at design flow and near stall flow. These were obtained at the end of the test series when the drive motor was experiencing serious problems. Since motor life was limited the compressor was held on condition for only about seven minutes while the fluorescent paint dried. This was sufficient time for the majority of the blade surface to dry, however the corner stall region remained wet and this caused the runs on the platform seen in the photographs. The motor failed completely at the end of the near stall run so a high flow test was not possible.

Figures 6.14 and 6.15 show photographs of the flow visualisation studies for the design flow and near stall respectively. The suction surface of both blades of the two bladed stator cassette were painted red, the platform green and the pressure sides blue. The circles beneath the stators shown in the platform view are the mounting bosses of the blades. At design flow the green platform dye moves onto the suction surface at approximately 10% chord, it quickly moves 10% height up the span (remembering that the casing is at the platform end so 'up' in the view of the photograph is towards the hub) and remains at this height until 50% chord. Up to this point the green platform paint has pushed away the red suction surface paint and very little mixing of the dyes has occurred perhaps indicating that the flow is attached. From 50% chord to the trailing edge a triangular section of purple colour is observed at the intersection with the platform. The purple colour indicates that the colours have mixed so the turbulence is high and the near surface velocities are low. This region marks the extent of an endwall corner stall and evidence of reverse flow within the region is seen by the blueish colours coming forward from the pressure surface.

Along the trailing edge of the suction surface a strip of deeper purple colour is seen at the last 10% of blade chord away from the corner stall. This is a 2D flow separation where reverse flow within the separation is moving the excess blue pressure surface paint from the trailing edge forward into the separation. At approximately 40% chord a dark band is apparent in the red suction surface paint. This feature is more easily seen in the view of the bottom right hand photo where it is clearly repeatable on both blade surfaces. This is a region of high boundary layer shear stress and it marks the transition from a laminar to a turbulent boundary layer.

On the pressure side a band of dark blue (more evident near stall) from the leading edge to approximately 5% chord is seen extending over most of the blade height. This marks a region of low boundary layer shear stress since the paint has not been scrubbed to the extend of the flow further downstream and is possibly a bubble separation. Further along the pressure surface towards the platform the near surface flow appears to bifurcate. This could be due to a blemish or dirt stuck to the base paint on that particular blade since the adjacent blade shows much less of an effect.

The platform flow shown in the bottom left hand side photograph shows strong evidence for the presence of a horseshoe vortex just ahead of the leading edge. The platform (casing) boundary layer on approach to the blade has vorticity in the pitchwise direction due to its radial velocity gradient. Since the vortex lines cannot be cut by the blade they stretch around the leading edge and their axes turn towards the axial between the blades. The dark lines stretching axially backwards from the leading edge on the pressure side appear to be the loci of these vortex lines. The region of blade just over the tip was

sprayed with black primer but was left unpainted by fluorescent dye. The photographs show how the first 30% of the clearance gap was left clean of dye and the remainder has blue dye swept over it from the pressure surface. On the suction surface near the tip there is evidence of the clearance flow rolling over the tip and interacting with the suction surface flow.

At near stall (figure 6.15) the nature of most of the flow features described above are very similar to the design flow results with the exception of the suction surface-endwall corner stall. At near stall the area of the purple stalled region is much larger and starts at around 30% chord instead of 50% chord for the design flow case. The flow of green dye from the platform to the suction surface ahead of the corner separation has disappeared at near stall. This could be due to the fact that at near stall the endwall blade section operates at a much greater incidence than at design flow so the flow deflection from the cross passage pressure gradient has to be much larger to get the endwall flow onto the blade surface so close to the leading edge. Another distinct difference between the flow visualisation studies at the two flows is at the leading edge on the pressure surface. At near stall the band of dark blue running the length of the blade is much more pronounced than at design flow. This is surprising since the feature appears to be a separation bubble yet it becomes more marked on the pressure surface at higher incidences where the pressure surface leading edge boundary layer loading should be decreased.

6.7 Throughflow analysis

A throughflow analysis has been completed using the experimental traverse data for each of the three flow conditions measured. Mass averaged radial profiles of total pressure and flow angle were calculated from area traverses obtained in the stationary frame. All the pressures were referenced back to a standard ambient pressure and data from missing planes (such as rotor 4 exit) were made up from traverses at similar planes (eg rotor 3 exit) with the pressure levels adjusted to match the overall rise of pressure through the machine. The overall performance of each calculation are shown by the circular symbols in figure 6.16 and are compared with the torquemeter derived characteristics. Further calculations were completed with 0.25° added to the measured angles (subtracted behind rotors so that relative flow angles increased in the same sense as the stationary bladerows) and also with 0.25° subtracted. These are shown on the figure by the H and cross bar symbols respectively.

The pressure ratios for the throughflow calculations all lie below the measured characteristic line and this is due to the sensitivity of the total pressure rakes to their circumferential position as discussed in section 6.2 on overall performance. The performance characteristics use four rakes at exit while the throughflow calculation uses

the stator 4 exit traverse averaged over two stator pitches to obtain the exit conditions. The levels of stage $\Delta H/U^2$ for the design and high flow calculations are very close to the characteristic line obtained from the torquemeter and this is very encouraging for the level of angular accuracy of the traverse measurements. The comparison at near stall is not so good, however, the error bands indicated by the additional calculations show that only a 0.5^o error in measured flow angle is necessary for this difference. The efficiencies for all the throughflow calculations fall below the measured characteristic. This is due mainly to the pressure ratios falling below the rake derived pressure ratio, if better rake coverage could be achieved by plumbing up all the ports and positioning them better then the throughflow efficiency at design and high flow might lie closer to the characteristic measurements.

The bars marked for the $\pm 0.25^o$ calculations show how sensitive the efficiency is to such small changes in measured flow angle. The subsequent change in rotor relative exit flow angle varies from $\pm 0.44^o$ for high flow to $\pm 0.57^o$ for near stall. While it is appreciated that individual errors on some angle measurements may be high and some canceling of errors will occur in a throughflow calculation, since the errors will not all be in the same direction, the angle measurements as a whole indicate a level of work that agrees very closely with the torquemeter.

Detailed results of the throughflow analysis of the experimental data (with no yaw angle change) are presented in figures 6.17a through to 6.19b for the design flow, near stall and high flow conditions respectively. Radial profiles of loss, loading parameters, swirl angle, incidence, deviation and stage efficiency are shown for all four stages using the colour coding shown in the key. The profiles of pressure loss coefficient (PLC) at design flow at rotor exit (figure 6.17a) show a large increase in loss in the first 40% of height for all stages. This feature increases in loss for the near stall data and decreases at high flow in line with the large hub endwall loss region shown earlier in the traverse results.

There is a large variation in stator loss coefficient between the stages, the low value for stator 4 could be due to a poor estimate of rotor 4 pressure levels that were estimated from the pressure rise through the compressor. Rotor 3 exit flow angles were used at rotor 4 and this explains why only three lines are visible on the rotor exit swirl angle plot; the rotor 3 line is under the rotor 4 line.

The losses for rotor 1 are higher than the others at all flow conditions. This is unexpected since the inlet to the first rotor is less turbulent and the indicated incidence over the lower half of the blade is lower than for the other rotors. Also, the profiles of diffusion factor show that rotor 1 is operating at a lower diffusion factor than the other three rotors. The unexpectedly higher loss at rotor 1 is therefore difficult to explain and could be due to

errors in the rotor 1 or IGV exit probe measurements. It may alternatively arise from the fact that rotor 1 is not an embedded rotor and is not obtaining any benefits that may arise from unsteady bladerow interactions of the embedded stages. After the first stage the remaining stages repeat fairly well and a repeating stage pattern appears to have been set up.

The rotor incidence variation at design flow (figure 6.17b) goes from -10° at 75% height to 20° at the hub. Since the calculation of blade leading edge angle is very sensitive for the blunt edges of the DERA LSRC blades the absolute level of incidence is somewhat arbitrary. The issue of incidence and loss buckets are discussed in more detail in chapter 7 where they are compared to the high speed C147 blades. While the level of incidence is somewhat arbitrary the radial variation of incidence shows a significant increase towards the hub for the rotor. This, together with the high diffusion factor and decreasing De Haller number explain why the rotor performance at the hub is so low. The stators, on the other hand have significantly lower levels of incidence variation. The lower diffusion factor and higher De Haller numbers of the stators help explain why the level of deviation measured for the stator is around 2-3° lower than for the rotors (particularly around 20% height). The implication for a 3D design of the datum blading is that there are more gains to made from improving the rotor aerodynamics than the stator, especially in the rotor hub region.

6.8 Conclusions

The datum low speed blades have been manufactured and tests conducted on the Cranfield University low speed research compressor. A comprehensive set of measurements have been obtained which include; overall performance mapping, stationary frame traversing at most planes, rotating frame traversing behind rotor 3, blade surface static pressure measurements at stage 3 and flow visualisation studies. With the exception of the flow visualisation all the measurements were obtained for three flow conditions; near stall, design flow and high flow.

Difficulties arose during the testing from having to split the tests into two parts to accommodate a Rolls-Royce test. Re-establishing the overall performance measured during the first phase was one such difficulty due to problems encountered with the torquemeter signal and persistent drive motor problems.

The overall performance measurements were very repeatable during the first phase of testing and the experimental spread of performance data much lower than has ever been obtained by Cranfield before. The 'totem pole' effect on performance produced by rotating the rake instrumentation is a symptom of a lack of coverage at inlet and exit to the compressor. It is recommended that the rakes be positioned in a vernier manner relative to the stationary blading and that all the eight rakes are plumbed up. This will also benefit

the performance measurement of subsequent 3D designs where circumferential movement of blade sections (ie through lean) could shift the blade losses away (or closer to) rake instrumentation and give a false impression of blade performance changes. Better rake coverage would also benefit the tie-up of the throughflow analysis of test data with the overall performance measurements.

Area traverse and flow visualisation measurements indicate that the stator is suffering from a relatively large thickening of the wake towards the casing. The flow visualisation shows that this is caused by a separation of the near endwall boundary layer due to casing endwall flow sweeping up onto the suction surface.

Rotating frame traverses and results from the throughflow analysis indicate a similar endwall feature is present at the hub of the rotor. This appears to be a significantly larger source of loss than for the stator and the throughflow analysis suggests this is due to (or exacerbated by) an increase in incidence and diffusion at the inner half of the blade.

Chapter 7 - Datum design appraisal

7.1 Introduction

A set of datum low speed blading (DERA1) has been designed to represent an embedded stage from the DERA C147 high speed research compressor. The aim of the design was to undertake a careful high-to-low speed transformation of the geometry of the high speed stage and evaluate the transformation process through comparing detailed flow measurements taken in both the high and low speed environments. The design of this datum blading is described in detail in chapter 5.

The blading has been manufactured and tests have been conducted at Cranfield University's low speed research compressor (LSRC) facility. Details of the LSRC facility and the instrumentation used are described in chapter 6 along with the results from the datum test measurements. This chapter draws on these results and compares them to measurements taken on the C147 high speed research compressor. These show that a good comparison of pressure, flow angle, and endwall loss distributions can be achieved despite the compromises inherent in the transformation process. The overall duty of the datum blading was significantly higher than the design intent and this is investigated and conclusions drawn on the design process.

In addition, 3D TRANSCode calculations have been performed for both the rotor and stator modelled in isolation using traverse measurements for the inlet conditions. These predictions model the endwall corner flow well but further work is needed to obtain better modelling of the clearance flow of both blade rows. These calculations used axisymmetric inlet conditions, further predictions using the full measured non-axisymmetric flow field are also presented. TRANSCode modelling of the high speed C147 stage is also presented and compared to the high speed test and low speed TRANSCode results.

Finally, a 2D unsteady calculation has been undertaken using the un-NEWT flow solver to attempt to understand and quantify the circumferential variations of total pressure that have been measured at rotor exit. Measurements of total pressure behind the first rotor and stator, measured by steady probes in the stationary frame, are compared to time averaged results from the unsteady calculation. Time sequences from the prediction are analysed to study the effect of the stator static pressure field on the rotor performance.

7.2 High-to-low-speed read-across

The high-to-low speed transformation process involves compromises due to both geometric and aerodynamic constraints. Geometric constraints include the parallel annulus of the low speed compressor and also its size and power which restrict the

Reynolds number that can be achieved. Aerodynamically the high speed blades have to be subsonic and the effects of Mach number on loss buckets and boundary layer development limit the extent to which a full high-to-low speed match is possible. The high-to-low speed design decisions and the final geometry are discussed in detail in chapter 5.

7.2.1 Overall performance

Figure 7.1 shows the overall performance of the low speed compressor compared to the fourth stage performance of the high speed C147 compressor, which was derived from stator mounted instrumentation. Va_{bar}/U has been calculated using the mean axial velocity and the mid-span blade speed; the mean axial velocity was derived from the overall mass flow, the annulus area and the inlet density. Experimental data from the datum tests have been plotted along with the design point calculations. Three vertical chained lines indicate the Va_{bar}/U corresponding to the traverse data. The design flow condition is close to that of the high speed SC90 calculation.

At the design flow the high and low speed polytropic efficiencies agree well at around 88%. The low speed compressor has a larger flow range and the $\Delta H/U^2$ characteristic remains relatively steep up to the instability limit whereas the C147 stage characteristic becomes less steep. The reduced sensitivity of the low speed sections to incidence changes (discussed in chapter 4) produces broader and shallower loss buckets and is the reason why the low speed flow range is so much larger, although the high speed stage flow range may be limited by other stages. The most striking difference is in the level of work shown in the $\Delta H/U^2$ plot. To help explain why this difference has occurred colour coded bars have been plotted to break down the step from design intent to test. Figure 7.2 shows the design and test profiles of work, flow and swirl angle. For reasons which are explained later, the test data are based on average values from the throughflow analyses carried out at the design and high flow conditions. Using these two figures the errors have been traced back as follows:-

1) The target for the design was the SC90 calculation which modelled all five C147 stages using predicted deviations and losses with some correction to line up with measured overall performance. The low speed design was based on results taken from the fourth stage .

2) The '2D' flow distribution from this SC90 calculation is shown in figure 7.2 by the dark blue line. These results are subject to blockage and the values used in the SC90 calculation start at 2% at the front of the compressor and rise to 6% at exit to the fourth stage. The low speed design used SC92H which takes 2D radial profiles of exit flow angle and loss and calculates its own blockage and 3D endwall effects. The output from SC92H therefore includes these effects and so the design was lined up on flow at mid-

height with the SC90 profile. The Va/Umid figure in 7.2 show these profiles matching well over most of the span with most of the differences occurring at the endwalls. The difference between the bulk Va/Umid for SC90 and SC92H, shown in figure 7.1, is due to differences in blockage. The effective level of blockage in the SC92H calculation is about 2%.

3) The datum design therefore proceeded at the higher flow of around 0.625 instead of 0.60 as shown by the SC90 and SC92H points in figure 7.1. The points are connected by a thick blue line which represents this mass flow difference. It should be noted that if Va_{mid}/U_{mid} were plotted instead of the bulk Va/U_{mid} then the two flows would agree well. The difference in $\Delta H/U^2$ between the two points is because, although the SC92H solution was designed to have the same general level of loading as SC90 over the mid span region, levels differ towards the endwalls.

4) The rest of the discrepancy between the SC92H point and the test data lie with the computational tools and the design process. Fortunately the flow condition of the SC92H calculation lies approximately mid-way between the design and high flow measurements, so comparisons can be made with profiles derived from an average of the experimental throughflows at these two flows, as mentioned earlier. These are shown by the dashed lines in figure 7.2.

5) Inspection of the rotor exit swirl angle profiles for the experimental and SC92H design curves shows a reasonable agreement, although there are some differences particularly at the endwalls. It is also encouraging that the results agree quite well with the fully 3D TRANSCode prediction (described later). However, at stator exit the SC92H calculation has around 2.5° extra swirl than the experimental results. The seven TRANSCode blade-to-blade sections (triangular symbols) were designed to line up with the C147 SC90 results, these are shown as the uniform distribution at a swirl of around 13.5° in the figure. The blade-to-blade TRANSCode solutions therefore overestimated the stator deviation so that the SC92H calculation under predicted the level of loading. Had the deviation error in the TRANSCode stator calculations been known the $\Delta H/U^2$ level would have been dropped to compensate.

6) The effect of the stator deviation error on $\Delta H/U^2$ has been calculated by taking the observed difference in stator exit swirl and applying this to all the stator exit swirls in a throughflow calculation based on the experimental data. Stator exit swirl differences from around 30% to 70% span were taken and extrapolated to the endwalls so that '2D' differences were applied. The difference in the $\Delta H/U^2$ from the standard throughflow solution was then obtained as an estimate of the effect of the stator deviation error. Overall, this difference accounts for approximately half of the discrepancy between test and the SC92H prediction. The remaining discrepancy has not been investigated in

detail but may be due to factors such as SC92H losses being different from test and the fact that the hand iterated S1-S2 design calculation was not completely converged.

The higher level of loading in the low speed stage does not significantly affect its relevance to the high speed case. This is because the original decision to maintain the level of $\Delta H/U^2$ was in any case somewhat arbitrary and overall diffusion levels will now be more representative. The mid-height De Haller numbers from test are 0.663 and 0.656 for the rotor and stator respectively and compare well to the high speed values of 0.643 and 0.654 (at the nominal design Va/U of 0.6).

7.2.2 Radial Profiles

Figure 7.3 shows the radial profiles of absolute total pressure and flow angle downstream of both the rotor and stator for the high and low speed stages. The high speed rotor exit data was obtained from the average of four radial traverses taken at different circumferential locations with steady state pneumatic wedge probes. The stator exit data is pitchwise averaged from an area traverse with the same type of probe. A total pressure coefficient has been calculated using the local and area average (AVG(Pt)) values of total pressure, both expressed relative to the local wall static pressure. Area averages for the low speed data were calculated over two passages and the radial profiles are pitchwise averages over two passages.

The measured flow angle distributions for high and low speed cases agree fairly well both in terms of radial variation and absolute levels. The total pressure curves are broadly similar, with the endwall loss regions and rotating hub work profiles extending to a similar percentage height in both cases. The biggest discrepancies occur near and below stator mid-height where there is a difference in pressure level. This may be connected with the pitchwise distortion at inlet to the stator which affects the total pressure downstream of the stator.

7.2.3 Stator exit flow field

Figure 7.4 shows contours of total pressure coefficient (defined as in Fig 7.3) behind the stator at design flow for the high speed experimental, low speed experimental and modelled low speed and high speed cases. The view is looking upstream and the rotor rotates from left to right. The TRANSCode high and low speed results are discussed later.

The extent of the traversing is indicated by the blank spaces above and below the data and the high speed (C147 stage 3) traverse limits are also shown on the low speed plots along with the hub and casing lines. The high speed test data show the wake thickening significantly from around 65% passage height towards the casing. The low speed traverse also shows this feature and compares well with the high speed wake. At

the hub the low speed blading has produced a significant region of low total pressure close to the pressure surface which is also seen in the high speed data. The main difference between these two data sets are in the mid passage flow where the low speed results show a circumferential distortion.

This distortion is present at stator inlet, as shown in figure 7.6, (discussed later) and arises at rotor 3 exit due to the response of the rotor to the potential field of stator 3 and to the wake structure from stator 2 passing through it. It is emphasized by the fact that equal blade numbers are used for all stator rows in the low speed compressor. Dissimilar numbers are generally used at high speed and Cherrett and Bryce (1991) show that for rotors these blade row number differences lead to a cyclic 'waxing and waning' of the blade loss regions in the circumferential direction. At low speed the repeating pattern means that some sensitivity to the relative circumferential positioning of subsequent stator rows might be expected (The stators here were in-line axially, but indexing of stator 2 is possible). Barankiewicz and Hathaway 1997, discuss the effects of stator indexing on low speed compressor performance and show that a 0.2 % change in efficiency is possible between the worst and best indexed positions. With unequal blade number counts the performance effects would be even smaller, but nevertheless stator-stator interactions could give rise to significant passage-to-passage differences which need to be allowed for in both experimental measurements and modelling. In the present case, the in-passage distortion over the inner half of the annulus appears to coincide with the region of relatively constant total pressure in figure 7.3. The absence of such effects at high speed may result from different levels of rotor-stator potential interaction or wake mixing as well as from dissimilar stator blade counts.

Figure 7.5 shows the pitchwise variation of total pressure coefficient (as used for figure 7.4) at stator exit at five heights up the span for all four data sets. The thickness and loss of the experimentally measured wakes agree well at 50% and 70% height while at 85% the high speed test data show more pressure deficit within the wake. Between the wakes the low speed test data shows a greater pitchwise variation in pressure; this is particularly noticeable at 70% height and corresponds to the mid-passage variation shown in the contour plots.

7.2.4 Rotor Exit

Figure 7.6 shows contours of absolute total pressure coefficient (based on stator exit wall static as in figure 7.4) measured at rotor 3 exit in the LSRC at three operating conditions. The strong circumferential variation in total pressure is of the same period as the number of stators and is partly attributed to the upstream wake structure of stator 2 and partly due to the potential interaction of stator 3 on rotor 3. The evidence for potential interaction comes from a traverse at rotor 1 exit (see figure 6.15) which shows

a similar total pressure field, where the period of circumferential variation is mostly commensurate with the stator pitch (134 blades) particularly at the hub with a weaker variation at the IGV pitch (96 blades) towards the casing.

The pitchwise distortions at stator inlet correspond to those seen in the stator exit field of figure 7.4. The position of the high pressure regions moves circumferentially across the stator passage inlet with changing flow condition. From the design condition to near stall the high pressure region moves towards the pressure surface. This means that it is split differently as it enters the stator passage, as can be seen by comparing the stator exit flow pattern shown in figure 6.16 for the near stall condition with that at design flow in figure 7.4. This highlights how strongly the stator exit flowfield is affected by the cross passage distortion.

Figure 7.7 shows the relative total pressure coefficient contours measured downstream of the low speed rotor using the rotating frame traverse compared with the predicted flow field. Turbulence intensity is shown for the high speed rotor. This was measured using a high frequency response dynamic pressure probe traversed radially behind the rotor. Records were taken that were phase locked to a rotor passing event and an ensemble average and unsteadiness calculated from these records. The turbulence field has been shown since this highlights the wake and overtip loss regions better than the time varying absolute total pressure field. TRANSCode predictions for the high and low speed rotors are also shown and these are discussed later in section 7.3.

The agreement between the loss regions indicated by the low speed measurements and those indicated by the turbulence in the high speed data is good. The wake broadens significantly towards the hub and this loss region is of a similar extent and shape in both cases. Evidence of a tip clearance loss region is also seen in both the low and high speed experimental data towards the pressure surface side of the nearest blade wakes. This feature is very similar to the vortical flow pattern reported by Cherrett and Bryce (1991) for the first three rotors of the second build of C147. The feature was attributed to a clearance flow vortex and the observed spatial position is a consequence of its cross-passage migration

7.2.5 Flow Visualisation

Figure 7.8 shows the results of a flow visualisation study carried out at design flow and near stall conditions for the low speed stator. They are compared with a picture of a C147 stage 3 stator taken after the C147 test series. The casing platform is at the bottom of the blade in these pictures. The dark regions on the C147 blade are dirt and oil deposited throughout the test series and therefore represent an average flow condition for the entire test period. A large proportion of this testing was, however, completed at

the 100% speed design flow condition. The procedure for taking the flow visualisation measurements is discussed in chapter 6.

The low speed stators show a significant corner stall at the fixed end which grows as the loading on the compressor is increased. The extent of the stalled region agrees well with that indicated by the area traverse at stator exit. A region of '2D' separated flow near the trailing edge is also apparent over the rest of the span. The darker region appearing up the span at 30-40% chord suggests where the start of transition is occurring. While the high speed results are less clear, similar corner stall and trailing edge separation regions are also apparent.

7.3 Comparison with TRANSCode predictions

TRANSCode predictions for both the high speed C147 stage and the low speed DERA1 stage have been completed. These were run as isolated bladerows using inlet conditions derived from the experimental measurements. For most of this work pitchwise mass averaged profiles were obtained from the traverse measurements and these were imposed at the inlet boundary as a circumferentially uniform field. This is the normal operating mode for TRANSCode.

In addition to these solutions, and to study the effects of the circumferential variations on the low speed stator performance, further predictions were obtained by imposing the full traverse flow field, for the low speed case, at inlet to the stator. The standard predictions are discussed in the following sections while the full field predictions are discussed in section 7.4. Figure 7.9 shows the grid used for the DERA1 rotor prediction and is typical of the grid used for the stator and later for the DERA2 geometry. The grid size is 41 x 135 x 41 and the clearance end is modelled by a 'pinched tip' where the blade thickness reduces to zero over three cells while the clearance gap is modelled by six cells. The C147 solutions were completed by Mike Spruce (from the Propulsion Department, DERA) using a 49 x 149 x 49 sized grid, similar in topology to the DERA1 rotor grid shown in figure 7.9.

7.3.1 Radial profiles

Figure 7.10 shows the radial profiles from the TRANSCode predictions for both the rotor and stator alongside the high and low speed test data (shown earlier in figure 7.3). The low-speed predictions capture the main qualitative features of the test data fairly well but there are some significant differences. The rotor prediction fails to model the clearance flow well and this is shown by the higher amount of turning towards the casing. The over-prediction of this tip-blockage flow increases the flow over the rest of the span producing a lower absolute frame rotor exit swirl. At stator exit an area of high pressure is predicted at around 20% height, but pressure levels close to the hub are

under-predicted. This high pressure area corresponds to that closer to the hub at rotor exit which is moved radially outwards by the clearance flow within the calculation. These modelling shortfalls are discussed further in considering the full area traverse results below. The stator deviation is over-predicted by around 1.5°-2°. This is consistent with the blade-to-blade design calculations for the stator where the over-prediction of deviation contributed to the extra level of work reported in section 7.2.1.

The C147 TRANSCode predictions are shown by the triangular symbols in the figure. At rotor exit the TRANSCode predictions for absolute swirl angle agree well with the high speed test data although the shape of the curve towards the casing suggests that the clearance features are not being modelled well. The distribution of pressure coefficient is reasonably good around mid-span but the code under-predicts the radial extents of the hub endwall flow and of the clearance flow near the casing. The C147 predictions for the stator appear worse than for the rotor although the distribution of swirl angle downstream of the stator is in reasonable agreement over the mid-span region. At the hub endwall, the region of the boundary layer having strong gradients of skew is predicted to be closer to the hub than on test, even though the distribution of pressure coefficient shows a similar hub endwall boundary layer extent. Towards the casing the limited radial extent of the test data restricts comparisons but total pressure levels appear to be underpredicted. Conversely, pressure levels near the hub are overpredicted mainly due to the pressure peak which appears closer to the wall than that predicted at low speed.

7.3.2 Stator exit flow field

Figure 7.4 shows the total pressure coefficient (defined as in figure 7.3) at stator exit for the low and high speed test and prediction. Comparison of the test data was discussed earlier in section 7.2.3. The prediction for the low speed case shows the wake thickening significantly towards the casing endwall and the size and shape of this loss region agrees fairly well with experiment up to the highest experimental measurement height. The hub clearance flow is not well modelled and the losses here are smeared across the passage instead of accumulating on the pressure side. The over-prediction of total pressure near 20% height has been commented on earlier. The failure of TRANSCode to capture the flow pattern around the clearance region may be partly due to the limitations of the Baldwin-Lomax model and to the highly skewed H-grid employed over the blade end region. Different levels of clearance and blade end shape were modelled to try to match the experimental clearance end flow but with little success. The prediction shown uses the design clearance with a squared-off end. The prediction also fails to predict the mid-passage distortion shown in the measurements

because it uses a circumferentially uniform inlet condition from a radial profile measured at rotor 3 exit.

Comparisons of the C147 stator exit prediction shown at the top of the figure with test are restricted by the limited extent of the high speed test data. There appears to be less evidence for the overprediction of clearance losses than at low speed but some indication that losses near the casing endwall are overpredicted. The pitchwise slices through these fields are shown in figure 7.5. For the high speed prediction the thinness of the wake at 50% height compared to test is clearly evident. At 85% height the over-prediction of loss at the casing is reflected in the line plot which shows the losses extending to fill 50% of the pitch. At 15% and 30% height the predictions overestimate the mid-passage pressure level and this obscures the accuracy of the wake modelling. A corresponding region of high pressure in the core flow near the hub was observed in figure 7.4 for both predictions. It is due to the high pressure rotor exit flow at the hub moving radially outwards, as it progresses through the stator, passing over the growing hub boundary layer.

7.3.3 Rotor exit flow field

The CFD result for the rotors (shown in figure 7.7 along with test data) show similar features to the stator prediction. The tip clearance loss region for the low speed prediction has been grossly over-predicted and the losses here extend across the entire passage. The hub region, however, compares reasonably well with the measurement, with the wake thickening to a similar extent. The low speed measurements also show somewhat thinner blade wakes but a rather thicker boundary layer at the hub which the computation fails to predict. This could be due to the extra blockage created elsewhere alleviating the diffusion occurring at the hub endwall.

Towards the hub the high speed rotor prediction shows very encouraging agreement with the test data and low speed prediction. There is generally good agreement with the region of loss indicated by the high speed measurement, although this perhaps shows the loss region extending further up the span. At the tip TRANSCode struggles to predict the clearance flow adequately, as for the stator case, although the losses are not so grossly over-predicted as they are in the low speed rotor solution.

7.3.4 Blade surface pressure distributions

A number of rotors and stators from the study (third) stage were instrumented with pressure tappings at a range of heights up the span. Blades instrumented on their suction surface were paired with blades with pressure surface tappings so that the same passage was measured for each surface at each respective height. Each pair had tappings along one spanwise station, plus a datum tapping that was at the same position on each

instrumented blade pair. The blade surface static pressure instrumentation is discussed in more detail in chapter 6.

Figure 7.11 shows the distributions of blade surface static pressure coefficient from the 3D TRANSCode prediction for the low speed compressor along with the experimental results from the LSRC. The pressure coefficient is calculated by the difference in local pressure from the datum divided by a rig reference inlet dynamic head. Three heights at 15%, 50% and 85% span are shown for each blade row. The agreement with the 3D TRANSCode prediction is generally good for the stator, but is not so good for the rotor especially towards the rotor tip. This is consistent with the rotor clearance flow modelling problems already commented on.

7.4 Full inlet flow field modelling

3D TRANSCode predictions have been carried out for the DERA1 stator using the measured inlet flow fields shown in figure 7.6 for the inlet boundary conditions instead of the previous circumferentially uniform fields. The axial location of the inlet grid plane was moved closer to the leading edge to line up with the traverse plane and the correct relative circumferential position was found from the instrumentation scheme. The experimental data was then interpolated onto the TRANSCode grid. At the endwalls the experimental data was extrapolated by taking the first order extrapolation of the pitchwise average profile, to obtain a good overall level, and then imposing the same circumferential variation as the nearest measured plane.

Results from the design flow, near stall and high flow predictions are shown in figures 7.12 to 7.14 respectively. Contour plots of stator exit total pressure are shown along with circumferential and radial slices through the flow field. The location of the slices are shown on the contour plots by the dashed lines. The blue lines denote the experimental data while the red is for the TRANSCode results. At design flow (figure 7.12) the high total pressure region is positioned towards the suction surface (to the right of the wake) in the upper half of the passage. TRANSCode shows the centre of this high pressure region at the same location and is therefore predicting the same transportation of the inlet field through the passage. However, the detailed structure of the inlet field is smoothed out as it passes through the inviscid mid-passage region. Also, the high pressure ridge in the lower half of the passage is close to the suction surface whereas the experimental data shows this crossing the passage towards the pressure side.

The high pressure zone near 15% height seen in the axisymmetric prediction (see figure 7.4) is absent in the full inlet flowfield modelling. Part of this is due to the fact that slightly different grid standards were used. For the later axisymmetric predictions, presented here in figure 7.4, more j-planes were used upstream of the leading edge. This helped maintain the high pressure region at exit from the rotor hub and enabled it to

convect through the passage, albeit moving radially outwards also. Earlier axisymmetric predictions looked more similar in this respect to the non-axisymmetric predictions presented here. Neither standard of grid is producing adequate solutions in this region since although the coarser grid solution looks closer to the experimental measurements, the high pressure region at exit from the rotor hub has diminished significantly before it has even reached the leading edge.

The mid-passage radial slice (slice B) and the mid-passage average (pitchwise average between slices A and C) show fairly encouraging agreement with test over most of the span. At the hub the clearance flow is not well modelled as was the case with the standard predictions. The pitchwise slices of total pressure show the wake thickness and pressure deficit to be over predicted up the whole span as is evident from the contour plot. The pitchwise variations of yaw angle from the test measurement show a large change in yaw across the wake. This is a feature of the cobra probes which over predict yaw angle in highly sheared flow.

At near stall (figure 7.13) the centre of the high total pressure region has moved away from the suction surface into the mid-passage. TRANSCode predicts a similar circumferential position for this but fails to model the foot of the high pressure region which has passed into the next passage. This is the high total pressure region close to the suction surface side of the wake and very close to the hub. In the TRANSCode solution this feature is drowned in the large clearance loss region which is smeared across the passage at the hub. At high flow (figure 7.14) the high total pressure region at inlet has been sliced by the stator and part of it passes either side of the blade. The stator wake becomes surrounded by high pressure fluid over most of the span producing kidney shaped contours of total pressure between the wakes. TRANSCode has modelled the slicing and convection of the high pressure region through the passage well, improving the mid passage predictions. However, the viscous endwall and clearance end modelling has not been improved compared to the axisymmetric solutions, although the wake predictions are better for this case.

The full inlet field modelling shows that the circumferential variations of total pressure and flow angle measured behind the rotors have a significant effect on the downstream stator's exit flow field. The relative circumferential position of this inlet field changes with flow condition along with blade loading due to the different absolute flow angles at rotor exit. In order to assess just the effect of this relative positioning on stator performance a series of TRANSCode predictions were carried out on the stator for the design flow condition with the inlet field stepped around circumferentially. Figure 7.15 shows the results of this exercise for five predictions where the inlet field has been stepped by 20% of the stator pitch between each solution in the pentagon. The exit total pressure has been plotted and the view is looking upstream as in the previous plots.

The zero pitch shift solution at the top of the page corresponds to the datum solution shown in figure 7.12 and the same contour legend applies. As the inlet field is stepped across the passage (from right to left in this view) the high total pressure region gets split either side of the stator then appears close to the pressure side of the wake before moving out into the middle of the next passage. When the high pressure region is close to the wake, as in the solution at 20% pitch shift, the wake appears thinner. The reverse happens when the high pressure area is away from the wakes as in the 80% pitch shift solution where the wakes appear thicker. This effect is mostly due to the fact that higher inlet total pressure is seen at the blade leading edge in the 20% case so if the same pressure deficit occurs across the blade section the exit total pressure level would also be elevated and so the wake would appear thinner.

The relative position of the inlet field total pressure distortion has a significant effect on the stator overall performance. In the middle of the page the overall pressure loss coefficient (calculated within TRANSCode and based on mass averaged quantities at inlet and exit to bladerow) has been plotted for each solution against percentage pitch shift of the inlet field. The loss varies from around 0.075 for the datum case to over 0.11 for the 40% shift case, an increase in loss of almost 50%. The 40% case shows a significant jump in loss over the other cases although this is not readily apparent from the contour plots. Although the 80% case appears to have the thickest wakes, and therefore possibly higher loss, the 40% case has the least total pressure within the core flow. It appears that the contribution of the mid-pitch core flow has a greater effect on overall loss than the wake deficit. However, the minimum loss case is not for the 80% shift position which shows the centre of high total pressure at mid pitch but for the datum case where there is closer proximity to the suction surface side of the passage. The two effects therefore contribute although the inviscid flow has the stronger effect.

The relative positioning of the circumferential variations at stator inlet will be dependent on the convected variations from upstream (due to upstream stator wakes) moving under the influence of the absolute swirl angle and also the potential variations (from the stator itself) which will depend on the stator loading. This exercise is therefore somewhat artificial since the whole inlet field has been shifted with no regard for the influence of the stator on the stator inlet flowfield. It does show, however, that the positioning of the inlet field variations could have a measurable effect on bladerow performance.

7.5 Un-NEWT modelling of datum stage

2D unsteady modelling of the first stage of DERA1 has been undertaken at mid-height using un-NEWT (Dawes 1993, Jackson and Angel 1997) with considerable help and guidance from Dr Brian Angel. The purpose of the investigation was to simulate the

unsteady interaction between the rotor and stator that was evident from the stationary frame traversing at the stator exits. The first stage was chosen because the inlet flow could be modelled as uniform (ignoring the effect of IGV wakes) and the measurement of total pressure variations of stator pitch wavelength at stator 1 exit was a clear indication of the stator influence on the rotor performance which warranted further investigation. The un-NEWT work presented here are preliminary results intended to give a rough guide to the magnitude and phase of any rotor-stator interaction. More detailed investigations are beyond the scope of this thesis, although fully 3D unsteady stage modelling of DERA1 is ongoing within the Propulsion Department.

The grid used in the investigation is shown in figure 7.16. The grid was generated from a TRANSCode geometry file and the j-planes therefore have constant axial positions. Three rotor passages were modelled along with four stators and this ratio compares well to the actual blade number ratio; 101:134 actual compared to 102:136 (3:4) modelled. The grid refinement was reduced (particularly towards the trailing edge) compared to the TRANSCode predictions to increase the maximum allowable timestep and decrease the computational burden per timestep so that a solution could be obtained within two weeks (previously finer grids were modelled with the solution taking around three weeks). The axial location of the traverse plane is also shown in the figure.

Figures 7.17 and 7.18 show the static pressure and blade relative flow angle contours respectively for snapshots in time covering one rotor passing event from the un-NEWT prediction at the design flow condition. While the overall quality of the solution may be impaired by some entropy generation at the slide plane and the rotor and stator wakes are somewhat thicker than those predicted by TRANSCode the solution obtained is useful for studying the potential field interaction effects. At the rotor leading edge the static pressure contours cycle between a more forward loaded distribution (top left when viewed in portrait) and an off-loaded distribution (bottom right). This is due to the static pressure field from the downstream stator; the circulation downstream of the rotor alters the rotor's circulation at certain relative positions so that the loading varies cyclically. In figure 7.18 the relative swirl angle contours show this cyclic loading is coupled to a varying rotor blade incidence.

The unsteady results have been time averaged at each circumferential position at the traverse plane so that the spatial variation due to the varying rotor performance could be evaluated and compared to test measurements. This is shown at the top of figure 7.19 along with traverse results from stator 1 and stator 3 inlet. Normalised total pressure (normalised to average level) has been plotted so that the magnitude and phase of the variations can be studied. The instantaneous flow fields from the un-NEWT calculation were output over one rotor period and not all the three that were modelled. Therefore the variations with wavelength between one and three rotor pitches are not fully represented

in the time averaging and this will bias the time averaged results so that a longer wavelength is superimposed on the stator pitch variations.

The unsteady prediction compares well to the measurements downstream of the first rotor and therefore reinforces the argument that the first rotor has a potential pressure field interaction with the downstream stator. The measurements at stage 3 show a much larger spatial variation than at stage 1; between 2.5 to 3 times larger in magnitude. This extra variation is due to the influence of the upstream stator wakes that has not been modelled in the unsteady calculation. As a rough guide we can conclude that approximately 65% of the circumferential variations seen behind the embedded rotors is due to upstream stator wakes passing through them and 35% due to the static pressure field of the downstream stator changing the circulation around the rotor blades.

These effects may be different at other spanwise positions. At the rotor hub, for example, the large endwall loss region may be more sensitive to static pressure variations than the flow at mid-span. In this case we may expect the stator interaction effect to be amplified by the corner flow. Indeed, the rotor 1 exit flow field (shown in figure 6.6) at the hub shows a stronger total pressure variation at the stator wavelength than towards the casing where the wavelength is more commensurate with the number of IGV blades.

The second plot in figure 7.19 shows a non-dimensional surface static pressure distribution around the rotor at five different instances in time (AVG(Ps) is average around the blade surface of all time instances). These distributions have been integrated to find the overall blade loading and this has been plotted in the third plot against fraction of stator passing rotor. The loading has a saw-tooth variation with a peak at around 50% and a minimum at around 90%. The zero position for this plot corresponds to the relative rotor and stator positions shown by the bottom left hand contour of figures 7.17 and 7.18. The relative flow angle from a group of cells just ahead of the rotor leading edge have been averaged at each instant in time to obtain an indication of rotor incidence and this has also been plotted against stator passing and is show in the final plot of figure 7.19. The variation of relative flow angle about the mean level has been plotted and this shows that the rotor incidence varies by over one degree as it passes the stator. The peak in incidence appears to lag behind the peak in loading.

7.6 Conclusions

The overall duty of the datum low speed blades is around 10% higher than intended in the original design. This discrepancy has been investigated and shown to be due partly to a difference in overall flow coefficient between the SC92H design calculation and the high speed SC90 solution. It was also partly due to the shortcomings of the SC92H throughflow model and deviation errors of around 2° in the blade-to-blade

TRANSCode design solutions for the stator. Although the $\Delta H/U^2$ level was higher than intended the De Haller numbers for both rotor and stator were closer to the C147 fourth stage blading.

Stationary frame traverses at rotor and stator exit show that the radial profiles of total pressure and flow angle agree fairly well with the high speed stage profiles although there were some discrepancies. The area traverse at stator exit shows good agreement with the high speed stator performance in terms of wake structure and endwall loss regions. However there was much more evidence of non-axisymmetric flow in the free-stream regions between blade wakes in the low speed tests and this needs to be recognised when interpreting data and comparing with CFD predictions. Rotor relative traverse measurements were compared with turbulence measurements in the high speed rig and the loss regions indicated by these two methods are also in good agreement.

Overall the measurements show that both primary and secondary flow features can be reproduced in the low speed environment inspite of the compromises in the high to low speed transformation process caused by both geometric and aerodynamic limitations.

Numerical predictions were carried out on each blade row using the DERA TRANSCode Navier Stokes flow solver for both the low speed and C147 blading. The low speed predictions showed fairly good agreement over much of the blade span including the fixed end of each blade row but failed to predict the size and structure of the clearance flow region. Similar results were apparent for the high speed predictions although the clearance flow modelling problems were less and the stator casing flow suffered from an over-prediction of loss. Further work to improve the modelling is needed on both the high and low speed predictions, particularly at the clearance ends.

The non-axisymmetric flow was found to be an important feature of the low speed flowfield and represented possibly the largest difference between the high and low speed environments. To study this effect TRANSCode modelling was carried out using the complete measured stator inlet flowfield. This study showed that the relative positioning of the stators to the inlet field could have a significant effect on overall performance. However, the circumferential variation was also shown (by unsteady modelling) to be partly due to the downstream stator itself so shifting the whole field circumferentially was somewhat artificial in this case.

Un-NEWT modelling of the mid-span sections of the first stage has demonstrated the potential interaction between the rotor and stator. The time averaged spatial variations of total pressure at rotor exit agree well with the level of pressure variation measured at rotor 1 exit. The variation at rotor 3 exit was shown to be higher than at

rotor 1 exit and this was attributed to the extra spatial variations arising from the upstream stator wakes passing through the rotor. Approximately 65% of the circumferential variations downstream of an embedded rotor was attributed to the upstream stator and 35% to the downstream stator. Although the overall effect on performance due to these circumferential variations is small they must be recognised when comparing detailed flow measurements with high speed data and when attempting to model the low speed flow with a flow solver.

Chapter 8 3D Blade Design

8.1 Introduction

The performance of multi-stage axial flow compressors can be seriously eroded by the complex, three dimensional viscous flows found in the endwall regions and wakes. Recent research work has focused on alleviating these endwall losses through the use of '3D' blade design approaches. These approaches attempt to control the endwall flows by locally reducing the loading in these regions. Several methods have been used to achieve this with varying degrees of success, these include; end-bends, leading edge recambering, section modification, lean and sweep. End-bends are near endwall blade twists that off-load the endwalls by reducing the level of turning required while leading edge recambering reduces loading by decreasing the incidence at the endwall. However, Wadia and Beacher (1989) show that the need to align the inlet metal angle precisely with the skewed inlet flow angle at the endwall is less than that indicated by 2D analyses due to the effects of three-dimensional relief.

Recent interest has focused on the more generic methods of lean and sweep to control the endwall flows. These methods involve stacking the blade on a non-radial stacking axis either forwards/backwards (sweep) or to the side (lean). By moving the endwall sections into regions of higher pressure they have less diffusion to achieve and therefore lower loading and loss.

This chapter outlines the design of a 3D set of blading for the Cranfield LSRC based on the previous datum design described in chapter 4. The aim of the 3D design is to improve upon the performance of the datum through the control of the endwall flows where losses can be considerable.

8.2 3D Blade Definition

The traditional approach to blade design is to use an essentially 2D method where sections are designed at given heights up the span using blade-to-blade calculations to guide the section design. These sections are then stacked on a straight axis to form the final blade shape. For a fully 3D design where there are no artificial restrictions to the final 3D form of the blade the design possibilities are endless. The extra dimension available to the designer creates a myriad of design combinations which can rapidly overwhelm the design task.

In order to retain some control but at the same time allow a certain amount of flexibility into the design system the 3D design in this study has been defined using a number of parameters. The stacking axis has been deformed within a single plane (initial studies also include deformations in two planes for the hub and casing respectively) and

the plane is allowed to rotate about a radial axis. The shape of the axis has been restricted to a symmetrical parabola for the final study but initial studies included asymmetric bends and bends more localised to the endwalls.

Figure 8.1 shows a blade-to-blade and meridional view of a series of blades progressively modified by a series of parabolic stacking axes of increasing 'strength'. The mid-span section is shown by a solid line and the end sections by the feint lines. For the case shown the plane of the axis is in a direction normal to the blade chord and this is defined as the 'Lean' direction. Positive lean is defined as the direction of lean that creates an obtuse angle between the suction surface and endwall. The parabola of the axis is defined by the general curve $Ax^2 + Bx$ where A controls the 'strength' of the curve and the parameter B is a function of A and is chosen to ensure symmetry about the 50% height position.

Figure 8.2 shows another blade-to-blade and meridional view, this time the angle of the stacking axis plane has been rotated through a series of angles. The angle of the plane to the lean direction has been defined as the angle α. When α is equal to zero the blade has pure lean, $\alpha=90^o$ corresponds to pure forward sweep and $\alpha=-90^o$ corresponds to pure backward sweep. Intermediate values of α correspond to a mixture of lean and sweep.

8.3 Computational Approach

Computations for this work have been carried out with the DERA 3D Navier-Stokes flow solver TRANSCode (Calvert, 1995) described earlier in chapter 4. A typical grid used for the 3D design work is shown in figure 8.3 which shows the overall grid and close up views of the leading, trailing and overtip regions. The grid size used was 41 x 149 x 41 and this was increased to 49 x 149 x 49 for some overtip modelling studies. The tip clearance end is modelled by a pinched tip and various thickness factor distributions were tried to improve the modelling in this region. The inlet and outlet planes were kept at the same constant axial position regardless of blade axial sweep.

The 3D design work falls into two distinct groups; those carried out before and those after measurement of the datum design. The pre-measurement work uses boundary conditions from the design SC92H throughflow analysis and the latter uses the measured conditions for the datum design. Figure 8.4 shows how these boundary conditions compare for the stator inlet and rotor inlet profiles of total pressure and swirl angle. The swirl angle profiles at stator inlet show greater incidence in the measured profiles towards the endwalls than the prediction. This greater incidence onto the stator endwalls has a large effect on the performance of the stator and on the improvements that can be achieved through 3D blade design.

8.4 3D Design approach

8.4.1 Initial Studies

The initial 3D design studies, using the design boundary conditions from SC92H, looked into the effects of a straight lean/sweep of the blade stacking axis. This work confirmed the findings of previous workers (Emmerson and Buchanan, 1996) that an obtuse angle between the suction surface and endwall (positive lean) can decrease the loss in that region. For acute angles (negative lean) the loss was found to increase significantly. The cause of the decrease in loss is due to a decrease in the local diffusion at the endwall. By leaning the blade in the positive direction the endwall section moves into a region of higher pressure because the pressure contours tend to remain radial. This means that the endwall section has lower diffusion and the losses decrease. This result is in agreement with the findings of other workers (see Denton and Xu 1998, Place 1997)

Sweeping the stacking axis forward decreased the endwall losses in a similar manner to positive lean. Similarly, backwards sweep was found to increase the losses. The driver for the loss reduction was a decrease in diffusion at the endwalls. The effects of lean and sweep can also be explained by viewing the blade as a line vortex. When the blade is leaned a component of vorticity is introduced in the circumferential direction which induces flow into the endwall region towards the trailing edge. Figure 8.5 shows the results of a simple line vortex study showing the first order effects of lean through perturbation contours. The study shows how the 2D meridional flow becomes perturbed by the pitchwise components of a line vortex. The pitchwise vortex strength is increased in a parabolic manner towards the endwalls as the pitchwise component of the line vortex increases due to the angle of lean. A series of mirror vortices are also set up ensuring the no flow condition is imposed through the endwalls.

Ahead of the line vortex pitch angle contours show that flow is induced towards the middle of the blade and then back towards the endwalls downstream of the vortex line. The axial velocity perturbation contours show how this causes a deceleration of the flow downstream of the vortex at mid height and an acceleration downstream at the endwalls. The mid-height section therefore becomes more highly loaded and the endwalls off-loaded. A yaw angle contour field has also been calculated using the axial velocity field and a constant tangential velocity field is assumed. This shows that there is a secondary effect of lean which is to increase the incidence at the endwalls.

Figure 8.6 shows a similar study looking at the effects of sweep. A cascade of line vortices were set up to model the effects of adjacent bladerows and further mirror vortices above and below the blades to ensure a no flow condition through the endwalls. The perturbation of flow parameters of pitch angle, swirl velocity and yaw angle along

with velocity vectors have been shown at the inlet plane. The contours of pitch angle show that flow is induced towards both endwalls near the suction surface and away from the endwalls near the pressure surface. The yaw angle contours show a decrease in incidence near the endwalls and an increase at mid span, these effect becomes greater nearer the blades. Sweeping the blade forward therefore increases the mid span loading and decreases the endwall loading in much the same manner as lean (the increased flow towards the endwalls downstream of the vortex line for the lean case compares with a similar increase of flow towards the endwalls on the suction surface side of the passage for the sweep case). Comparison with the lean study is difficult because of the different planes considered, this is due to the different geometric directions in which the vorticity is applied. Lean therefore produces a more axisymmetric perturbation while sweep appears to affect the cross-passage flow more.

Another difference with sweep is that the endwall incidence appears to decrease whereas it increases with lean. The similar behaviour of lean and sweep together with their different secondary effects lead to the idea that they could be used in combination to produce a 3D blade with moderate incidence increase near the endwalls while still off-loading the endwalls.

3.4.2 Physical Effects of 3D modifications

TRANSCode solutions were calculated for a series of lean and sweep cases to investigate the effects of lean and sweep on the 3D viscous flow around the blades. Figure 8.7 shows the pitchwise averaged relative Mach number difference contours for increasingly strong rotor lean cases using a parabolic stacking axis (the inlet Mach number is around 0.2 and the scale therefore represents a ±10% change in total velocity). The flow field has been averaged across the pitch at each point and the difference from the local pitchwise average calculated. The resulting contour field represents the effect to the bulk flow of introducing the lean. The leading edge flow at each endwall has decreased in velocity while at the mid-span the velocity has increased. This is in agreement with the vortex model shown in figure 8.5. At the clearance end the flow velocity has increased towards the rear of the blade section. As the lean is increased the effects become increasingly stronger. Although a parabolic distribution of lean was applied, the effects at the endwalls are very radially localised, in a similar manner to the line vortex perturbations. This result highlights the fact that localised blade geometry changes are not necessarily needed to produce localised flow changes.

Figure 8.8 shows the effect of sweep and a lean/sweep combination on the pitchwise average Mach number flowfield of the rotor. The pure sweep case shows no reduction in the endwall velocity as seen in the lean case. There is also no marked

increase in mid-span leading edge velocity. The lean/sweep blend case shows the effects of both the lean and sweep cases and shows that the effects also appear to combine in a linear manner.

Figure 8.9 shows the same averaging carried out on the pitch angle for the stator case with lean, sweep and a combination of lean and sweep. The introduction of lean has induced more bulk flow towards the mid-span ahead of the blade and towards the endwalls downstream of the leading edge. This agrees with the idea of introducing vortex elements in the pitchwise direction at the endwalls as shown in figure 8.5. The pure sweep case shows less pitch angle variation (particularly upstream of the leading edge) and most of the changes are localised behind the leading edge with less effect on the rear 50% of chord. The lean/sweep combination case also shows that the effects of both the lean and sweep cases appear to combine in a linear manner. By varying the relative amounts of lean and sweep the distribution and magnitude of flow into the endwall can be controlled.

Figure 8.10 shows the pitchwise average yaw angle difference contours for the same case. The increase in yaw angle at the endwalls is shown by the red contours which extend a further distance upstream of the bladerow for the lean case than for the sweep case. The line vortex study also showed that yaw angle would increase towards the endwalls for the lean case, and for sweep the vortex model predicted a decrease in yaw angle, although the viscous predictions show a small increase in endwall flow angle. At mid-span and downstream of mid-chord at the clearance endwall the yaw angle decreases. The slight increase in flow angle at the midspan region downstream of the bladerow is a result of the increased deviation due to the increased loading at midspan. The effect on the rotor was very similar to the stator. The effects at their respective clearance and fixed ends behaved in a broadly similar manner.

The overall effect of lean on the pitchwise average radial exit profiles is shown in figure 8.11. The exit total pressure profile is shown for the stator case and it can be seen that the total pressure at the endwall increases and the mid-span total pressure decreases as the lean strength is increased. The profile therefore becomes progressively flatter with cleaner endwall flow as lean is increased. As the lean strength is increased further the midspan loading becomes so great that separation occurs and the overall loss increases greatly. Before this point is reached however, there is a net improvement in loss where the gains made at the endwall outweigh the losses at the midspan. At a certain balance point the losses are minimised before the overall loss increases up to the mid-span stall condition.

8.4.3 Combined Lean/Sweep approach

The 3D viscous studies indicated that lean and/or sweep could improve the endwall flow and overall performance of the datum blades. A systematic approach was therefore employed to study the effects of combining lean and sweep to produce a better 3D blade that did not suffer so much from secondary effects such as increased endwall incidence and mid-span loading. The stacking axis was therefore rotated through a series of directions from lean to sweep (see figure 8.1) for different parabola strengths (see figure 8.2).

Figure 8.12 shows the summary of this exercise for the rotor. Two cases have been run, one uses a complete parabola and the other has local axis bends using half parabolas close to the endwalls. The axes were rotated from -15° to 105° in steps of 15°. The overall pressure loss coefficient is shown and for most of the cases the improvement over the datum case (shown by the triple chain line) is significant. The constant parabola case shows greater improvement than the other case and there is a minimum at an axis rotation of 30°. This corresponds to a combination of positive lean and forward sweep. The optimum rotation for the local end case is at the lower angle of 0°. The optimum therefore changes with the particular axis deformation used.

A similar study was also carried out to see if a minimum loss could be obtained from an increasingly strong single parabola stacking axis at 0° rotation. In figure 8.13 the magnitude of the factor A which controls the parabola shape has been plotted against the pressure loss coefficient. A minimum loss is found at a factor A of 12 after which the loss rises sharply and a solution could not be obtained after a value of 16 due to the onset of a large mid-span separation. The square symbol in the figure indicates the value of A used for the single parabola case in figure 8.12. It is interesting to note that the minimum loss coefficient achieved in both studies are very similar but that the lean/sweep minimum is achieved at a lower factor A and therefore would suffer less from blade stress than the pure lean case with a higher level of overhang.

The same study was carried out for the stator geometry and is shown in figures 8.14 and 8.15. Figure 8.14 shows the results for the stacking axis rotation plotted against pressure loss coefficient. The minimum obtained for the stator case occurs at a rotation of -30° instead of the +30° found for the rotor. This corresponds to a positive lean and backwards sweep combination. The lean strength study at zero rotation shown in figure 8.15 shows a similar trend to the rotor case. The minimum occurs at a strength factor A of 9 which is the same factor used in the axis rotation study. However, the minimum found in the axis rotation study is lower than in the pure lean study and demonstrates that

by combining lean and sweep the loss can be reduced more for a given blade overhang or axis strength.

8.4.4 Effects of leading edge recambering

The reduction in loss achieved in the lean/sweep study was around 9% for the rotor and 6% for the stator when using the SC92H inlet conditions. The high degree of incidence that is found at the endwalls together with the increase in incidence due to the secondary effects of lean/sweep suggest that more efficiency gains may be found by recambering the leading edges to point in the expected flow direction.

Studies were carried out on the best case lean/sweep geometry and the datum straight blade geometry using leading edge recambering of varying degrees at both fixed and free ends of the blades. The recambering was achieved by increasing the camber of both suction and pressure surfaces via the blade definition parameters that control the shape of each section. Restaggering the blade section was necessary to achieve the appropriate blade exit angles. This produced a section that was smooth and continuous on both surfaces and allowed the modification to be blended into the rest of the blade by progressively altering the definition parameters up the span.

Leading edge recambering (LER) was found to be beneficial at the fixed ends of both rotor and stator but increased the loss when applied to the clearance ends. The benefits were found for both the straight blade datum case and the lean/sweep case. Figure 8.16 shows the pressure loss coefficient versus mass flow curves for the datum, lean/sweep and lean/sweep with LER cases for the rotor (these used experimental measurements and are all at a higher level of loss than seen in figure 8.12 and 8.13). The figure shows that the further improvement achieved by using LER is of a similar magnitude as that from using just the lean/sweep combination approach. Figure 8.17 shows the same format of plot for the stator case. The improvements achieved in the stator case show a similar trend to the rotor case but the gains are of a lower magnitude for both lean\sweep and LER.

.4.5 Effects of Profile modification

The lean/sweep combination study showed that a trade off existed between a reduction in loss at the endwall and an increase in the mid-span losses as the blade was increasingly leaned. If the losses at mid-span could be reduced by careful design of the mid-span section to cope with the increased loading then there would be even greater potential for blade performance improvement. This idea is made more attractive by the fact that the endwall flow is highly 3-dimensional in nature and therefore more difficult to control. The mid-span flow on the other hand is essentially 2-D and designing a 2-D

section to a certain loading level should be easier than designing an endwall blade region. The idea, therefore, was to use the lean/sweep approach to clean up the endwall flow and then carry out a 2D section design at mid span to limit the damage done to the mid span flow.

Various profile modifications were tried at the mid span region which included moving the peak camber point forwards and backwards and varying the amount of camber and stagger. None of the modifications were found to improve the mid span losses and the original blade section was found to be approximately the best section that could be achieved for the mid span region using the given blade section generator.

8.4.6 Effects of section re-stagger

Other 3D geometric features were investigated during the initial design phase, these included the use of end-bends or restaggered sections towards the endwalls. Restaggering the whole section has the disadvantage over leading edge recambering of changing the exit flow angle and therefore the radial blade loading distribution. Restaggering also suffers from the fact that the design then becomes optimised for one flow condition and the benefits are not generally found over the entire operating range.

Locally restaggering the blade sections near the endwalls introduces local lean/sweep effects which may reduce the performance of the blade. For example, if the stagger is increased towards an endwall about the section's centroid then negative lean is set up along the front half of the chord and positive lean towards the back half. The static pressure field that is set up under these circumstances will serve to increase the endwall losses towards the leading edge in an unexpected manner. The lesson learned from this exercise is that the blade cannot be regarded as a series of 2-D sections that can be stacked up to line up with the incoming flow direction, but rather that the whole 3-D shape must be taken into account. An endbend design is therefore, by definition a 3D design based on 2D ideas of flow behaviour.

8.5 Final design

The final design work was carried out using the measured inlet flow conditions from the datum tests. The design improvements achieved in the initial investigations using the SC92H conditions were not obtained with the measured conditions. This was attributed to the fact that the flow angles were larger and therefore the incidence onto the blade rows was increased. This reduction in improvement with incidence for lean/sweep geometries has been observed in earlier studies (Emmerson and Buchanan, 1996).

The final design was based on the best design indicated by the CFD, although time was not wasted further refining the design based on CFD results. This was due to the

limitations with the computational model along with experimental inaccuracies in the measured inlet conditions, so the CFD results were used mainly to guide the design process. The final design consisted of a lean/sweep combination with leading edge recambering at the fixed ends of both blade types. The design parameters for the rotor and stator are shown in Table 8.1. The performance improvement predicted on an isolated blade row calculation show the new rotor design producing a 10% reduction in loss and the stator a 2-3% reduction in loss. Although the stator showed less of an improvement than the rotor both rotors and stators were changed for the 3-D redesign test so that the effects of both together could be assessed.

The amount of leading edge recambering was kept as low as possible without destroying the predicted beneficial effects. The recambering was blended in smoothly to the rest of the blade to about 12% height and the stacking position of the recambered section altered to minimise the adverse lean/sweep effects that would occur towards the leading edge. This was achieved by moving the section towards the suction surface and forwards to reduce leading edge barrelling effects.

The final designs were checked for smoothness and continuity for axial and circumferential variations in the radial direction. Stereolith models were made of both the rotor and stator geometries to check the final 3D form before committing the design to manufacture.

Figure 8.18 shows the rotor exit total pressure field for the datum and 3D design predicted using TRANSCode along with experimental data for the datum design. The view is looking upstream and the rotor rotates from left to right. Towards the hub endwall the losses increase from around 30% height for both the experiment and TRANSCode flow fields. Although the flow prediction is reasonable in this region at the casing the clearance flow features are poorly modelled. Various tip clearances and grid combinations were used to try to improve the prediction in this region with little success. Comparing the TRANSCode predictions for the datum and 3D (designated DERA2) designs shows how and where the losses are being reduced. The large loss region towards the hub endwall has been reduced and is spread more evenly up the span in this region. This is in agreement with the initial studies which showed that the primary effect of lean/sweep was to unload the endwalls and load up the mid span. Although the clearance modelling was generally poor, the code also indicated an improvement to the level of loss generated at the casing.

Figure 8.19 shows a similar view to figure 8.18 but for the stator exit flow field. The comparison between the experiment and predicted flow fields for the datum design is similar to the rotor comparison; the fixed end of the blade is modelled reasonably well

while the clearance end is poorly modelled. In addition, a mid passage circumferential variation in the pressure field is seen in the experimental data. This is attributed to a bladerow interaction effect which is reinforced by the fact that identical repeating stages are used throughout the machine. The rotor flowfield responds to the potential field of the downstream stator and to the wake structure from the upstream stator passing through it. Comparing the 3D design stator with the datum using TRANSCode shows a similar trend to the 3D rotor. The losses at the fixed end (the casing) have been reduced while the profiles losses over the mid span region have increased.

Throughout the design process the mass averaged total pressure loss coefficient has been used as the parameter to minimise in order to obtain the best blade. While it is difficult to predict the correct absolute level of loss coefficient using modern CFD tools it was considered possible to rank candidate designs using this method. Other methods for ranking blade designs might be to look at how large the areas of reverse flow are and to minimise these regions. This method requires judgement from the designer for each design and inhibits parametric studies when large candidate numbers are involved. For the final 3D design the near suction surface axial velocity contours have been plotted and compared with the datum blade. This is shown in figures 8.20 and 8.21 for the rotors and stators respectively, the zero velocity contour is shown by the thicker contour line.

The datum rotor has a large region of reverse flow at the hub which extends out to 40% towards the trailing edge. At the casing end a smaller region of reverse flow is also apparent at 95% height. The 3D rotor shows no signs of reverse flow and the contours of axial velocity are more evenly spread up the span indicating a balanced distribution of load. For the datum stator a smaller region of reverse flow is seen at the casing, extending down the blade to 70% height at the trailing edge. There are no reverse flow regions associated with the clearance end. The 3D stator has eliminated the reverse flow region and, as with the 3D rotor, also has an even distribution of axial velocity contours along most of the span.

Figure 8.22 compares the static pressure coefficient distributions for the datum and 3D designs for both the rotor and stator at five heights up the span. The datum designs are shown by the solid lines while the 3D designs are plotted using dashed lines. The peak suction surface loading at mid height of both blades is increased for the 3D blades and is reduced towards the endwalls. Figure 8.23 shows in more detail the differences between the two pressure distributions. The difference between the loading (indicated by the difference between the suction surface and pressure surface pressure coefficients) for the two designs is shown against fraction chord length. The distributions indicate that the sections are loaded up more over the forward half and less towards the trailing edge than the datum sections. Since the section shapes are identical over most of the span this

implies that the streamtube thickness variations have changed. The drop in loading at the leading edge for most of the sections indicate a reduction in the incidence.

8.6 Multistage considerations

The TRANSCode solver used throughout the design process solves isolated bladerows only and therefore the multistage implications of the 3D design could not be assessed directly. To get a first order idea of the effect of the 3D design of one bladerow on the performance of the other, calculations were carried out with inlet conditions modified by the effect of the new upstream bladerow. This was achieved by using the measured inlet profile to each bladerow and modifying this profile by the change in exit profile calculated between the datum and 3D blades for the upstream bladerow.

The results of this calculation are shown in figures 8.24 and 8.25 for the rotor and stator respectively. Absolute total pressure and swirl angle are shown for each station and the solid line represents the isolated 3D bladerow with measured inlet conditions (from datum build) while the chained line shows the effect of the upstream 3D bladerow. For the rotor the presence of the 3D stator produces an inlet profile that is flatter and more full at the endwalls. This new profile slightly improves the performance of the 3D rotor and the exit total pressure is increased over the whole span. The higher mid-span loading of the 3D stator increases the stator mid-span deviation. The effect of this is to decrease the incidence onto the rotor which is also more loaded at the mid-span due to the effect of the lean/sweep.

For the stator the presence of the 3D rotor has more of an effect than the 3D stator did for the 3D rotor. The profile at exit from the 3D rotor is flatter and more full towards the casing than the datum rotor profile. The smaller endwall boundary layers with lower levels of overturning improve the stator performance and result in an even flatter profile at stator exit. The overall performance implications of the modified inlet conditions are shown in figures 8.16 and 8.17 where the datum design and final 3D design (Case 11 with LER) are shown with the inlet effect of the 3D design of the other bladerow. The rotor and stator show around 2.5% reduction in pressure loss coefficient from their respective isolated bladerow case. A picture of the final 3D blades along with the datum blades is shown in figure 8.26.

8.7 Conclusions

A set of blading has been designed for the Cranfield LSRC. The blading was based on the datum low speed DERA blading which was designed to represent the fourth stage from the high speed research compressor C147 build 3. The design incorporates a combination of lean, sweep and leading edge recamber to reduce the endwall and 3D losses found in the datum design. A single parabolic arc was chosen to define the

modified stacking axis and a study was undertaken to find the optimum level of axis deformation. The axis was rotated through a blend of lean and sweep and an optimum rotation, based on minimum predicted loss, found for each blade. The following observations were made:

1) Positive lean (obtuse angle between suction surface and endwall) off loads the endwalls and loads up the mid span. Negative lean has the opposite effect. Positive lean also increases the flow angle onto the blade near the endwalls and decreases it at mid span.

2) Sweep has a similar effect to lean except the incidence increase at the endwalls is much smaller and the re-distribution of chordwise loading here makes the endwall sections become more aft loaded.

3) For both rotor and stator a trade-off between the decrease in losses at the endwalls and the increase at mid span produced a net decrease in overall loss as the lean was applied. Beyond a certain level of lean the overall loss then increased as the mid span blading began to suffer flow separation and high loss.

4) Rotating the stacking axis from lean to sweep showed that a minimum loss exists for both bladerows for a certain blend of lean and sweep. For the rotor the blend involved positive lean and forward sweep while the stator calculations showed that positive lean with a little backsweep was necessary for minimum loss.

5) Combining lean and sweep produced a blade shape with less overhang than a pure lean or pure sweep blade of the same loss. Stresses could therefore be lower for combination blades than pure lean blades.

Leading edge recambering was applied close to the endwalls of the fixed ends of both blades. This was achieved by modifying the blade section definition parameters of sections near the endwall. The benefits of leading edge recambering indicated by the CFD were of a similar order of magnitude as the benefits arising from the lean and sweep.

Multistage effects of the 3D design were considered through a simple perturbation model of the inlet flow fields of each bladerow. Although this did not take into account blade force and unsteady effects, encouraging results were produced which indicated that the improved flow through one 3D bladerow benefitted the next bladerow in turn.

Near suction surface axial velocity contours for the rotor and stator show that regions of reversed flow at the hub and casing of the datum design were eliminated for the 3D design. The resulting contours were also more uniformly distributed across the span of each blade.

Chapter 9 3D design aerodynamic measurements

9.1 Introduction

This chapter presents and describes the experimental results obtained from the Cranfield University low speed research compressor for the advanced 3D blade design (DERA2) described in detail in chapter 8. Along with the overall performance, area traverses were obtained in the stationary and rotating frame and blade surface static pressure data were also measured for rotors and stators. The majority of the traversing was completed using 2D cobra pneumatic probes as for the datum build measurements. In addition, however, two new 3D cobra probes were designed and manufactured at Cranfield and used with success at stator 1 and stator 3 exit.

Results of a flow visualisation test using fluorescent dye on a stator cassette are also presented at the three test flow conditions. A throughflow analysis has been undertaken using radial profiles obtained from the stationary frame traverse data and these are compared with the measured overall performance. Comparison of the 3D blade design performance with the datum design and the implications for 3D high speed designs are discussed in detail in chapter 10.

9.2 Overall Performance

The overall performance measurements are shown in figure 9.1 along with the datum design performance levels. Two characteristics are shown for the 3D design, these were the most repeatable from a number of characteristic measurements that all suffered to a varying extent from a jumpy torquemeter signal. The efficiency curve shows a significant increase in isentropic efficiency over the datum design; around 1.5% at design flow rising to almost 3% at near stall. The flow range has also increased with a 25% increase in design-to-stall flow margin over the datum design. This is reflected in the pressure rise curve where the pressure rise towards stall continues to rise strongly towards stall.

Although the scatter in the performance measurements is greater for the 3D design measurements than for the datum measurements, due to problems with the torquemeter, they indicate a clear improvement in performance above that predicted by the design 3D TRANSCode predictions (around 1% improvement at design).

A number of performance measurements were also made at the design flow condition with the rake instrumentation stepped around circumferentially relative to the stators. These are shown as the vertical line of points at design flow. The purpose of this test was to confirm that the level of performance measured was not a result of fortunate instrumentation positioning (see discussion in section 6.3 on datum overall performance) and to try to quantify the effect of believing the fixed rake position data

on measured performance improvement at design flow. Unfortunately the circumferential instrumentation sweep for the advanced design was completed at one degree angular spacings (i.e. 1°, 2°, 3° etc. corresponding to 37.2%, 74.4%, 11.6% stator pitch) while the datum design measurements were completed at even stator-relative spacings across a stator pitch. The 3D design measurements were therefore unevenly distributed relative to a stator pitch and the variation of measured efficiency with stator relative position was therefore not obtained.

If measurements of the 3D build re-start in the future it is recommended that performance measurements be taken with the same instrumentation sweep positions as used for the datum design. It will therefore be possible to determine the true performance difference by averaging the rake data over a stator pitch and comparing this with the performance difference obtained from the set instrumentation position. This exercise will quantify the biasing effect of the rake instrumentation on performance measurement and lead to a better indication of the minimum rake instrumentation coverage needed.

9.3 Blade surface static scans

The blade surface static pressure measurements are shown in figures 9.2 and 9.3 for the rotor and stator respectively. Seven heights up the span were instrumented and these are shown as a column of plots for each of the three flow conditions. The coefficient used is the difference in pressure from an average of the three reference ports (blade surface instrumentation is described in chapter 5) normalised by the inlet dynamic head to the compressor.

The distributions are very similar to the datum design distributions with a high level of loading towards the leading edge and a chordwise distribution of loading which characterises controlled diffusion blading. At the rotor hub the effect of the leading edge recambering can be seen by the largely reduced forward loading of the hub section. Differences between the datum and 3D blade distributions are discussed in more detail in chapter 10.

Contour plots of the suction surface for each blade at each operating condition are shown in figure 9.4. The blade surface is represented as a normalised square extending from 0% to 100% chord and from 0% to 100% passage height. This normalised view eliminates the effect of the sweep in the blades but allows for a direct comparison with the datum surface pressure data. The extent of the instrumentation is indicated by the white space surrounding the colour filled contours.

The increase in peak suction near the leading edge of the stator towards the endwalls indicate that both endwalls are operating at a higher incidence than the mid-height region. This appears to be in stark contrast to the rotor pressure distributions

where the near-leading-edge-peak suction tails off towards both endwalls for all operating conditions. The pressure closest to the leading edge, however, rises towards the endwalls as it does for the stators, this is more apparent in the line plots of figures 9.2 and 9.3. The change in static pressure distributions between the datum and 3D design is discussed in more detail in chapter 10.

9.4 Stationary frame area traversing

Stationary frame area traverses were completed for the 3D build using 2D pneumatic cobra probes at the exit to every bladerow and two 3D pneumatic cobra probes were used at stator 1 and stator 3 exit. The 2D and 3D probes and calibrations are described in more detail in chapter 5. Measurements behind the nine bladerows were completed in two sets since a maximum of six probes can be traversed at any one time. The second set was used to accommodate the two 3D probes in positions already covered by 2D probes in the first set. This allowed back-to-back comparisons to be made between the 2D-probe and 3D-probe derived yaw angle and total pressure fields.

9.4.1 2D cobra probe measurements

The traverse grid used was the same as for the datum measurements; 60 evenly spaced (1/8th of a degree) circumferential points by 21 radial points (distributed closer at both endwalls). The probe setting angles were set to the design expected mean flow angle at each height to save time repeating measurements that may be outside the yaw angle tolerance of $\pm 5^{o}$. The traverse control files used in the final 2D-probe data sets are shown in table 9.1. Table 9.2 shows the axial locations where traverse measurements were made for each data set. The repeat measurements at stator 4 exit were made to verify that the two data sets of each flow condition were measured at the same flow condition. The data presented in the following figures use stator 4 results from the first set and the agreement at stator 4 exit at all three conditions was good.

Figures 9.5 to 9.7 show area contour plots of total pressure coefficient for the design, near stall and high flow conditions respectively. The rotor results are shown in the left hand column and the stators on the right; the stages run from the first stage at the top to the fourth stage at the bottom. The rotor rotates from left to right and the view is looking upstream so that flow to the right of the stator wakes is from the suction surface. The total pressure coefficient used is the same as that used in the datum measurements reported in chapter 6 ({Pt-Pswall}/(Ptave-Pswall]).

At rotor exit there is a similar circumferential non-uniformity of the flow at all three conditions to that seen in the datum design measurements. Since this was partly due to a potential interaction between the rotor and downstream stator the

circumferential position of the non-uniformity at each radial height is dependant upon the nature of the relative bowing of the rotor and stator blade rows. The rotor suction surfaces face different directions to the stator suction surfaces and both are bowed with their suction surfaces making an obtuse angle with the endwalls. The potential fields from the mid-span sections will therefore interact first and this interaction will quickly move towards both ends of the blades as the rotor passes the stator. The 3D blades will therefore have different unsteady flow features from the datum blades. Investigation of the 3D unsteady performance of the 3D and datum blading is outside the scope of this thesis and is recommended for future work.

The stationary frame traverses downstream of the stators show that the wake loss increases from around 65% passage height to the casing in a similar manner to the datum stator wakes. These loss peaks tend to migrate radially away from the endwall especially near stall. At mid-passage the radial distribution of total pressure is improved towards the hub where an island of high total pressure resides. This fuller total pressure profile has convected through from the upstream rotor and is evidence of an improvement to the rotor hub performance over the datum design. The losses associated with the stator clearance flow have also been reduced compared to the datum stators. Further comparisons with the datum results are presented in chapter 10.

Figure 9.8 shows radial profiles of total pressure ratio measured behind the rotors, stators and IGV at design flow, near stall and high flow respectively. The profiles were calculated from pitchwise mass averages of the stationary frame area traverse data. The radial profile at a total pressure ratio of around 1.0 is for the IGV and the following pairs of profiles are for the four stages from front to back. The Z shaped profiles correspond to rotor exit and the profiles immediately to the left of them correspond to their respective stator; the difference between them represents the pressure loss through the stator.

The profile of total pressure at stator 2 exit for all flows (though for design flow in particular) show a significant drop in pressure at mid-height. This 'hole' is almost filled at stator 3 and 4 exit. This feature arises from the presence of the high total pressure towards the outer passage (also seem in the datum design) and the improvement in pressure near the hub producing a now noticeable hole in the middle. It is probably exacerbated by the increased level of mid-span loading and decreased endwall loading that is characteristic of bowed blading. The harder worked mid span generates more loss than the ends producing an 'M' shaped work profile. This difference increases as the blading is driven harder towards stall and is highlighted by the near stall flow visualisation pictures of the stator 3 cassette where a strong mid span separation is evident (see discussion on figure 9.18).

Figure 9.9 shows the radial profiles of absolute yaw angle at rotor and stator exit for the near stall, design and high flow operating conditions. The profiles were derived from pitchwise mass averages of the area traverse data. The first stage rotor shows the largest difference from other rotors over the outer half of the annulus. This is similar to the datum compressor where the lower turning was put down to the higher rotor 1 incidence in this region due to the reduced absolute flow angle at IGV exit. The largest difference between the two compressors is that the 3D blading has generally more '2D' and uniform profiles than the datum blading.

9.4.2 3D cobra probe measurements

Figures 9.10 and 9.11 show contour plots of total pressure for stator 1 and stator 3 exit respectively. They show results as measured by the 2D and 3D cobra probes for near stall, design and high flow conditions. The dark bands at the casing for the 3D probe data cover data points where calibrations could not be applied to the measured data. This has probably occurred due to the increased interference of the extra fourth port above the pitot port with the casing endwall. This would give a false pitch angle reading and send the calibration lookup routine outside the calibrated range of the probe. Generally the comparison between the two data sets is good with the general flow features well captured in both cases. There are some differences in the mid passage region but the main differences arise from a slight decrease in measured total pressure for the 3D probe. Overall the results are encouraging and increase confidence in the 2D data while helping to validate the 3D probe design.

Fig 9.12 shows the same comparison as figures 9.10 and 9.11 but for the measured yaw angle at stator 3 exit. The measurement of yaw angle by the 2D probe is expected to be less accurate in a 3D flowfield than the 3D probe which has been calibrated over a range of pitch angles. The differences are therefore expected to be larger towards the endwalls where there is more radial flow present in clearance vortices and corner loss regions. Results at stator 1 exit have not been shown since the probe is known to have slipped in the traverse cradle throughout the traverse. When traversing was complete the traverse cradle was taken off the rig and mounted on the calibration tunnel where a 7 degree turn of the probe was necessary to null the probe. This is similar to the yaw angle error measured by the last sweep but a correction to the traverse data is not possible since it is not known when and how the probe slipped during the traverse. It is recommended that a more substantial arrangement for mounting the probe be found for future work. This may involve machining a flat onto the probe stem to act as a reference face and stop any unexpected rotation.

At stator 3 exit the yaw angles agree well and demonstrate that the probe design is working in a manner consistent with the 2D cobra probe design. Figure 9.13 shows the secondary velocity vector flow fields for stator 1 and stator 3 exit at all three flow conditions. The velocities were derived from the measured static and total pressure fields and assume no air density change from ambient conditions. The velocity components were then calculated using the measured pitch and yaw angles and the velocity components secondary to the main flow direction (defined as the average yaw and pitch direction between 35% and 65% height) were derived. The secondary velocity vectors show a clear vortex structure towards the hub to the pressure side of the nearest stator wake for both stator 1 and stator 3 exit. This corresponds in location to the centre of a total pressure loss core shown in the 2D stator exit area traverses and confirms that the feature is the clearance vortex from the previous blade.

At the hub the rotational effect of the endwall on the flow can be seen, this produces an underturning of the flow. There is a large amount of radial flow in the wake towards the hub. This could be due to the clearance flow vortex from the previous blade inducing radial flow in the slower moving wake fluid. This radial flow is stronger at high flow for stator 3 than for stator 1. The sharp rise in radially outward flow near the casing as measured by both probes for all flow conditions is most likely where probe-endwall interference effects start to increase. As the upper port nears the casing the flow velocities over the top of the probe will increase and the measured upper port pressure decrease. This will give the probe the impression that it is operating in a high pitch angle flow. This effect will not occur at the hub since both the upper port and the probe stem are away from the endwall.

The results from the 3D probes are encouraging and they have demonstrated an improvement over the conventional 2D cobra probes. While appreciating that there is nothing new about 3D probes, their every day use in the Cranfield rig as a replacement to the 2D probes would greatly improve the usefulness of the traverse measurements for only a small increase in measurement effort. If sting mounted probes were manufactured along with insertion plugs (to allow replacement of the probes from outside the casing) then probe stem effects would be reduced, the sensing head could be more easily and accurately machined and different axial planes could be measured including the possibility of traversing inside the blade passage.

9.5 Rotating frame area traversing

Rotating frame area traverses were completed at rotor 3 exit for design flow and near stall flow conditions. Problems were experienced with the rotating Scanivalve and slipring so traversing at high flow was not possible because of lack of time due to delays arising and the urgency of a planned Roll-Royce test following the DERA

measurements. Planned measurements at inlet to rotor 3 were also cut from the programme as in the datum build measurements.

Figures 9.14 and 9.15 show results from the rotating frame traverse work for design flow and near stall respectively. Contour plots of total pressure coefficient are presented, these have been calculated in a similar manner to the stationary frame results except that the mid-height static pressure (derived from the probe measurements) was used instead of P_{wall} because the effect of the radial pressure gradient changed the coefficients significantly from the stator results. Contour plots of relative flow angle are also shown along with radial profiles of total pressure ratio (ratioed to atmospheric pressure) and relative yaw angle. The view in the contour plots is looking upstream and the rotor rotates from left to right.

The black blocks on the contours mask regions where the probe calibration failed to find a result. This occurred in the mid height region at both flow conditions despite extrapolating the probe calibration map out to $\pm 60^{o}$. This problem did not occur for the datum design measurements and is most probably due to the closer proximity of the rotor trailing edge to the probe for the swept blades than for the datum blades. The probe traverse plane is approximately 30% chord downstream of the datum rotor trailing edge and 10% chord downstream of the 3D rotor trailing edge at mid height.

During traversing the measured mean pressure level for consecutive sweeps often increased or decreased in an inconsistent manner and this was due partly to a build up of copper deposits on the slip rings and also a faulty Scanivalve power supply cable that had been squashed and was partially short circuiting thereby changing the power to the rotating Scanivalves. Repairing the power supply cable improved the signals but did not solve the problem completely. Up to three sweeps could be completed before the rig had to be stopped and the slipring blown through with a high pressure air line so that signal levels were restored. A radial traverse measurement was made between the rotor wakes so that the levels of each sweep could be adjusted to produce an overall contour plot. Unfortunately this method did not produce sensible results so the pressure levels were adjusted until the mass average pressure level at each height matched the rotor relative exit pressures from the experimental throughflow analysis.

The problems encountered with the rotating frame measurements for the 3D build make quantitative comparisons with the datum measurements difficult. At near stall the wake position steps across circumferentially at different heights producing a zig-zag effect at some positions. This is because there is no feedback on the probe position and so the probe start position is set by eye through the laser window using a

stroboscope. The presence of backlash in the rotating traverse system and the fact that it sometimes misses a command to move on to the next point add to the problem.

At design flow the large thick wake region seen in the datum design towards the hub has decreased with the losses moving further out towards the mid span. This is consistent with the 3D design TRANSCode predictions which show the endwall loading decreasing and the mid span loading increasing as the blade lean/sweep is increased. There is a marked improvement in the mainstream flow in the lower half of the passage where the total pressure level has been maintained towards the hub. At the casing the region of low total pressure indicating the clearance vortex region has reduced in size and is positioned closer to the nearest rotor wake. The comparison of the 3D rotor performance with the datum rotor is discussed in more detail in chapter 10.

9.6 Flow visualisation

Figures 9.16 to 9.18 show photographs of the flow visualisation studies for the design flow, near stall flow and high flow conditions respectively. The blades were painted in the same colours as for the datum build flow visualisation; suction surface red, platform green and the pressure surface blue. At the design flow condition (figure 9.16) platform flow moves onto the suction surface at around 15% chord. The flow moves along the blade span as it progresses downstream marking out a triangle of platform-originating boundary layer flow. The affected region is slightly smaller than that seen for the datum design and does not have the same rapid initial flow onto the suction surface. The 3D stator also does not have the region of recirculating flow indicated by the purple region towards the casing endwall.

At high flow this corner flow feature is reduced in extent, due to the reduced cross-passage pressure gradient, while at near stall the feature takes on a completely different nature. The boundary layer flow onto the suction surface takes two distinct paths, a shallow path similar to the high flow and design flow corner feature, and a steep path which bifurcates suddenly at around 50% chord. One branch of this second path travels axially downstream while the other heads in a spanwise direction before turning downstream at approximately 40° to the axial direction. Just downstream of the second branch a clearly defined parabolic shaped flow separation is seen. The pattern described is repeated well on the second blade of the cassette demonstrating that it is a real and repeatable effect. Evidence of this separation is seen in figure 9.6 but not in the steady blade surface static pressure measurements and it is therefore possible that the separation is unsteady. If the separation fluctuated in size with every rotor passing event this could explain why distinctly different secondary flow paths

occur (each one for a different state of blade loading) and why the steady surface pressure measurements failed to detect it.

If the separation size is fluctuating then when it is at a maximum the extra mid-height blockage created will act to relieve the endwall diffusion and the endwall flow moves onto the suction surface at a shallow angle, as it does for the high flow case. When the diffusion is restored the strong cross passage pressure gradient drives the flow up the suction surface, as it did for the datum stator at near stall. On approaching the unsteady separated region this second branch is forced to move around the blockage on either side. The timescale for the boundary layer motion up the blade is probably longer than the unsteady up and downstream perturbations that are linked to blade passing frequency. The resulting dye path is therefore a history of this dynamic boundary layer motion and not simply the result of a series of instantaneous states.

9.7 Throughflow analysis

A throughflow analysis has been completed for the 3D blade design using the experimental traverse data for each of the three flow conditions measured. Mass averaged radial profiles of total pressure and flow angle were calculated from area traverses obtained in the stationary frame at the exit to each blade row. All the pressures were referenced back to a standard ambient pressure. The overall performance of the three calculations are shown in figure 9.19 along with the performance characteristics measured using the torquemeter and the instrumented rakes and the datum build results.

The difference in pressure ratio between the throughflow and measured characteristic is due to the fact that the outlet rakes (used for characteristic) do not obtain as good a representation of the exit total pressure as the traverse at stator 4 exit (used in throughflow). As with the datum build the difference in pressure at each condition is similar at all three conditions. If the difference in exit pressure measurement is taken into account the efficiencies at design flow would closely match. The close agreement of $\Delta H/U^2$ at design flow indicate that the yaw angle measurements agree well with the level of work derived by the torquemeter, this was also the case for the datum measurements. At near stall and high flow the agreement is not so good but the measurement error needed to produce these discrepancies is of the order of 0.5^{o} as shown by the error bands on the datum calculations (see section 6.8).

The performance improvement of the 3D design over the datum of around 1.5% at design flow shown by the characteristic measurements is confirmed by the throughflow analysis. Significantly, the 4% efficiency improvement between the datum and 3D throughflow results at near stall show that the large improvement in stall margin and performance at near stall is genuine.

Detailed results of the throughflow analysis of the experimental data (with no changes to measured angles or pressures) are presented in figures 9.20a to 9.22b for the design flow, near stall and high flow conditions respectively. Radial profiles of loss, loading parameters, exit flow angle, incidence, deviation and stage efficiency are shown for all four stages using the colour coding shown in the key. The profiles of pressure loss coefficient (PLC) at design flow at rotor exit (figure 9.20a) show a significant reduction in loss over the first 30% height compared to the datum rotors. This is where most of the performance improvement is coming from with little discernible difference in the stator performance. The performance at the rotor tip is also improved.

The rotor hub and stator casing incidence has been greatly reduced due to the leading edge recambering and increased axial velocity in this region. This has improved the rotor hub De Haller number and the reduction in incidence near the casing for the stator has left a region of relatively higher incidence at 70% height. This increased incidence could be exacerbated by more flow passing through the hub region. This could be causing the area of separation seen in the flow visualisation at near stall which is at a similar height. Generally the loading and deviation profiles are more '2D' or radially uniform than the datum profiles. The losses and stage efficiencies are also more consistent from stage to stage than the datum results.

The first stage performs differently from the other stages, this is shown by the dark blue line in the diffusion factor, De Haller number and $\Delta H/U^2$ plots in the figures. This is similar to the datum design which also shows the work and loading levels of the first stage to be lower than the following stages. The datum design shows more of a spread in the stator loss profiles than the 3D design and this is possibly due to the fact that data at some planes were missing and had to be inferred from other stages. A more detailed appraisal of the 3D design is given in chapter 10.

9.8 Conclusions

The 3D (DERA2) low speed blades have been manufactured and tests have been conducted on the Cranfield University low speed research compressor. A comprehensive set of measurements have been obtained which include; overall performance mapping, stationary frame traversing at all planes, rotating frame traversing at rotor 3 exit, blade surface static pressure measurements at stage 3 and flow visualisation studies. With the exception of the rotating frame traversing all the measurements were obtained for three flow conditions; near stall, design flow and high flow.

In addition to the standard instrumentation used in the datum (DERA1) test measurements, two 3D pneumatic probes were designed, manufactured and used at

Cranfield on the 3D build. These proved to be successful in mapping the 3D nature of the flow behind the first and third stators. Comparison of the yaw angle profiles and total pressure profiles derived from conventional 2D probes and the new 3D probes show encouraging agreement. The probes did, however, show strong signs of endwall interference at the casing due to the arrangement of the upper port. This may be improved by a better head design mounted on a sting to reduce the probe stem effects.

It is recommended that further 3D probes be developed and routinely used on the Cranfield rig since they offer improved understanding of the 3-dimensional aspect of the flow field. This need will become increasingly important as designers focus on controlling these areas of the flow by applying 3D design concepts.

The overall performance measurements show an efficiency improvement over the datum design of around 1.5% at design flow. This improvement extends over the entire flow range and increases to around 3% at the datum design stall point. The 3D design also has a significantly improved stall margin which other recent 3D designs have failed to achieve (an increase in efficiency at design often comes with the penalty of reduced stall margin and near stall efficiency). The design also has a stronger pressure rise characteristic which increases steadily up to the stall point.

Rotating frame area traverses and throughflow analysis show that the performance improvement is coming mainly from the new rotor design. The large hub endwall loss region of the datum rotor has been significantly reduced and the wake losses more evenly spread up the blade height. This change in performance was predicted in the TRANSCode design solutions.

Flow visualisation measurements on the stator show the 3D design behaving very differently from the datum design at near stall. The resulting flow pattern suggests a mid-height '2D' flow separation linked to an increase in incidence at this height. This is possibly an unsteady feature since it is not observed in the steady state surface pressure measurements.

Chapter 10 - 3D design appraisal

10.1 Introduction

A set of 3D low speed blading based on the datum blading (reported in chapters 5 and 6) has been designed and tested at the Cranfield University low speed research facility. The aim of the design was to improve upon the performance of the datum blading through the use of '3D' design concepts such as lean and sweep. The details of the design are reported in chapter 8 and the test measurements are reported in chapter 9.

This chapter appraises the 3D design (designated DERA2) through comparing detailed performance and traverse measurements with the datum design. The differences between the two blade sets are drawn out of the test measurements and the throughflow analysis for the three flow coefficients measured.

In addition, an unsteady 2D prediction of the mid-height sections of stage 1 has been calculated using un-NEWT for the design flow condition. This was similar to the unsteady calculations carried out for the datum stage where potential field interactions were predicted between the stator and rotor. These were found to be responsible in part for the circumferential variations in flow at exit from all the rotors. For the DERA2 blading the prominent axial sweep of the rotor has moved the mid-span rotor section closer to the stator when compared to DERA1. The effect of this closer proximity has been modelled and the results compared to test and to the datum design results.

Finally, the implications for a future high speed 3D design, based on the success of the low speed 3D design, is discussed. The transformation back to the high speed environment is addressed along with the geometric restraints that a high speed design must accommodate.

10.2 Performance improvement

10.2.1 Overall performance

Figure 9.1 shows the overall performance of the 3D design compared to the datum design for efficiency, $\Delta H/U^2$ and pressure rise coefficient. The 3D design demonstrates a significant increase in efficiency at design flow (around 1.5%) which increases to around 3% at near stall along with a significant improvement in stall margin. This performance is achieved at the same level of stage loading as the datum but with a strengthened pressure rise curve over the whole flow range. At near stall the pressure rise coefficient maintains a negative slope up to the instability limit and does not turn over as it does for the datum blading. This is an encouraging result for high speed applications as it should give a more robust stage, inspite of the differences between high and low speed cases at off-design conditions.

A tare torque calibration has not been made although a correction has been applied to the torque measurements based on a previous tare torque test carried out for a hub/tip ratio of 0.85 and corrected to 0.91 via an empirical formula. The absolute level of efficiency may therefore not be as accurate as the change in performance measured between the two builds. The traverse based throughflow analysis shown in figure 9.20 confirms the change in efficiency between the two builds although at a slightly different absolute level of efficiency. It can therefore be concluded with confidence that the 3D design demonstrates a significant improvement over the datum blading.

10.2.2 Radial Profiles

Figures 10.1 and 10.2 show where these improvements have arisen from. They show radial profiles of pressure loss coefficient, incidence deviation and Va/U for the rotor and stator respectively for the near stall, design flow and high flow operating conditions. The 3D design results are shown by the solid lines while the chained lines represent results from the datum blading. The results were obtained from the experimental throughflow calculations and are discussed in more detail in chapter 9. The average of the last three stages have been plotted (the first stage behaviour usually differed from the following stages) to eliminate stage-to-stage variations which were more significant in the datum results.

The radial profiles of pressure loss coefficient show a large increase in loss across the rotor in the datum design at the hub (from around 10% to 30% height). This feature has been curtailed in the 3D design and the resulting loss profile is generally more uniform over the whole span. At the tip the datum rotor suffered another significant increase in loss from around 85% to the casing. This loss has also been significantly improved in the 3D design although some increase in loss in this region does remain. For the stator there is a less discernible difference between the two loss profiles, especially in view of the fact that the datum stator losses were less consistent from stage to stage than the 3D stator losses (see figure 6.27a).

As the flow coefficient drops from the high flow condition to near stall (although the 3D design is not so near to stall) the bulge in loss for the datum rotor near 20% height increases in a progressive manner affecting a larger portion of the annulus. The peak loss associated with the clearance flow however remains relatively constant as the flow condition is changed. The 3D design also shows this trend (although to a lesser extent) with the hub losses spreading out radially with reduced flow. The stator losses change less with operating point for both designs.

The profiles of incidence show a large spanwise variation (from -10 to 20 degrees) for the datum rotor and this is due mainly to the calculation of blade leading edge angle rather than flow angle variations. The problems with calculating the leading edge angles

arise from the bluntness of the low speed blade, this is discussed in more detail in chapter 7 where the operating condition of a near-hub section is shown to be near the bottom of its loss bucket and therefore at a sensible incidence despite the high indicated value. For comparison purposes differences between the datum and 3D blade incidences should be considered rather than absolute levels. It should also be noted that chapter 4 showed the loss buckets of the low speed sections to be considerably broader than their high speed counterparts so changes in incidence with flow will be significantly larger than at high speed.

Figure 10.1 shows the 3D rotor incidence is greatly reduced over the datum from the hub to around 25% height. This is mostly the effect of the leading edge recambering at the hub of the 3D rotor although the Va/U over the first 25% height has increased, contributing to the incidence reduction at the hub. For the stator the leading edge recambering and increased flow at the casing has greatly reduced the incidence in this region by up to 10 degrees. This has left an island of relatively higher incidence at 70% height, particularly near stall, which is the most likely explanation for the presence of a separated flow region at this height seen in the flow visualisation results and discussed later. Between 10% and 15% height the 3D stator has a region of incidence reduced by around 4 degrees while between 30% and 80% height the incidence has increased by around 2-3°. This pattern is reflected in the distribution of stator inlet Va/U (also figure 10.2). The flow through the inner and outer 20% height has increased while from 20% to 80% it has decreased significantly compared to the datum design. The distributions of Va/U for both the rotor and stator are very similar and show that the flow has moved towards both endwalls decreasing the endwall incidence and increasing the mid-span incidence.

The profiles of deviation show that while the overall deviation for the rotor and stator is generally higher for the 3D design than for the datum the profile at design flow is arguably more uniform up the span (particularly for the rotor at design flow. The 3D design therefore has improvements due to the reduction of severe incidences in endwall regions from the leading edge recambering and improvements due to the spanwise redistribution of flow arising from the blade lean and sweep.

10.2.3 Stator exit flow field

Figure 10.3 compares the stator exit total pressure coefficient contours of the datum and 3D stators for the three measured operating conditions at the third stage. The 3D stator wakes appear curved in the measurement plane due to the bowing of the blade and the pressure loss deficit near the casing is reduced compared to the datum. The centre of the near casing wake loss is further from the endwall than for the datum blade and the losses are spread further down the span. This is because the endwall losses have

reduced and the loading at around 75% has increased due to the increased incidence here. At the hub the 3D blade shows a reduced area of loss at the foot of the wake, this region is attributed to total pressure loss associated with the clearance vortex from the previous blade. During the design phase the 3D TRANSCode predictions failed to capture the structure and detail of the clearance flow but did predict a reduction in loss in this region for the 3D blading. This loss reduction is therefore most probably due to first order effects such as the general reduction in endwall diffusion/loading arising from the blade lean/sweep.

Between the wakes the core flow is more evenly spread up the span for the 3D stator although figure 9.5 shows that this has developed through the compressor; at stator 1 exit a large island of high total pressure resides towards the casing with a smaller region at the hub, these two regions merge more at the latter stages. The datum blading remains unevenly distributed in the mid-passage region throughout the stages. The improvement at the hub for the 3D stator is due mainly to improvements in the rotor hub flow (as discussed above for the throughflow radial profiles) and the way these improvements cascade through the compressor. The improvement in the first stage performance produces better inlet conditions, near the endwalls, for the next bladerow which in turn performs better and improves the flow in the next bladerow. This is seen in the throughflow results presented in figures 9.21 to 9.23, where the first stage is generally out performed by the other stages, and in the numerical investigation of repeating stage effects presented in chapter 8 on the 3D design.

At near stall the stator wakes thicken and the regions of high total pressure in the core flow become more polarised. The core flow pattern is shifted towards the adjacent pressure surface (to the right in the figure) due to the increased inlet flow angle (the inlet field convects further to the right). This starts to expose a mid-span region of low total pressure towards the middle of the passage. At high flow this low total pressure region resides at the centre of the passage. The kidney shaped high total pressure region at high flow is very similar in both the datum and 3D stator flow fields. The absolute frame total pressure coefficient contours at rotor 3 exit are shown in figure 10.4. These show how the circumferential variations at stator inlet have changed for the 3D blading. At design flow and near stall the distortions are more radially aligned and evenly distributed. These inlet patterns are convected through the stator as shown in the stator exit results (figure 10.3). The stator performance may therefore benefit from the 3D rotor exit flow field, particularly at design flow where the improvement at the mid-passage near the hub is considerable.

At design flow and near stall the stator wake losses (figure 10.3) near the casing appear to be linked more with the endwall flow for the datum blading than is the case for the 3D blading. For the latter the increased incidence at 70% height, shown in the radial

profiles and the separation at this height shown latter in the flow visualisation, suggest the increased loss at this height is more 2D in nature. The 3D blading has higher levels of Va/U at the endwalls, as seen in the radial profiles, and hence the losses are more two dimensional and away from the endwalls than for the straight datum blades.

10.2.4 Rotor exit flow field

Figure 10.5 compares the rotor exit flow field measured for the datum (left hand column) and 3D rotor at near stall, design and high flow (no high flow data was measured for the 3D rotor). Total pressure coefficient is presented using total pressure measured in the rotating frame of reference at rotor 3 exit. The view is looking upstream and the rotor rotates from left to right. The measurements for the 3D rotor were more problematic to obtain due to instrumentation problems and these were the best that could be obtained in the time available. The pressure levels of individual sweeps were inconsistent and so the resulting 3D rotor flow field has been corrected to produce the same radial pitchwise-averaged total pressure profile as the experimental throughflow results. This is discussed in more detail in chapter 9. The total pressure coefficient profile, obtained by mass averaging the rotating frame traverse data, is compared to the rotor relative pressure profile from the throughflow calculation in the lower right hand plot. This plot is for the datum rotor at design flow and shows a generally good level of agreement. The corrected 3D rotor data, while not ideal, should therefore give a good indication of rotor performance.

Despite these difficulties the 3D rotor exit data clearly shows a significant improvement over the datum rotor. The large region of wake loss near the hub merges with the hub endwall boundary layer flow at exit from the datum rotor. The 3D rotor has a significantly thinner wake and endwall boundary layer in this region. Also the core flow shows a region of higher total pressure extending down to 15-20% span. At the tip the losses associated with the clearance vortex are reduced in size and loss in a similar manner to the 3D stator flow field.

At near stall the 3D rotor remains well behaved with only a gradual increase in loss, although the data quality is poorer here (the pitchwise shifts in wake position are due to traverse movement problems and should be ignored). These rotor exit traverses support the experimental throughflow results (derived from stationary frame data) that show the largest improvement of the 3D design to be at the rotor hub.

10.2.5 Blade surface pressure differences

Blade surface static pressure measurements have been made for both the datum and 3D design blading from the third stage rotor and stator. The instrumentation and experimental setup for these measurements are discussed in chapter 5 and the results are

reported in chapters 6 and 9 respectively. The differences between the static pressure distributions of the two designs are difficult to appreciate by comparing the contour plots or distributions alone due to the small level of difference between them. Changes between the designs have been highlighted by plotting contours of the differences between suction surface static pressure coefficient. These are shown in figure 10.6 for the rotor and stator at the three measured flow coefficients. A thick contour denoting zero change has been plotted to clearly separate the regions of positive and negative change. The blade surface has been plotted as a normalised square in the same manner as figure 6.14 and figure 9.4.

The first point to note is that the differences between the static pressure distributions are very small, hence the jaggedness of the difference contours. Despite these low levels a definite and repeatable pattern is observed which strengthens towards stall. The DERA2 rotor has a region of higher suction (than the datum rotor) which is centred around 25% chord and covers most of the mid-span region. At the leading edge the peak in suction has been reduced significantly (this is shown by the dark blue band). The DERA2 rotor therefore shows lower leading edge loading than the datum and the diffusion occurs more gradually over the blade chord.

Higher levels of positive difference are observed for the stator than the rotor. At design flow the stator contours show a peak in suction at mid-height at around 20% chord. Upstream of this the leading edge is split into two regions; the lower half has reduced loading while the outer half has increased loading. This is broadly in agreement with the incidence variation shown in figure 10.2 although these cross each other at around 25% height.

The surface static pressure measurements presented here are somewhat surprising. The main feature of the 3D rotor flow is the large reduction in hub incidence due to leading edge recambering. A larger decrease in leading edge loading at the hub compared to the mid-span was therefore expected in the pressure data. A similar trend was also expected at the stator casing where an incidence reduction of around 15° was indicated by the throughflow analysis.

10.2.6 Flow Visualisation

Figure 10.7 compares the flow visualisation results for the datum and 3D designs at near stall, design and high flow (high flow results are not available for the datum stator). Details of the measurements and further views are presented in chapters 6 (for datum) and 9 (for 3D design). The nature of the respective stator flow patterns has also been discussed in detail in these chapters and the purpose of this figure is to draw out the main performance differences.

The datum stator has a relatively large endwall flow feature at the platform end (the casing). This is evident from the mixing which occurs between the platform dye (green) and the suction surface dye (red) which results in a triangular region of purple coloured dye (some blue pressure surface dye may also have moved onto the suction surface from around the trailing edge). Platform flow is clearly moving onto the blade producing the region of high wake loss near the casing (see the stator exit traverse results). This purple region was the only area of dye which had not dried completely after the cassette was held on condition in the compressor. The shear stresses are therefore much lower here and it is likely that the boundary layer is separated in this region. This region extends further upstream and up the span from the design flow to near stall flow condition.

The 3D stator shows a stark contrast to this behaviour. At design flow no separated flow region is evident, although the platform flow does move onto the blade suction surface the coloured dyes remain largely un-mixed. This result is in agreement with the near suction surface velocities predicted by TRANSCode (reported in chapter 8) which show the datum stator suffering from a large region of reverse flow near the casing and the 3D stator having no reverse flow.

At near stall the corner flow region does not simply grow across the blade as it does for the datum stator. Instead a rather complex flow pattern is set up which possibly arises from an unsteadiness in the endwall flow producing a number of branched flow paths. This flow pattern is discussed in more detail in chapter 9. At 60-70% blade height (the cassette is viewed with the casing platform at the bottom) a parabolic shaped region of mixed dye is seen. The blue dye from the pressure surface has mixed with the red suction surface dye and reversal of the boundary layer flow has clearly occurred. This region shows more evidence of a shear stress than the datum stator corner separation because the dye is fully dried and the base paint is almost visible. This supports the view that the separation may be unsteady.

This separated region is linked with the centre of high wake loss seen in the stator exit traverses and the high incidence seen in the radial profiles. The stall margin for the 3D design has improved significantly and it is interesting that the nature of the stator surface flow at near stall has changed from being dominated by a three dimensional corner flow feature for the datum blade to a predominantly two dimensional blade-to-blade separation for the new design.

10.3 Un-NEWT modelling

2D unsteady modelling of the mid-span sections of the first stage of the datum design was undertaken to study the effects of the downstream stator pressure field on the rotor performance and to understand the pitchwise variations in total pressure that have

been measured in the stationary frame behind the rotors. This work, which demonstrated how the pitchwise variations were occurring, is reported in chapter 7.

The 3D design uses largely the same section shapes as the datum design and at mid-span the two designs are exactly the same for both rotor and stator. The difference between the 3D and datum stages at mid span is the change in blade axial spacing due to the sweep of the blading. The 3D stator design incorporated mostly pitchwise movement of the middle section whereas the rotor design incorporated forward sweep of the endwall sections and therefore rearward movement of the mid span section (because the mounting boss position remained centred on the hub section centroid).

Since axial movement of blade sections is almost unavoidable if 3D design methods are to be used and since the interaction effects of the datum low speed compressor were relatively strong an unsteady calculation was undertaken at the reduced bladerow spacing of the 3D design. The aim of the study was to assess the impact on the pitchwise flow non-uniformities of bringing the rotor closer to the stator and comparing the prediction results with traverse measurements.

Figures 10.8 and 10.9 show the static pressure and relative flow angle contour histories for the mid-height of the first stage from the 3D design. The prediction was carried out on a similar grid to that reported in chapter 7 using the same boundary conditions and running options. The rotor geometry was moved closer to the stator so that the grid upstream of the rotor trailing edge shifted uniformly and the grid between the rotor trailing edge and stator leading edge compressed to accommodate the reduced gap. The 3D stage axial spacing is 78% of the datum stage axial spacing.

The static pressure contours and flow angles show a similar time history to the prediction at the datum axial spacing although the quality of the solution around the slide plane is degraded, possibly due to increased interference from the bladerows. Figure 10.10 shows the time averaged results and compares them to the datum spacing solution (DERA1) and the measured results from DERA2 at stages 1 and 2. Also shown are the static pressure coefficient distributions around the rotor at different fractions of stator passing.

The solid black line in the normalised total pressure plot shows a lower magnitude of variation than that predicted for the DERA1 (Blue line) spacing. This result appears to be greatly affected by interference from the slide plane. The pressure loading and relative yaw angle plots shown further down the page give a better indication of the effect of reducing the axial spacing since these results rely on a larger area of the solution away from the slide plane. The experimental results in the first plot compare well in terms of magnitude of total pressure variation. At the first stage the magnitude is relatively low compared to the variation at stage 3. In chapter 7 the extra variation at the

third stage was attributed to the upstream stator wakes passing through the rotor in addition to the influence of the downstream stator.

It can be argued that the measured difference in phase between the datum and DERA2 blades for the variations in normalised total pressure at stage 3 could be due to the differences in circumferential transport of wakes between bladerows due to the different distances between blade rows. The DERA2 measured data has been shifted by just over 25% of a stator pitch to the right in the figure to take into account the circumferential movement of the mid-section of the bowed stator blade relative to the start position of the traverse measurements. At exit from the upstream stator the wake structure transports circumferentially under the influence of the inter-stage swirl. At exit from the rotor the circumferential variations transport at a much larger swirl. By moving the rotor mid-section backwards, through sweeping the rotor, the two transport phases change in duration and a circumferential shift relative to the stator leading edge is possible. Since the relative axial spacing between the bladerows varies with span (due to the lean/sweep) the circumferential shift in total pressure variations will also vary with span. This can be seen in figure 10.4 where a significant straightening of the higher pressure region at rotor 3 exit is apparent.

The rotor pressure loading histories have been plotted in the third plot of figure 10.10. These were calculated by integrating the instantaneous pressure loadings, shown for DERA2 in the second plot, around the blade. The DERA2 (black line) loading history shows a similar pattern and phase as the DERA1 prediction but has a much greater amplitude. The relative yaw angle history shown at the bottom of the page shows a similar result. A group of nodes just upstream of the leading edge were used to find an average relative rotor inlet angle at each instant in time. This has been plotted from the rotor's perspective; ie against fraction of the downstream stator pitch passing the rotor. The relative yaw angle for the closer spaced case changes by just over $\pm 2^{o}$ compared to $\pm \frac{1}{2}^{o}$ for the datum spacing. This appears to be large considering the gap reduction was only around 25%. However, these results demonstrate the increased pressure potential interaction of the bowed blading over the datum blading leading to greater unsteady incidence variation and load variation even though the magnitude of the total pressure variations remain largely unchanged (compare stage 3 measurements at top of figure).

10.4 High speed 3D design

The work so far has concerned the transformation of a high speed compressor to a datum low speed design, the evaluation of this process and the re-design of the datum low speed design using 3D design methods. Although the transformation of the 3D low speed design back to high speed blading is beyond the scope of this thesis it is worth briefly discussing this issue for completeness.

It is the author's opinion that the high speed transformation of DERA2 blading would be undertaken indirectly by using the same methodology and approach as was used in the low speed design rather than directly transforming back from the DERA2 geometry using some kind of rule of thumb. For example a parabolic stacking axis would be employed and the C147 fourth stage blading used as a datum from which to start the design process. Parametric studies of stacking axis 'strength' and orientation would then be undertaken using the same goals as before and using the same constraints. The final 'strength' of the stacking axis parabola would therefore result from the same process of balancing the mid-span and endwall losses. Leading edge recambering of the fixed ends of the blades would follow along similar lines although the radial extent of the section changes would be restricted to the same fraction of span as the low speed blades.

It is likely that the resulting high speed 3D design would have less overhang and leading edge recambering than the low speed blading. The change in endwall diffusion due to the blade lean arises from the radial pressure gradient set up by the component of blade force in the radial direction. It is the authors opinion that the same blade lean angle is needed in the high speed design to produce the same curvature of the streamtubes towards the endwalls as the low speed design. However, since the flow in the high speed compressor is compressible the density will change across the bladerows and therefore less area contraction will be needed for a given change in diffusion. Therefore the high speed blades are expected to require less lean than the low speed blading. The greater sensitivity of high speed blading to changes in incidence, as shown in chapter 4, means that less leading edge recambering will be required for the high speed blades.

The combination of lean and sweep in the low speed 3D design has resulted in less overhang (normal to blade section) than would have been the case if only lean were used. At high speed this should result in lower stresses within the blade roots since the centre of gravity of the blades will be closer to the mounting axis. Also, space restrictions between bladerows limit the extent to which forward axial sweep can be employed. By using a flexible approach to the design problem (by incorporating sufficient parametric freedom while still maintaining the size of the problem) high speed blades can be optimised for a balanced aerodynamic load distribution within the space available. Unsteady blade interaction effects may become more of an issue for bowed high speed blades where space restrictions result in closer bladerow gaps at certain heights. These effects may reduce aerodynamic performance and increase the dynamic blade loadings.

10.5 Conclusions

The 3D advanced blading (DERA2) has demonstrated a significant and measurable improvement over the datum low speed blading design. At design flow the efficiency improvements are around 1.5% rising to around 3% near stall. The stall margin has also improved significantly and a stronger pressure rise coefficient has been measured towards stall. Experimental throughflow analysis using radial profiles derived from traverse data also support these findings. They show an improved axial velocity profile with higher flow towards both endwalls compared with the datum design.

Radial profiles of loss coefficient from the throughflow analysis show that most of the improvement is coming from the rotor hub and tip rather than from the stator. They also indicate that the incidence on to the rotor hub is greatly reduced from 0 to 25% span. The reduction in hub incidence can be attributed to both the leading edge re-cambering and the increased axial flow at the hub. The reduction in tip loss has arisen purely from the lean/sweep combination. The measurements support the general findings of the design calculations which show the leading edge recambering in the rotor produces benefits of similar magnitude to the lean/sweep.

Rotating frame traverses at rotor exit support the stationary frame based throughflow results. They show a greatly reduced hub endwall boundary layer and a thinner rotor wake from 40% height to the hub. The losses associated with the clearance flow (indicated by the throughflow) are also greatly reduced when compared to the datum rotor exit measurements.

The flow visualisation results indicate that no separated corner flow is present for the 3D design at the suction surface of the stator towards the casing; this was a significant feature of the datum stator flow field. These results therefore confirm the general results of the traverse data, ie the reduction in wake loss towards the casing at stator exit. At near stall the DERA2 stator displays a distinctly different flow pattern to the datum stator. Whereas the datum stator suffers from an increase in the '3D' endwall losses at the casing the DERA2 stator suffers a '2D' flow separation closer to mid-height.

Unsteady calculations of mid-height sections at stage 1 using un-NEWT have been carried out. These indicate an increase in unsteady loading on the rotor due to the closer proximity of the mid-span rotor section to the stator section. However, neither the measured nor predicted circumferential variations in total pressure increase in magnitude over those for the datum spacing. This suggests that the potential interactions are less important than the viscous flow from the upstream stator on the total pressure variations.

The restrictions to axial movement of high speed blade sections will limit the extent to which lean and sweep can be employed. The possibility of extra bladerow

interaction and unsteady loading (such as that observed here at low speed) will also be an important consideration during the design process of high speed blading. A high speed equivalent of the DERA2 blading would use the same design approach but would be guided by the high speed aerodynamics to tailor the amount of lean/sweep and leading edge recambering. Similar performance improvements should be expected at high speed.

Chapter 11 - Conclusions

This Thesis has presented the design and test of two builds of the Cranfield low speed research compressor. The first design aimed to represent an existing high speed highly loaded stage as closely as possible, to evaluate how well the low speed environment can replicate the high speed multistage core compressor flow. The second design was based on the first and incorporated the '3D' design features of lean, sweep and leading edge recambering to improve upon its performance.

Improved measurement and calibration procedures, along with a new intake configuration, helped to ensure that the measurements taken at Cranfield for this work were among the most comprehensive and successful made to date. They show that the first (datum) design successfully reproduces both the primary and secondary flow features measured in the high speed target stage (the fourth stage of C147 build 3). The second design (DERA2) demonstrated a 1.5% improvement in efficiency at design flow, rising to around 3% at stall, along with a significant improvement in stall margin and a strengthened pressure rise characteristic.

Although concluding remarks have been made at the end of each chapter throughout the Thesis the opportunity is taken here to focus upon the main results from the work. This is followed by a section on recommendations for future work.

11.1 Datum design work

The TRANSCode flow solver has been modified to run at the low Mach numbers found in low speed research compressors by implementing the method of pseudo-compressibility. The modifications were implemented as an alternative running option so that either compressible or incompressible flows can be modelled with the same code but using different time marching procedures. Evaluation work on a low speed stage showed that the stator exit flow angle was over-predicted by about a degree at mid-height while the rotor relative exit swirl angle was slightly under-predicted. These conflicting results together with the uncertainty associated with experimental test data meant that it was difficult to judge whether a deviation correction was necessary. However, the DERA1 design calculations experienced a similar pattern of deviation error for the rotor and stator which ultimately contributed to an increased level of work over the design intent.

The DERA1 design approach used was a manual S1-S2 method which used the low-speed TRANSCode solver to calculate the blade-to-blade flow (S1) and SC92H to calculate the throughflow (S2). This method ensured consistency of approach with the high-speed stage design which used a coupled S1-S2 method employing S1BYL2 and SC90. The blade sections were designed to match the high speed normalised surface

velocity distributions. Good agreement was achieved for both blade rows and the variation of the distributions with incidence appears to be small.

The high-to-low speed transformation process has involved compromises due to both geometric and aerodynamic constraints. Geometric constraints include the size and power of the rig which restrict the Reynolds number. Aerodynamically the effects of Mach number on loss buckets and boundary layer limit the extent to which full high-low speed readacross can be achieved.

11.2 Instrumentation and rig changes

The Cranfield University research compressor facility was significantly modified for the DERA tests. The most significant change was the increase in hub/tip ratio from 0.85 to 0.91 and the alterations that had to be made to accommodate this. The opportunity was taken to improve the intake arrangement and this proved to be successful in producing a clean steady inlet flow, enabling the compressor to be readily set up on flow condition.

The compressor instrumentation and measurement methods were also improved. These include improvements to the method of setting the probe angles, to the resolution of the probe calibration data and to the measurement of overall total pressure rise through increased rake coverage. In addition to the standard instrumentation used for testing, 3D probes were designed and manufactured at Cranfield University. These were successfully used for the first time during the DERA2 test programme. Flow visualisation studies using fluorescent dye were also successfully executed for both DERA1 and DERA2 stator blading.

11.3 Datum performance

A comprehensive set of measurements for the datum design has been obtained which include; overall performance mapping, stationary frame traversing at most planes, rotating frame traversing behind rotor 3, blade surface static pressure measurements at stage 3 and flow visualisation studies. With the exception of the flow visualisation all the measurements were obtained for three flow conditions; near stall, design flow and high flow.

The overall duty of the datum low speed blades is around 10% higher than intended in the original design. This discrepancy has been investigated and shown to be due partly to a difference in overall flow coefficient between the SC92H design calculation and the high speed SC90 solution. It was also partly due to the shortcomings of the SC92H throughflow model and deviation errors of around 2° in the blade-to-blade TRANSCode design solutions for the stator. Although the $\Delta H/U^2$ level was higher than

intended the De Haller numbers for both rotor and stator were closer to the C147 fourth stage blading.

Stationary frame traverses at rotor and stator exit show that the radial profiles of total pressure and flow angle agree fairly well with the high speed stage profiles although there were some discrepancies. The area traverse at stator exit shows good agreement with the high speed stator performance in terms of wake structure and endwall loss regions. However there was much more evidence of non-axisymmetric flow in the free-stream regions between blade wakes in the low speed tests and this needs to be recognised when interpreting data and comparing with CFD predictions. Rotor relative traverse measurements were compared with turbulence measurements in the high speed rig and the loss regions indicated by these two methods are also in good agreement.

Both rotating frame traverses and results from the throughflow analysis of the stationary frame traverse data indicate a region of increased loss at the rotor hub. This is similar to the increased loss seen at the casing end of the stator, but appears to be significantly larger than for the stator. The throughflow analysis suggests this is due to (or exacerbated by) an increase in incidence and diffusion at the inner half of the blade. Overall, the measurements show that both primary and secondary flow features can be well reproduced in the low speed environment. However, much stronger periodic, non-axisymmetric flow features were found to be an important aspect of the low speed flowfield and these represented possibly the largest difference between the high and low speed environments.

11.4 CFD comparisons

Numerical predictions were carried out on each blade row using the DERA TRANSCode Navier Stokes flow solver for both the low speed and C147 blading using test measurements as inlet conditions. The low speed predictions showed fairly good agreement with test over much of the blade span including the fixed end of each blade row, but failed to predict the size and structure of the clearance flow region. Similar results were apparent for the high speed predictions although the over prediction of clearance effects was less evident and the stator casing flow suffered from an over-prediction of loss.

To study the effect of the non-axisymmetric stator inlet flow field TRANSCode modelling was carried out using the complete area traverse measurements for the inlet boundary condition. This study showed that the relative positioning of the stators to the inlet field could have a significant effect on overall performance. However, the circumferential variation was also shown (by unsteady modelling) to be partly due to the

downstream stator itself so the exercise of shifting the whole field circumferentially was somewhat artificial in this case.

Un-NEWT unsteady modelling of the mid-span sections of the first stage demonstrated a pressure potential interaction between the rotor and stator. The time averaged spatial circumferential variations of total pressure at exit from rotor 1 agree well with the measured level of pressure variation. The measured variation at rotor 3 exit was shown to be higher than at rotor 1 and this was attributed to the extra effects arising from the upstream stator wakes passing through the rotor. Approximately 65% of the circumferential variations downstream of an embedded rotor was attributed to the upstream stator and 35% to the downstream stator. Although the overall effect on performance due to these circumferential variations is small they must be recognised when comparing detailed flow measurements with high speed data and when attempting to model the low speed flow with a flow solver.

11.5 DERA2 design work

The DERA2 design was based on the datum design and incorporated a combination of lean, sweep and leading edge recamber to reduce the endwall and 3D losses. A single parabolic arc was chosen to define the modified stacking axis and a study was undertaken to find the optimum level of axis deformation. The axis was rotated through a blend of lean and sweep and an optimum rotation giving minimum predicted loss was found for each blade. The following observations were made:

1) Positive lean (obtuse angle between suction surface and endwall) off loads the endwalls and loads up the mid span. Negative lean has the opposite effect. It also increases the flow angle onto the blade near the endwalls and decreases it at mid span.

2) Sweep has a similar effect to lean except the incidence increase at the endwalls is much smaller and the re-distribution of chordwise loading makes the endwall sections become more aft loaded.

3) For both rotor and stator a trade-off between the decrease in losses at the endwalls and the increase at mid span produced a net decrease in overall loss as the lean or sweep was applied. Beyond a certain level the overall loss then increased as the mid span blading began to suffer flow separation and high loss.

4) Rotating the stacking axis from lean to sweep showed that a minimum loss exists for both bladerows for a certain blend of lean and sweep. For the rotor the blend involved positive lean and forward sweep while the stator calculations showed that positive lean with a little backsweep was necessary for minimum loss.

5) Combining lean and sweep produced a blade shape with less overhang than a pure lean or pure sweep blade of the same loss. Stresses should therefore be lower for combination blades than pure lean blades.

6) For both the rotor and stator areas of reversed flow found on the datum blade suction surfaces were eliminated in the optimum 3D designs. In addition, further loss improvements resulted from allowing for the effects of a 3D row upstream.

7) The philosophy for these blades was to produce a 'balanced' design. Since sharp changes in blade lean or sweep can seriously increase the loading near the point of maximum change a parabolic distribution for the stacking axis was used. The gradual change of blade loading brought about by this type of bowing did not affect the pressure rise of the bladerow.

11.6 DERA2 performance

The overall performance measurements show an efficiency improvement over the datum design of around 1.5% at design flow. This improvement extends over the entire flow range and increases to around 3% at the datum design stall point. The 3D design also has a significantly improved stall margin which other recent 3D designs have failed to achieve (an increase in efficiency at design often comes with the penalty of reduced stall margin and near stall efficiency). The design also has a stronger pressure rise characteristic which increases steadily up to the stall point. Experimental throughflow analysis using radial profiles derived from traverse data also support these findings. They show an improved axial velocity profile with higher flow towards both endwalls compared with the datum design.

Radial profiles of loss coefficient from the throughflow analysis show that most of the improvement is coming from the rotor hub and tip rather than from the stator. The large hub endwall loss region of the datum rotor has been significantly reduced and the wake losses more evenly spread up the blade height. This change in performance was predicted in the TRANSCode design solutions. The throughflow analysis also indicates that the incidence on to the rotor hub is greatly reduced from 0 to 25% span and that the losses associated with the clearance flow are also greatly reduced. Rotating frame traverses at rotor exit support the stationary frame based throughflow results. They show a greatly reduced hub endwall boundary layer and a thinner rotor wake from 40% height to the hub.

The flow visualisation results indicate that no separated corner flow is present for the 3D design at the suction surface of the stator towards the casing; this was a significant feature of the datum stator flow field. These results are consistent with the traverse data, which show a reduction in wake loss towards the casing at stator exit. At the near stall operating condition the DERA2 stator displays a distinctly different flow

pattern to the datum stator. Whereas the latter suffers from an increase in the '3D' endwall losses at the casing the DERA2 stator suffers a '2D' flow separation in a region further from the casing which is indicated by the throughflow analysis to suffer from increased incidence.

Unsteady calculations of mid-height sections at stage 1 indicate an increase in unsteady loading on the rotor due to the closer proximity of the mid-span rotor section to the stator section. However, neither the measured nor predicted circumferential variations in total pressure increase in magnitude over those for the datum spacing. This suggests that the potential interactions have a less important effect on the total pressure variations than the viscous flow from the upstream stator.

11.7 Recommendations for future CFD and design work

Designing a high speed equivalent of the DERA2 blading would prove a useful exercise in helping to determine the extent to which the benefits demonstrated at low speed can be fulfilled in real high speed compressors. The restrictions to axial movement of high speed blade sections in real engines may limit the extent to which lean and sweep can be employed. The possibility of extra bladerow interaction and unsteady loading (such as that observed here at low speed) will also be an important consideration during the design process of high speed blading. The high speed version of DERA2 should use the same design approach but be guided by the high speed aerodynamics to tailor the amount of lean/sweep and leading edge recambering. Similar performance improvements should be expected at high speed.

The quality of the current design work has been strongly dependent on the accuracy of the TRANSCode modelling. For the datum build, shortfalls in TRANSCode's ability to model the measured stator deviation contributed to the build having a higher work duty than intended. A careful calibration of TRANSCode on previous Cranfield builds could improve design point prediction through the use of deviation correction factors.

Modelling of clearance flows for both Cranfield builds was also of limited quality and this has an impact on the 3D design process. Since this involved the careful optimisation of balancing losses at the middle and the ends of the blades through lean/sweep combinations the performance of the resulting design was dependant on the quality of the CFD tool used. Further development of TRANSCode is therefore needed to enable better prediction of low speed flows. This may involve improving the gridding methods employed, particularly in the clearance region, and improving the turbulence modelling.

With better 3D CFD calculations it may then be worth running the DERA2 case predictions using the measured DERA2 inlet flow conditions. The 'multi-stage' aspects

of the DERA2 design, such as the improvement to the Va/U profiles through the compressor, warrant further investigation and multi-stage calculations could be undertaken to assess how these effects would have altered the 3D design.

Fully 3D unsteady calculations of the DERA1 stage are presently underway and these should help the interpretation of the measurement data, particularly where the 3D effects of the unsteady interactions influence the endwall losses.

11.8 Recommendations for future testing

A follow on programme of experimental work could then centre on an improved 3D design born out of the improved CFD tools. On the measurement side, instrumentation and data acquisition software need to be improved to speed up test times and improve the productivity of the facility. This could be achieved through the use of radial traverse actuators and dedicated Scanivalve transducers to reduce scanning time and automate the traverses more fully. A feedback signal on the position of the rotating probe would eliminate time wasted taking data at the wrong grid position.

The 'totem pole' effect on performance produced by rotating the rake instrumentation is due to a lack of coverage at inlet and exit to the compressor. It is recommended that the rakes be positioned in a verniered manner relative to the stationary blading and that all the eight rakes be plumbed up. Better rake coverage would also benefit the tie-up of the throughflow analysis of test data with the overall performance measurements.

The present work has shown that unsteady bladerow interaction effects are present in the LSRC. Further work could include a series of stator indexing measurements to investigate this phenomenon. This could be supplemented by unsteady laser velocimetry measurements and hot wire measurements to support the unsteady CFD calculations. Further measurements on DERA2 may also benefit from additional traversing closer to stall so that its performance limiting behaviour can be better understood. The unsatisfactory rotating frame traverses for DERA2 could usefully be repeated and extended to this operating condition.

Appendix A - Cycle efficiency calculation

Cycle efficiency is the ratio of net work out to heat input ie;

$$\eta = \frac{Work_{OUT} - Work_{IN}}{Heat_{IN}}$$

$$\eta = \frac{c_P(T_{03} - T_5) - c_P(T_{02}' - T_a)}{c_P(T_{03} - T_{02}')}$$

rearranging:-

$$\eta = 1 - \left(\frac{T_5 - T_a}{T_{03} - T_{02}'}\right), \text{ which can be expressed as } \eta = 1 - \left(\frac{\frac{T_5}{T_{03}} - \frac{T_a}{T_{03}}}{\frac{T_{03}}{T_5} - \frac{T_{02}'}{T_5}}\right) \cdot \left(\frac{T_{03}}{T_5}\right)$$

If we define $t = \left(\frac{T_{03}}{T_a}\right)$ the turbine entry to atmospheric temperature ratio

we get:-

$$\eta = 1 - \left(\frac{\frac{T_5}{T_{03}} - \frac{1}{t}}{\frac{T_{03}}{T_5} - \frac{T_{02}'}{T_a} \cdot \frac{1}{t} \cdot \frac{T_{03}}{T_5}}\right) \cdot \left(\frac{T_{03}}{T_5}\right)$$

overall compression efficiency is defined as: $\eta_c = \frac{T_{02} - T_a}{T_{02}' - T_a}$

and $\left(\frac{T_{02}}{T_a}\right) = r^{\frac{\gamma-1}{\gamma}}$ (from the isentropic relationship) where $r = \left(\frac{P_{02}}{P_a}\right)$

therefore: $\left(\frac{T_{02}'}{T_a} - 1\right) \cdot \eta_c = \left(\frac{T_{02}}{T_a} - 1\right)$

so $$\frac{T_{02}'}{T_a} = \frac{\left(r^{\frac{\gamma-1}{\gamma}} - 1\right)}{\eta_c} + 1$$

also

$$\left(\frac{P_{02}}{P_a}\right) = \left(\frac{P_{03}}{P_5}\right) \therefore \left(\frac{T_{02}}{T_a}\right) = \left(\frac{T_{03}}{T_5}\right) = r^{\frac{\gamma-1}{\gamma}}$$

substituting these expressions into the expression for cycle efficiency:

$$\eta = 1 - \left(\frac{\left(\frac{1}{r}\right)^{\frac{\gamma-1}{\gamma}} - \left(\frac{1}{t}\right)}{r^{\frac{\gamma-1}{\gamma}} - \left(\frac{r^{\frac{\gamma-1}{\gamma}} - 1}{\eta_c} + 1 \right) \cdot \left(\frac{1}{t}\right) \cdot r^{\frac{\gamma-1}{\gamma}}} \right) \cdot r^{\frac{\gamma-1}{\gamma}}$$

therefore:-

$$\eta = 1 - \left(\frac{\left(\frac{1}{r}\right)^{\frac{\gamma-1}{\gamma}} - \left(\frac{1}{t}\right)}{1 - \left(\frac{r^{\frac{\gamma-1}{\gamma}} - 1}{\eta_c} + 1 \right) \cdot \left(\frac{1}{t}\right)} \right)$$

The cycle efficiency is therefore a function of pressure ratio and the cycle temperature ratio. When the compressor efficiency is 100% the expression becomes:-

$$\eta = 1 - \left(\frac{\left(\frac{1}{r}\right)^{\frac{\gamma-1}{\gamma}} - \left(\frac{1}{t}\right)}{1 - \left(r^{\frac{\gamma-1}{\gamma}} \right) \cdot \left(\frac{1}{t}\right)} \right) = 1 - \left(\frac{1 - \left(\frac{r^{\frac{\gamma-1}{\gamma}}}{t} \right)}{1 - \left(\frac{r^{\frac{\gamma-1}{\gamma}}}{t} \right)} \right) \cdot \left(\frac{1}{r}\right)^{\frac{\gamma-1}{\gamma}}$$

Therefore the ideal cycle efficiency is:-

$$\eta = 1 - \left(\frac{1}{r}\right)^{\frac{\gamma-1}{\gamma}}$$

which is not a function of the temperature ratio.

Appendix B- Propulsive efficiency calculation

Propulsive efficiency (η_p) is defined as the ratio of the useful thrust power to the sum of that energy and the unused kinetic energy of the jet.

$$\text{Kinetic energy of jet} = \frac{m\left(C_j - C_a\right)^2}{2}$$

$$\text{Thrust power} = F \cdot C_a = mC_a\left(C_j - C_a\right)$$

$$\eta_p = \frac{mC_a\left(C_j - C_a\right)}{mC_a\left(C_j - C_a\right) + \tfrac{1}{2}m\left(C_j - C_a\right)^2} = \frac{C_a\left(C_j - C_a\right)}{\tfrac{1}{2}\left(C_j^2 - C_a^2\right)}$$

also; $$\tfrac{1}{2}\left(C_j^2 - C_a^2\right) = c_p\left(T_{03} - T_5\right) - c_P\left(T_{02}^{'} - T_a\right)$$

$$\tfrac{1}{2}C_a^2 = c_P\left(T_{01} - T_a\right)$$

and:

$$\tfrac{1}{2}C_j^2 = c_P\left(T_{04} - T_5\right)$$

therefore:-

$$\eta_p = \frac{2\sqrt{\left(T_{01} - T_a\right)\cdot\left(T_{04} - T_5\right)} - 2\left(T_{01} - T_a\right)}{\left(T_{03} - T_5 - T_{02}^{'} + T_a\right)}$$

$$\eta_p = \frac{2\sqrt{\left(\frac{T_{01}}{T_{03}} - \frac{T_a}{T_{03}}\right)\left(\frac{T_{04}}{T_{03}} - \frac{T_5}{T_{03}}\right)} - 2\left(\frac{T_{01}}{T_{03}} - \frac{T_a}{T_{03}}\right)}{\left(\frac{T_{03}}{T_a} - \frac{T_5}{T_a} - \frac{T_{02}^{'}}{T_a} + 1\right)} \times \left(\frac{T_{03}}{T_a}\right)$$

using the same relations derived in Appendix A we get:-

$$\eta_p = \frac{2\sqrt{\left(\frac{T_{01}}{T_{03}}\cdot\frac{T_a}{T_a} - \frac{1}{t}\right)\left(\frac{T_{04}}{T_{03}}\cdot\frac{T_a}{T_a} - \frac{1}{r^{\frac{\gamma-1}{\gamma}}}\right)} - 2\left(\frac{T_{01}}{T_{03}}\cdot\frac{T_a}{T_a} - \frac{1}{t}\right)}{\left(t - \frac{t}{r^{\frac{\gamma-1}{\gamma}}} - \left(\frac{r^{\frac{\gamma-1}{\gamma}} - 1}{\eta_c} + 1\right) + 1\right)} \times t$$

we can now define the aircraft's Mach Number M_a as

$$M_a^2 = \frac{C_a^2}{\gamma R T_a} = \frac{2c_p\left(T_{01} - T_a\right)}{\gamma R T_a}$$

$$M_a^2 = \frac{2\left(\frac{T_{01}}{T_a} - 1\right)}{\gamma - 1} \quad \text{hence,} \quad \frac{T_{01}}{T_a} = \frac{M_a^2(\gamma - 1)}{2} + 1$$

also:-

$$½\, C_j^2 = ½\, C_a^2 + c_p\left(T_{03} - T_5 - T_{02}^{'} + T_a\right)$$

so, $$c_p\left(T_{04} - T_5\right) = c_p\left(T_{01} - T_a\right) + c_p\left(T_{03} - T_5 - T_{02}^{'} + T_a\right)$$

rearranging:- $$T_{04} = T_{01} + T_{03} - T_{02}^{'}$$

therefore, $$\frac{T_{04}}{T_a} = \frac{T_{01}}{T_a} + \frac{T_{03}}{T_a} - \frac{T_{02}^{'}}{T_a}$$

$$\frac{T_{04}}{T_a} = \left(\frac{M_a^2(\gamma - 1)}{2} + 1\right) + t - \left(\frac{r^{\frac{\gamma-1}{\gamma}} - 1}{\eta_c} + 1\right)$$

substituting into the expression for η_p we get:-

$$\eta_p = \frac{2t\sqrt{\left(\frac{M_a^2(\gamma-1)}{2t}\right)\left(\frac{1}{t}\cdot\left(\frac{M_a^2(\gamma-1)}{2} + 1 + t - \left(\frac{r^{\frac{\gamma-1}{\gamma}} - 1}{\eta_c} + 1\right)\right) - \frac{1}{r^{\frac{\gamma-1}{\gamma}}}\right)} - M_a^2(\gamma - 1)}{\left(t - \frac{t}{r^{\frac{\gamma-1}{\gamma}}} - \left(\frac{r^{\frac{\gamma-1}{\gamma}} - 1}{\eta_c}\right)\right)}$$

Appendix C - Calculation of Specific thrust

If nozzle is choked specific thrust is the sum of momentum change and pressure change at nozzle outlet:

$$F_s = \left(C_5 - C_a\right) + \frac{A_5}{m}\left(P_c - P_a\right)$$

$$F_s = \left(\left(\gamma RT_c\right)^{1/2} - C_a\right) + \frac{1}{\rho_5 C_5}\left(P_c - P_a\right)$$

$$T_c = \left(\frac{2}{\gamma+1}\right)T_{04}, \rho_5 = \frac{P_c}{RT_c}, C_5 = \left(\gamma RT_c\right)^{1/2}$$

$\therefore$

$$F_s = \left(\gamma R\left(\frac{2}{\gamma+1}\right)T_{04}\right)^{1/2} - C_a + \frac{RT_c}{P_c\left(\gamma RT_c\right)^{1/2}}\left(P_c - P_a\right)$$

$$F_s = \left(\gamma R\left(\frac{2}{\gamma+1}\right)T_{04}\right)^{1/2} - C_a + \frac{R\left(\frac{2}{\gamma+1}\right)T_{04}\left(1-\frac{P_a}{P_c}\right)}{\sqrt{\gamma RT_c}}$$

$$P_c = P_{04}\left(1-\frac{1}{\eta_j}\left(\frac{\gamma-1}{\gamma+1}\right)\right)^{\frac{\gamma}{\gamma-1}}$$

$$F_s = \left(\gamma R\left(\frac{2}{\gamma+1}\right)T_{04}\right)^{1/2} - C_a + R\left(\frac{2}{\gamma+1}\right)\left(\frac{T_{04}}{\sqrt{\gamma R\left(\frac{2}{\gamma+1}\right)T_{04}}}\right)\left(1-\frac{P_a}{rP_{01}\left(\frac{T_{04}}{T_{03}}\right)^{\frac{\gamma}{\gamma-1}}\left(1-\frac{1}{\eta_j}\left(\frac{\gamma-1}{\gamma+1}\right)\right)^{\frac{\gamma}{\gamma-1}}}\right)$$

$$T_{01} = T_a + \frac{C_a^2}{2c_{pa}}$$

$$T_{04} = \left(T_{03} - \frac{c_{pa}}{c_{pg}}\left(\frac{T_{01}}{\eta_c}\right)\left(r^{\frac{\gamma-1}{\gamma}} - 1\right)\right)$$

$$P_{01} = P_a\left(1+\frac{C_a^2}{2c_{pa}T_a}\right)$$

c_{pa} = Specific heat for air
c_{pg} = Specific heat for gas mixture
C_a = Aircraft speed

Appendix D - Probe calibration coefficients

The probe calibration coefficients used for the 2D cobra probes are:-

$$Cyaw = \frac{(S2 - S3)}{(Pt - Ps)}$$

$$Cs = \frac{(0.5 * (S2 + S3) - Ps)}{(Pt - Ps)}$$

$$Ctot = \frac{(P1 - Pt)}{(Pt - Ps)}$$

where: Cyaw is the yaw coefficient

Cs is the static pressure coefficient

Ctot is the total pressure coefficient

Pt is the tunnel total pressure

Ps is the tunnel static pressure

P1 is the middle probe port

S2 and S3 are the side probe ports

For the 3D probes the following coefficients were used which include an extra coefficient for the pitch direction:-

$$Cyaw = \frac{(S3 - S2)}{(Pt - Ps)}$$

$$Cs = \frac{(Ps - 0.5 * (S2 + S3))}{(Pt - Ps)}$$

$$Ctot = \frac{(P1 - Pt)}{(Pt - Ps)}$$

$$Cpit = \frac{(P1 - U4)}{(Pt - Ps)}$$

where: Cpit is the pitch angle coefficient

U4 is the upper fourth port

This page is intentionally blank

References

Ahmed N A, Charnley B A (1992)
V2500 datum blading, Through traverse build study on the Cranfield LSRC
RCR 91132 (CIT report with RR top sheet)

Ahmed N A, Charnley B A (1993)
V2500 New end bend (NEB1) study on the Cranfield LSRC
RCR 91106 (CIT report with RR top sheet)

Ahmed N A
Preliminary investigations of unsteady flows in a multi-stage axial compressor
(CIT report) to be issued.

Barankiewicz W S, Hathaway M D (1997)
Effects of stator indexing on performance in a low speed multistage axial compressor
ASME Paper 97-GT-496

Barton J P (1992)
Results of the first test at datum rotor tip clearances carried out on the Cranfield Low Speed Research Compressor for the BRITE/EURAM tip clearance project
RCR 91120

Barton J P (1992b)
Interim report on the New End Bend test 1 (NEB1) carried out on the Cranfield 4-stage low speed research compressor
RCR 91092

Barton J P (1992c)
Cranfield probe calibration conventions and probe characteristics in blade wakes
RCR 91133

Barton J P (1994)
Results of the first NEB1D or BRITE straight-bladed test, at datum tip clearances, carried out on the Cranfield Low Speed Research Compressor
RCR 91139

Behlke R F (1986)
The Development of a Second Generation of Controlled Diffusion Airfoils for Multistage Compressors
Trans. ASME Journal of Turbomachinery Vol 108 pp32-41

Bolger J J (1991)
BRITE/EURAM Blading design for the 4-stage CIT compressor
RCR 91077

Breugelmans F A H, Carels Y, Demuth M (1984)
Influence of Dihedral on the secondary flow in a two-dimensional compressor cascade
Trans. ASME, Journal of Eng for Gas Turbines and Power, Vol 106

Breugelmans F A H (1987)
Investigation of dihedral effects in compressor cascades
AGARD CP421

Calvert W J, Ginder R B (1985)
A quasi three dimensional calculation system for the flow within transonic compressor bladerows
ASME Paper 85-GT-22

Calvert W J, Ginder R B, McKenzie I R I, Way D J (1989)
Performance of a highly loaded HP compressor
ASME Paper 89-GT-24

Calvert W J (1995)
Development of Version 1.0 of the TRANSCode Reynolds Averaged Navier-Stokes Code for Turbomachinery
DRA Technical Report, DRA/AS/PTD/TR95033/1

Calvert W J, Stapleton A W, Emmerson P R, Buchanan C R, Nott C M (1997)
Evaluation of a 3D viscous code for turbomachinery flows
ASME Paper 97-GT-78

Camp T R (1995)
A new method to improve accuracy of rotor exit traverse measurements using stator exit data
DNS 21378

Camp T R
Aspects of the off-design performance of axial compressors
PhD thesis. Cambridge University
to be issued.

Casey M V (1990)
The use of large scale low-speed rotating rigs in turbomachinery research and development
RCR 91043

Chang J L C, Kwak D (1984)
On the method of Pseudo compressibility for numerically solving incompressible flows
AIAA Paper 84-0252

Cherrett M A, Bryce J D (1992)
Unsteady viscous flow in a high-speed core compressor
ASME Journal of Turbomachinery, Vol.114 pp 287-294.

Chorin A J (1967)
A numerical method for solving incompressible viscous flow problems
Journal of Computational Physics, 2 12-26

Copeland G A, McFarlane C W (1990)
Viscous end-bend blading study on the Cranfield LSRC
RCR 91018 (CIT report issued with RR top sheet)

Cumpsty N A (1989)
Compressor Aerodynamics
Longman 1989

Dawes W N (1986)
A numerical method for the analysis of 3D viscous compressible flow in a turbine cascade; application to secondary flow in a cascade with and without dihedral
ASME Paper 86-GT-145

Dawes W N (1993)
Simulating unsteady turbomachinery flows on unstructured meshes which adapt in both time and space
ASME Paper 93-GT-104

Denton J, Xu L (1998)
The exploitation of 3D flow in turbomachinery design
IMechE Seminar 'The successful exploitation of CFD in turbomachinery design', ppr 4.

Dong Y, Gallimore S J, Hodson H P (1987)
Three-dimensional flows and loss reduction in axial compressors
Trans ASME Journal of Turbomachinery 109:354-61

Dunham J, Britton A J, Calvert W J (1990)
A new Turbomachinery throughflow program using the streamline curvature method
RAE Tech Memo P1175

Dunham J (1994)
Application of a new endwall model to the Cranfield Low Speed Research Compressor
DRA Technical Report, TR 94043

Dunham J (1994b)
A new endwall model for axial compressor throughflow calculations
ASME Paper 94-GT-75

Emmerson P R, Buchanan C R (1996)
Investigations of sweep and lean effects on a highly loaded compressor cascade using a 3D viscous analysis
DERA Report DRA/AS/PTD/TR95056

Emmerson P R, Buchanan C R, Ginder R B (1996)
Numerical studies of the C148 single-stage transonic fan including a conceptual redesign of the stator row
DERA Report DRA/AS/PTD/TR96047

Fottner L (1990)
Test cases for Computation of Internal flows in Aeroengine Components
Propulsion and Energetics Panel Working Group 18, AGARD Advisory Report No. 275

Freeman C (1978)
The design of ends for compressor blades
RR Report RCM 61163

Gardiner I D, Robinson C J (1988)
A three year research programme for the Cranfield Low Speed Compressor rig
RCR 90971

Ginder R B, Britton A J (1987)
Blading design for build 2 of the C147 multistage compressor
RAE Technical Report 87053

Ginder R B (1990)
Definition and test objectives for Build 3 of the C147 Research Compressor
DRA Technical Report, TR 90058

Ginder R B (1991)
Design and Performance of advanced blading for a high-speed HP compressor
ASME Paper 91-GT-374

Harris D (1989)
A three year research programme for the Cranfield 4-stage, low-speed compressor rig SMP 3301/13
RCR 90993 (Addendum 2)

Harris D (1990)
A three year research programme for the Cranfield 4-stage, low-speed compressor rig SMP 3301/13
RCR 91021 (Addendum 3)

Howard M A, Gallimore S J (1993)
Viscous Throughflow Modelling for Multi-stage Compressor design
Transactions of the ASME, Journal of Turbomachinery, Vol 115

Howard M A, Ivey P C, Barton J P, Young K F (1993)
Endwall effects at two tip clearances in a multi-stage axial flow compressor with controlled diffusion blading
ASME Paper no. 93-GT-299

Howell A R (1945)
Fluid dynamics of axial compressors
Proc. I. Mech E 153: 441-82

Inoue M, Kuroumaru M, Fukuhara M (1986)
Behaviour of tip clearance flow behind an axial compressor rotor
Trans ASME Journal for Gas Turbines and Power 106:455-67

Jackson R, Angel B N (1997)
Extension of the NEWT and Un-NEWT codes for temperature distortion and unsteady flow studies
DERA/AS/PTD/CR97047/1

Keogh A (1991)
Design of DCM blading for the Cranfield Low speed research compressor
RCR 91068

Keuthe A M, Chow C Y (1976)
Foundations of Aerodynamics
Wiley and Sons, pp. 15-18 and pp 255-279

Lakshminarayana B, Horlock J H (1967)
Leakage and secondary flow in compressor cascades
Aeronautical Research Council R and M 3483

Lakshminarayana B, Sitaram N, Zhang J (1986)
Endwall and profile losses in a low speed axial flow compressor rotor
Trans ASME Journal for Gas Turbines and Power 108:23-31

LeJambre C R, Zacharias R M, Biederman B P, Gleixner A J, Yetka C J (1995)
Development and Application of a multistage Navier-Stokes Flow Solver Part II: Application to a High Pressure Compressor Design
ASME Paper 95-GT-343

Liemann H W, Roshko A (1957)
Elements of Gas Dynamics
Wiley and Sons, pp 253-263

McDougall N M, Dawes W N (1987)
Numerical simulation of the strong interaction between a compressor blade clearance jet and stalled passage flow
Seventh GAMM conference on Numerical Methods in Fluid Mechanics, Louvain, Belgium

McDougall N M (1988)
Stall Inception in Axial Flow Compressors
PhD Dissertation, University of Cambridge

McKenzie A B (1988)
A Rational design method for end-bend axial compressor blading
Rolls Royce Internal note

Paramour M D (1995)
Future technology requirements for UK combat engines

Philpot M G (1992)
Practical considerations in designing the engine cycle

Place J M M (1991)
The Aerodynamic design of a low speed single stage research compressor representative of a core compressor stage.
RCR 91040

Place J M M (1995)
New End Bend (NEB1) Tests on the Cranfield Four Stage Low Speed Compressor
DNS 20256

Place J M M (1997)
Three-dimensional flow in core compressors
PhD thesis, Cambridge University

Rhie C M, Gleixner A J, Spear D A, Fischberg C J, Zaharias R M (1995)
Development and Application of a Multistage Navier-Stokes Solver Part 1: Multistage Modelling using Bodyforces and Deterministic Stresses
ASME Paper 95-GT-342

Robinson C J (1985)
Blading Design for the Cranfield 4-stage compressor
RCR 90897

Robinson C J (1986)
Low reaction blading design for the Cranfield four stage compressor
RCR 90932

Robinson C J (1986b)
End-bent low reaction blading for the Cranfield low speed compressor
RCR 90933

Robinson C J (1987)
End-bent low reaction blading for the Cranfield low speed compressor specification of tapered trench geometry and spend summary
RCR 90952

Robinson C J (1987b)
End-bend blading for the Cranfield low speed compressor Addendum 2
RCR 90967

Robinson C J (1988)
Test of the Cranfield LSRC with low reaction blading at increased tip clearance with area traversing through all four stages and instrumentation refinement
RCR 90972

Robinson C J, Northall J D, McFarlane C W R (1989)
Measurement and calculation of the three-dimensional flow in axial compressor stators, with and without end-bends
ASME paper no. 89-GT-6

Robinson C J (1991)
DCM Blading design for the Cranfield LSRC
RCR 91095

Robinson C J (1991b)
Low speed, 4-stage compressor research at the Cranfield Institute of Technology 1991-1992
RCR 91056

Robinson C J (1991c)
End-wall flows and blading design for axial flow compressors
PhD Thesis, Cranfield University

Robinson C J (1991d)
End-bend blading for the Cranfield low speed four stage research compressor: Comparison of DCA datum, controlled vortex, inviscid and viscous end-bend blading
RCR 91072

Robinson C J (1993)
End-bent low reaction blading for the Cranfield low speed compressor
RCR 91151, Final Report

Sasaki T, Breugelmans F (1997)
Comparison of sweep and dihedral effects on compressor cascade performance
ASME Paper 97-GT-2

Saunders E J Sqrd Ldr (1998)
Private Communication

Schäffler A (1979)
Experimental and Analytical Investigation of the Effects of Reynolds Number and Blade Surface Roughness on Multistage axial flow compressors
ASME Paper 79-GT-2

Serovy G K, Dring R P
Test cases for computation of internal flows in aeroengine components: Test case E/CO-1 Single low speed compressor rotor, AGARD AR-275

Shang E, Wang Z Q, Su J X (1993)
The experimental investigations on the compressor cascades with leaned and curved blade
ASME Paper 93-GT-50

Shapiro A H (1953)
The Dynamics and Thermodynamics of Compressible Fluid Flow
Wiley and Sons. pp 322-323.

Smout P D (1994)
Aerodynamic probe calibration discrepancies
Internal Memorandum

Stapleton A W (1997)
Evaluation of a fully viscous CFD code for the V2 compressor cascade
DERA report, DRA/AS/PTD/TR96066

Storer J A, Cumpsty N A (1990)
Tip leakage flow in axial compressors
ASME Paper 90-GT-127

Swoboda M, Wenger U, Gümmer V (1998)
An experimental examination of cantilevered and shrouded stators in a multistage axial compressor
ASME Paper 98-GT-282

Tweedt D L, Okiishi T H (1986)
Stator Endwall Leading-Edge Sweep and Hub Shroud Influence on Compressor Performance
ASME Paper 86-GT-197

Wadia A R, Beacher B F (1989)
Three-dimensional relief in turbomachinery blading
ASME Paper 89-GT-151

Walker P J (1987)
Blade lean in axial turbines: Model turbine measurements and simulation by a novel numerical method.
PhD Thesis, University of Cambridge.

Weingold H D, Neubert R J, Behlke R F, Potter G E (1995)
Reduction of compressor stator endwall losses through use of bowed stators
ASME Paper 95-GT-380

Weingold H D, Neubert R J, Behlke R F, Potter G E (1997)
Bowed Stators: An Example of CFD Applied to improve Multistage Compressor Efficiency
ASME Journal of Turbomachinery, Vol 119 pp161-168

Wennerstrom A J (1984)
Experimental study of a high throughflow transonic axial compressor stage
Trans ASME Journal of Gas Turbines and Power 106: 552-60

Wilson A G (1992)
Rotating flow phenomena on the DCM build of the CIT 4-stage low-speed rig
RCM 91987

Wilson A G (1993)
Aerodynamic design of the Leading Edge Recamber (LER) build of the Cranfield 4 Stage rig
RCR 91094

Wisler D C (1984)
Loss reduction in axial-flow compressors through low-speed model testing
ASME Paper 84-GT-184

Wood P J (1984)
Description of the concepts involved in end-bend blading and flow modelling
RCR 90889

Young K F (1993)
Results from the DCM build of the Cranfield LSRC (Part 1)
RCR 91170 (DNS 13748)

Young K F (1994)
Results from the DCM build of the Cranfield LSRC (Part 2)
DNS 15222

Young K F (1992)
Pre-test document for Cranfield LSRC DCM build
RR response to CIT draft
RCM 91967

Young K F (1993)
Aerodynamic design of the BRITE blading (NEB1D) and the end-bend version of these aerofoils (NEB1)
RCR 91143

Young K F
An overview of the new acquisition/Analysis software suite for use on the Cranfield LSRC
DNS 16039

Young K F (1992)
BRITE/EURAM tip clearance investigation report on second CIT compressor build
RCR 91122

Young K F (1994)
Statistical checking of new Cranfield data acquisition system
DNS 13555 (RCR 91207)

Young K F (1993)
Results from the TTB and NEB1 builds of the Cranfield LSRC
RCR 91141

Zhongqi W, Jiexian S, Jingjun Z (1994)
The effect of the pressure distribution in a three-dimensional flow field of a cascade on the type of curved blade
ASME Paper 94-GT-409

	Harrier Fleet (Flying Hrs)			Tornado Fleet (Flying Hrs)				
	GR7	**T10**	**Total**	**F3**	**GR1**	**GR1A**	**GR1B**	**Total**
Jan-97	1039.6	274.9	1314.6	2396.0	1725.4	485.0	414.0	5020.4
Feb-97	862.2	209.8	1071.9	2049.4	1600.6	431.3	411.1	4492.4
Mar-97	963.1	233.8	1196.9	2151.9	1467.3	628.3	246.2	4493.8
Apr-97	1237.5	232.8	1470.3	2179.4	1995.4	497.3	270.3	4942.4
May-97	762.3	155.3	917.7	2518.4	1336.7	360.8	941.6	5157.5
Jun-97	1281.4	157.4	1438.8	2562.1	1813.1	405.1	472.7	5252.9
Jul-97	1193.9	211.8	1405.8	2413.5	1655.3	420.3	476.3	4965.4
Aug-97	859.0	203.7	1062.8	1795.9	1553.2	316.8	397.8	4063.7
Sep-97	1367.6	245.3	1612.9	2503.3	2077.1	301.9	454.2	5336.4
Oct-97	1306.2	241.1	1547.3	2409.4	1756.5	362.4	551.8	5080.2
Nov-97	976.4	201.0	1177.4	2033.8	1858.7	409.8	328.1	4630.5
Dec-97	838.9	105.9	944.8	1555.5	1393.3	257.5	254.3	3460.7
	12688	2473	**15161**	26568	20233	4877	5218	**56896**

Harrier (Single Engine) Fuel Costs					
Flying Hours	Fuel (Ltrs)	Cost (£/Ltr)	Fuel/Hr (Ltr)	Cost/Hr	Total Cost
15161	56000000	0.135	3694	499	**£7.56 M**
Tornado (Twin Engine) Fuel Costs					
Flying Hours	Fuel (Ltrs)	Cost (£/Ltr)	Fuel/Hr (Ltr)	Cost/Hr	Total Cost
56896	264000000	0.135	4640	626	**£35.64 M**

Grand Total	**£43.2M**

Table 2.1 Cost of aviation fuel for RAF Harrier and Tornado fleet for 1997 (Saunders, 1998)

Parameter	**LSRC**		**C147 (4th Stage)**	
Mass flow rate (kg/s)	10.6		17.0 (corrected)	
Stage Pressure ratio	1.025		1.36	
$\Delta H/U^2$	0.495		0.495	
Va/U	0.60		0.60 → 0.50	
Reaction	0.586		0.605	
Reynolds Number	2.95×10^5 (Rotor)		11×10^5 (Rotor)	
RPM	1045		6893	
Tip Speed (m/s)	70.2		312.5	
Casing radius (mm)	609.6		433.77 → 432.09	
Hub/Tip ratio	0.91		0.906 → 0.911	
α_0	14.0		14.0 →13.5	
	Rotor	**Stator**	**Rotor**	**Stator**
Tip clearance	1.1%	1.12%	1.1%	1.12%
Flow deflection	24.5°	32.0°	20.5°	34.5°
Solidity	1.655	1.925	1.819	2.270
Aspect ratio	0.91	1.04	0.94	1.03
Rel Mach number	0.206	0.177	0.79	0.61
Blade number	101	134	111	158
Thick/chord (mid)	10%	9.2%	6%	6%
de Haller (pitchline)	0.698	0.728	0.643	0.654
Incidence (pitchline)	-9.0°	0.5°	-0.9°	-4.0°

Table 4.1 High and low speed aerodynamic and geometric parameters

Rotor	Z1	R1	Z2	R2	Camb	Stag	TC	AC	Redge	Chord	AIL	AIT
1	0.0	394.12	36.05	394.73	33.07	30.55	7.875	42.5	6.00	41.77	19.975	5.0
2	0.0	397.92	35.56	398.37	30.75	32.40	7.500	42.5	6.15	42.12	19.000	5.0
3	0.0	405.53	34.58	405.65	27.23	35.50	6.750	42.5	6.45	42.52	17.050	5.0
4	0.0	413.13	33.60	412.93	25.20	37.80	6.000	42.5	6.75	42.52	15.100	5.0
5	0.0	420.70	32.62	420.20	24.66	39.30	5.250	42.5	7.05	42.12	13.150	5.0
6	0.0	428.27	31.65	427.48	25.60	40.00	4.500	42.5	7.35	41.32	11.200	5.0
7	0.0	432.05	31.16	431.12	26.63	40.05	4.125	42.5	7.50	40.77	10.225	5.0
Stator	Z1	R1	Z2	R2	Camb	Stag	TC	AC	Redge	Chord	AIL	AIT
1	0.0	394.56	30.80	394.46	46.83	26.34	5.000	43.13	7.00	37.50	11.000	5.0
2	0.0	398.17	30.74	398.07	45.76	25.61	5.200	42.50	6.90	37.45	11.700	5.0
3	0.0	405.44	30.57	405.29	44.23	24.61	5.600	41.45	6.70	37.35	13.100	5.0
4	0.0	412.72	30.40	412.51	43.62	24.03	6.000	40.69	6.50	37.25	14.500	5.0
5	0.0	420.00	30.23	419.73	43.93	23.87	6.400	40.20	6.30	37.15	15.900	5.0
6	0.0	427.28	30.07	426.95	45.13	24.16	6.800	40.00	6.10	37.05	17.300	5.0
7	0.0	430.92	30.00	430.56	45.98	24.44	7.000	40.00	6.00	37.00	18.000	5.0

Table 4.2 C147 fourth stage design parameters

Section	1	2	3	4	5	6	7
Radius (m)	0.5548	0.5615	0.5722	0.5827	0.5936	0.6043	0.6096
Chord (mm)	58.937	59.430	60.000	60.000	59.430	58.302	57.526
CAMB	21.5	20.4	19.0	18.2	18.0	18.0	18.0
STAG	24.8	27.9	31.4	33.9	35.1	35.1	34.8
TC	4.0	4.0	4.0	4.0	4.0	4.0	4.0
AC	49.0	48.5	48.0	47.6	47.3	47.1	47.0
REDGE	11.0	11.0	11.0	11.0	11.0	11.0	11.0
AIL	12.1	11.7	10.95	10.1	9.2	8.4	8.0
AIT	1.9	2.25	2.6	2.78	2.91	3.01	3.04
CAMB2	28.0	28.6	29.5	30.4	31.2	32.0	32.4
STAG2	24.8	27.9	31.4	33.9	35.1	35.1	34.8
TC2	17.2	17.35	17.55	17.73	17.84	17.9	17.9
AC2	32.0	31.5	30.92	30.45	30.05	29.85	29.8
RLE	23.0	21.1	18.6	17.0	16.9	17.5	18.0
ALPHA	17.0	18.7	21.0	22.3	23.05	23.2	23.2
A_B	3.4	3.4	3.4	3.4	3.4	3.4	3.4
Rextra	6.0	6.0	6.0	6.0	6.0	6.0	6.0

Table 4.3 Rotor design parameters

Section	1	2	3	4	5	6	7
Radius (m)	0.5555	0.5618	0.5719	0.5822	0.5926	0.6029	0.6080
Chord (mm)	52.913	52.842	52.701	52.560	52.419	52.277	52.207
CAMB	41.0	39.0	35.7	33.0	32.1	32.0	32.0
STAG	23.6	23.2	22.55	21.95	21.7	21.75	21.8
TC	6.7	6.7	6.7	6.7	6.7	6.7	6.7
AC	41.7	41.72	41.77	41.83	41.9	41.97	42.0
REDGE	11.0	11.0	11.0	11.0	11.0	11.0	11.0
AIL	16.9	16.5	15.94	15.4	15.1	15.35	15.7
AIT	3.5	3.452	3.372	3.29	3.207	3.124	3.083
CAMB2	32.8	33.3	33.9	34.2	34.3	34.3	34.3
STAG2	23.6	23.2	22.55	21.95	21.7	21.75	21.8
TC2	14.79	15.0	15.33	15.67	16.01	16.35	16.52
AC2	34.5	34.04	33.36	32.8	32.5	32.34	32.3
RLE	21.0	20.3	19.6	19.3	19.2	19.15	19.15
ALPHA	31.0	29.5	27.0	25.0	23.5	23.0	23.0
A_B	2.7	2.9	3.14	3.2	3.23	3.25	3.25
Rextra	4.0	4.0	4.0	4.0	4.0	4.0	4.0

Table 4.4 Stator design parameters

	Part 1a			Part 1b		
	Design flow	Near stall	High flow	Design flow	Near stall	High flow
% Height	Calib3C	Calib5C	Calib6C	Calib6A	Calib7B	no data
2.10	NAC017	NAC118	NAC155	NAC166	NAC193	n/a
3.94	NAC092	NAC117	NAC154	NAC168	NAC194	"
6.13	NAC091	NAC116	NAC153	NAC169	NAC195	"
8.57	NAC090	NAC115	NAC152	NAC170	NAC196	"
11.23	NAC089	NAC114	NAC151	NAC171	NAC197	"
14.68	NAC086	-	NAC133	NAC172	NAC198	"
19.17	NAC083	-	NAC134	NAC173	NAC199	"
25.01	NAC081	NAC100	NAC135	NAC174	NAC200	"
32.42	NAC084	NAC101	NAC136	NAC175	NAC201	"
41.02	NAC082	NAC102	NAC137	NAC176	NAC202	"
50.00	NAC033	NAC103	NAC138	NAC177	NAC203	"
58.98	NAC034	NAC104	NAC139	NAC178	NAC204	"
67.58	NAC035	NAC105	NAC140	NAC179	NAC205	"
74.99	NAC036	NAC106	NAC141	NAC180	NAC206	"
80.83	NAC037	NAC107	NAC142	NAC181	NAC207	"
85.32	NAC060	NAC108	NAC143	NAC182	NAC208	"
88.72	NAC061	NAC109	NAC144	NAC183	NAC209	"
91.43	NAC062	NAC110	NAC145	NAC184	NAC210	"
93.87	NAC063	NAC111	NAC146	NAC185	NAC216	"
96.06	NAC070	NAC112	NAC150	NAC186	NAC212	"
97.90	NAC071	NAC119	NAC149	NAC188	NAC213	"

Table 6.1 Stationary frame traverse control files (Datum design)

	Part 1a			Part 1b		
Axial location	Design Flow	Near Stall	High Flow	Design flow	Near stall	High flow
	Calib3C	Calib5C	Calib6C	Calib6A	Calib7B	no data
IGV	✓	✓	✓		✓	
R1	✓	✓	✓			
S1	✓	✓	✓	✓		
R2				✓	✓	
S2	✓	✓	✓	✓	✓	
R3	✓	✓	✓			
S3	✓	✓	✓	✓	✓	
R4						
S4				✓	✓	

Table 6.2 Axial locations of stationary traverses (Datum build)

	Rotor	**Stator**
Stacking axis shape	**Parabola**	**Parabola**
Parabola strength factor A	**9.0**	**9.0**
Axis rotation (α)	**+30°**	**-30°**
Nominal blade stagger	**+30°**	**+22°**
Axis rotation to pitchwise direction	**+60°**	**-8°**
Overhang in axial direction	**3.4mm**	**-0.9mm**
Angle of axis to radial in axial direction	**13.4°**	**3.8°**
Overhang in pitchwise direction	**5.9mm**	**6.7mm**
Angle of axis to radial in pitchwise direction	**22.5°**	**25.3°**
Leading Edge Recamber at hub	**+20°**	**None**
Leading Edge Recamber at Casing	**None**	**+18°**
L.E.R. Endwall Section Parameters:		
Section Number	**1 (Hub)**	**7 (Casing)**
CAMB	**40.5**	**50.0**
CAMB2	**48.0**	**54.3**
STAG	**28.6**	**25.8**
AC	**41.0**	**40.0**

Table 8.1 Design parameters of final 3D design

% Height	Design Flow		Near Stall		High Flow	
	NBA002	NBA004	NBA011	NBA014	NBA021	NBA022
2.10	NBC002	NBC081	NBC029	NBA104	NBC058	NBC125
3.94	NBC003	NBC082	NBC030	NBA149	NBC059	NBC126
6.13	NBC004	NBC083	NBC031	NBA150	NBC060	NBC127
8.57	NBC005	NBC084	NBC032	NBA107	NBC061	NBC128
11.23	NBC006	NBC085	NBC033	NBA108	NBC062	NBC129
14.68	NBC007	NBC086	NBC034	NBA109	NBC063	NBC130
19.17	NBC008	NBC087	NBC035	NBA110	NBC064	NBC131
25.01	NBC009	NBC088	NBC036	NBA111	NBC065	NBC132
32.42	NBC010	NBC089	NBC037	NBA112	NBC066	NBC136
41.02	NBC011	NBC090	NBC038	NBA113	NBC067	NBC137
50.00	NBC012	NBC091	NBC039	NBA114	NBC068	NBC138
58.98	NBC013	NBC103	NBC040	NBA151	NBC069	NBC139
67.58	NBC021	NBC093	NBC041	NBA116	NBC070	NBC140
74.99	NBC015	NBC094	NBC042	NBA117	NBC071	NBC141
80.83	NBC016	NBC095	NBC043	NBA118	NBC072	NBC142
85.32	NBC017	NBC096	NBC044	NBA119	NBC073	NBC143
88.72	NBC018	NBC097	NBC045	NBA120	NBC074	NBC144
91.43	NBC025	NBC098	NBC046	NBA121	NBC075	NBC145
93.87	NBC024	NBC099	NBC047	NBA122	NBC076	NBC146
96.06	NBC022	NBC100	NBC048	NBA123	NBC079	NBC147
97.90	NBC023	NBC101	NBC057	NBA124	NBC078	NBC148

Table 9.1 Stationary frame traverse control files (3D design)

Axial Location	Design Flow		Near Stall		High Flow	
	NBA002	NBA004	NBA011	NBA014	NBA021	NBA022
IGV	✓		✓		✓	
R1	✓		✓		✓	
S1	✓	✓ (3d)	✓	✓ (3d)	✓	✓ (3d)
R2		✓		✓		✓
S2		✓		✓		✓
R3	✓		✓		✓	
S3	✓	✓ (3d)	✓	✓ (3d)	✓	✓ (3d)
R4		✓				✓
S4	✓	✓	✓		✓	✓

(3d) = Four hole probe used

Table 9.2 Axial locations of stationary traverses (3D build)

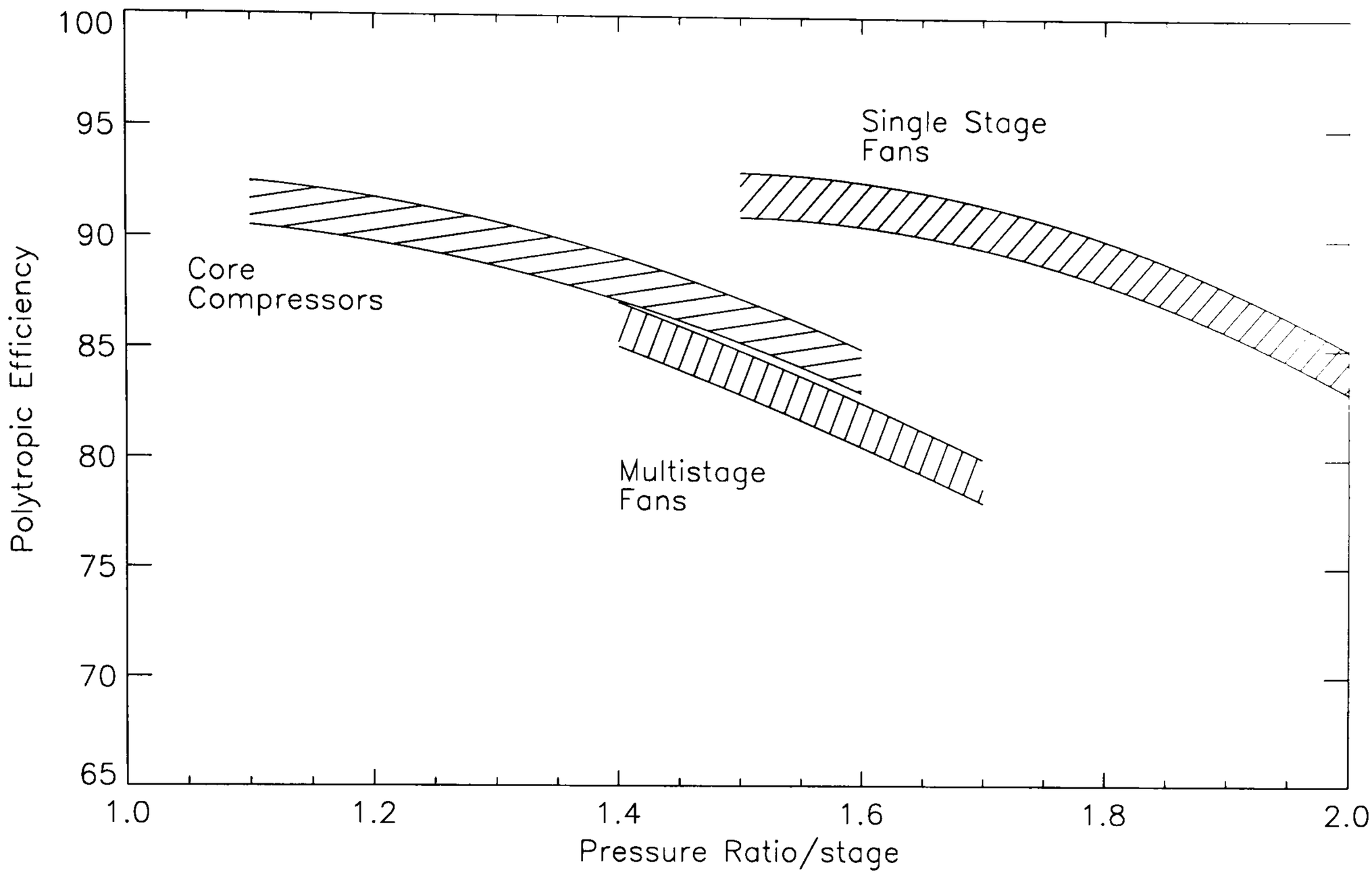


Figure 2.1 Compressor efficiencies - Effects of loading

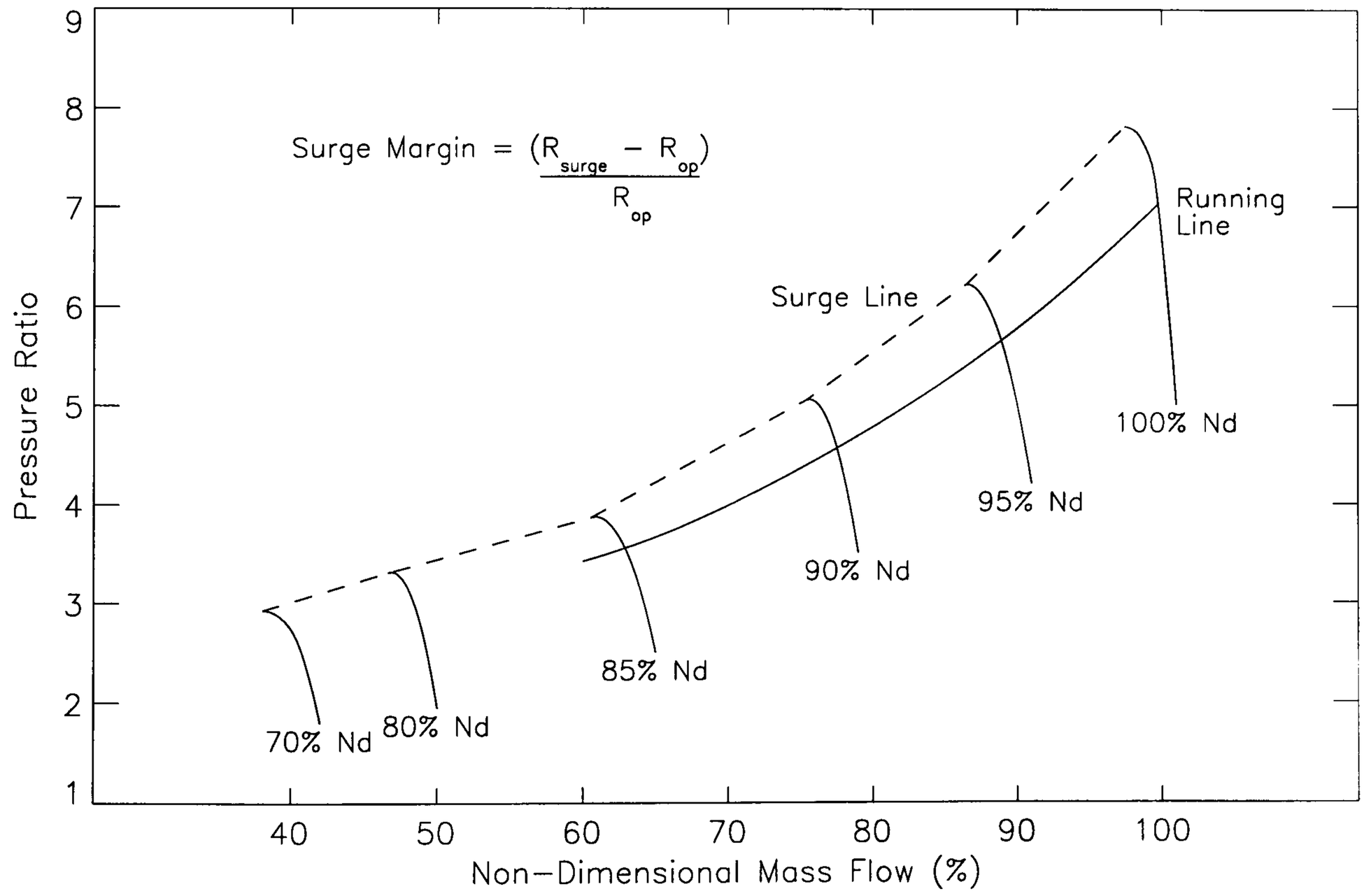
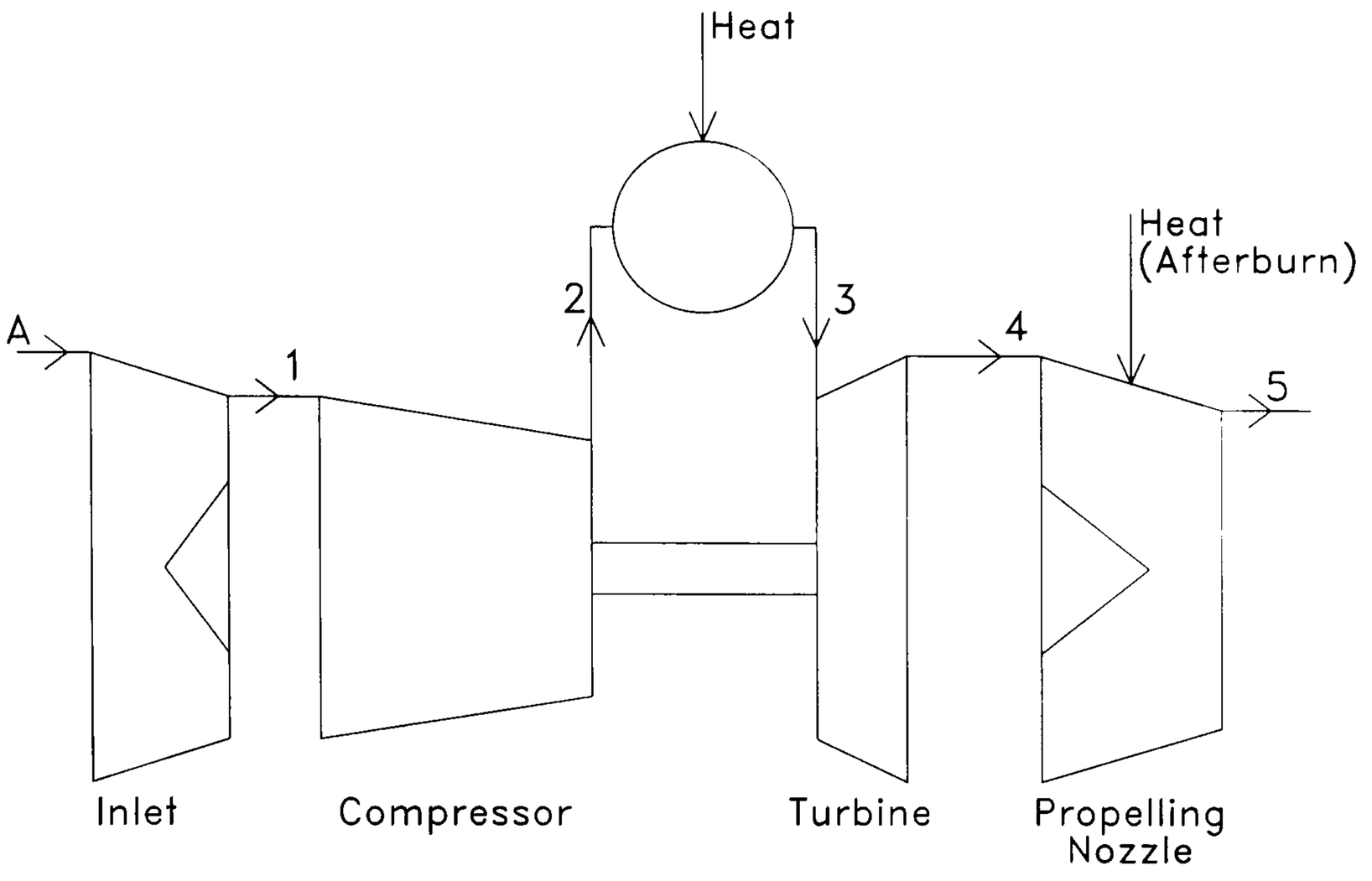


Figure 2.2 Typical military HP compressor characteristic



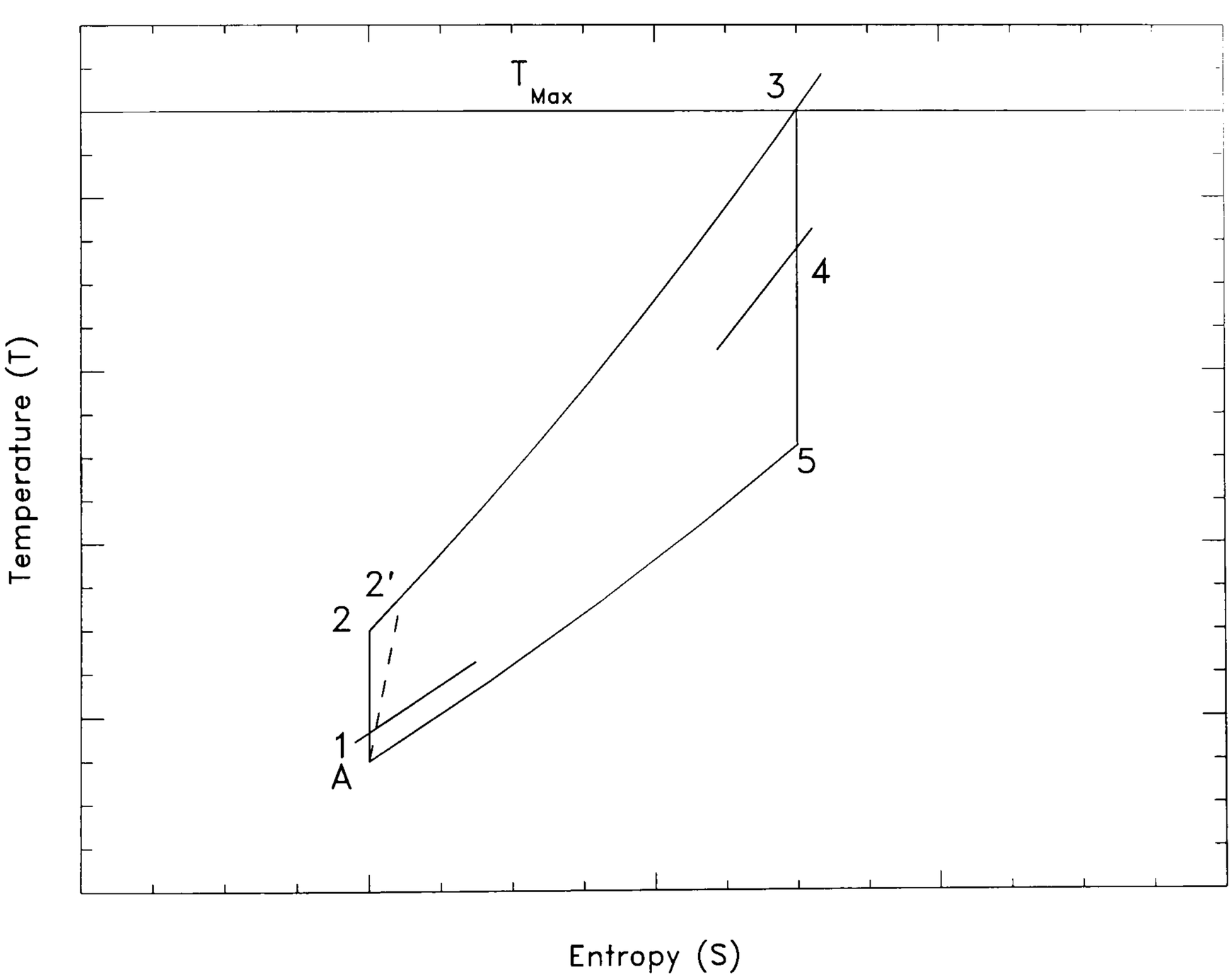


Figure 2.3 Ideal Joule cycle for a simple gas turbine

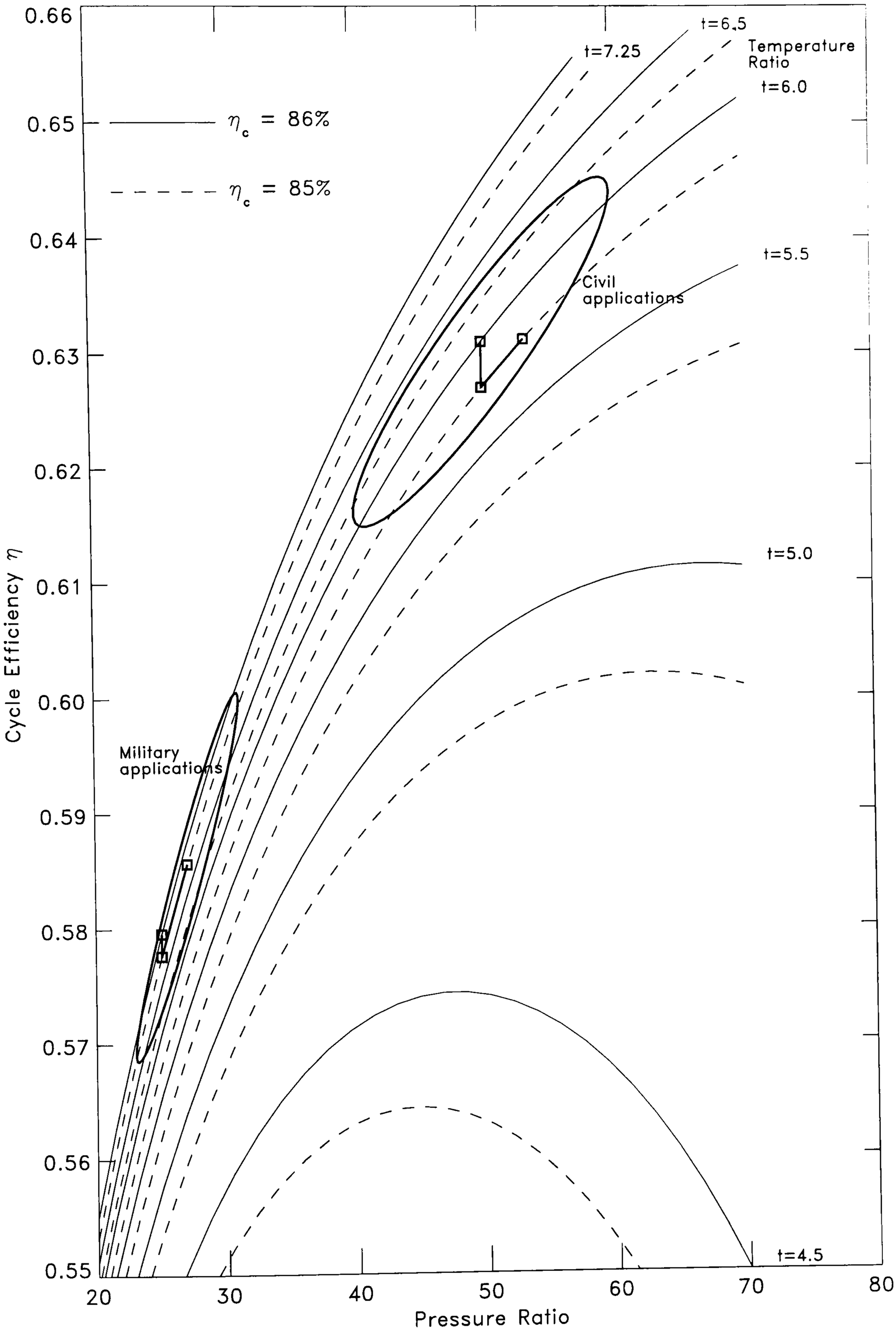
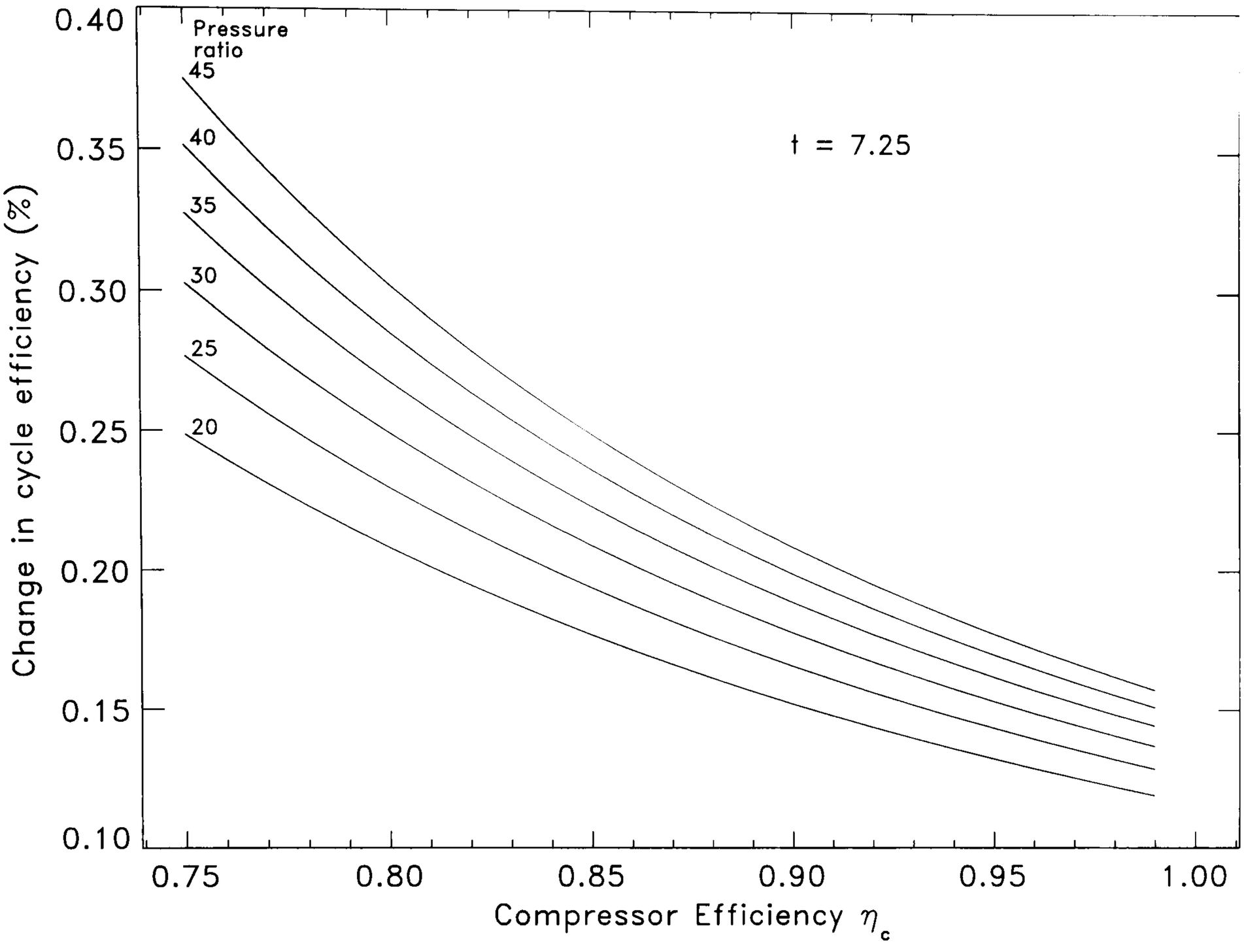


Figure 2.4 Cycle efficiency vs pressure ratio



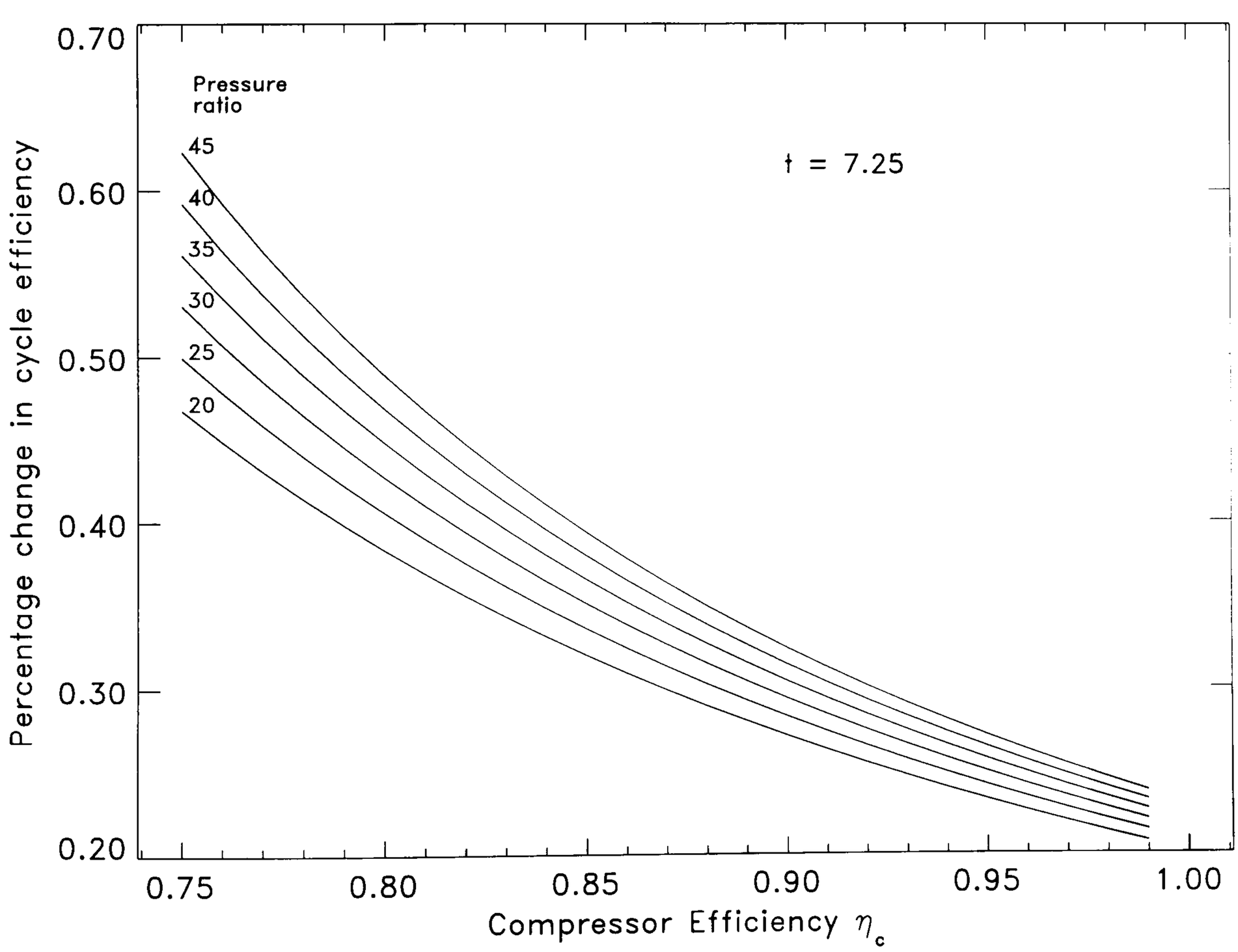
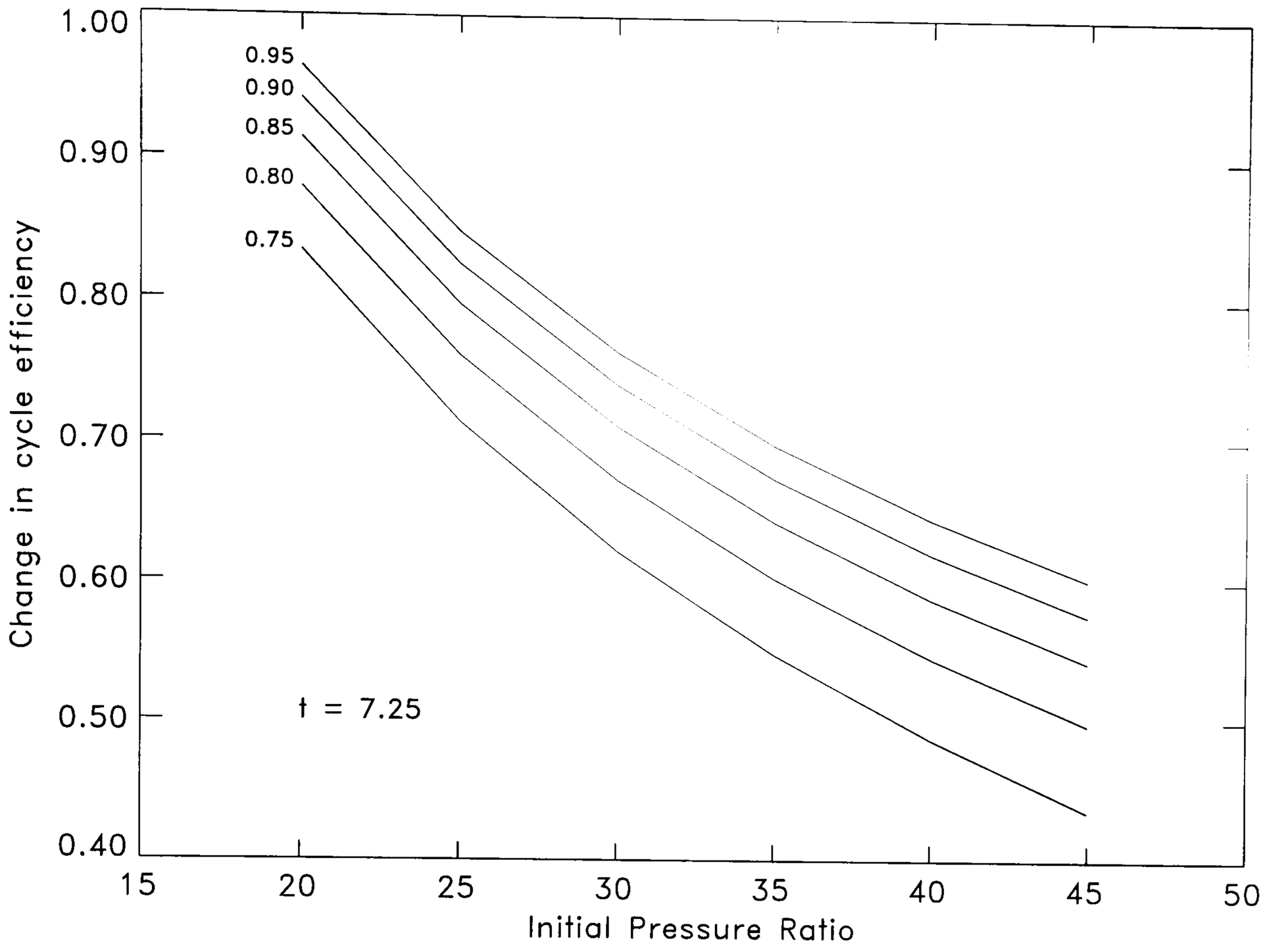


Figure 2.5 Effect of 1% improvement in compressor efficiency



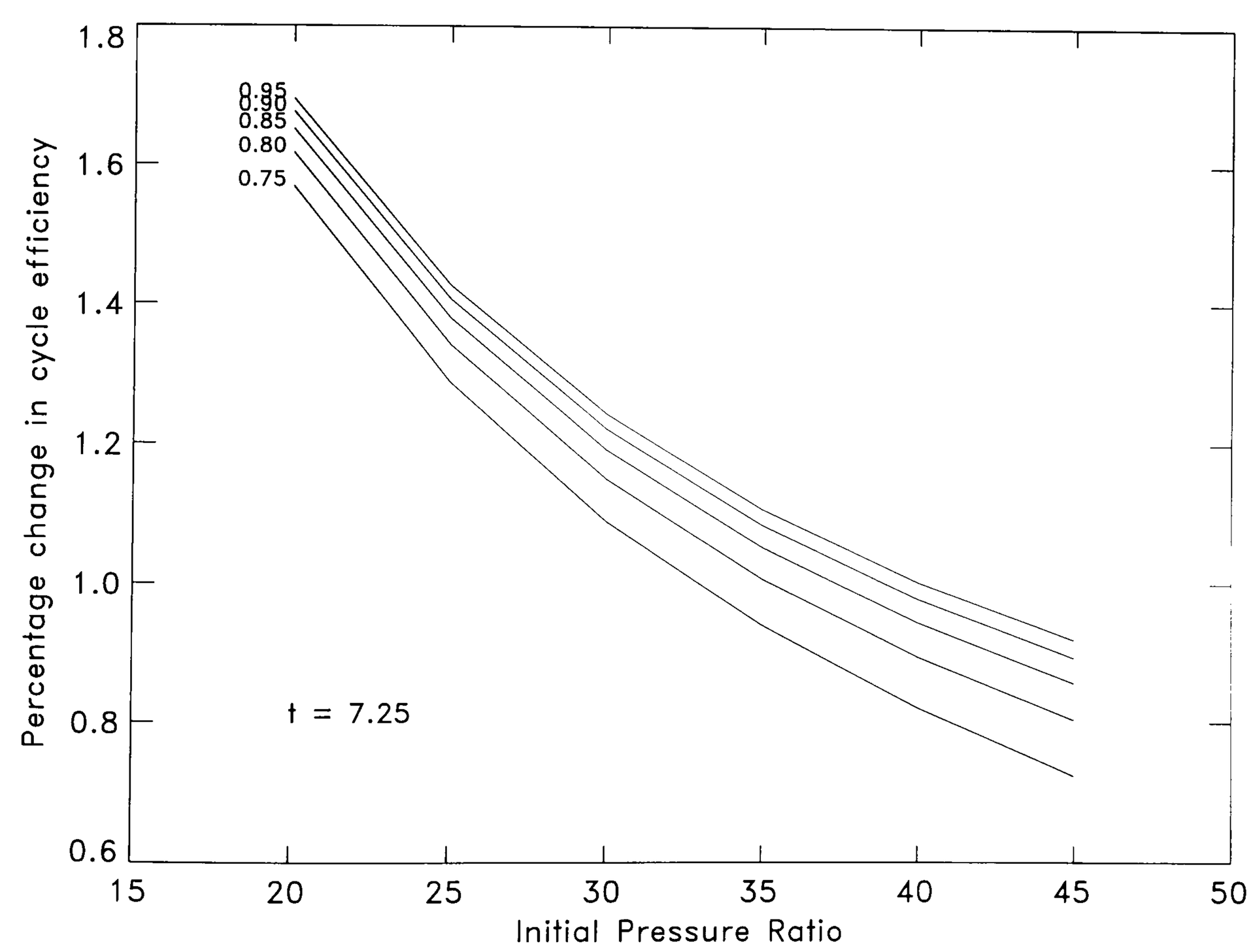


Figure 2.6 Effect of Pressure Ratio Increase on Cycle Efficiency

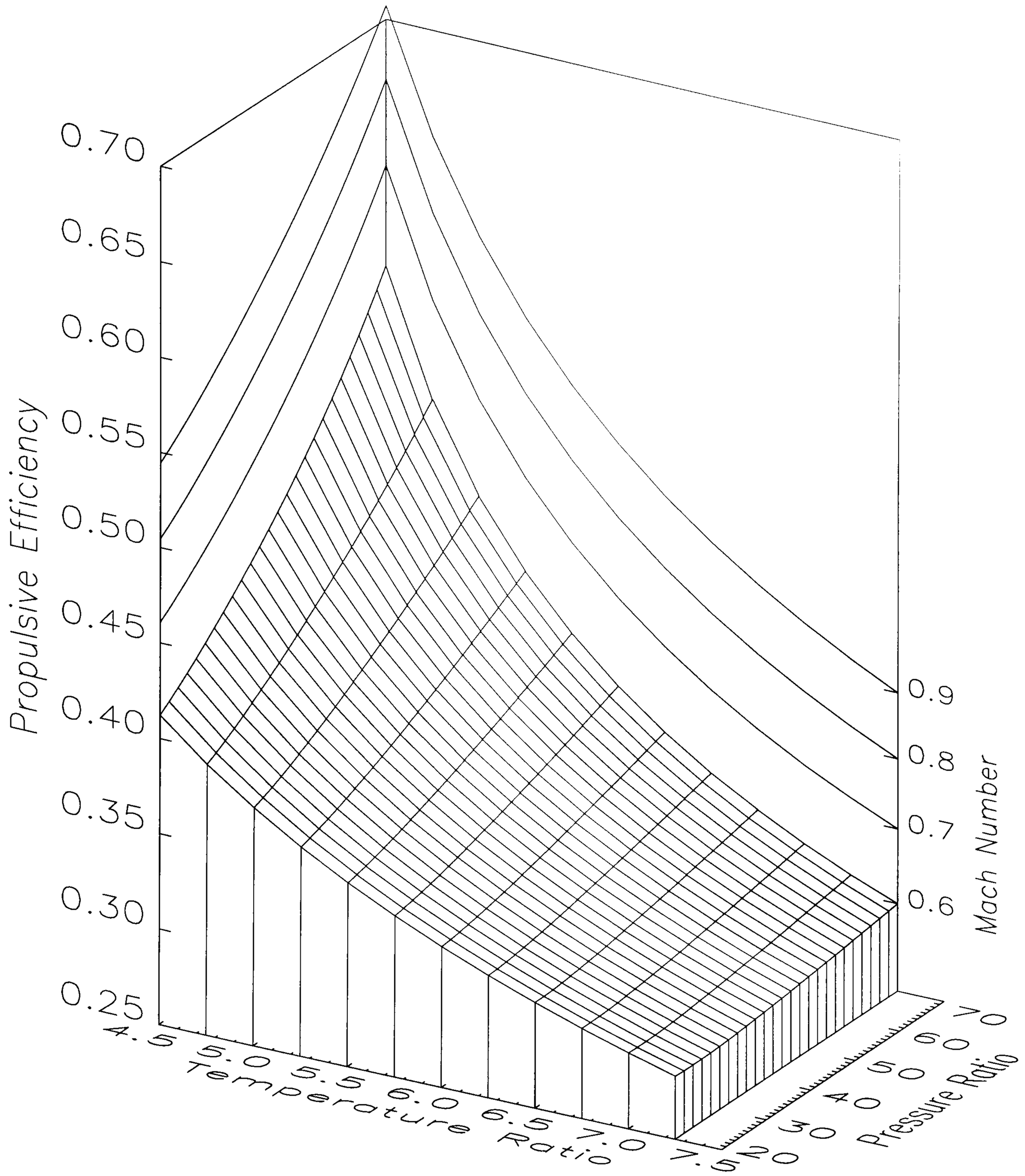


Figure 2.7 Propulsive efficiency distribution

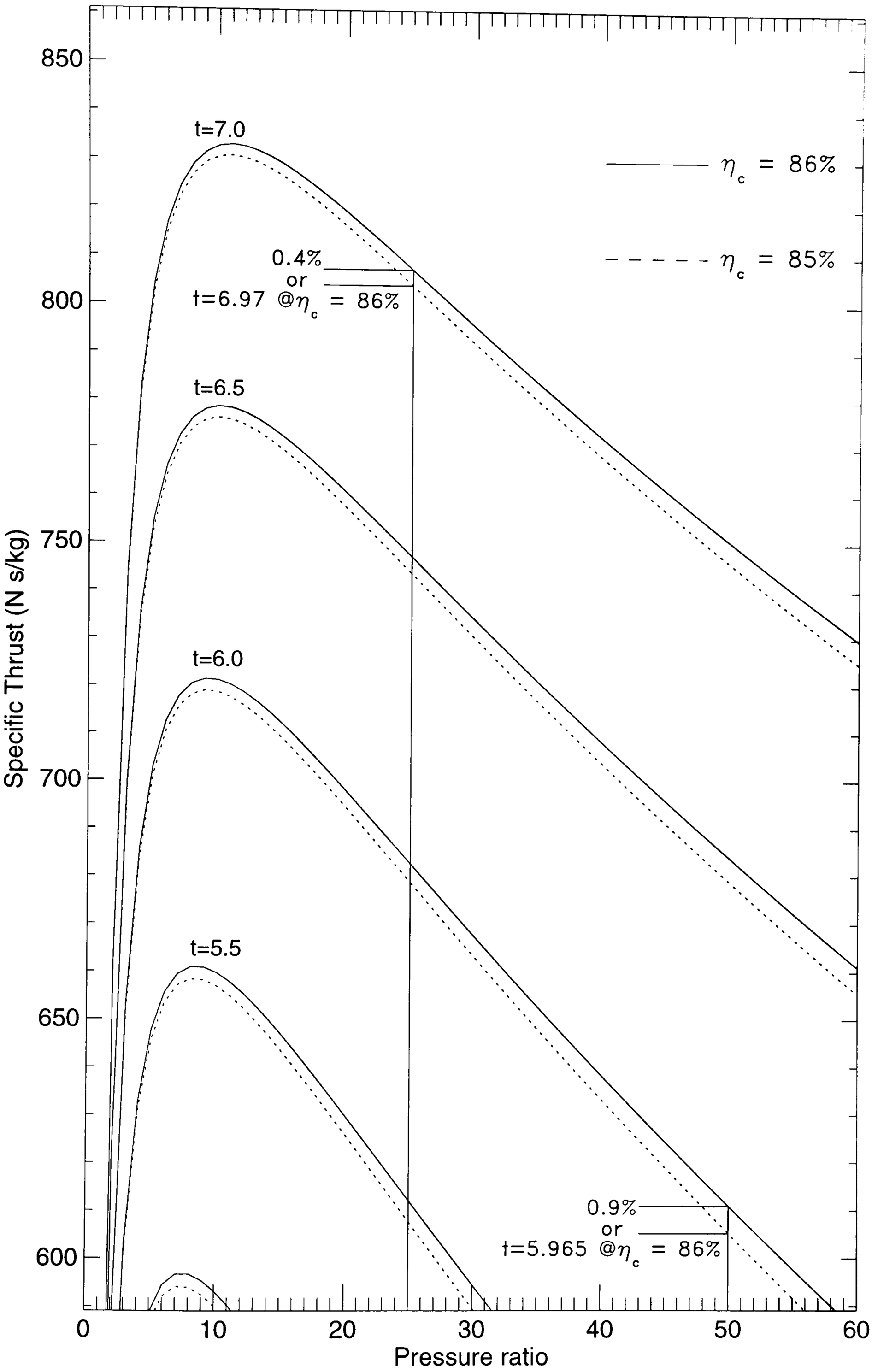


Figure 2.8 Effect of compressor efficiency increase on specific thrust

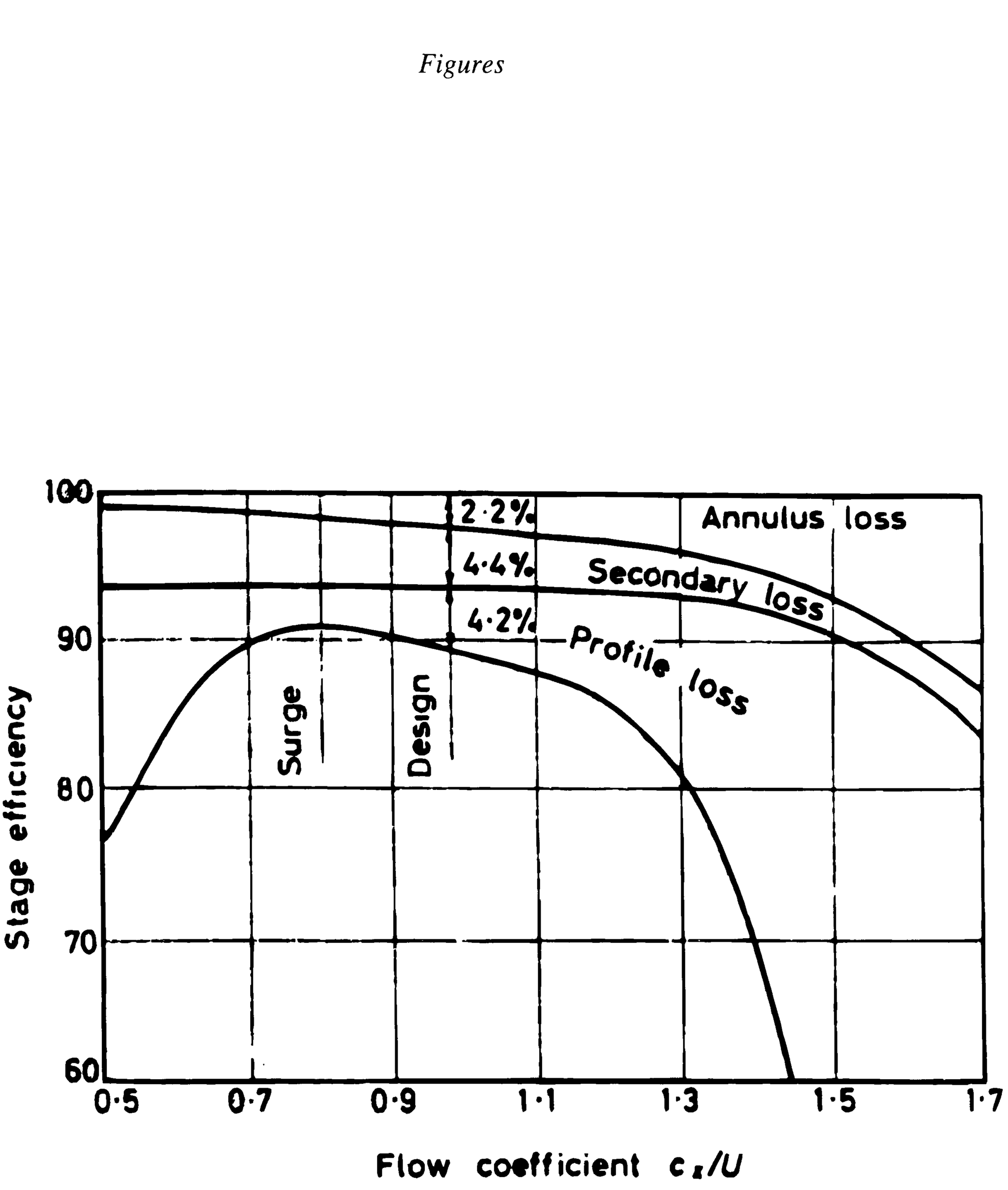


Figure 3.1 Losses in a compressor stage (Howell, 1945)

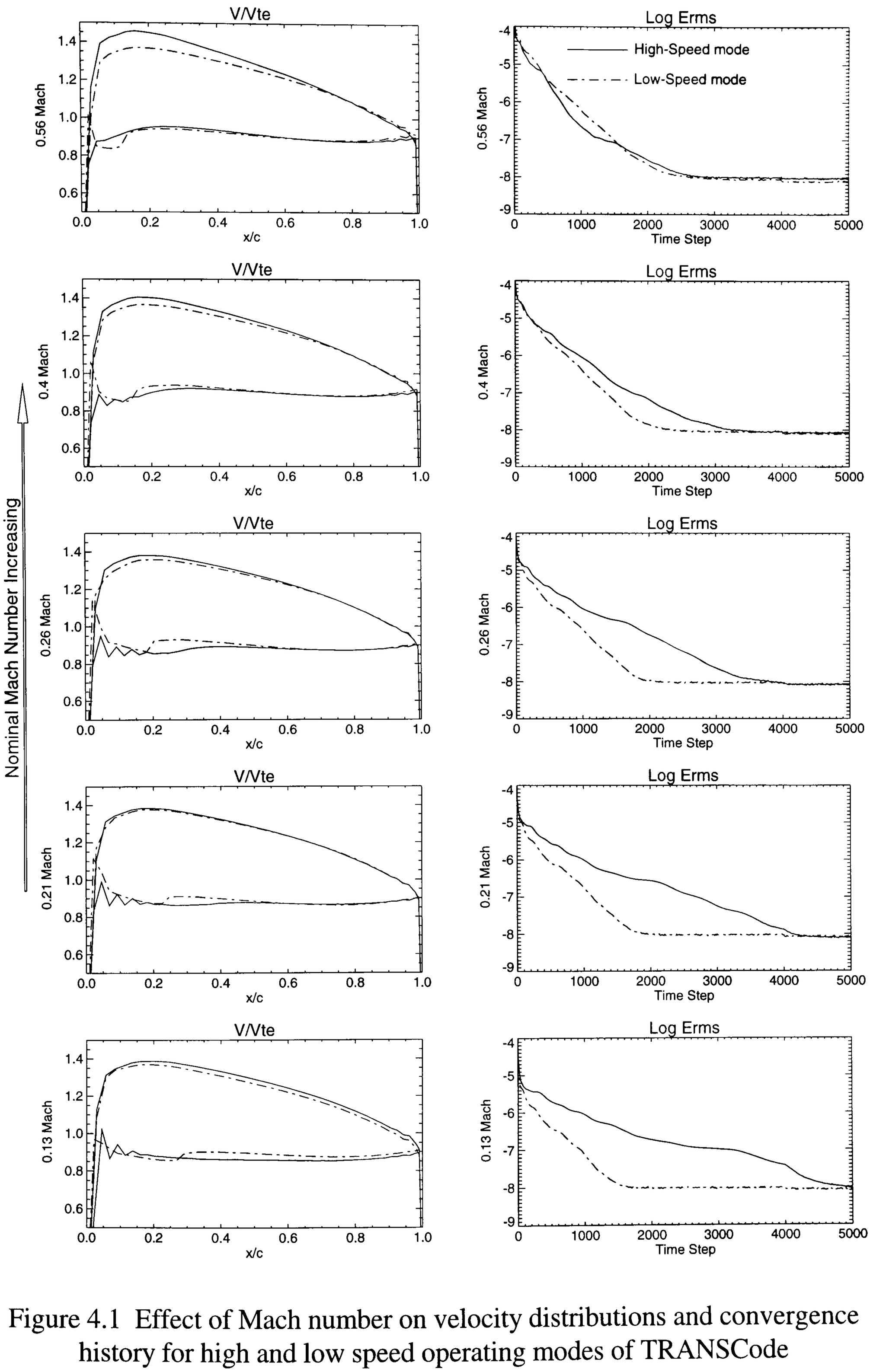


Figure 4.1 Effect of Mach number on velocity distributions and convergence history for high and low speed operating modes of TRANSCode

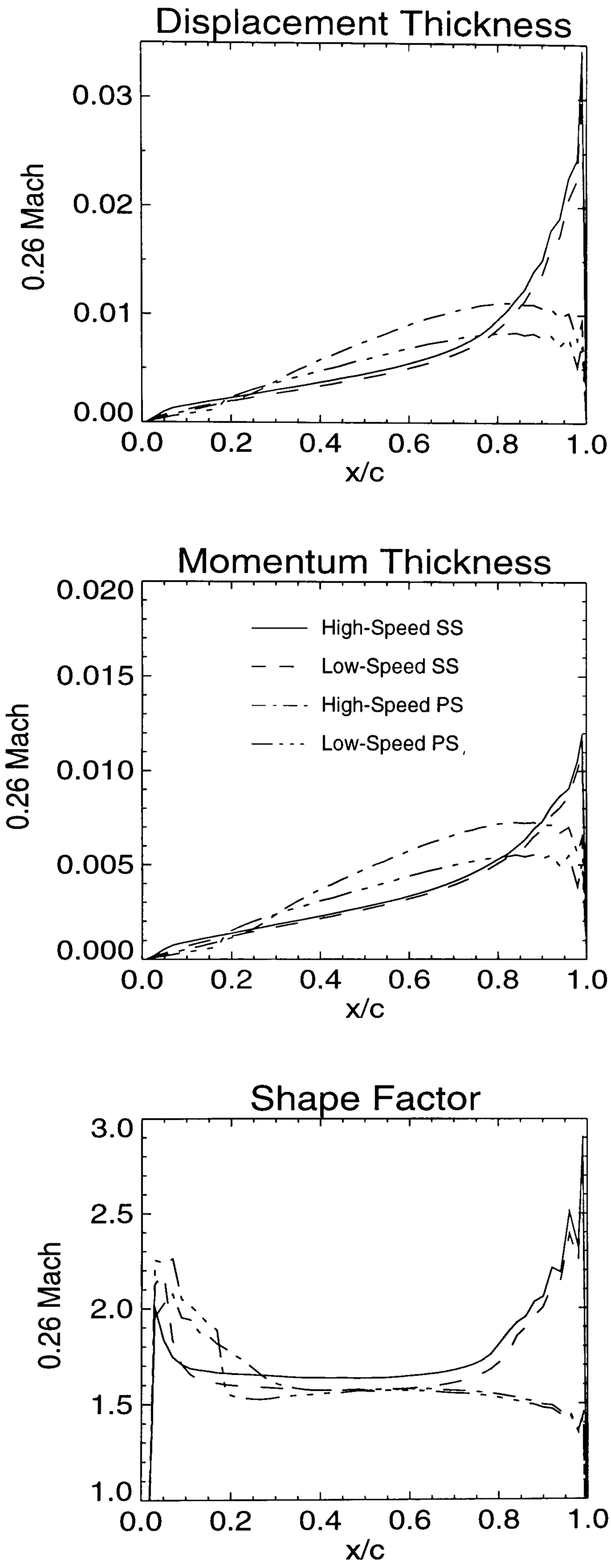


Figure 4.2 Boundary layer parameters for high and low speed operating modes at 0.26 indicated Mach number

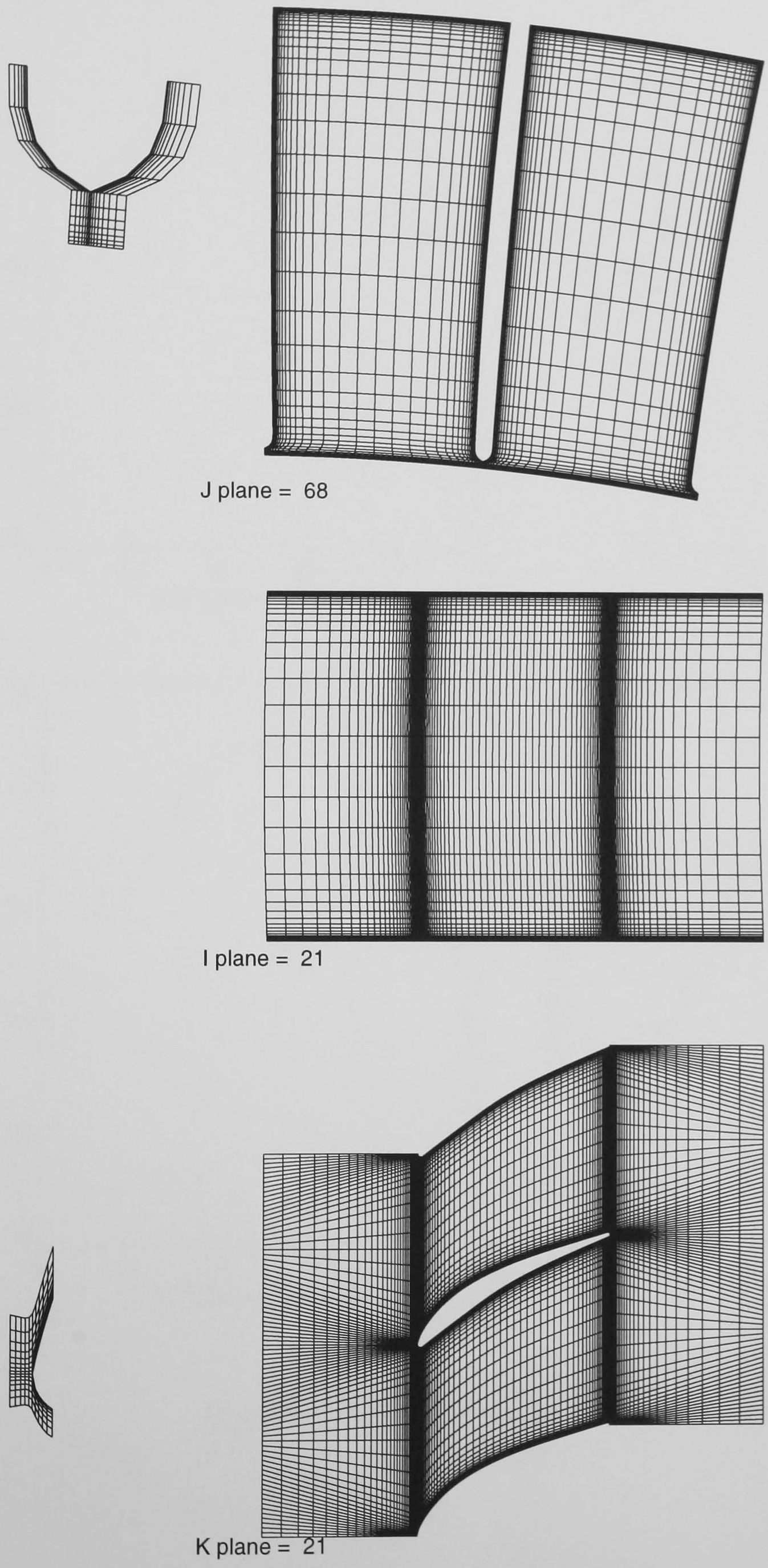
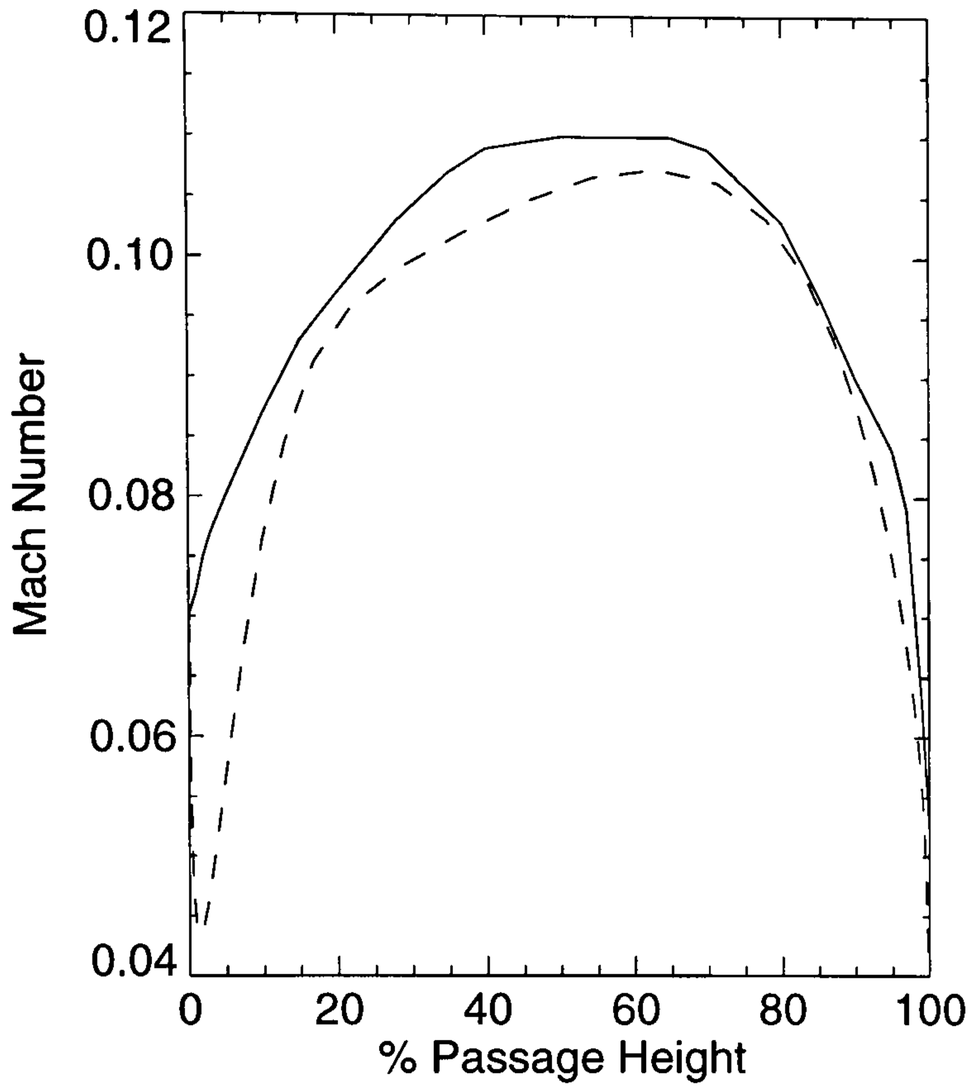
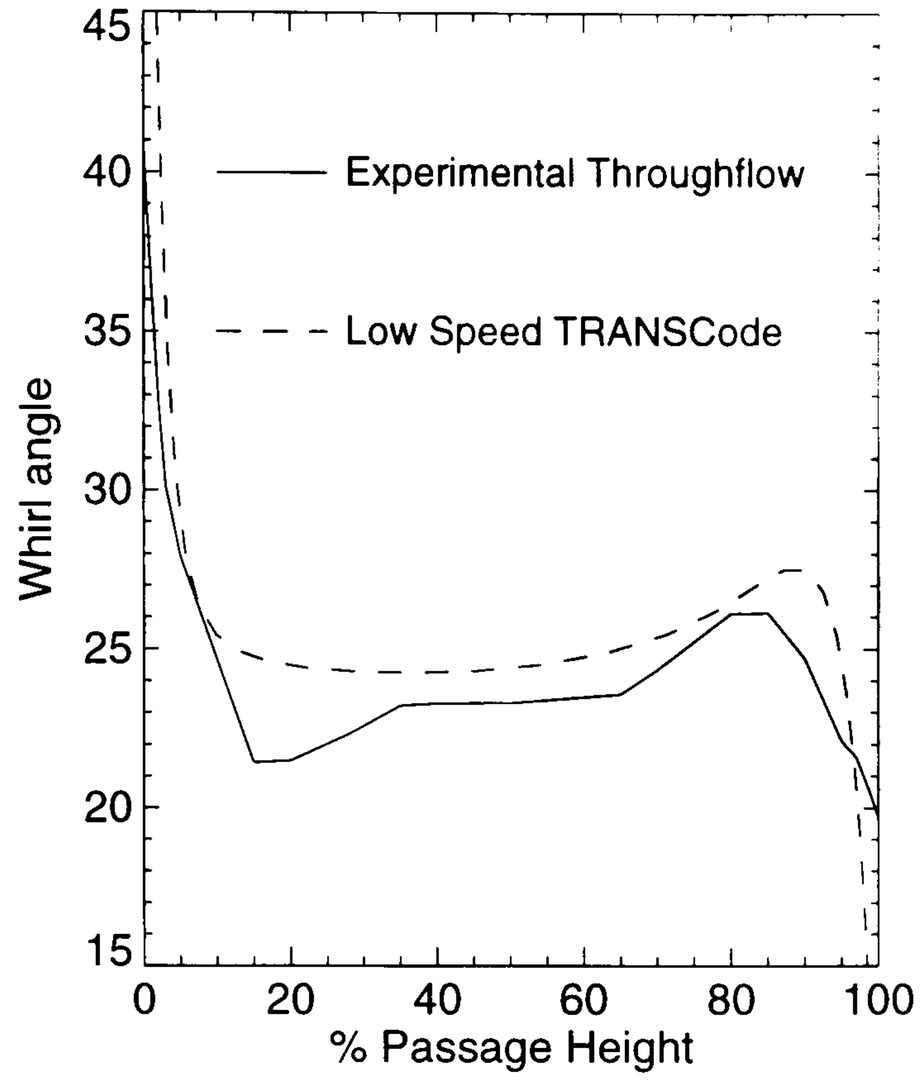
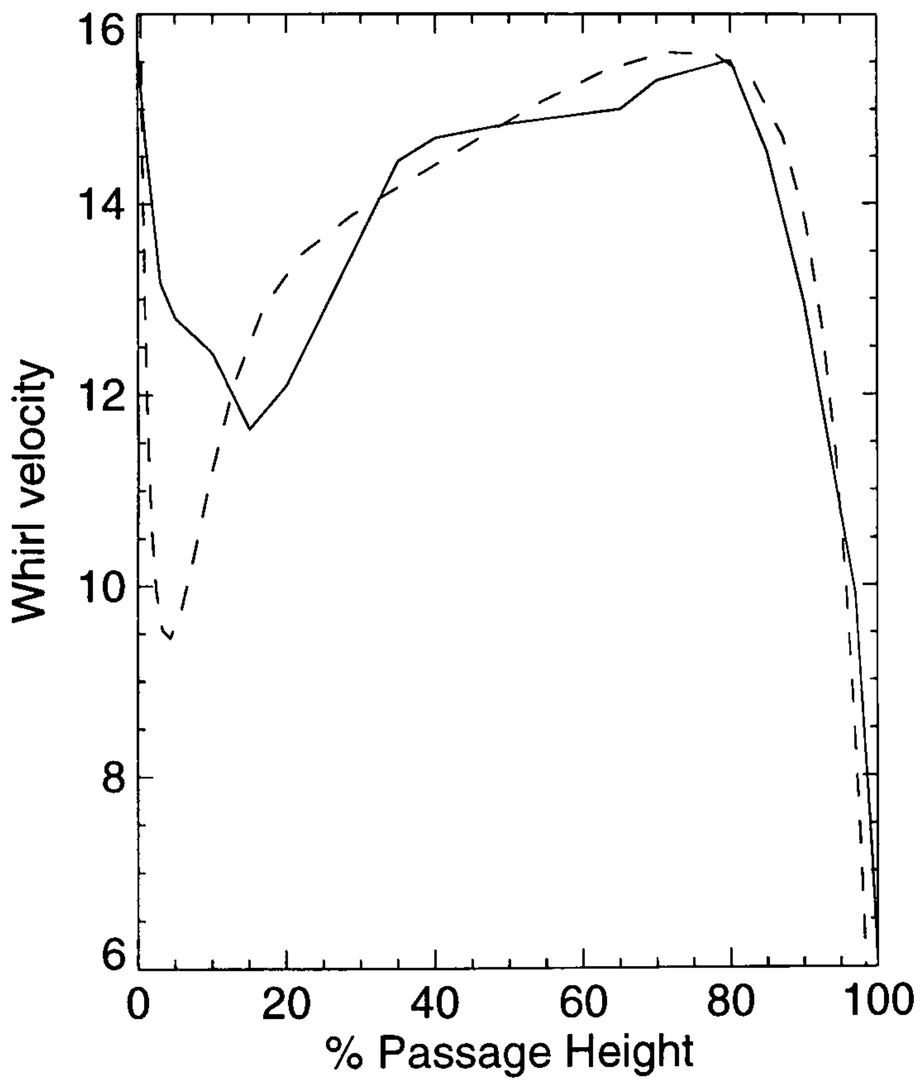


Figure 4.3 TRANSCode grid used for NEB1D stator solutions







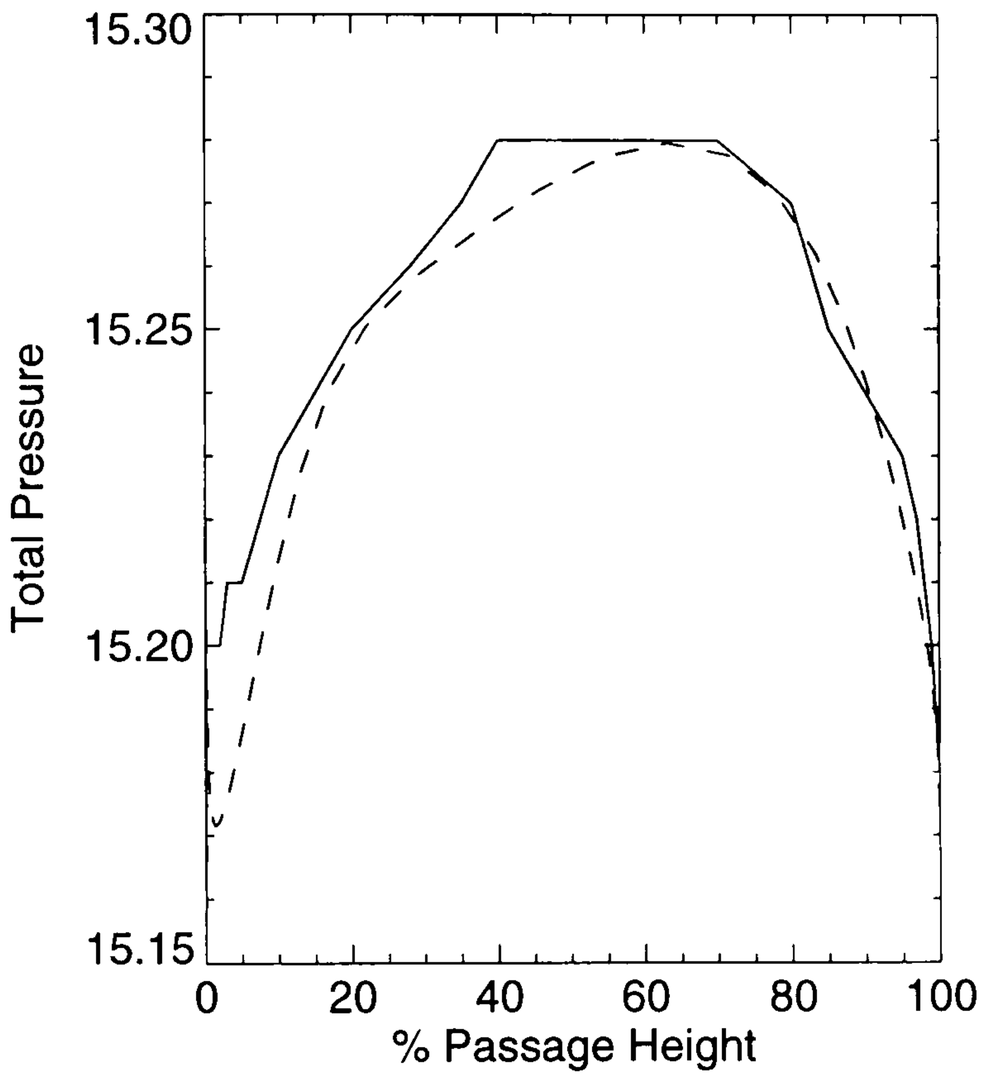
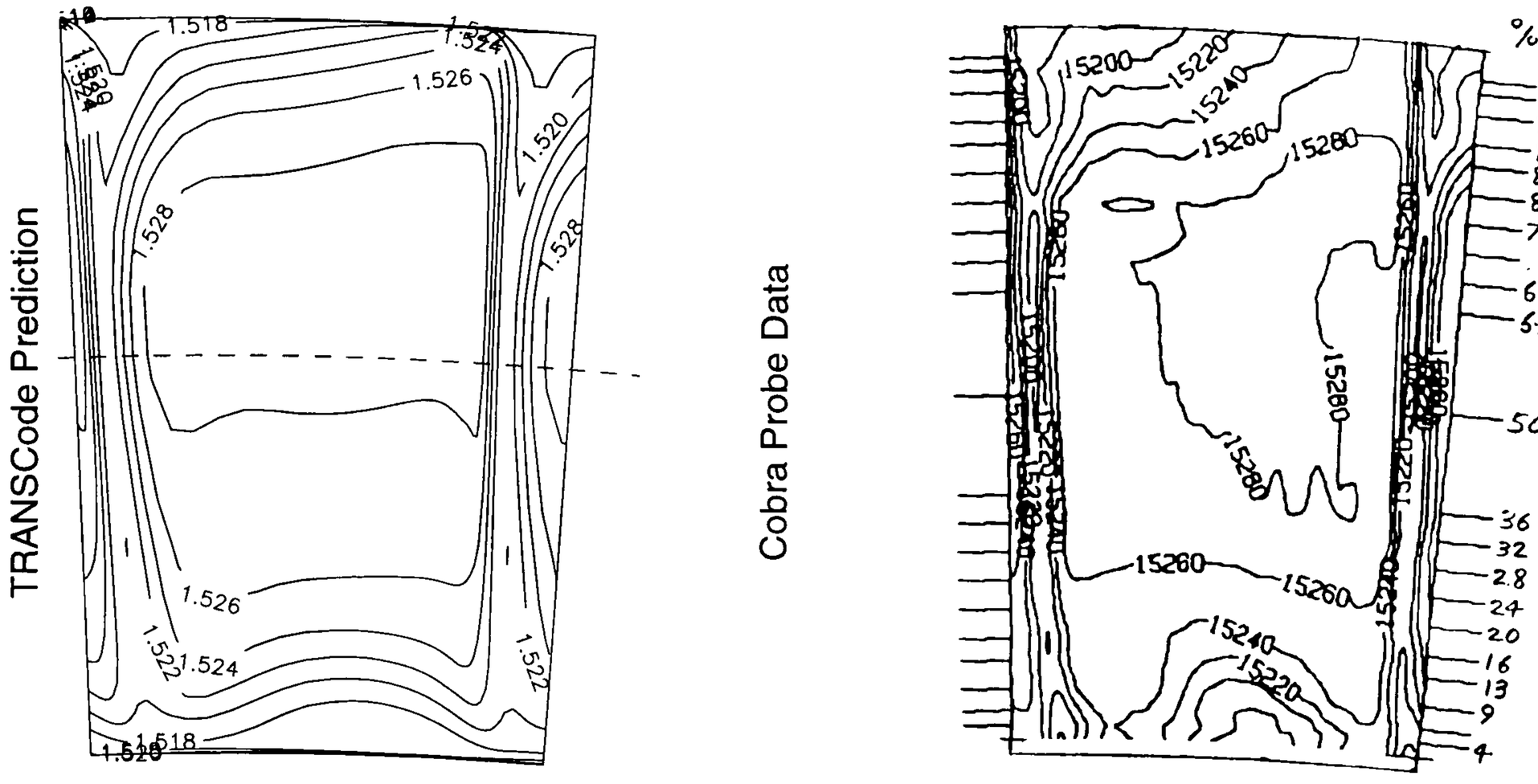


Figure 4.4 NEB1D Stator exit profiles



Contours of Total Pressure downstream of Stator 3
(PSIA x 1000) Max efficiency point

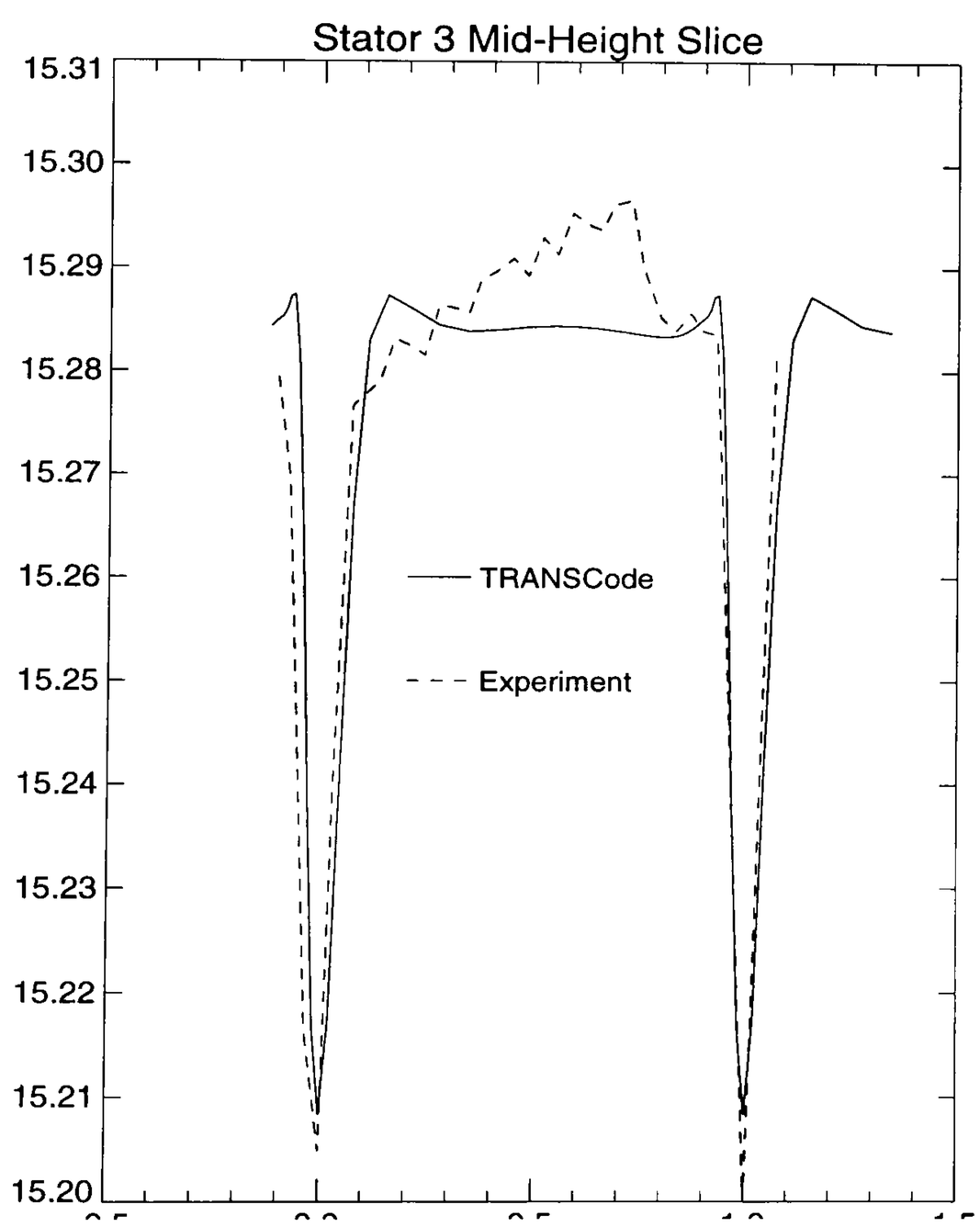
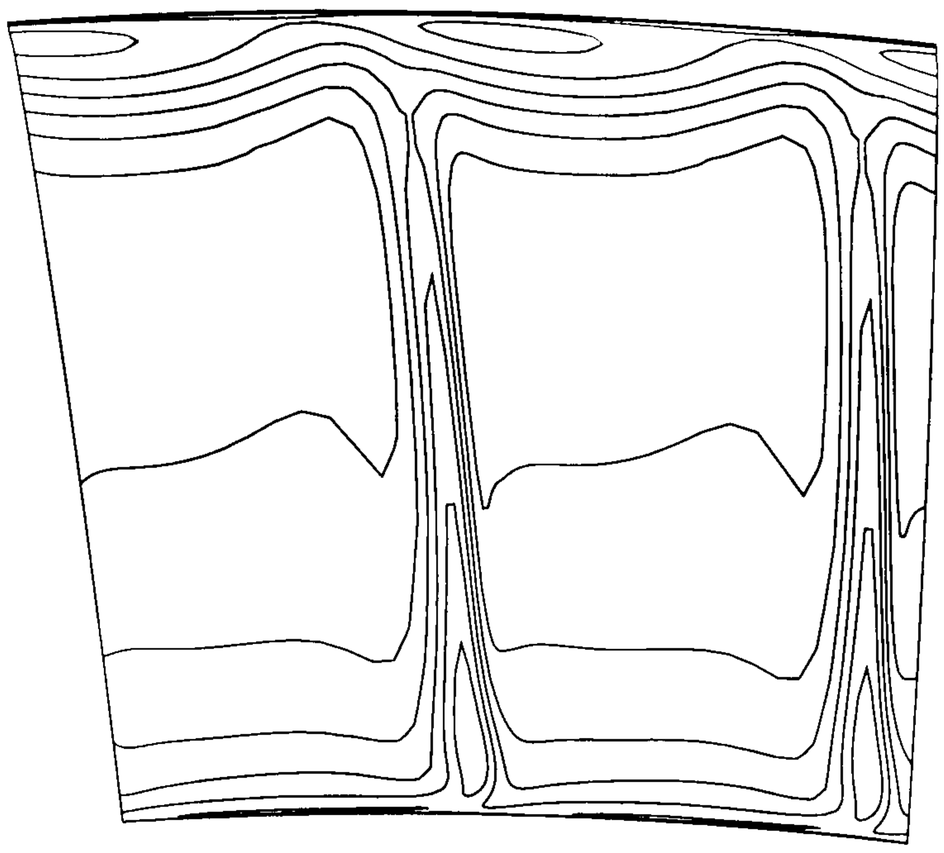
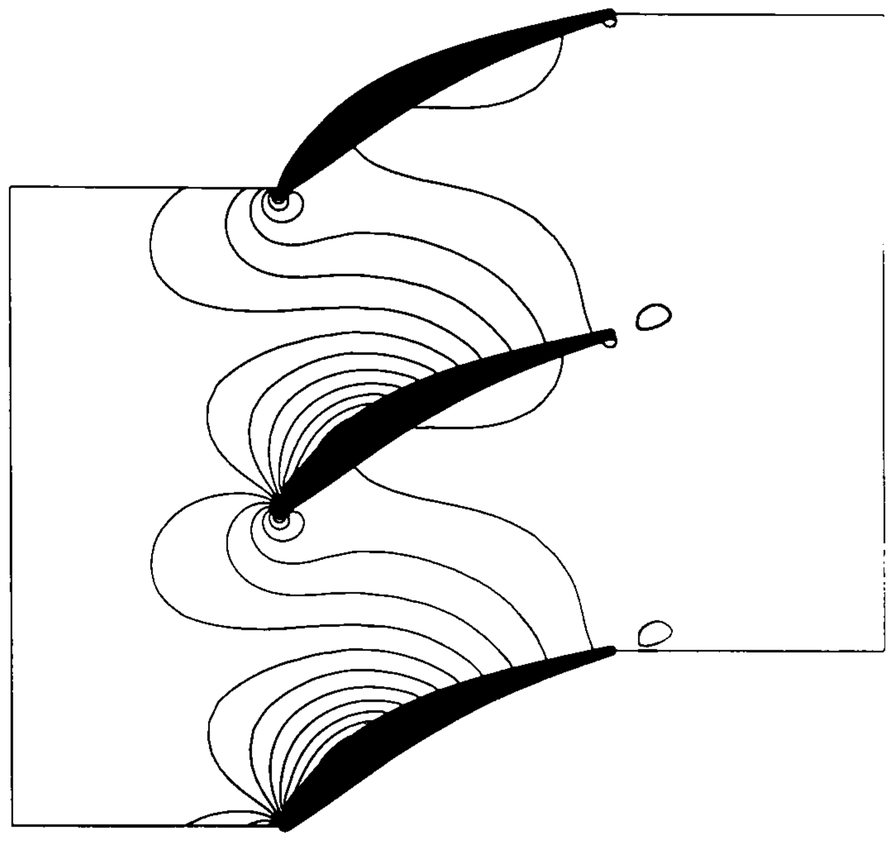


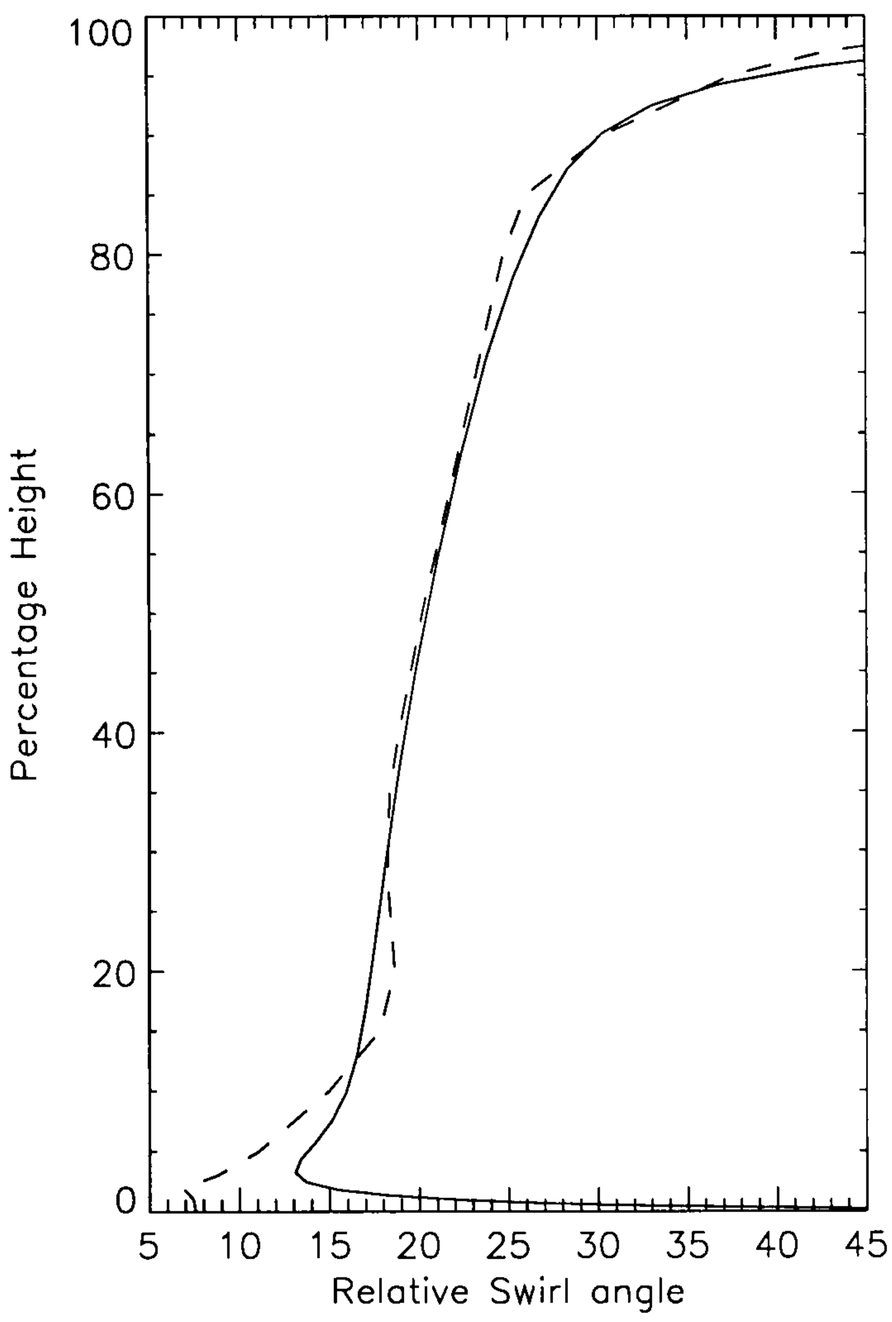
Figure 4.5 Comparison of NEB1D stator exit total pressure field with experiment



Total pressure at rotor exit



Static pressure at mid–height



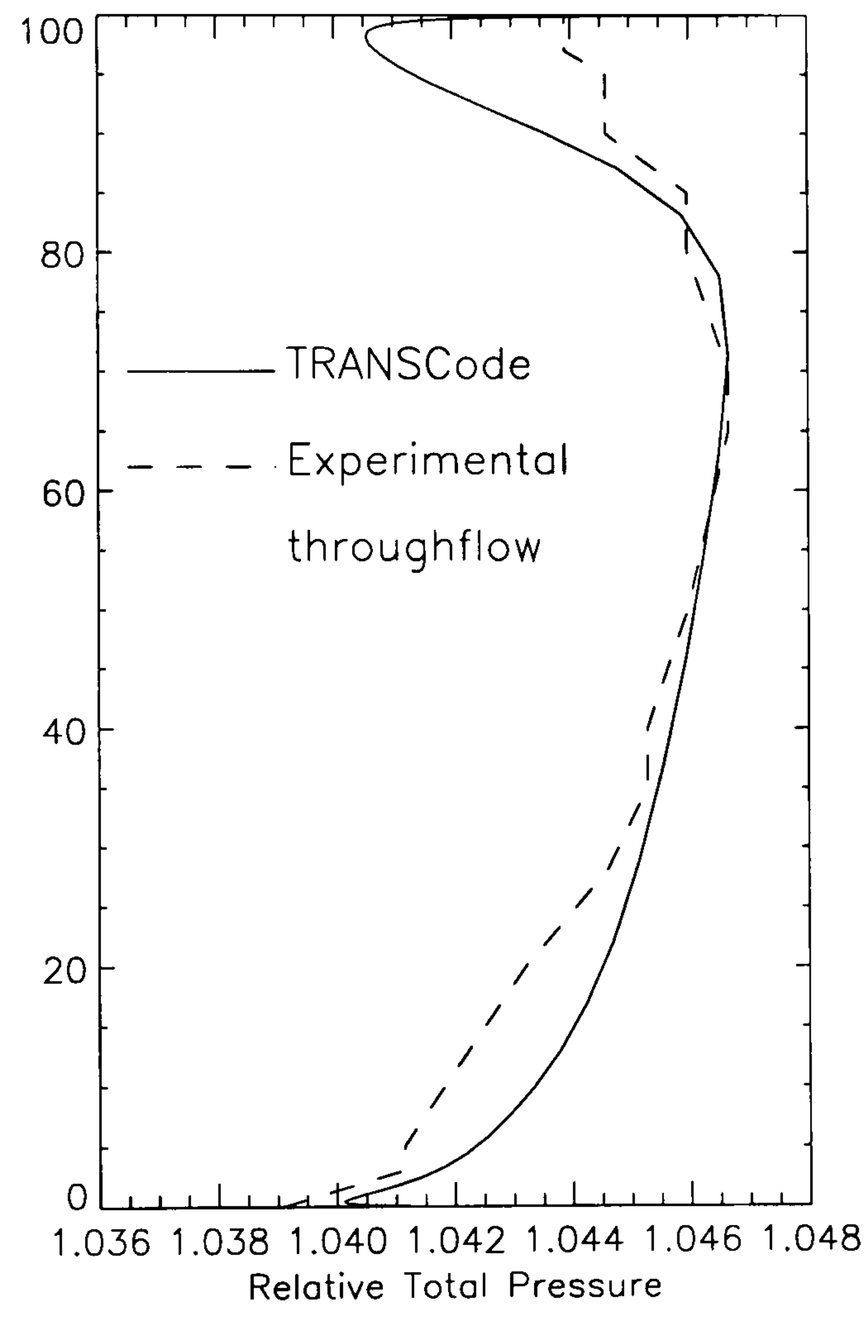


Figure 4.6 NEB1D rotor exit results

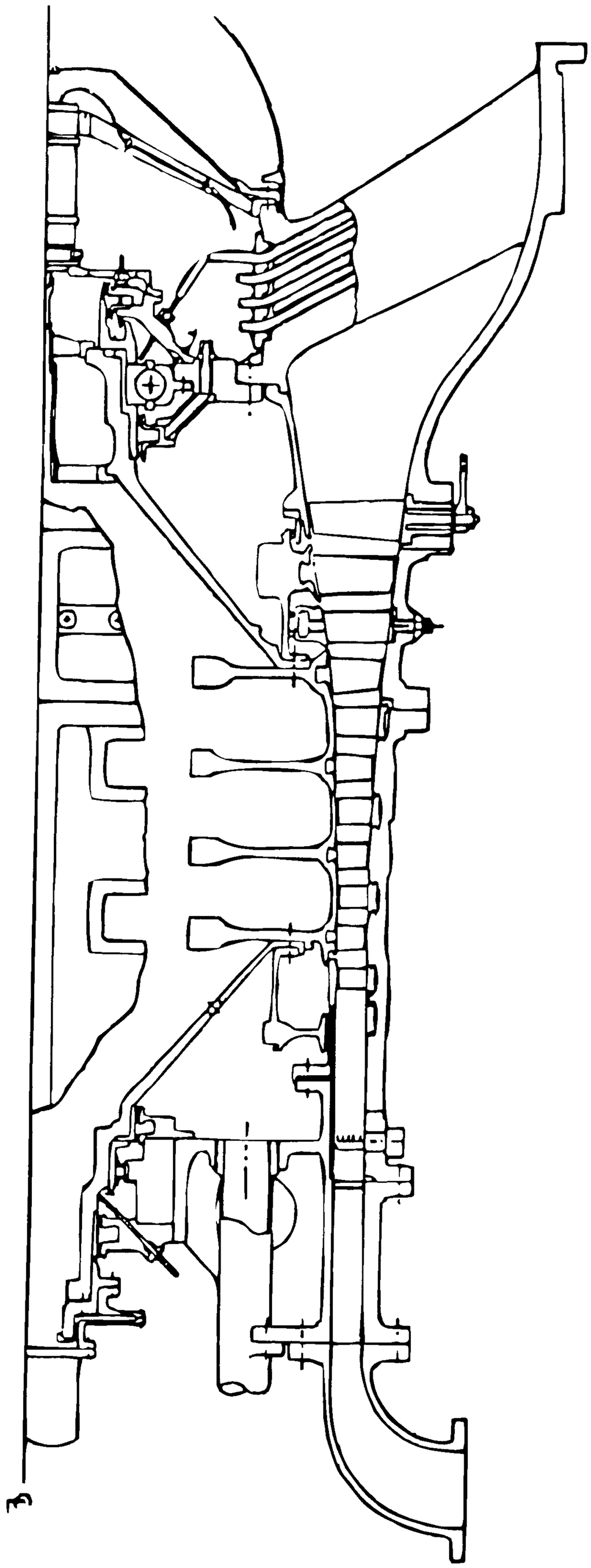


Figure 4.7 Section through C147

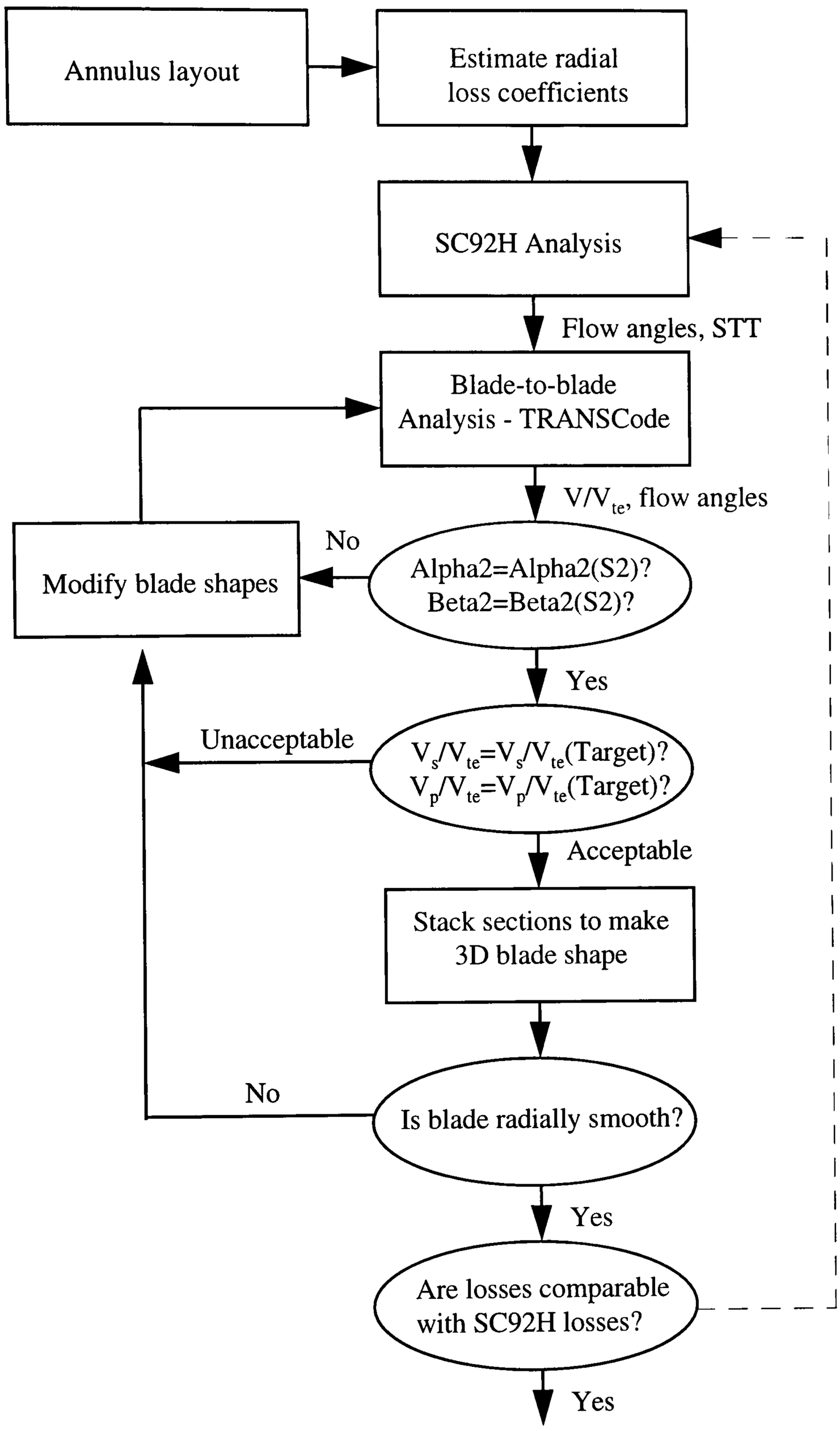


Figure 4.8 Design flow diagram

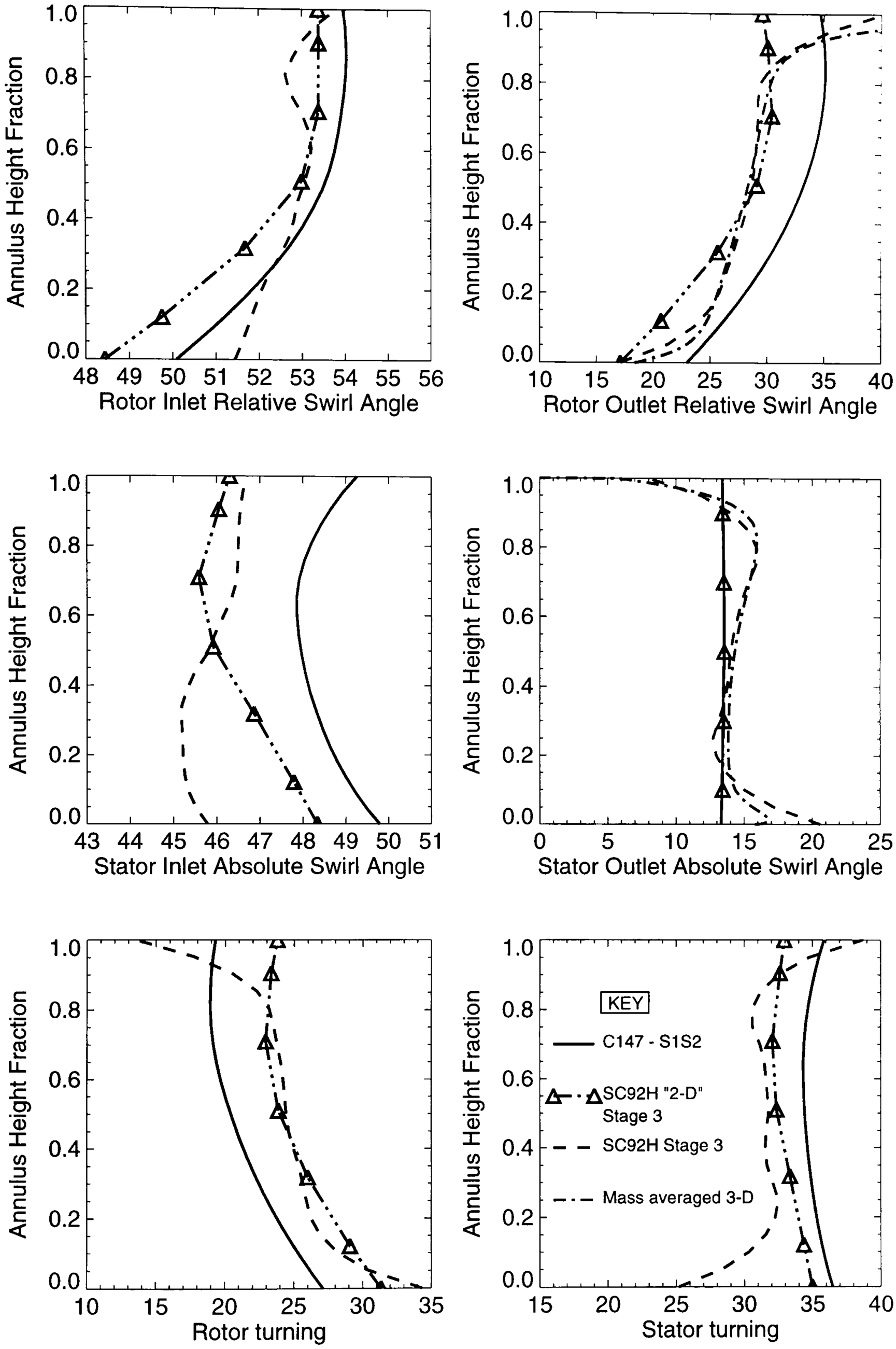


Figure 4.9 Throughflow calculation results

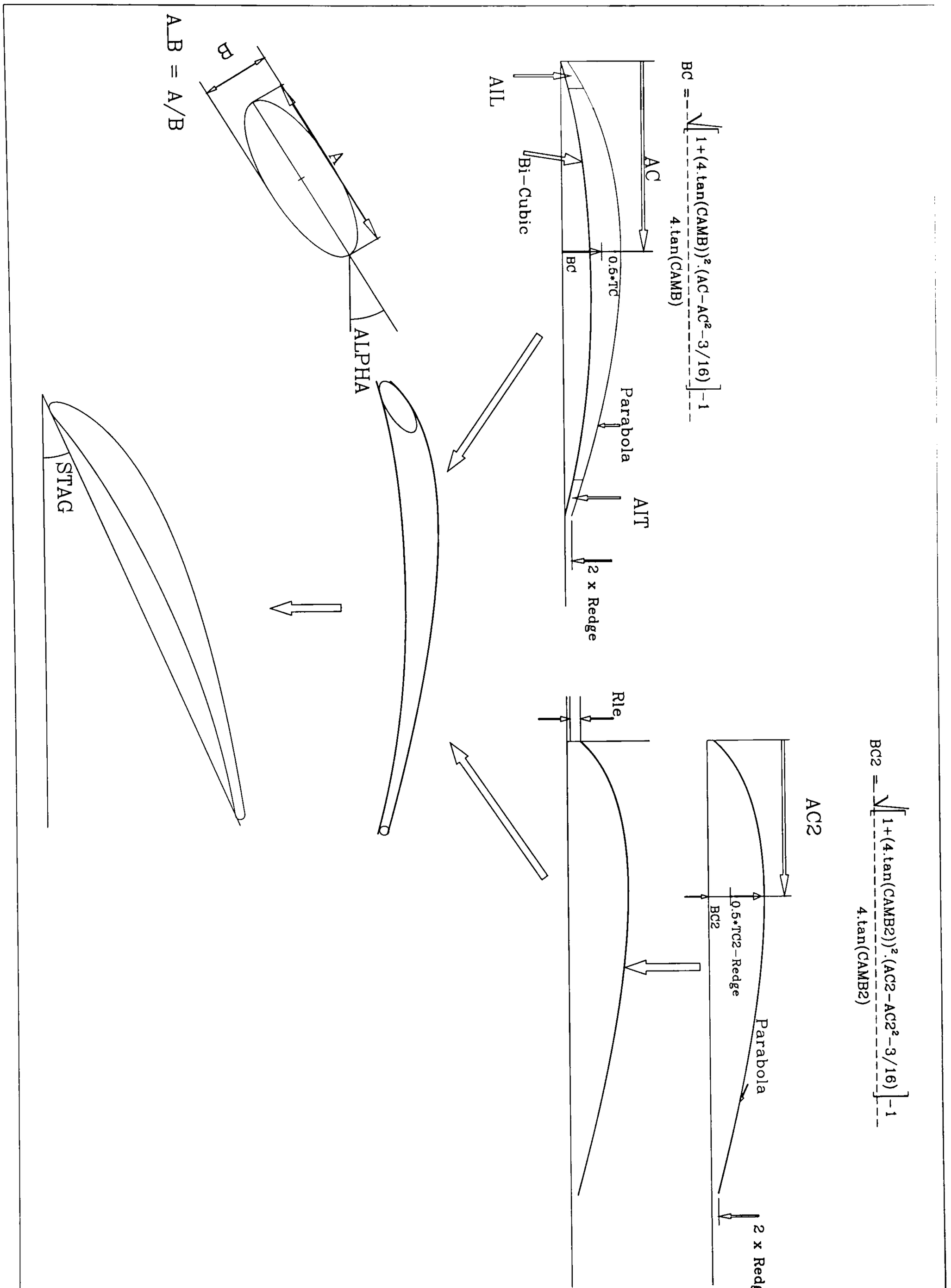


Figure 4.10 Blade profile generator

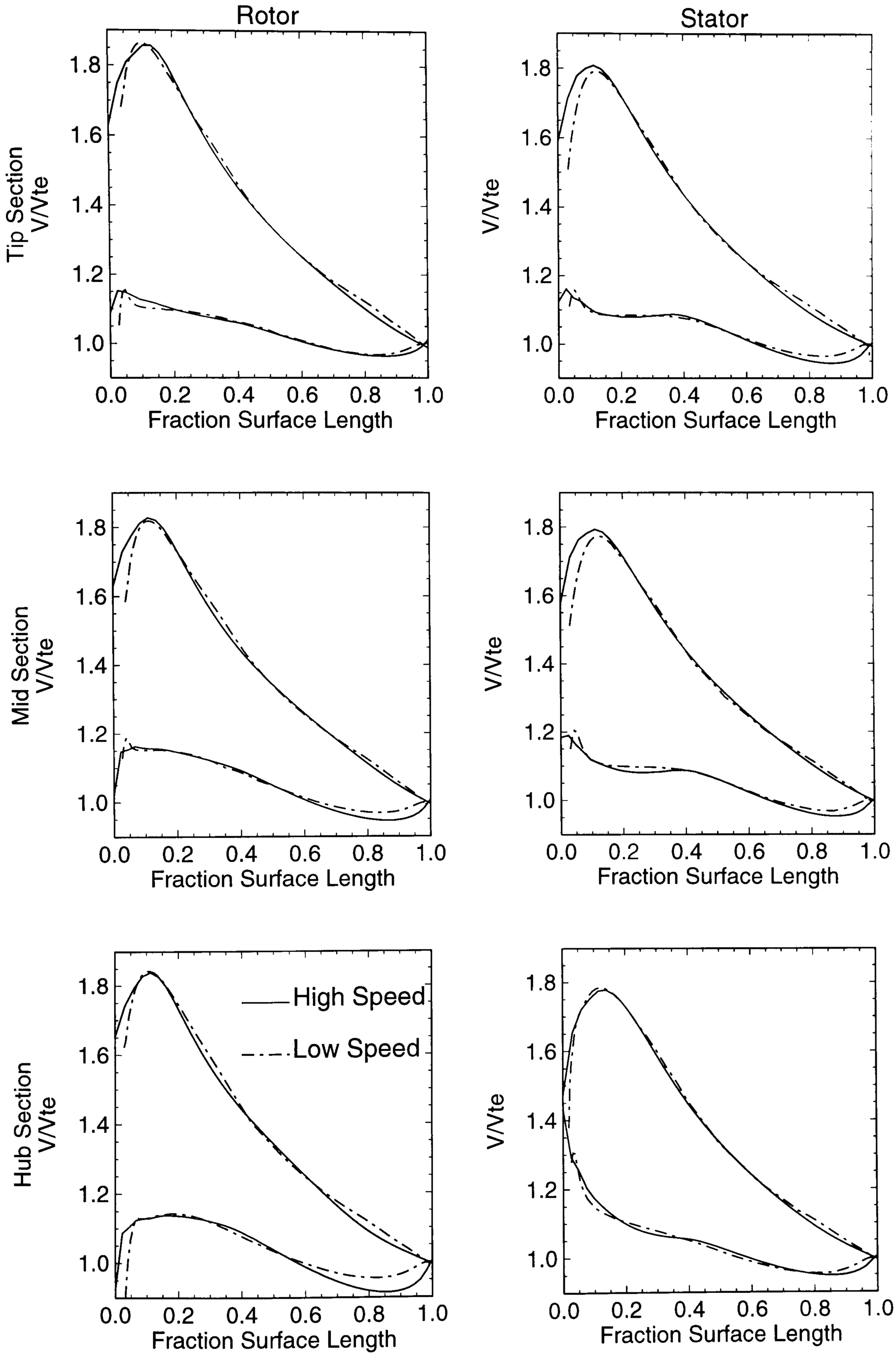


Figure 4.11 Rotor normalised velocity distributions

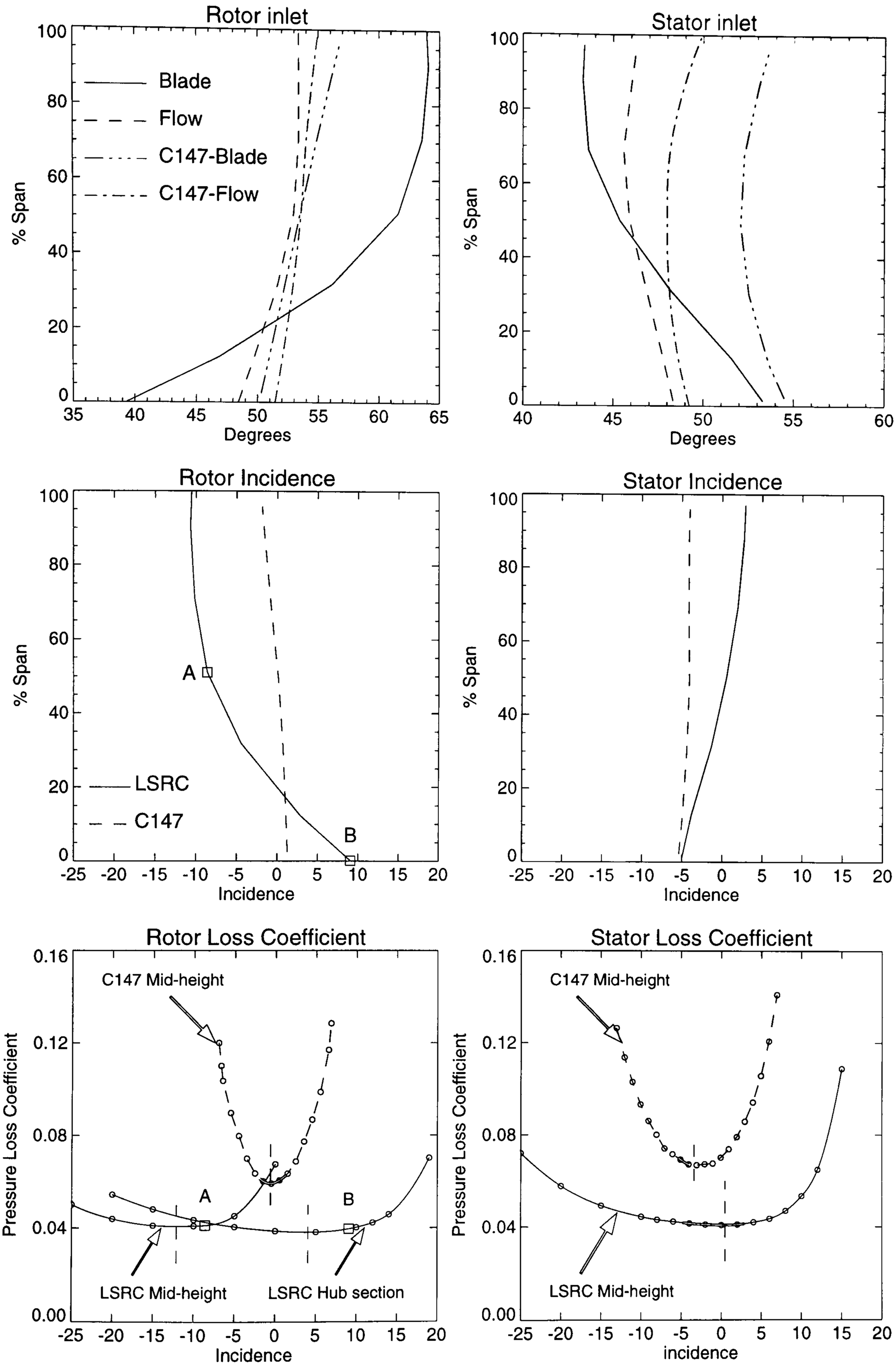


Figure 4.12 High and low speed incidence and loss

Figures

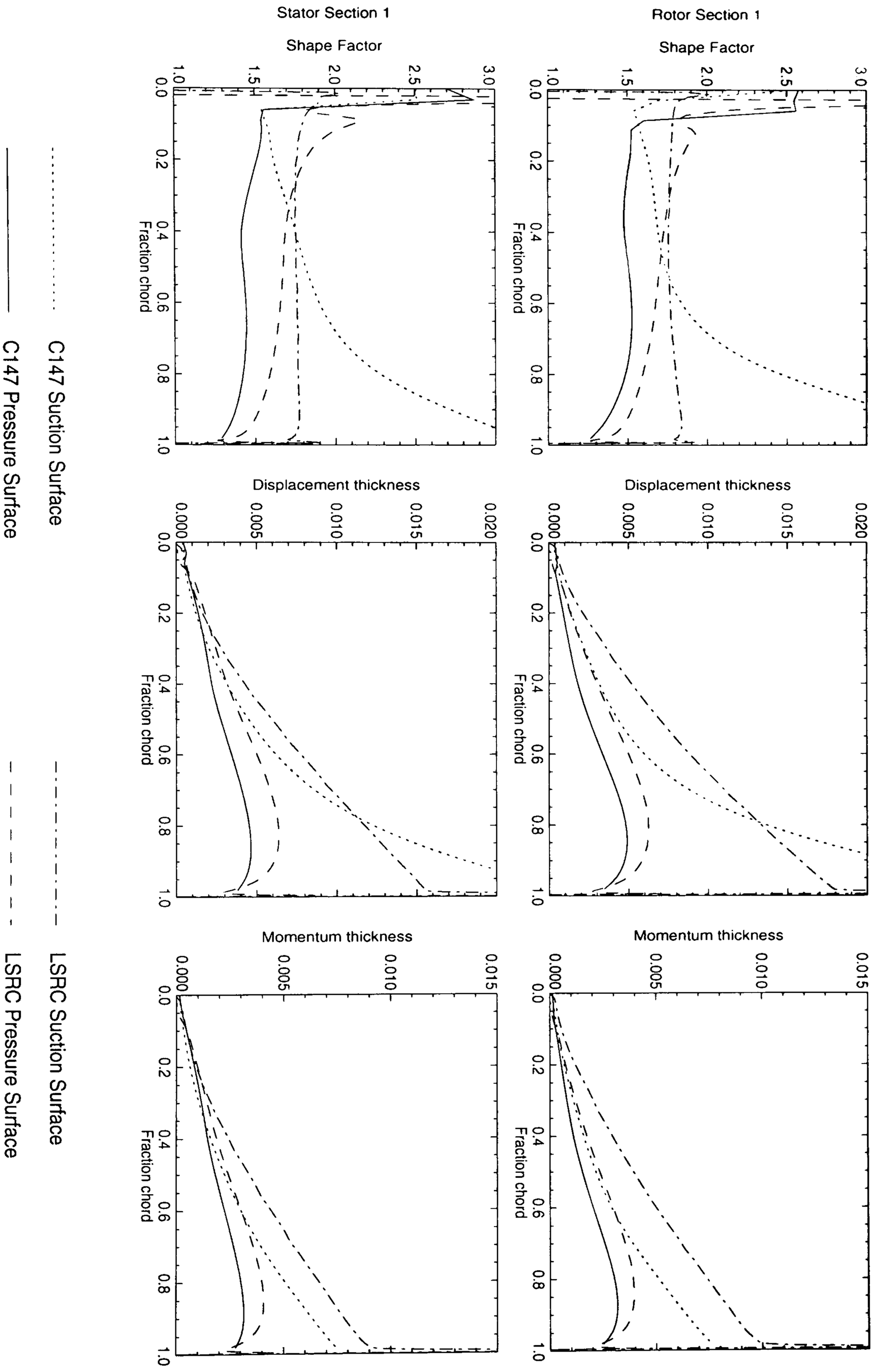


Figure 4.13 Boundary layer parameters

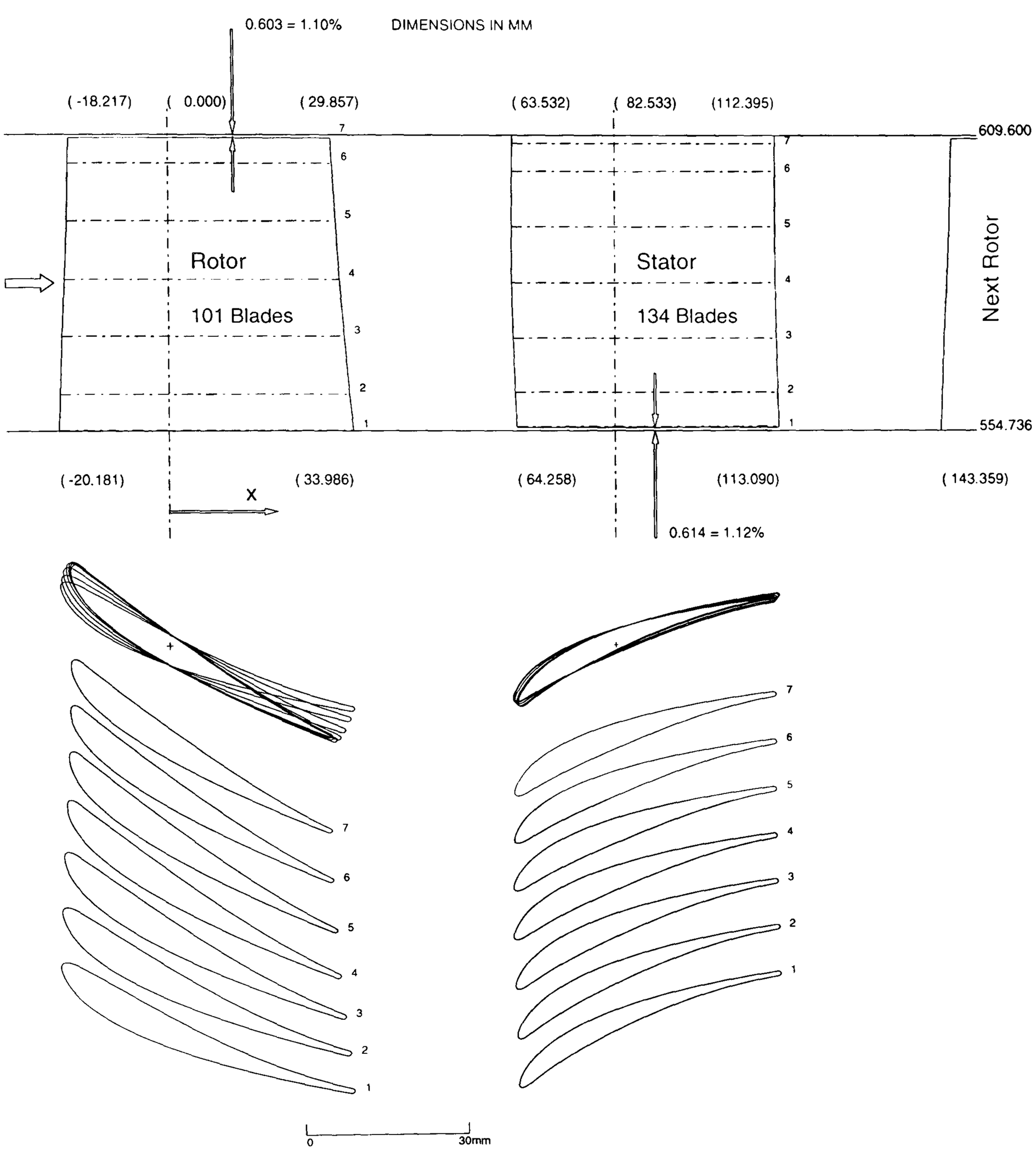


Figure 4.14 Final Geometry

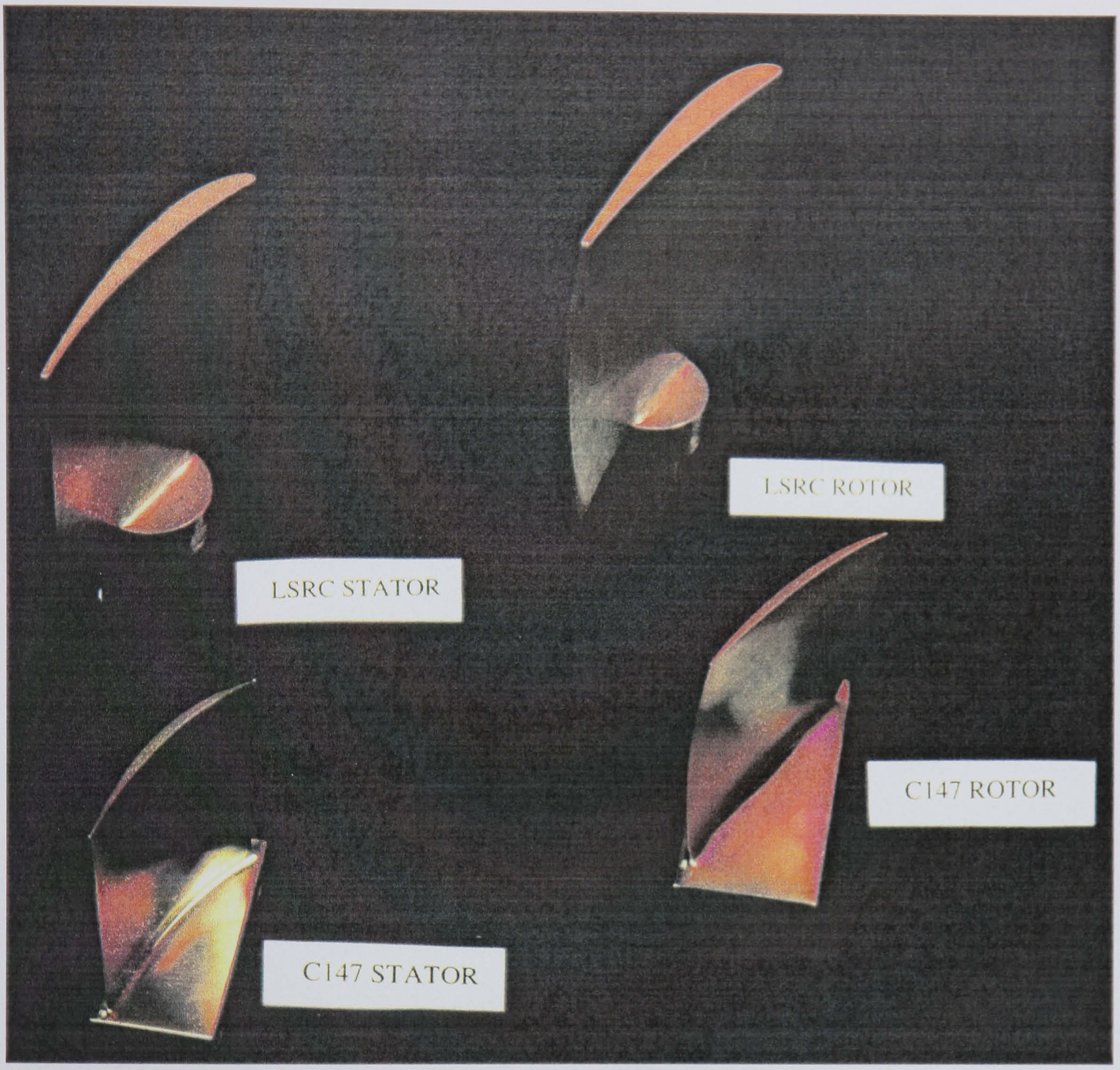


Figure 4.15 Photograph of LSRC and C147 blading

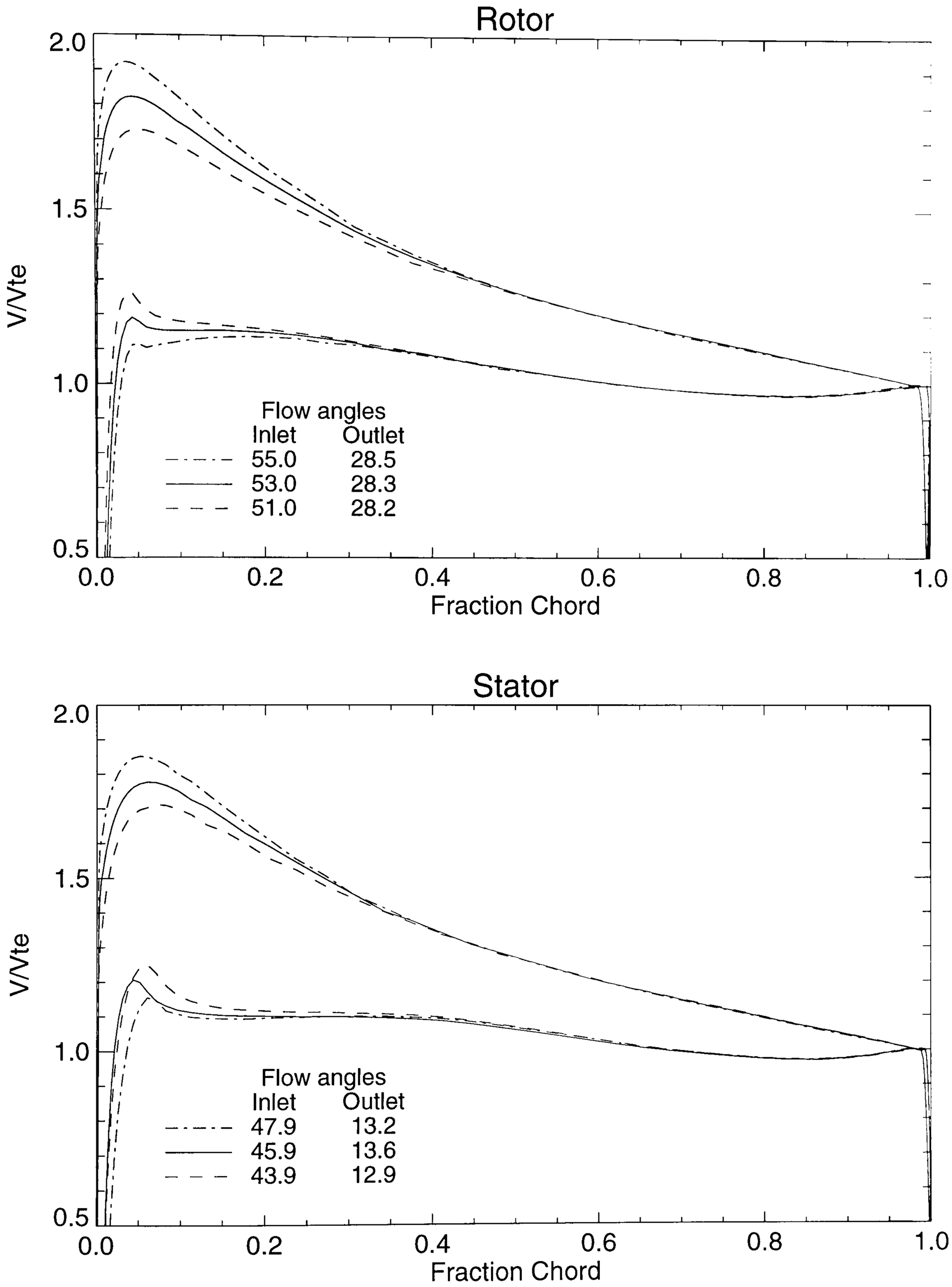
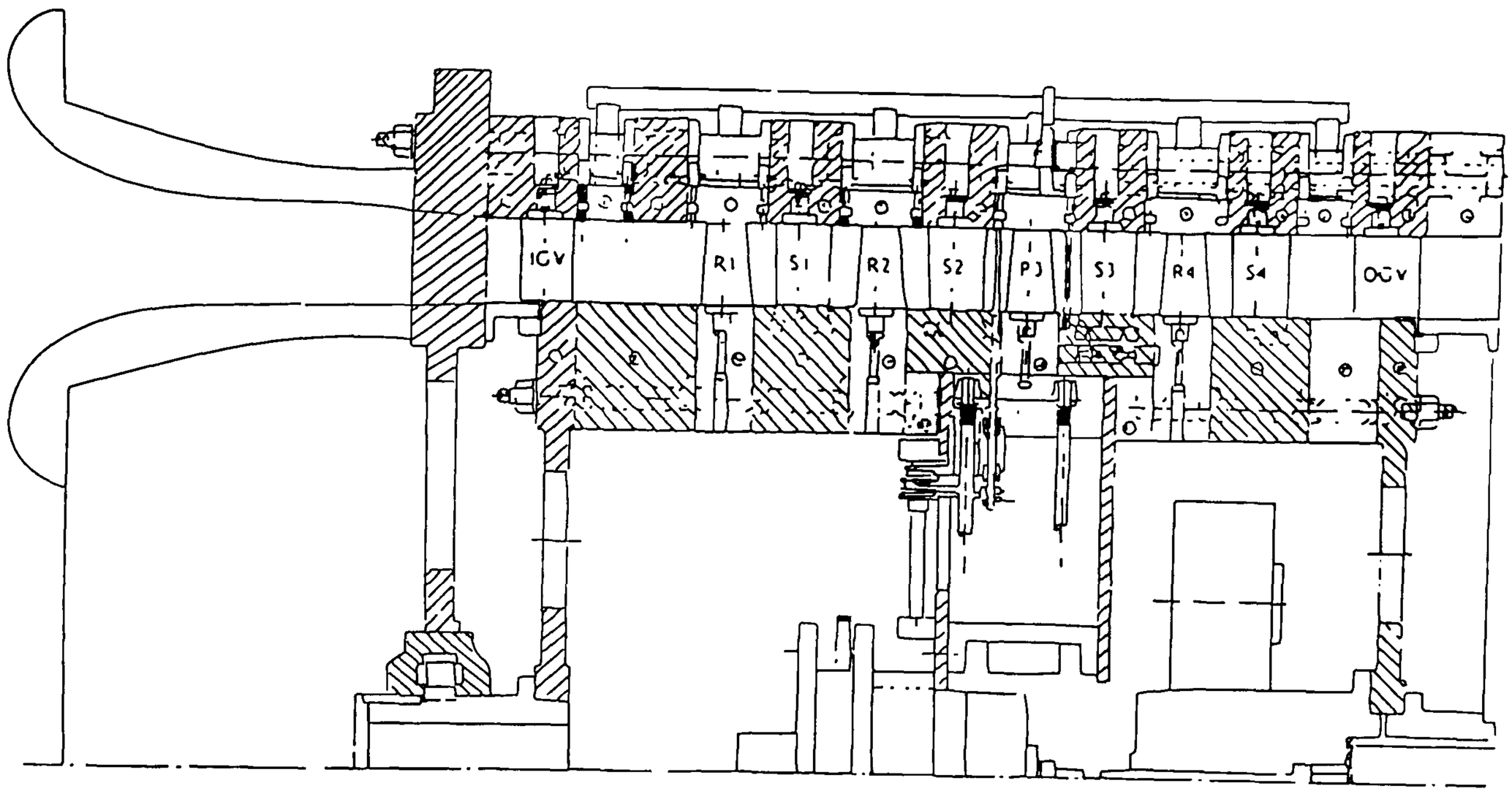
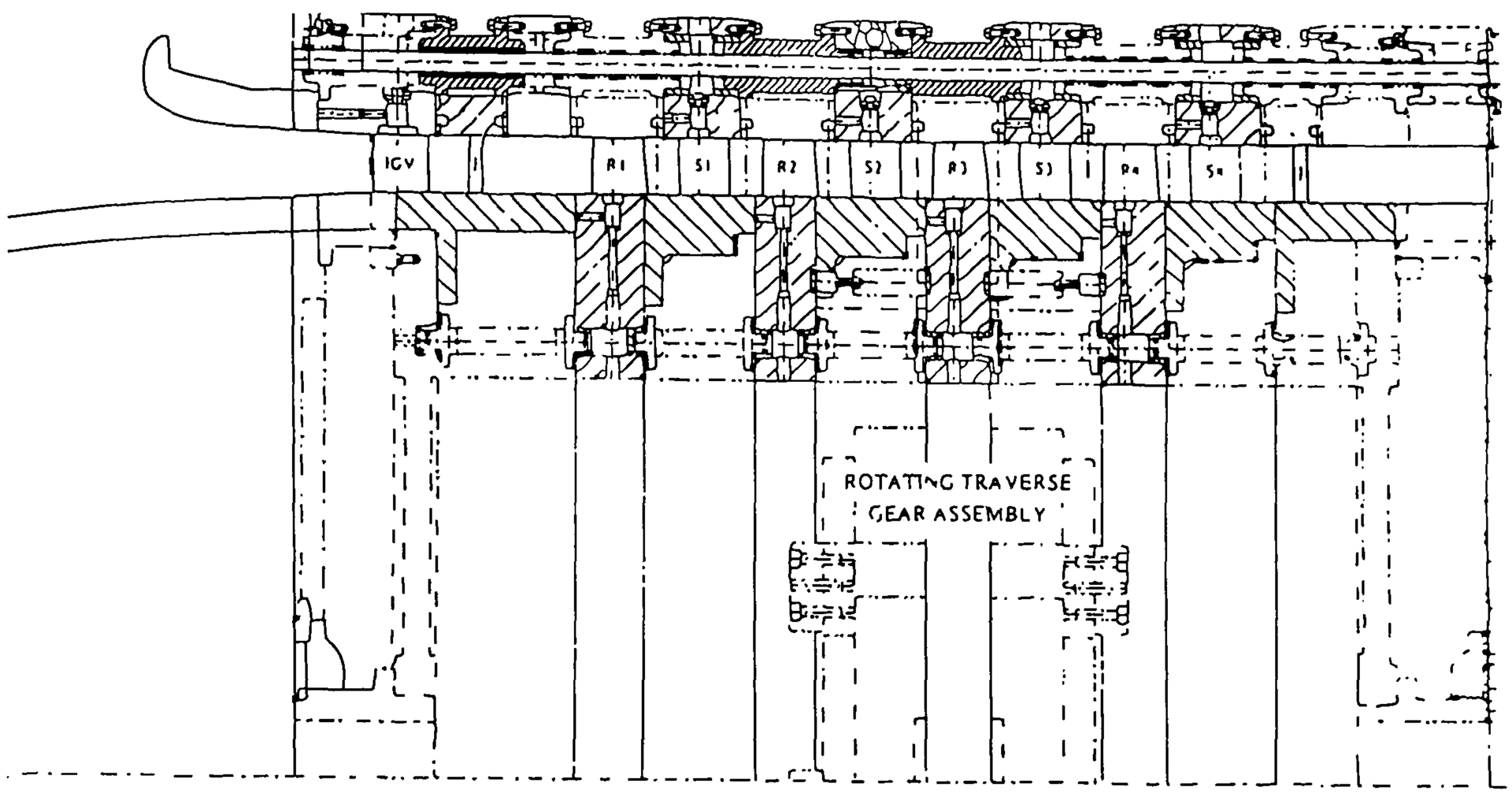


Figure 4.16 Effect of flow angle on velocity distribution



Original LSRC configuration (0.85 hub/tip ratio)



DERA LSRC configuration (0.91 hub/tip ratio)

Figure 5.1 Annulus layouts for original and DERA builds of LSRC

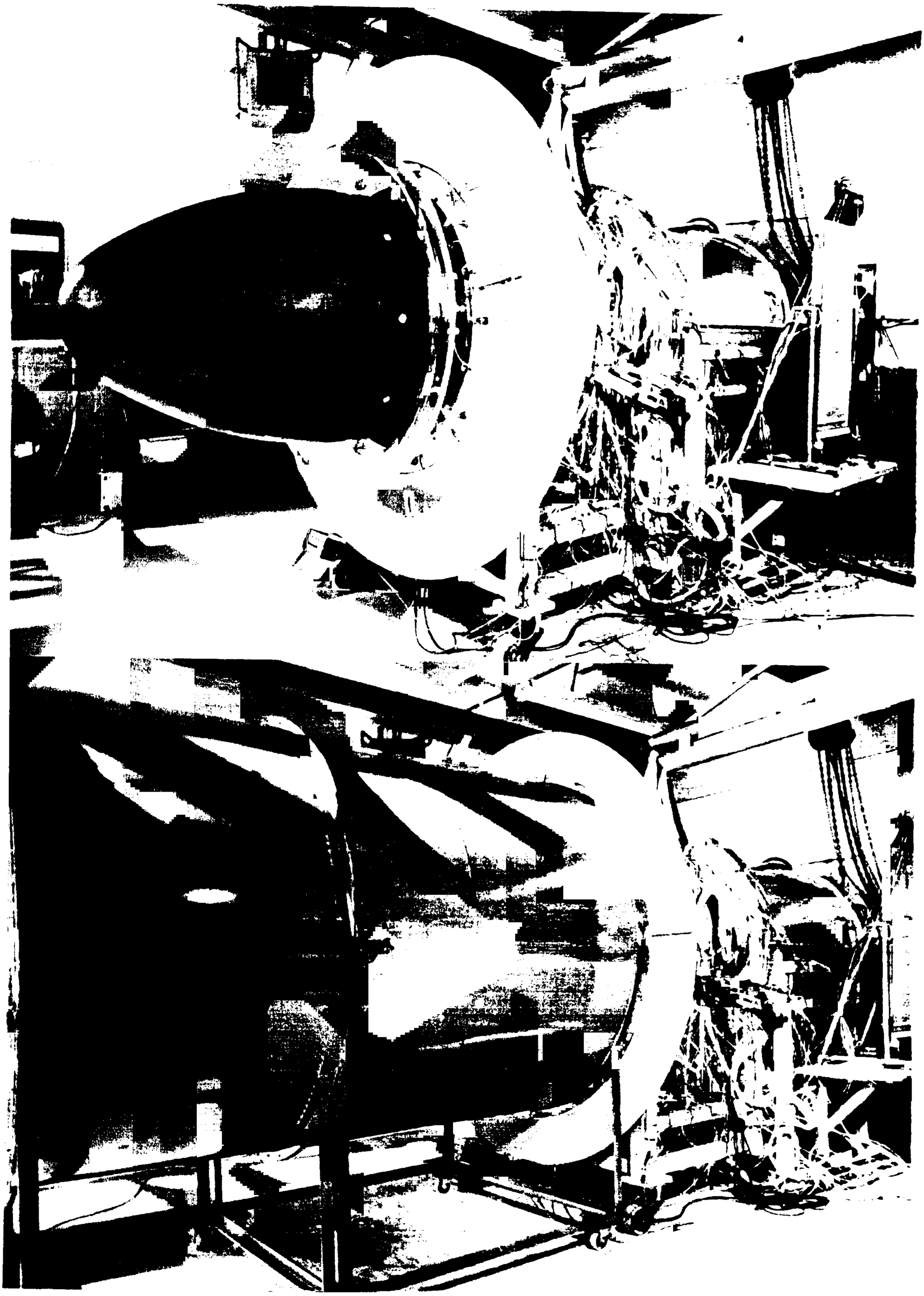


Figure 5.2 Photos showing inlet bullet, outer flare and inlet ducting arrangement

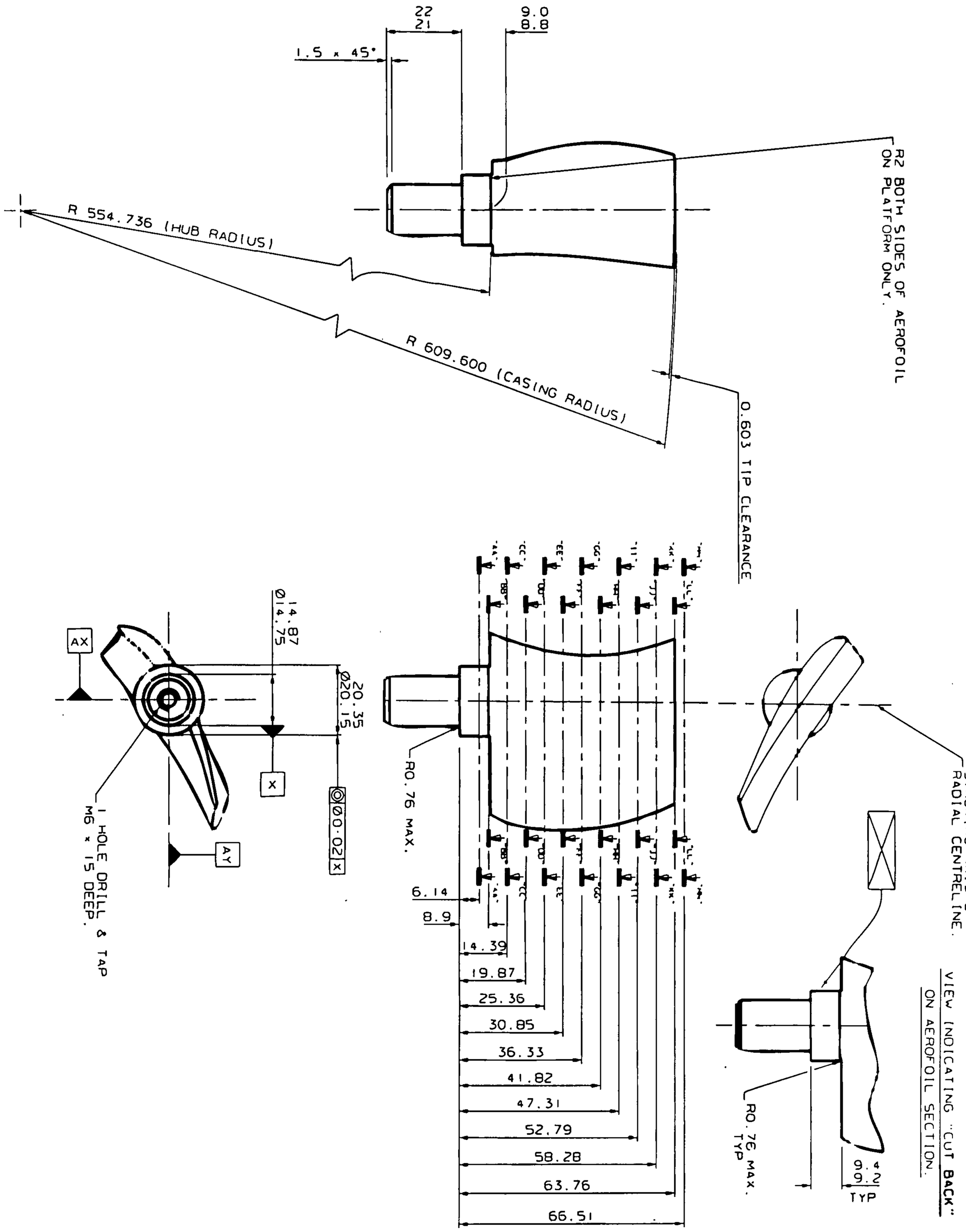


Figure 5.3 Engineering drawing of a DERA low speed blade showing spindle detail and sections defining the aerodynamic surfaces.



Figure 5.4 Photograph of instrumentation rake

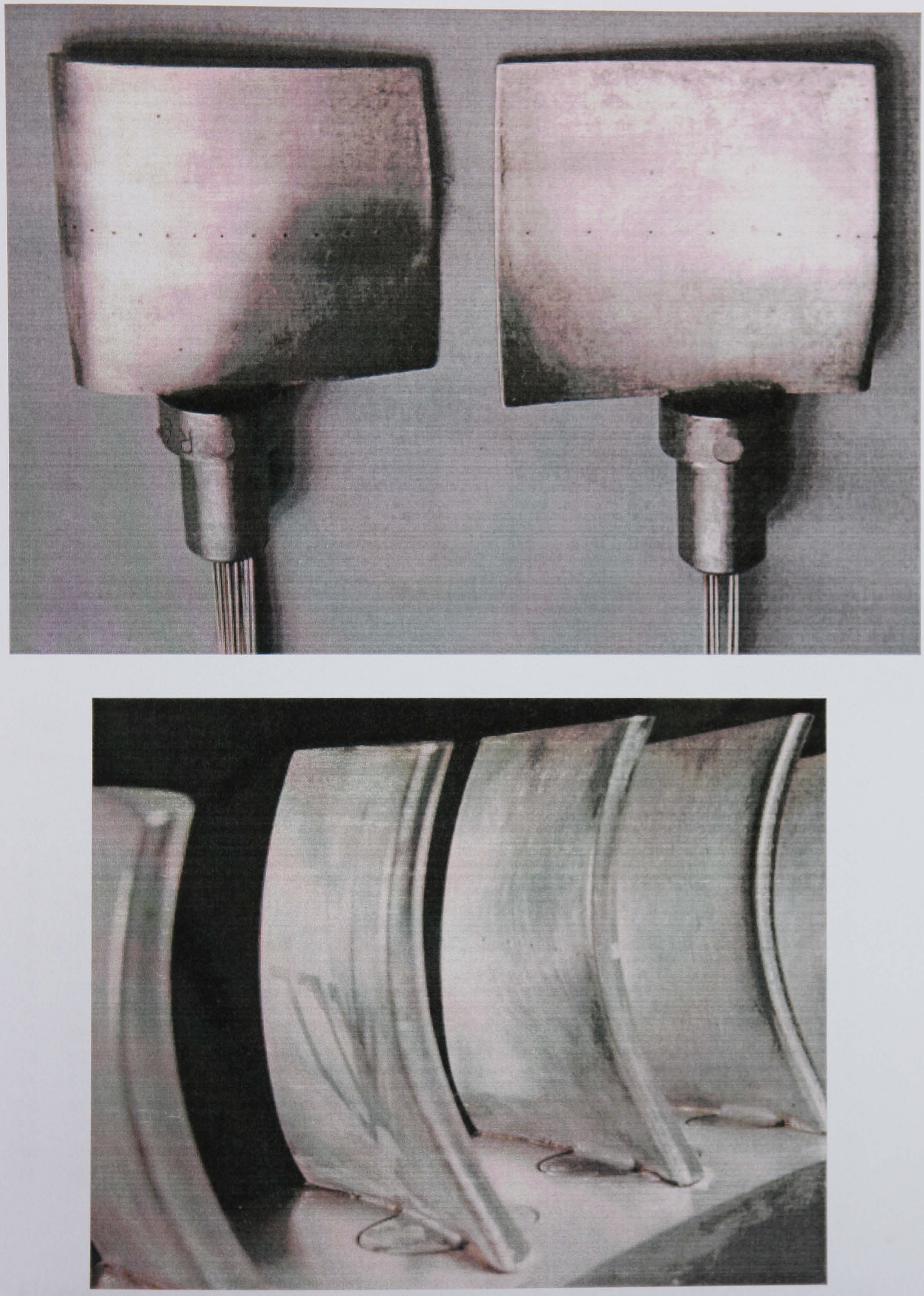
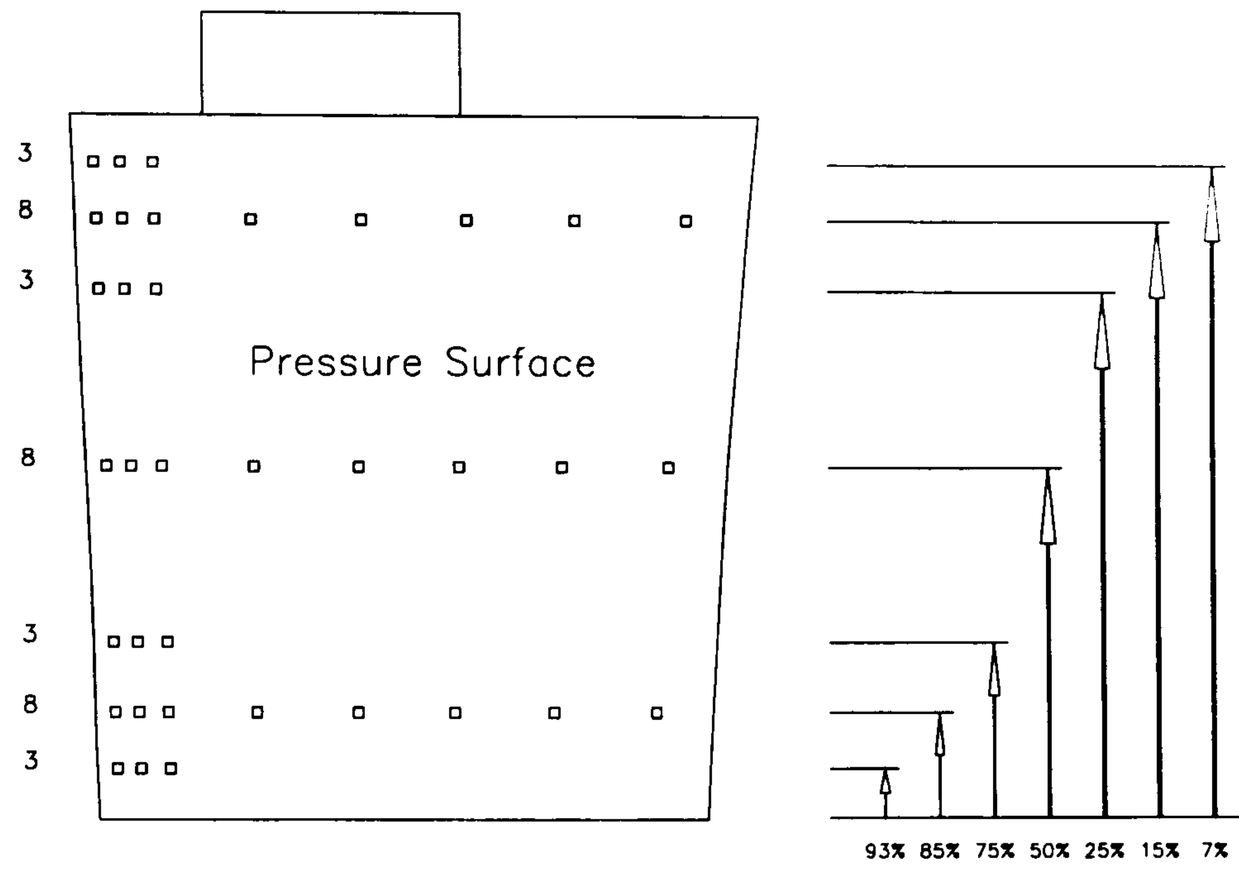


Figure 5.5 Photographs of instrumented blades

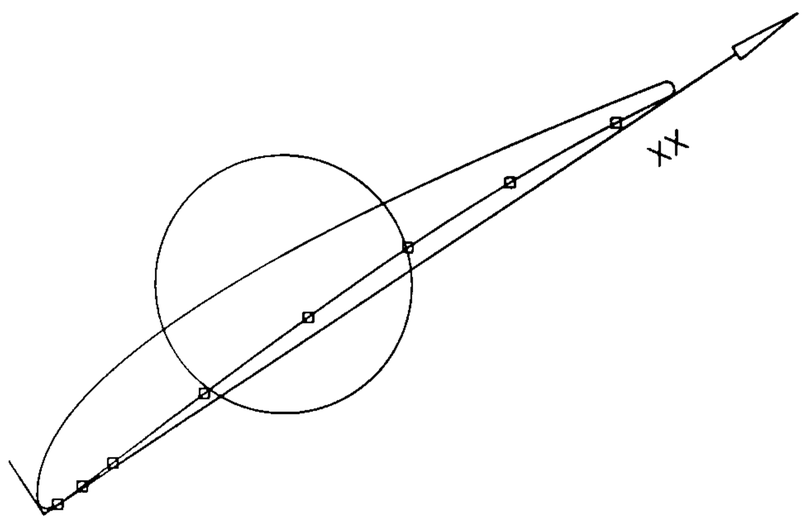
Rotating Frame

Rotor Instrumentation

Tap	%	XX(Mid)#
1	2.0	1.20
2	6.0	3.60
3	11.0	6.60
4	26.0	15.60
5	43.0	25.80
6	59.0	35.40
7	75.0	45.00
8	91.0	54.60

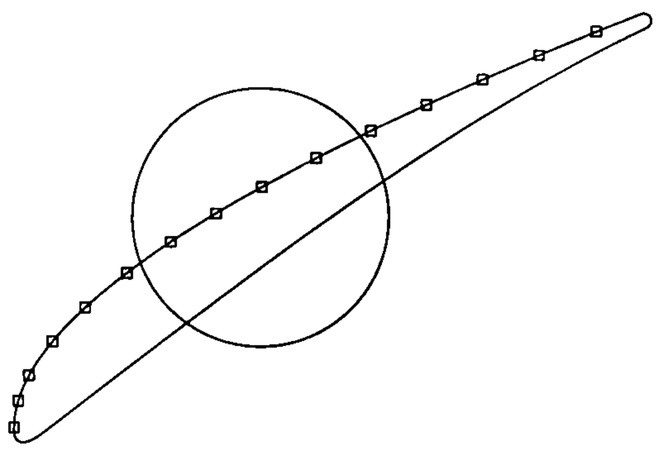


7% + 25% tappings with 15% blade
93% + 75% tappings with 85% blade



10 Instrumented Blades
141 Instrument Taps
18 Reference Taps
TOTAL = 159 Tappings

Mid–Height Section



Pressure surface blades paired with suction surface blade for common reference taps and blade passage.

50% ss paired with 50% ps
15% ss paired with 15% ps
85% ss paired with 85% ps

Use % true chord values for other sections

▣ Reference Taps

Tap	%	XX(Mid)#
1	0.7	0.42
2	3.0	1.80
3	6.0	3.60
4	11.0	6.60
5	17.0	10.20
6	24.0	14.40
7	31.0	18.60
8	38.0	22.80
9	45.0	27.00
10	53.0	31.80
11	61.0	36.60
12	69.0	41.40
13	77.0	46.20
14	85.0	51.00
15	93.0	55.80

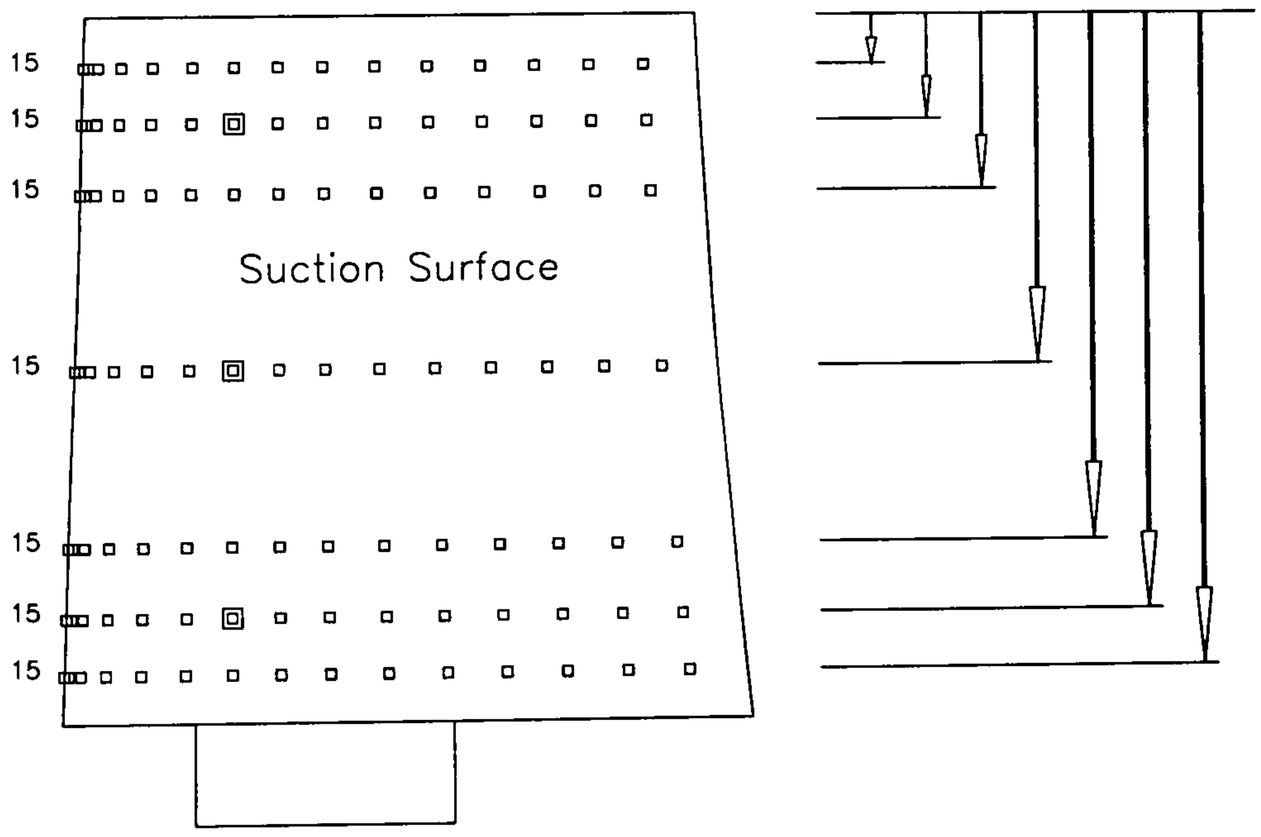


Figure 5.6 Blade surface static pressure instrumentation scheme for rotor blades



Figure 5.7 Photograph of 3D and 2D cobra probes

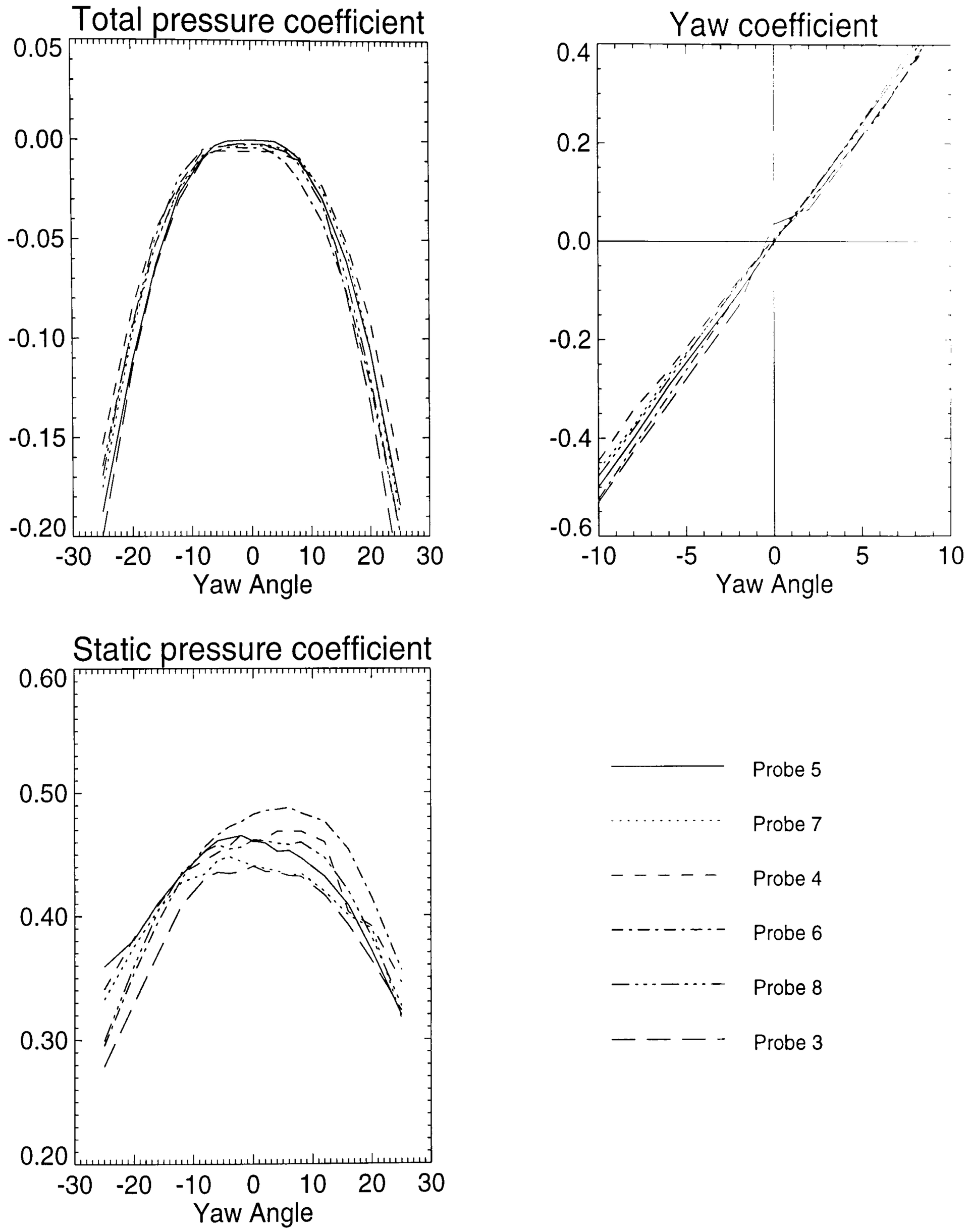


Figure 5.8 Calibration coefficients for 2D cobra probes

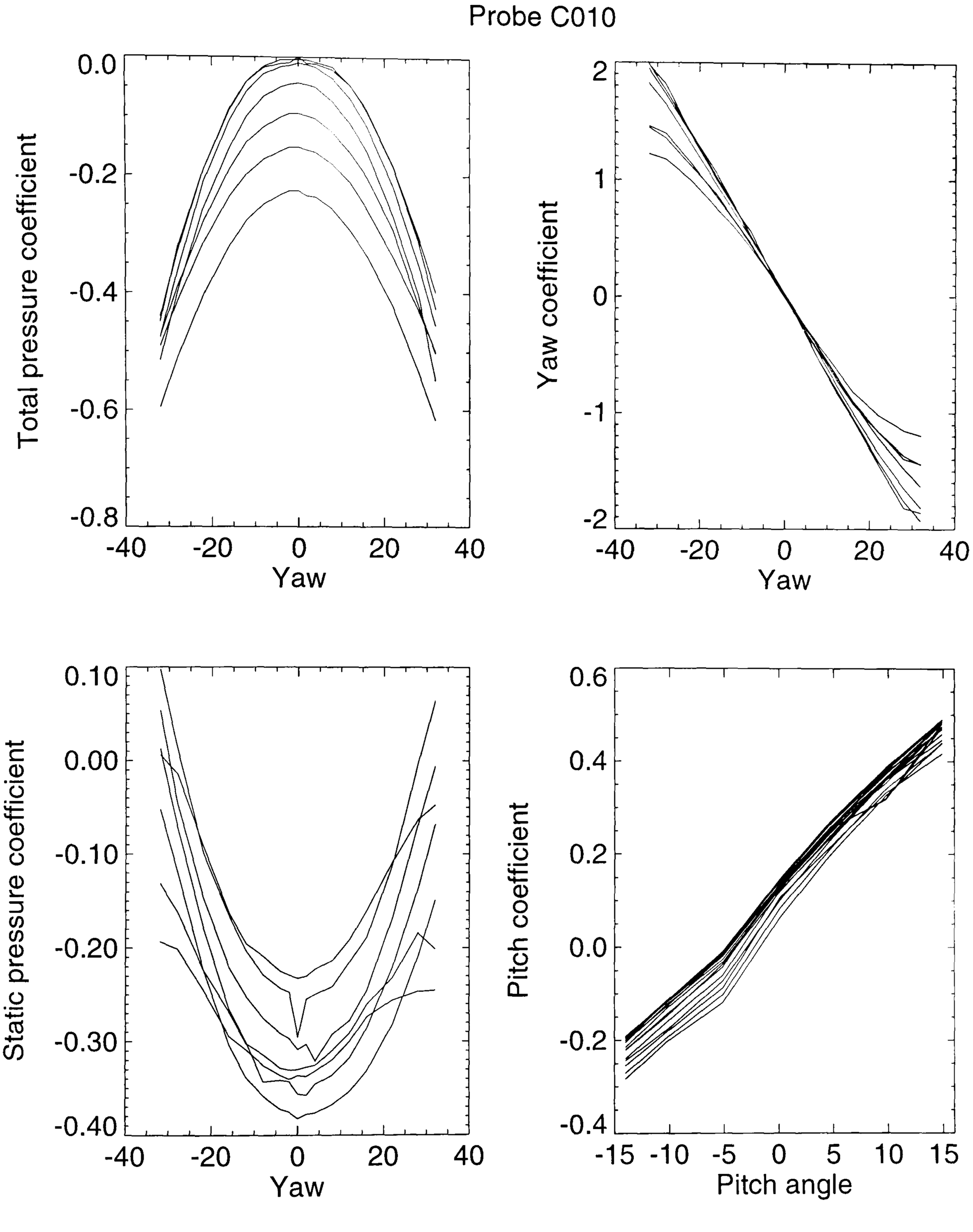


Figure 5.9 Calibration coefficients for 3D cobra probe C010

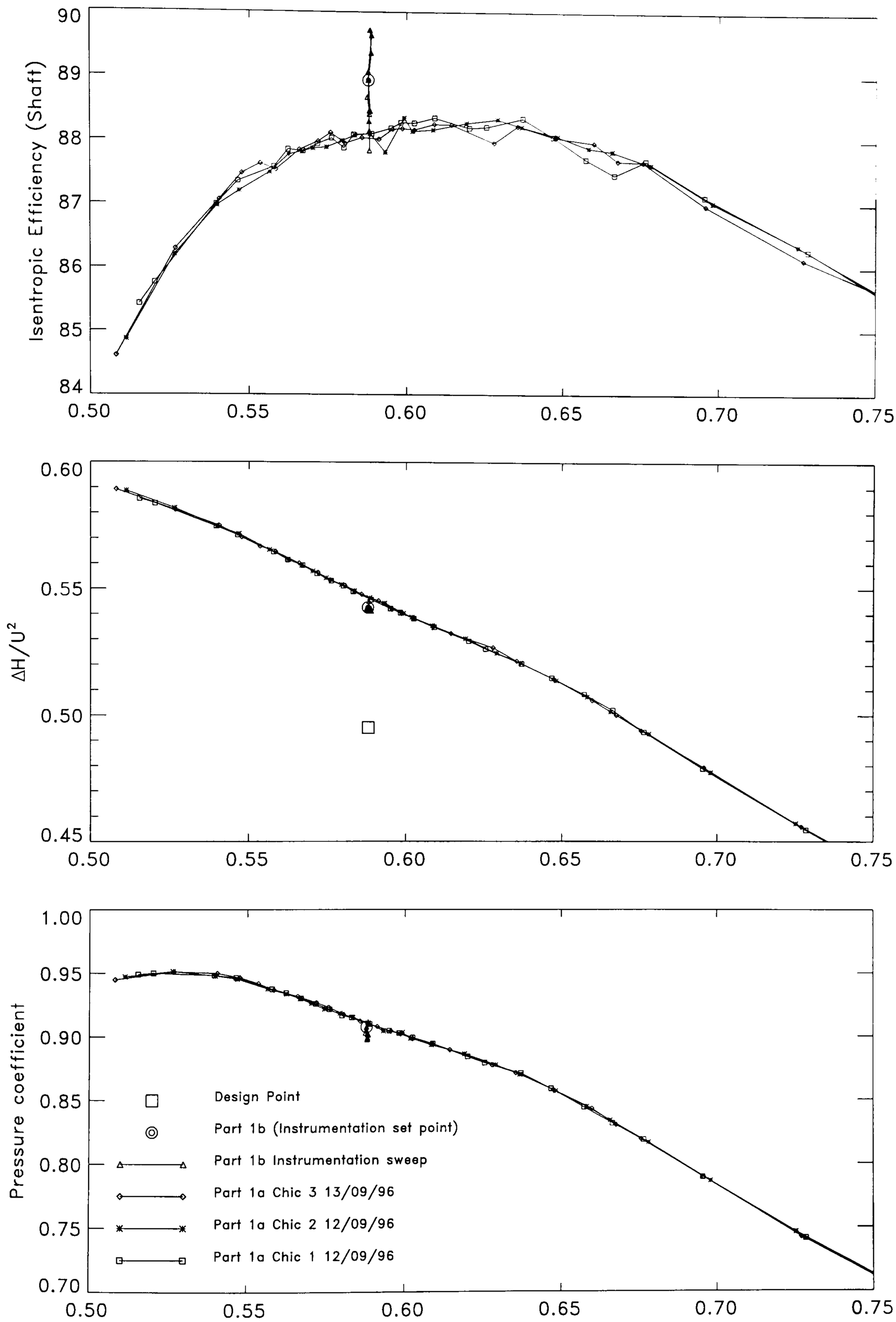


Figure 6.1 Datum build characteristic

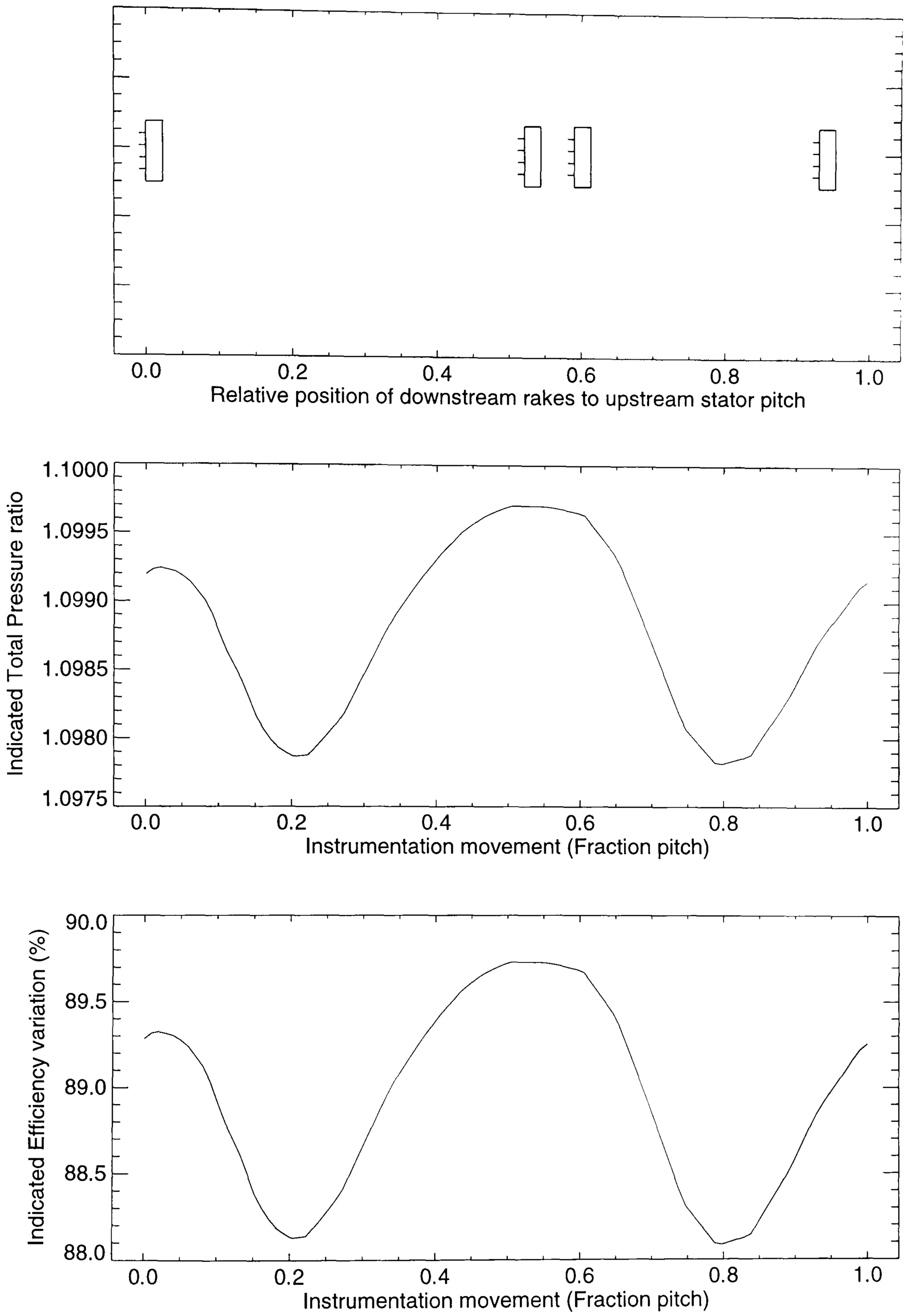


Figure 6.2 Results of analysis of performance variation by sampling stator 4 traverse data at exit rake relative positions

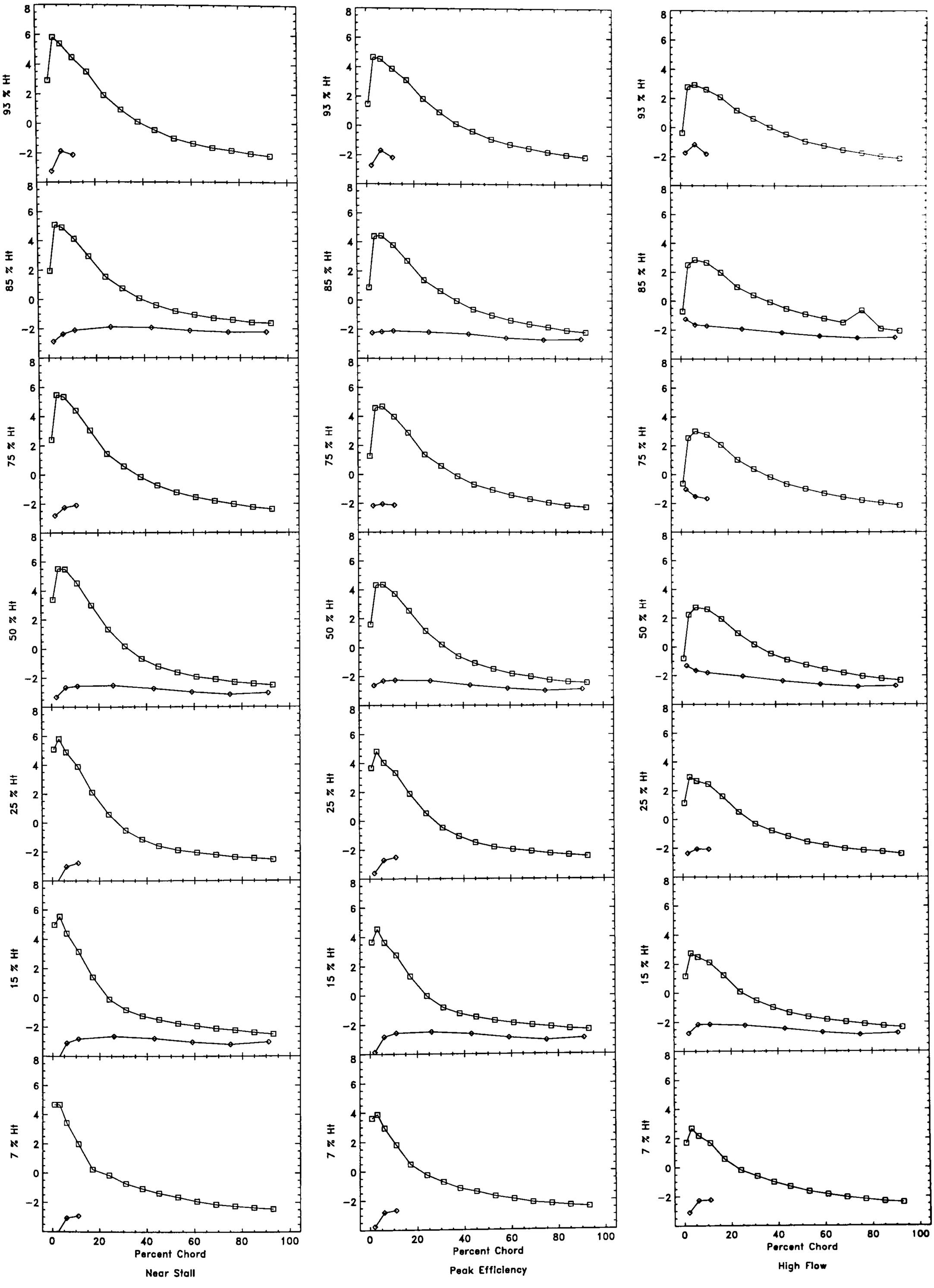


Figure 6.3 Datum rotor surface static pressure coefficient distributions

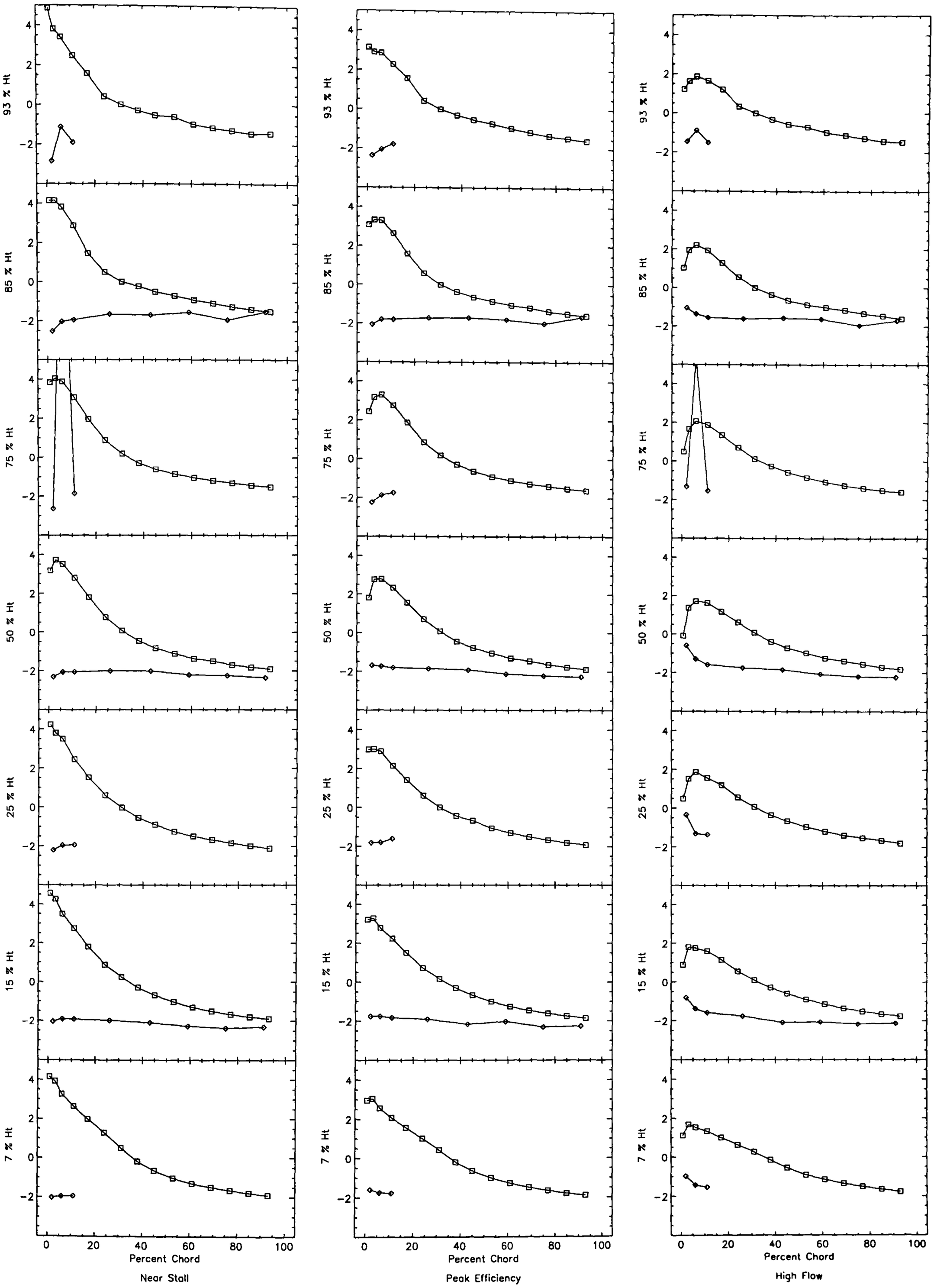


Figure 6.4 Datum stator surface static pressure coefficient distributions

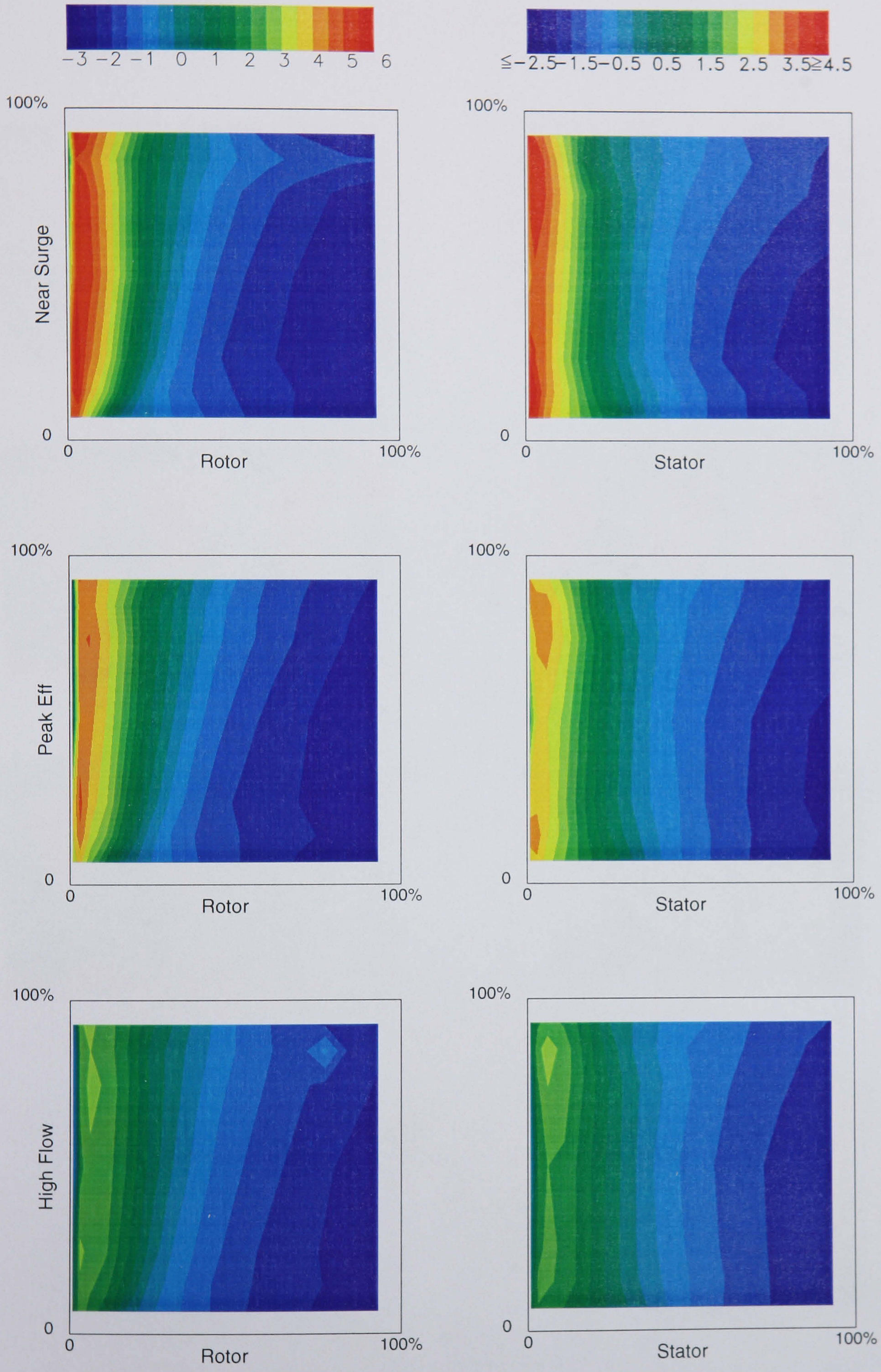


Figure 6.5 Suction surface pressure coefficient contours (datum)

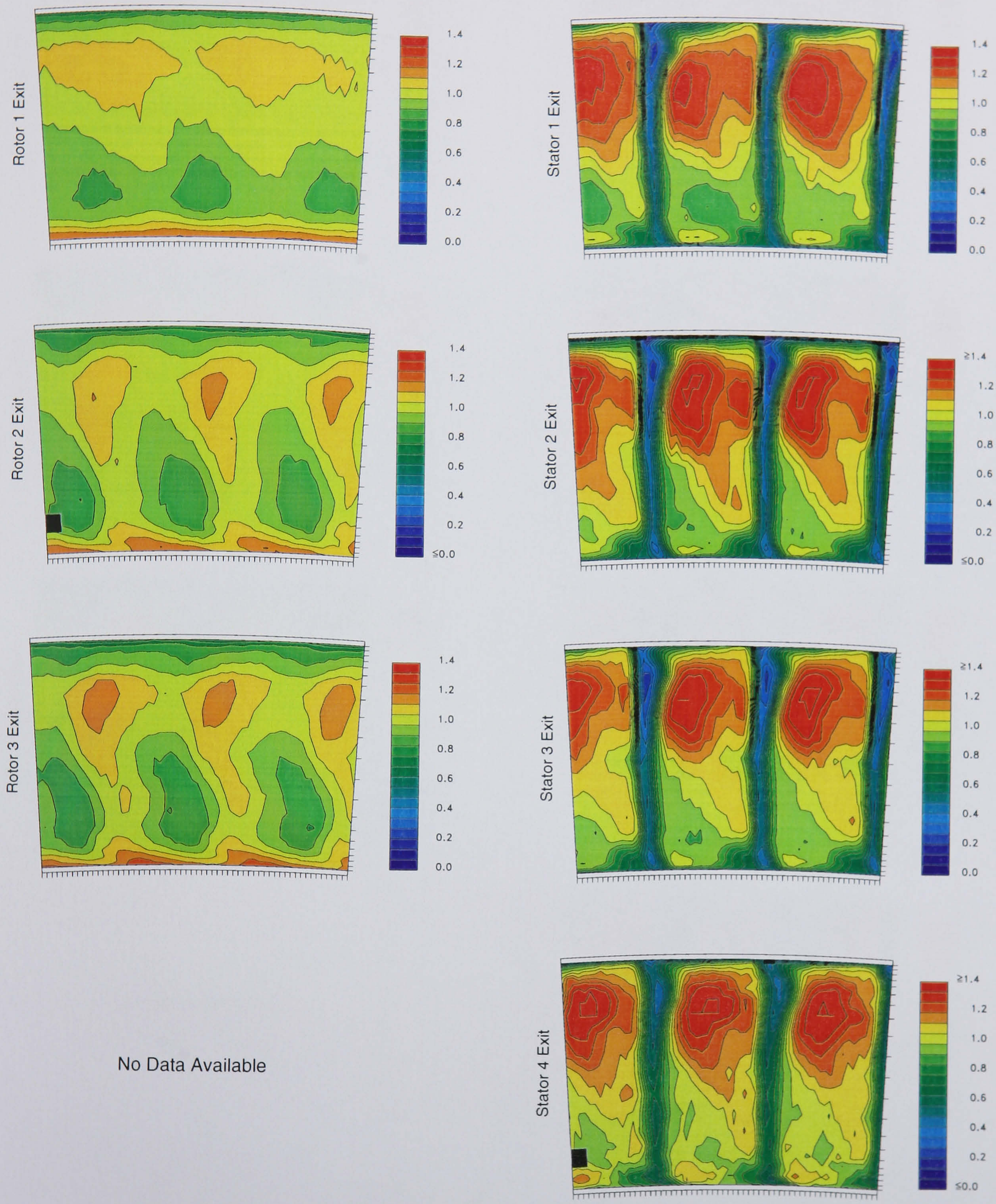


Figure 6.6 Total pressure coefficient contours at design flow (datum)

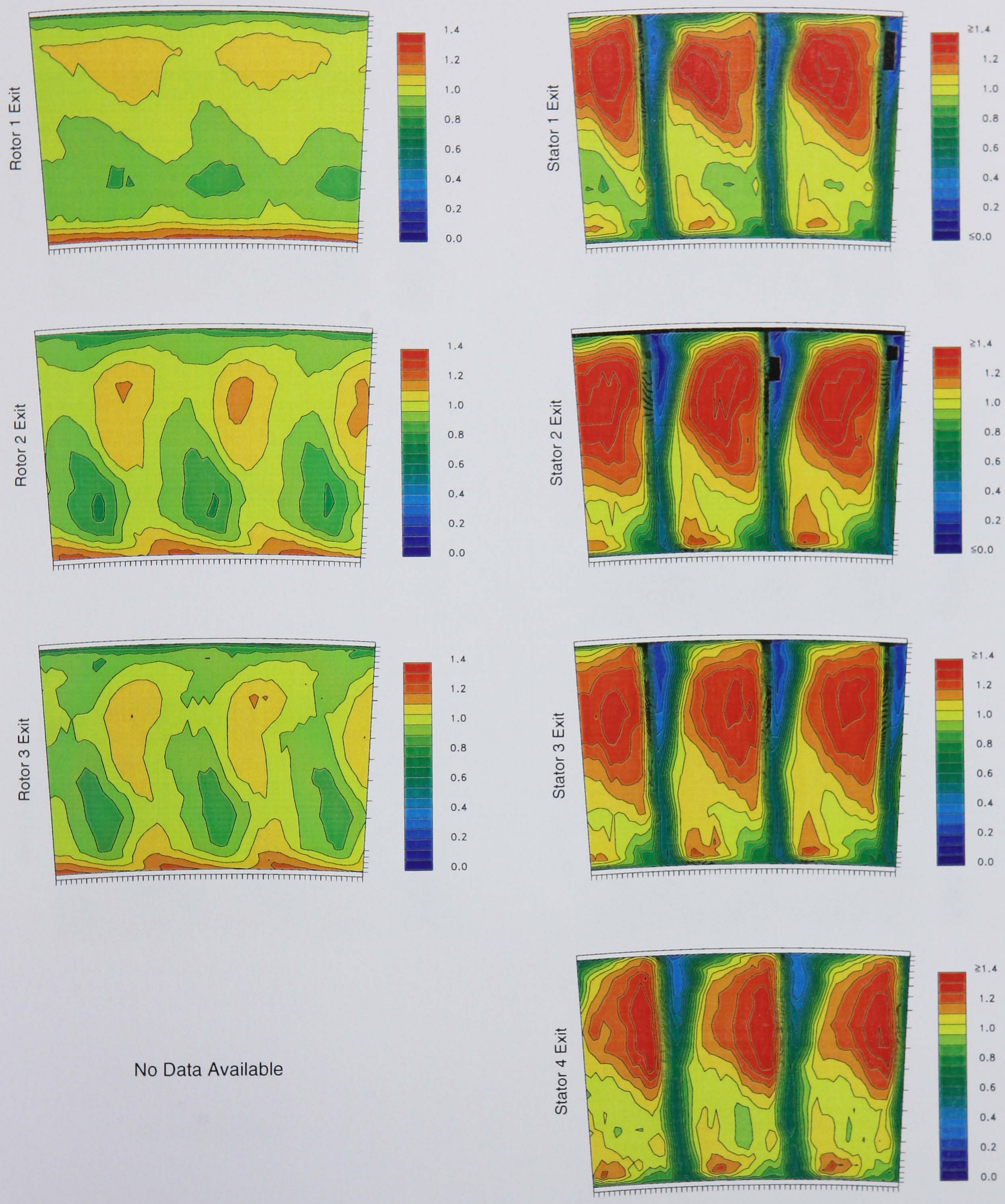
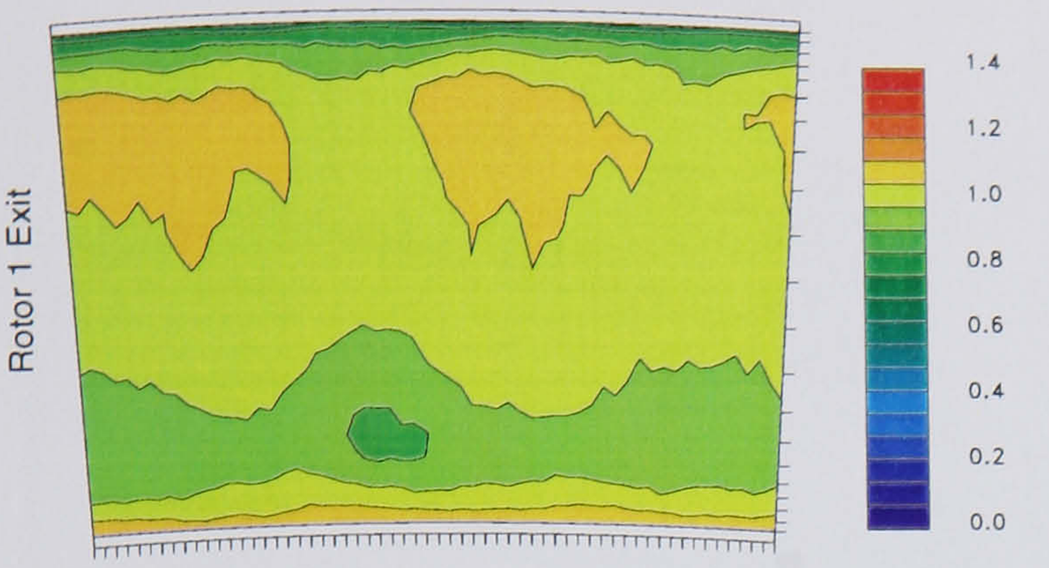
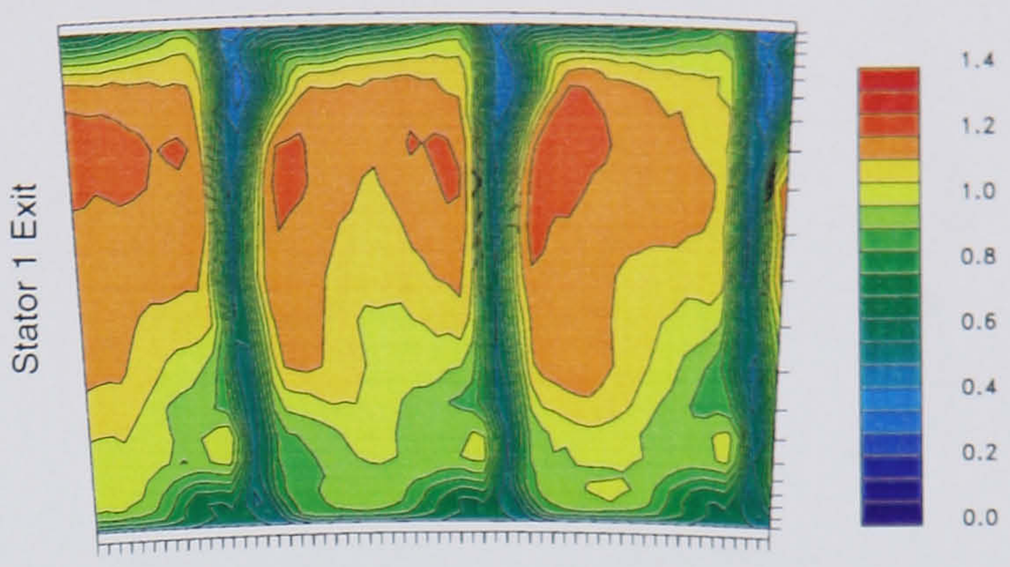
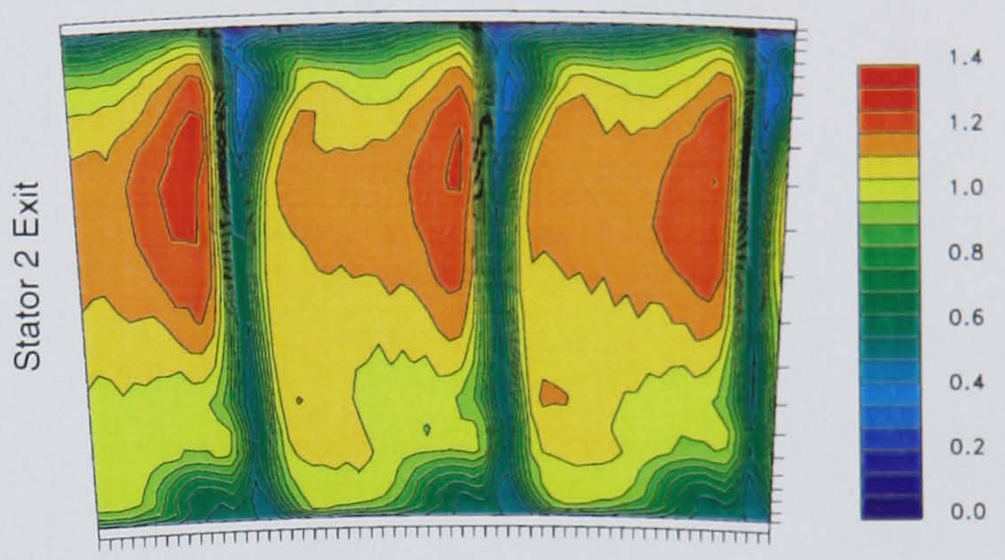


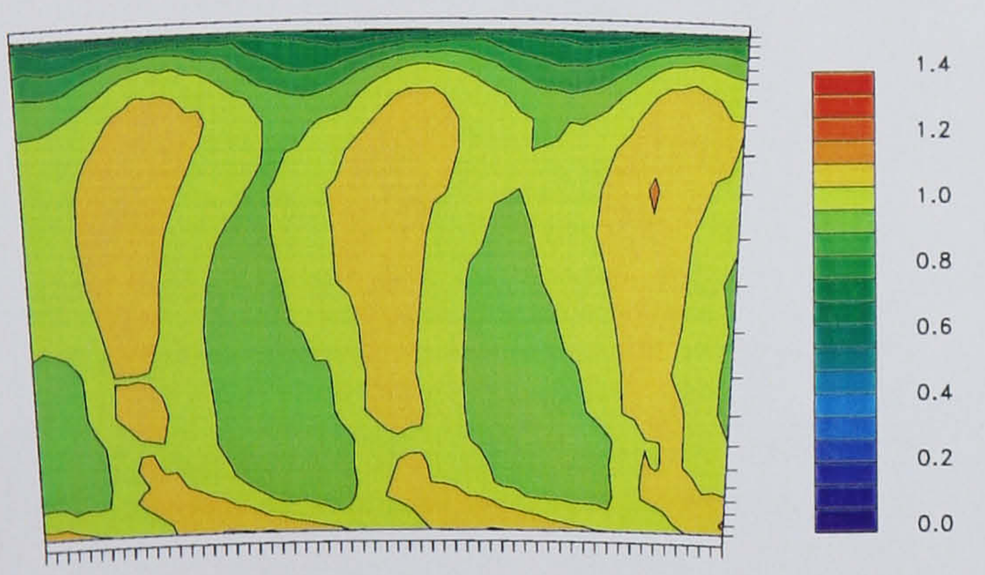
Figure 6.7 Total pressure coefficient contours at near stall (datum)

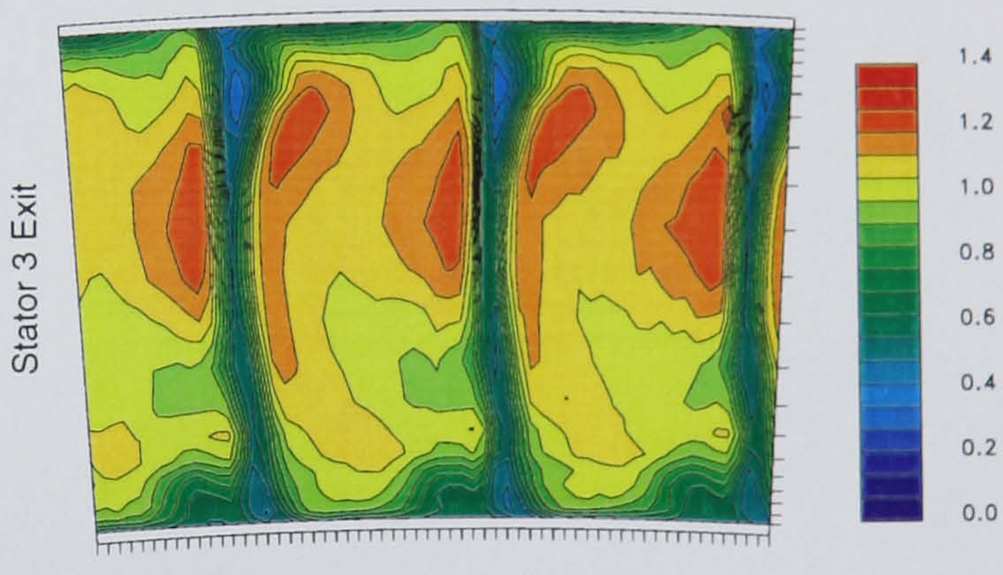




No Data Available







No Data Available

No Data Available

Figure 6.8 Total pressure coefficient contours at high flow (datum)

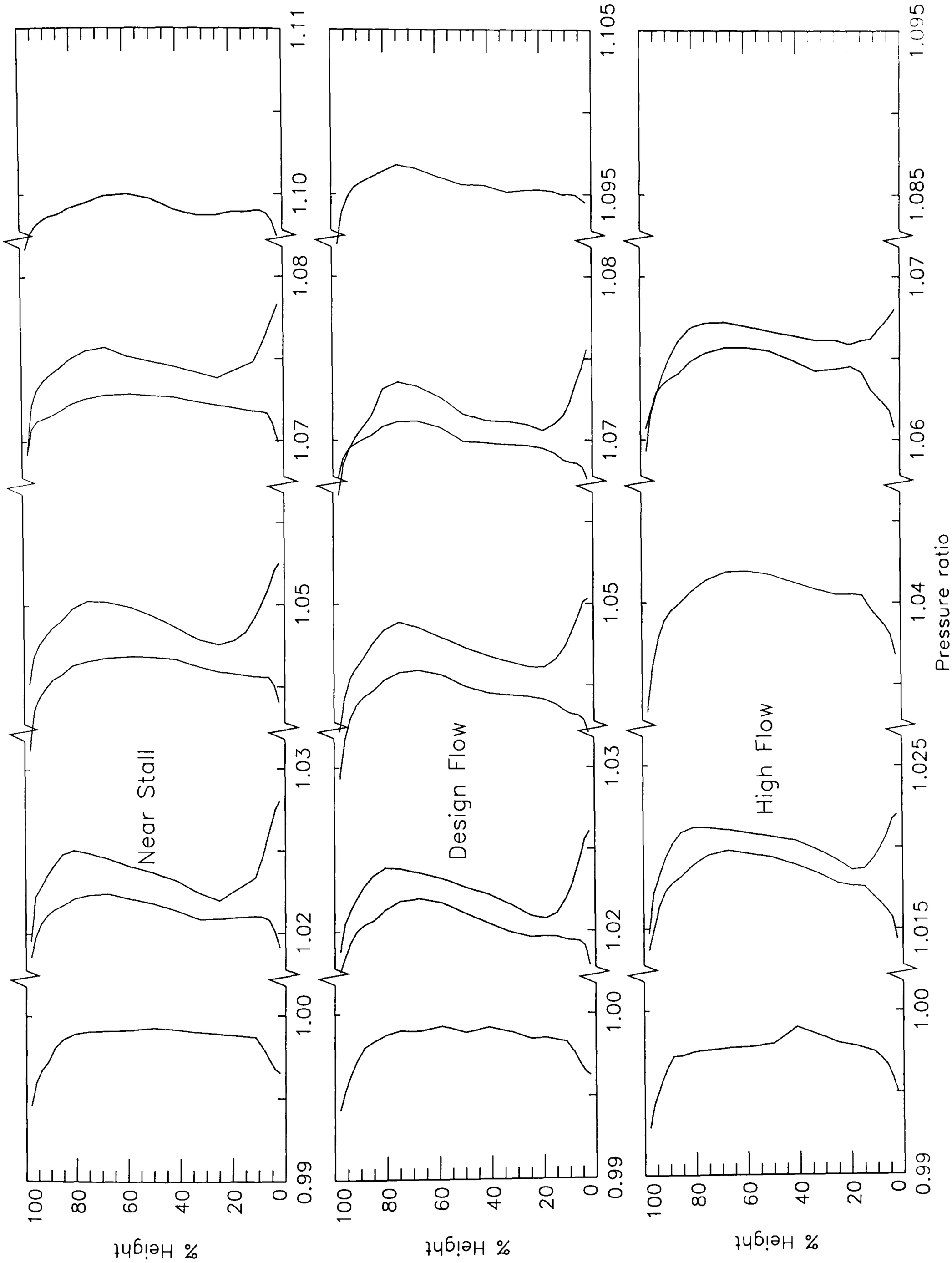


Figure 6.9 Radial profiles of pressure ratio at near stall, design flow and high flow (datum build)

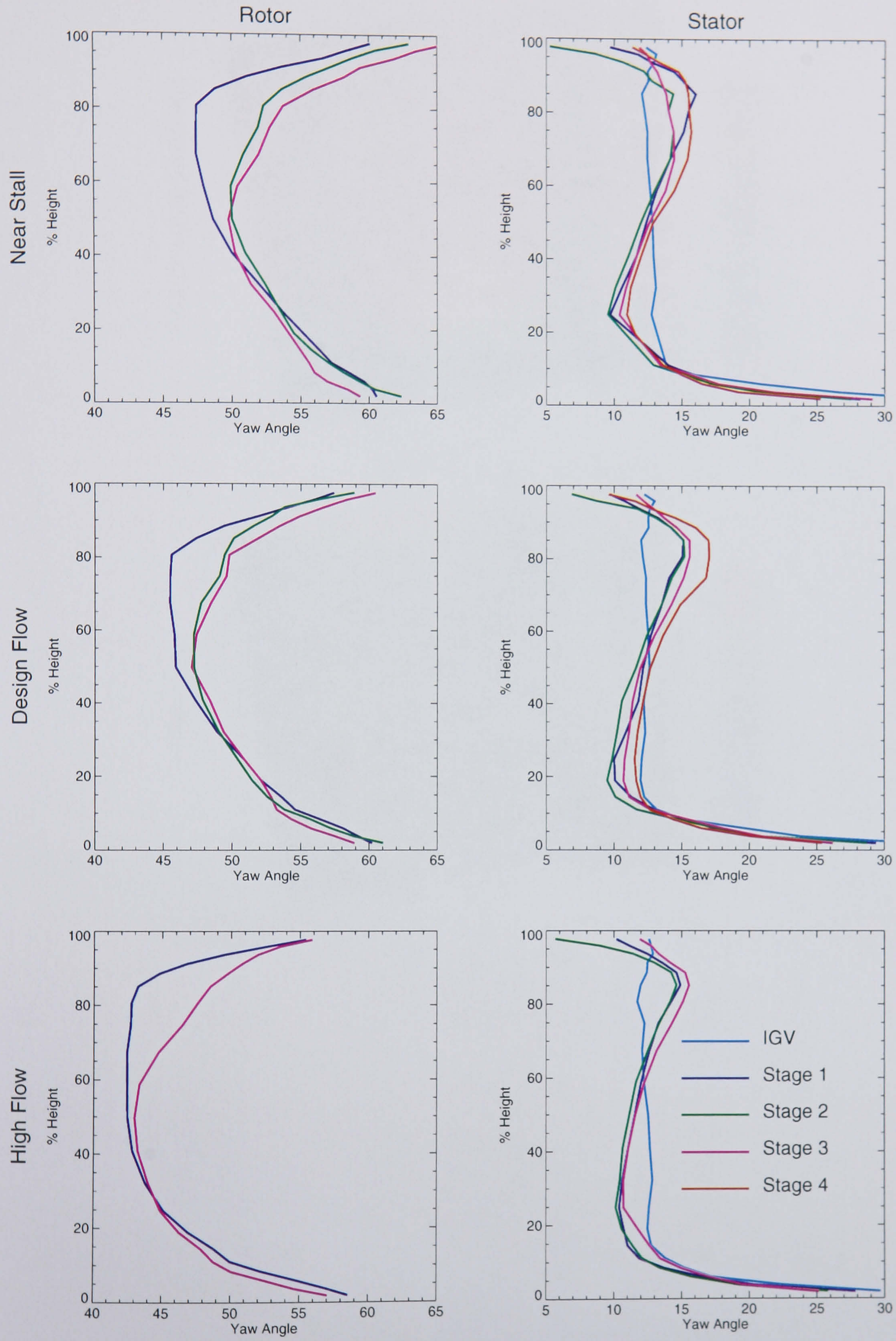


Figure 6.10 Radial profiles of yaw angle at near stall, design flow and high flow (datum build)

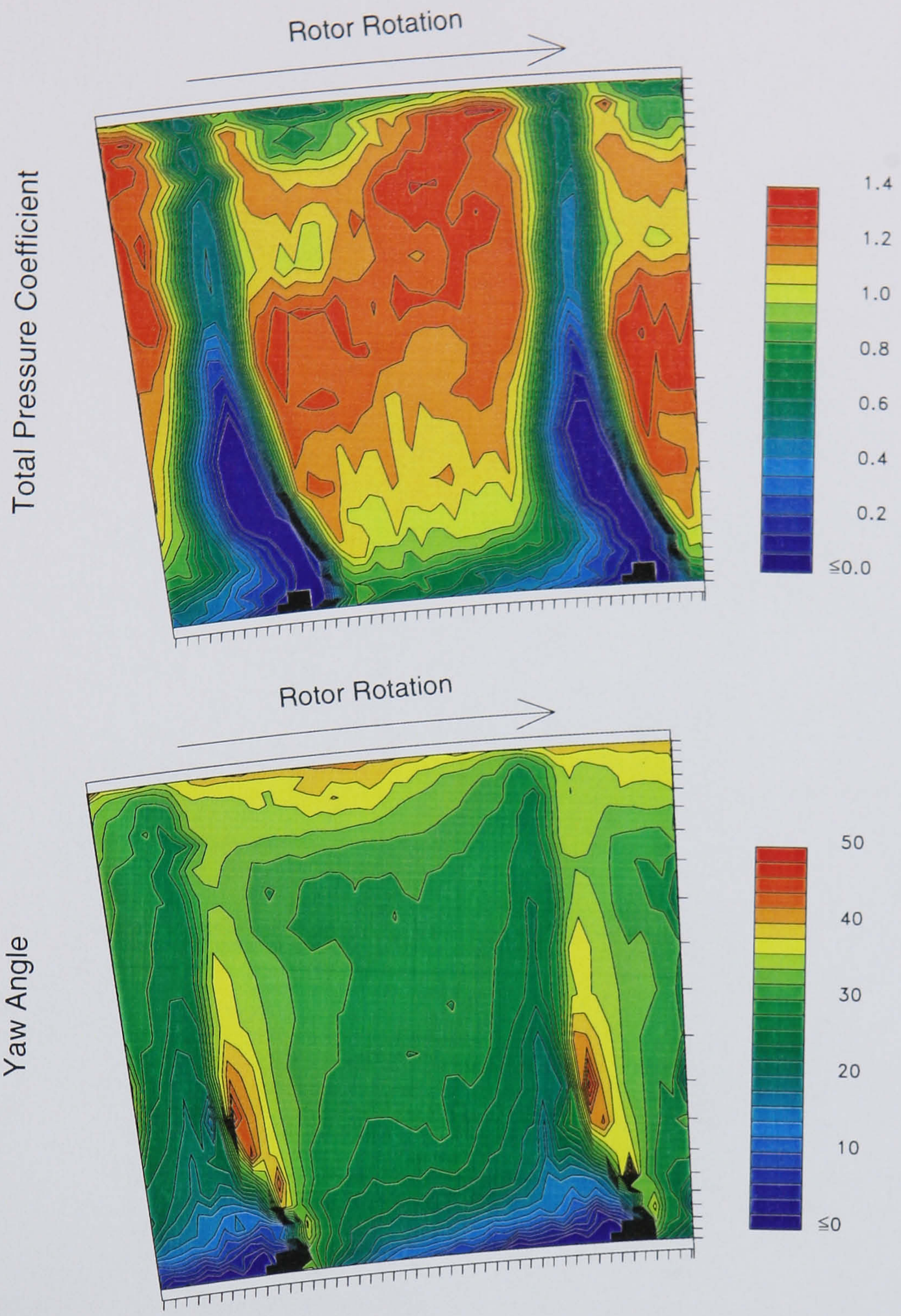


Figure 6.11 Rotor 3 exit total pressure and yaw angle contours and pitchwise average profiles at near stall measured in the rotating frame

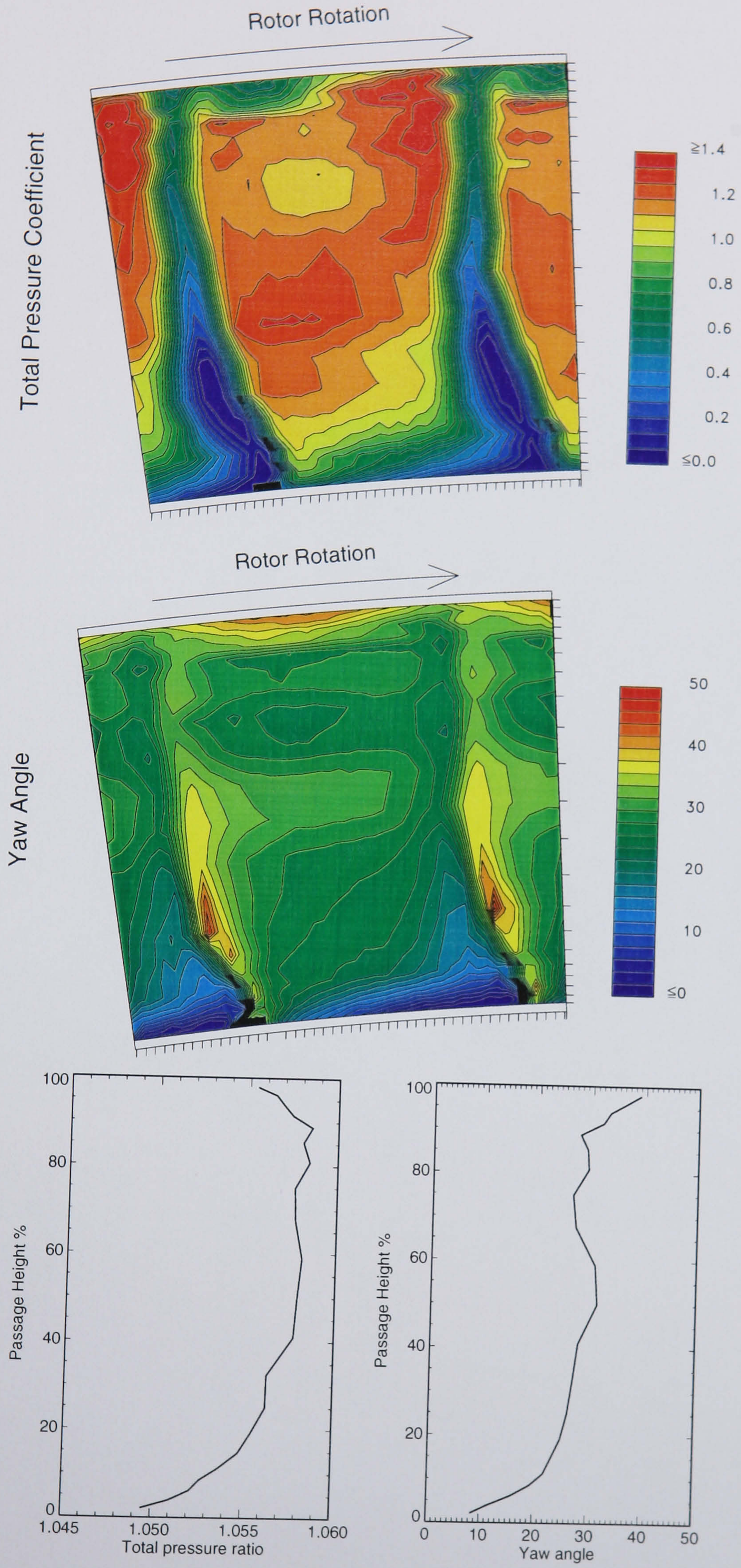


Figure 6.12 Rotor 3 exit total pressure and yaw angle contours and pitchwise average profiles at design flow measured in the rotating frame

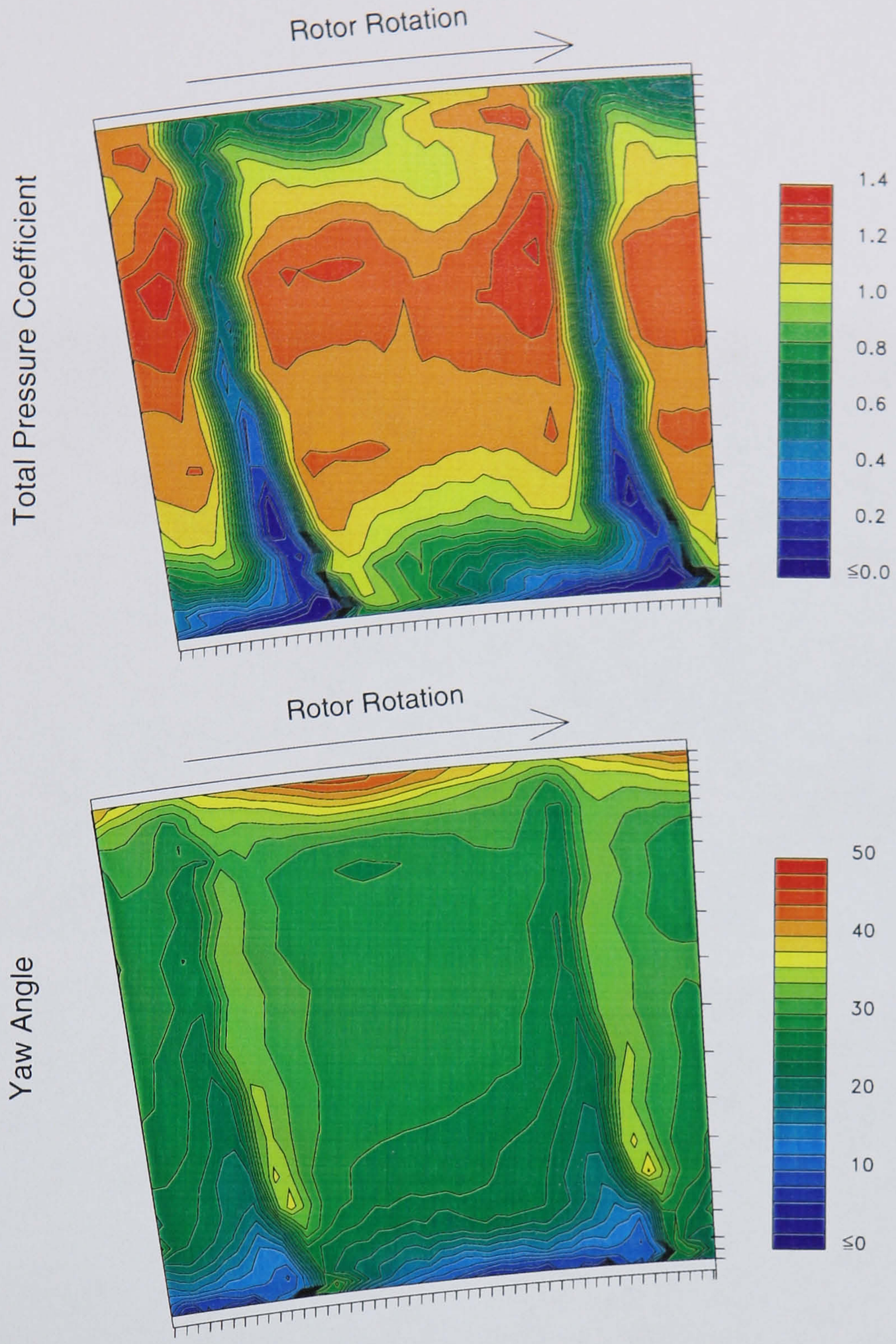


Figure 6.13 Rotor 3 exit total pressure and yaw angle contours and pitchwise average profiles at high flow measured in the rotating frame

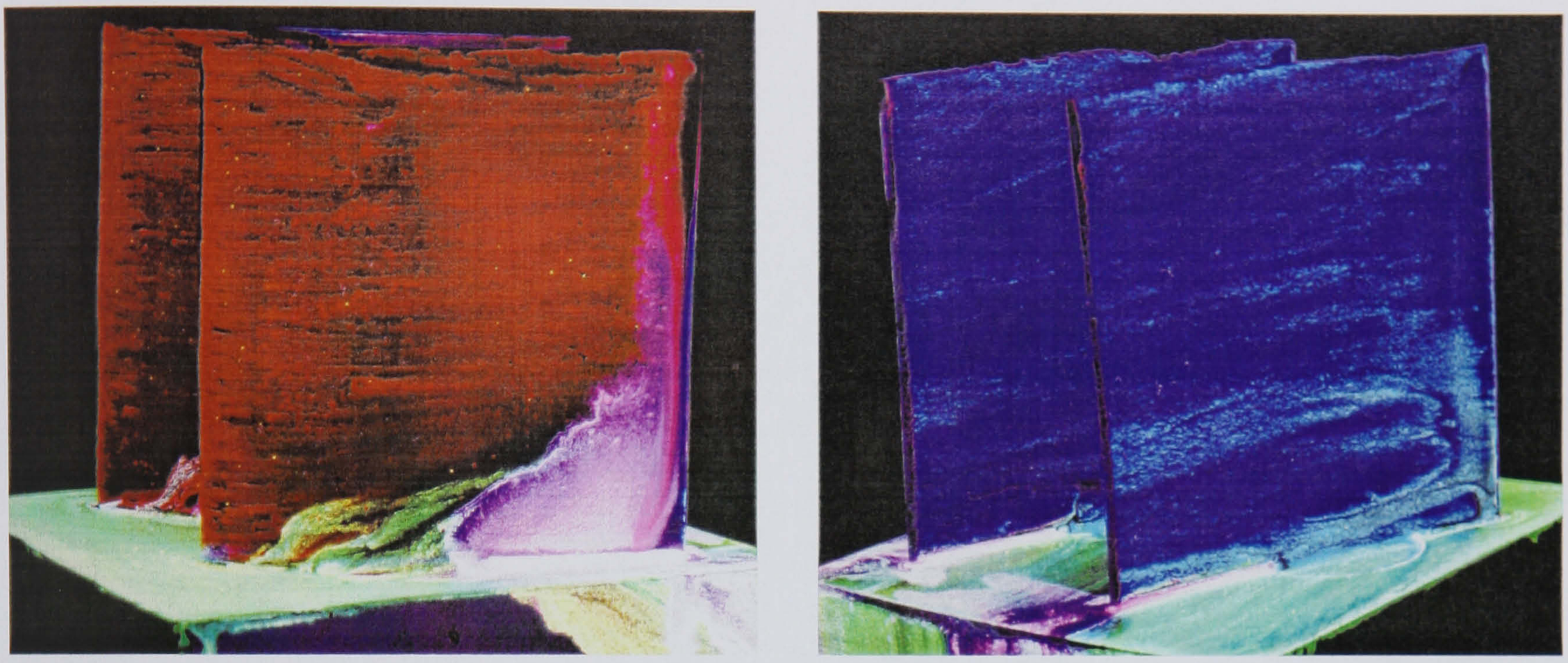


Figure 6.14 Stator flow visualisation at design flow

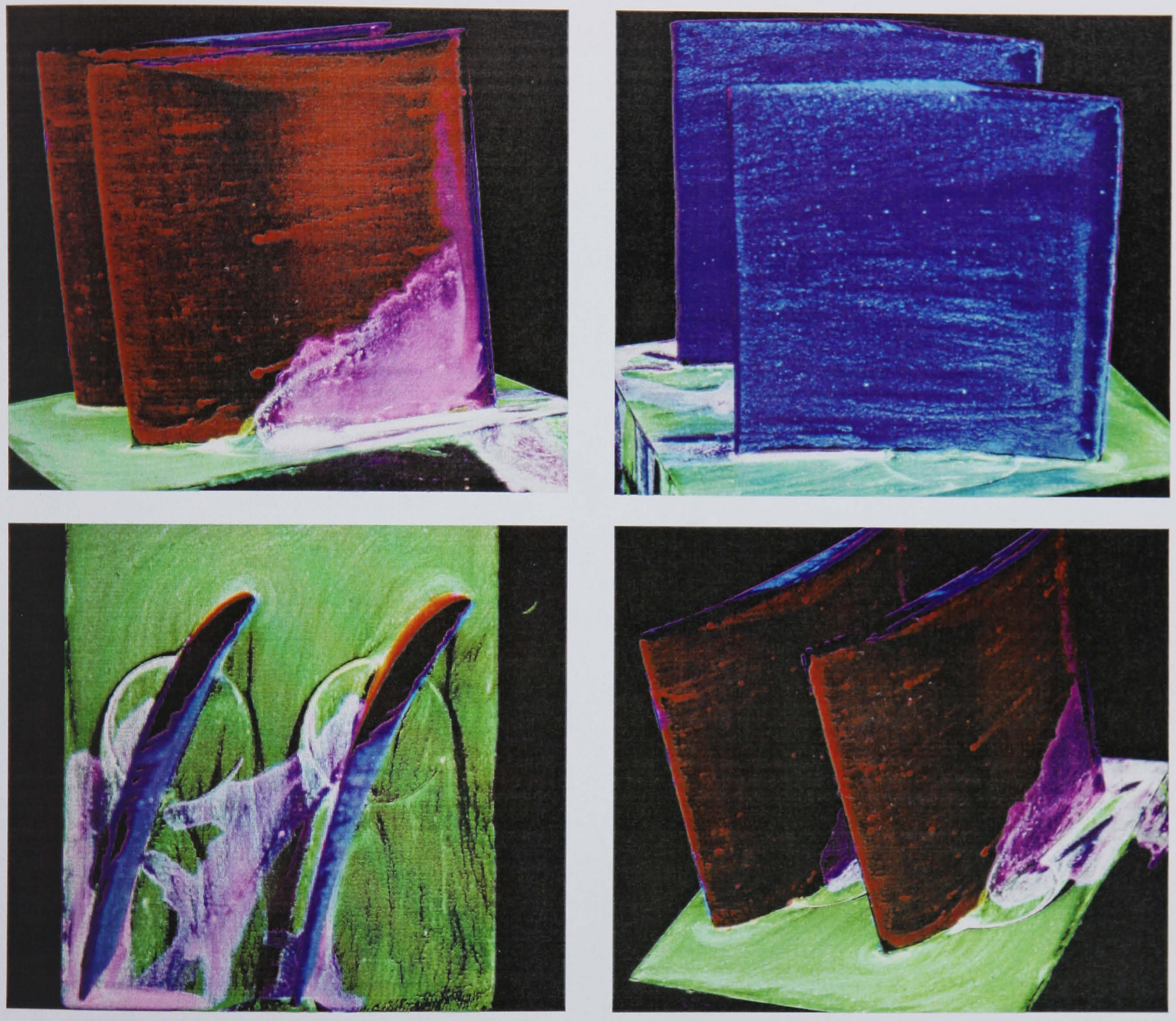


Figure 6.15 Stator flow visualisation at near stall

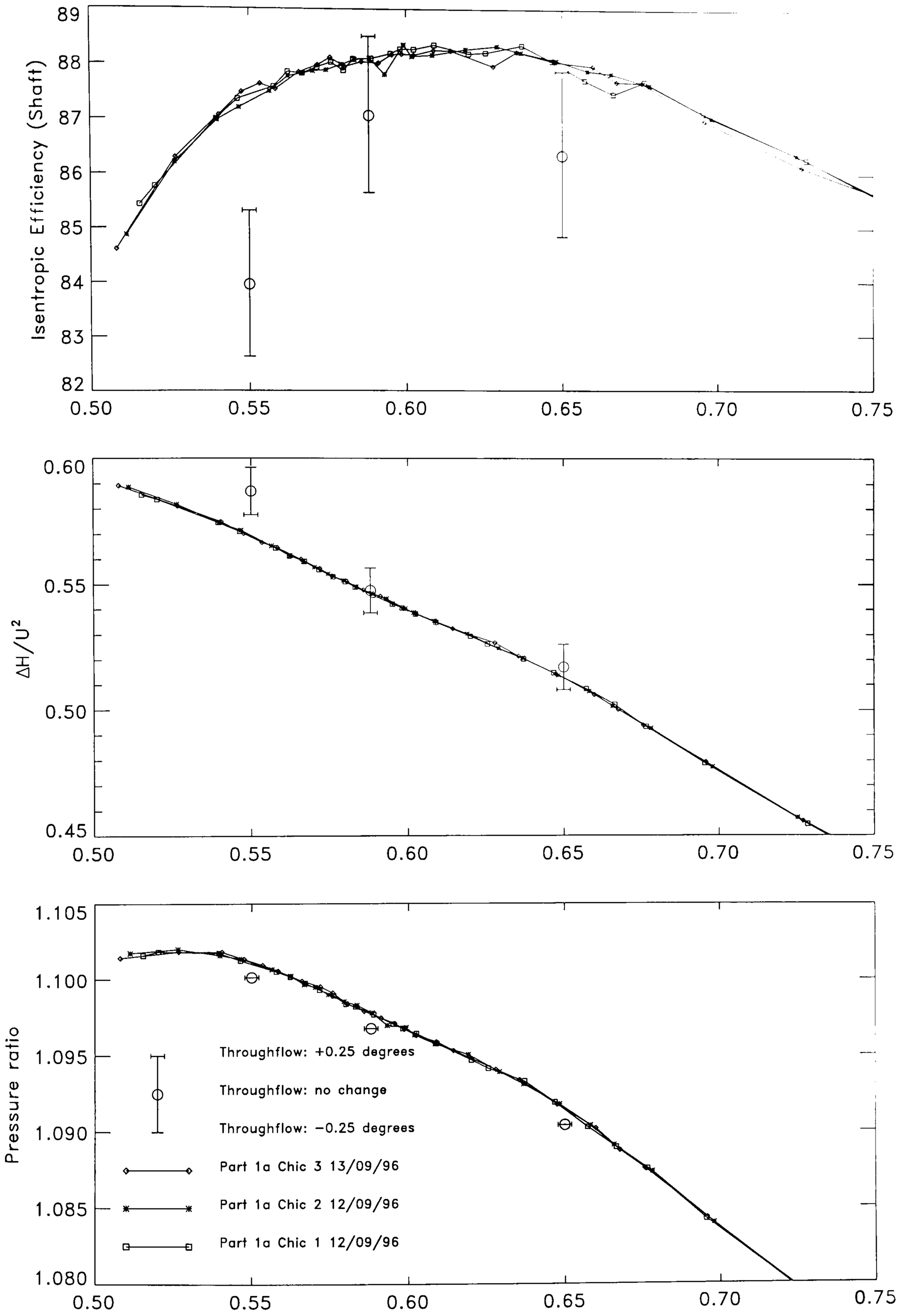


Figure 6.16 Overall performance of throughflow calculations

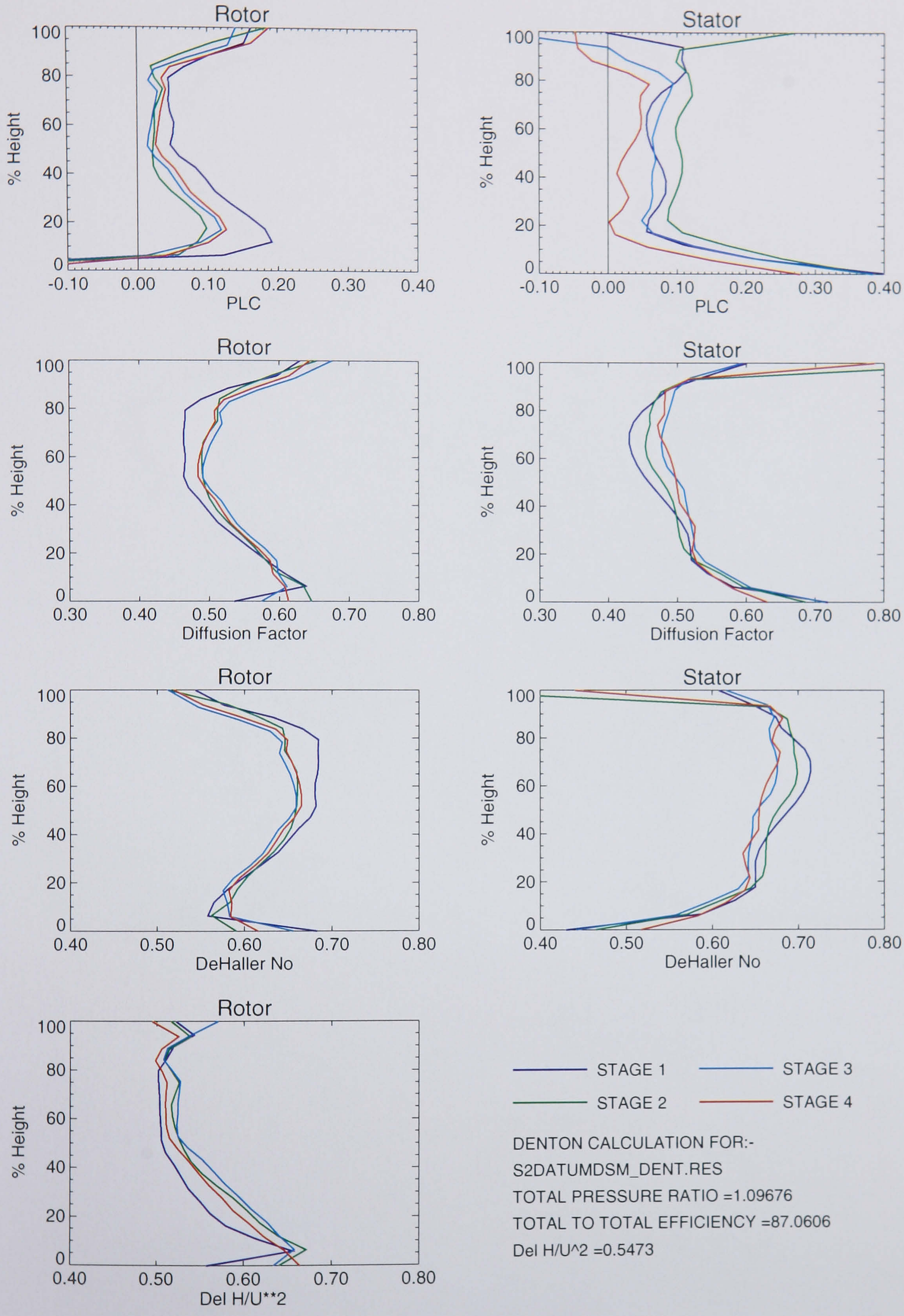
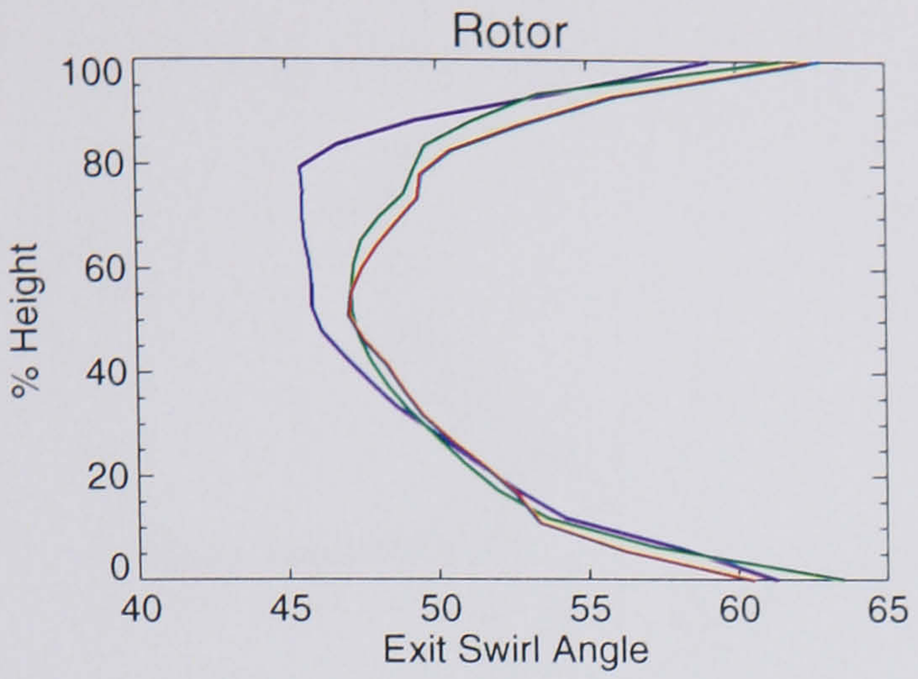
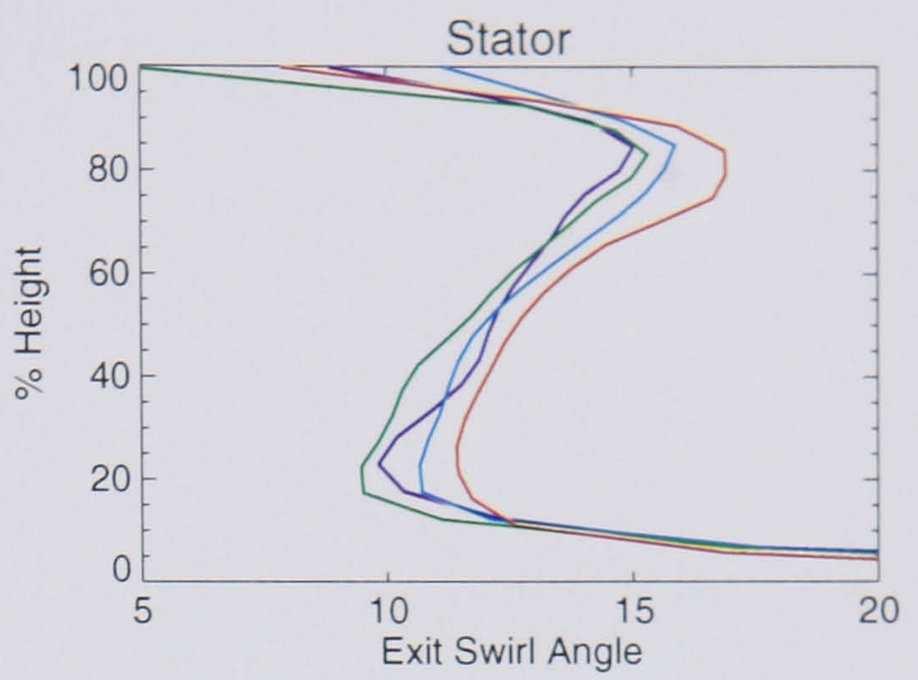
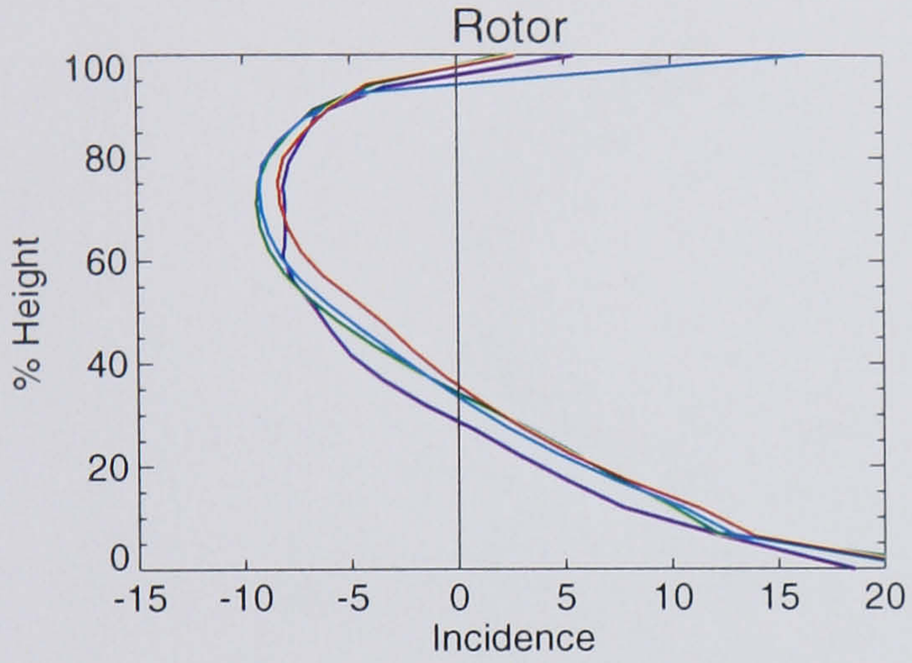
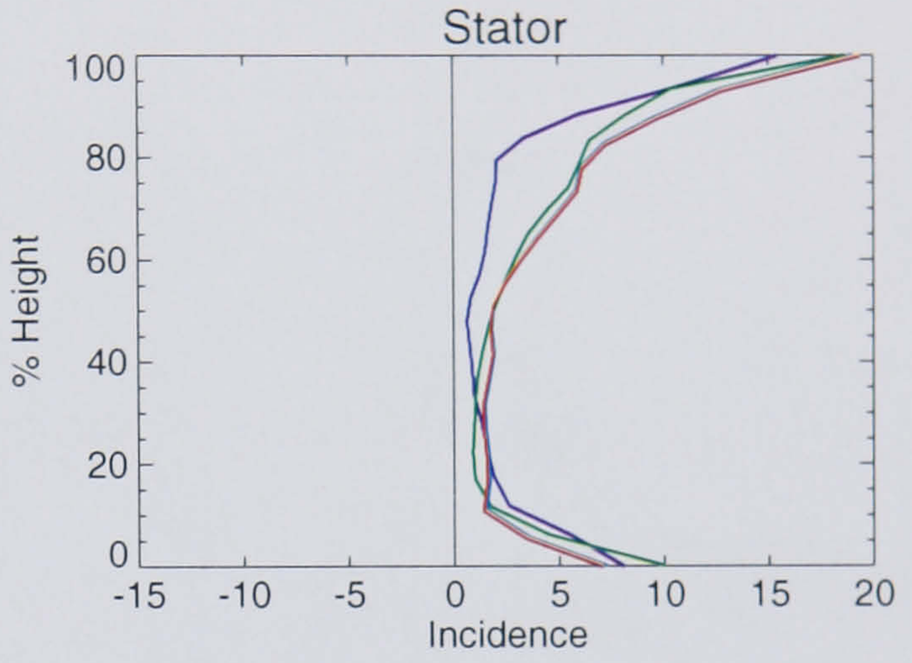


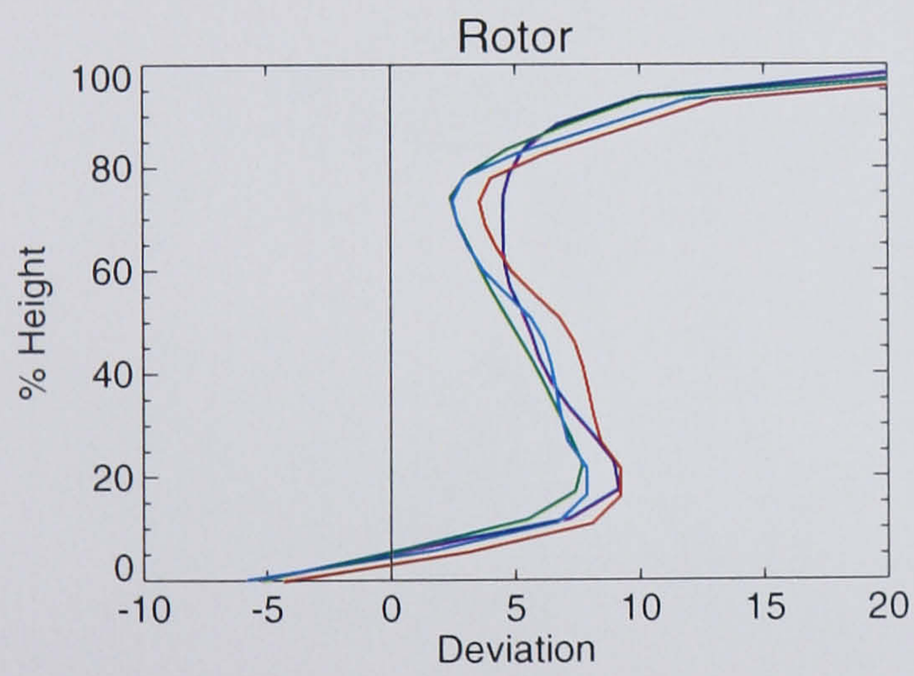
Figure 6.17a Results of throughflow calculation at design flow

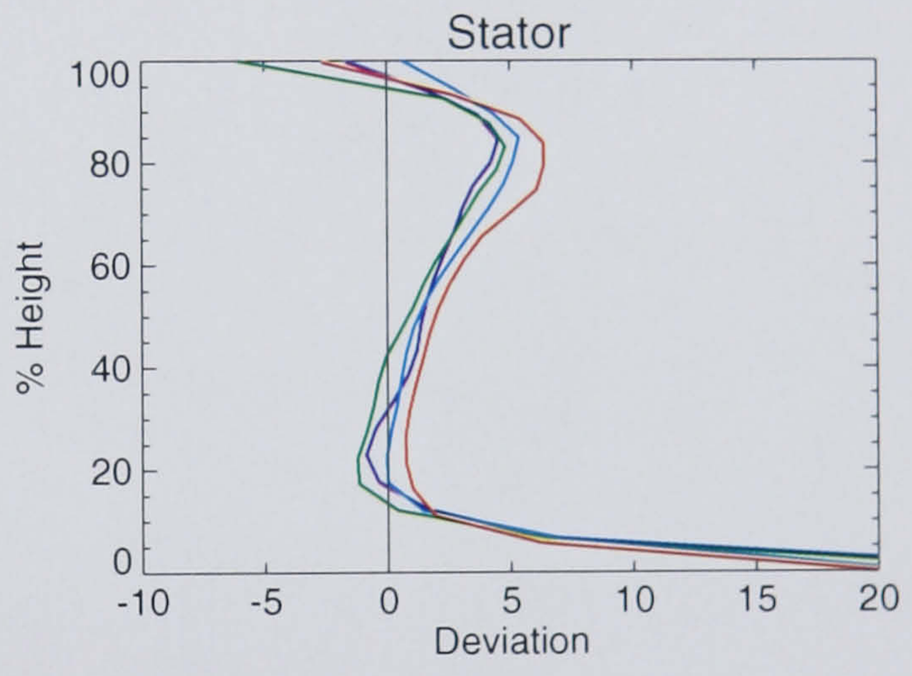


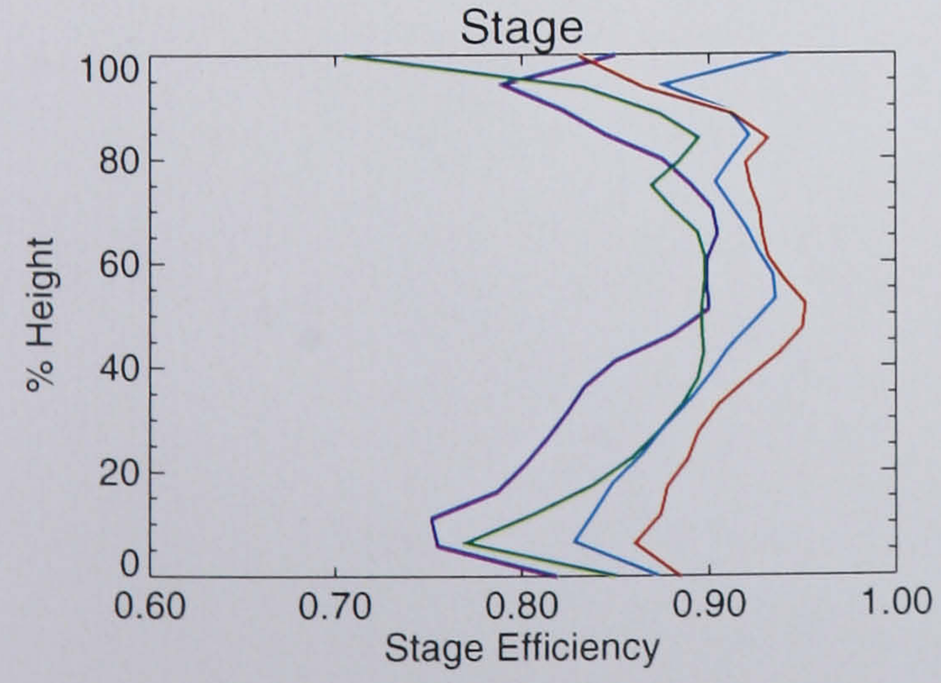












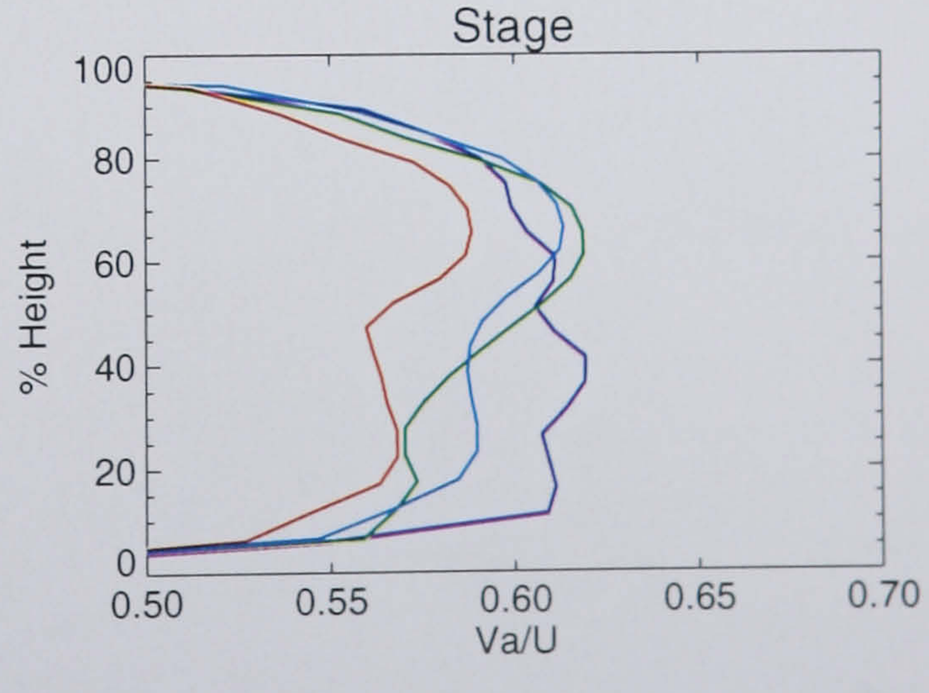


Figure 6.17b Results of throughflow calculation at design flow continued

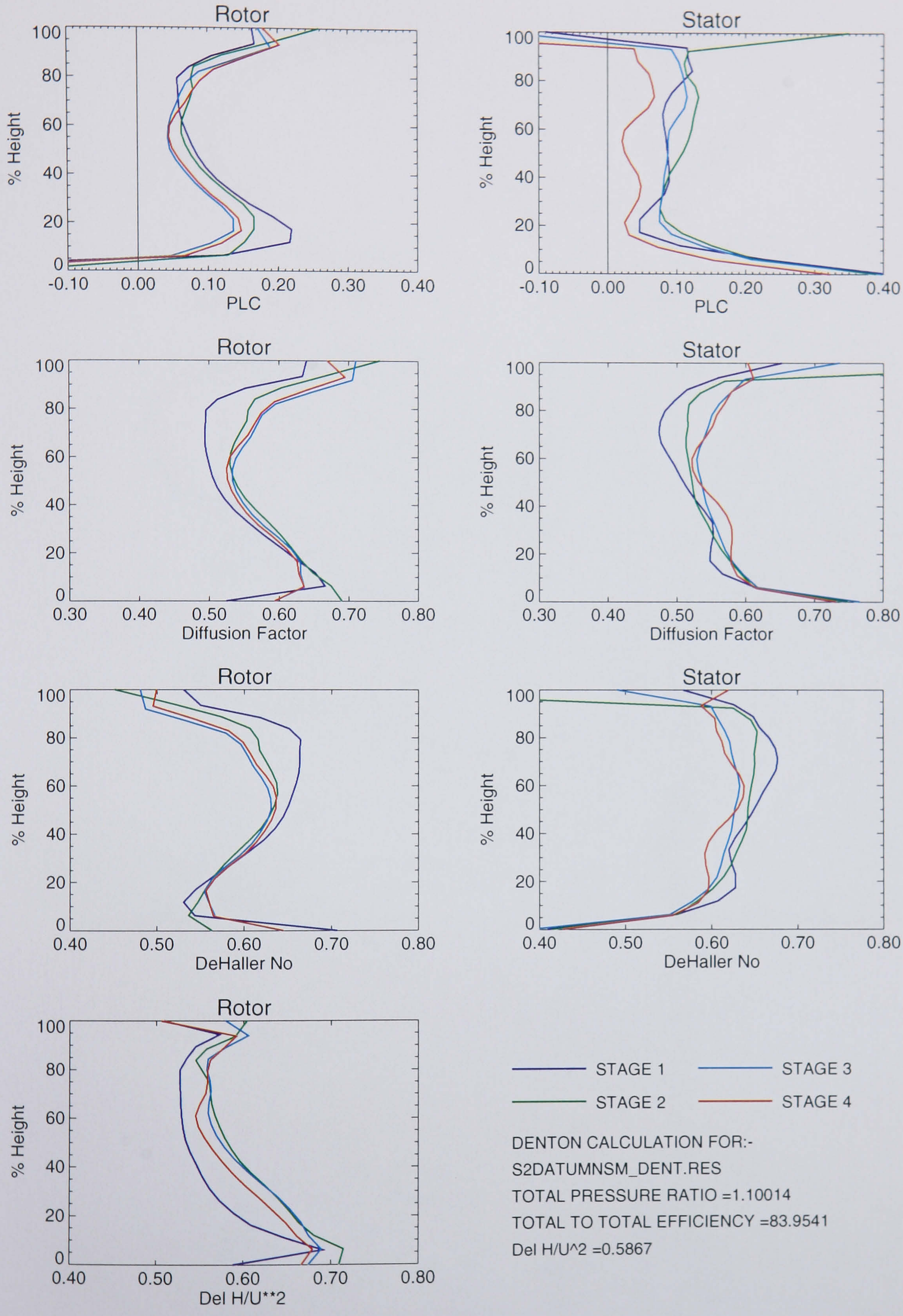
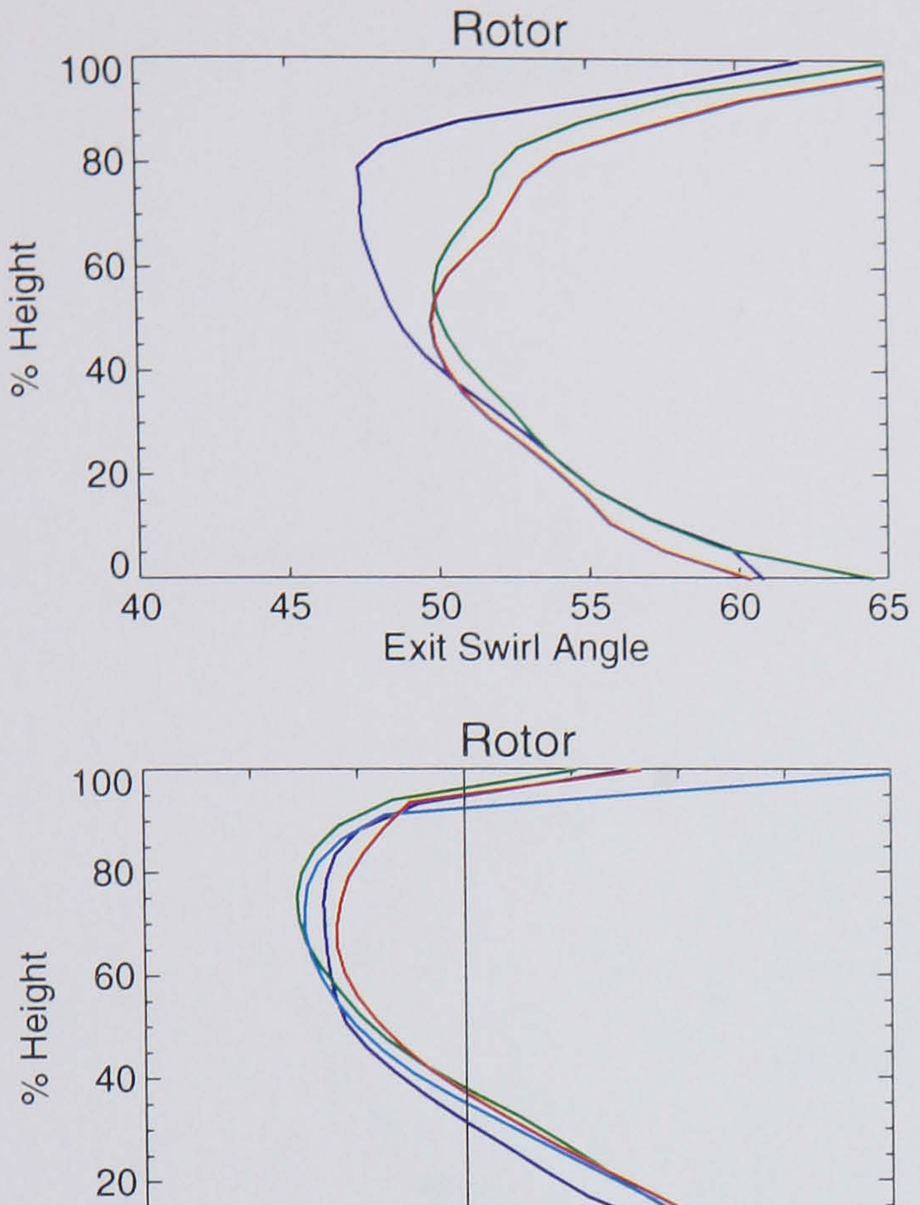


Figure 6.18a Results of throughflow calculation at near stall



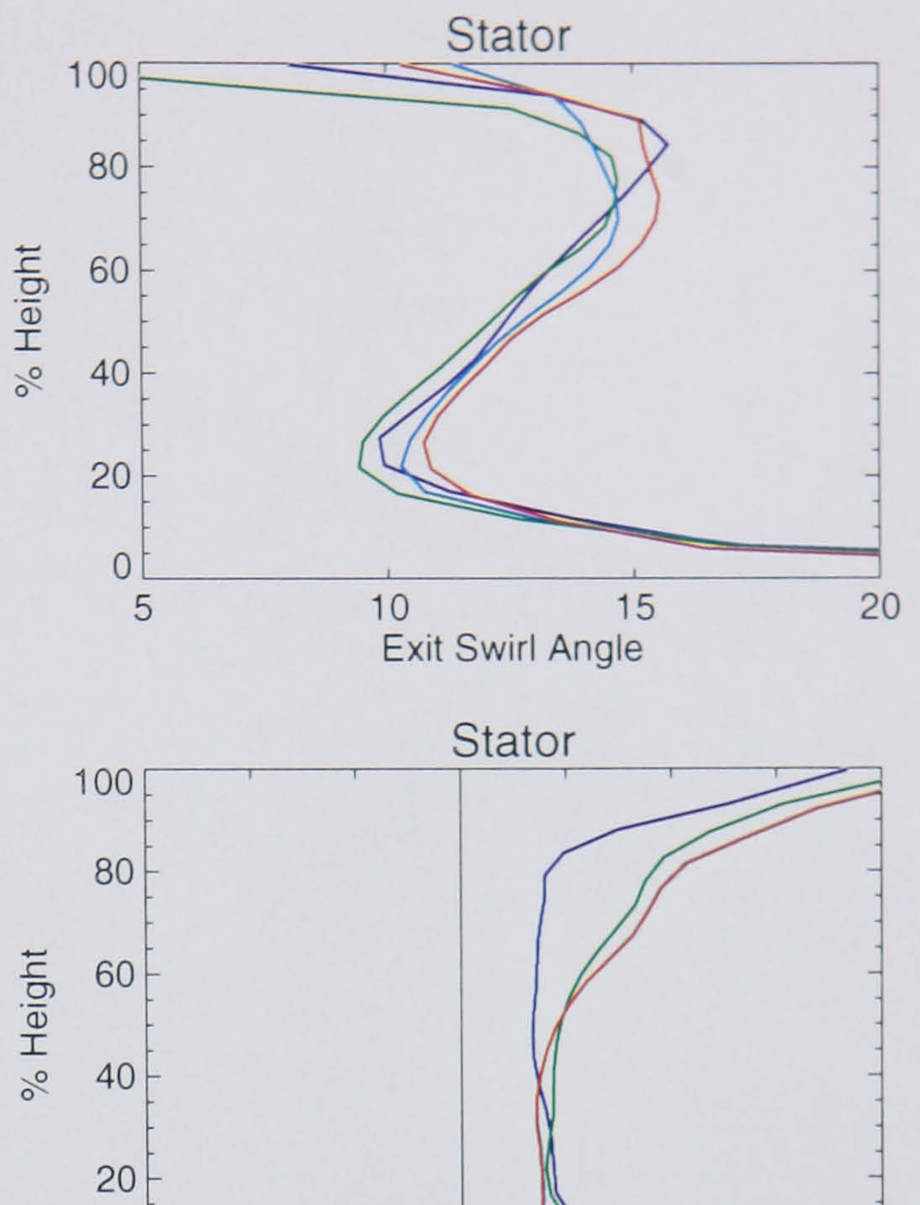


Figure 6.18b Results of throughflow calculation at near stall continued

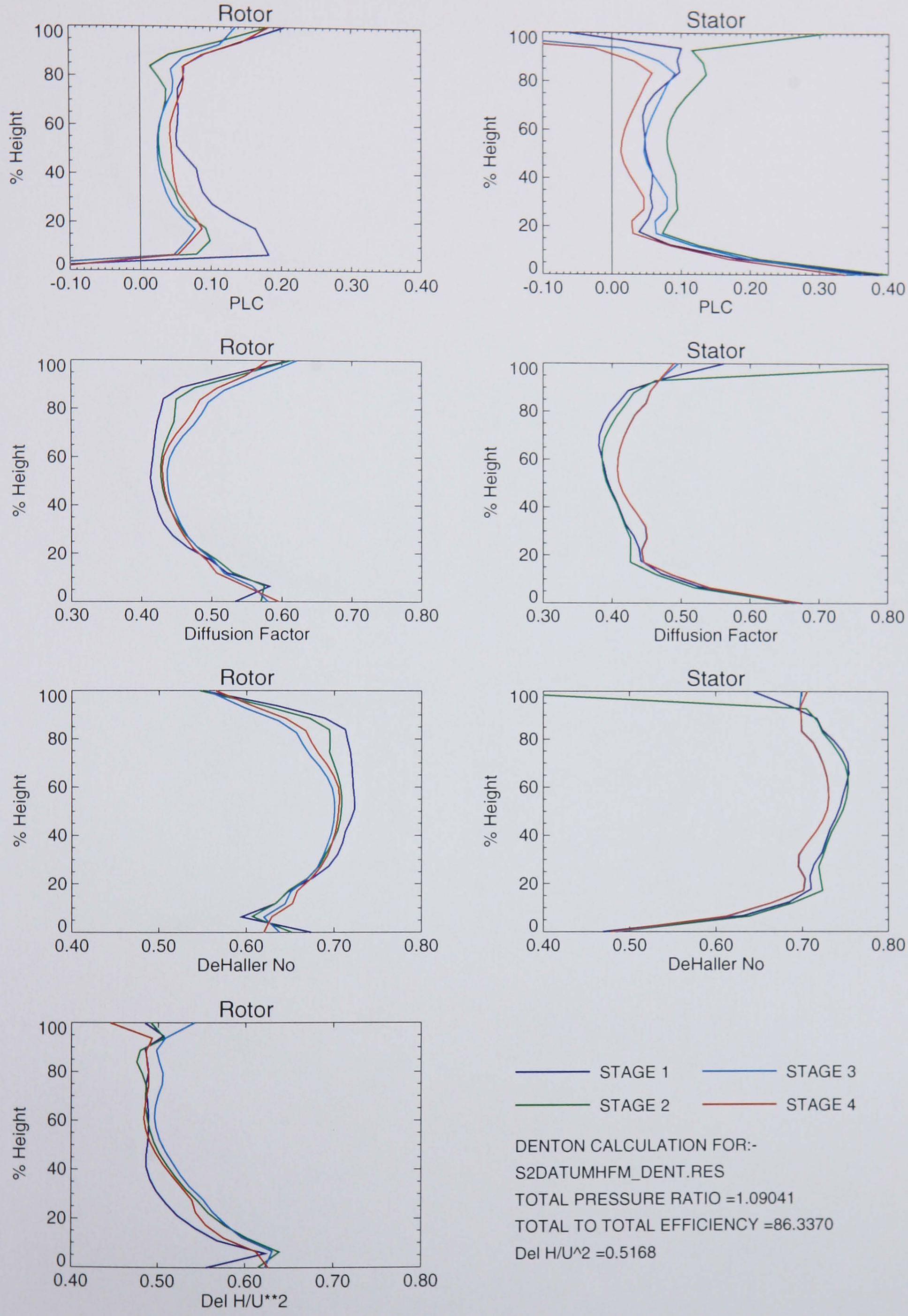
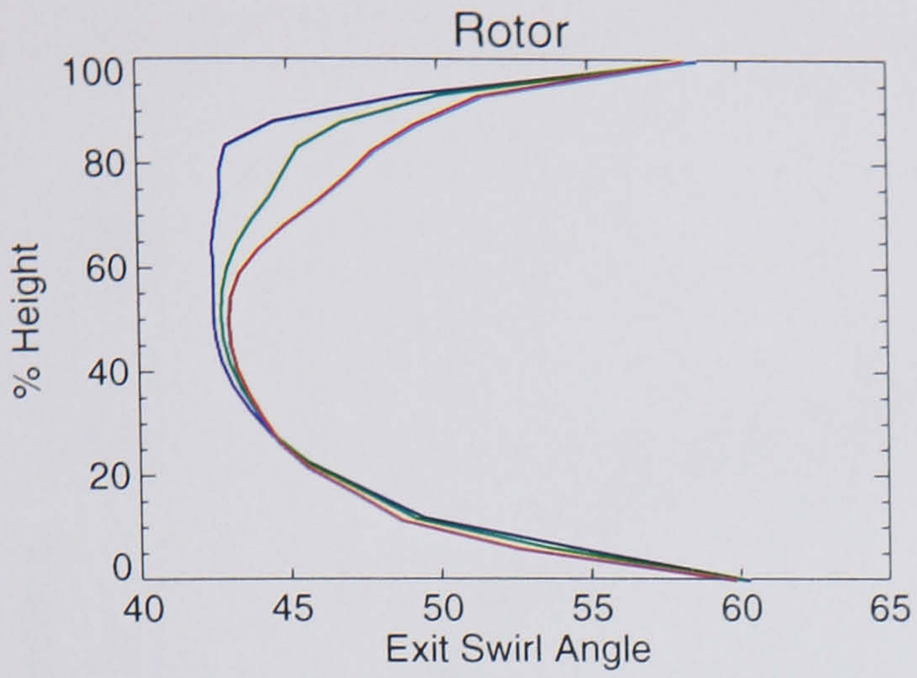
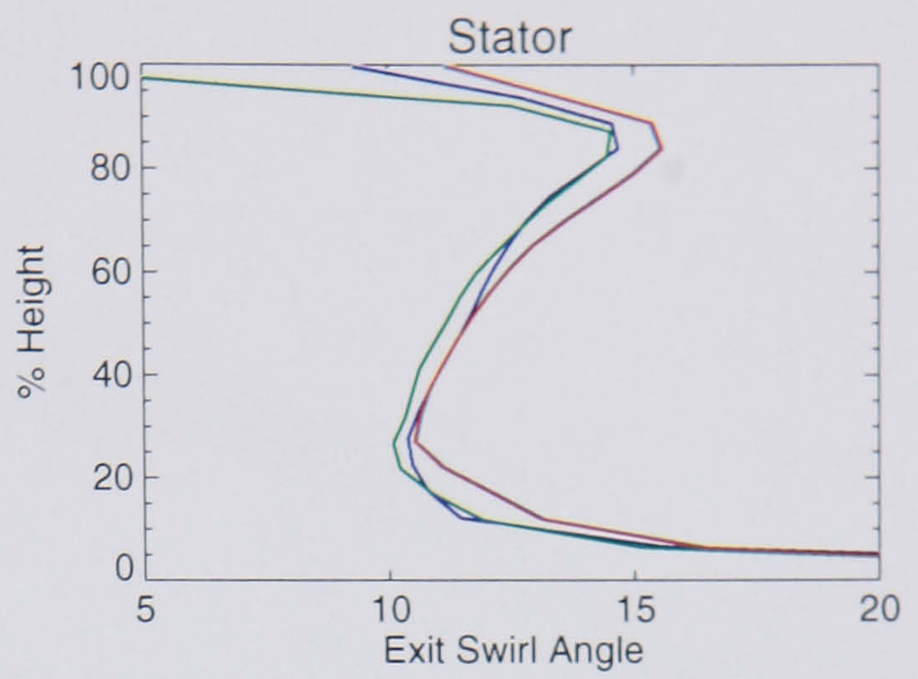
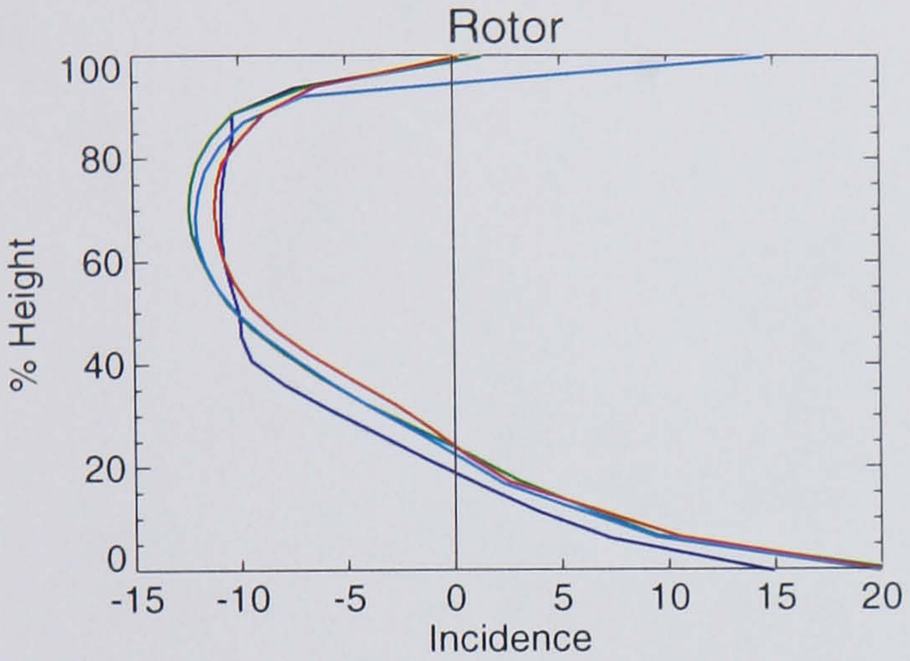
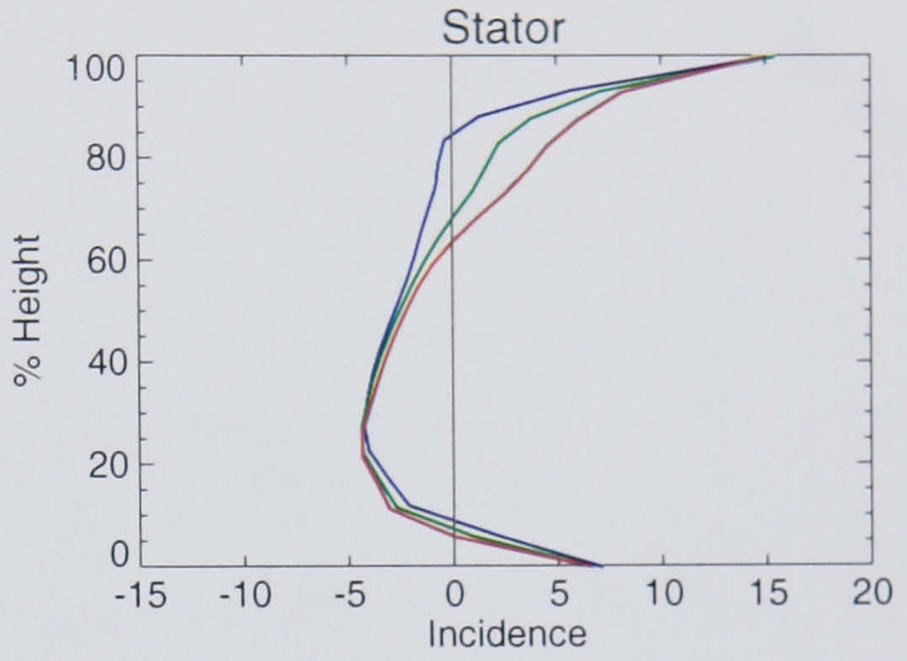


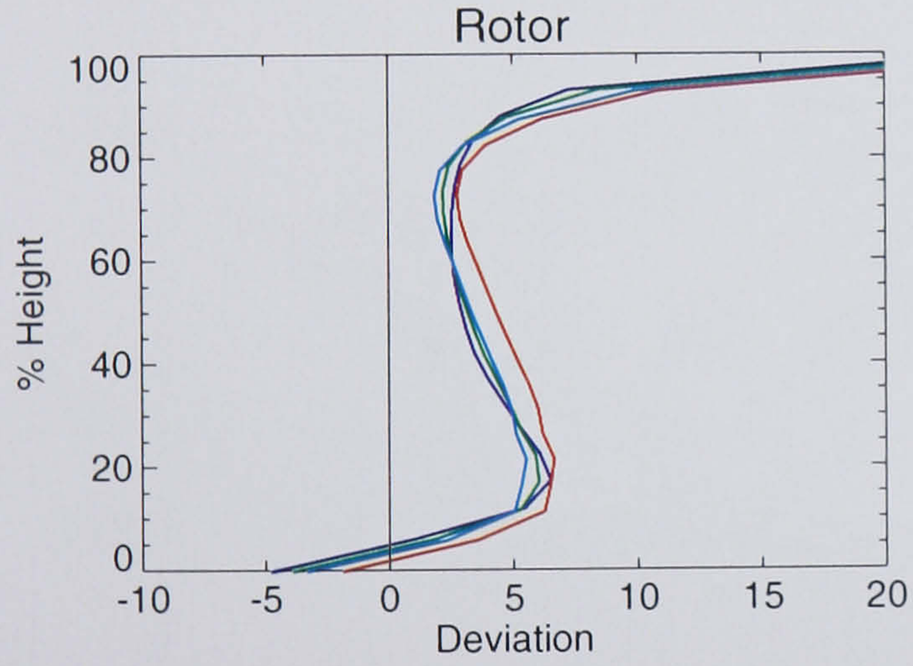
Figure 6.19a Results of throughflow calculation at high flow

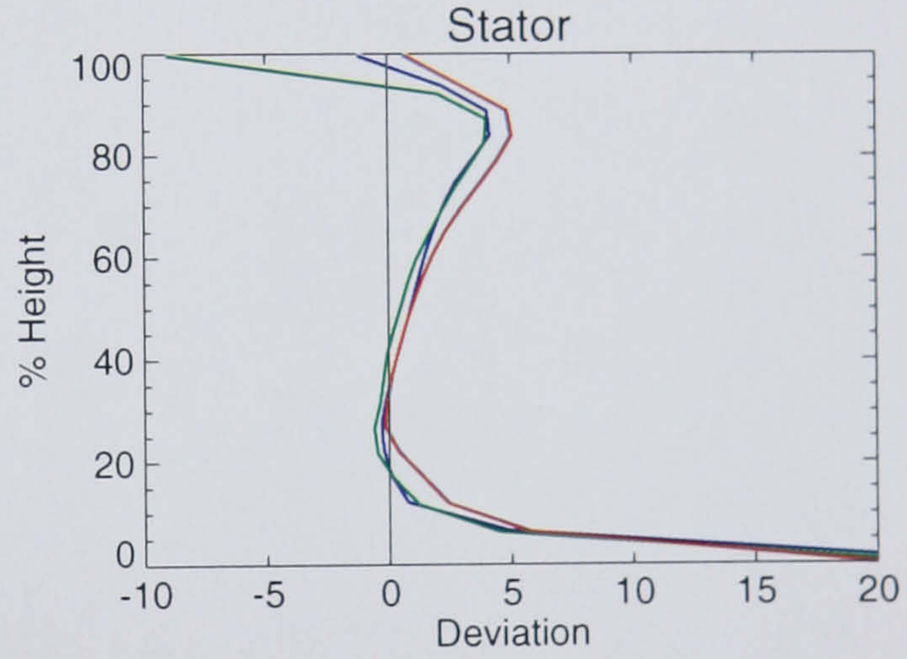


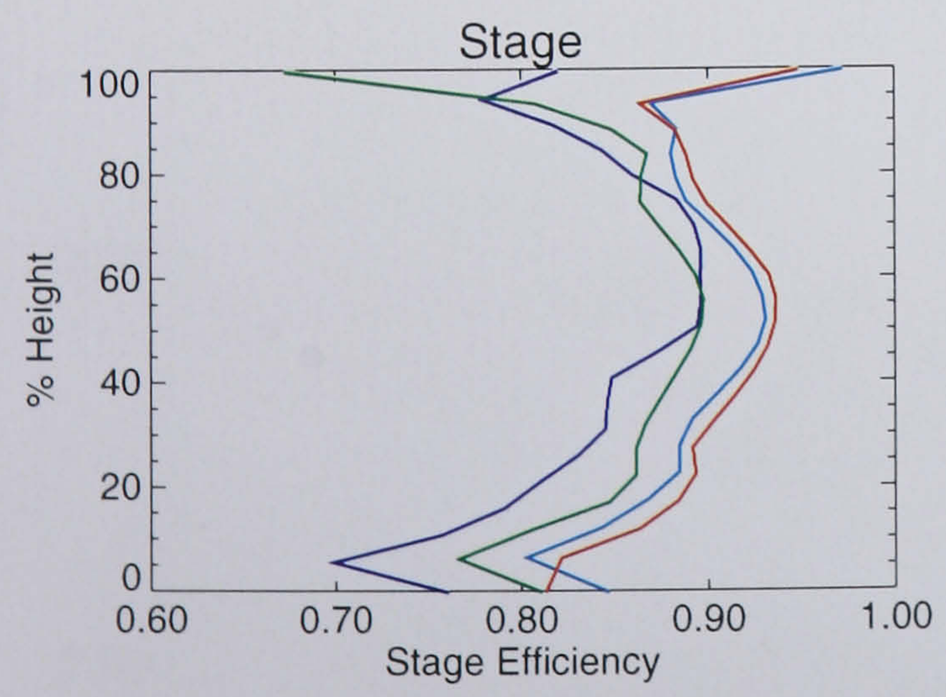












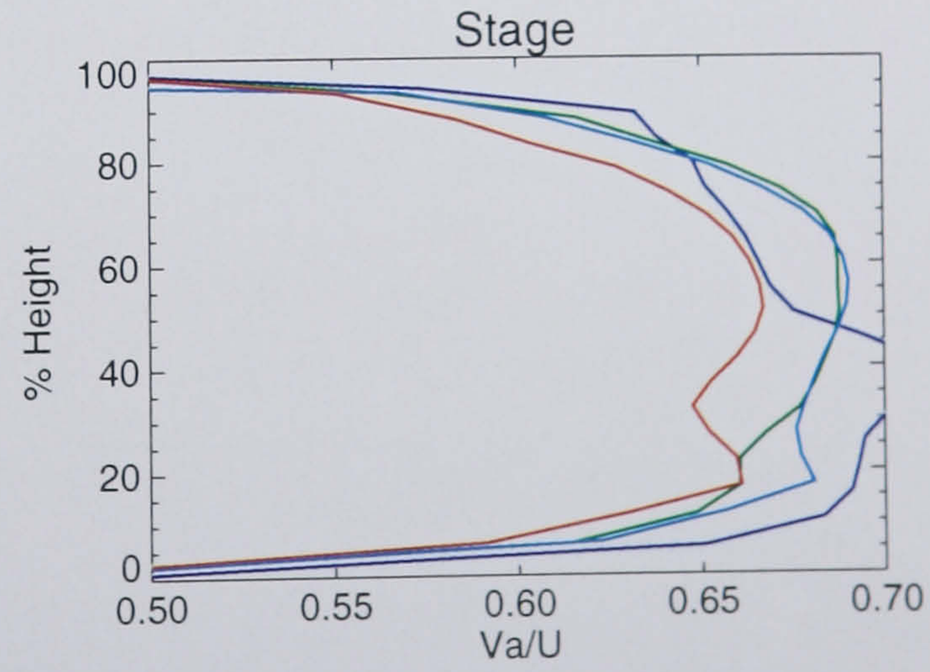


Figure 6.19b Results of throughflow calculation at high flow continued

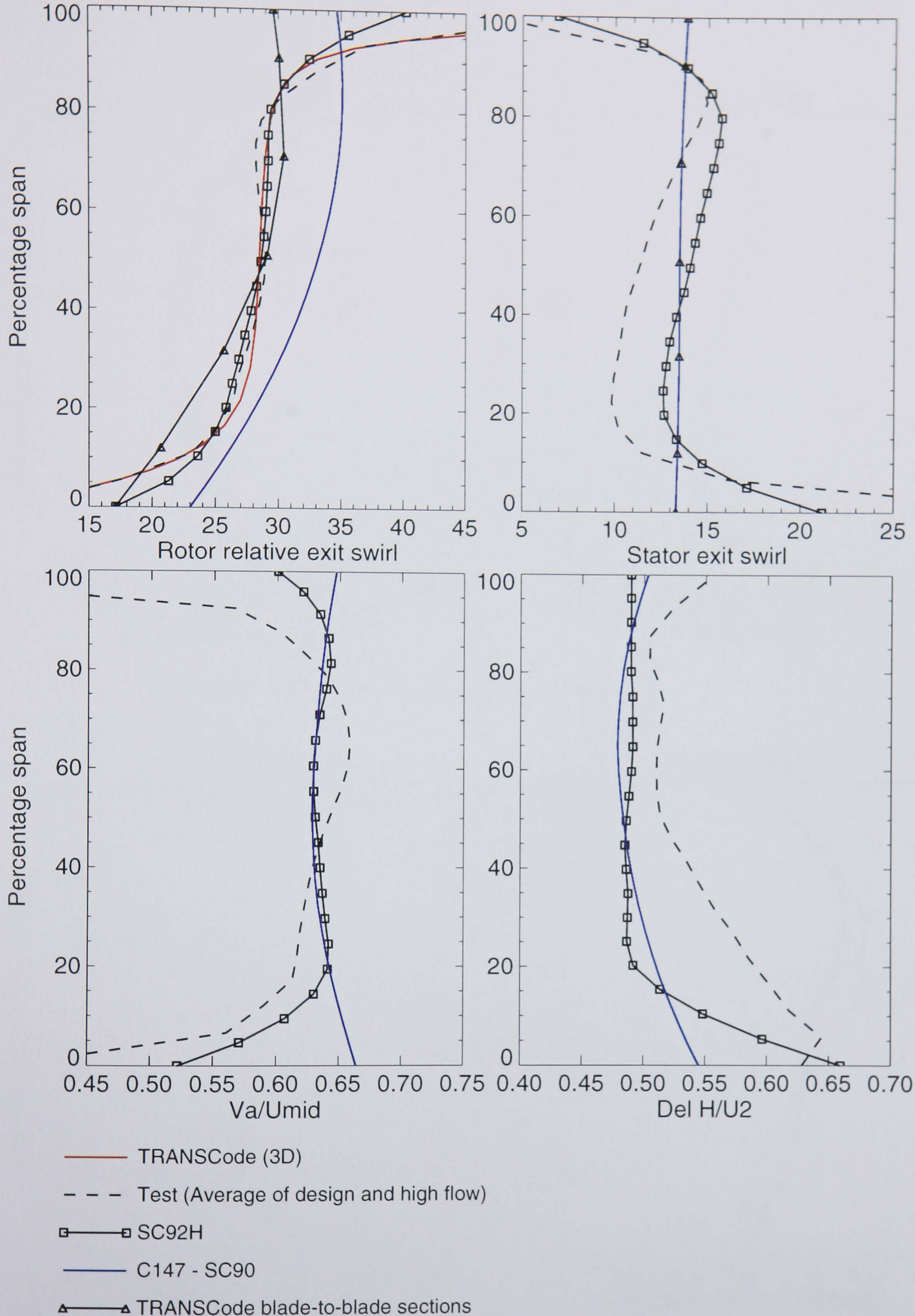
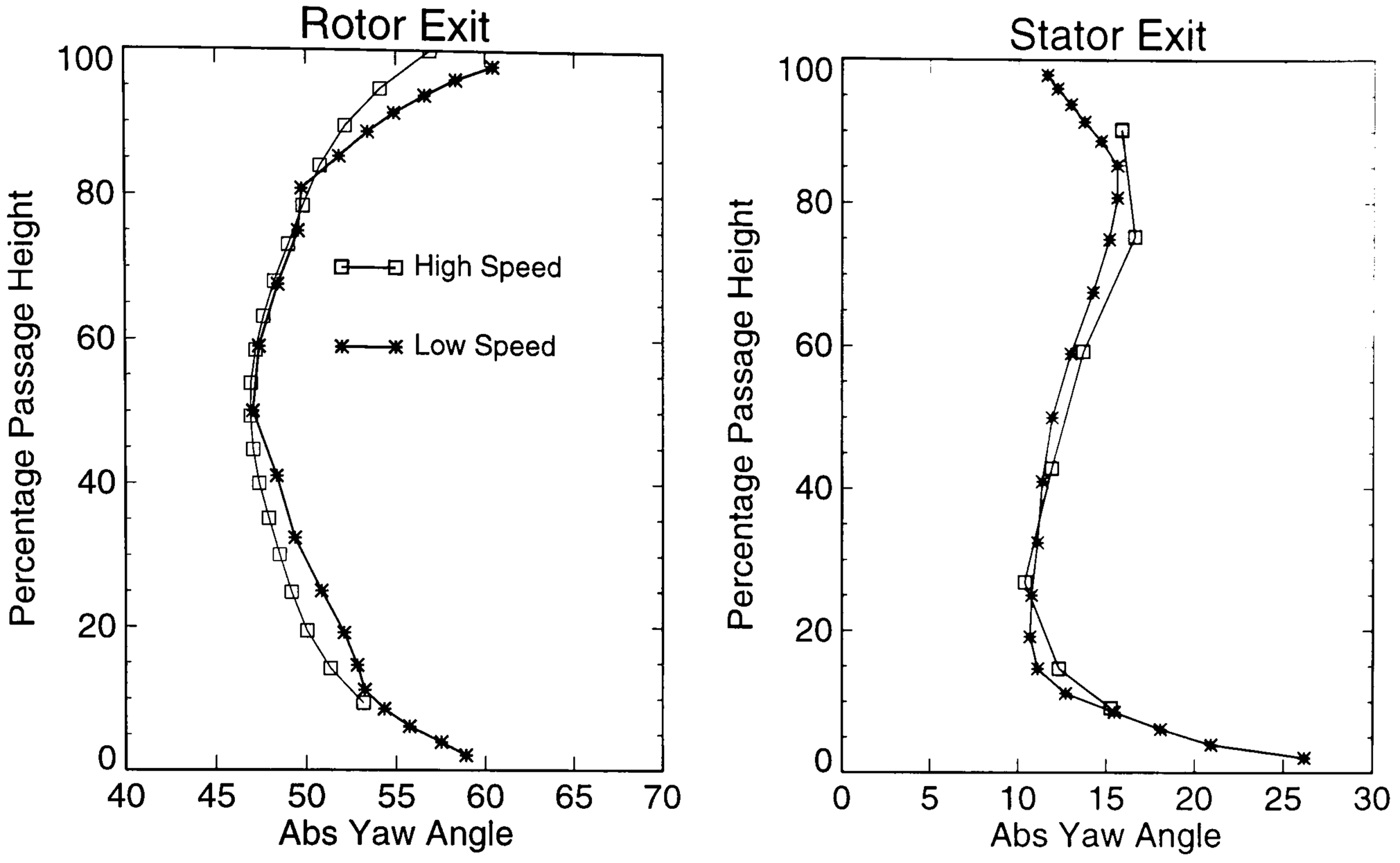


Figure 7.2 DERA1 design profiles and work anomalies



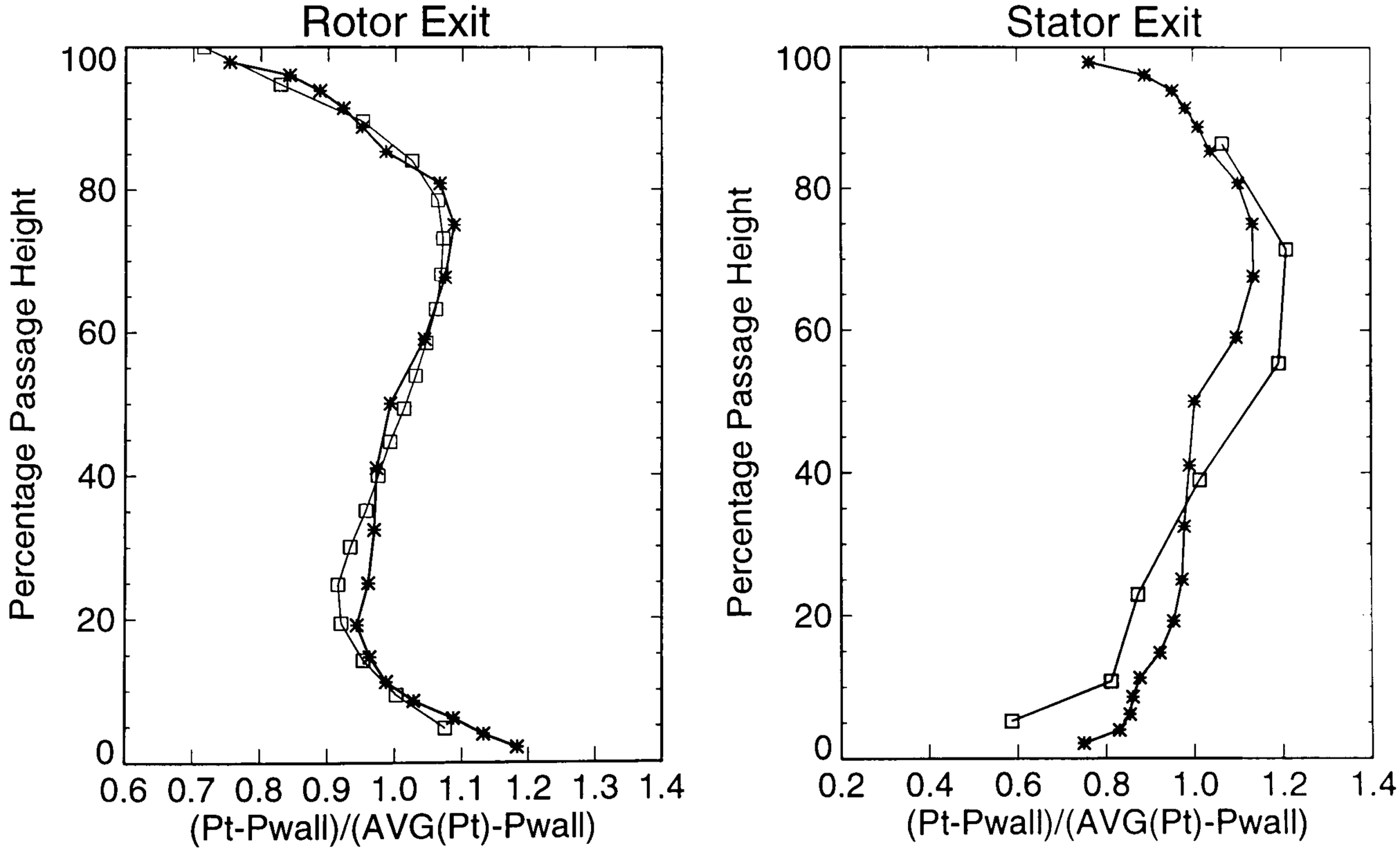


Figure 7.3 Rotor and stator exit radial profiles

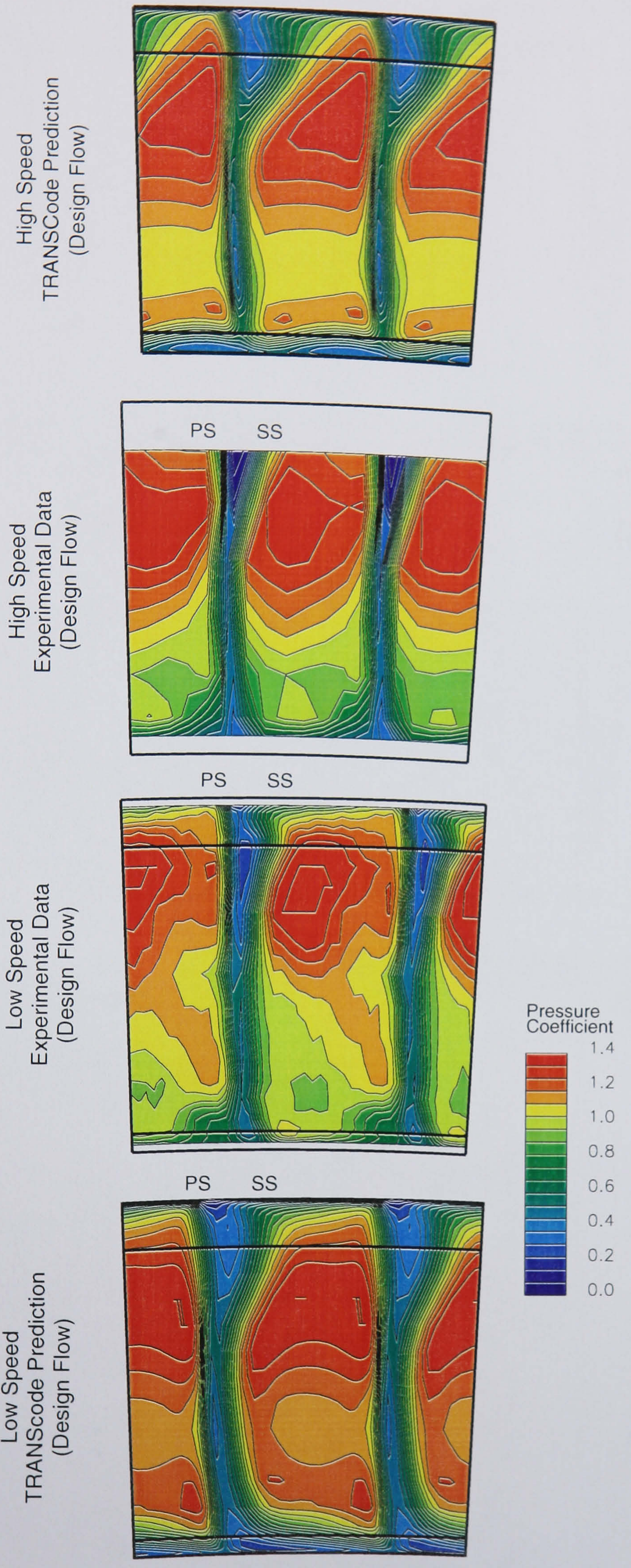


Figure 7.4 Total pressure coefficient at stator exit

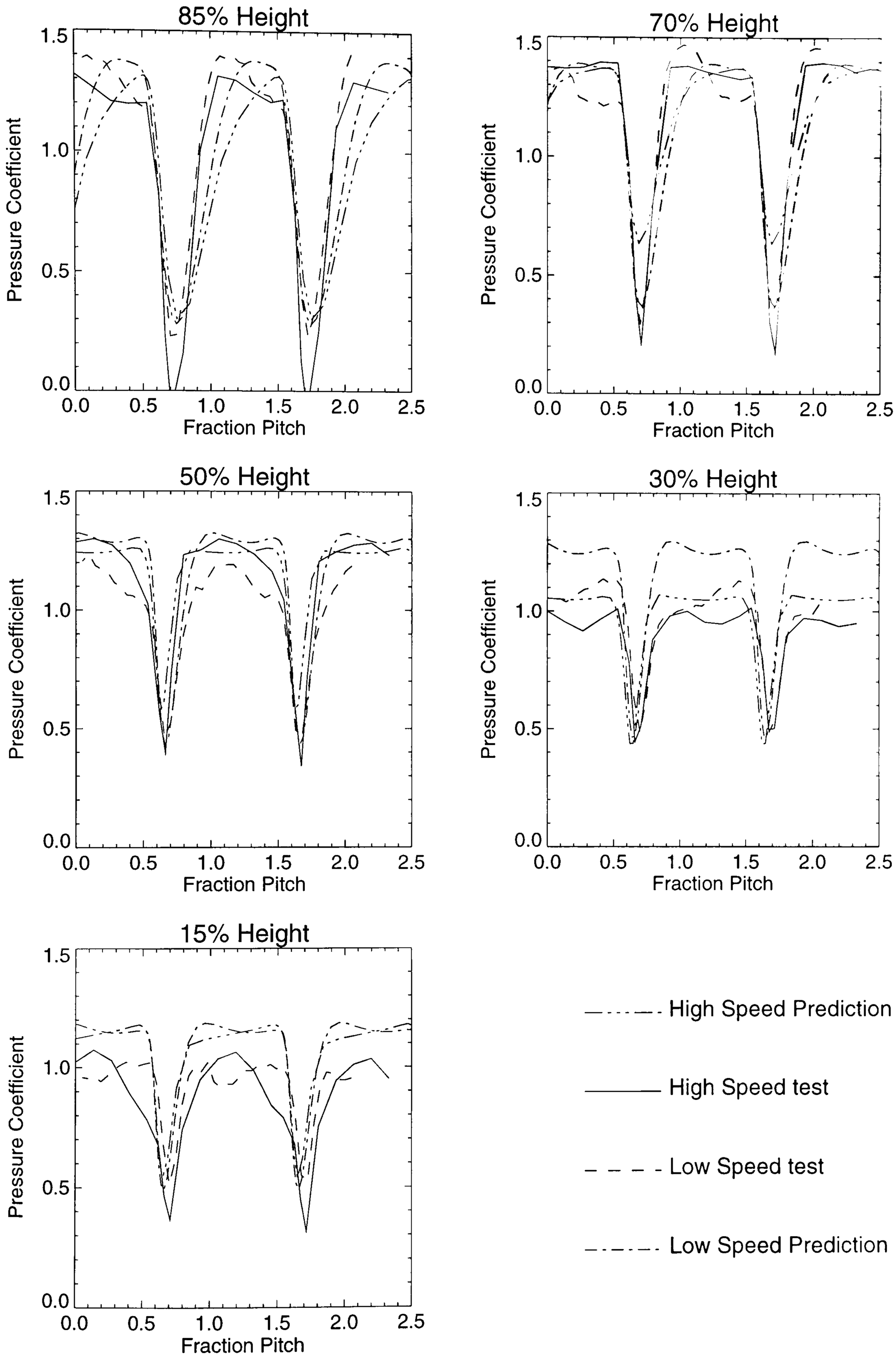


Figure 7.5 Pitchwise variations in pressure coefficient at stator exit

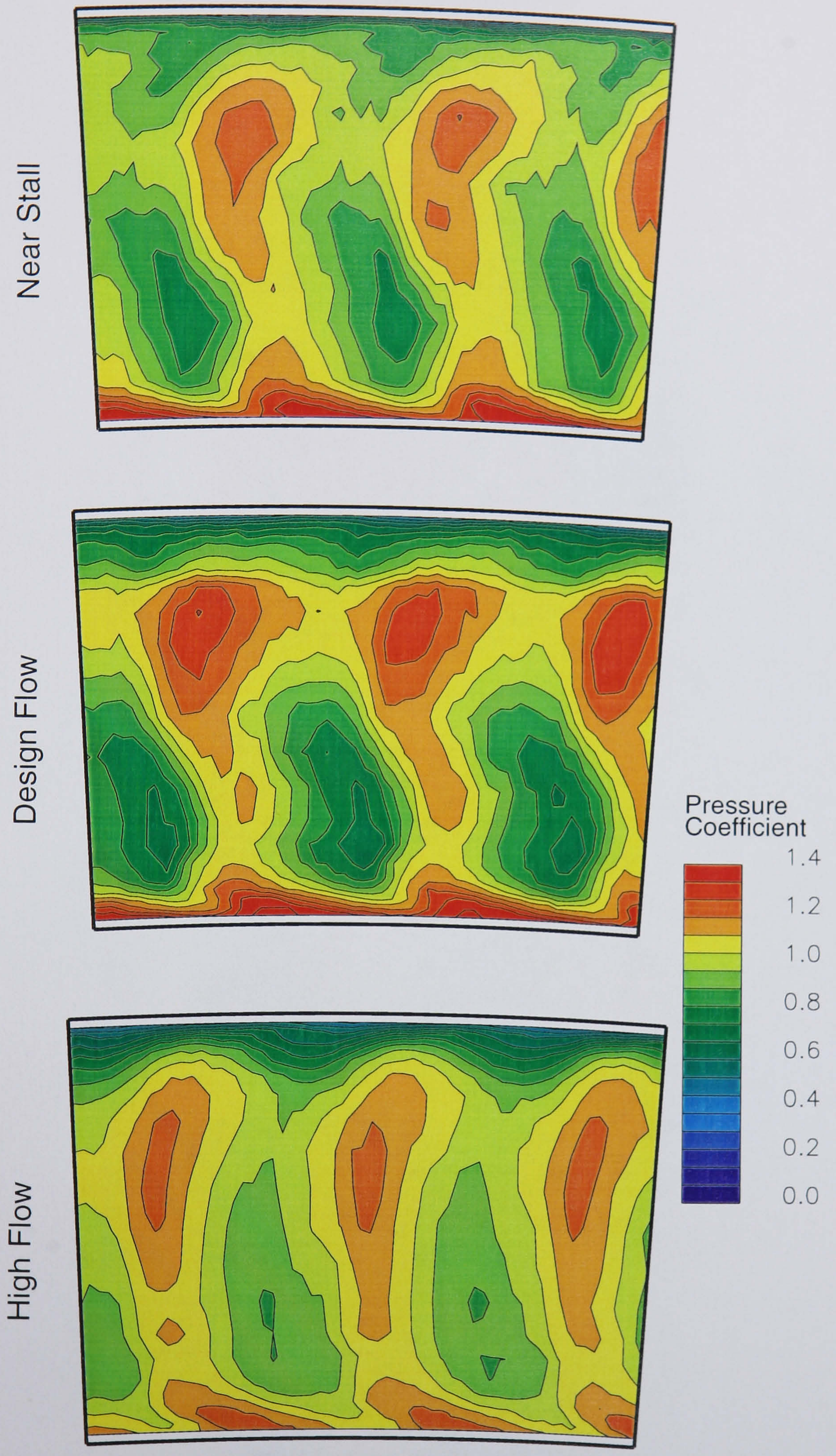


Figure 7.6 Total pressure coefficient contours at rotor exit (Absolute frame)

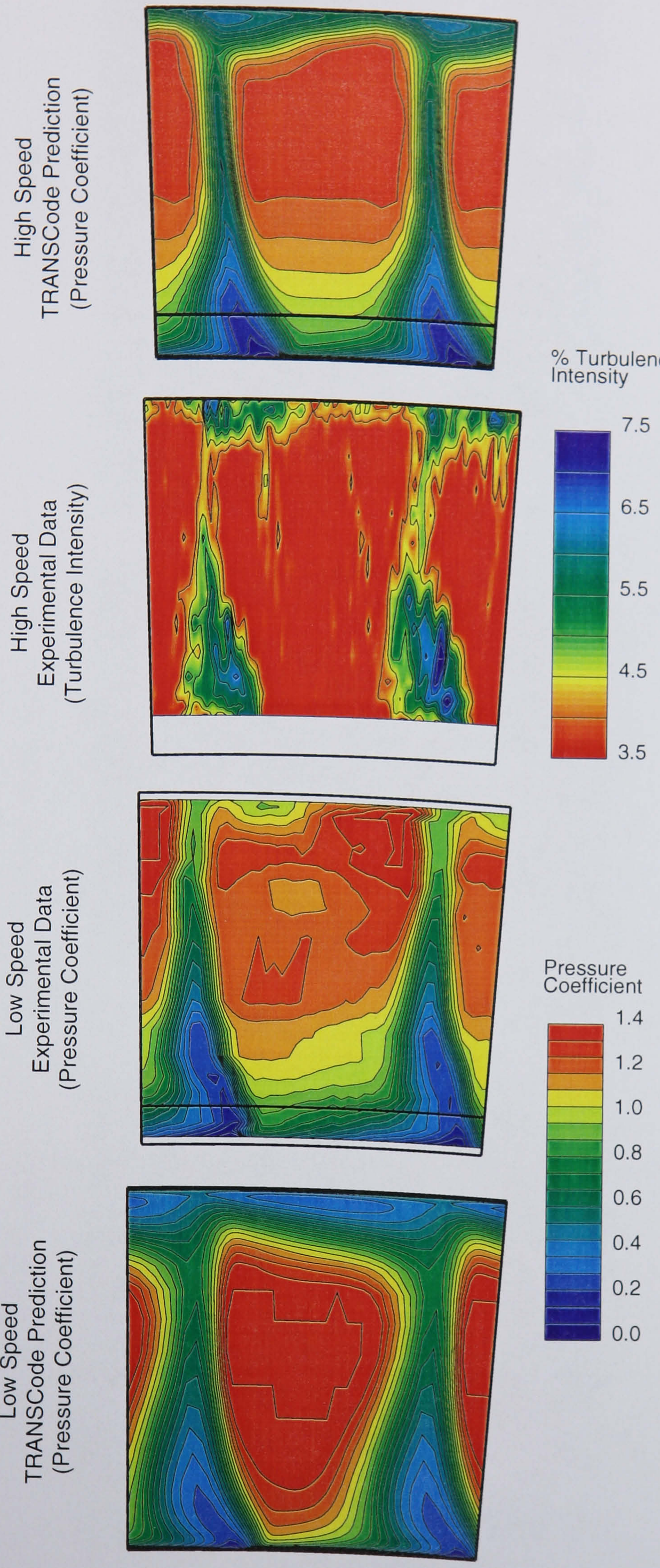
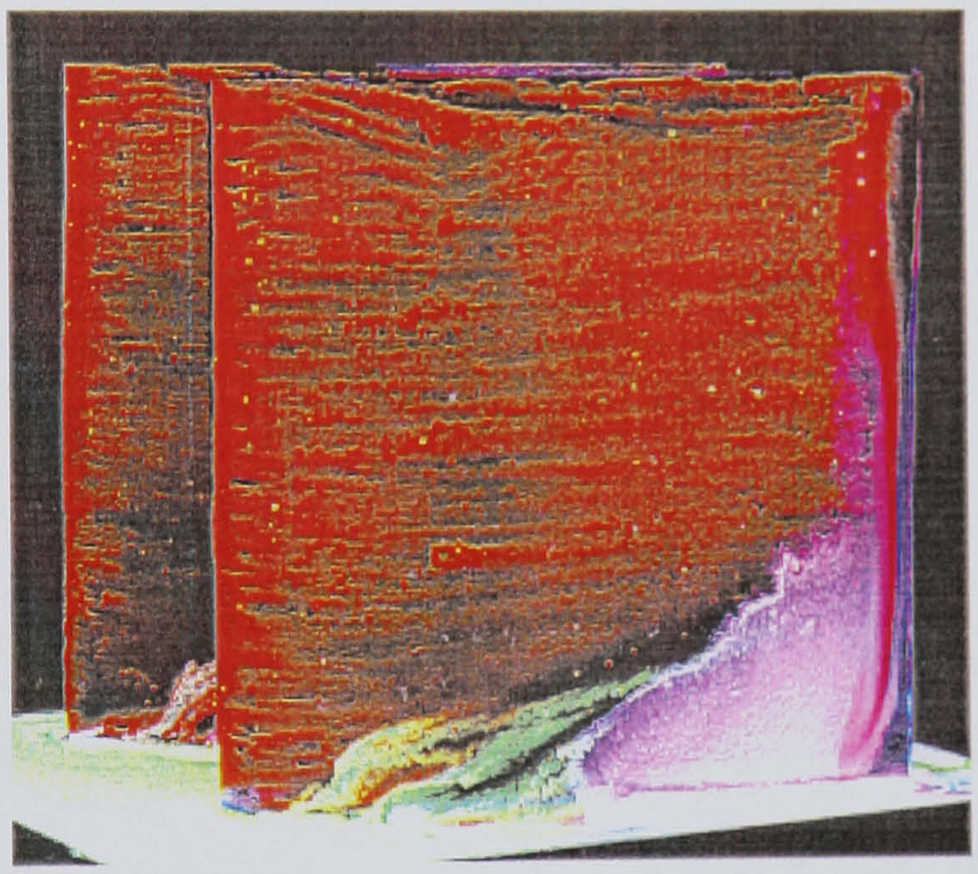


Figure 7.7 Total pressure and turbulence contours at rotor exit

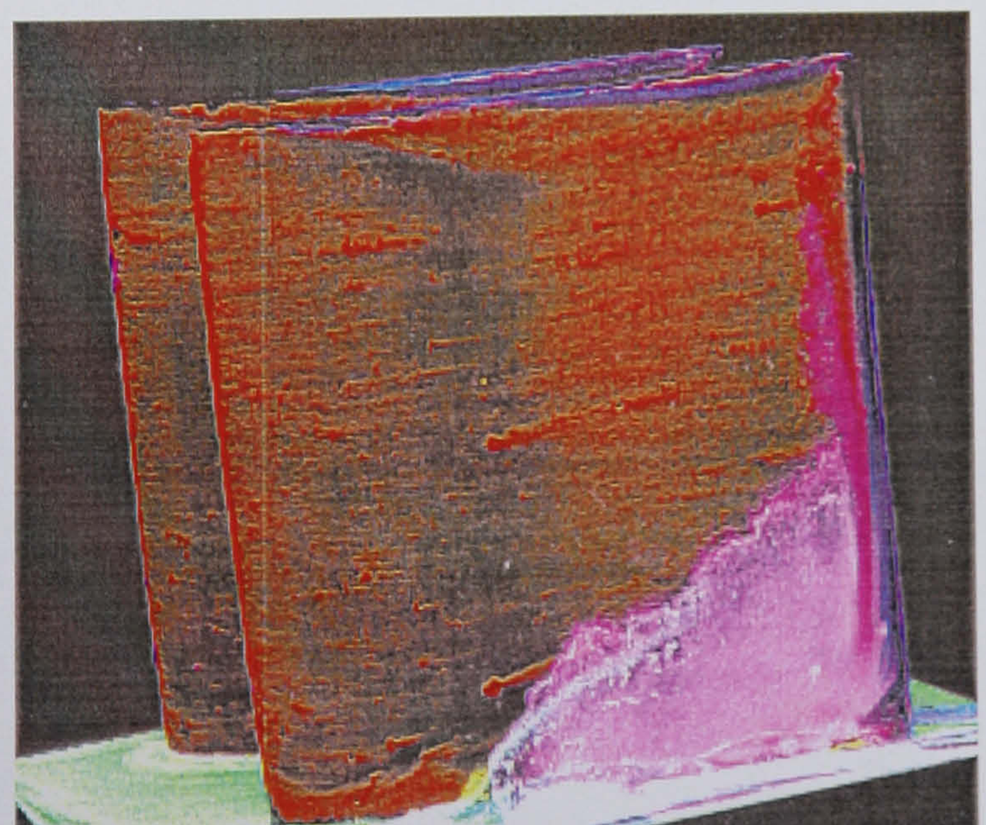
(Relative frame)



C147 stator



DERA1 Design Flow



DERA1 Near Stall

Figure 7.8 C147 and DERA1 stator flow visualisation

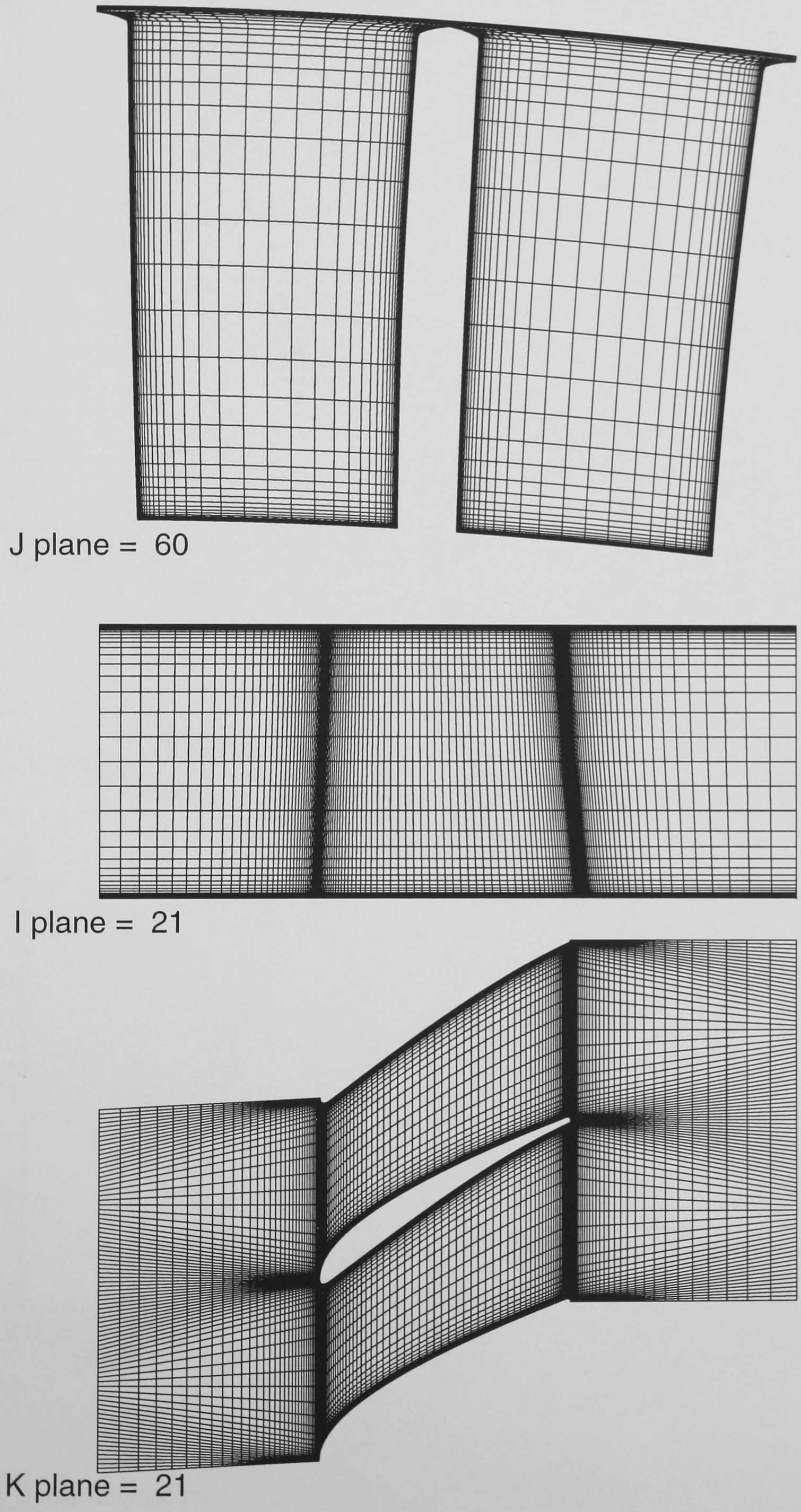
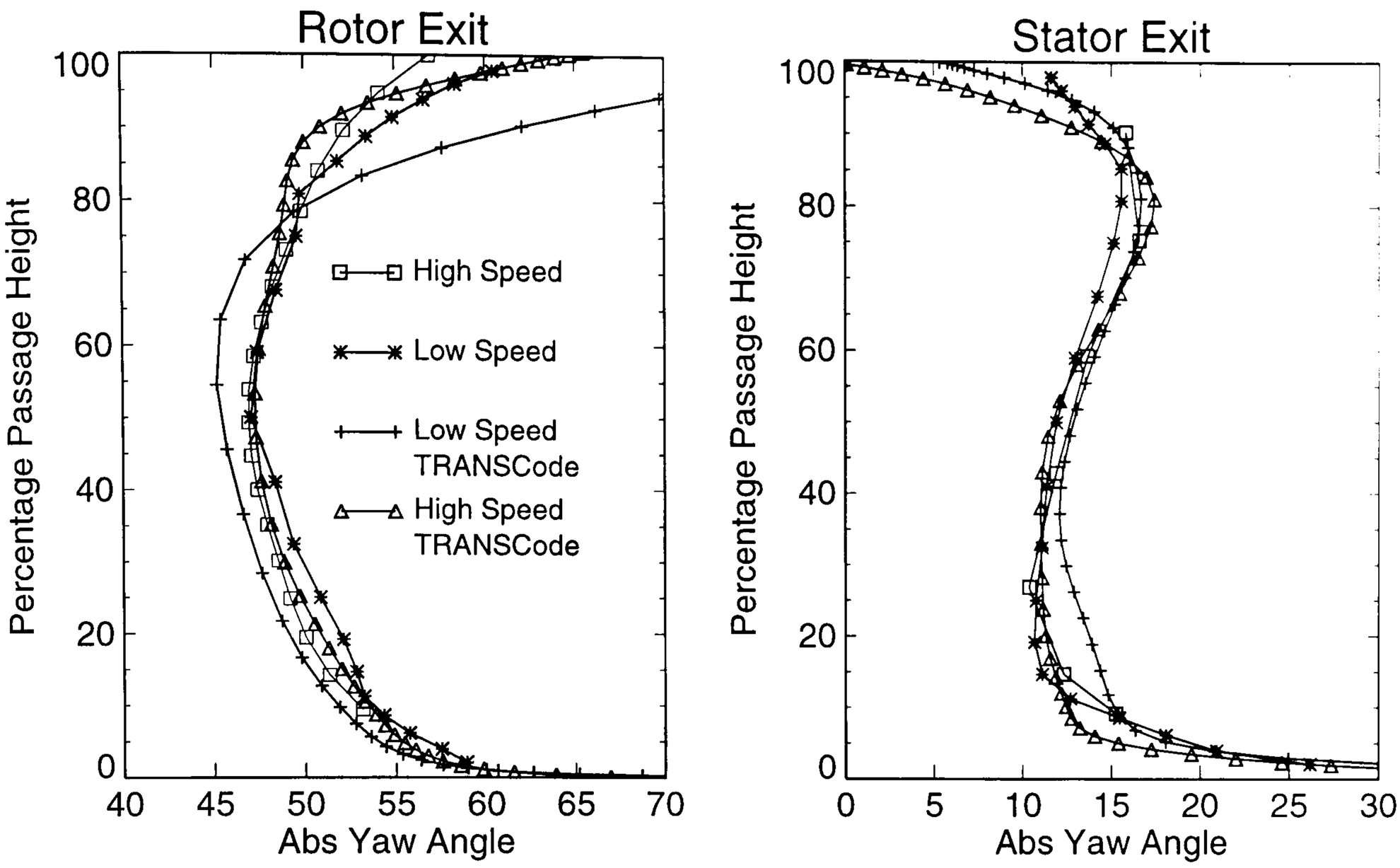


Figure 7.9 TRANSCode grid for DERA1 rotor



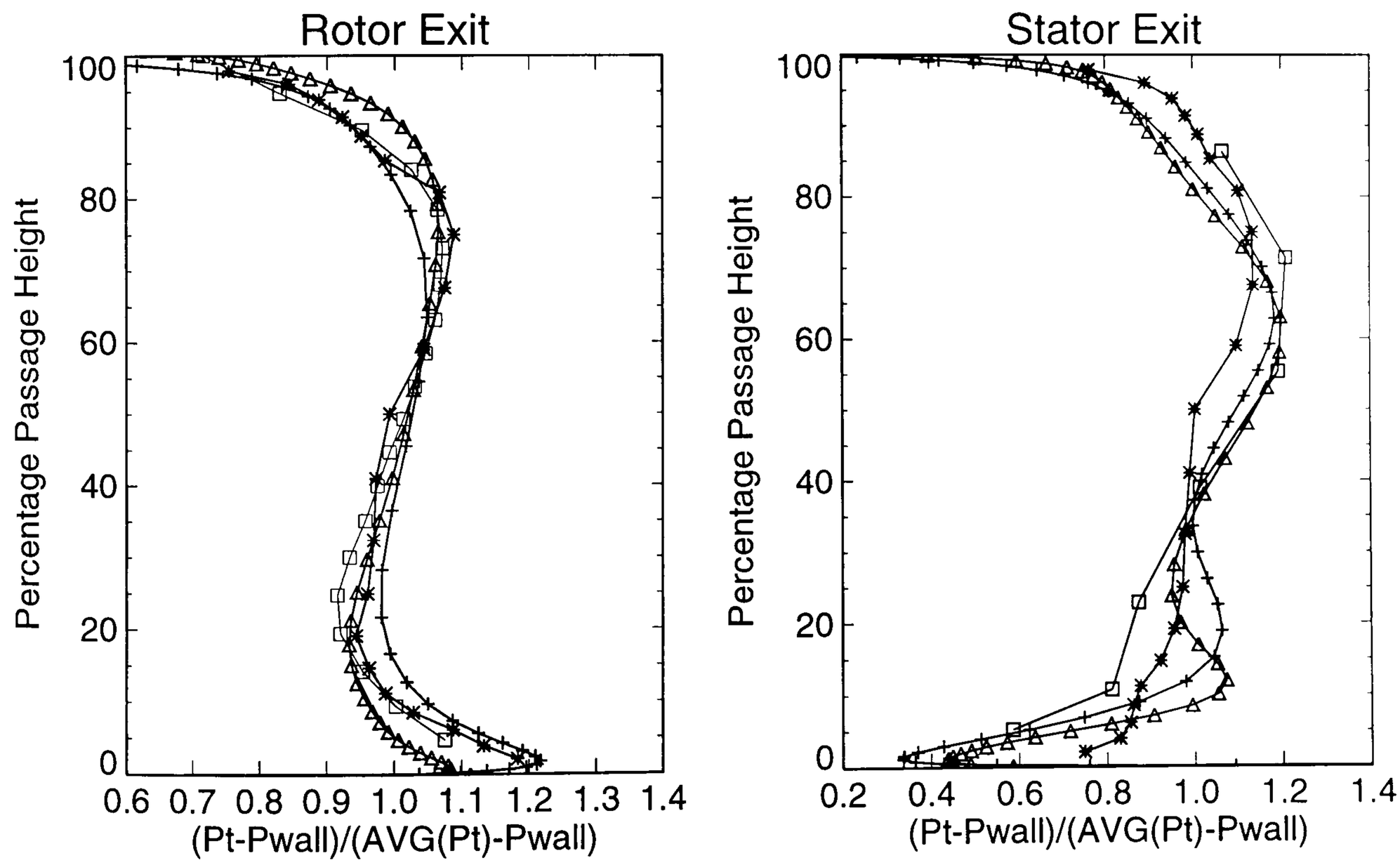


Figure 7.10 Rotor and stator exit profiles (including TRANSCode predictions)

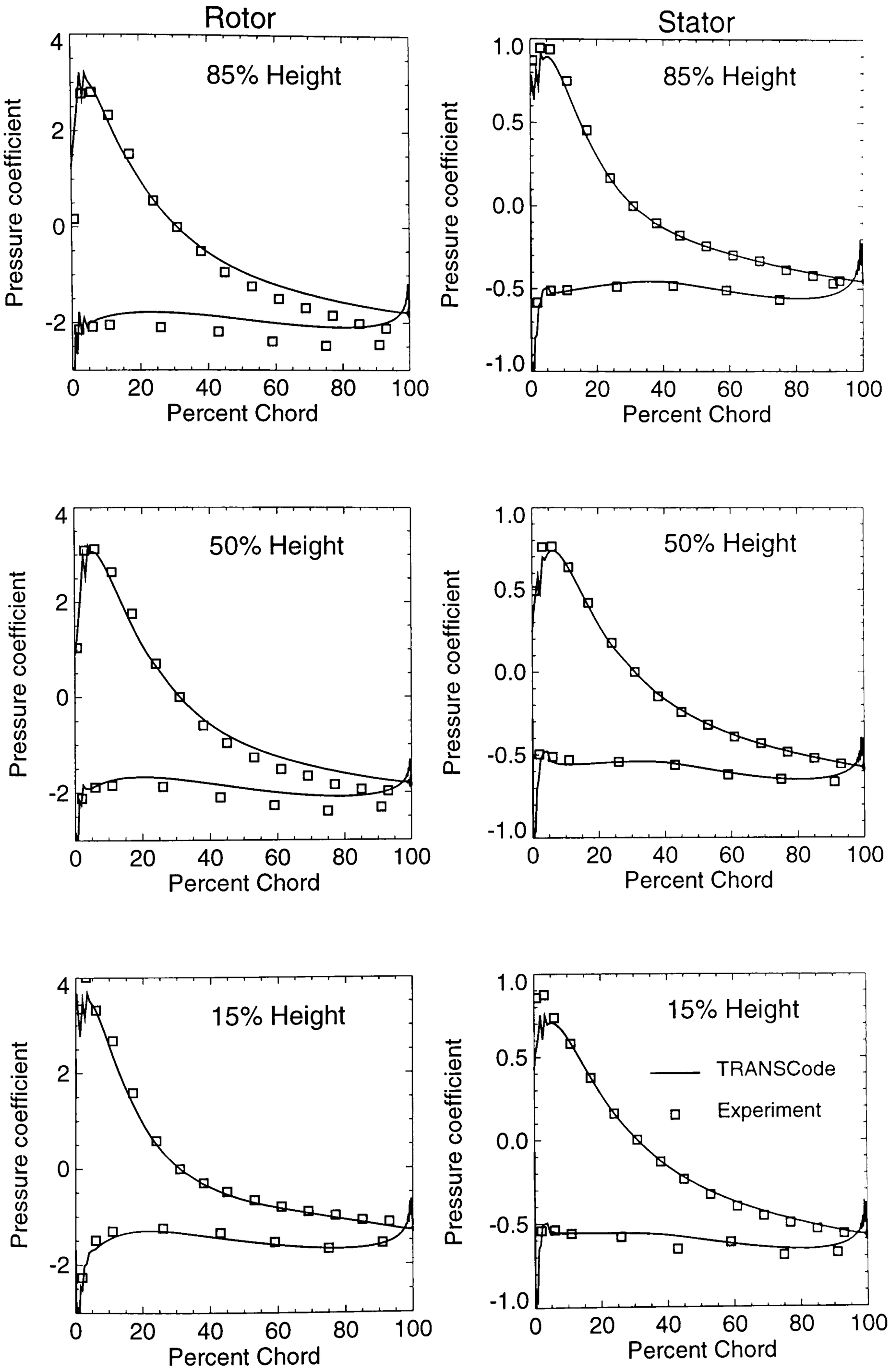
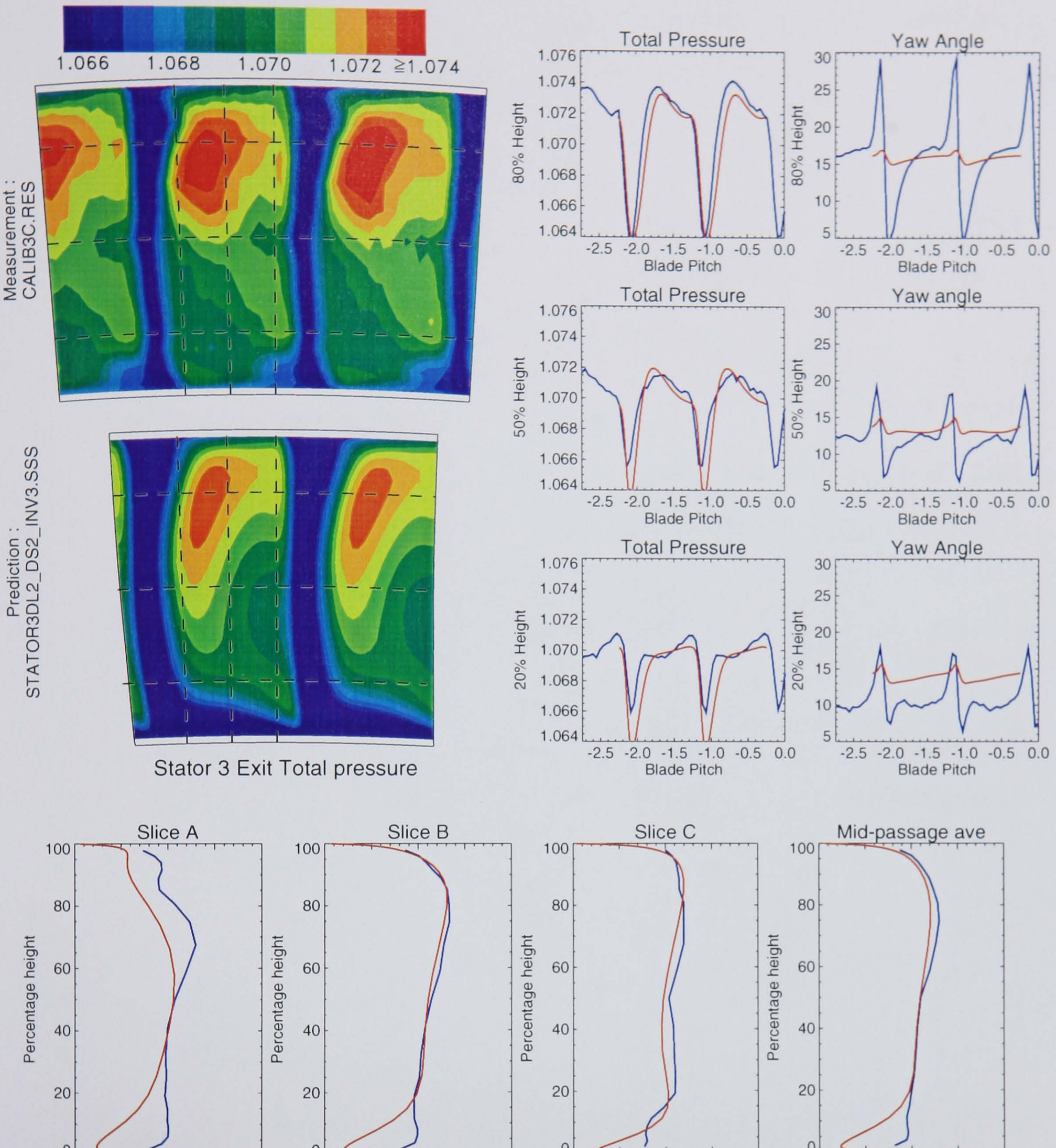
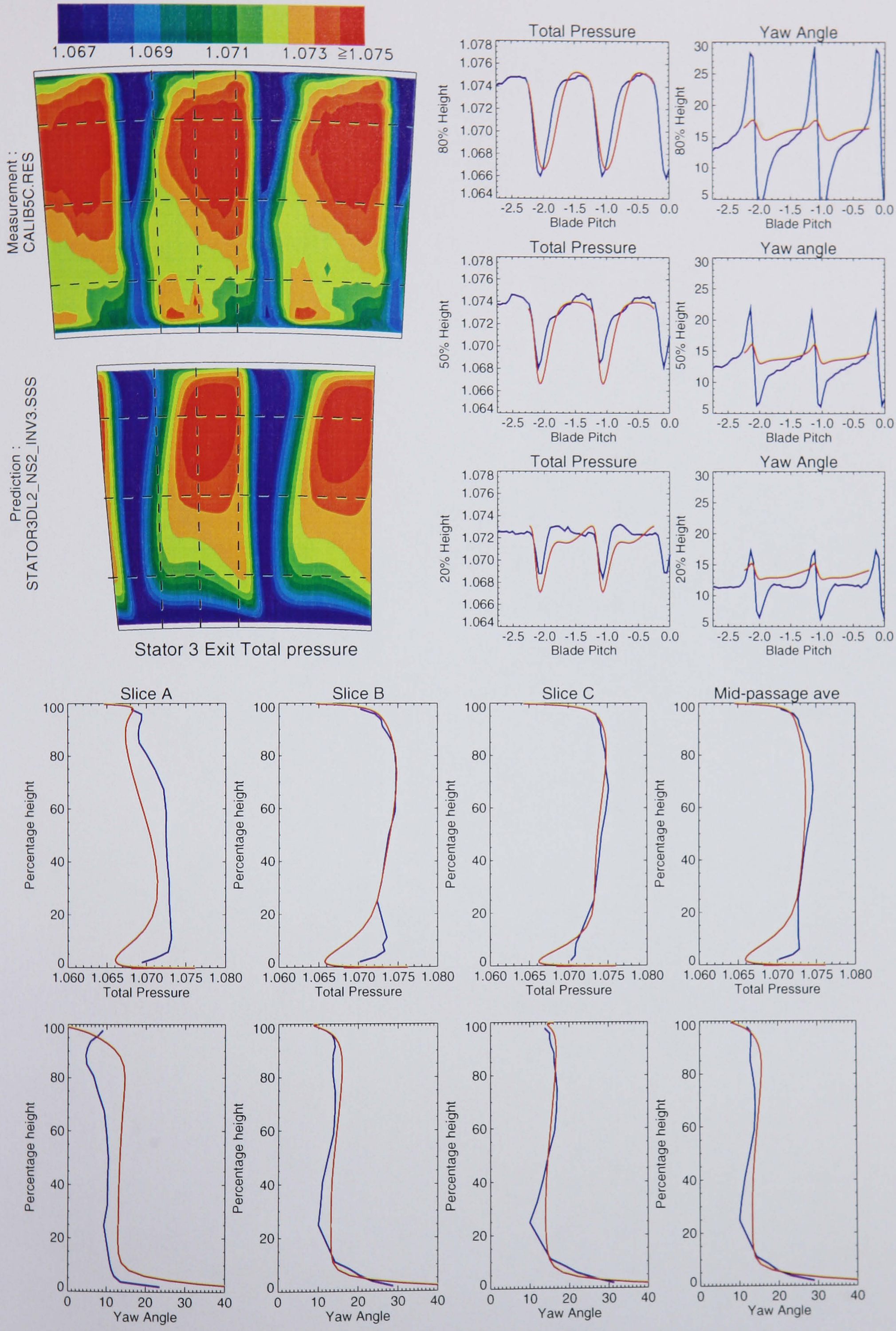


Figure 7.11 Blade surface static pressure distributions



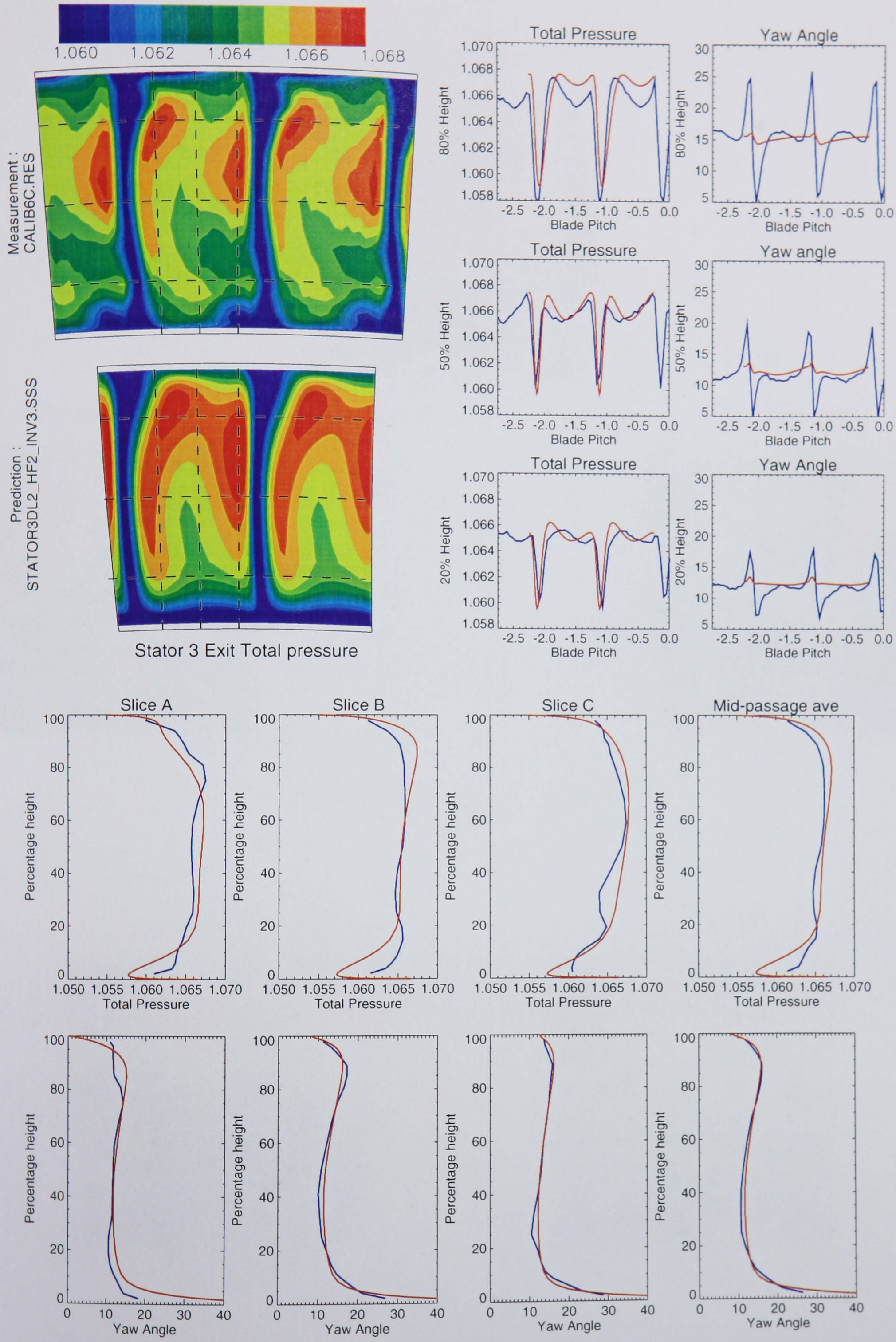
Stator 3 Exit Total pressure

Figure 7.12 Comparison of TRANSCode solution with inlet boundary circumferential variation to test at design flow



Stator 3 Exit Total pressure

Figure 7.13 Comparison of TRANSCode solution with inlet boundary circumferential variation to test at near stall flow



Stator 3 Exit Total pressure

Figure 7.14 Comparison of TRANSCode solution with inlet boundary circumferential variation to test at high flow

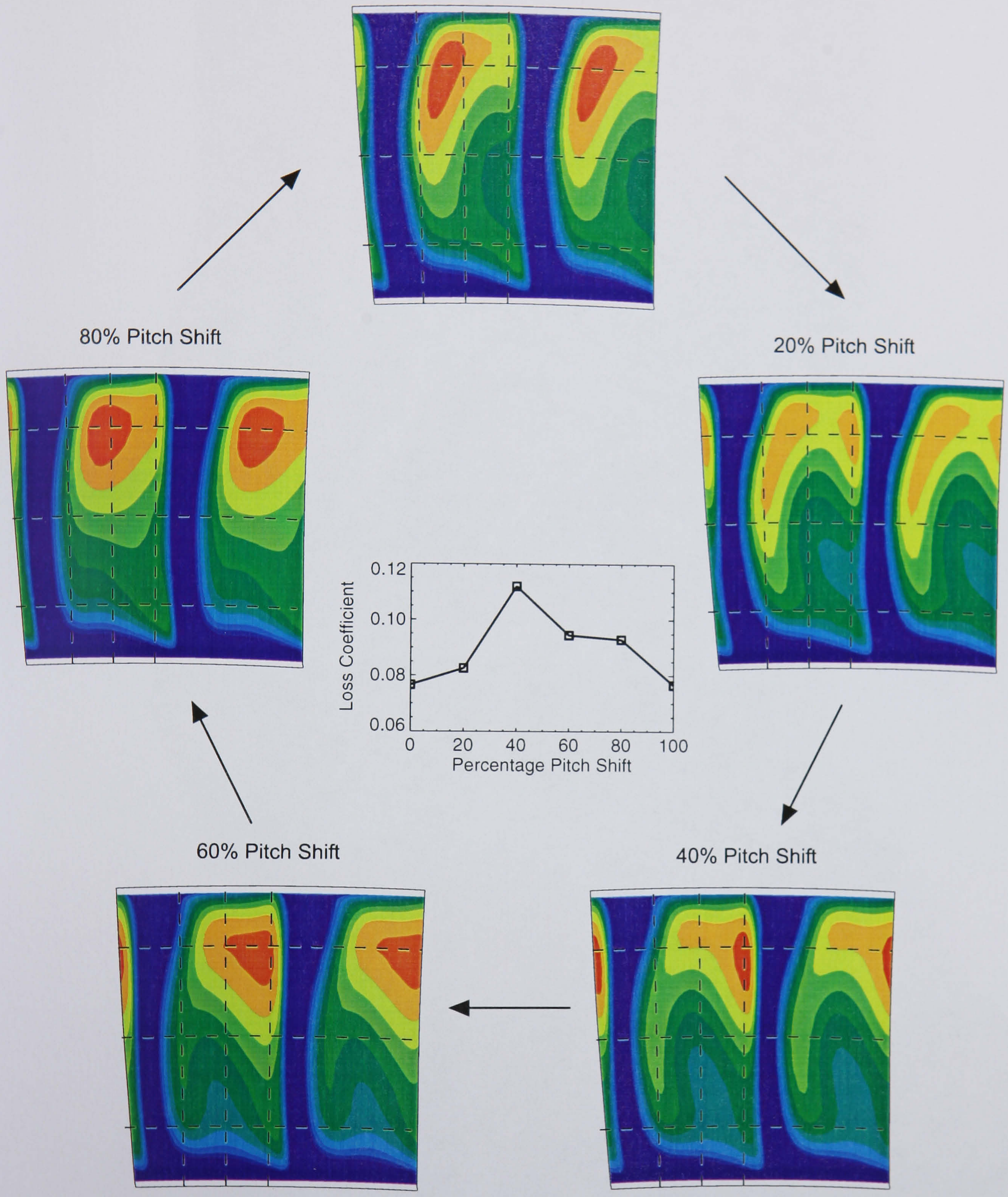


Figure 7.15 Effect of changing relative circumferential position of upstream total pressure field on stator 3 exit

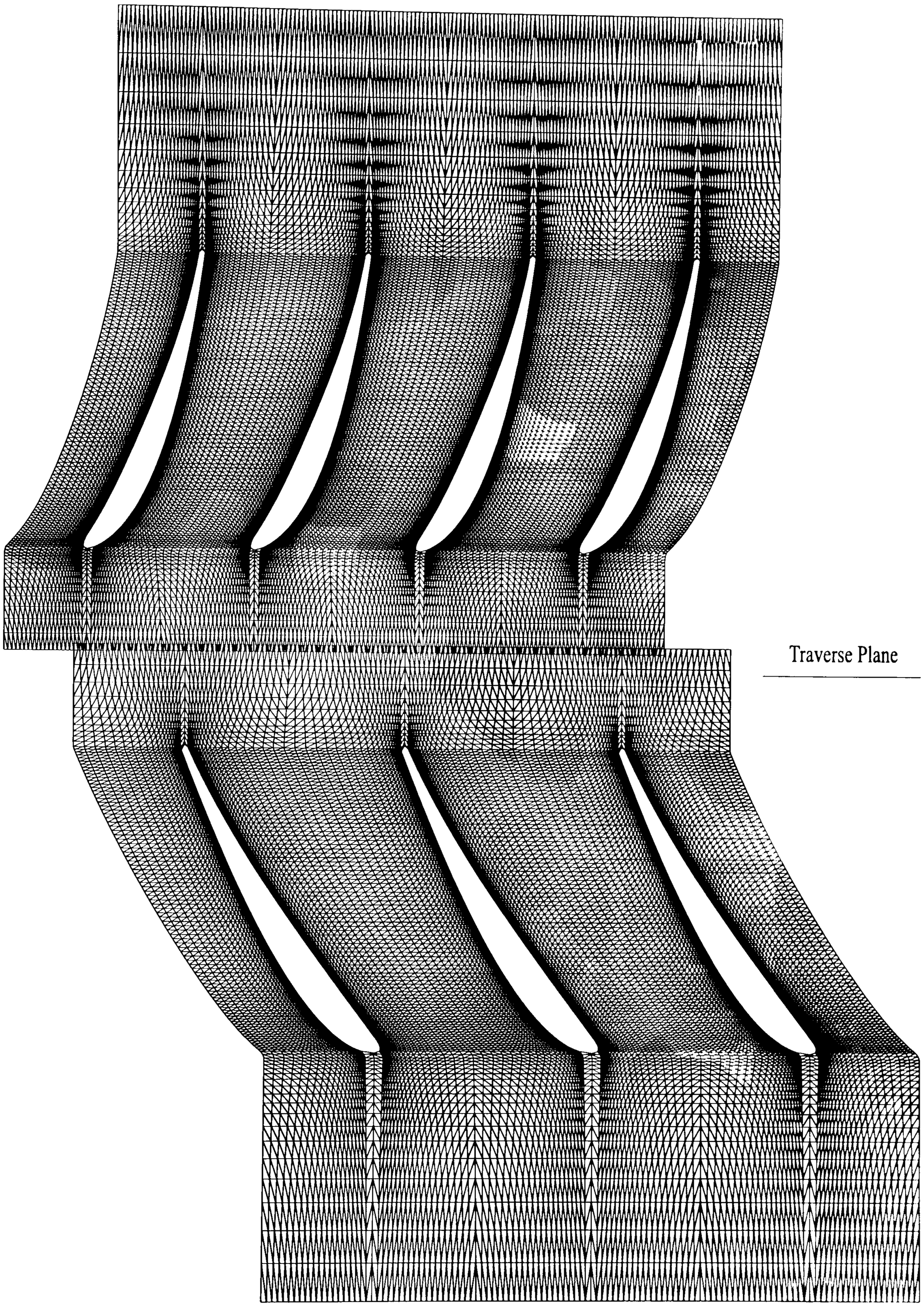


Figure 7.16 Un-NEWT blade-to-blade grid

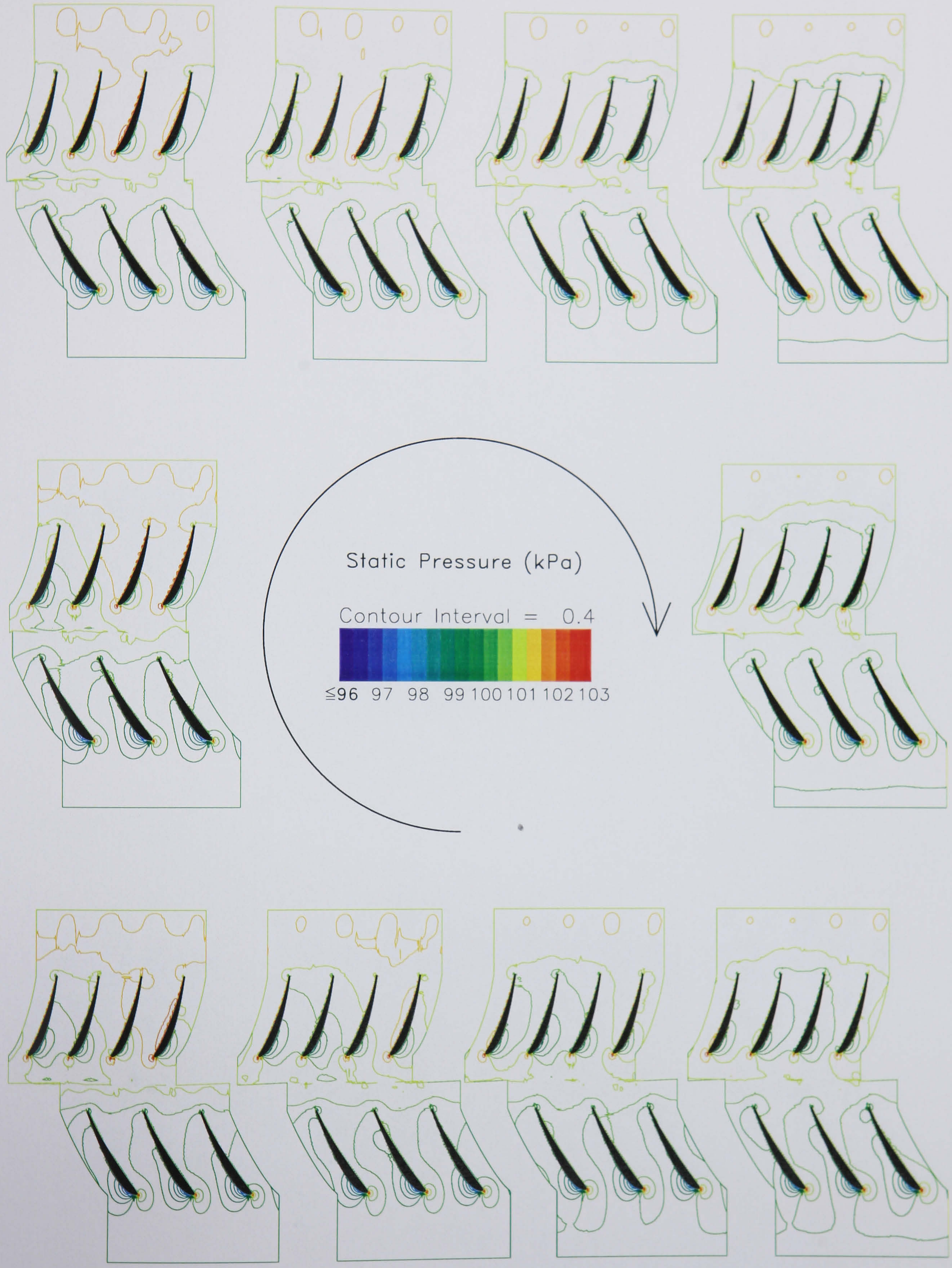


Figure 7.17 Static pressure variations from Un-NEWT

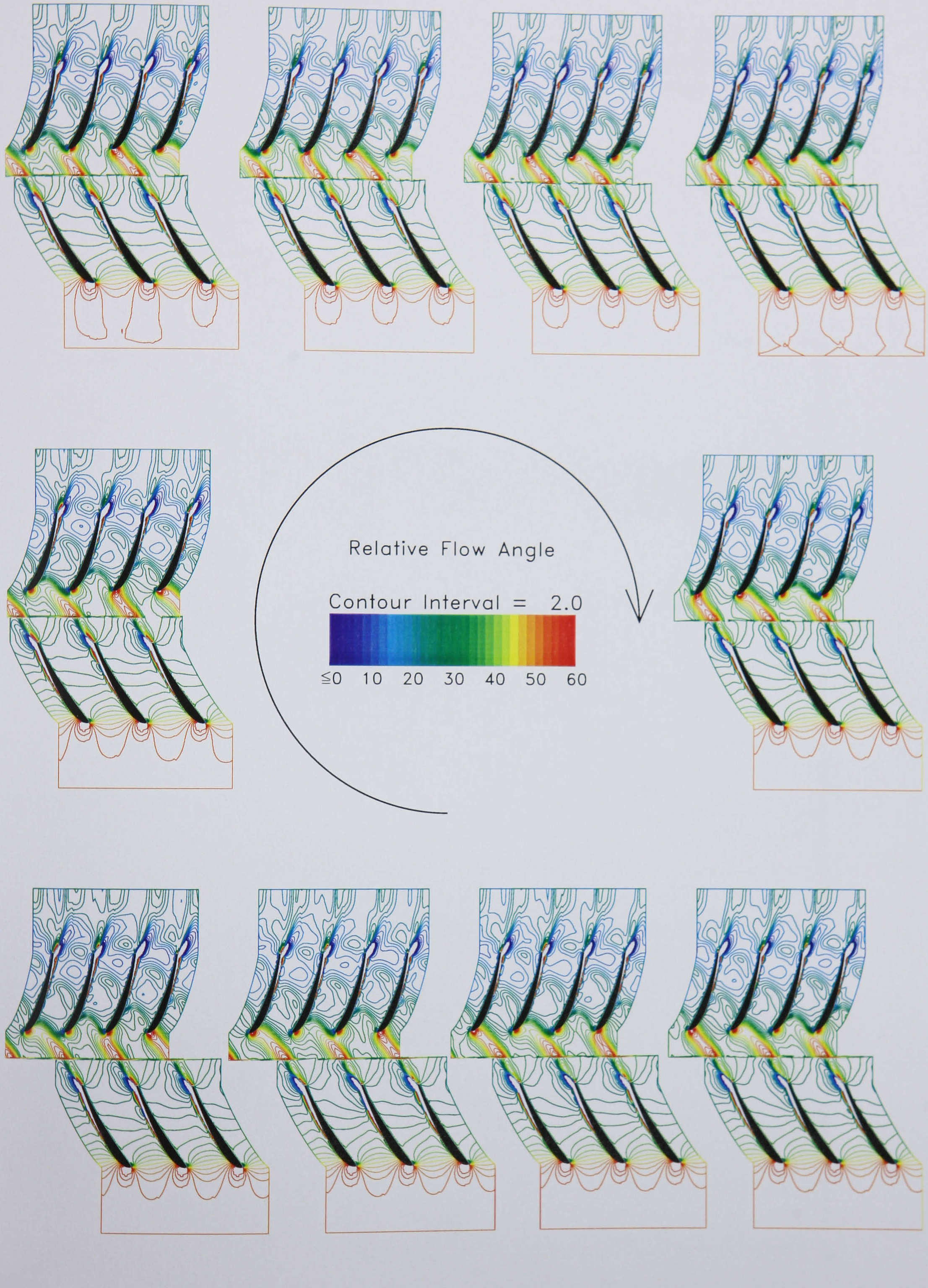


Figure 7.18 Relative flow angle variations from Un-NEWT

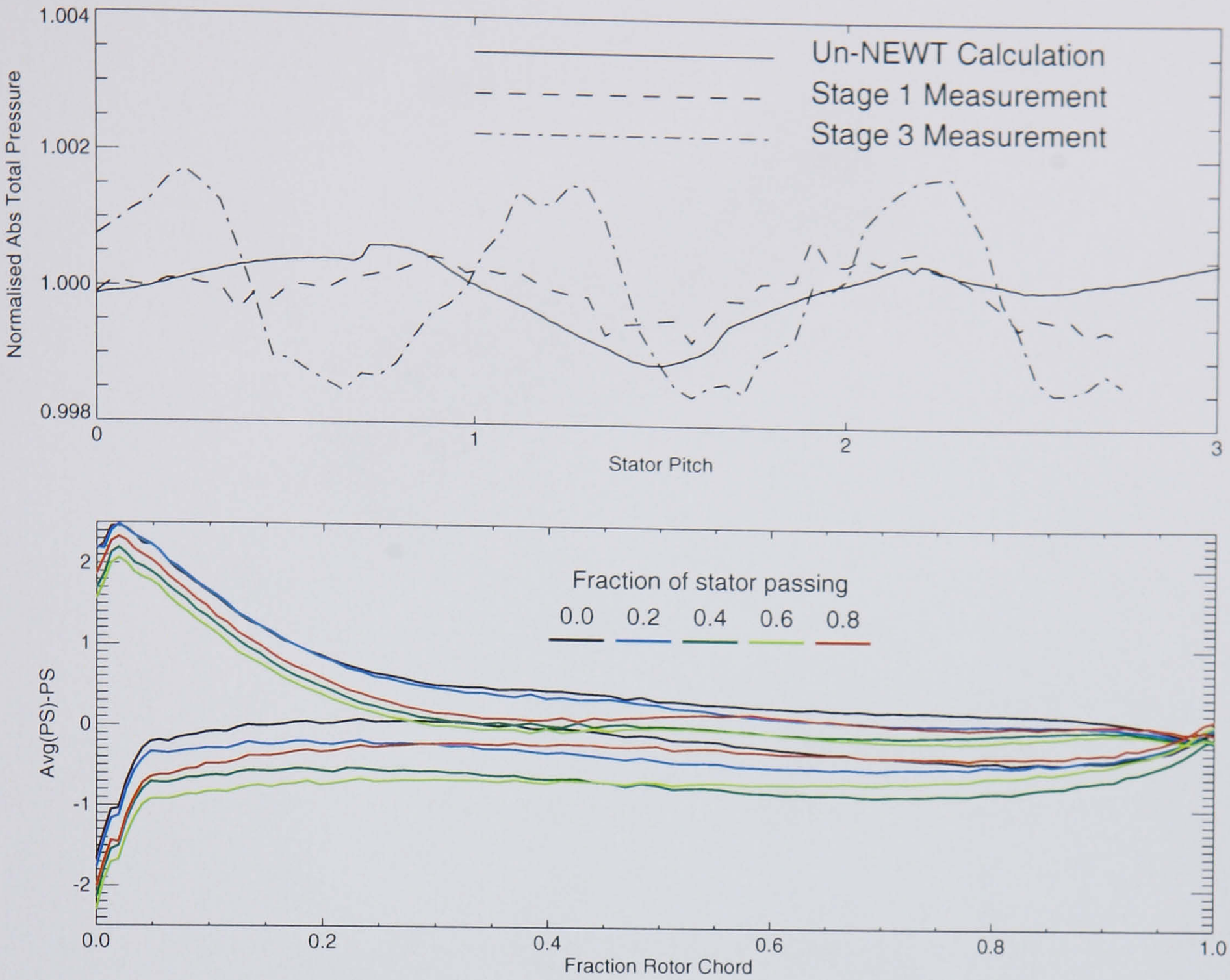


Figure 7.19 Rotor performance variations due to downstream stator

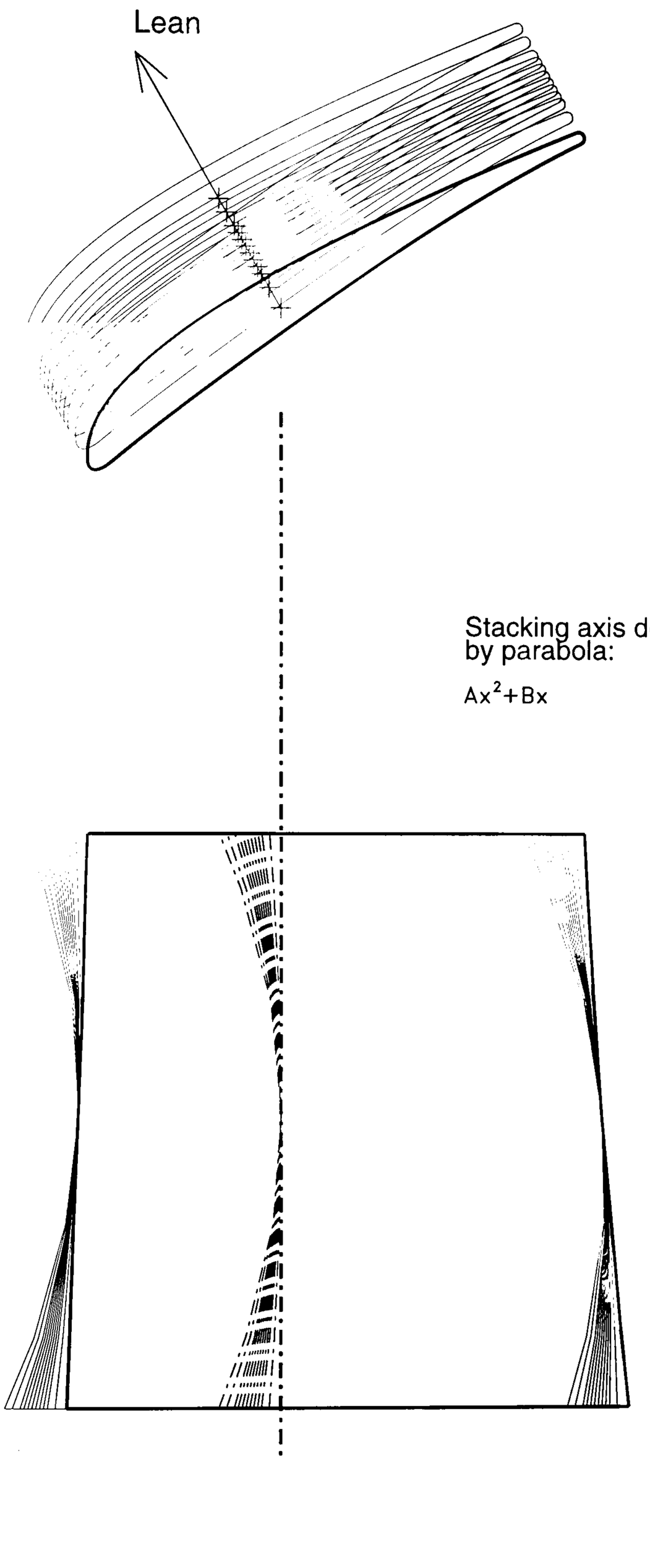
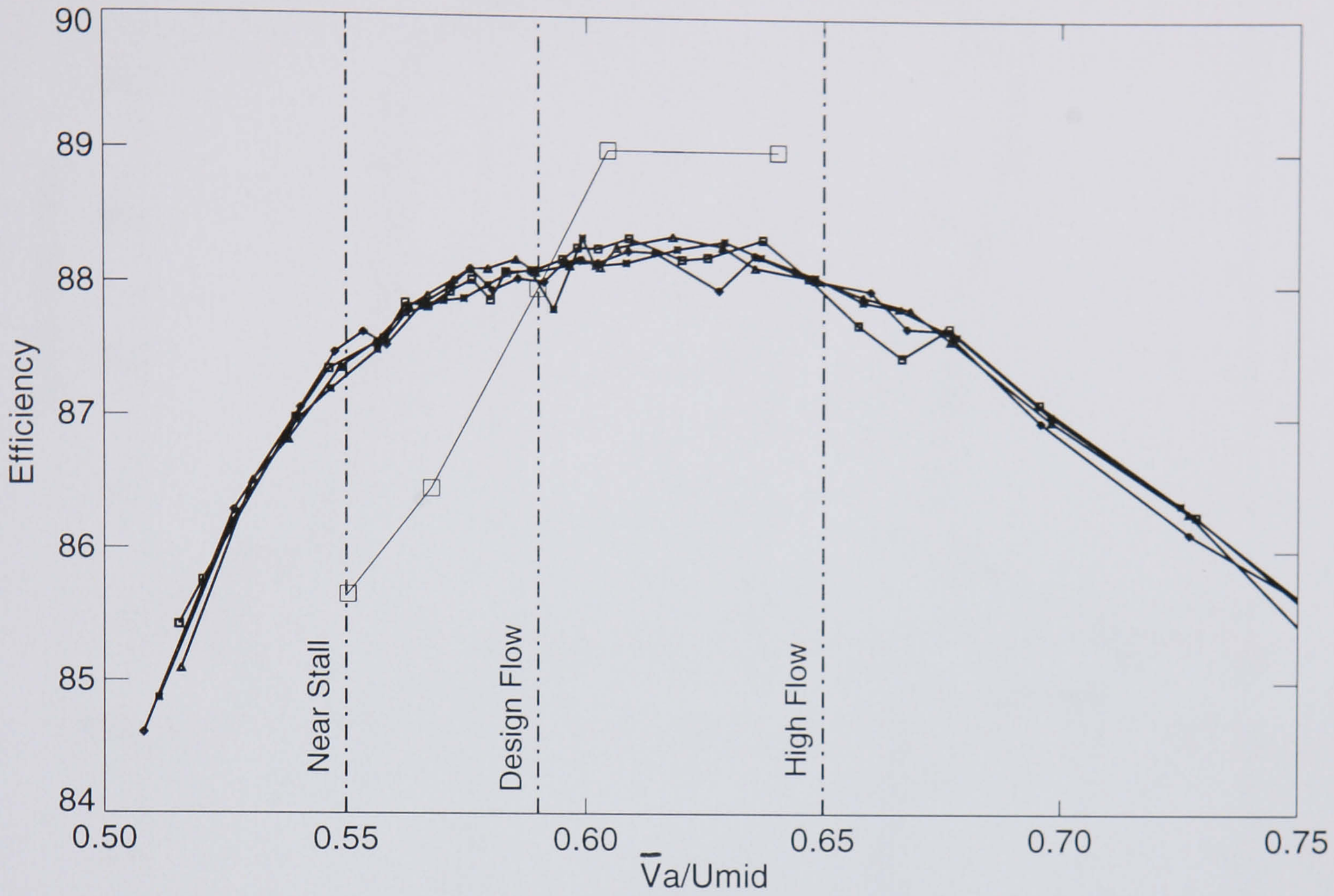


Figure 8.1 Definition of lean used in 3D design



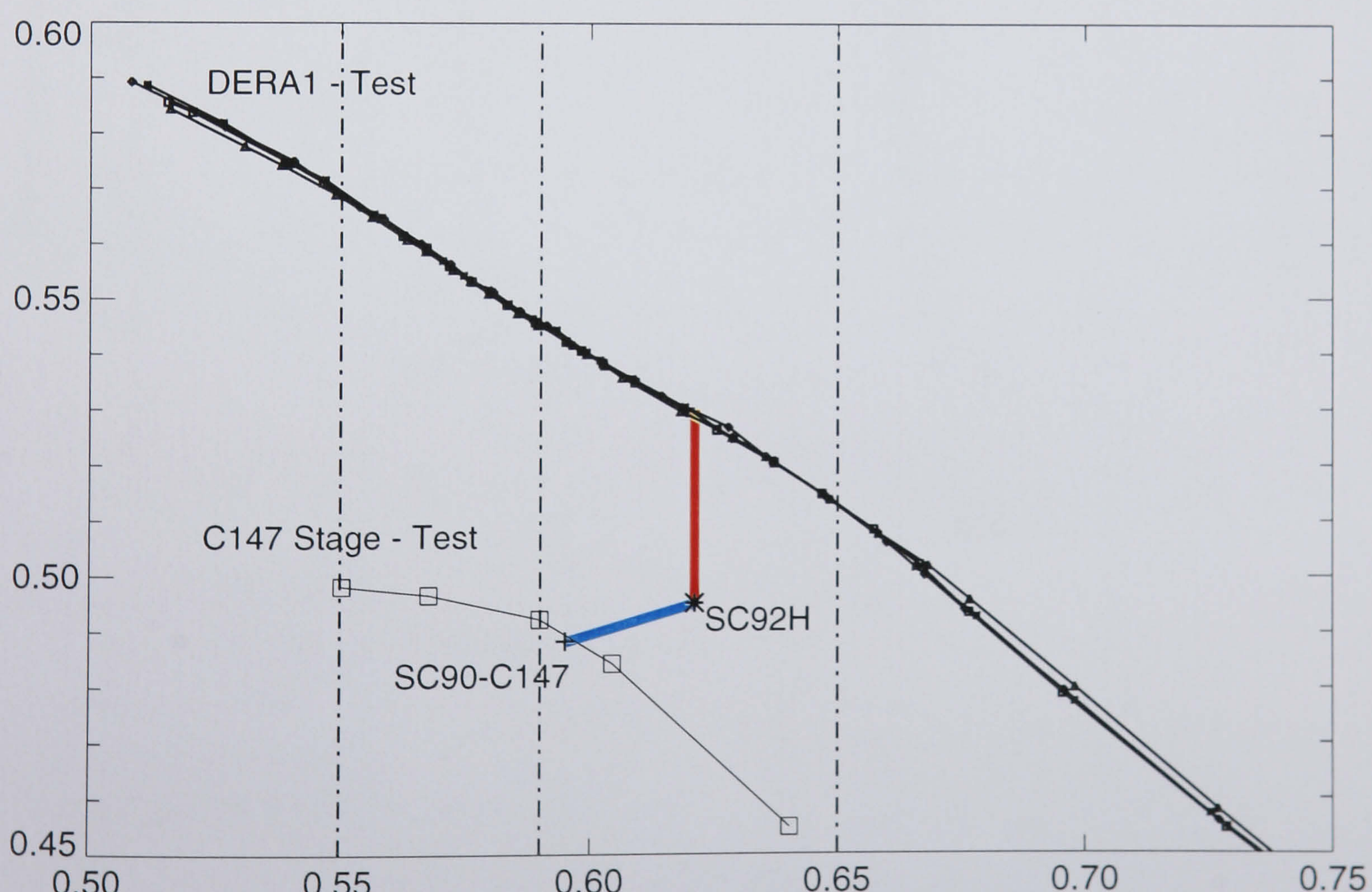


Figure 7.1 High and low speed stage performance

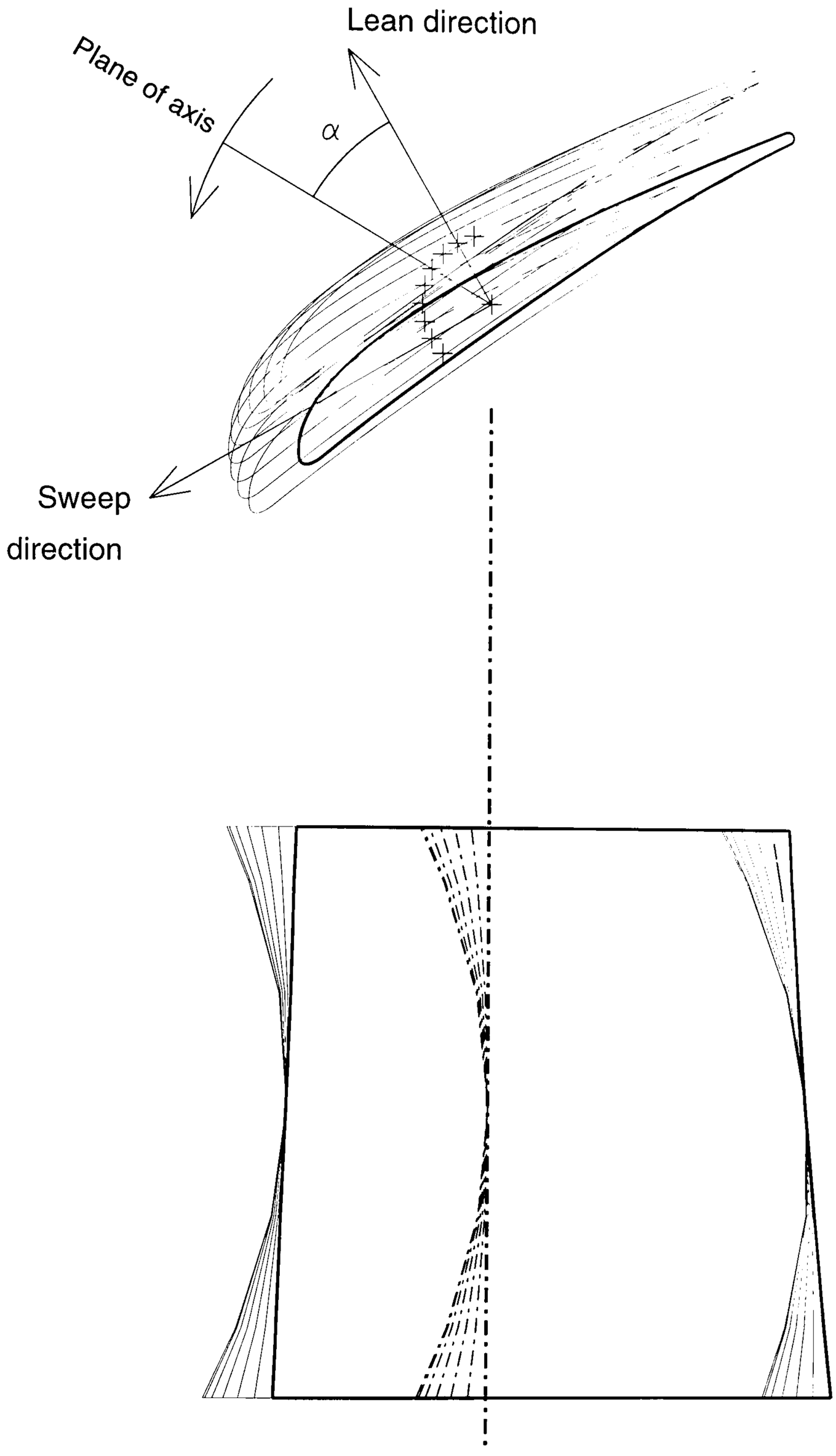


Figure 8.2 Definition of stacking axis direction angle

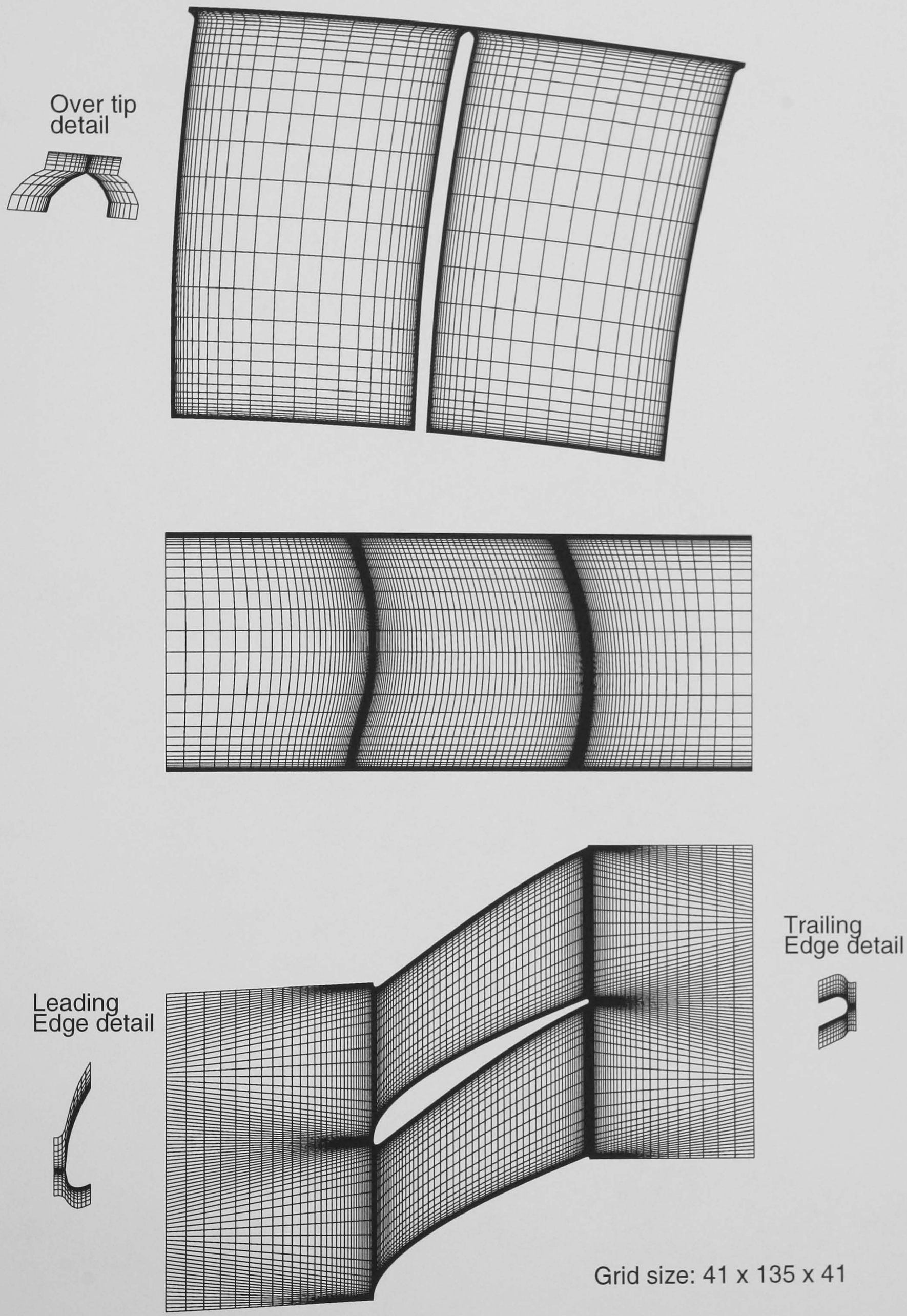


Figure 8.3 Typical grid used in 3D TRANSCode calculation

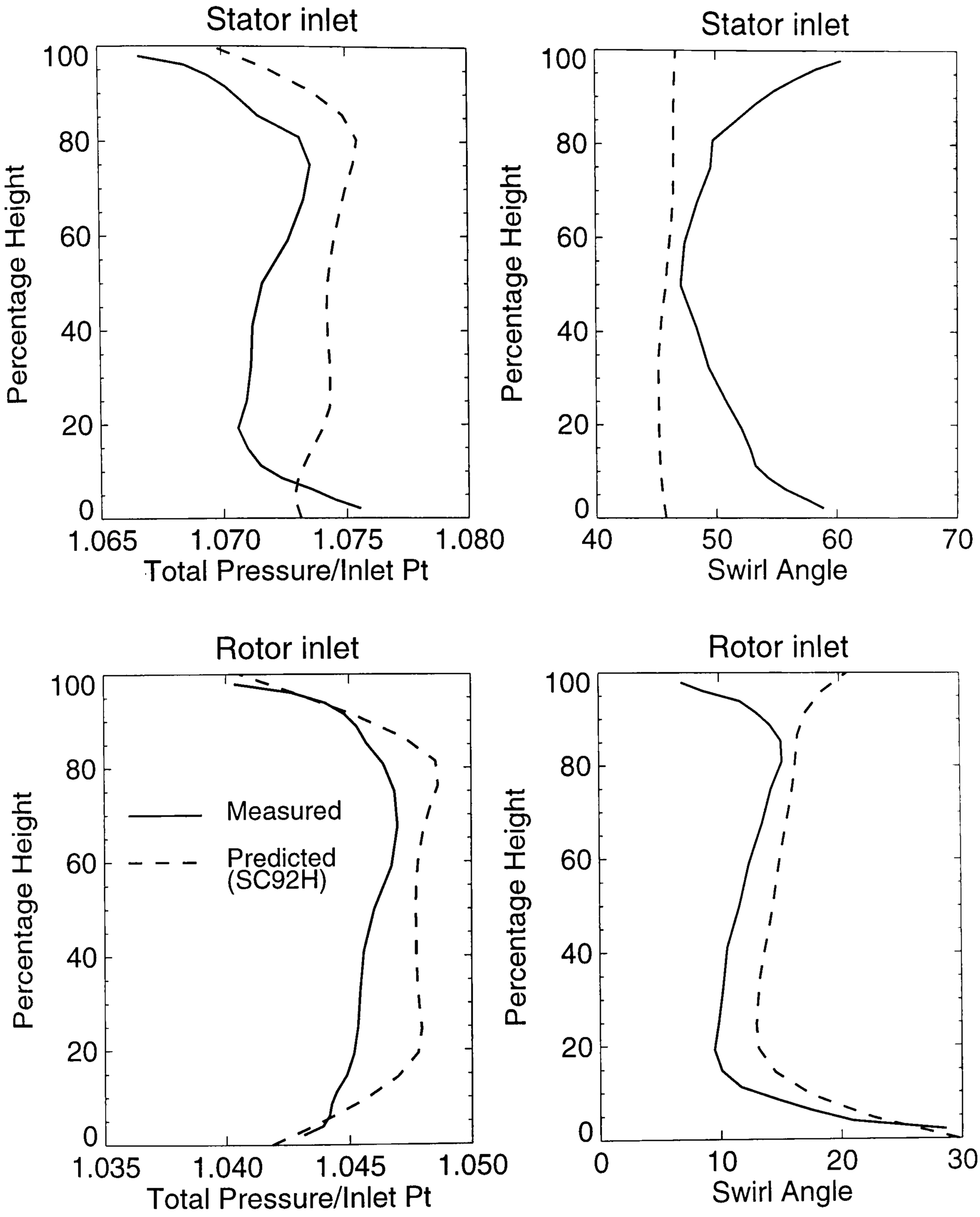


Figure 8.4 Comparison of measured and SC92H predicted rotor inlet profiles

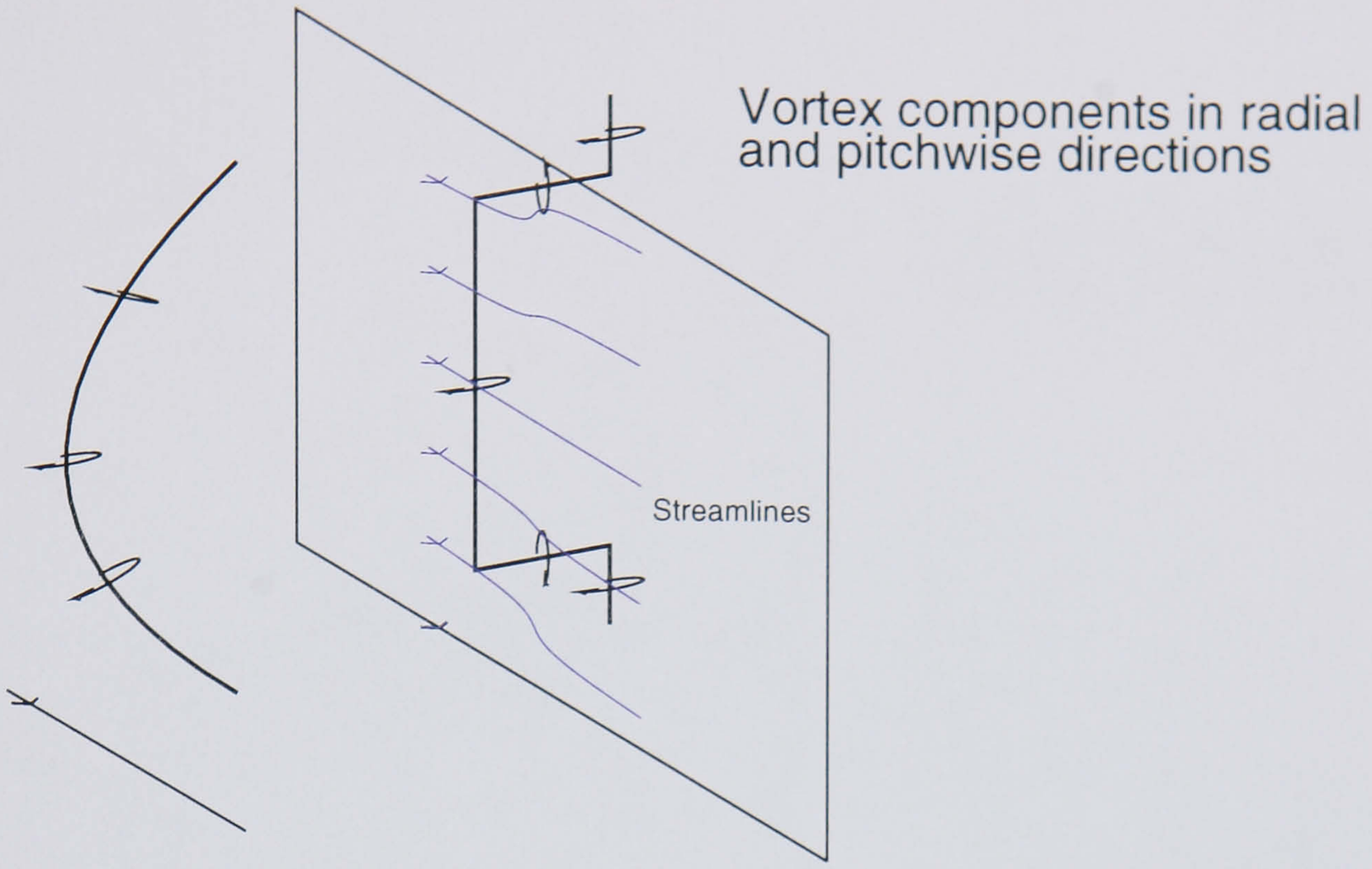


Figure 8.5 Line vortex study of the effect of lean

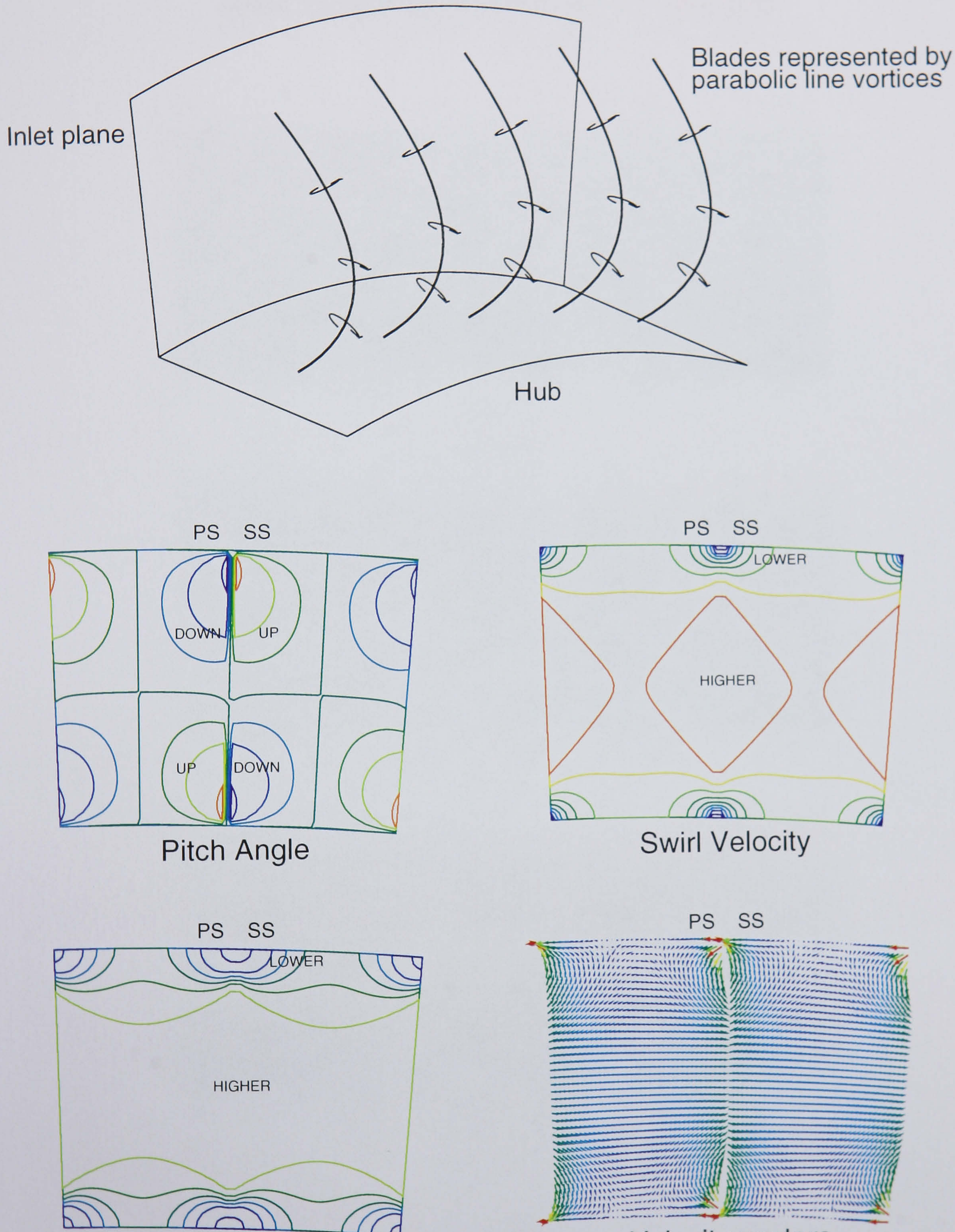


Figure 8.6 Line vortex study of the effects of sweep

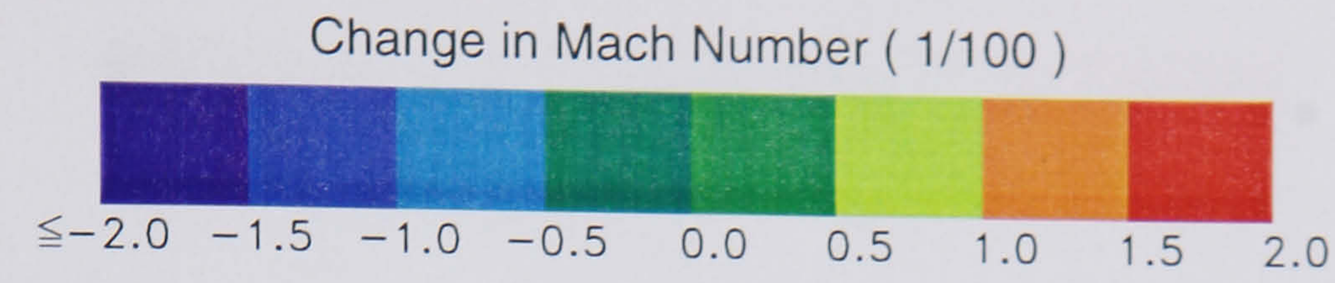


Figure 8.7 Pitchwise average Mach number difference contours (Rotor)

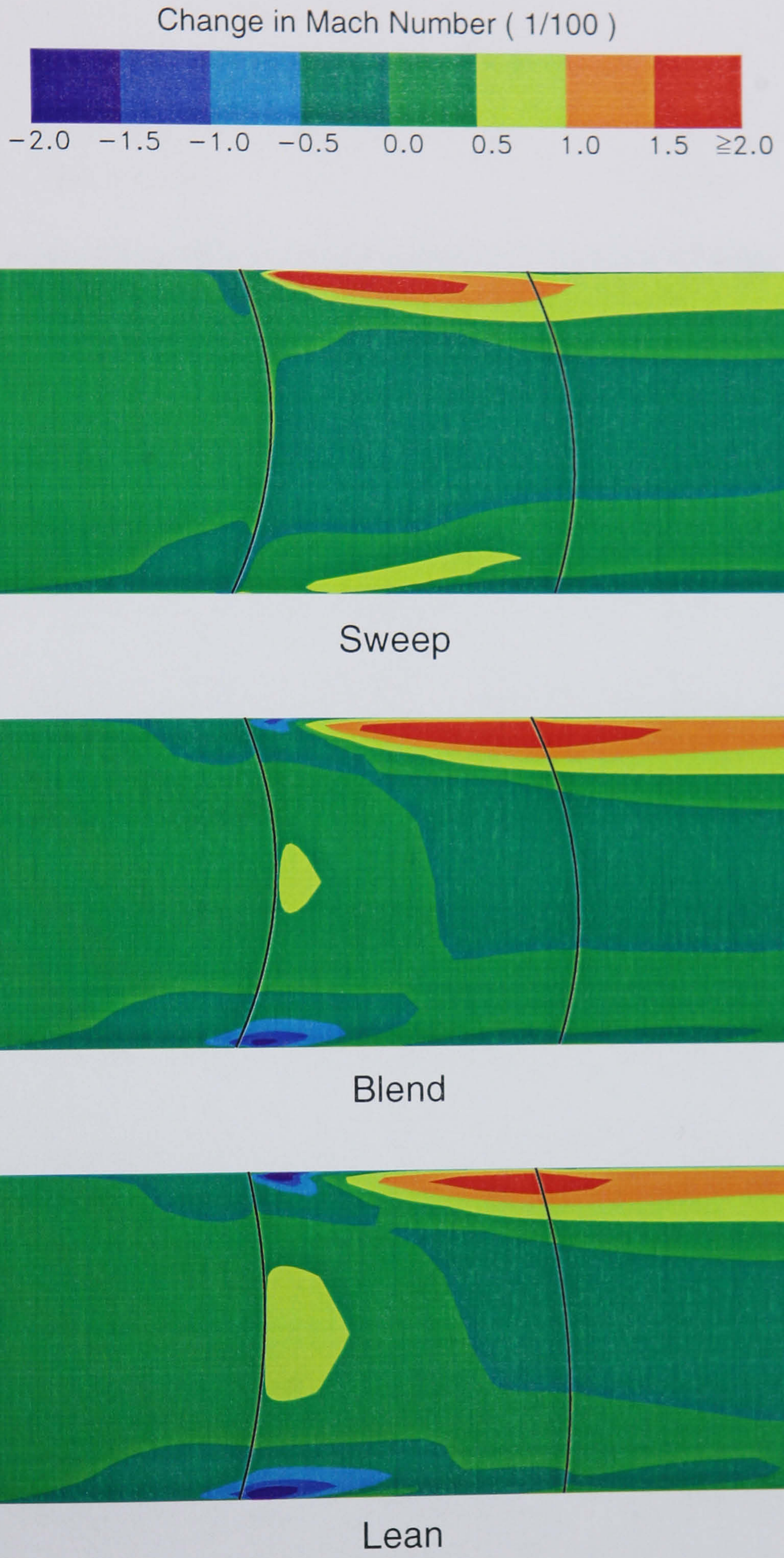


Figure 8.8 Pitchwise average Mach number difference contours (Rotor)

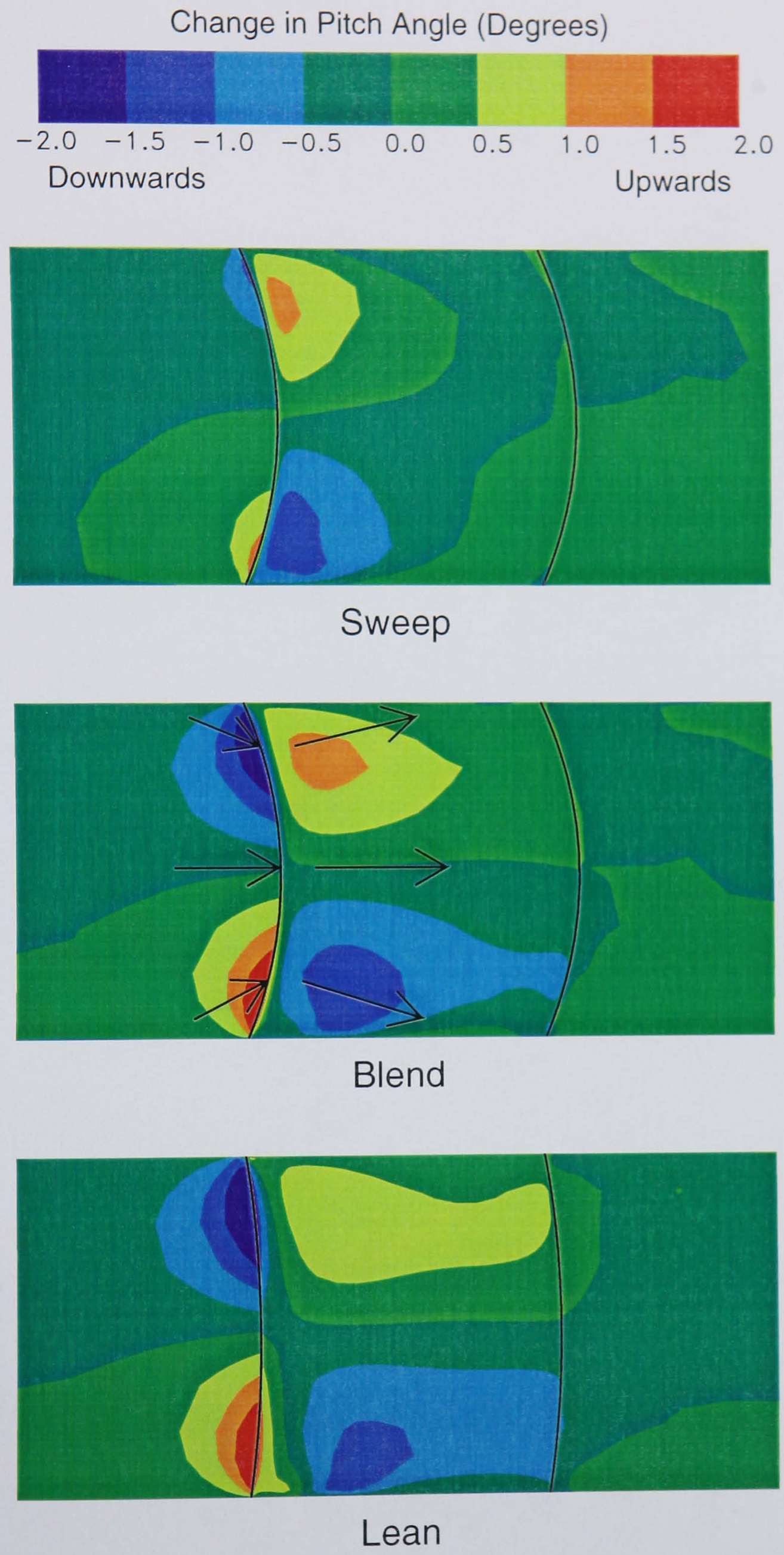


Figure 8.9 Pitchwise average pitch angle difference contours (Stator)

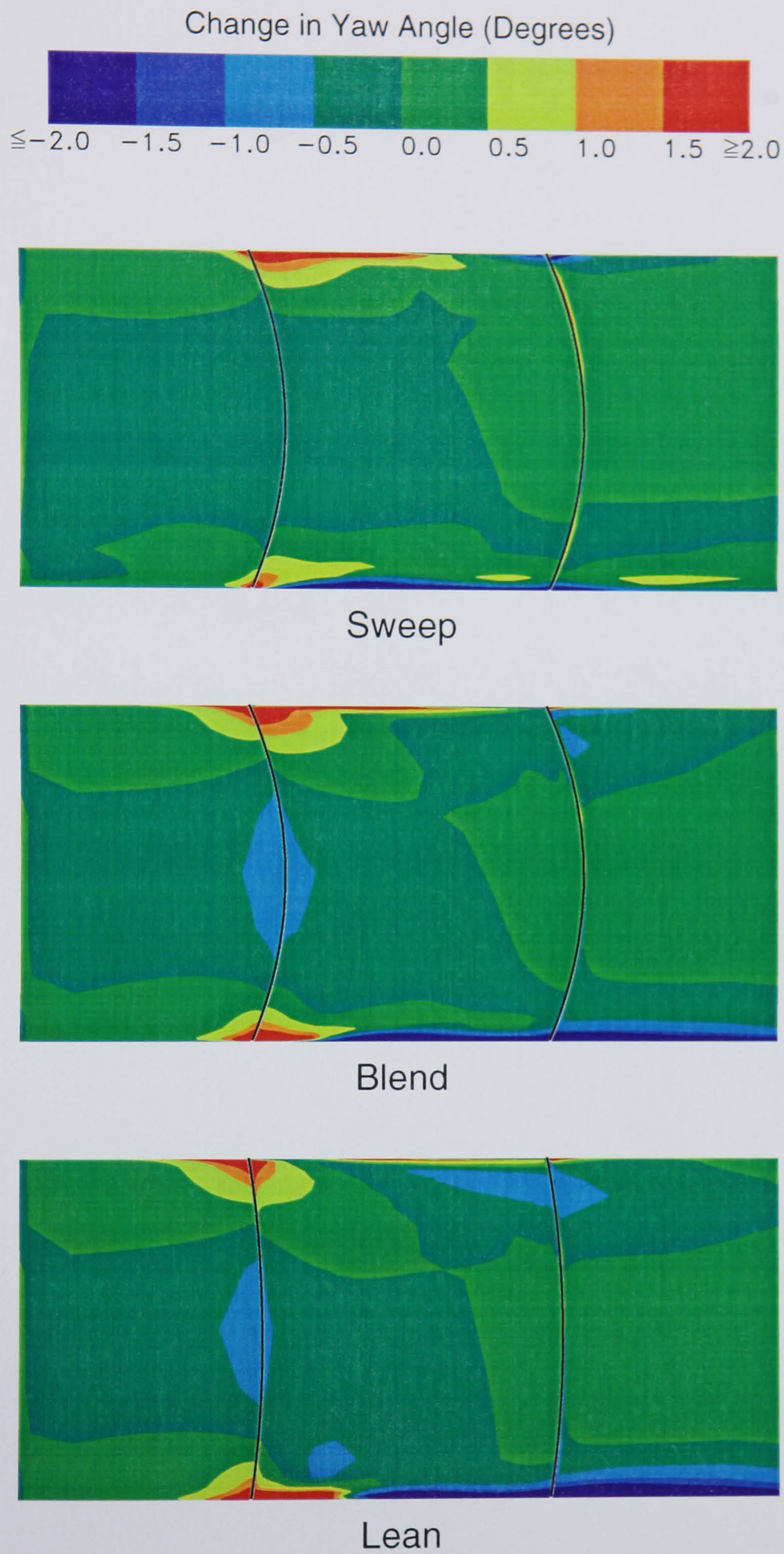


Figure 8.10 Pitchwise average yaw angle difference contours (Stator)

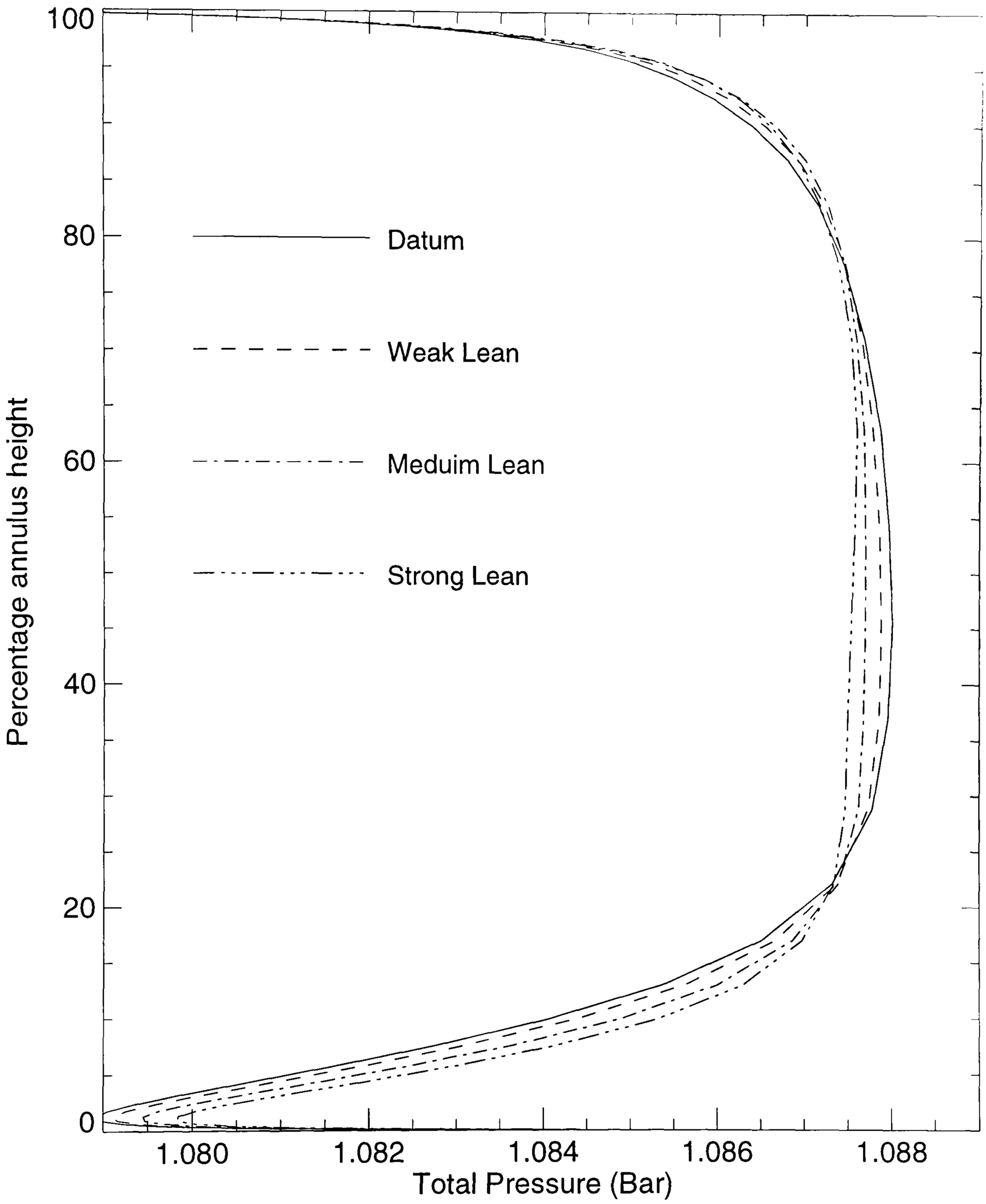


Figure 8.11 Effect of lean on exit total pressure profile (Stator)

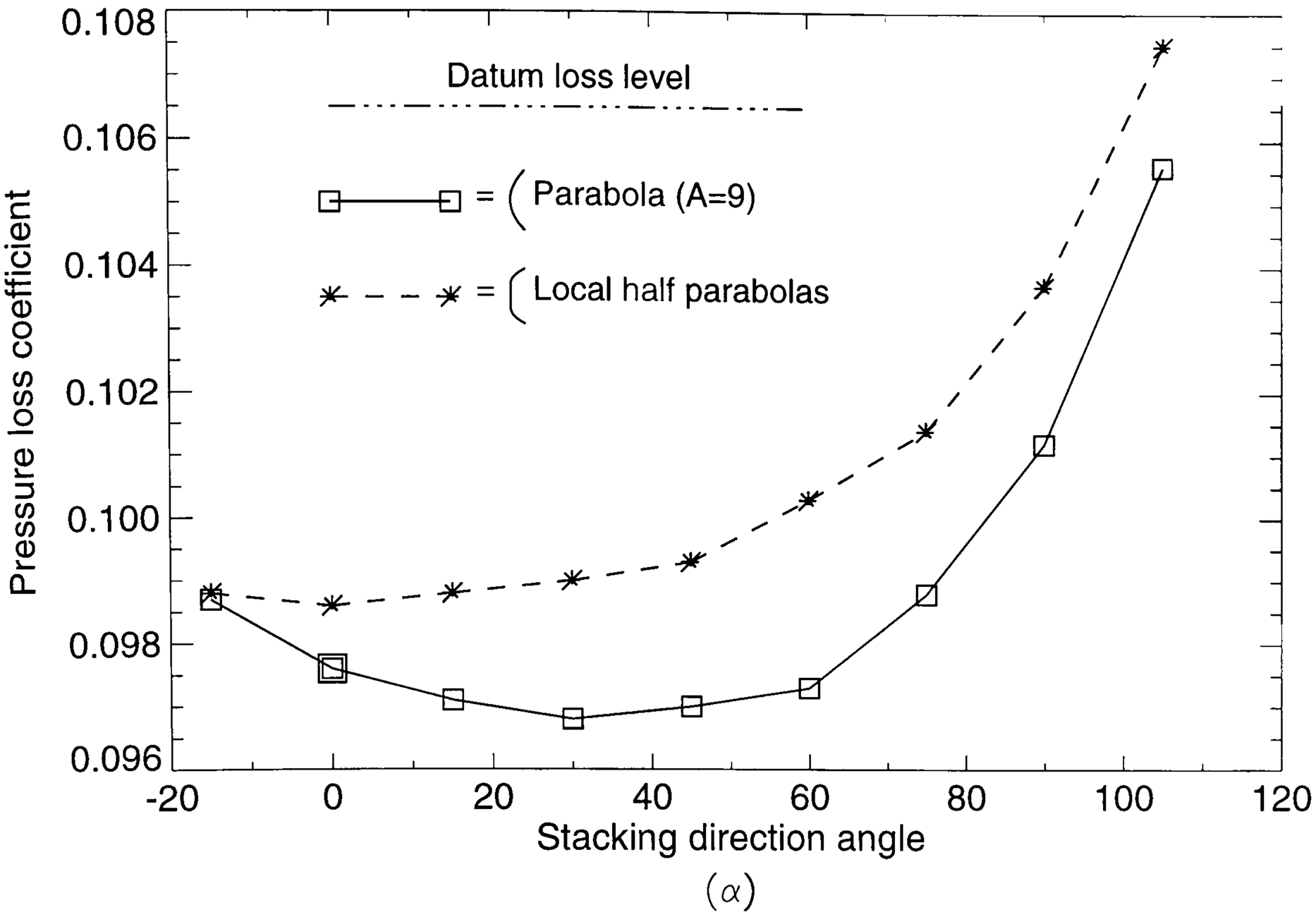


Fig 8.12 Pressure loss coefficient vs stacking direction for rotor

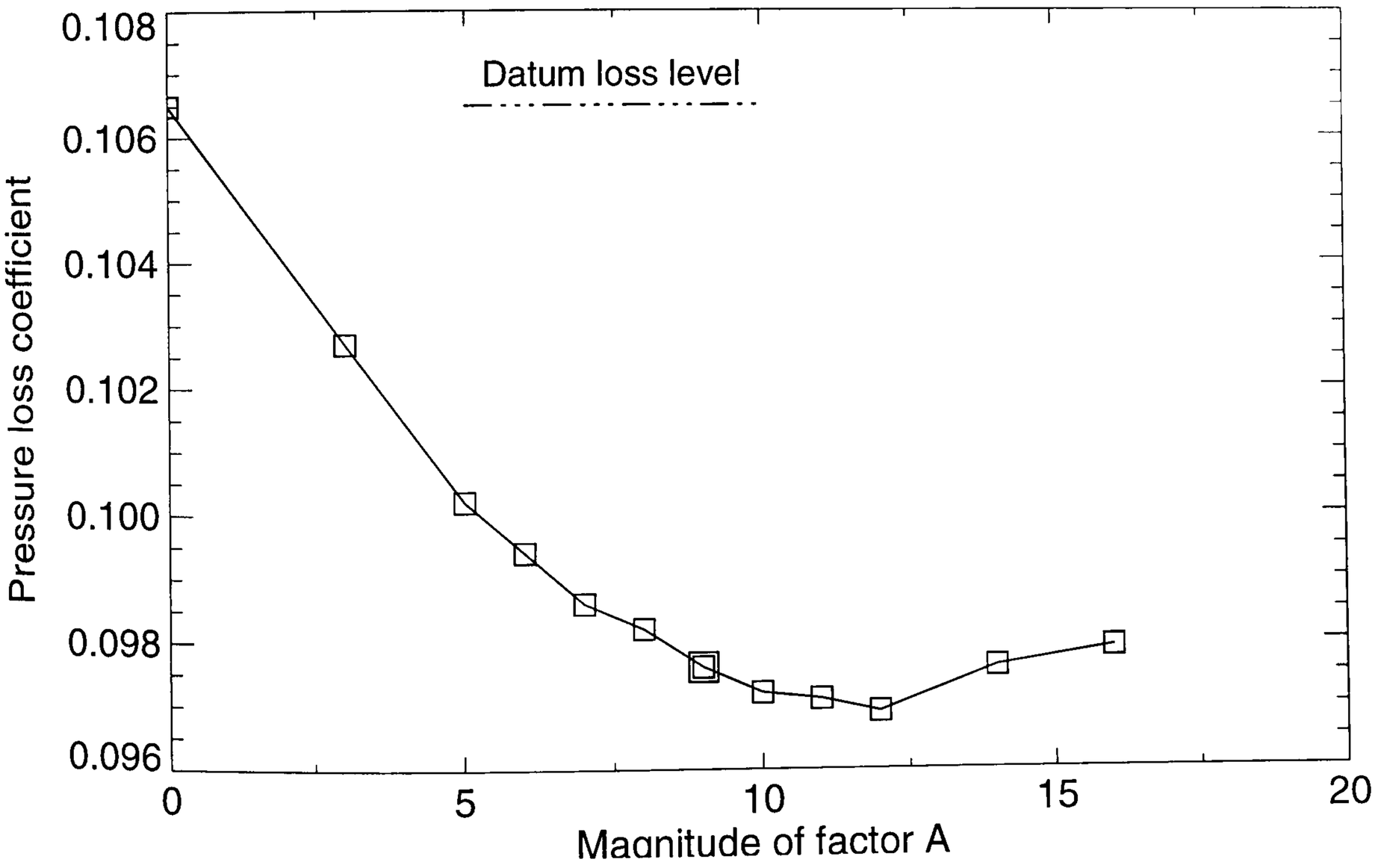


Figure 8.13 Pressure loss coefficient vs stacking axis lean strength for rotor

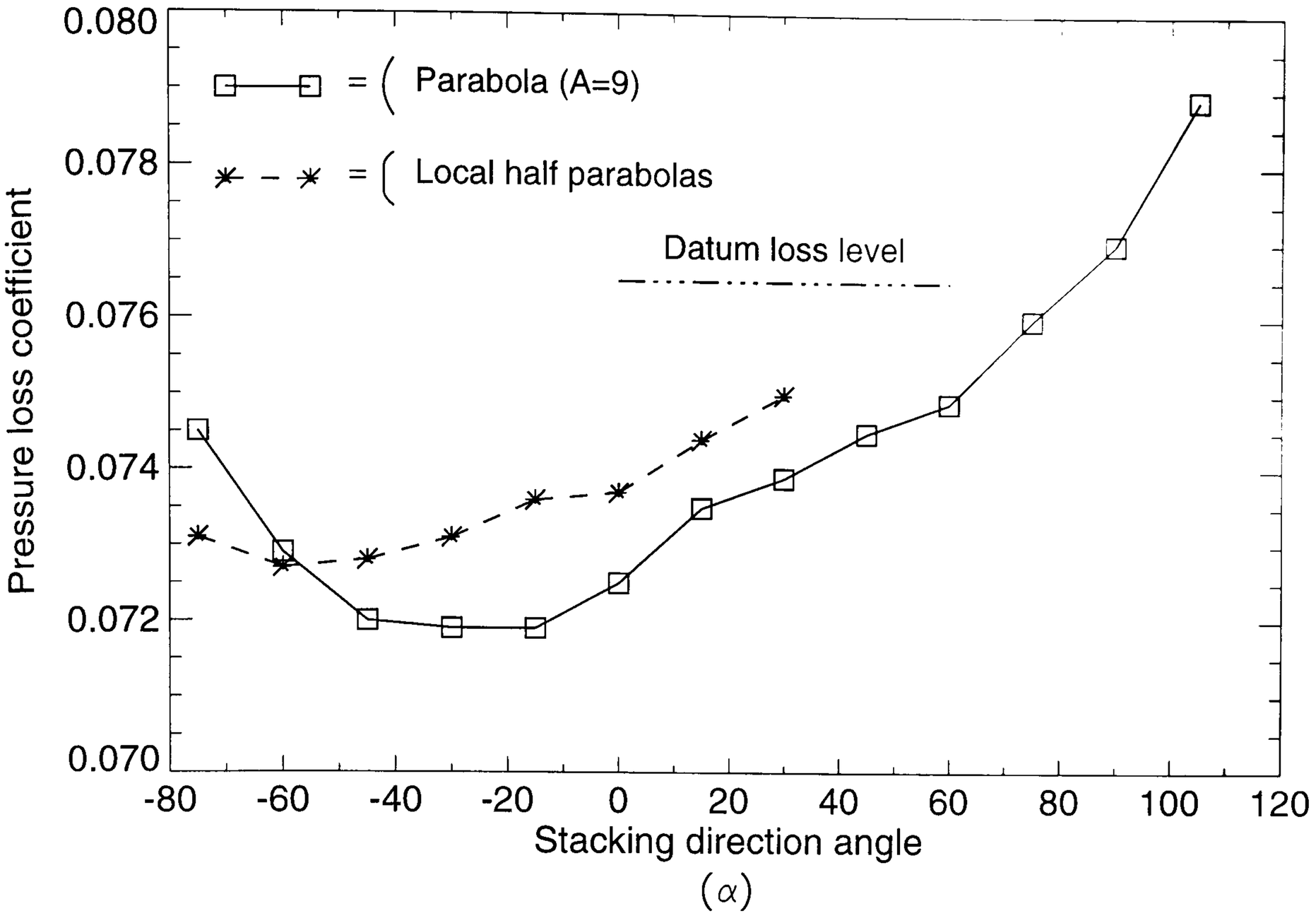


Fig 8.14 Pressure loss coefficient vs stacking axis direction for stator

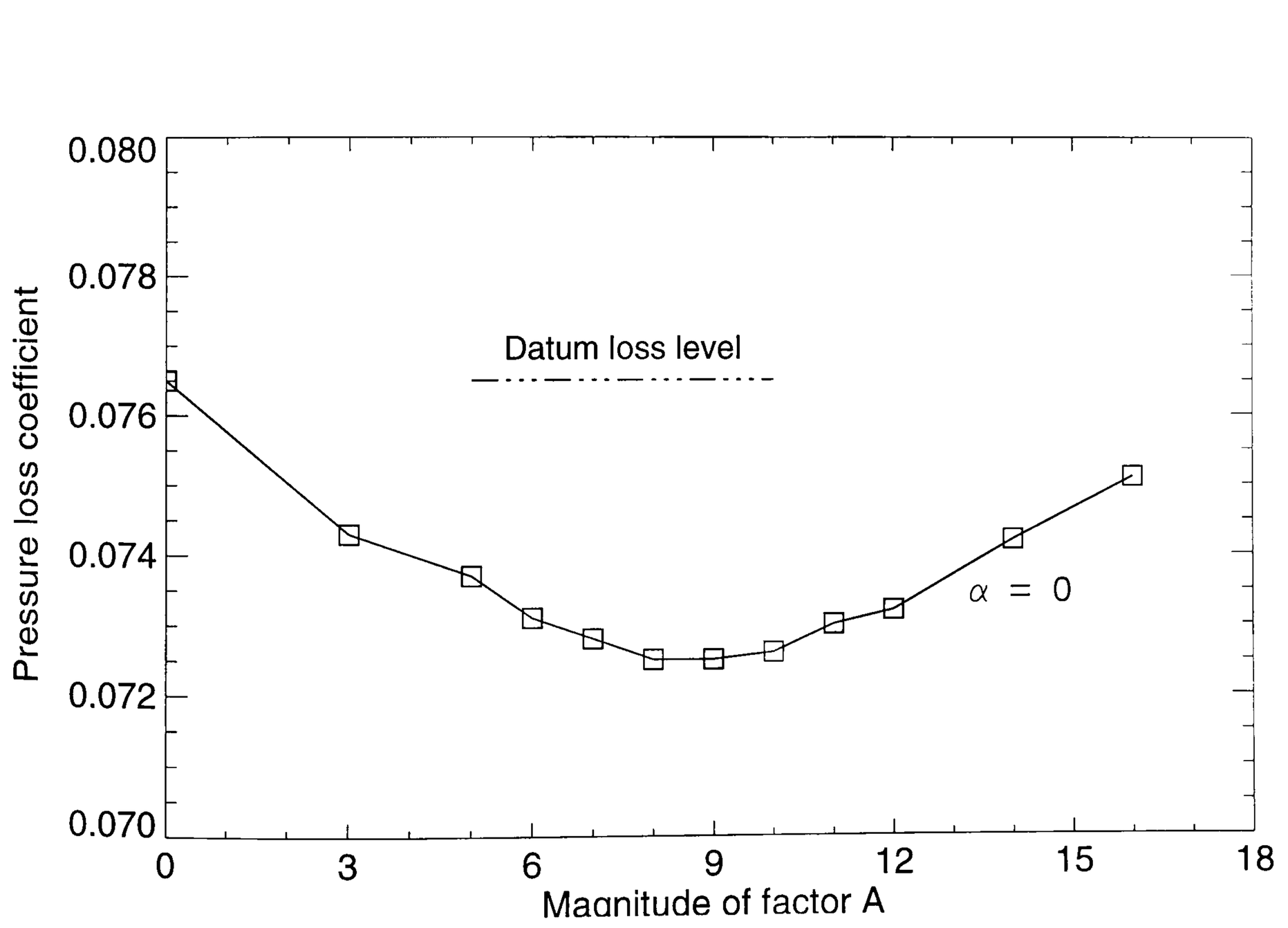


Figure 8.15 Pressure loss coefficient vs stacking axis lean strength for stator

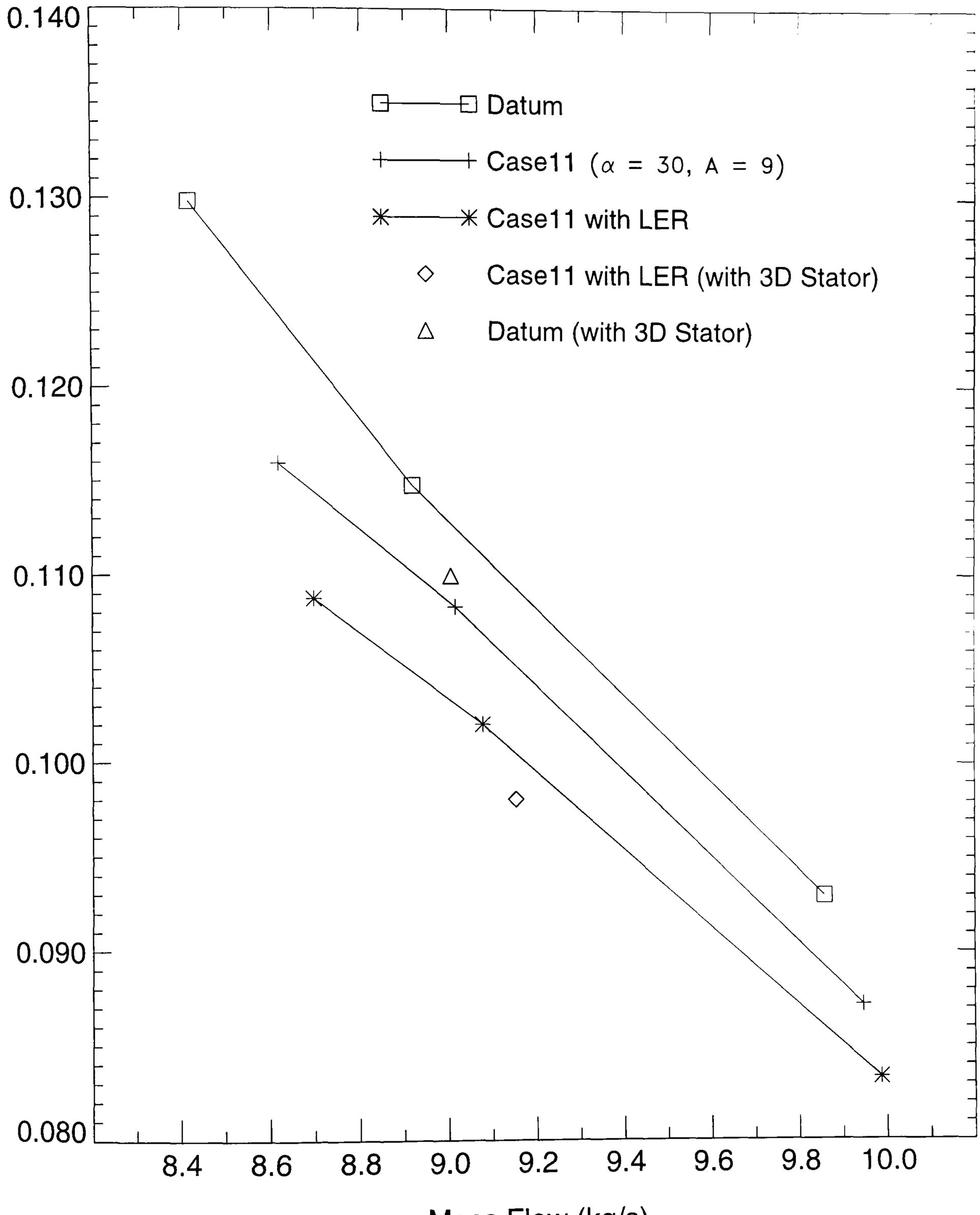


Figure 8.16 Pressure loss coefficient vs mass flow (Rotor)

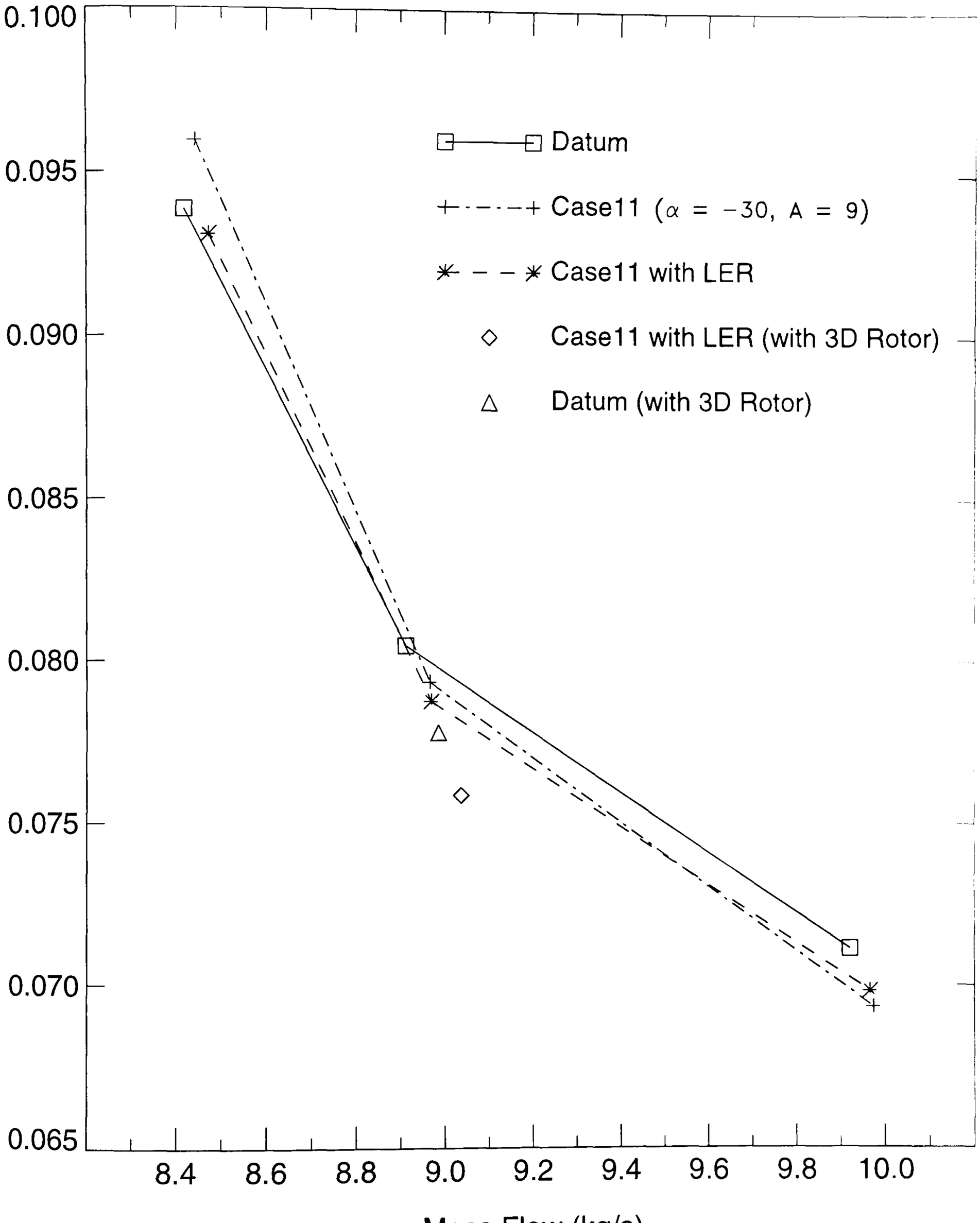


Figure 8.17 Pressure loss coefficient vs mass flow (Stator)

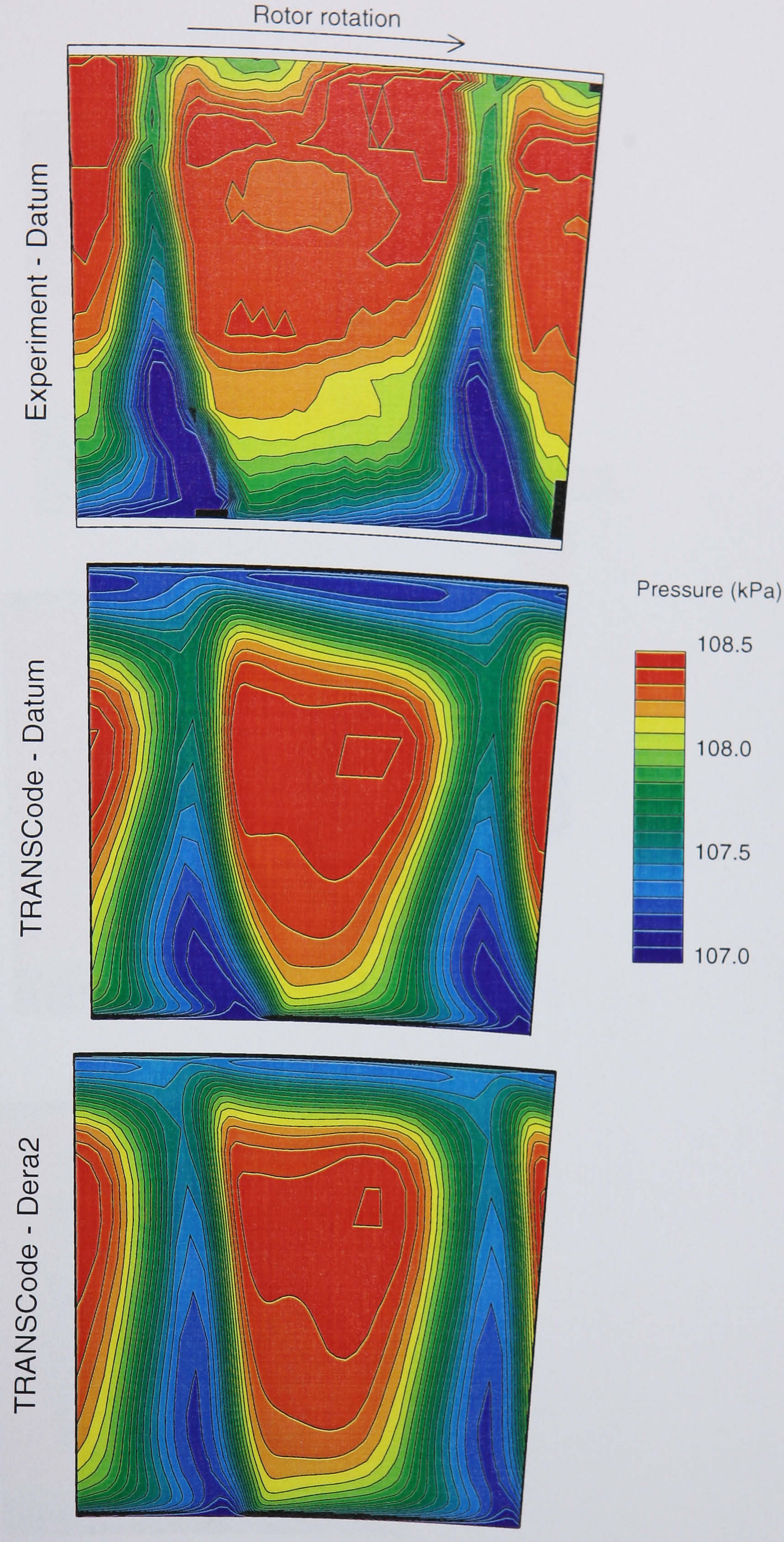


Figure 8.18 Rotor exit total pressure field

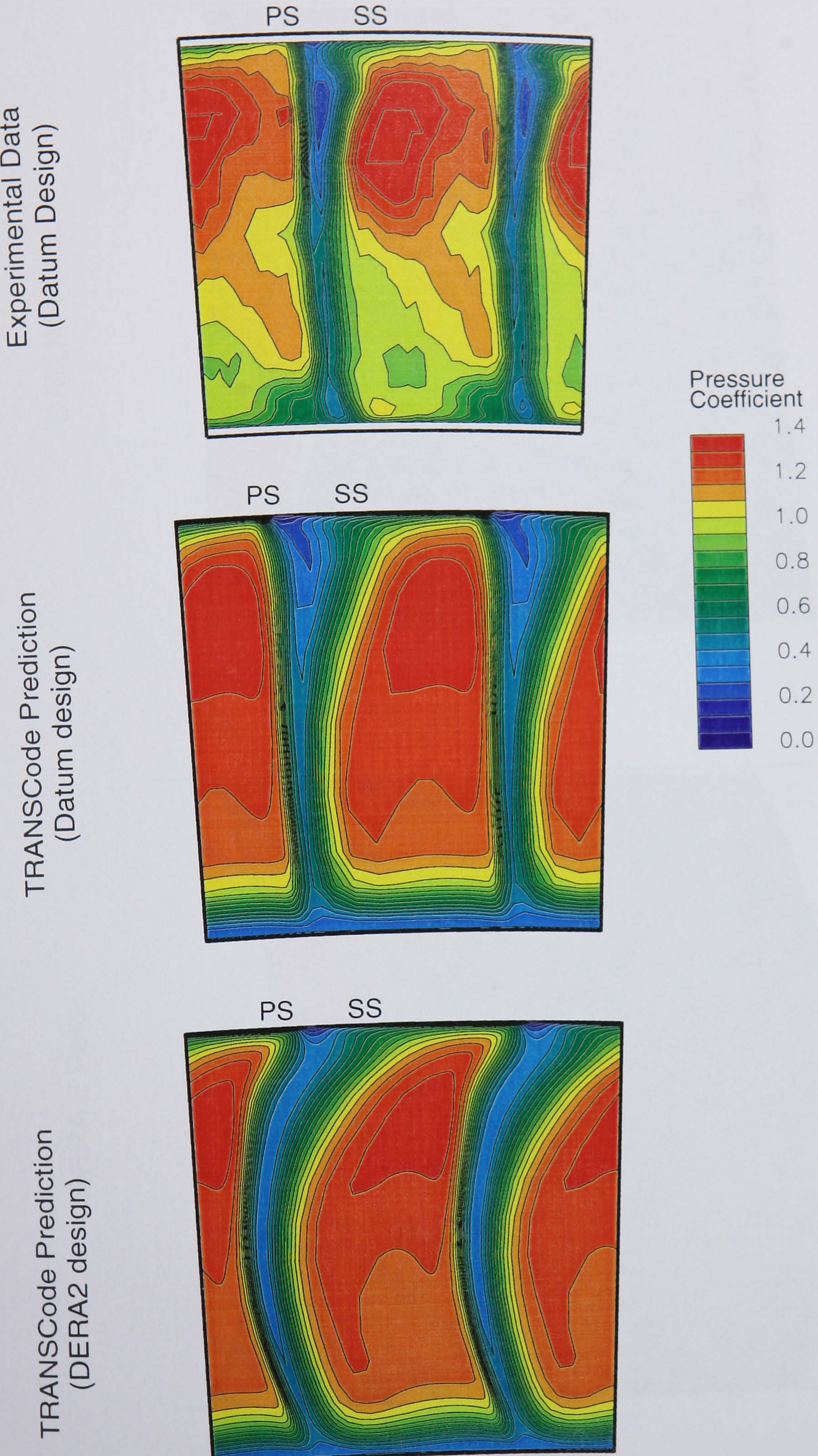


Figure 8.19 Stator exit total pressure field

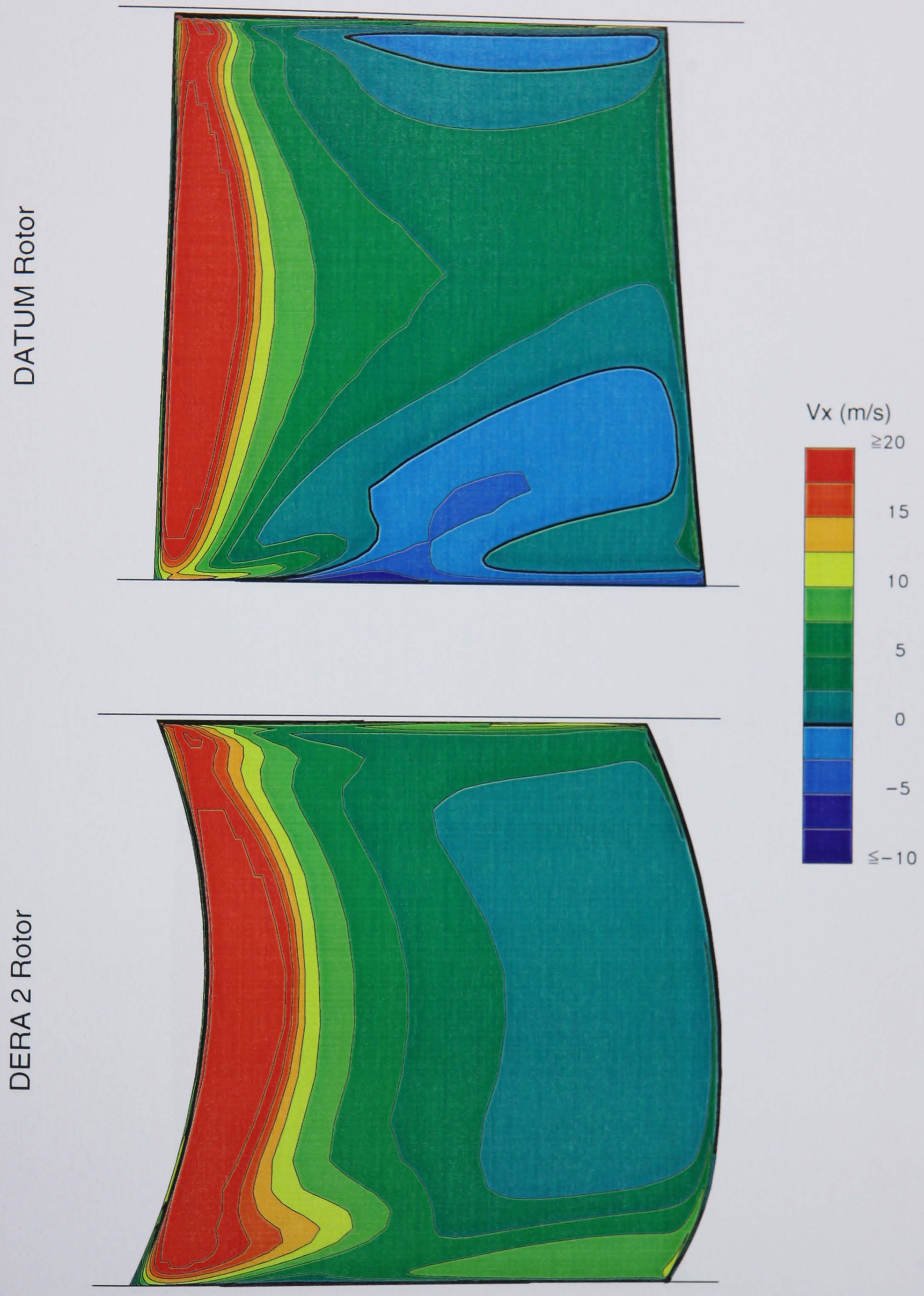


Figure 8.20 Near suction surface axial velocity contours (rotor)

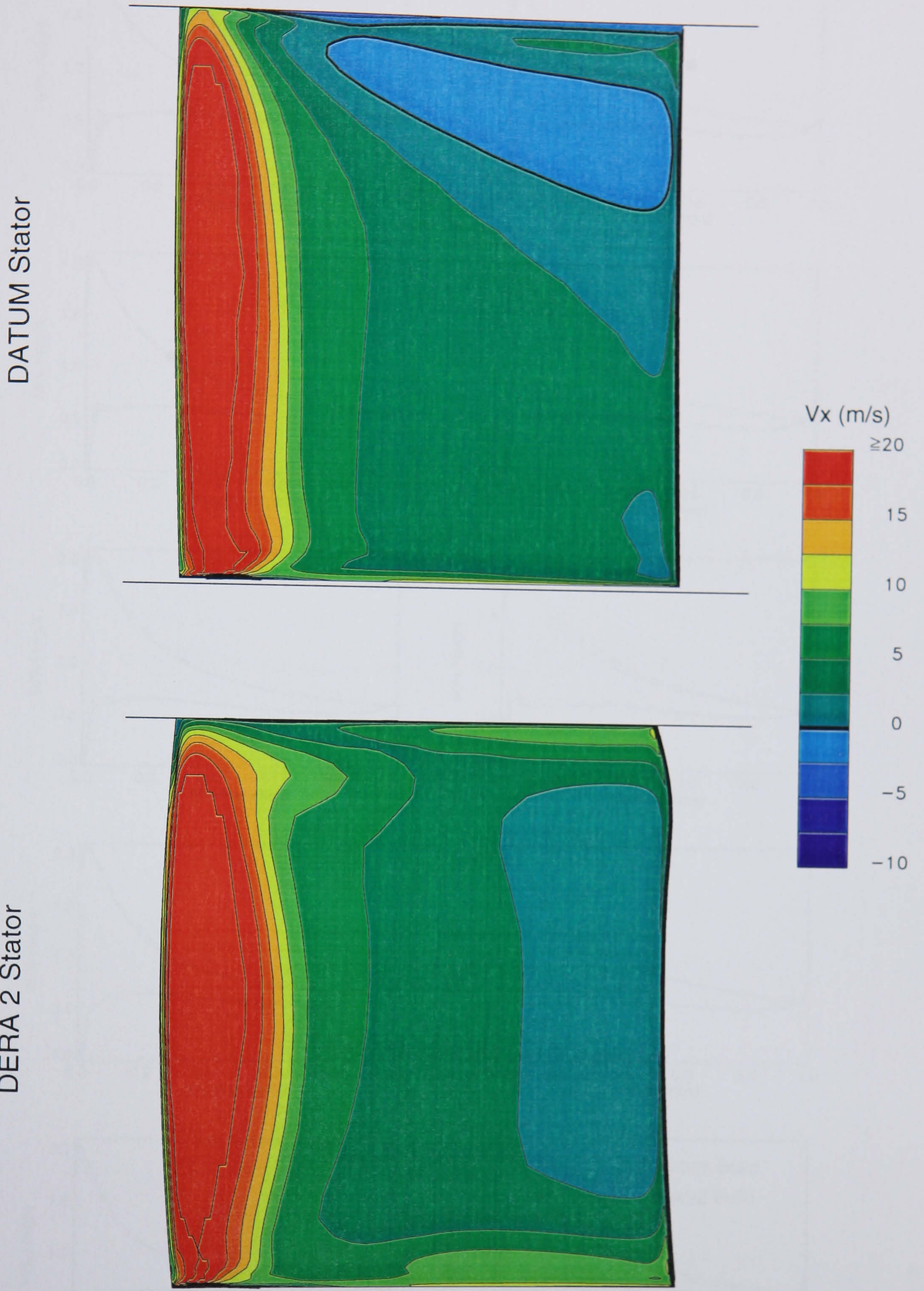


Figure 8.21 Near suction surface axial velocity contours (stator)

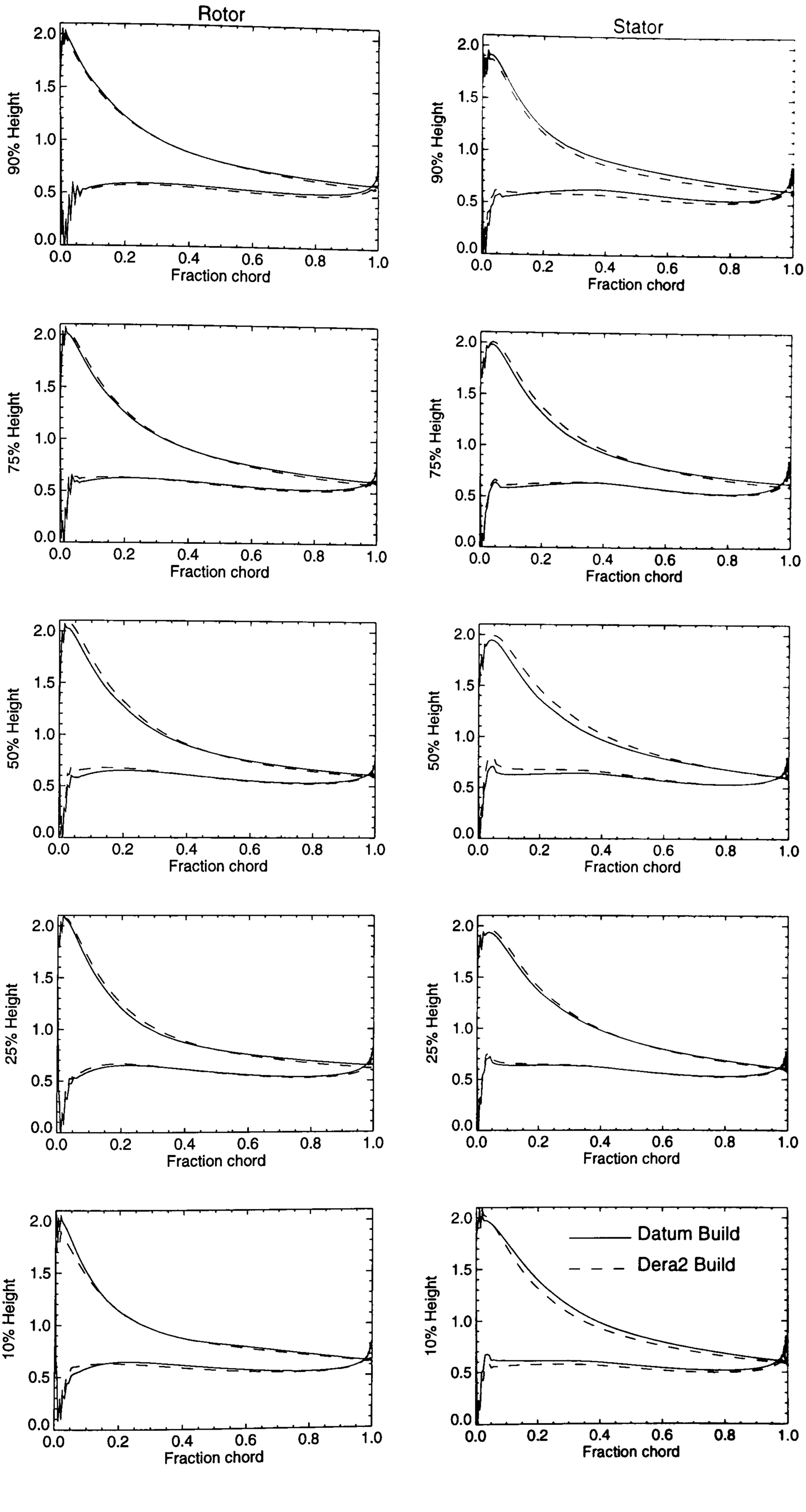


Figure 8.22 Blade surface static pressure coefficient distributions

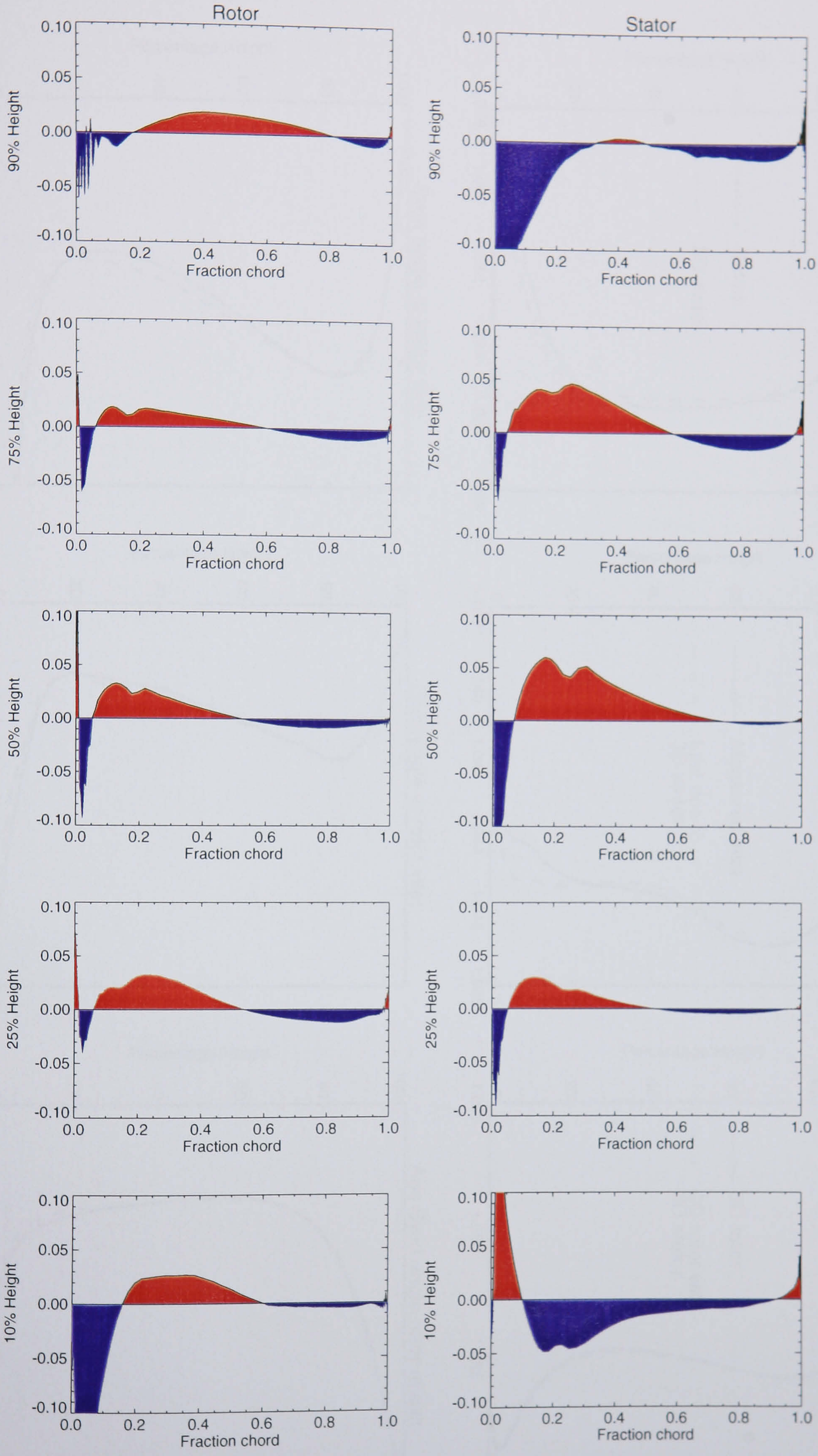


Figure 8.23 Blade surface static pressure coefficient difference distributions between datum and DERA2 blading

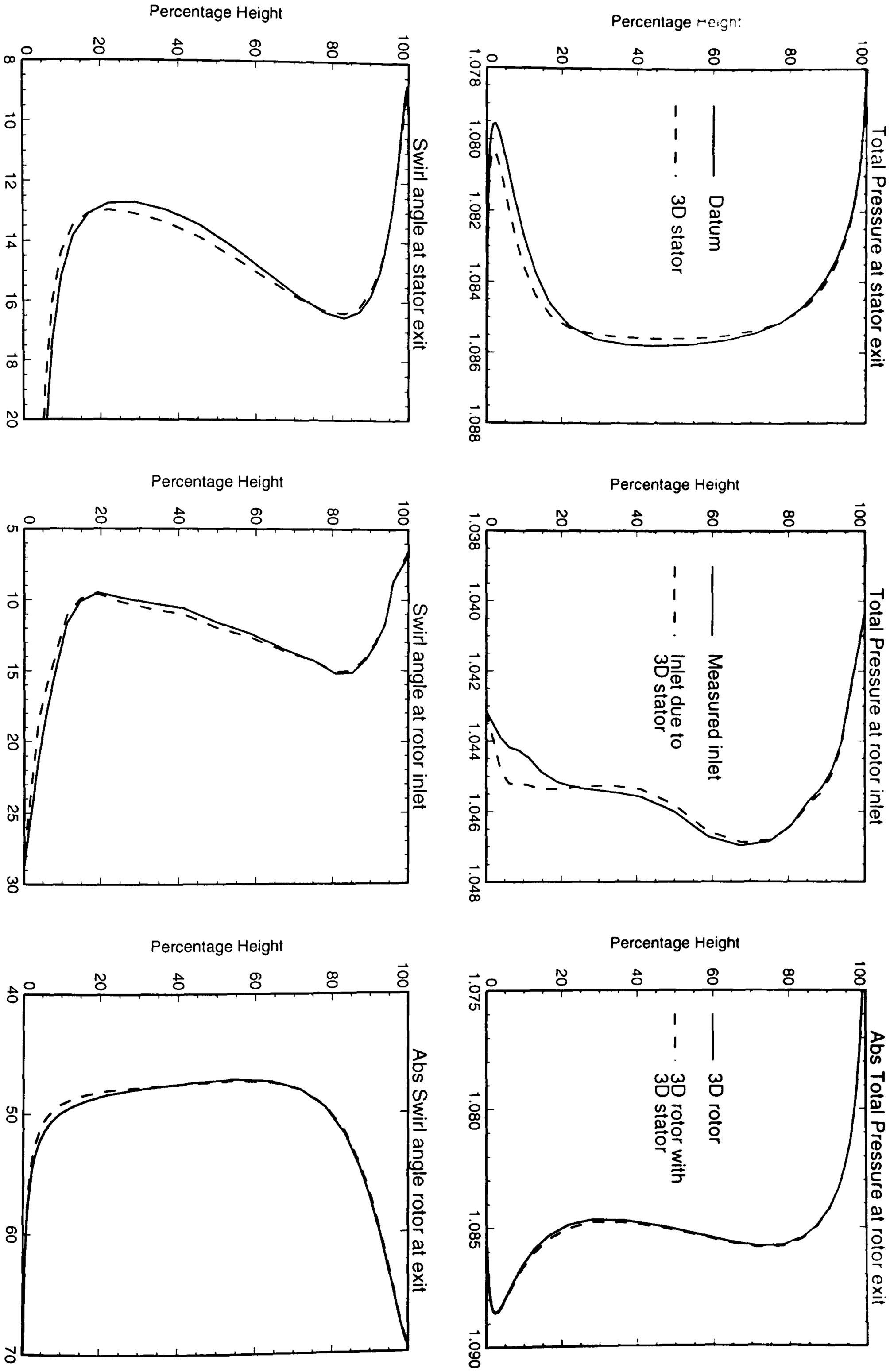


Figure 8.24 Effect of 3D stator design on 3D rotor radial profiles

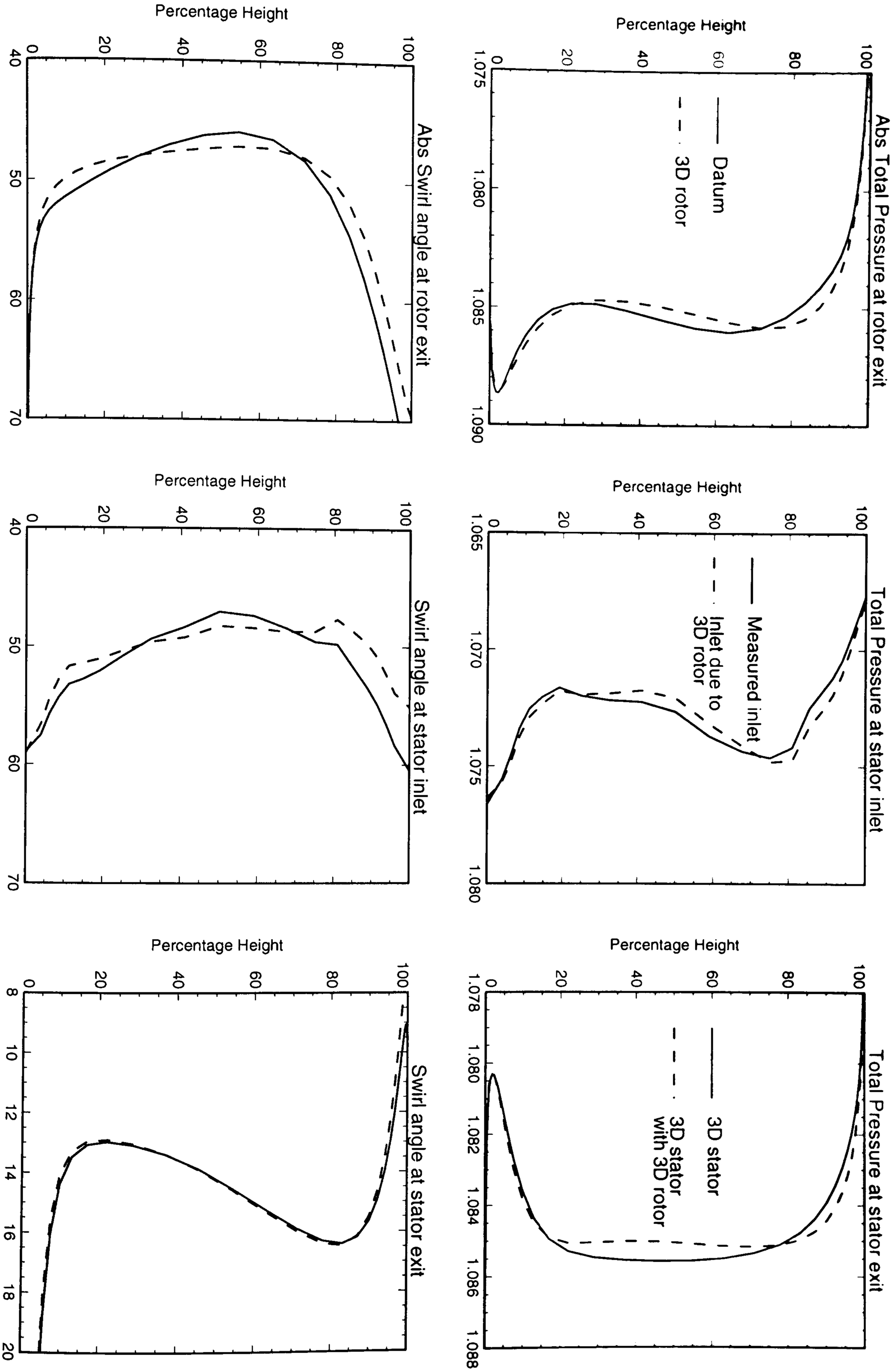


Figure 8.25 Effect of 3D rotor design on 3D stator radial profiles

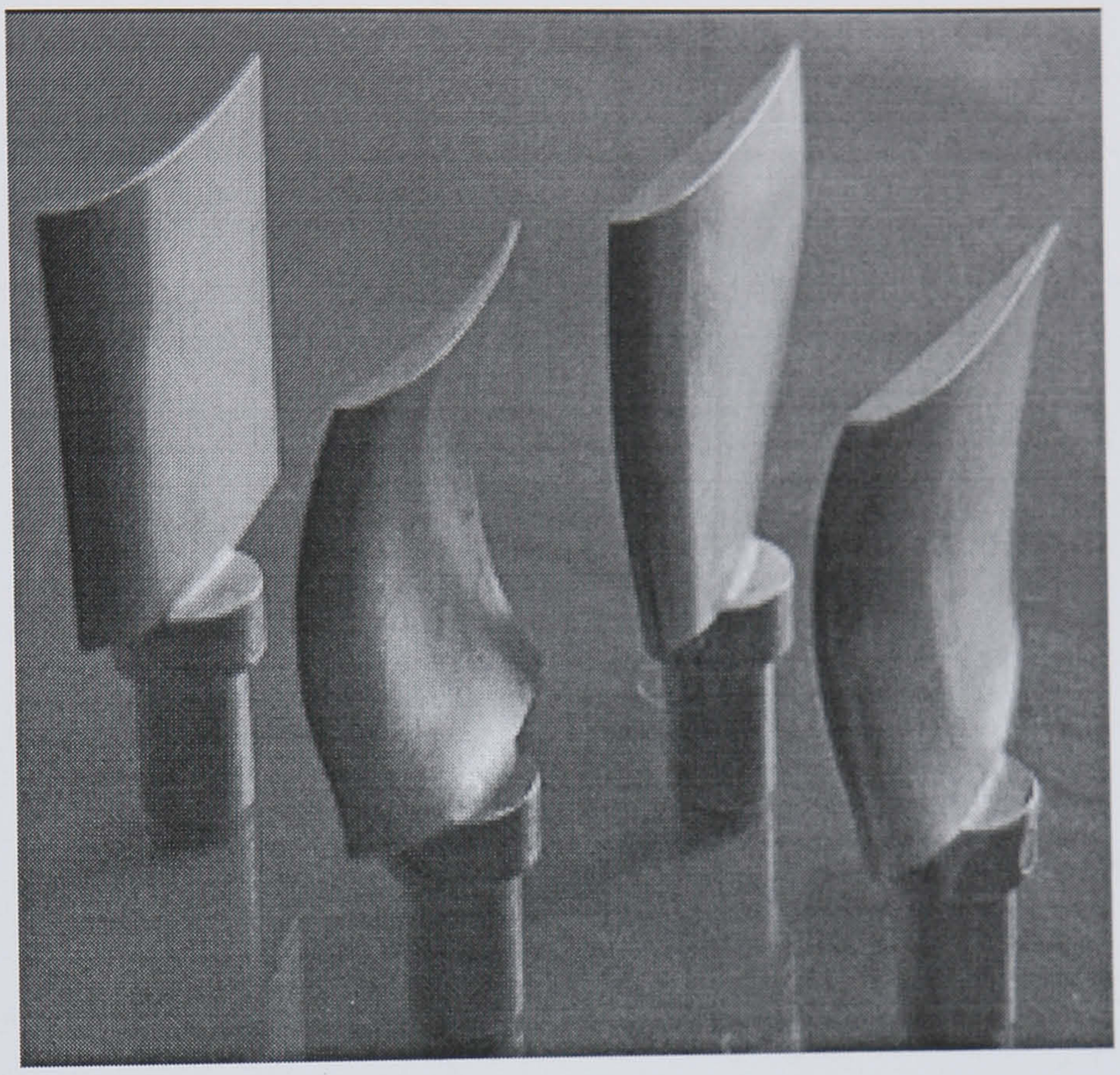


Figure 8.26 Photograph of datum and 3D blades

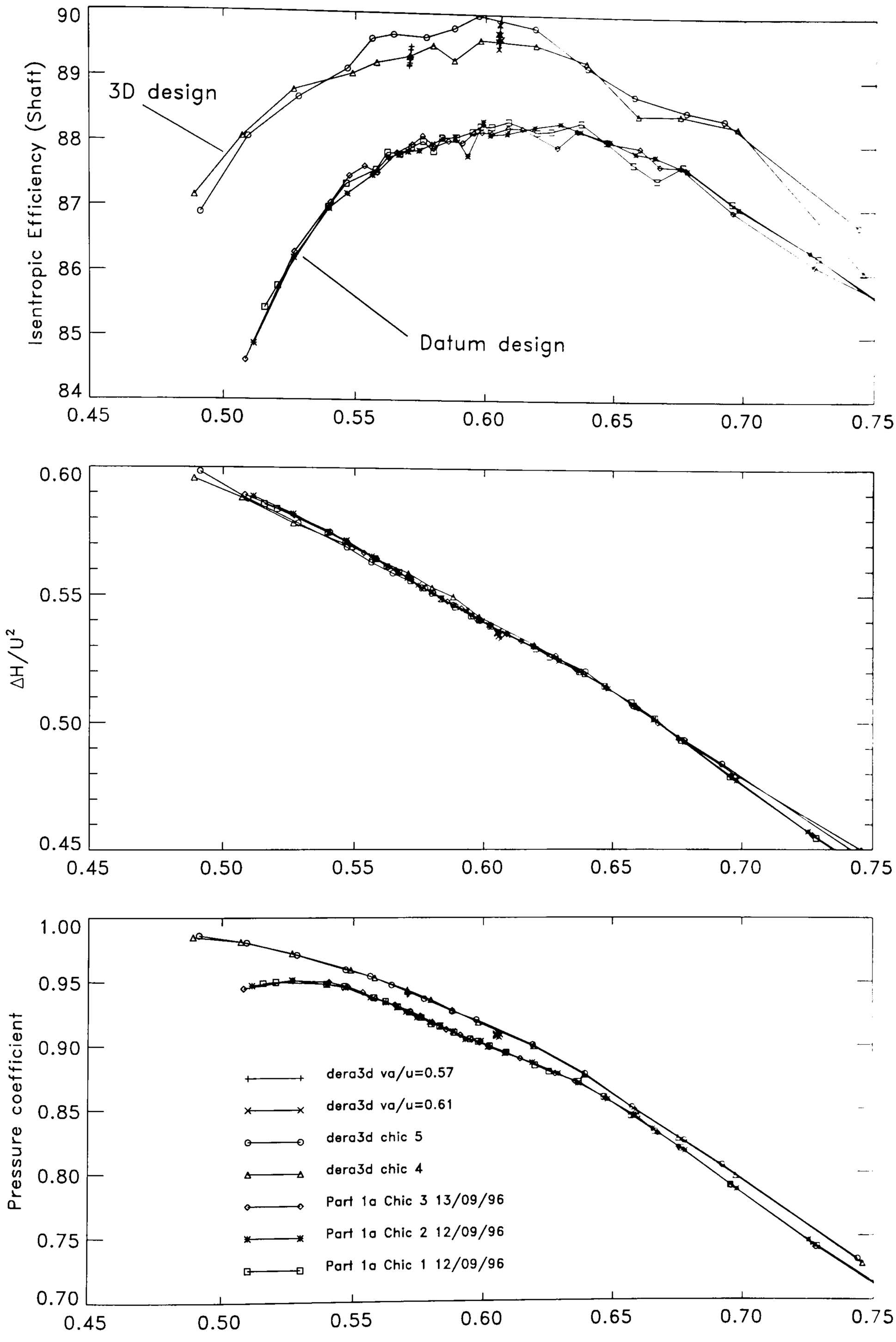


Figure 9.1 Overall performance characteristic of 3D design compared to datum design performance

Figures

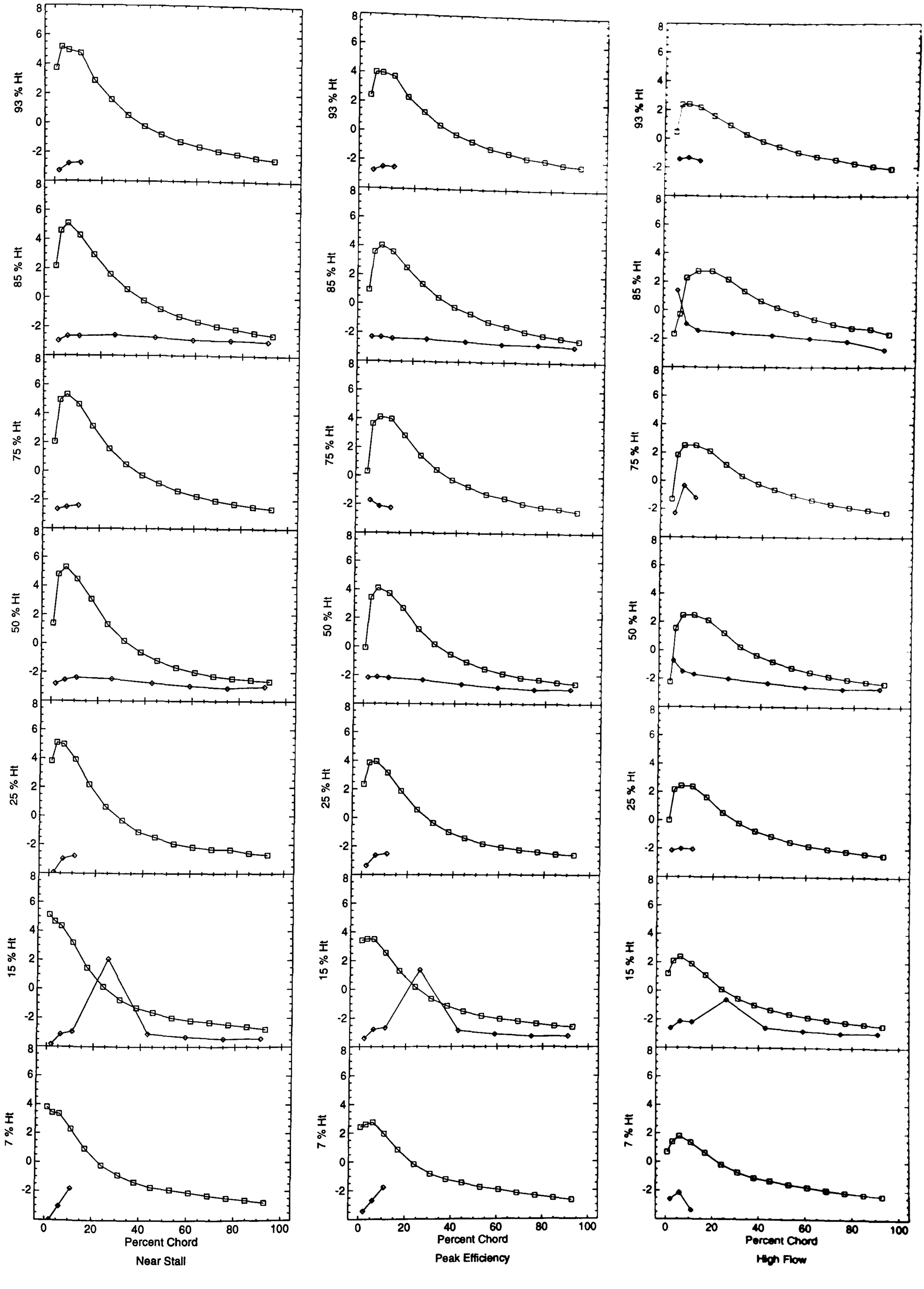


Figure 9.2 3D rotor surface static pressure coefficient distributions

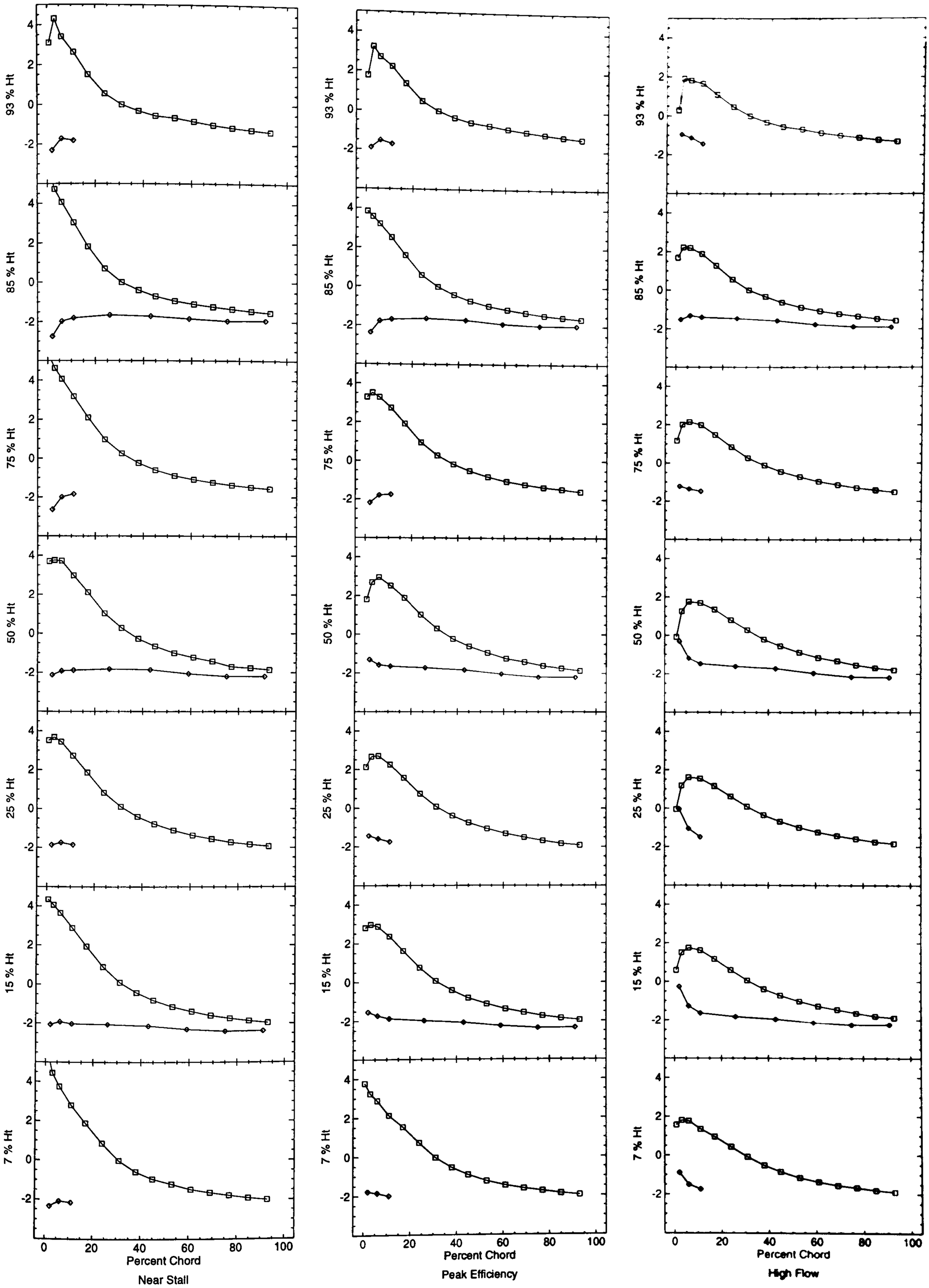


Figure 9.3 3D stator surface static pressure coefficient distributions

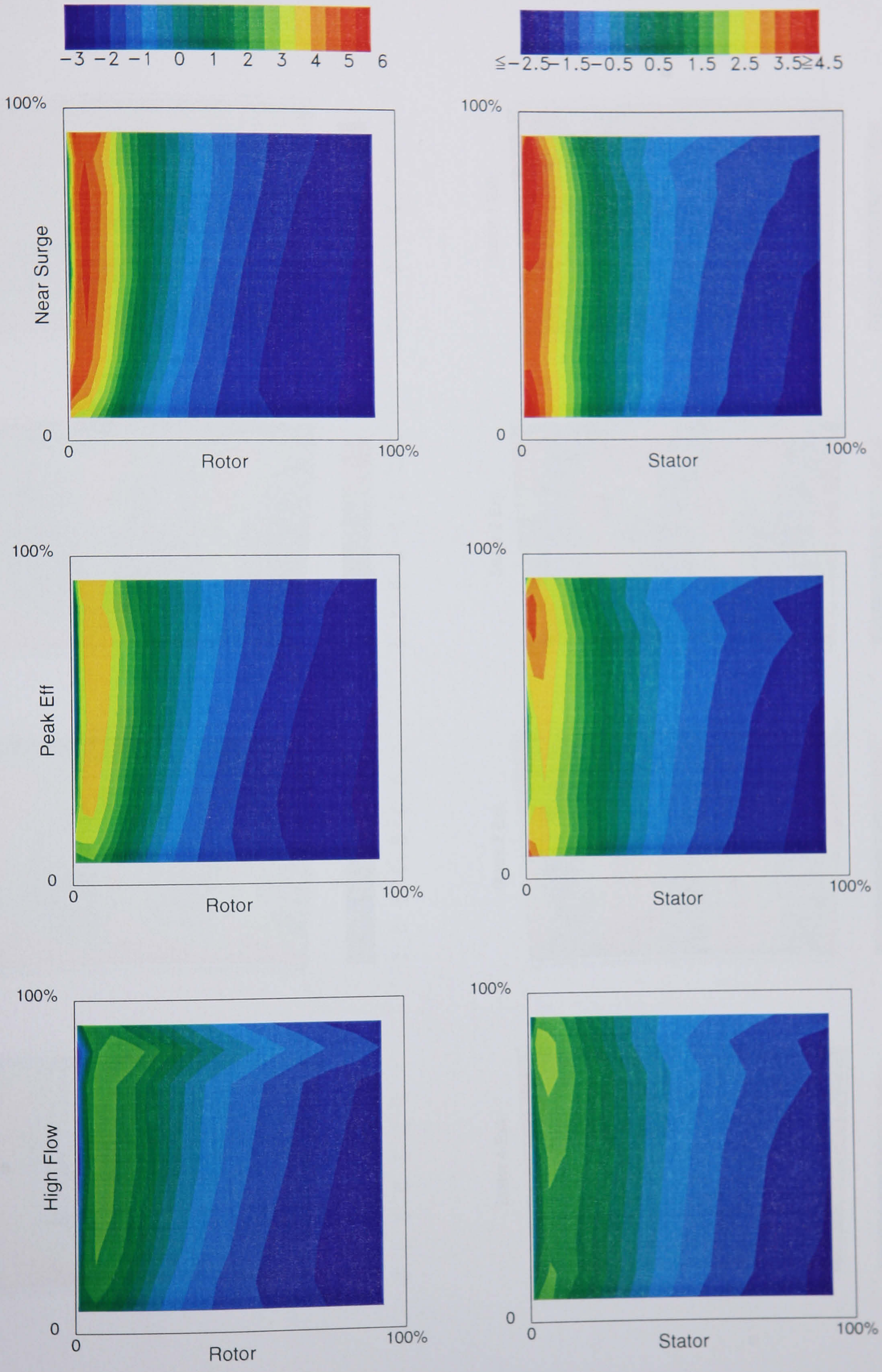


Figure 9.4 Suction surface pressure coefficient contours (3D design)

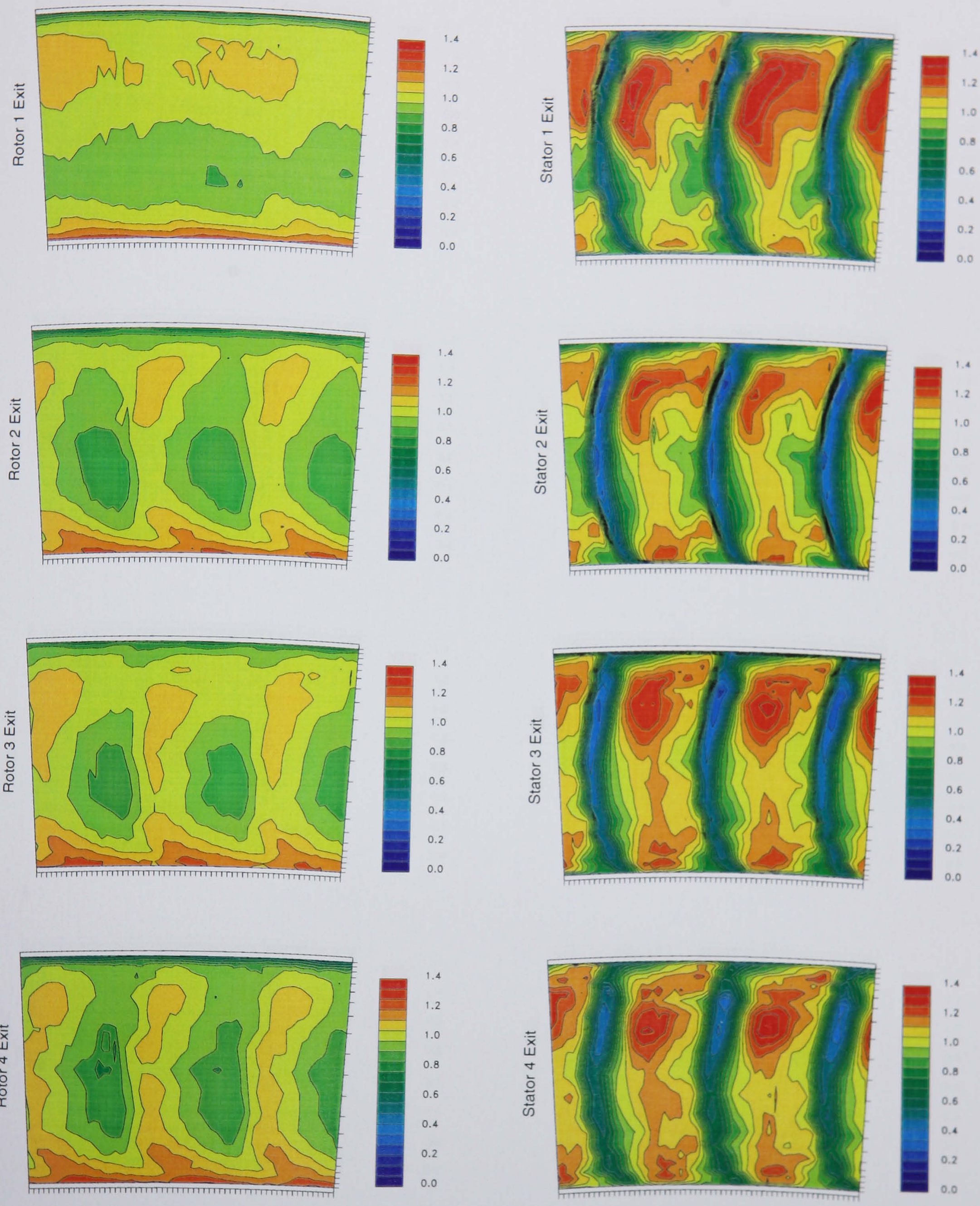


Figure 9.5 Total pressure coefficient contours at design flow (3D design)

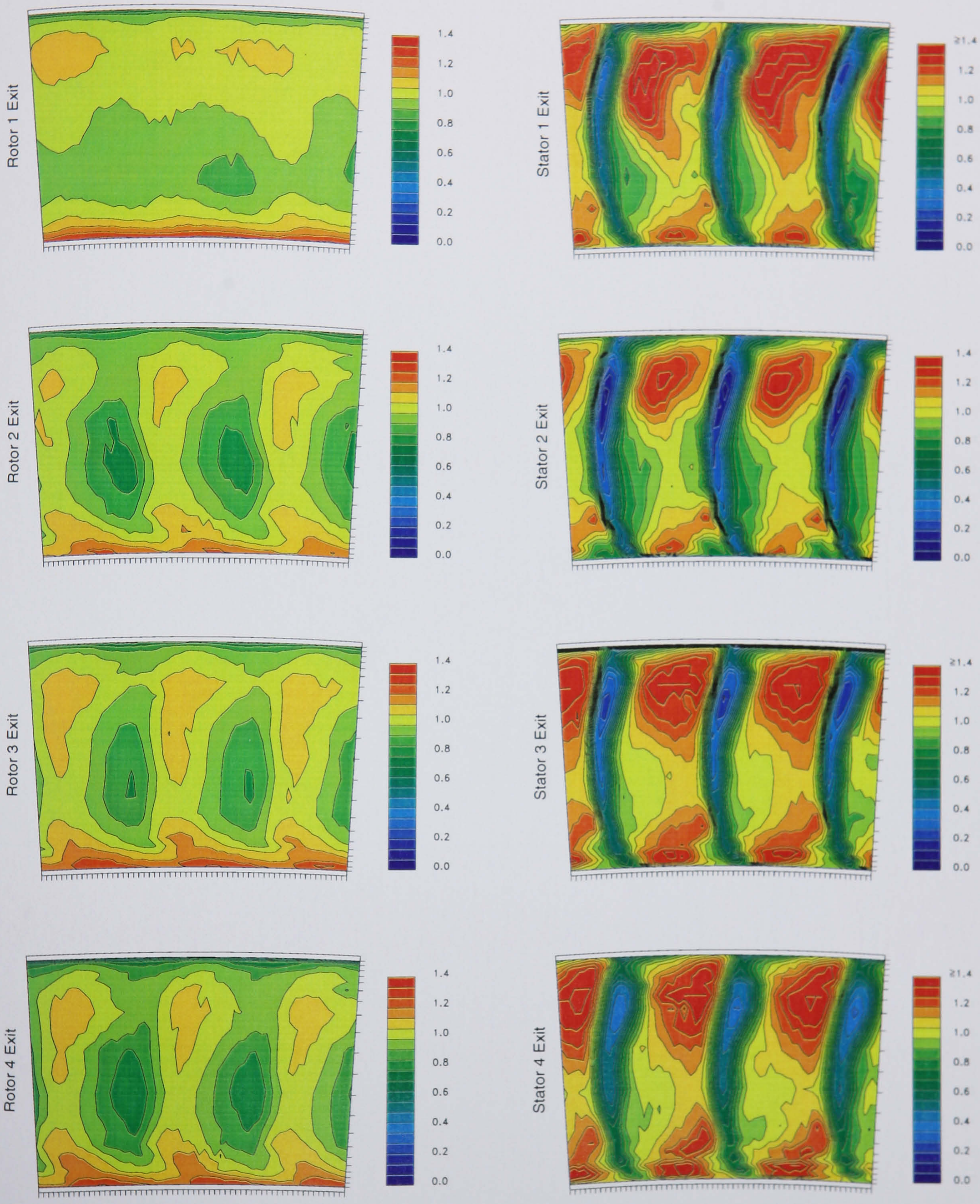


Figure 9.6 Total pressure coefficient contours at near stall (3D design)

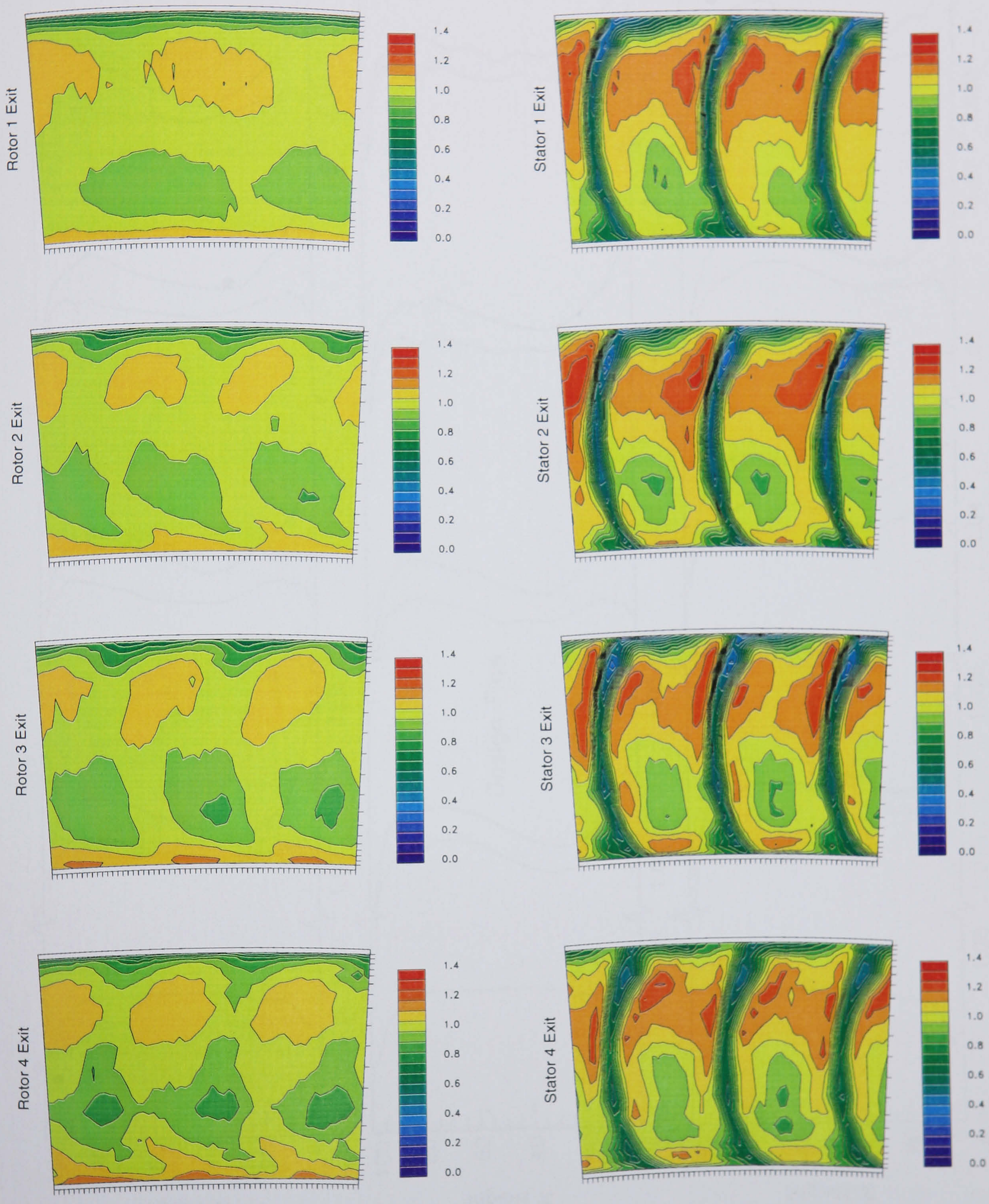


Figure 9.7 Total pressure coefficient contours at high flow (3D design)

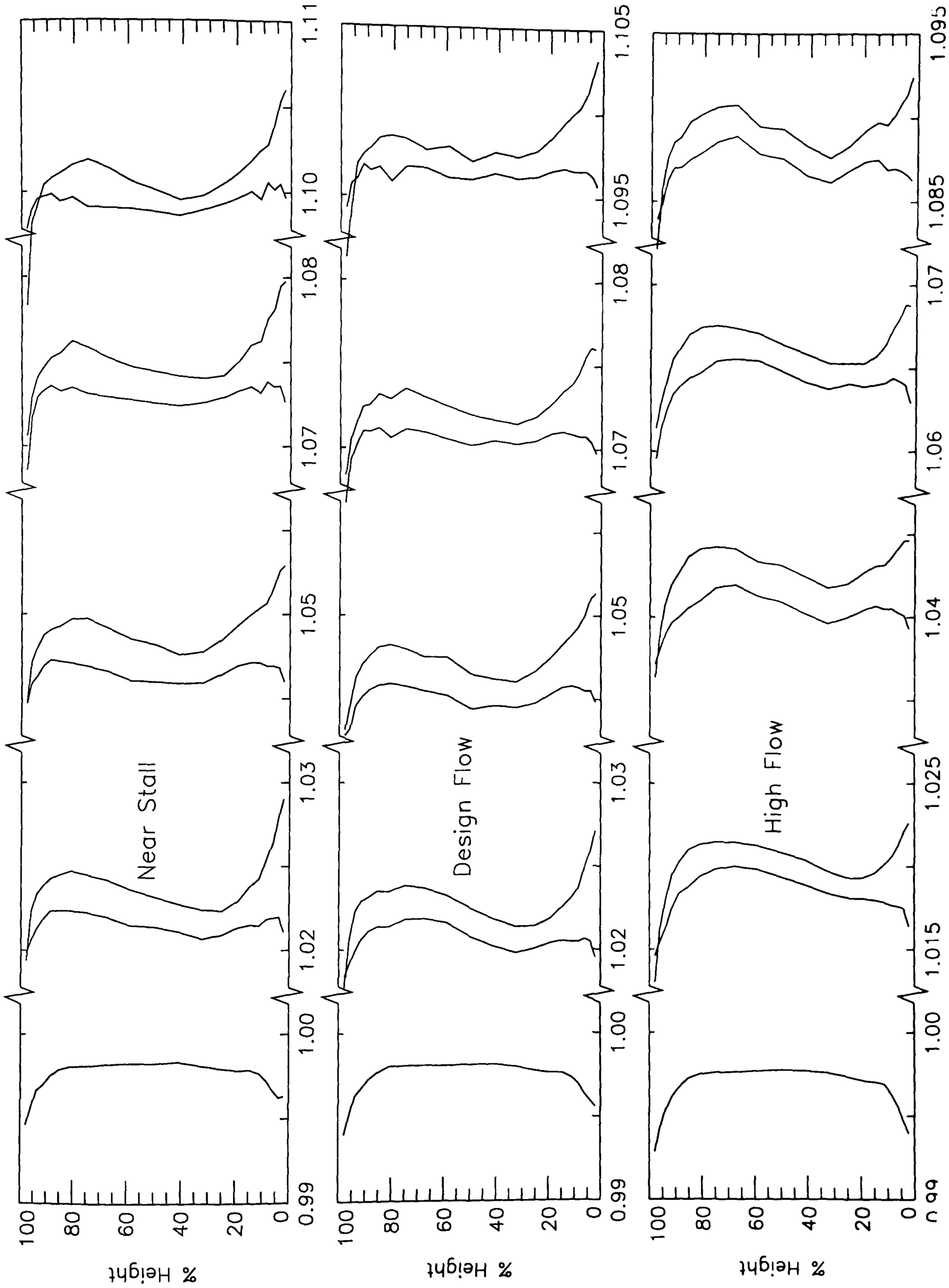


Figure 9.8 Radial profiles of pressure ratio at near stall, design flow and high flow (3D design)

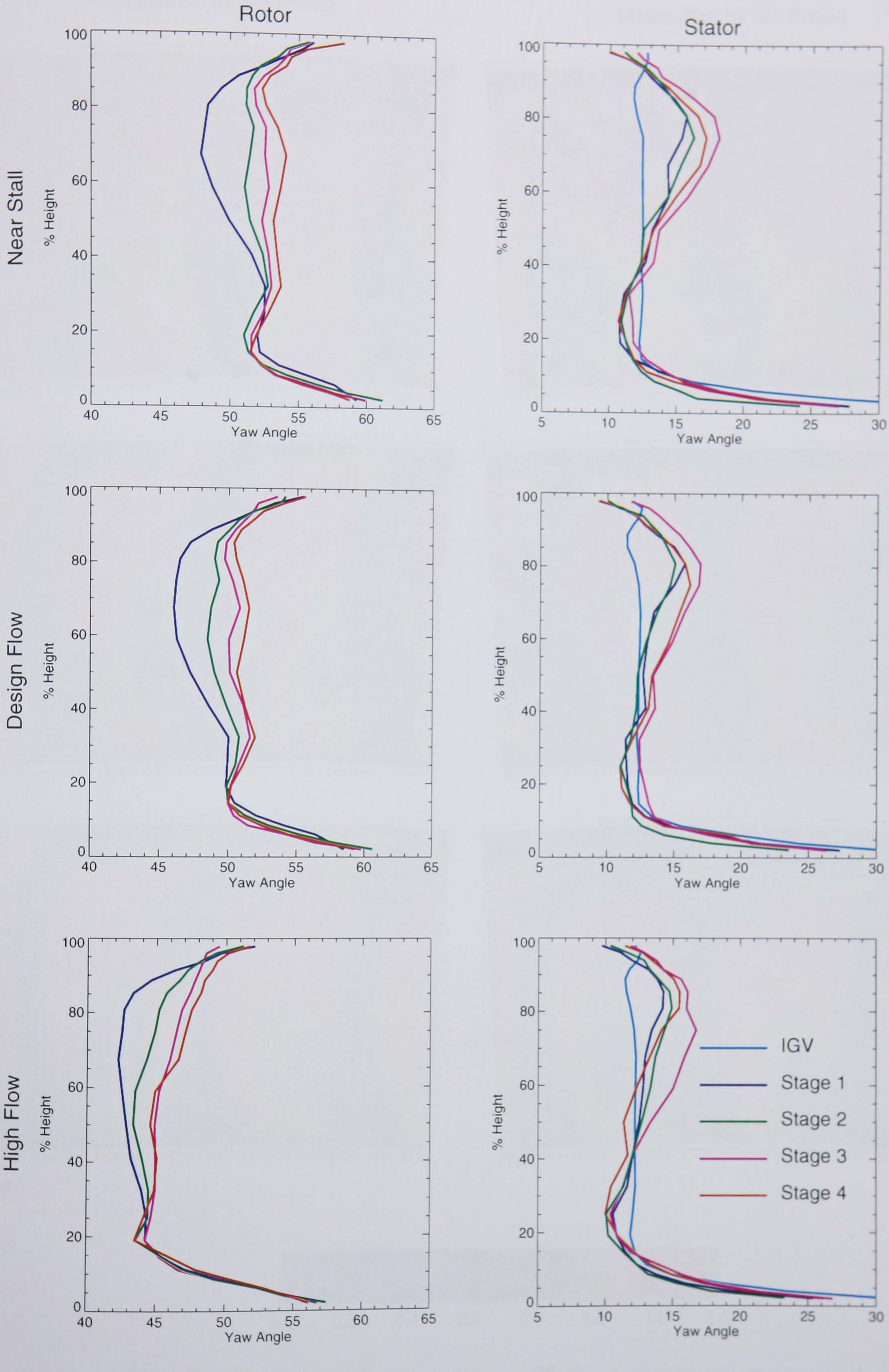


Figure 9.9 Radial profiles of pressure ratio and flow angle at near stall (3D design)

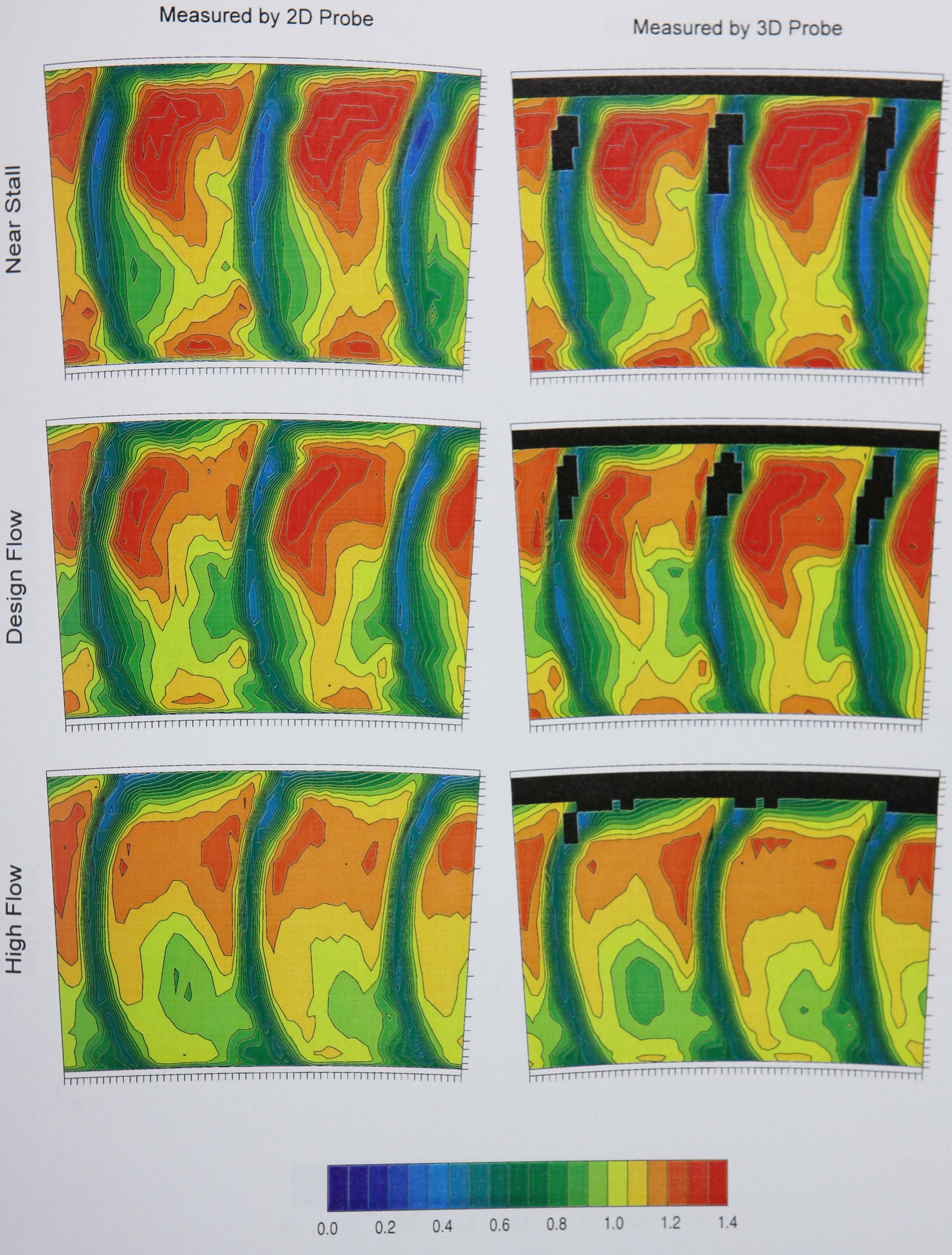


Figure 9.10 Comparison of pressure coefficient contours measured at stator 1 exit for 2D and 3D cobra probes

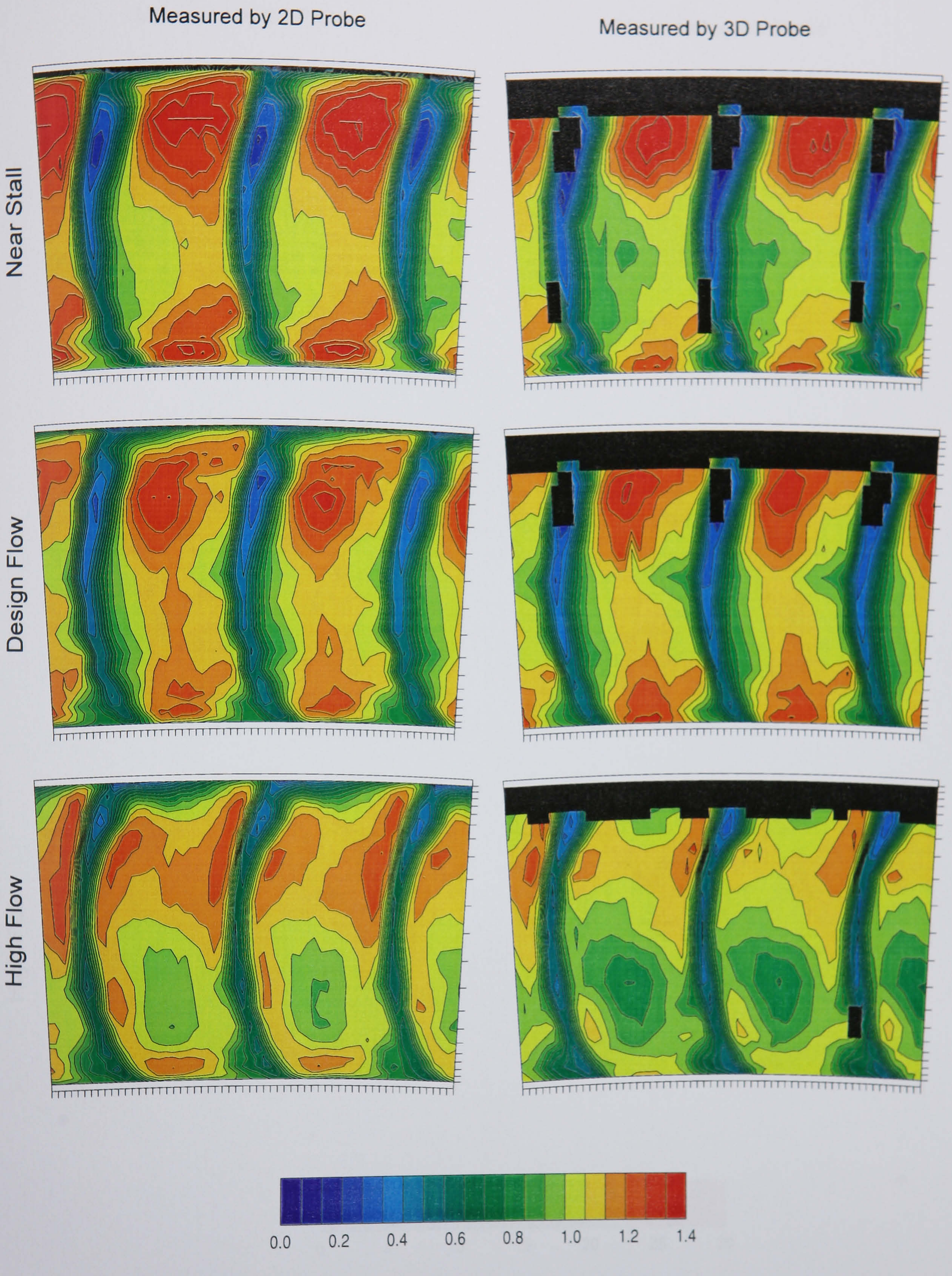


Figure 9.11 Comparison of pressure coefficient contours measured at stator 3 exit for 2D and 3D cobra probes

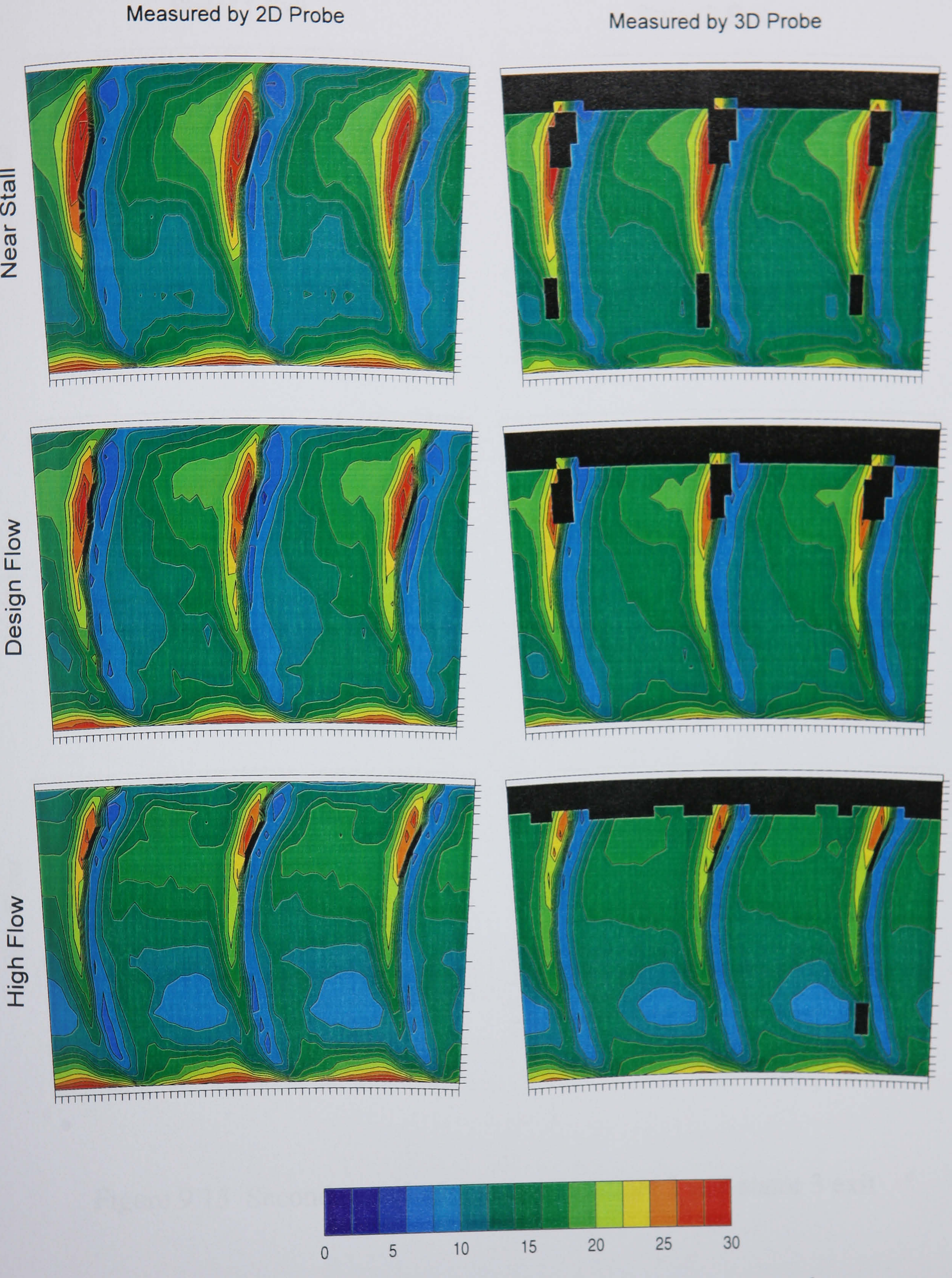


Figure 9.12 Comparison of yaw angle contours measured at stator 3 exit for 2D and 3D cobra probes

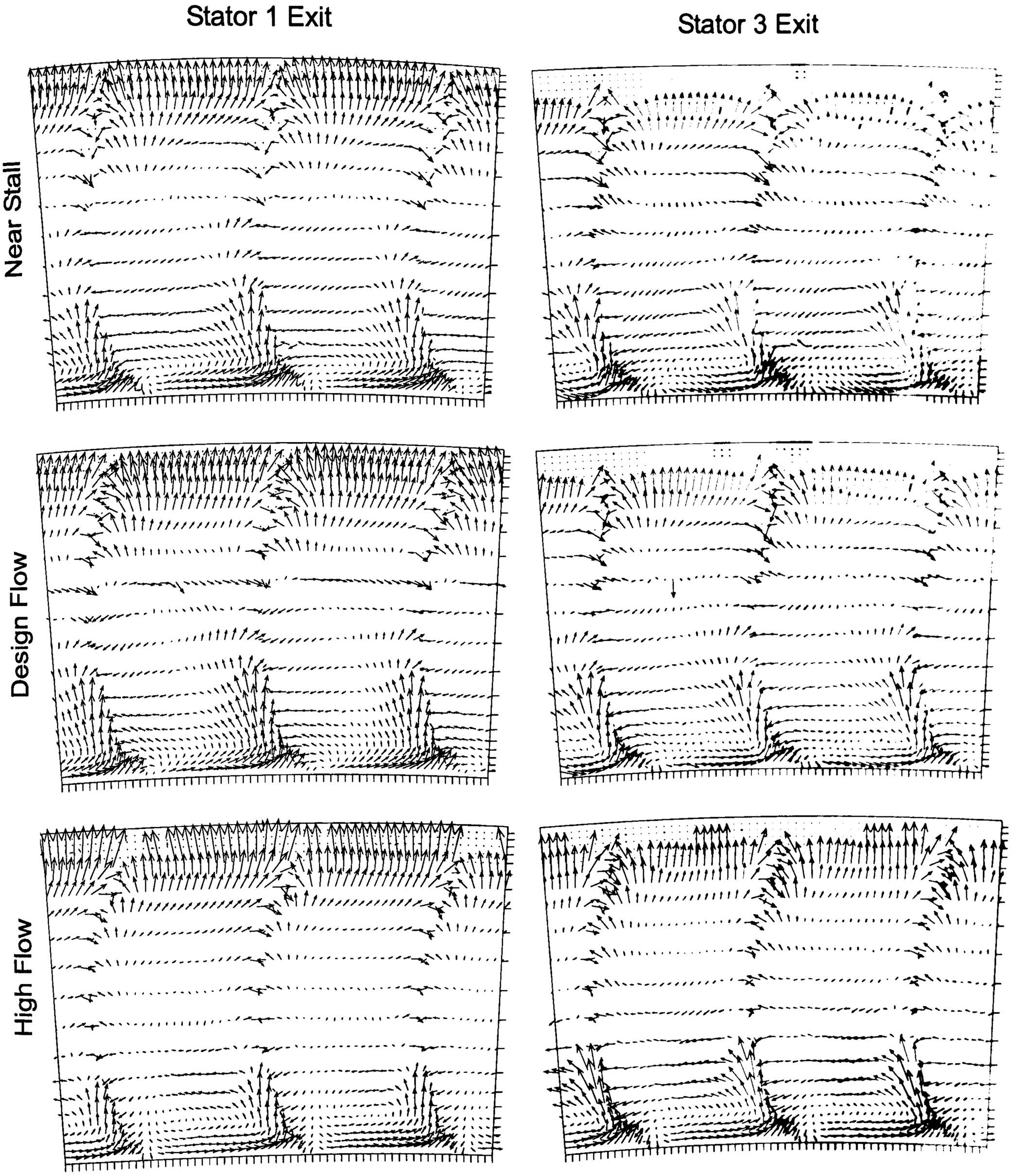


Figure 9.13 Secondary velocity vectors at stator 1 and stator 3 exit

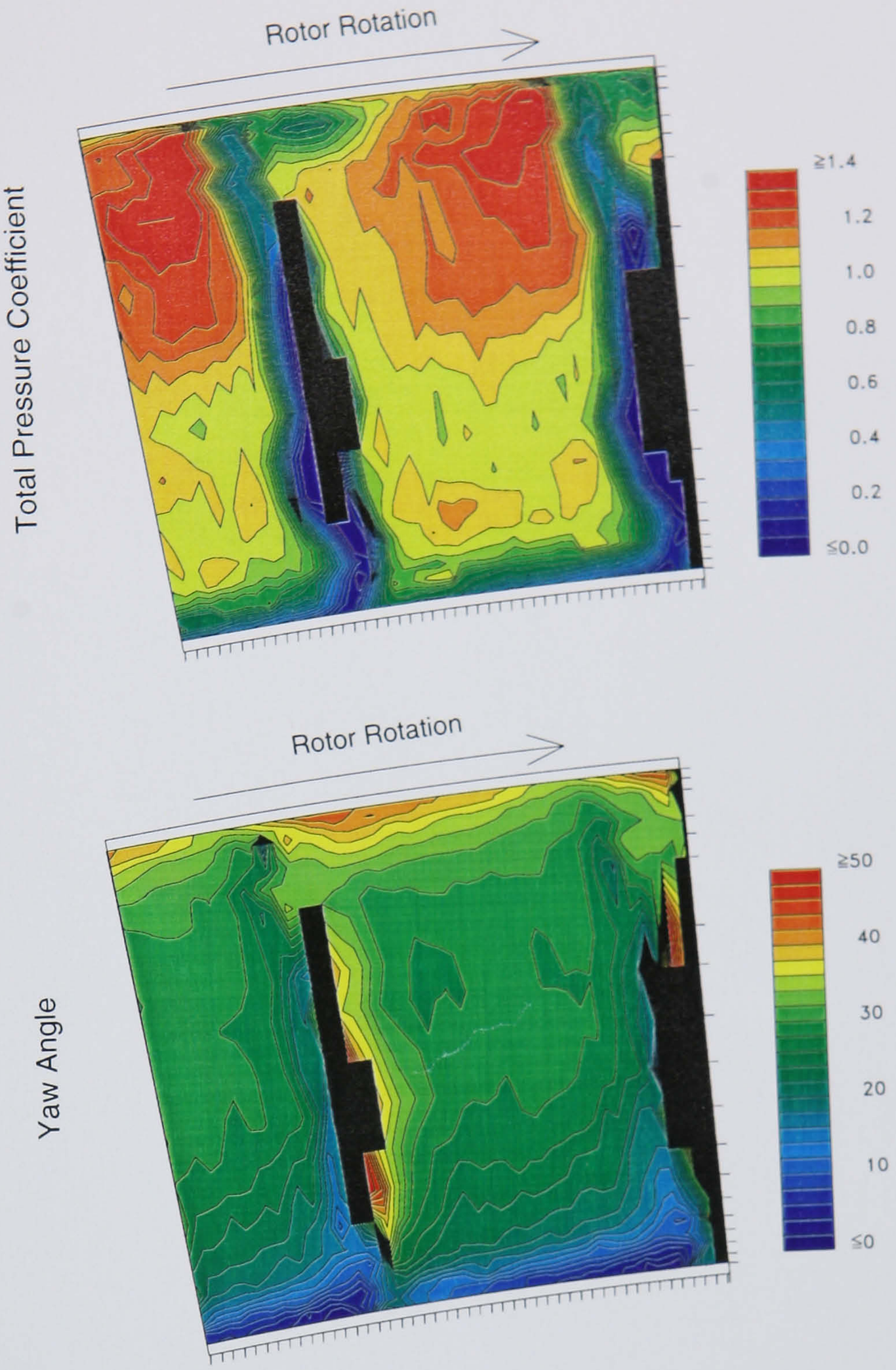


Figure 9.14 Rotor 3 exit total pressure and yaw angle contours and pitchwise average profiles at design flow measured in the rotating frame

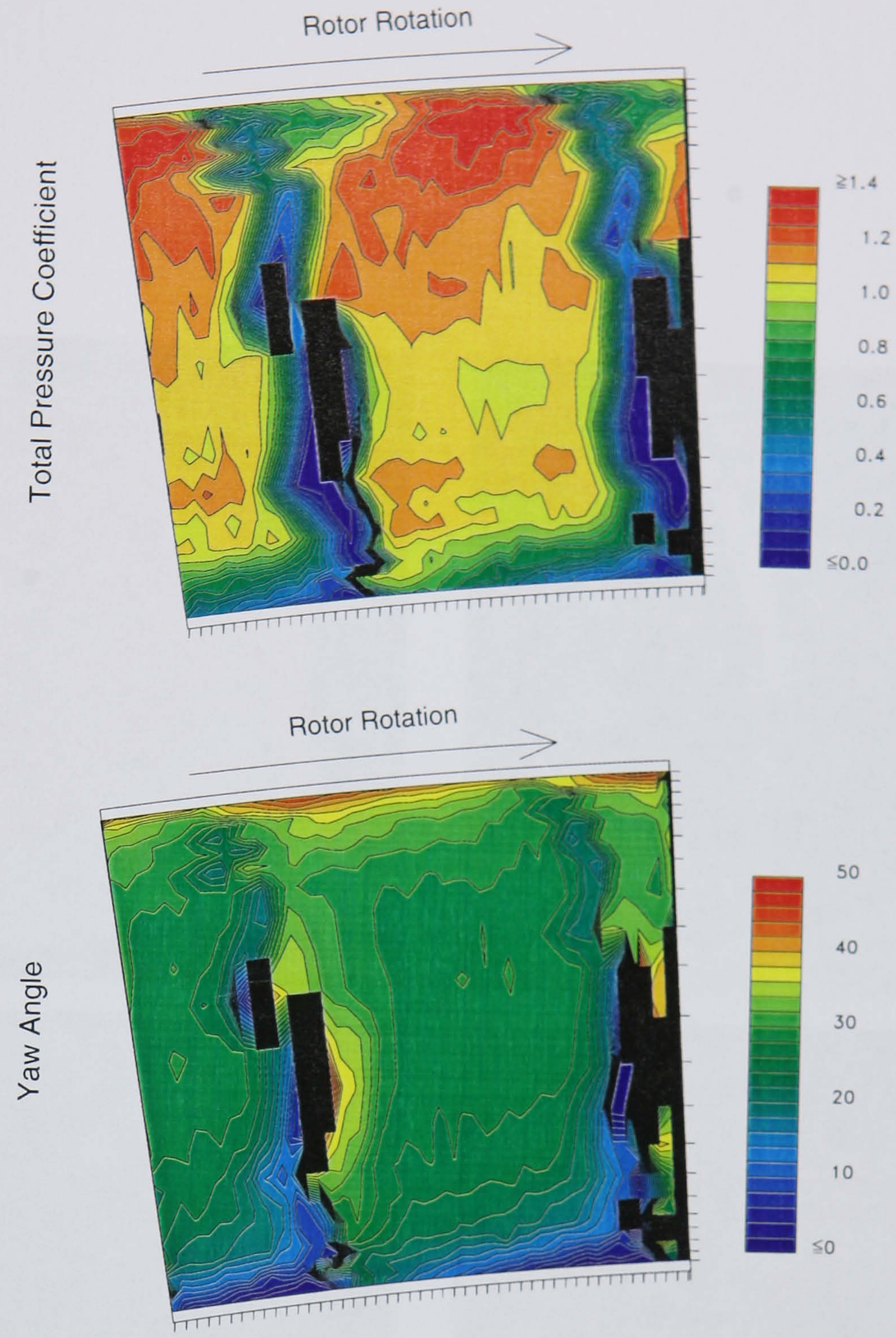


Figure 9.15 Rotor 3 exit total pressure and yaw angle contours and pitchwise average profiles at near stall measured in the rotating frame

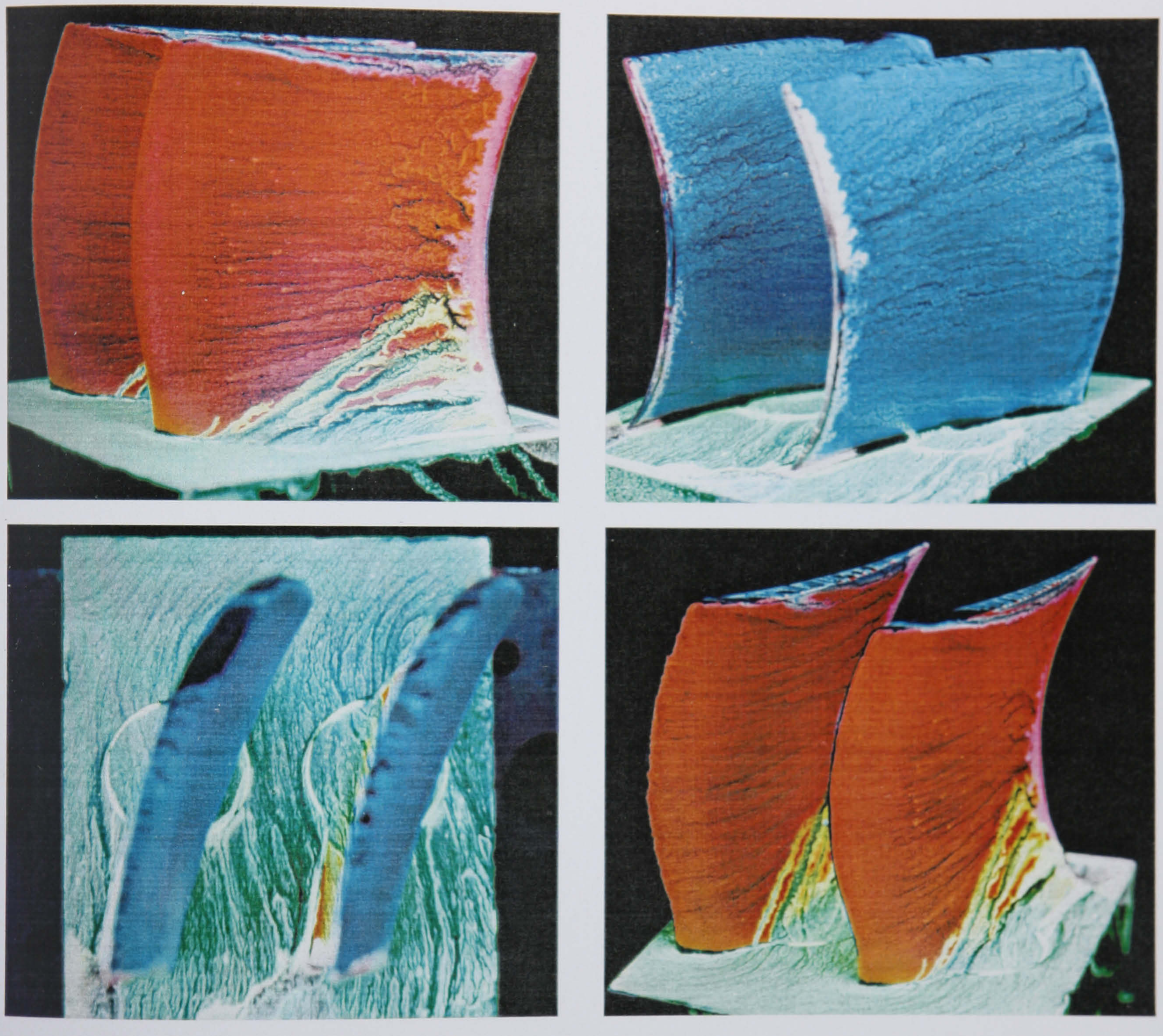


Figure 9.16 Flow visualisation at design flow

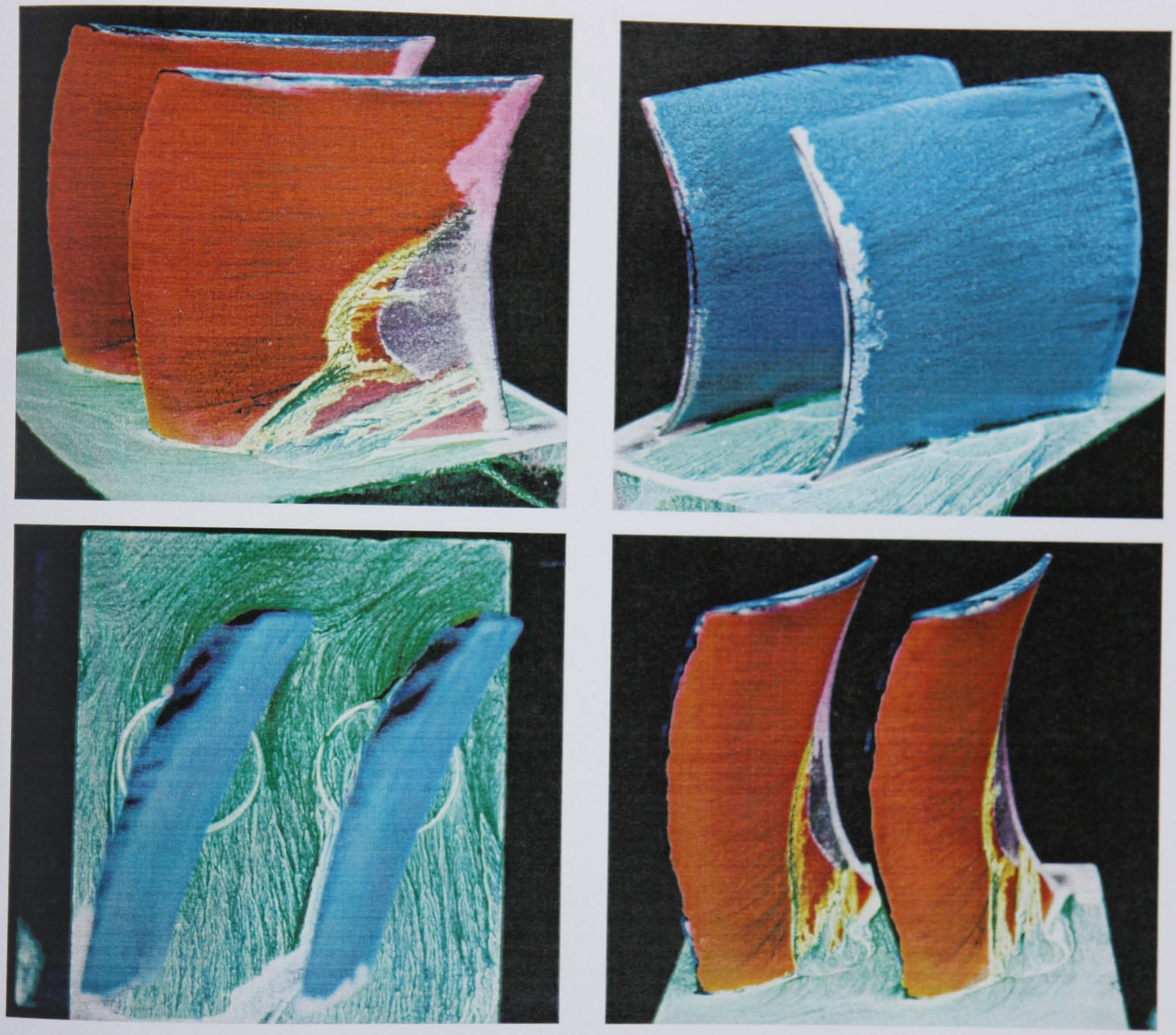


Figure 9.17 Flow visualisation at near stall

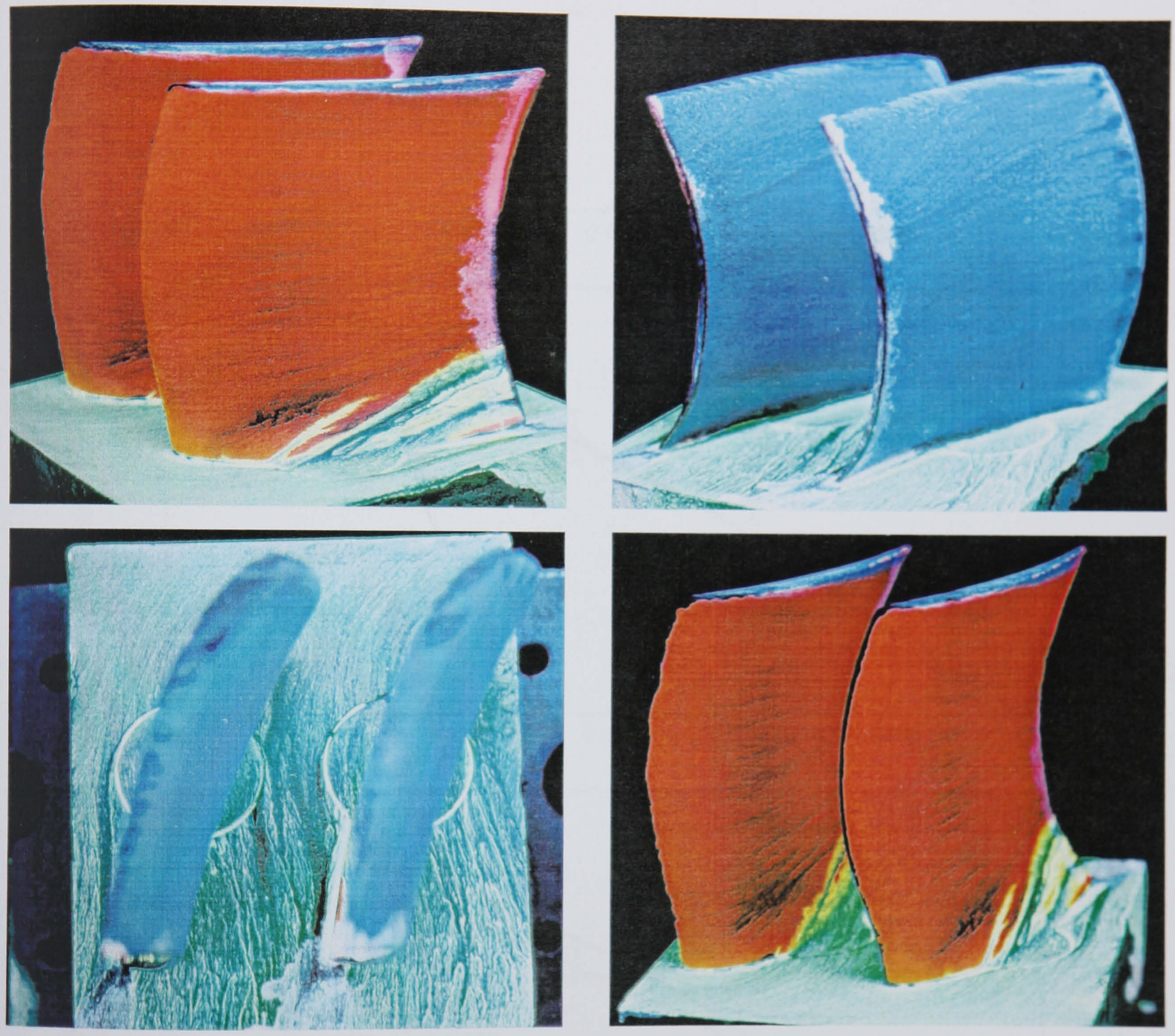


Figure 9.18 Flow visualisation at high flow

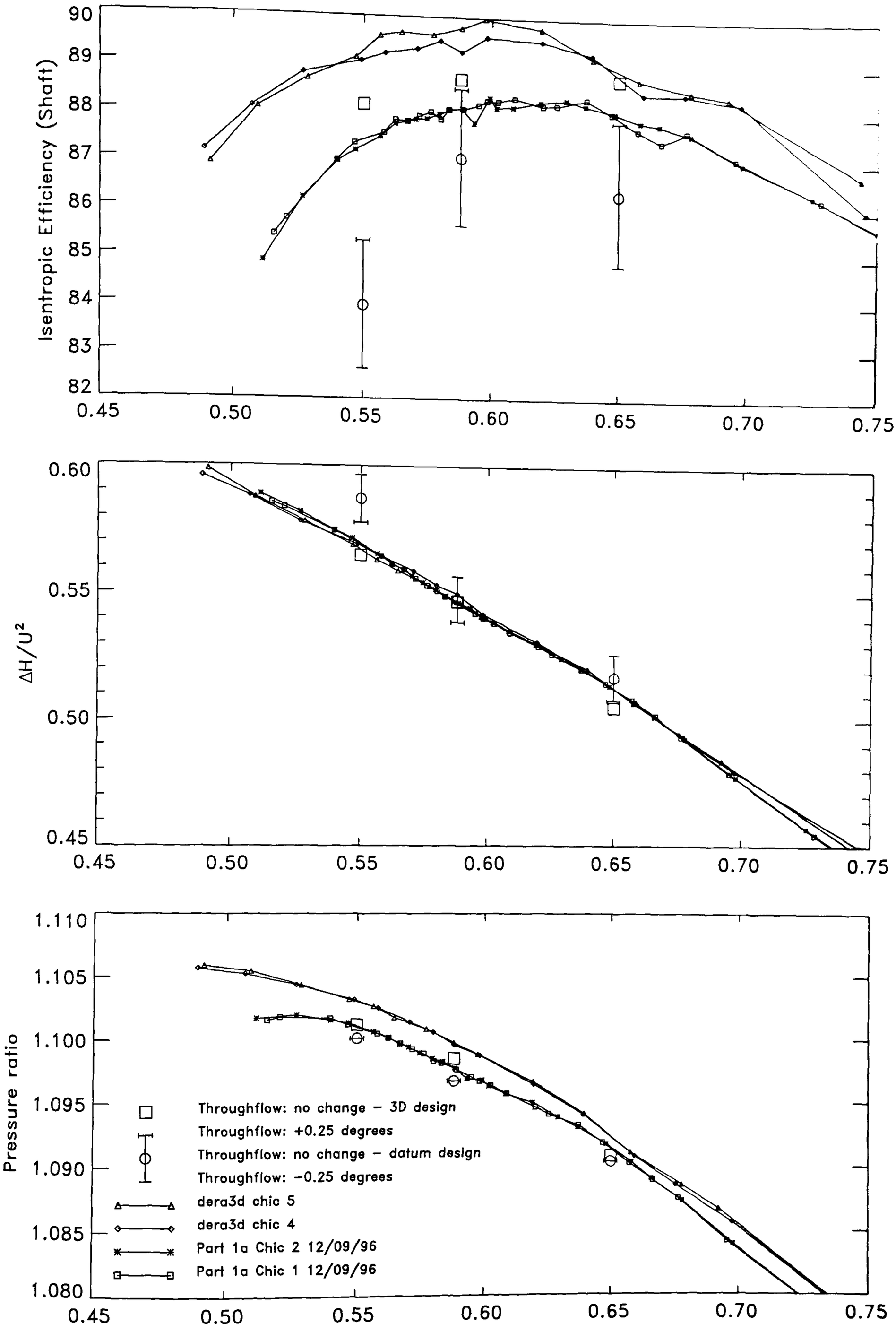


Figure 9.19 Overall performance of throughflow calculations

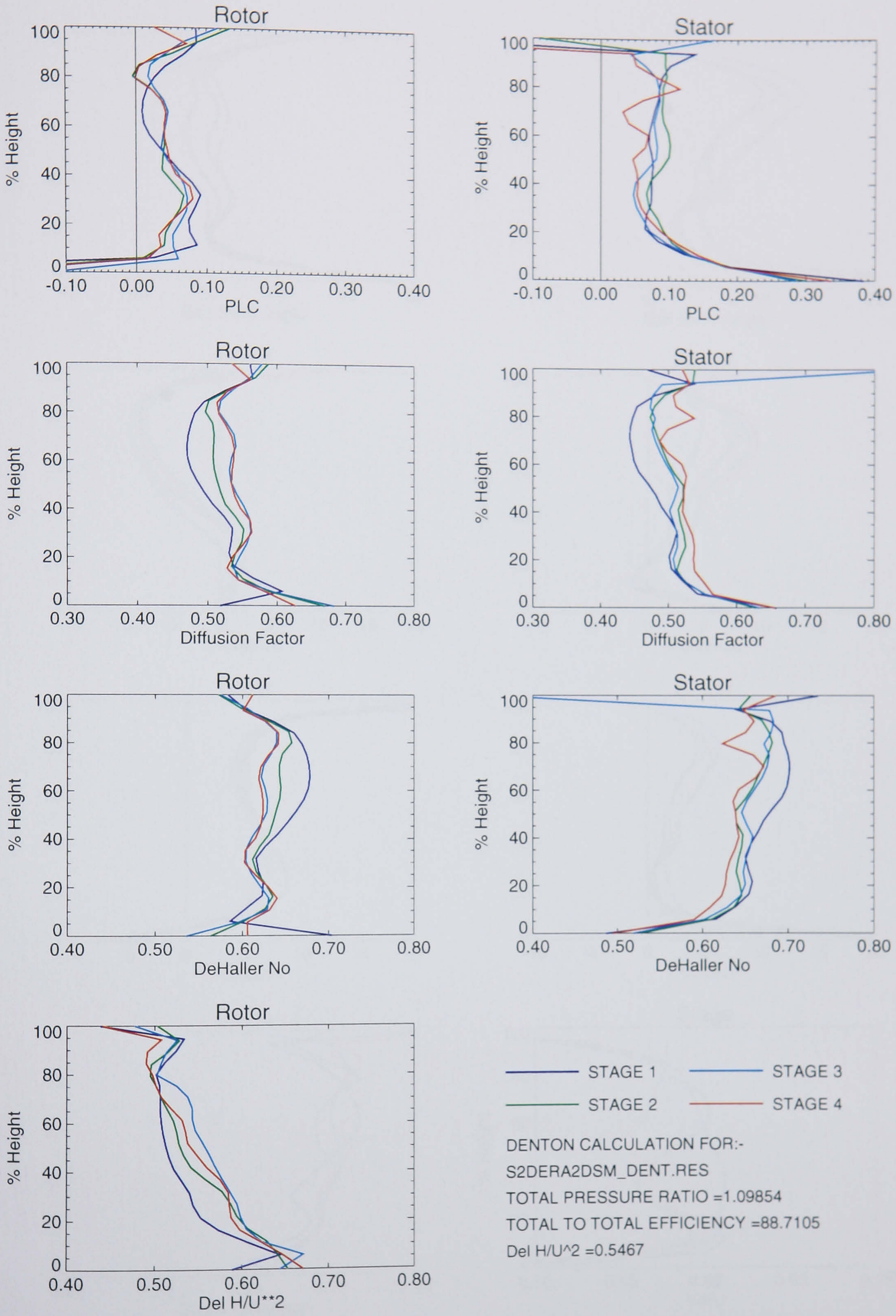


Figure 9.20a Results of throughflow calculation at design flow

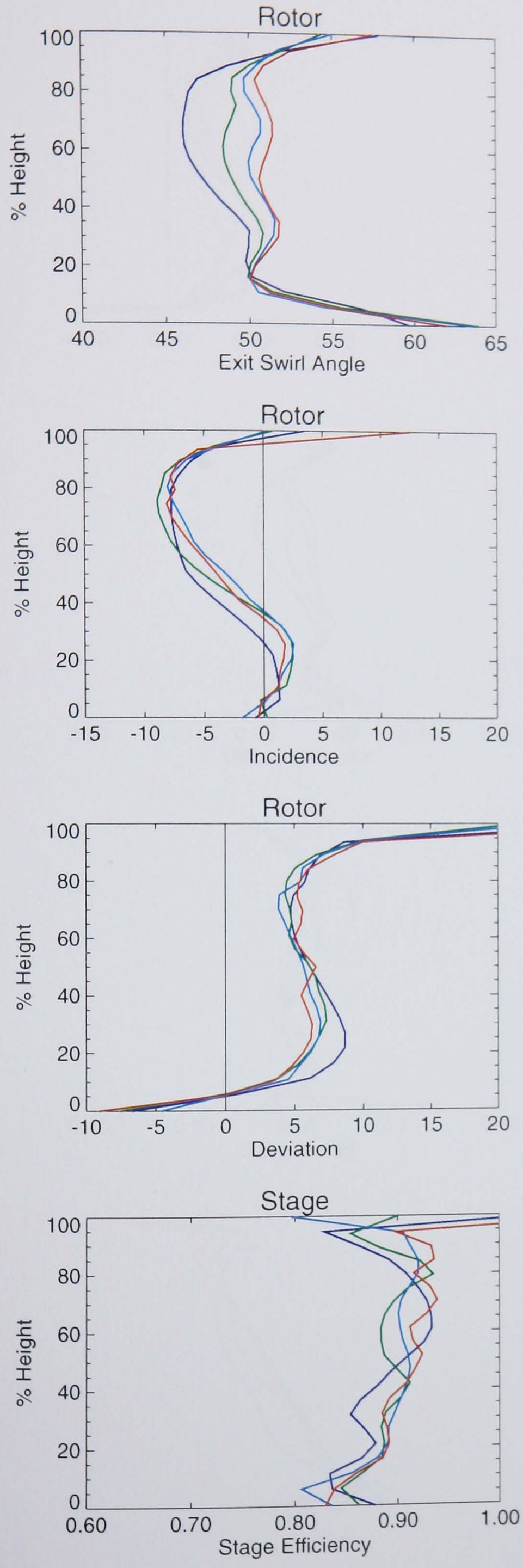


Figure 9.20b Results of throughflow calculation at design flow continued

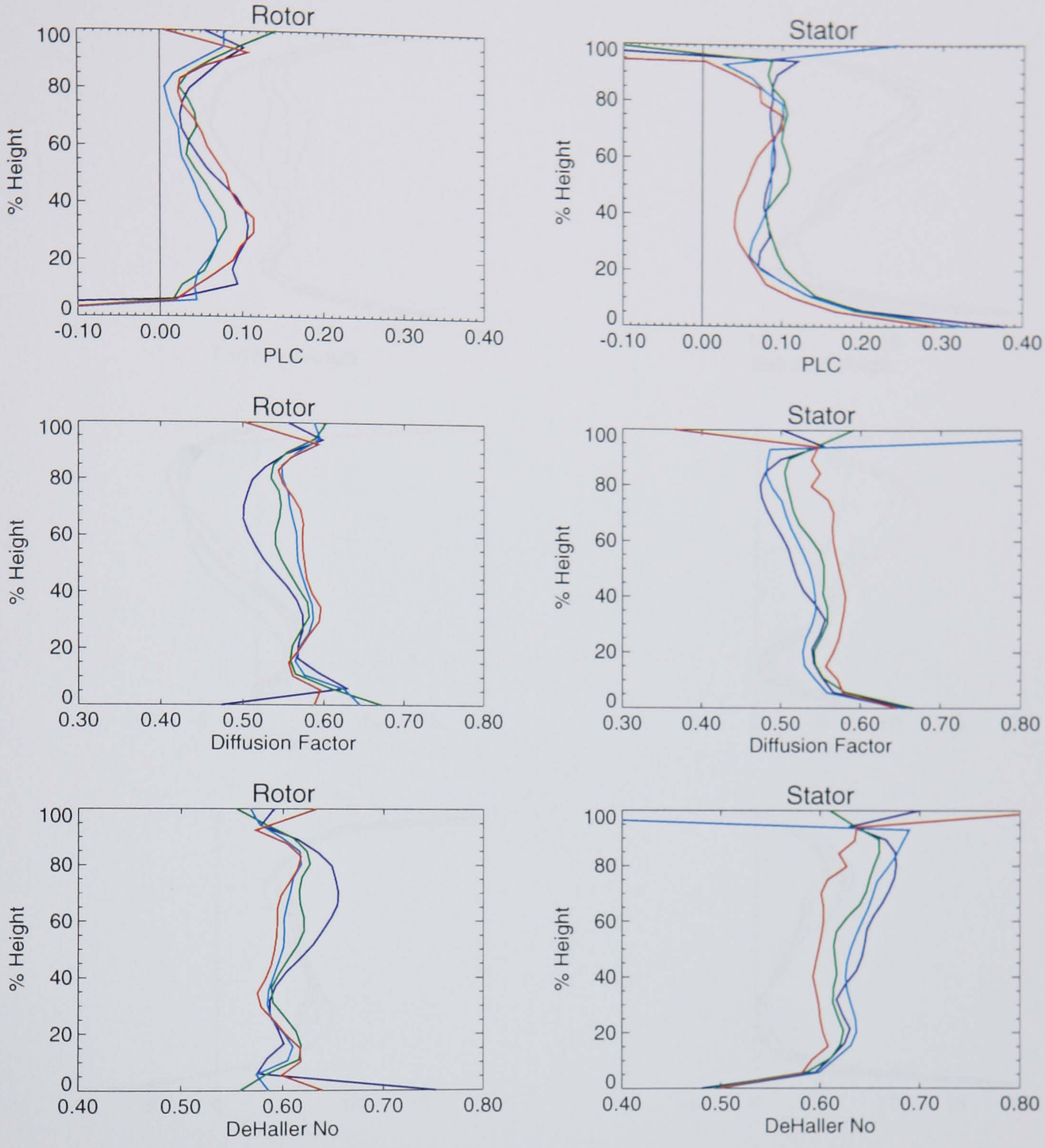


Figure 9.21a Results of throughflow calculation at near stall

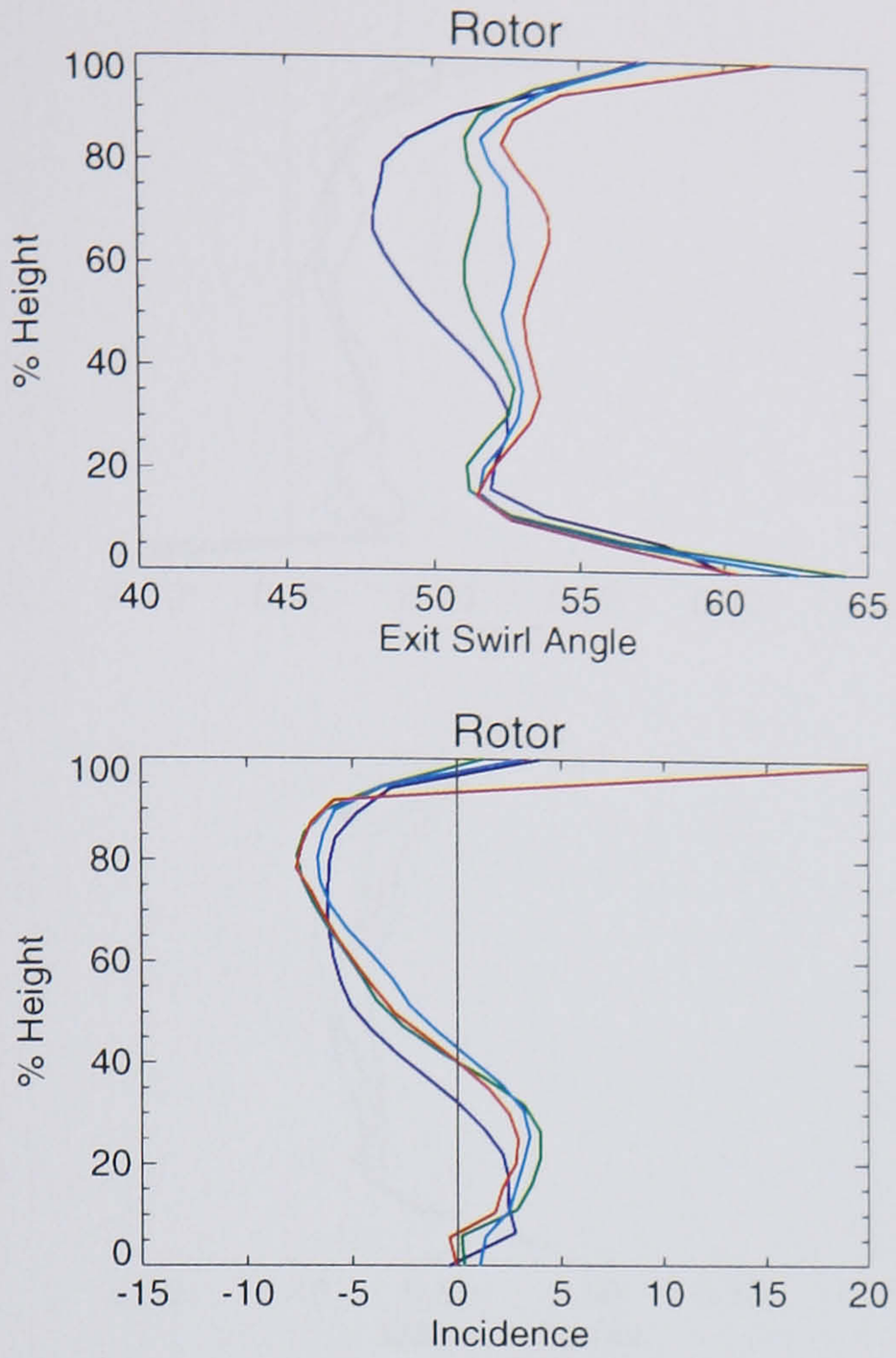


Figure 9.21b Results of throughflow calculation at near stall continued

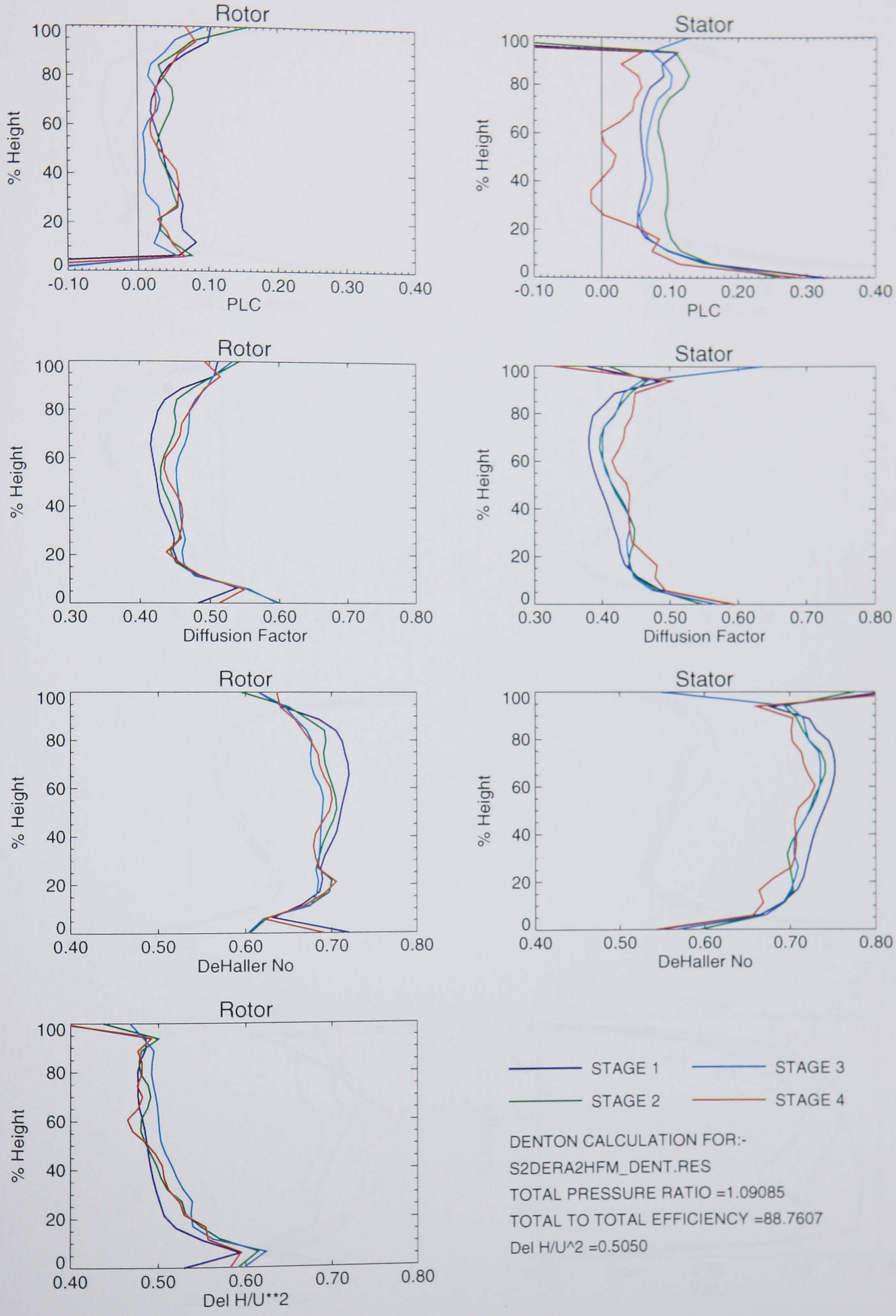
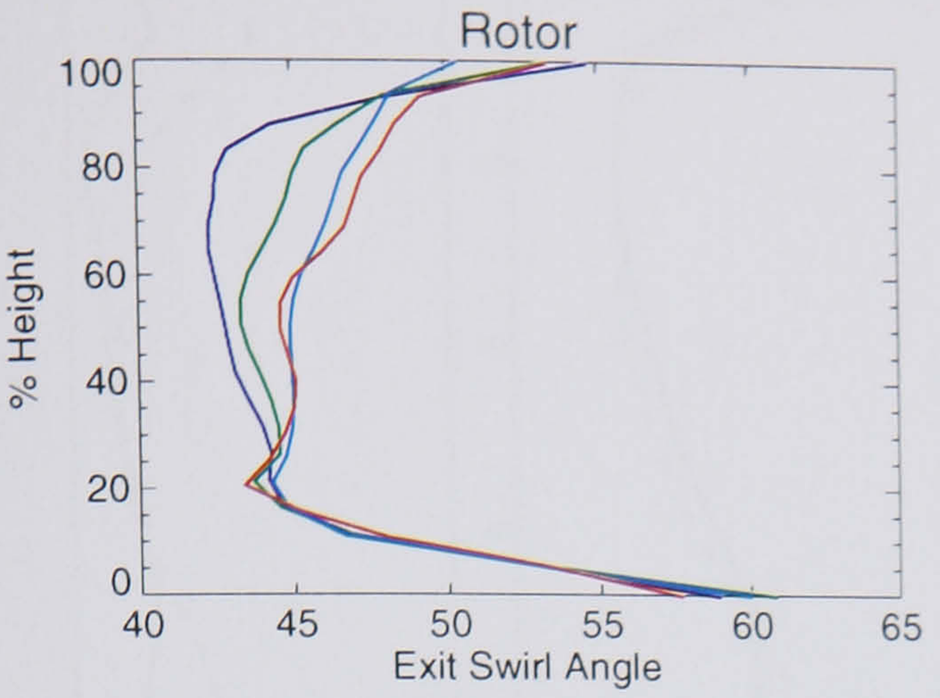
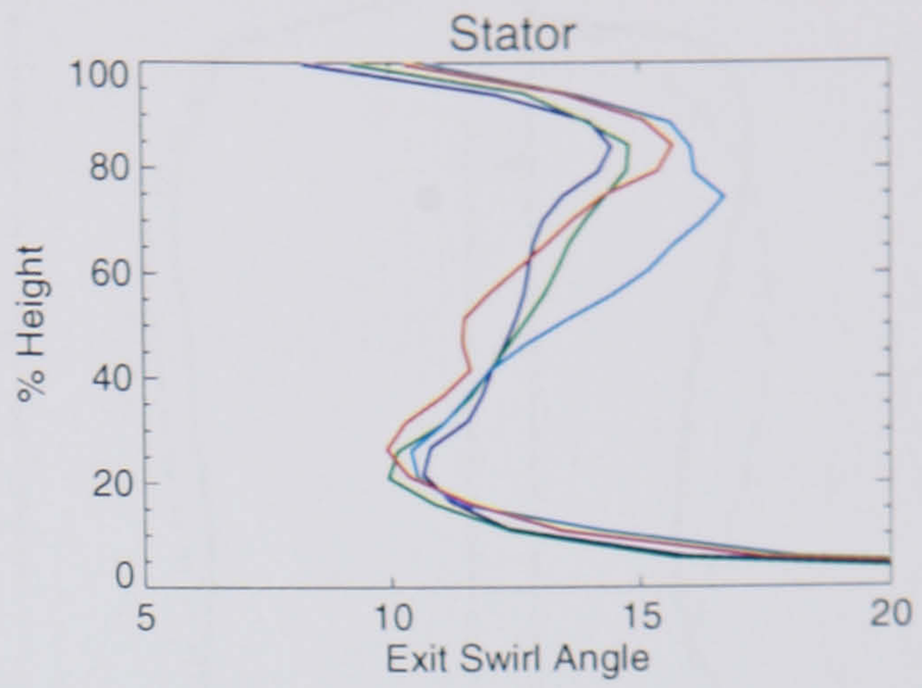
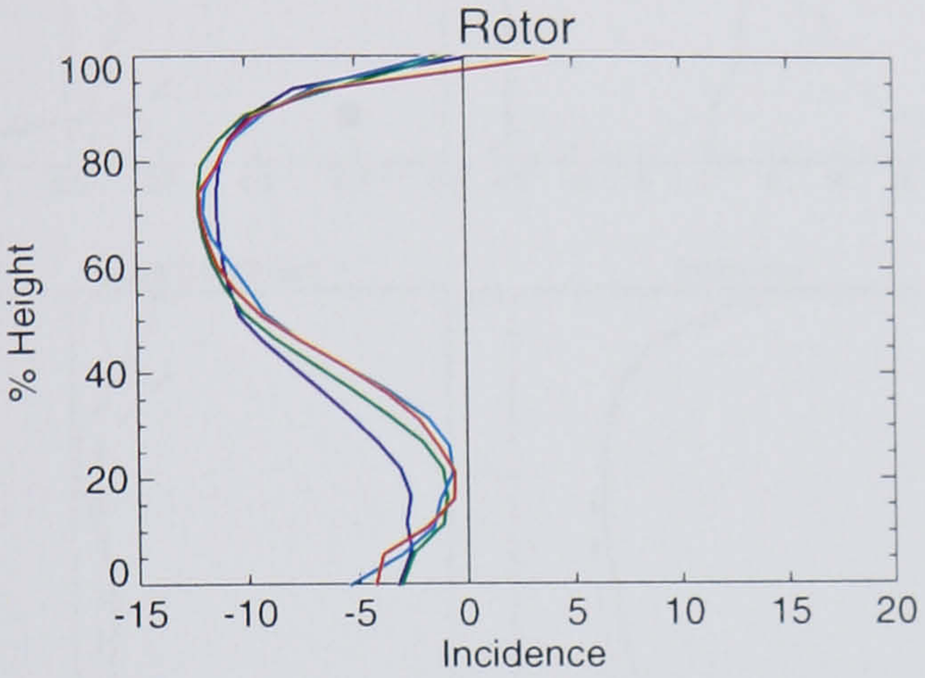
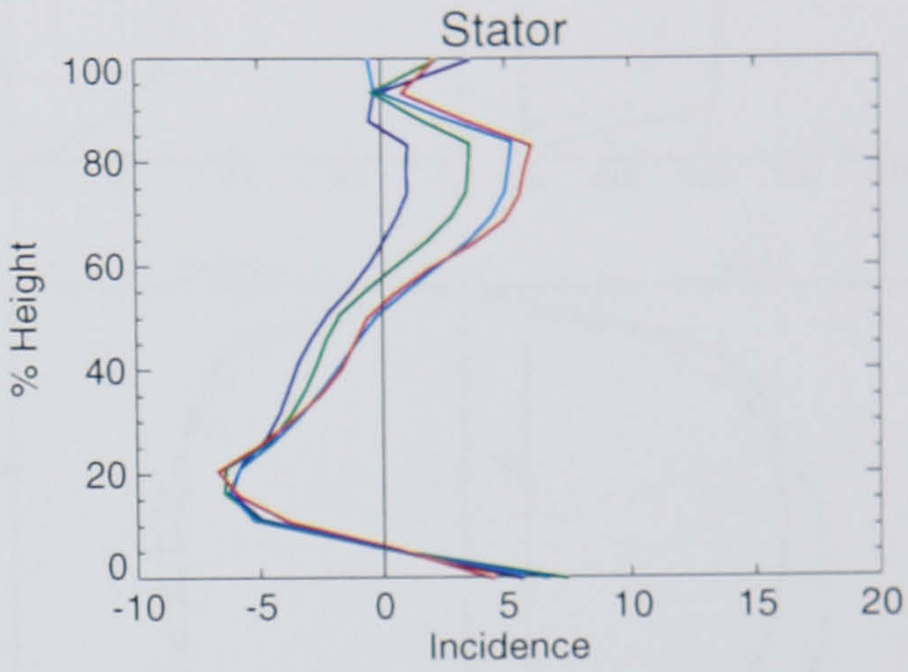


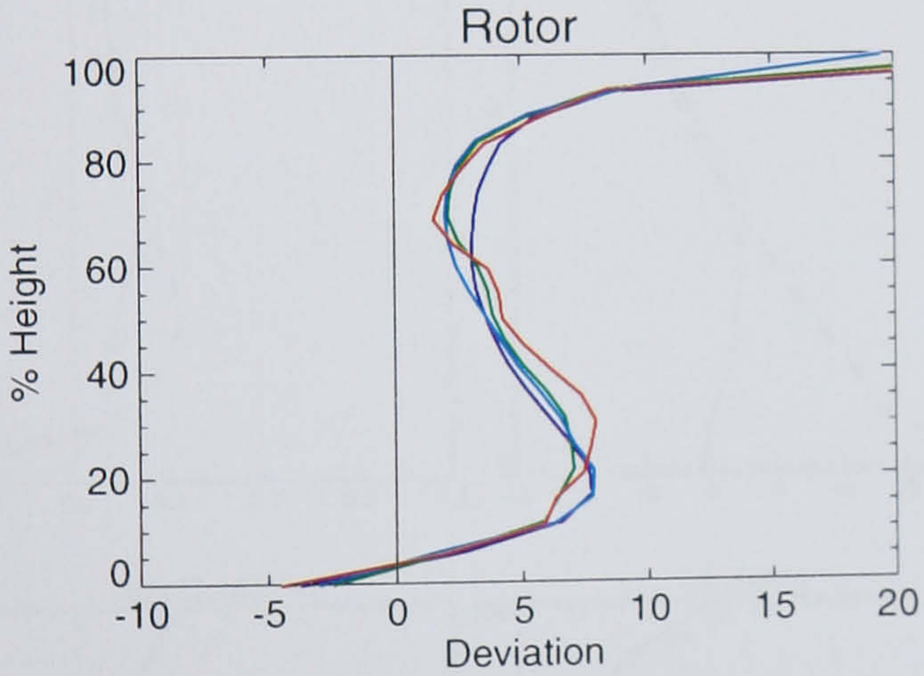
Figure 9.22a Results of throughflow calculation at high flow

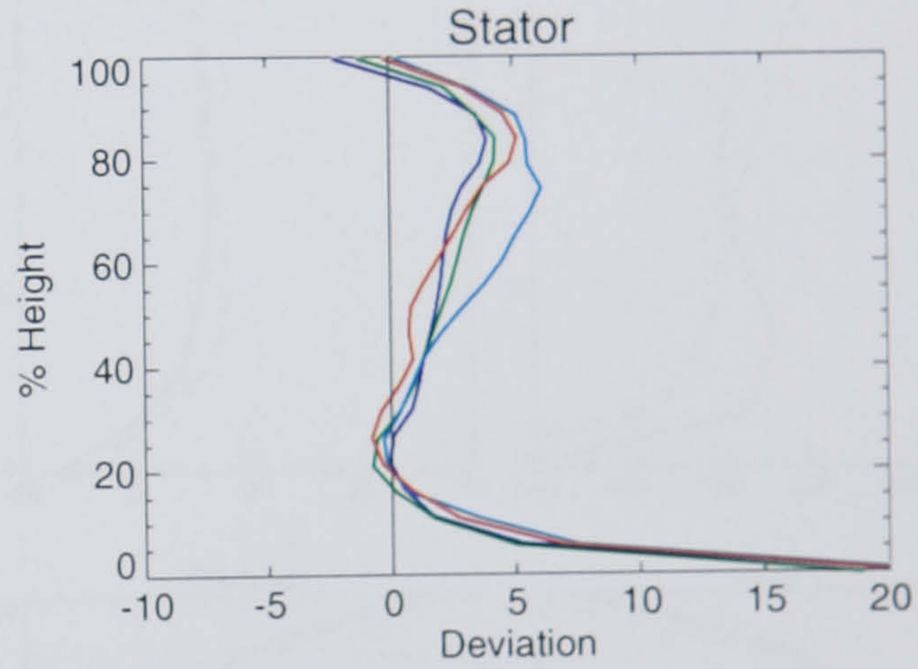


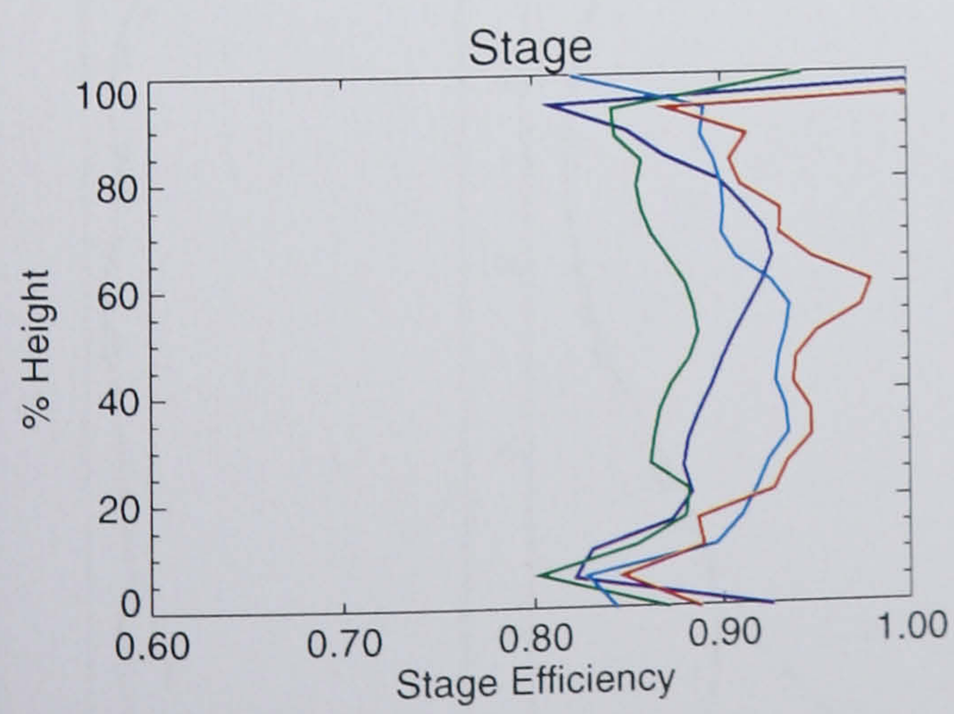












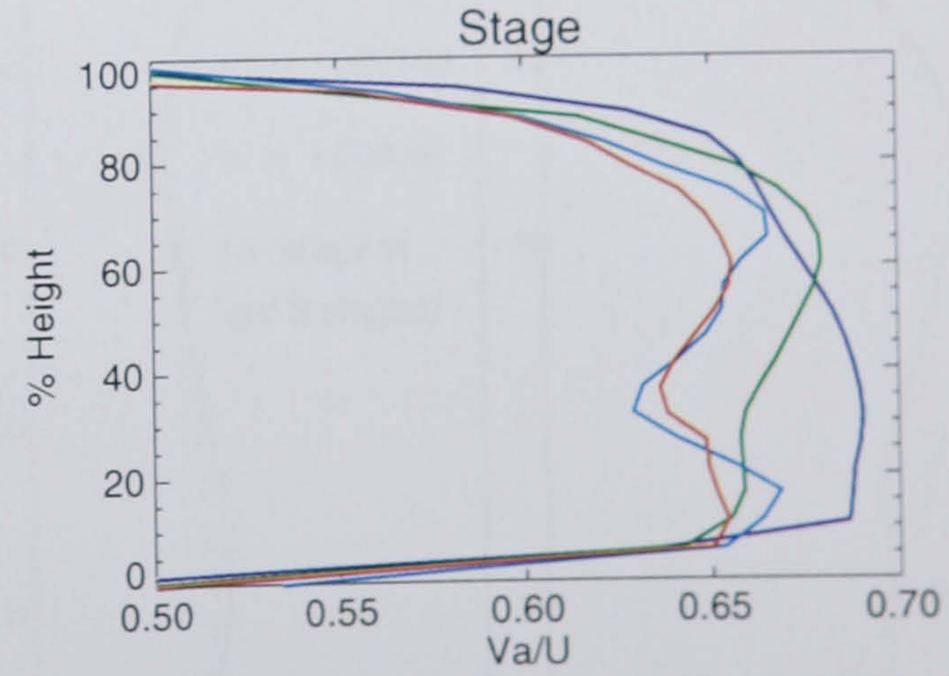


Figure 9.22b Results of throughflow calculation at high flow continued

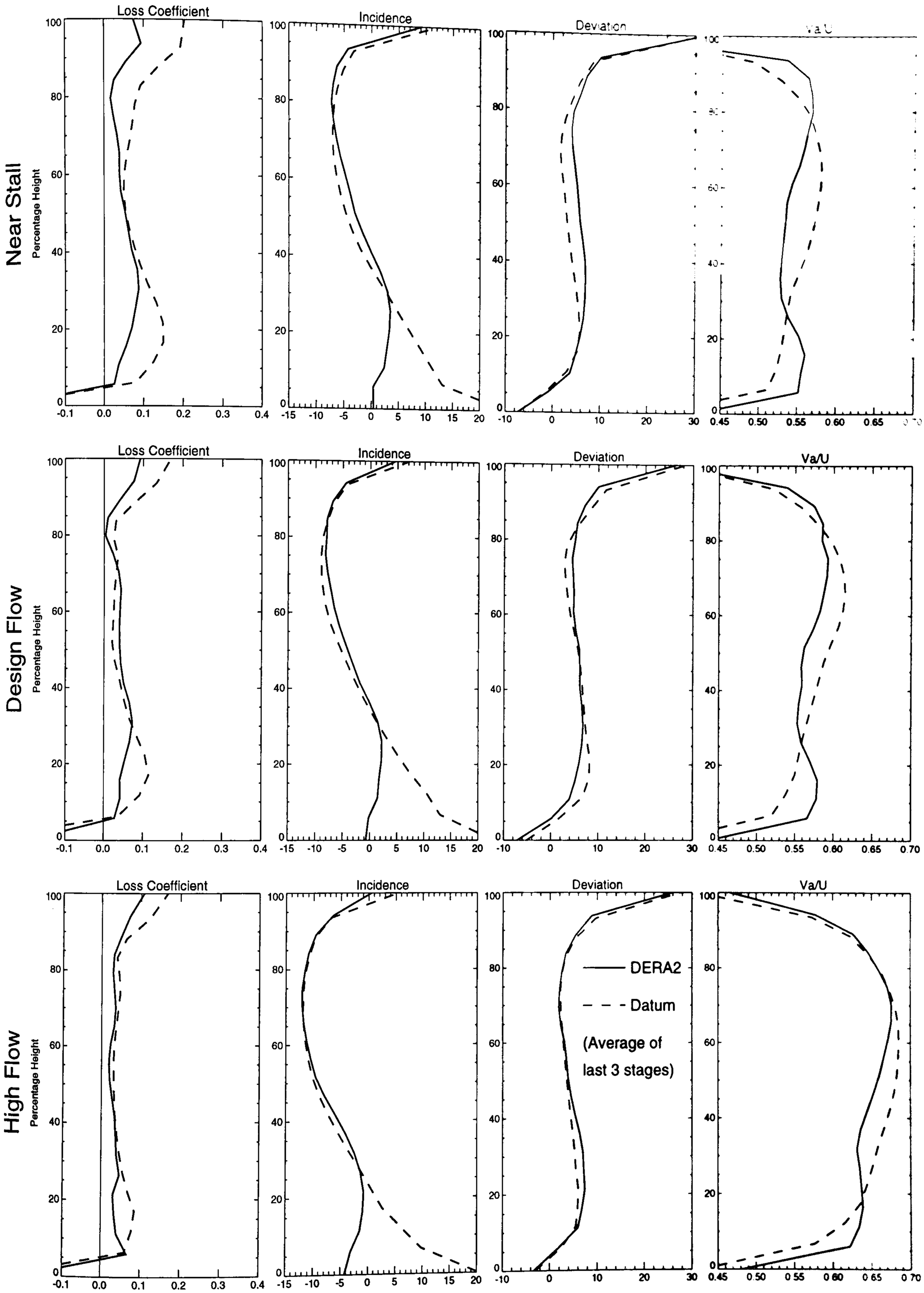


Figure 10.1 Radial profiles from experimental throughflow for rotor

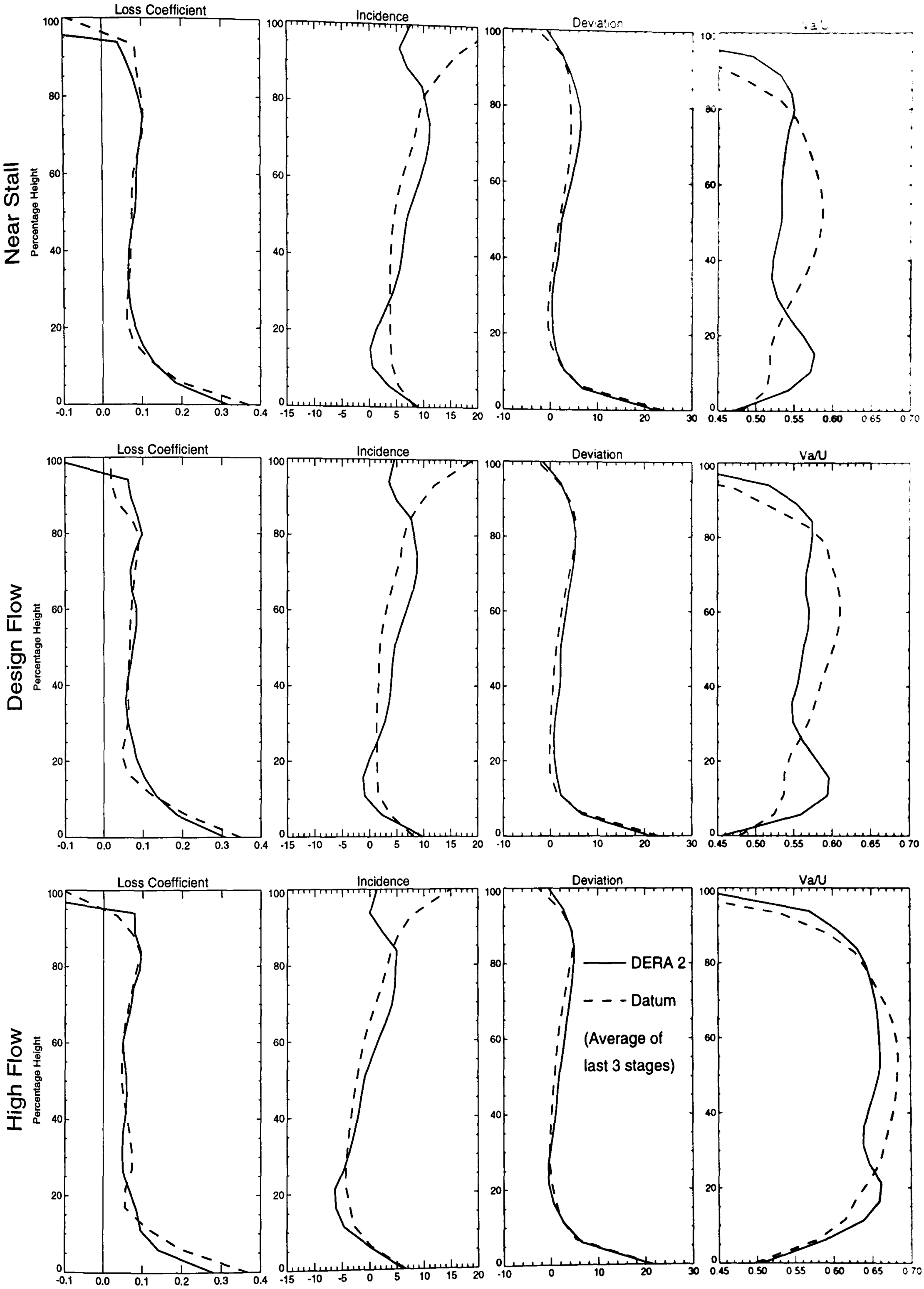


Figure 10.2 Radial profiles from experimental throughflow for stator

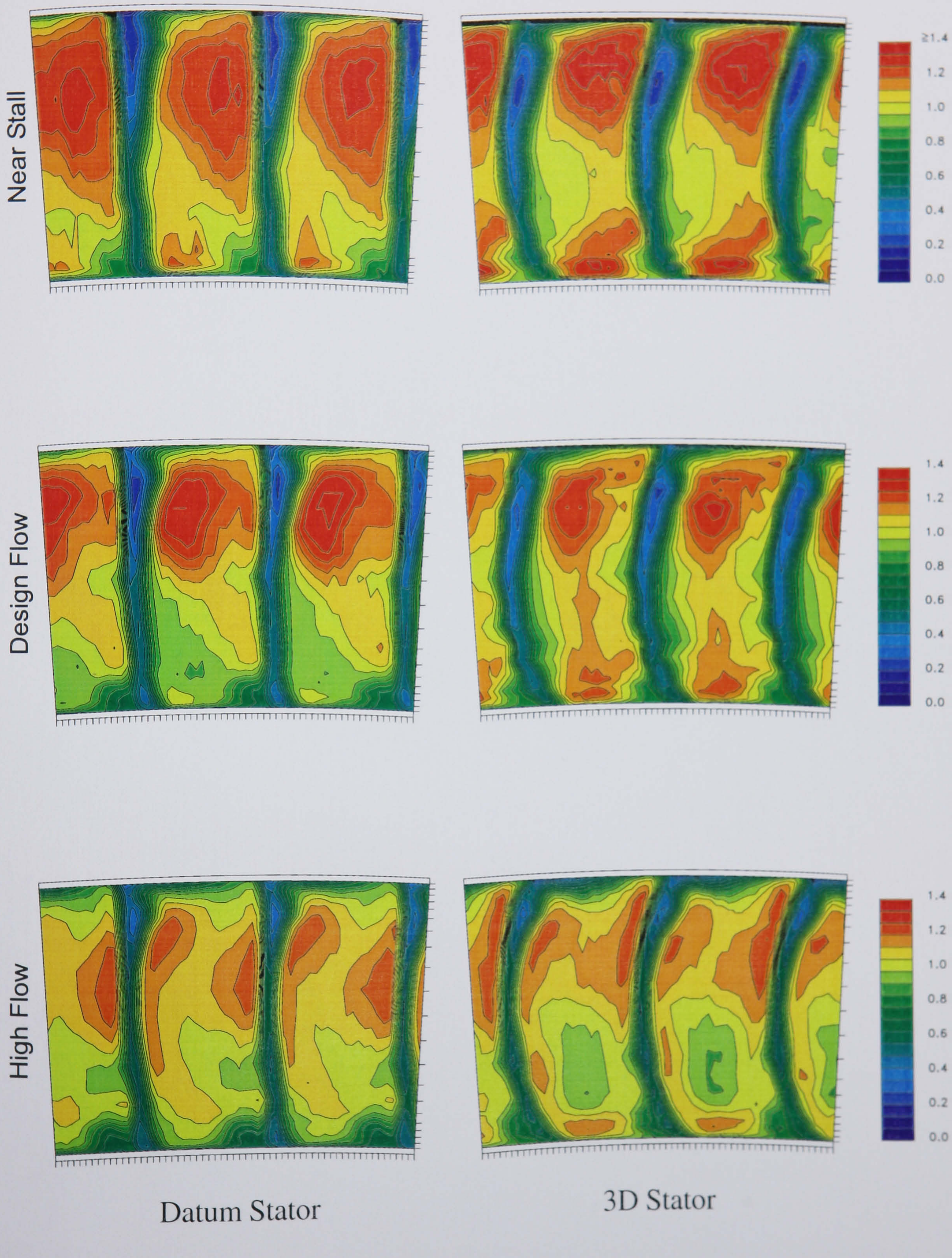


Figure 10.3 Comparison of stator 3 exit pressure coefficient contours

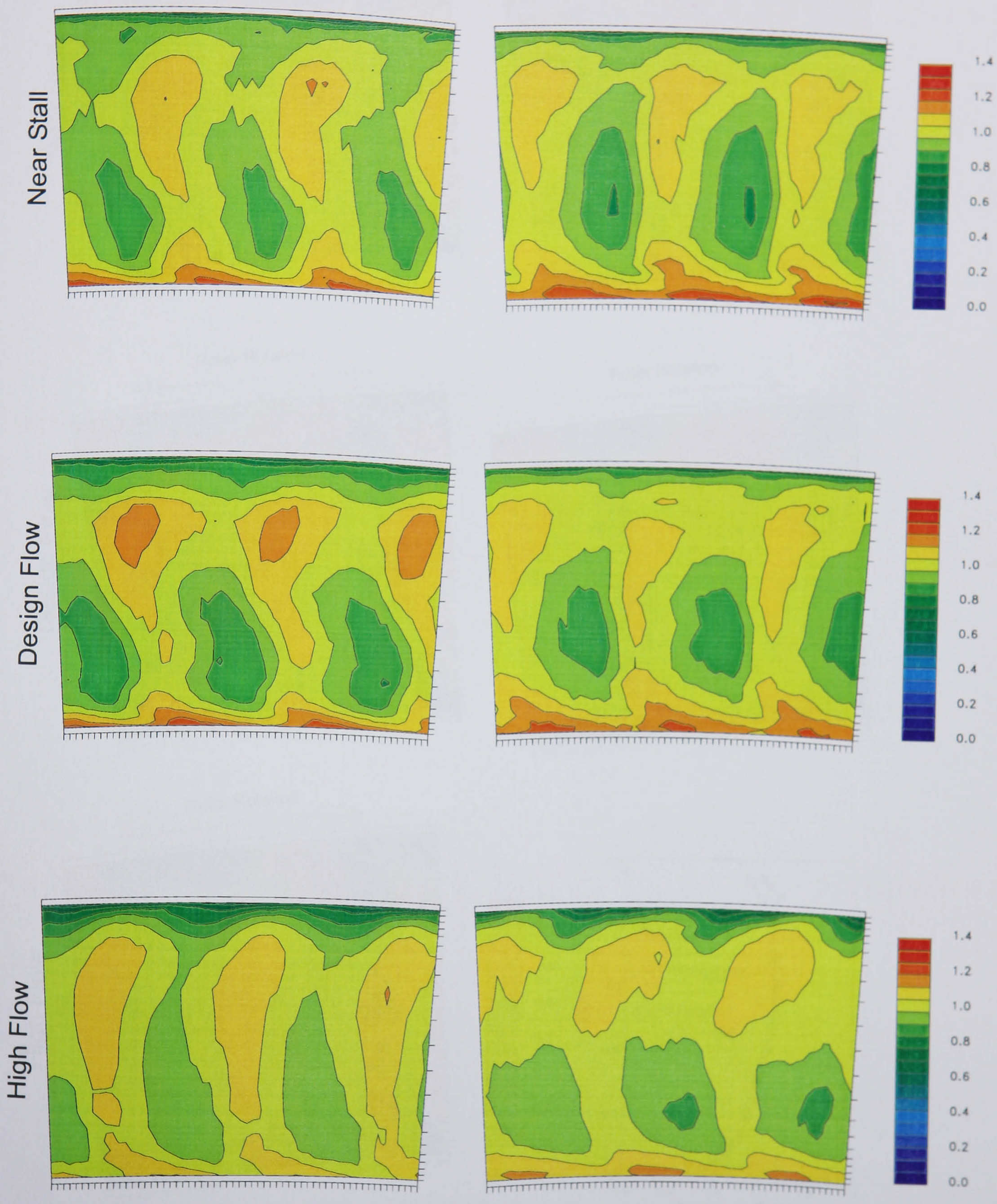
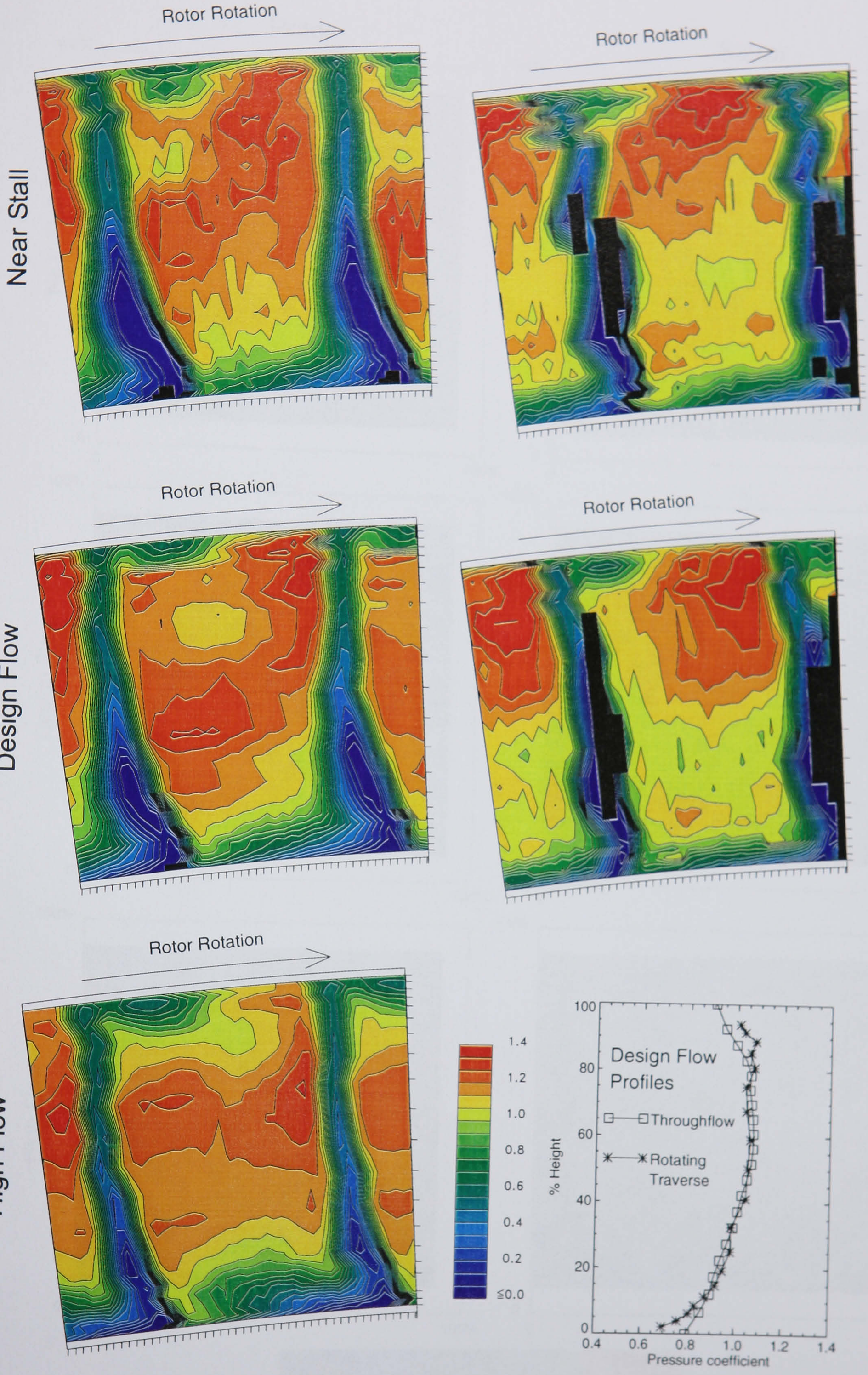


Figure 10.4 Comparison of rotor 3 absolute exit pressure coefficient contours



Datum Rotor

3D Rotor

Figure 10.5 Comparison of rotor 3 exit relative total pressure coefficient contours

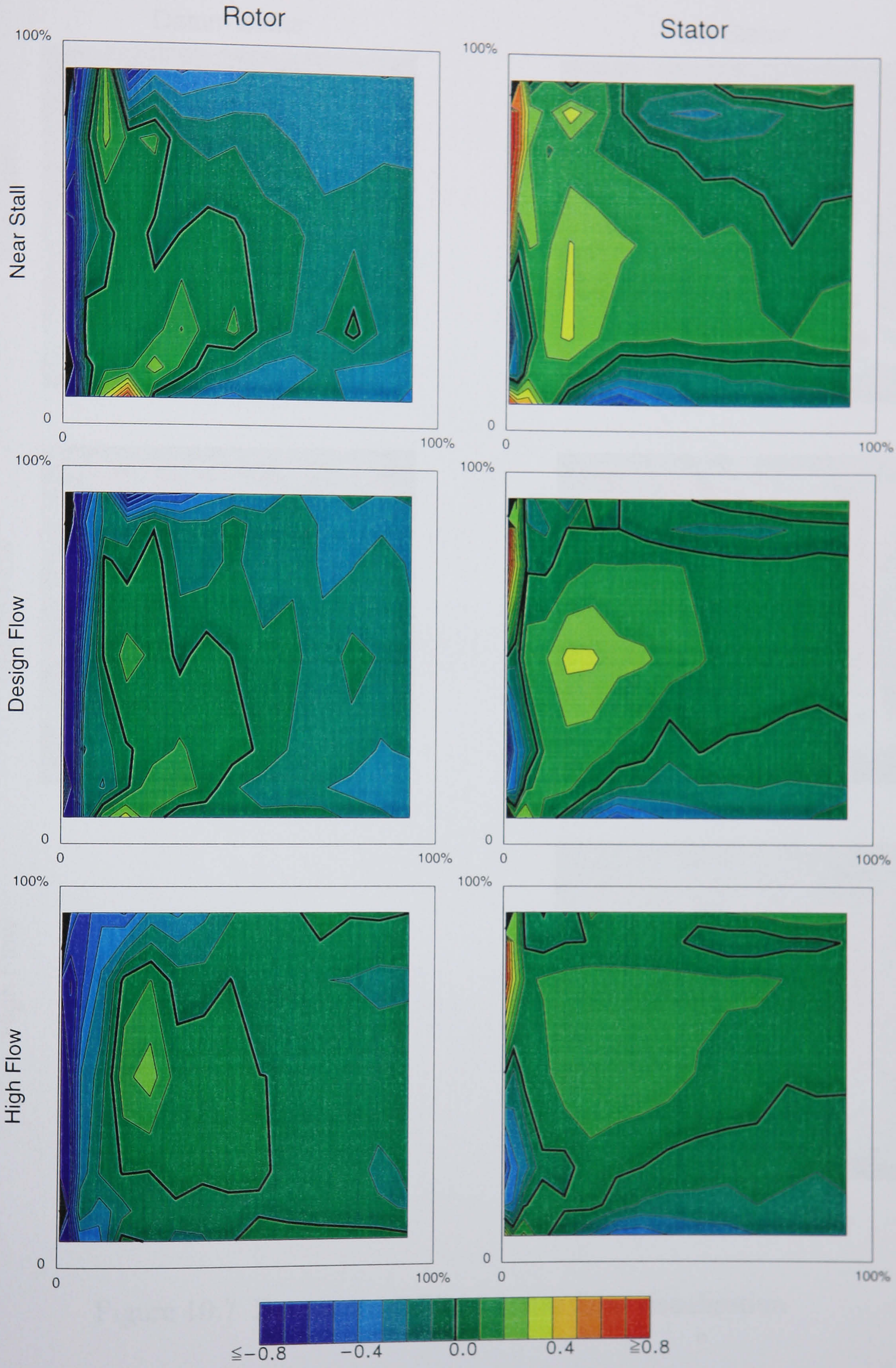


Figure 10.6 Blade surface pressure coefficient difference contours between DERA2 and datum measurements

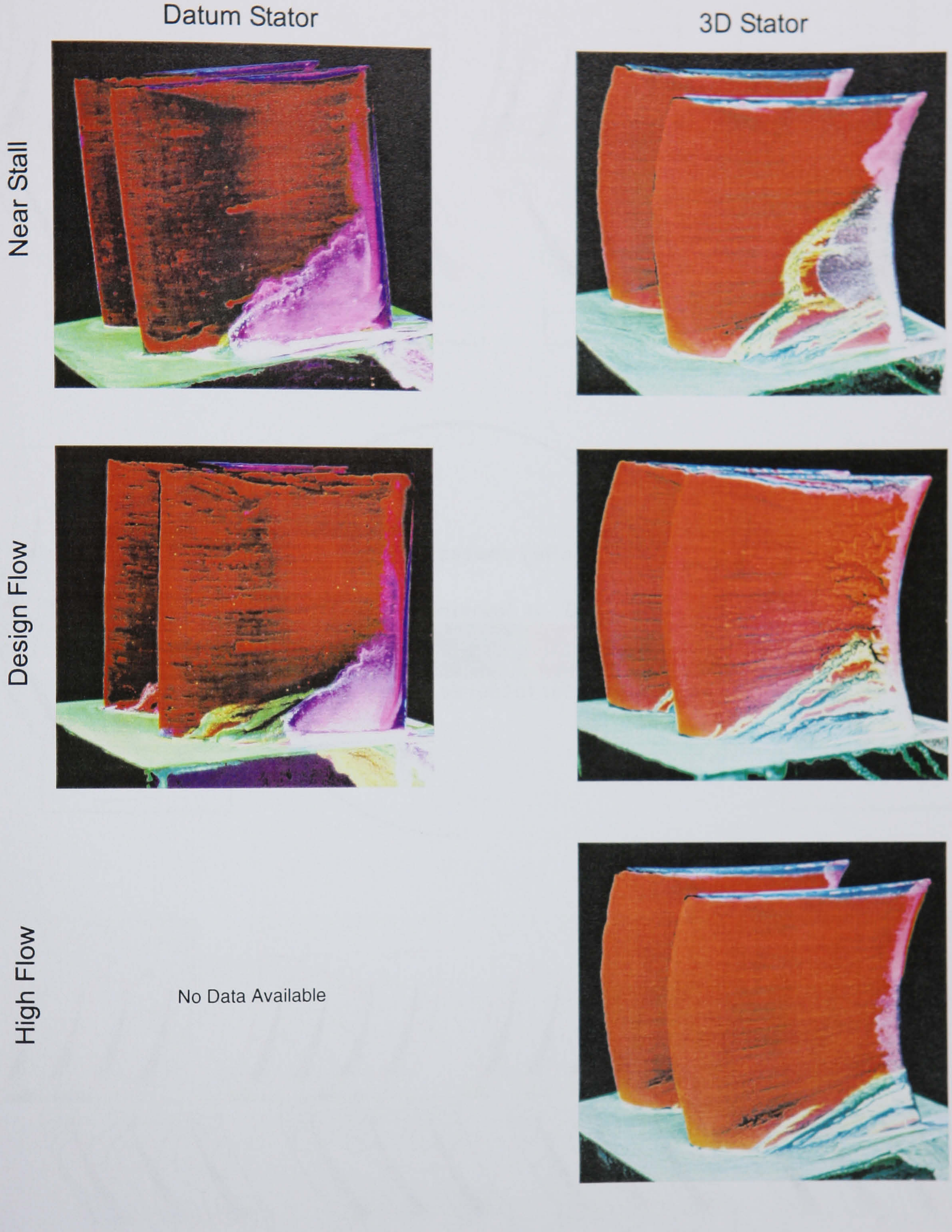


Figure 10.7 Datum and DERA2 stator flow visualisation

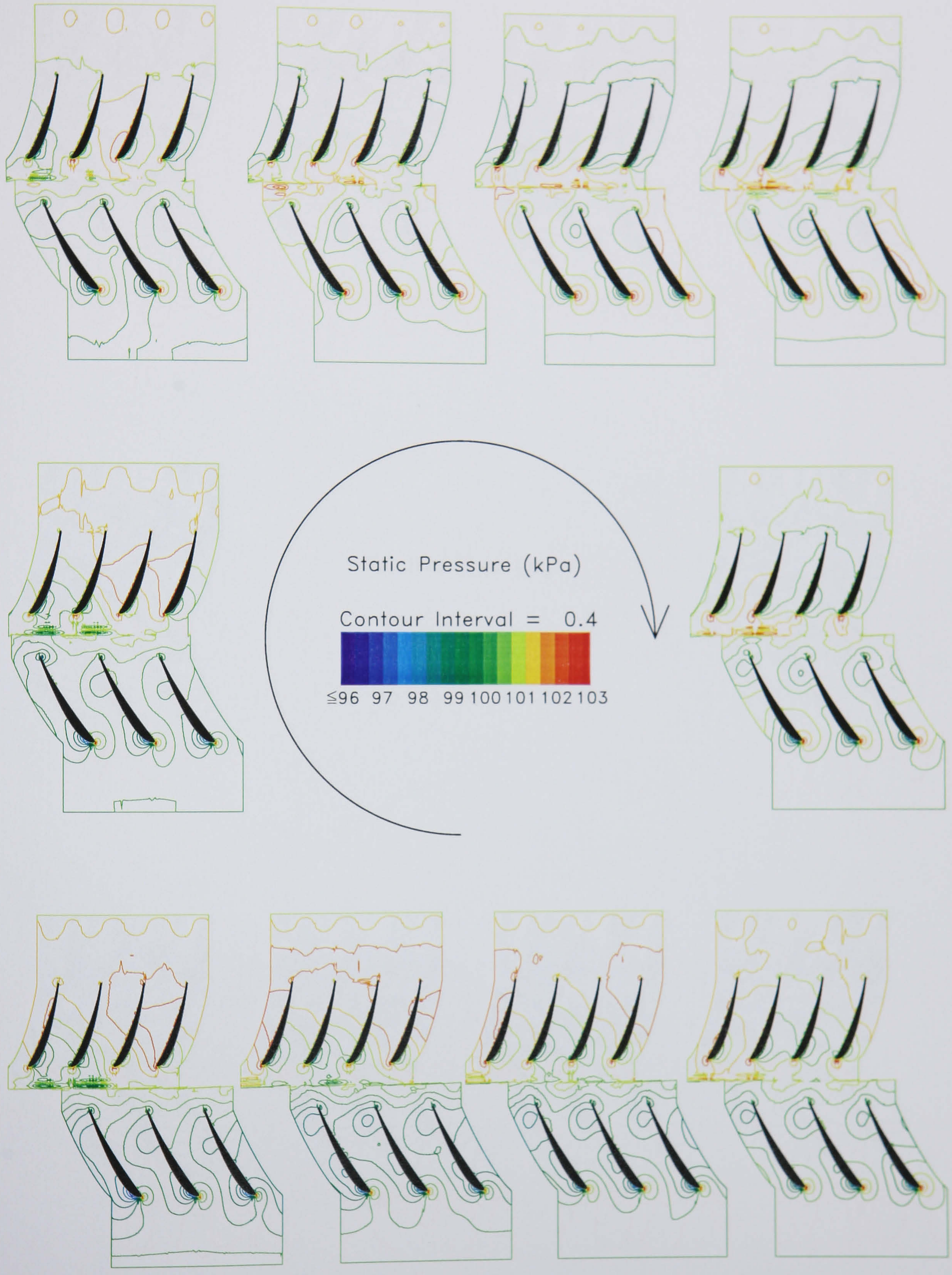


Figure 10.8 Un-NEWT static pressure contours

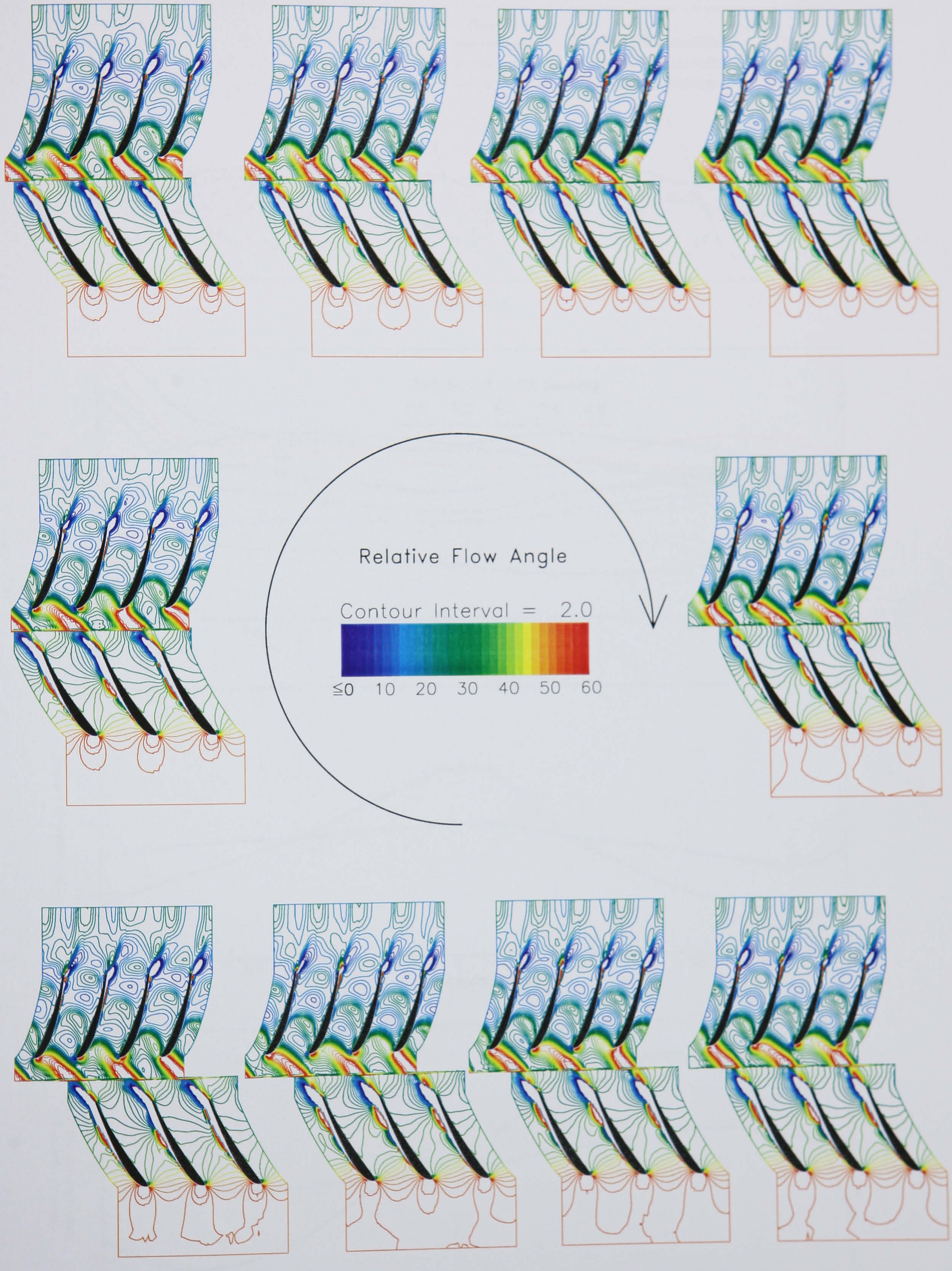


Figure 10.9 Un-NEWT relative flow angle contours

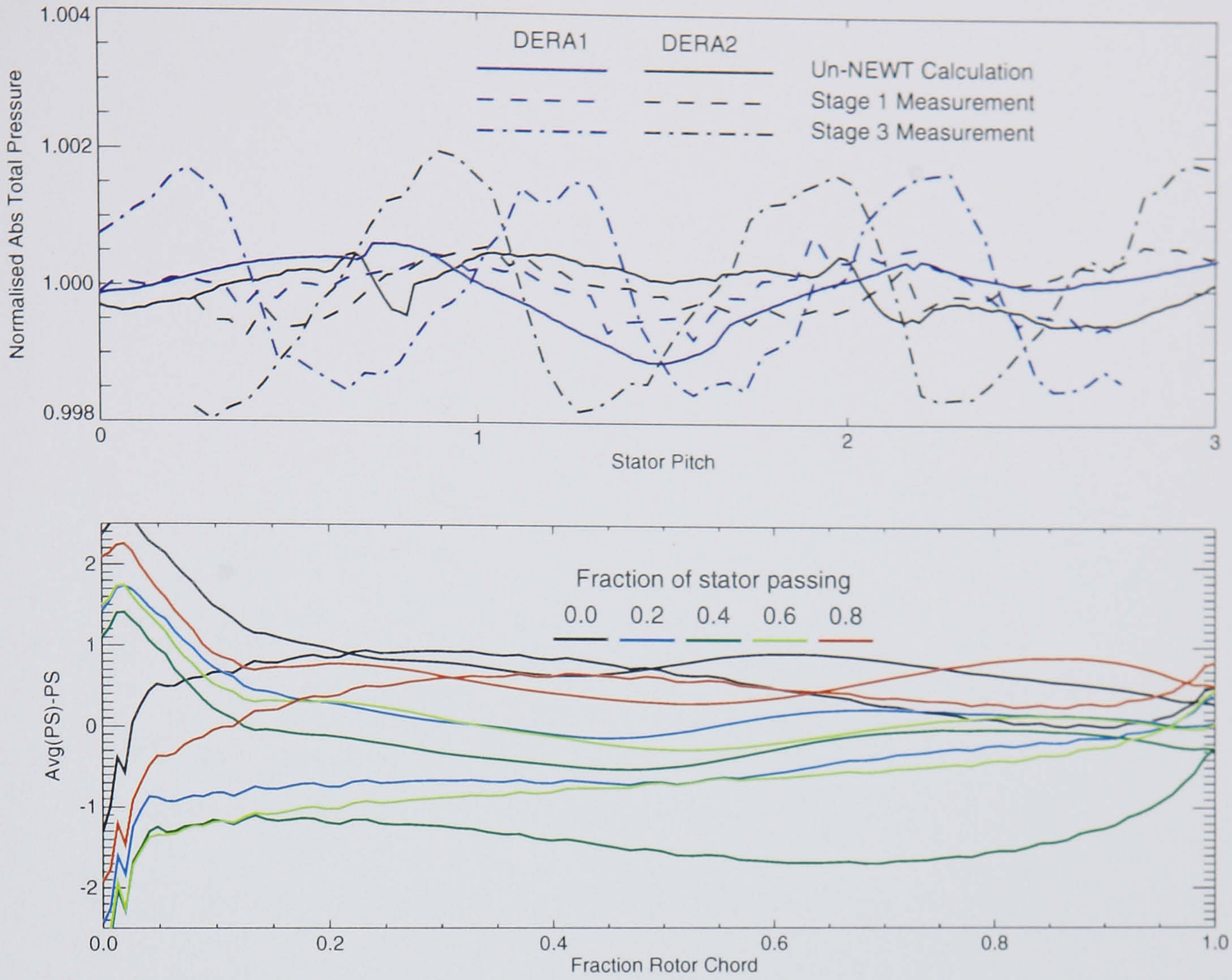


Figure 10.10 Un-NEWT time averaged results; DERA2 compared with datum spacing